frontiers | Research Topics

The use of geosciences for exploring and predicting natural resources

Edited by
Ahmed M. Eldosouky, Amin Beiranvand Pour, Luan Thanh Pham and Biswajeet Pradhan

Published in
Frontiers in Earth Science
Frontiers in Environmental Science

ISSN 1664-8714
ISBN 978-2-83251-674-4
DOI 10.3389/978-2-83251-674-4

About Frontiers

Frontiers is more than just an open access publisher of scholarly articles: it is a pioneering approach to the world of academia, radically improving the way scholarly research is managed. The grand vision of Frontiers is a world where all people have an equal opportunity to seek, share and generate knowledge. Frontiers provides immediate and permanent online open access to all its publications, but this alone is not enough to realize our grand goals.

Frontiers journal series

The Frontiers journal series is a multi-tier and interdisciplinary set of open-access, online journals, promising a paradigm shift from the current review, selection and dissemination processes in academic publishing. All Frontiers journals are driven by researchers for researchers; therefore, they constitute a service to the scholarly community. At the same time, the *Frontiers journal series* operates on a revolutionary invention, the tiered publishing system, initially addressing specific communities of scholars, and gradually climbing up to broader public understanding, thus serving the interests of the lay society, too.

Dedication to quality

Each Frontiers article is a landmark of the highest quality, thanks to genuinely collaborative interactions between authors and review editors, who include some of the world's best academicians. Research must be certified by peers before entering a stream of knowledge that may eventually reach the public - and shape society; therefore, Frontiers only applies the most rigorous and unbiased reviews. Frontiers revolutionizes research publishing by freely delivering the most outstanding research, evaluated with no bias from both the academic and social point of view. By applying the most advanced information technologies, Frontiers is catapulting scholarly publishing into a new generation.

What are Frontiers Research Topics?

Frontiers Research Topics are very popular trademarks of the *Frontiers journals series*: they are collections of at least ten articles, all centered on a particular subject. With their unique mix of varied contributions from Original Research to Review Articles, Frontiers Research Topics unify the most influential researchers, the latest key findings and historical advances in a hot research area.

Find out more on how to host your own Frontiers Research Topic or contribute to one as an author by contacting the Frontiers editorial office: frontiersin.org/about/contact

The use of geosciences for exploring and predicting natural resources

Topic editors

Ahmed M. Eldosouky — Suez University, Egypt

Amin Beiranvand Pour — INOS University Malaysia Terengganu, Malaysia

Luan Thanh Pham — VNU University of Science, Vietnam

Biswajeet Pradhan — University of Technology Sydney, Australia

Citation

Eldosouky, A. M., Pour, A. B., Pham, L. T., Pradhan, B., eds. (2023). *The use of geosciences for exploring and predicting natural resources*.

Lausanne: Frontiers Media SA. doi: 10.3389/978-2-83251-674-4

Table of contents

frontiers in Earth Science

ORIGINAL RESEARCH
published: 21 March 2022
doi: 10.3389/feart.2022.851737

Earthquake Occurrences of the Major Tectonic Terranes for the Arabian Shield and Their Seismic Hazard Implications

Sherif M. Ali[1,2]* *and Kamal Abdelrahman*[3]

[1]National Research Institute of Astronomy and Geophysics (NRIAG), Cairo, Egypt, [2]Preparatory Commission for the Comprehensive Nuclear-Test-Ban Treaty Organization (CTBTO), International Data Centre (IDC), Vienna, Austria, [3]Department of Geology and Geophysics, College of Science, King Saud University, Riyadh, Saudi Arabia

The Arabian Shield, which contains a group of diverse terranes accreted during the Late Proterozoic, has experienced considerable historical and recent earthquake activities. From north to south, the Midyan terrane, Tabuk-Neom area, Hijaz terrane, Jeddah terrane, and Asir terrane make up the western section of the Arabian shield. In order to determine the earthquake occurrences and earthquake recurrence characteristics in the study area, an earthquake dataset containing 2,991 seismic events recorded between 1941 and 2019 with magnitudes of 1.0 and 6.2 and depths between 0 and 50 km was examined. The data were compiled by combining phase readings and information, such as origin times, hypocenter parameters, and magnitudes reported by the International Seismological Centre. The maximum likelihood method has been applied to calculate the Gutenberg–Richter recurrence parameters (a- and b-values) and magnitudes of completeness (Mc). The range of b-values is 0.53–1.04, which indicates that the study region experienced different stress level accumulations that cause earthquakes with different magnitudes. The Hijaz terrane is characterized by a high b-value (1.04 ± 0.34), which indicates a relatively low stress regime that resulted from the earthquakes stress release. The Midyan terrane is characterized by a low b-value (0.53 ± 0.10), which could be indicative of a relatively higher stress regime associated with a dominantly extensional stress. Mc values were found to be 1.4 in Midyan and Jeddah terranes. The lower value of Mc at Midyan terrane demonstrates appropriate station distribution and high earthquake rates. However, at Jeddah terrane, the seismic activities are poorly detected that probably lead to the small value of Mc. Higher Mc are evident in Hijaz terrane (Mc = 2.3) and Tabuk-Neom (Mc = 2.4), where the station distribution is very poor. The maximum expected magnitudes (Mmax) are found to be 6.0 for Midyan terrane, 5.4 for Tabuk-Neom, 4.7 for Hijaz terrane, 4.8 for Jeddah terrane, and 7.7 for Asir terrane. The average recurrence intervals of earthquakes with the Mmax are ~7, ~20, ~6, ~120, and ~200 years for each seismic terrain,

OPEN ACCESS

Edited by:
Ahmed M. Eldosouky,
Suez University, Egypt

Reviewed by:
Melouah Oualid,
University of Ouargla, Algeria
Franck Eitel Kemgang Ghomsi,
National Institute of Cartography, Cameroon
Erdinc Oksum,
Süleyman Demirel University, Turkey
Mostafa Toni,
Helwan University, Egypt

***Correspondence:**
Sherif M. Ali
sherifmohamed.ali@hotmail.com

Specialty section:
This article was submitted to Solid Earth Geophysics, a section of the journal Frontiers in Earth Science

Received: *10 January 2022*
Accepted: *08 February 2022*
Published: *21 March 2022*

Citation:
Ali SM and Abdelrahman K (2022) Earthquake Occurrences of the Major Tectonic Terranes for the Arabian Shield and Their Seismic Hazard Implications. Front. Earth Sci. 10:851737. doi: 10.3389/feart.2022.851737

Abbreviations: NRIAG, National Research Institute of Astronomy and Geophysics; CTBTO, Preparatory Commission for the Comprehensive Nuclear-Test-Ban Treaty Organization; IDC, International Data Centre; ISC, The International Seismological Centre; Mc, magnitudes of completeness; Mmax, the maximum expected magnitudes; G–R, the Gutenberg–Richter relationship; FMD, frequency–magnitude distributions.

respectively. The probability of occurrence and returned periods of different magnitudes in each region indicate that regions related to the Najd strike-slip fault system are the regions for large probable earthquake occurrences.

Keywords: seismicity, magnitude of completeness (Mc), b-value, the International Seismological Centre (ISC), seismic hazard, Arabian Shield

1 INTRODUCTION

The Arabian Plate, bounded by relatively active tectonic regions is characterized by dominant earthquake activities (Girdler, 1991; Al-Haddad et al., 1994; Ghebreab, 1998; Stern and Johnson, 2010; Al-Amri, 2013; Youssef, 2015). The Dead Sea transform fault bounds the Arabian Plate on the northwest and extends from southern Turkey in the north through Syria and the Dead Sea to the Gulf of Aqaba. A rise to the Turkish–Iranian Plateau due to the collision between the Eurasian Plate and the Arabian Plate has led to convergent boundaries, which border the Arabian Plate from the east and the north, while at the west (the Red Sea) and the south (Gulf of Aden), divergent margins originated as a result of sea floor spreading and rifting (**Figure 1**).

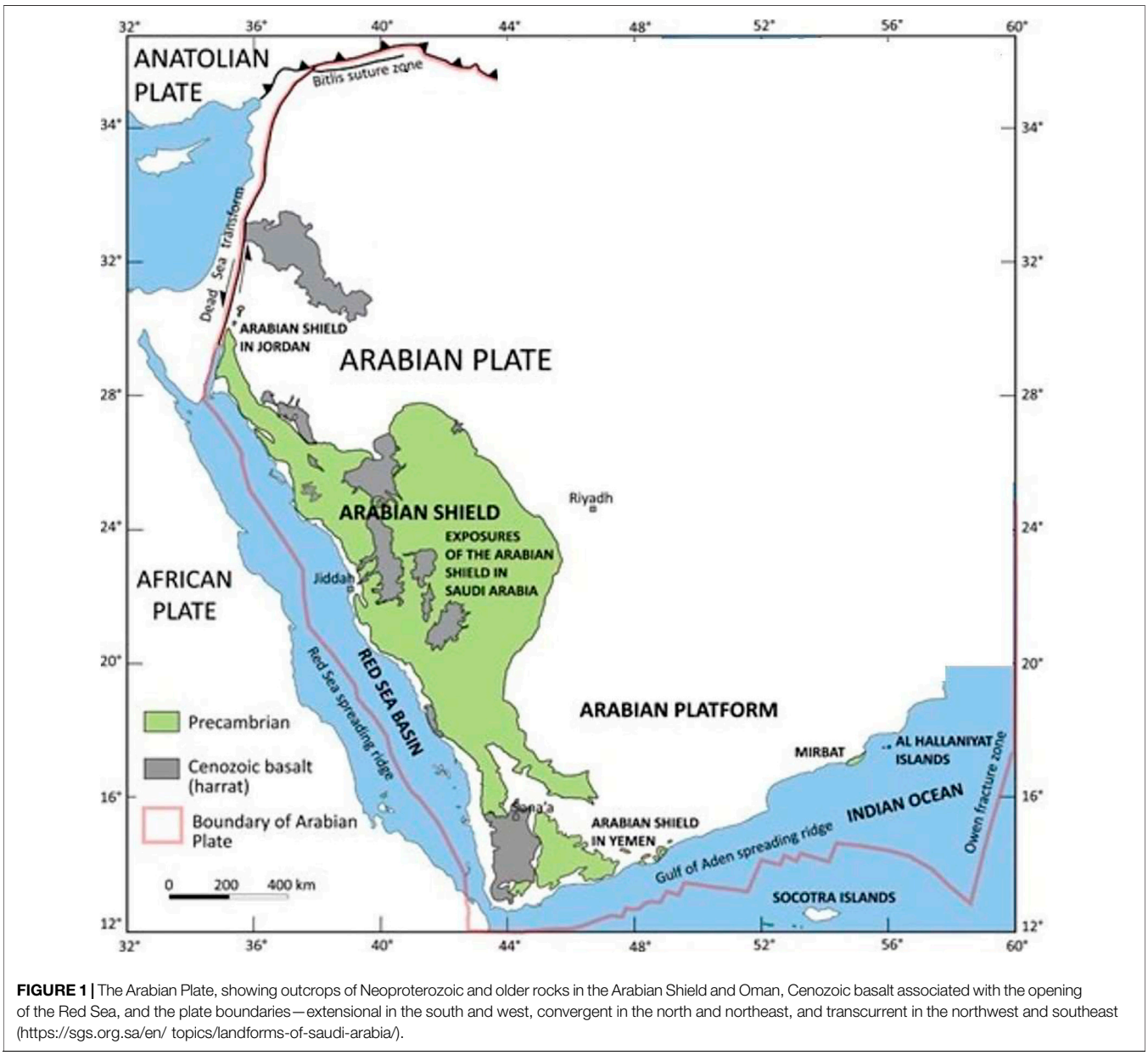

FIGURE 1 | The Arabian Plate, showing outcrops of Neoproterozoic and older rocks in the Arabian Shield and Oman, Cenozoic basalt associated with the opening of the Red Sea, and the plate boundaries—extensional in the south and west, convergent in the north and northeast, and transcurrent in the northwest and southeast (https://sgs.org.sa/en/ topics/landforms-of-saudi-arabia/).

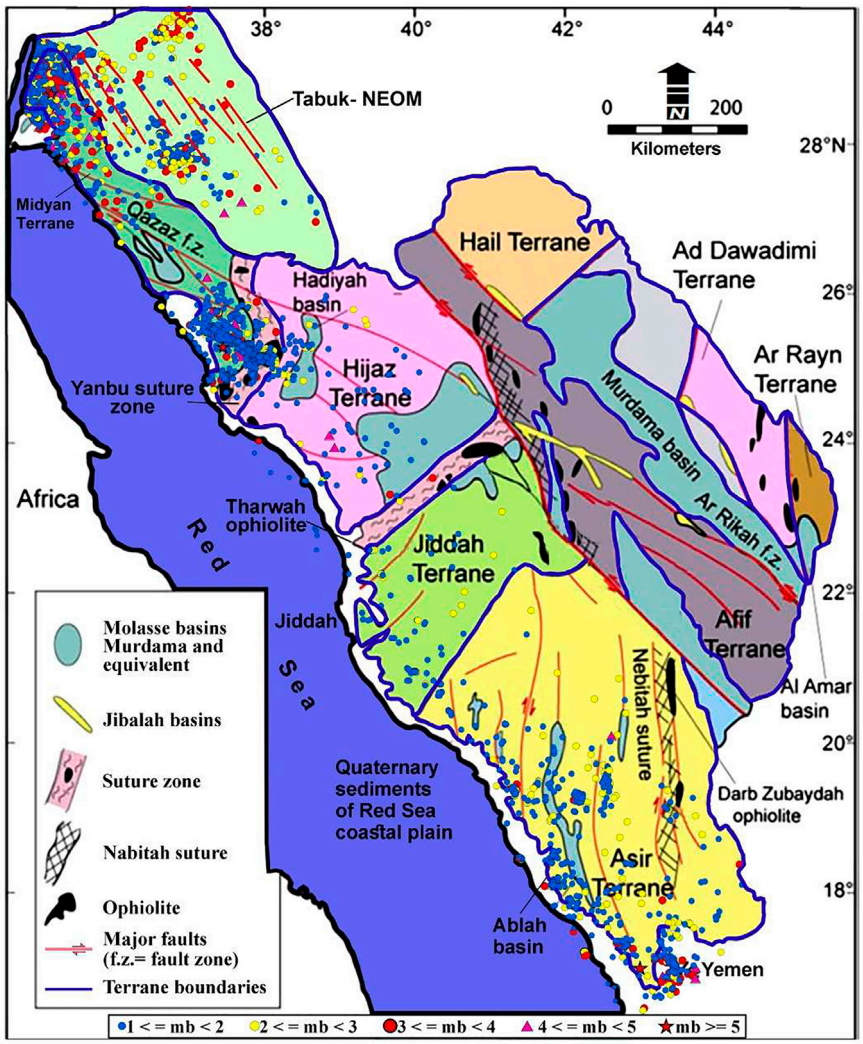

FIGURE 2 | Geologic map of the Arabian Shield showing the major geologic terranes and their boundaries, Najd fault system, and sedimentary basins (modified after Al-Amri et al., 2004) and the seismic activity from 1980 to 2019 using the International Seismological Centre catalog (ISC, 2021).

In the past, the Arabian shield experienced considerable earthquake records (Ambraseys and Adams, 1988; Ambraseys and Melville, 1988, 1989). However, it has incomplete pre-instrumental earthquakes activities due to sparse population, which reveal the prominent tectonic activities in the Cenozoic. During the last century, several moderate-sized to large earthquakes shock the area and the adjacent territories. Two large magnitude earthquakes were recorded on January 11, 1941 and November 22, 1995 with magnitudes of MS = 6.5 and MW = 7.3, respectively (Ambraseys et al., 1994; Klinger et al., 1999). The seismic sources are divided into three types including active geological faults, area source zones, and smoothed seismicity. The active fault is the dominant, especially when the magnitude and focal mechanism are well recognized.

The Arabian Shield, a prehistoric land mass with a trapezoidal shape is surrounded by Phanerozoic sediments and separated from the Red Sea by tight coastal plain of Cenozoic sediments (Kroner, 1985). It is a stable craton, which comprises a crystalline basement, predominantly metavolcanic, metasedimentary, and plutonic rocks of Precambrian continental crust of about 40–45 km thick (Davidson et al., 1994; Genna et al., 2002). Its slightly arched surface is a peneplain sloping very gently toward the north, northeast, and east.

The accumulation of oceanic island arcs along suture zones defined by ophiolites forms the Arabian shield (Stoeser and Camp, 1985). The accretion produces tectonostratigraphic terranes, which are divided by significant suture zones oriented north and northeast, and lined by serpentinite ultramafic rocks (tectonic slices and ophiolites) or major NW trending faults (**Figure 2**). The Midyan terrane, the Tabuk-Neom area, the Hijaz terrane, the Jeddah terrane, and the Asir terrane formed the western half of the Arabian Shield, from north to south (Johnson, 1998; Stern and Johnson, 2010). These terranes are separated by major suture zones, namely, Yanbu, Bi'r Umq, Afif, Nabitah, and Al Amar suture zones.

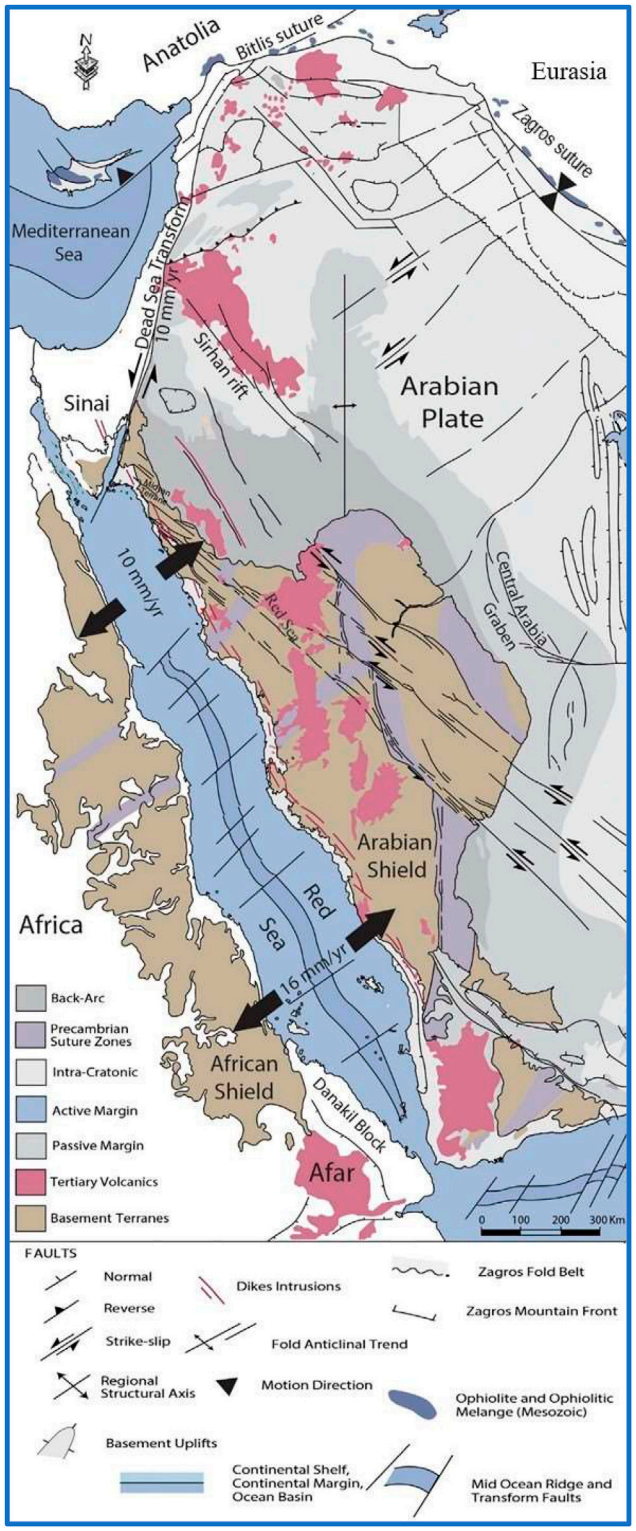

FIGURE 3 | Geological and tectonic elements map of the Arabian Plate and surrounding regions modified after Sharland et al. (2001). Geodetic observations estimate extensional rates along the Red Sea between 7 and 15 mm/year from north to south, and between 15 and 19 mm/year from west to east, left lateral slip rates along the southern Dead Sea Transform in (*Continued*)

FIGURE 3 | the range of 4.5–4.7 mm/year (e.g., ArRajehi et al., 2010). Counterclockwise rotation of Arabia relative to Eurasia was reported after Reilinger et al. (2006) in the range of 20–30 mm/year, leading to left lateral strike slip (East Anatolian Fault) along the northern boundary of the Arabian Plate with GPS slip rates in the range of 17–24 mm/year from east to west Turkey. The slip rates increase eastward along the Zagros mountain belts from 18 to 25 mm/year (Walpersdorf et al., 2006).

Aldaajani et al., 2021 stated that, at the northern boundary of the Arabian Plate, the boundary forces seem to have changed from compression to strike-slip style, due to the oblique collision between Anatolian and Arabian plates, which led to lateral escape tectonics of the Anatolian Plate (**Figure 3**) (Reilinger et al., 2006). This may have occurred simultaneously with the crustal extension in the Red Sea. Following the collision of Arabia and Eurasia and the Red Sea initiation, the strength contrast between Afro-Arabia continent and the oceanic lithosphere of the Mediterranean may have initiated movement along the Dead Sea Transform soon after a dike intrusion event along the western margin of the Arabian Plate (ArRajehi et al., 2010). This ultimately resulted in the development of the Sinai microplate (Beydoun, 1999).

The purpose of this study is to characterize the seismic activities related to these main terrains in the Arabian Shield. Furthermore, the study aims to indicate the dominant tectonic regimes of the studied regions and identify their related faulting types as well as characterize the earthquake rate changes and the risk of higher magnitude earthquakes related to each terrane, and obtain some seismicity parameters [a- and b-values and magnitude of completeness (Mc)]and seismic hazard parameters (earthquake recurrence and maximum expected magnitude) to be able to perform actions for seismic risk reduction in the studied region.

2 TECTONIC ENVIRONMENTS

Saudi Arabia occupies the majority of the Arabian plate that was formed between 25 and 30 million years ago. Because of rifting along the northeastern African continent's boundary, the Red Sea, and the Gulf of Aden opening, the rocks that make up the Arabian Peninsula, Jordan, Syria, Iraq, and westernmost Iran are found to split up from the African continent. Although the plate is a relatively new tectonic unit, it combines materials that have formed over a long period of geologic time. These rocks comprise a 45-km-thick layer of continental crust. Because of Mesozoic and Cenozoic uplift, Precambrian rocks are exposed toward southwest of the plate. In other places, the Precambrian rocks are obscured by a low-dipping succession of Phanerozoic deposits, which can be more than 10-km thick in the Arabian Gulf (Johnson, 1998). Precambrian shields typically have sufficiently thick and cold lithosphere that mantle earthquakes could occur. Their exceedingly low strain rates, including those within Arabia, cause mantle earthquakes to be particularly rare beneath shields (Frohlich et al., 2015). Volcano-seismicity, with mantle and lower-crustal earthquakes likely caused by early-stage

pooling and mixing of asthenospheric melt at the base of or within the lower-crust, are also rare in cratons, including Arabia, given their low heat flow (Prieto et al., 2017).

Tectonically, the movement of the Arabian plate northeast away from Egypt and Sudan is accompanied by compression and strike-slip displacement along the Zagros and Bitlis zones, and by strike-slip faulting along the Dead Sea transform. The northern part of the Arabian plate moves northwest toward the Eurasian plate with a rate of 20 ± 3 mm/year (Johnson, 1998; Jamali et al., 2006). The tectonic pattern of the western Arabia is congenital from the basement tectonics of ancient Nubian–Arabian shield, which received its main structural imprint during late Precambrian orogenic stages. The most important tectonic features are the NW-SE strike faults parallel to the extension of the Red Sea, Gulf of Suez rift, Aqaba fault trend, Najd faults system, NE-SW, and E-W (Tethyan trend) that affect the north and the NW Red Sea region.

The Najd strike-slip fault system is the Arabian shield's most notable structural feature. It extends in a zone >1,200 km in length and >300 km wide over the north-eastern Arabian Shield. This faults trend NW-SE with strike lengths >500 km, small sinistral displacements <25 km, and cumulative displacement across the zone >240 km. The Najd system's shear zones separate the western and eastern geologic terranes. From the NE coast of the Red Sea to the SE shield area, where the fault system is hidden beneath Mesozoic sedimentary strata, at least four major NW-SE trending left-lateral wrench zones of Najd intersect the shield. On the Najd system, cumulative Precambrian left-slip fault is estimated to be around 240 km (Brown, 1970). The Arabian Shield is made up of metamorphosed rocks that are overlain by a thick succession of Phanerozoic sedimentary rocks to the east, north, and south, and the Red Sea to the west. The shield's rocks are mostly Cenozoic basaltic volcanic lava fields, known as Harrat (an active volcanic field located along the western edge of the Arabian Shield, east of the Red Sea rift margin, beneath which earthquakes occurred within the lithospheric mantle), whereas those to the west of it are Cenozoic rocks from the Red Sea basin. The Red Sea and Gulf of Aden basins and phanerozoic rocks are typically slightly deformed and impacted by block faulting and open folds. The western and southern edges of the Arabian Plate were uplifted and partly surrounded by subaerial flood basalt during the previous 25 million years, culminating in the development of the Red Sea Cliff and Harrat (Davidson et al., 1994).

3 SEISMICITY OF THE ARABIAN SHIELD

The Arabian Plate has a clustered seismicity along the Dead Sea transform fault, the Red Sea rifting, Zagros fold and thrust belt, Makran subduction zone and Biltis thrust. Along the Red Sea rifting, the Gulf of Aden and Gulf of Aqaba, seismic activity is largely controlled and confined. It is concentrated near the axial trough of the Red Sea (Al-Malki and Al-Amri, 2013).

The spreading of the Red Sea floor and volcanism are linked to the distribution of earthquakes in the western half of the Arabian Shield. Several moderate-sized earthquakes struck the Arabian

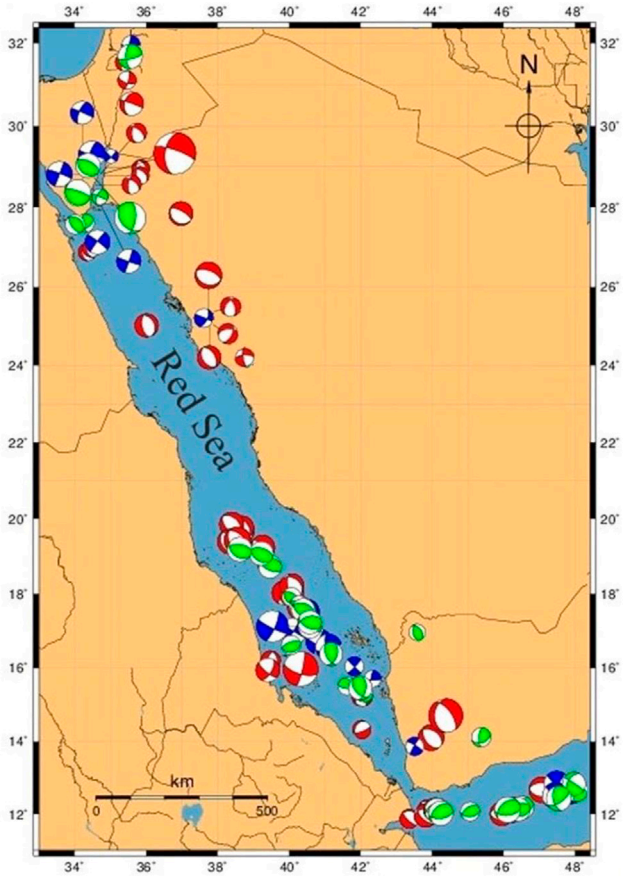

FIGURE 4 | Focal mechanism solutions of the 122 earthquakes in the Arabian Shield and its surrounding regions during the period from 1977 to 2021. Normal faulting solutions (in red). Strike-slip solutions (in blue) and thrusting solutions (in green). Size of focal sphere is proportional to magnitude.

Peninsula's extreme southwest. On January 11, 1941, near the modern Saudi Arabia–Yemen border, one of the greatest occurrences of magnitude Ms = 6.5 happened. It resulted in the deaths of several hundreds of people and the destruction of 1,700 buildings, 300 of which were destroyed, and 400 were severely damaged (Ambraseys et al., 1994). On January 23, 2014, an earthquake sequence was recorded around 50 km northeast of Jizan city, with the greatest occurrence having a local magnitude of Ml = 5.1 (El-Hadidy et al., 2015; Youssef, 2015). The earthquake fault plane solution indicates mainly a strike-slip northeast–southwest faulting mechanism, which, together with the aftershock distribution, matches the known NE-SW faults.

The northwestern Arabian Shield is characterized by strong historical earthquakes (Ambraseys and Melville, 1989; El-Isa and Al Shanti, 1989); the largest earthquake took place in AD 1068 with an intensity ~IX. It caused nearly 20,000 deaths and huge damages in Tabuk City, the Sinai Peninsula, and near the Dead Sea (Ambraseys and Melville, 1989; El-Isa and Al Shanti, 1989). Many recent moderate-to-large earthquakes are located in the study area, including a series of earthquakes in June 2004, about

TABLE 1 | Number of earthquakes, magnitude, and depth ranges; seismicity and seismic hazard parameters for the studied regions in the Arabian Shield.

Regions	Total no. of events	No. of events M ≥ 1.0	Depth range (km)	Max mag	a-value	b-value	Mc	Mmax
Midyan terrane	16,483	1,521	0–51	5.5	3.73	0.53 ± 0.10	1.4 ± 0.35	6.0
Tabuk-NEOM	1,012	899	0–35	4.9	4.35	0.76 ± 0.13	2.4 ± 0.48	5.4
Hijaz terrane	103	55	0–59	4.2	3.88	1.04 ± 0.34	2.3 ± 0.56	4.7
Jeddah terrane	114	68	0–19	4.3	2.70	0.70 ± 0.19	1.4 ± 0.38	4.8
Asir terrane	716	448	0–57	6.2	3.72	0.83 ± 0.23	1.6 ± 0.44	6.7

60 km southwest of Tabuk. The largest earthquake in this series took place on June 22, 2004 with a magnitude of Ml = 5.2. On August 27, 2009, an earthquake with a magnitude of Ml = 5.1 took place about 45 km north of Badr City. On May 19, 2009, the area was hit by an earthquake swarm in Harrat Lunayir with magnitudes of Ml = 5.4 for the main event, which was felt in Al Madinah (Youssef, 2015; Zahran et al., 2016).

4 FOCAL MECHANISM SOLUTIONS

Several approaches are used to understand the earthquake phenomena. One such approach is the focal mechanism solutions (FMS). The main purposes of focal mechanism analysis are to identify seismic faults from seismological observations and to study the type of displacement and the relative motion between the different plates' boundaries. The focal mechanism solutions, together with the distribution of seismic activity are very useful indicators for the seismotectonic setting, the earthquake generating processes, and the stress regime of a certain region. Determination of the focal mechanism solutions provides extensive information about the sense of fault movements and the state of stress in the lithosphere. In this study the most recently compiled focal mechanism dataset given for the Arabian Shield and surrounding regions are considered. Focal mechanism data were mainly obtained from the International Seismological Centre (ISC) catalog for the region from 12° to 32°N latitudes and between 34° and 48°E longitudes). The final compiled focal mechanisms catalog is comprised of a total number of 122 solutions spanning the time period from 1977 to 2021. These solutions, which are presented in **Figure 4**, demonstrate a majority of normal faulting mechanism. Some scarcely strike-slip and thrust faulting mechanism solutions are also noticed. The normal mechanism with centroid depths at 12–19 km, a strike-slip mechanism with centroid depths at 10–22 km and a thrust mechanism with centroid depths at 10–25. The focal mechanism solutions show a dominant extensional regime with almost horizontal NE-SW trending.

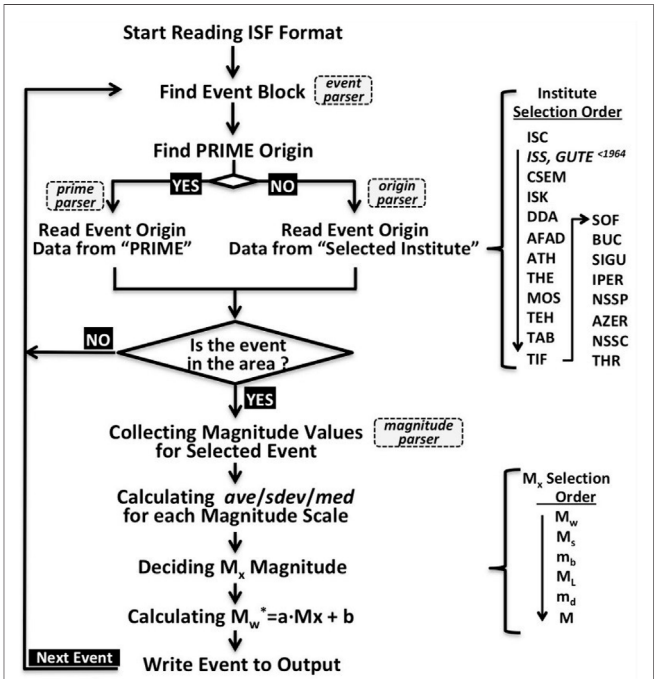

FIGURE 5 | Flowchart of the International Seismological Centre (ISC) database processing. Ave, average (mean); Med, median; Sdev, standard deviation. Mw is equivalent moment magnitude. See **Appendix A** for the institute codes.

5 ANALYSIS OF SEISMICITY PARAMETERS

5.1 Gutenberg–Richter relationship

The Gutenberg–Richter (G–R) relationship is the common recurrence relationship, which describes the seismicity of a seismic region. Once the earthquakes take place, the relationship between their frequency of occurrences and magnitude distributions (FMD) can be given by the following equation:

$$\log N(M) = a - b\,M \tag{1}$$

where the cumulative number of earthquakes N(M) is computed for all magnitudes M and greater. The a and b parameters are the seismicity constants that are indications for the seismic activity level and the slope of the FMD, respectively.

The a-value is the seismic activity rate that illustrates the above equation when it cuts across at M = 0. This variable parameter changes with the changes of seismic activity, the time, and term of observation, the earthquake magnitude, and the stress regime of the region under study (Gutenberg and Richter, 1944). With the increasing earthquake magnitudes in a region, the slope of its frequencies is determined by the b-value. It can also present the

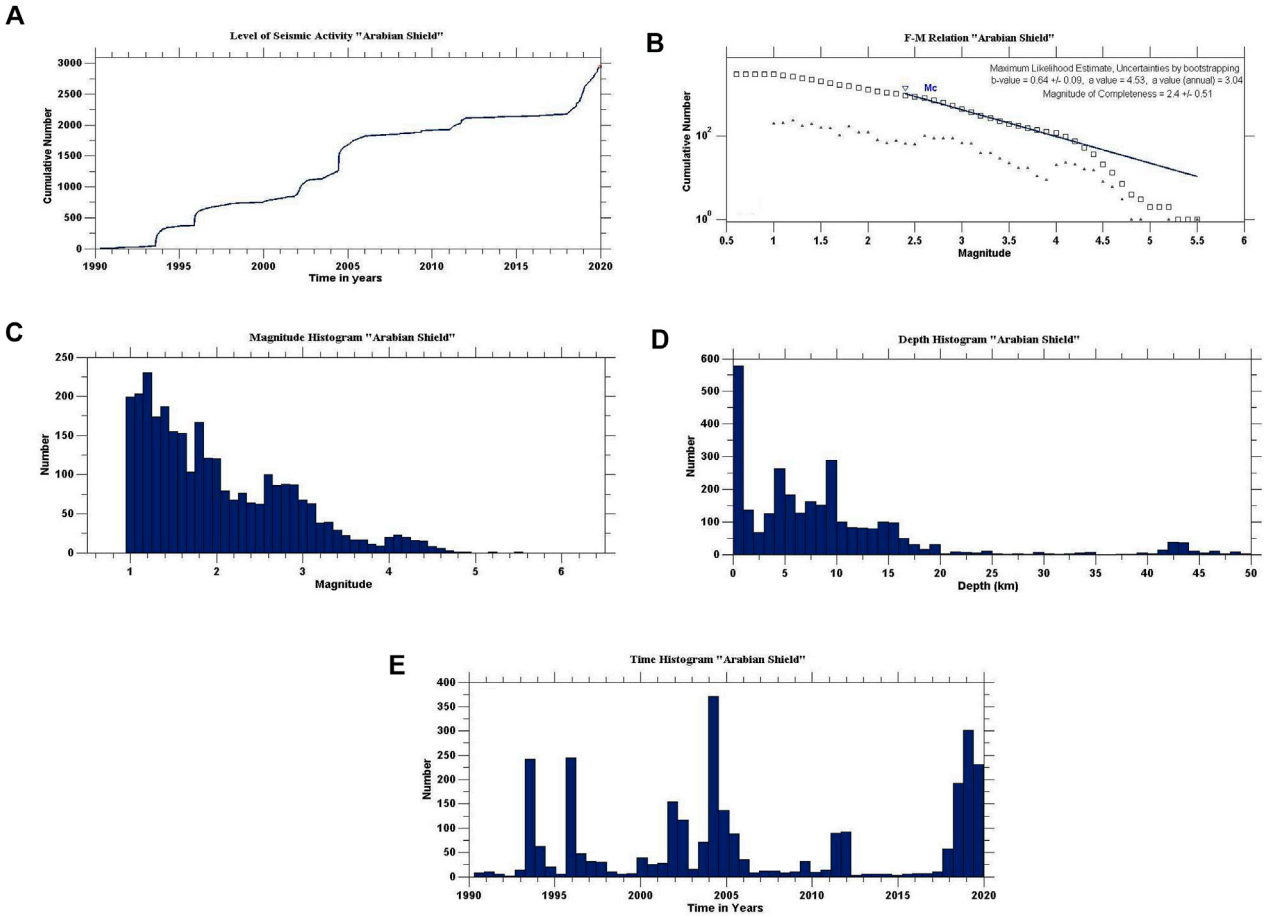

FIGURE 6 | The statistical analysis results of the Arabian Shield region using the whole dataset. **(A)** The evolutions among the levels of seismic activities, **(B)** the magnitude–frequency relationship, Mc is the cutoff magnitude (triangles and squares show earthquake numbers and the cumulative earthquakes for each magnitude value, respectively), **(C)** the magnitude histogram, **(D)** the depth distributions, and **(E)** the time histogram.

proportion of the earthquake sizes in numbers. The b-value is changing by the stress and strain distribution as well as the type of the rock. It is close to unity for most tectonically active regions (Schorlemmer et al., 2005). Areas with low heterogeneities (reduced geological complexity or crack density) and low thermal gradients are characterized by low b-values, while high heterogeneous regions, which are characterized by low velocity of deformation and less stress and strain, are the areas of higher b-values (Mogi, 1962; Manakou and Tsapanos, 2000). The correlation between b-values and the faulting mechanisms has been inferred from some previous studies, which relates normal faults to b-values ~1.1, strike-slip faults to b-values ~0.9, and thrust faults to b-value ~0.7 (Schorlemmer et al., 2005).

5.2 Magnitude of completeness

The magnitude of completeness (Mc) is defined as the lowest magnitude above which most of earthquakes are detected in space–time volume (Wiemer and Wyss, 2000; Ali and Shanker, 2017; Hafiez and Toni, 2020; Ali and Akkoyunlu, 2022). The accurate estimation of Mc is crucial, where increasing the values of Mc lead to take insufficient data and decreasing the Mc values lead to take a huge number of bogus data (Mignan and Woessner, 2012). The completeness magnitude is a basic requirement for modeling the seismicity in a region. The maximum curvature technique, the most reliable method to estimate Mc, is utilized to locate the maximum curvature point that refers to the magnitude of completeness by computing the first derivative maximum value of the slope of earthquake curve (Wiemer and Wyss, 2000).

There are various other methods to determine the magnitude of completeness. Some of these methods are the Mc by b−value stability, median-based analysis of the segment slope, and goodness-of-fit test. Although, the maximum curvature technique is easily applicable, Mc can be misjudged for the gradually curved FMDs. Consequently, utilizing other methods provide more reasonable estimates for Mc (Michael, 2014). When using more homogeneous local dataset, the maximum curvature technique gives more reasonable values for Mc (Mignan et al., 2011; Hafiez and Toni, 2020). The maximum curvature method requires less events compared with other methods, where uncertainties are also applicable by applying the Monte Carlo approach of the bootstrap technique (Efron, 1979). When the

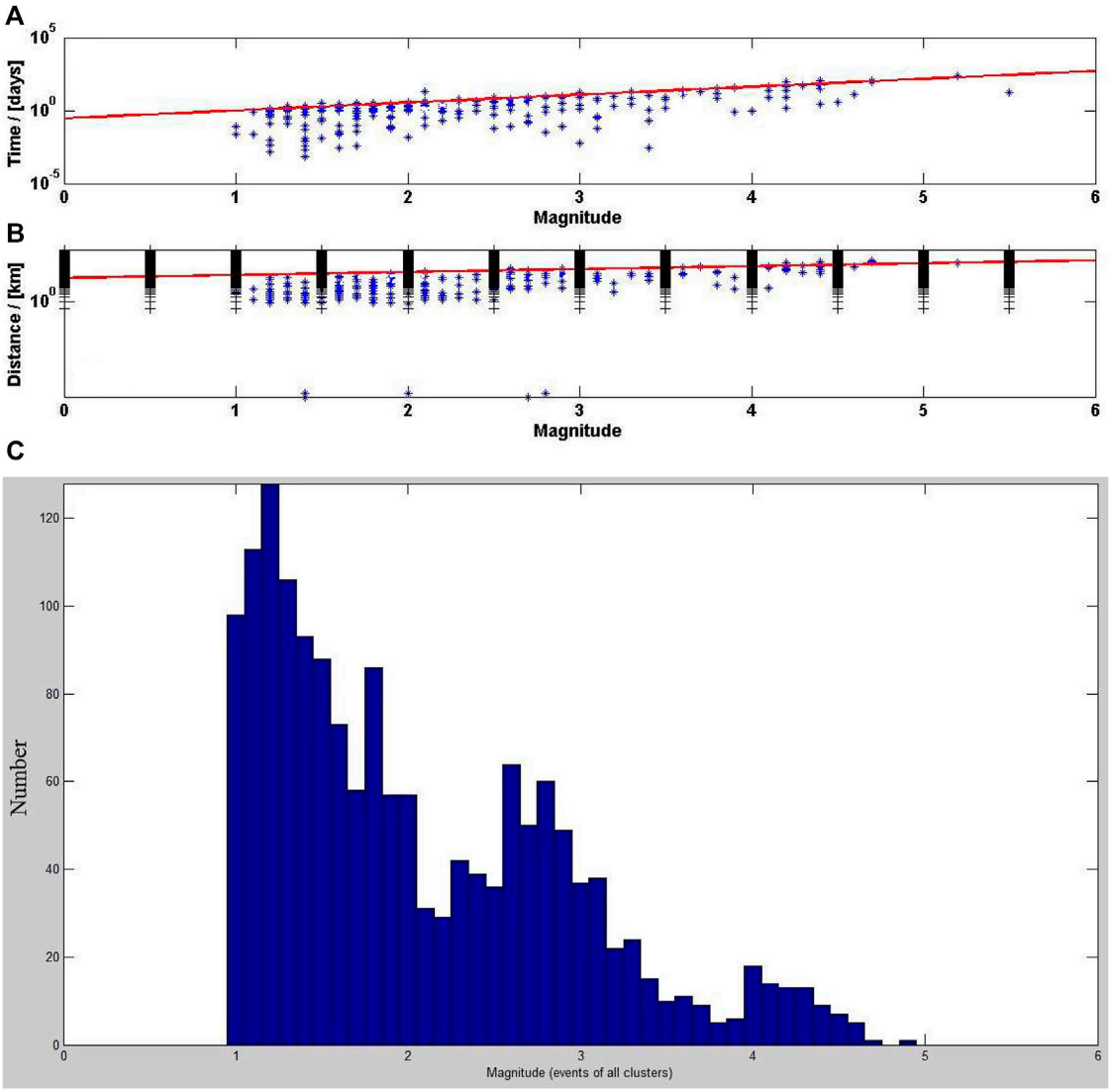

FIGURE 7 | Distribution of events through **(A)** time and **(B)** latitude for foreshock, mainshock, and aftershock sequences. **(C)** The magnitude histogram of the declustered catalog.

number of events is small, it leads to higher uncertainty values, and when the sample size is large enough (≥150 events), it allows a better estimation for Mc.

5.3 Seismic hazard parameters

The assessment of the previous earthquake distribution and their magnitudes in a seismotectonic region, as well as the calculation of the seismicity parameters, is the main stride to estimate the earthquake probability. The a- and b-values in the Gutenberg–Richter FMD can be employed to foresee the probability of future earthquakes of various magnitudes and recurrence intervals (Mogi, 1962; Scholz, 1968).

The earthquake probability of magnitude M (in any period T) is calculated by the Poisson model, a base model to calculate the probabilistic seismic hazard that have been used in the maps of the National Earthquake Hazard (Frankel, 1995), in the California Seismic Hazard Maps (Petersen et al., 1996), and in fault lengths and global earthquakes (Leonard et al., 2001). This method is defined by the following equation:

$$P\ (M) = 1 - e^{-N(M)*T} \tag{2}$$

where $P\ (M)$ is the probability that at least one earthquake will take place within certain periods (T), M is computed by **Eq. 1**. According to the Poisson model, the recurrence interval (Q) is given by the following equation:

$$Q = 1/N\,(M) \tag{3}$$

The relationship between the magnitude and reputed length (L) is employed for computations of the maximum expected earthquake magnitudes. The most likely magnitude for a certain maximum rupture is estimated by (L), which is not the maximum

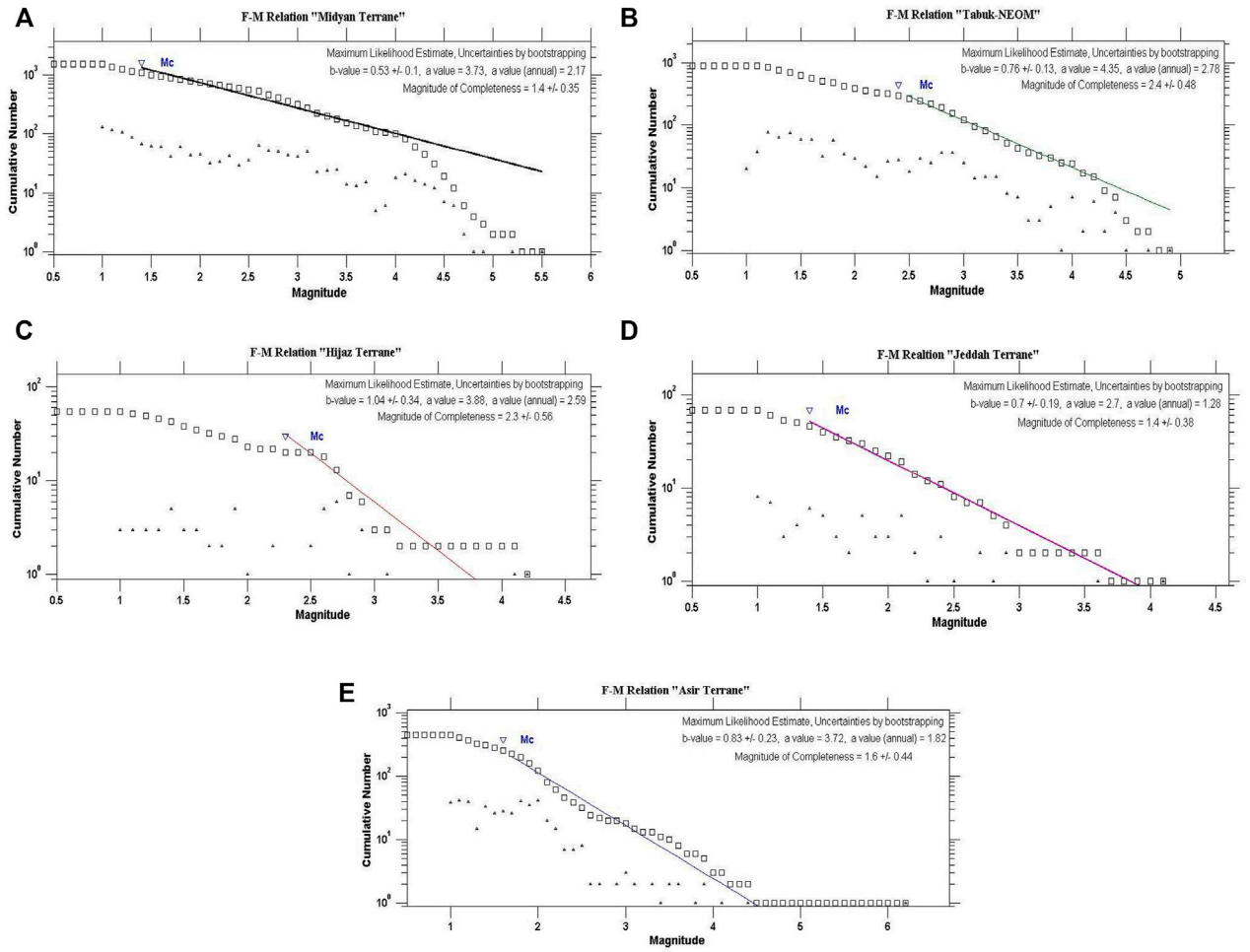

FIGURE 8 | (A–E) Frequency–magnitude relations of the studied seismic regions calculated by the maximum curvature technique. Mc is the cut-off magnitude (squares and triangles show the cumulative earthquakes for each magnitude value, as well as the earthquake numbers, respectively).

magnitude, but rather the magnitude that could be anticipated to overtake in half of the earthquakes correlated with that rupture length.

$$M = 5.08 + 1.16*\log(L) \quad (4)$$

It is possible to use the regression models to estimate the expected magnitude. Wells and Coppersmith (1994) used the documented and published historical and recent reports to take out relations between the rupture length and average surface displacement. The maximum expected magnitude (Mmax) was obtained by adding 0.5 units to the maximum observed magnitude (Kijko, 2004) (**Table 1**).

6 SEISMICITY CATALOG

The earthquake catalog is one of the most important outputs of seismology. It presents a broad dataset in earthquake events, which comprises the seismicity analysis in space–time volume, seismotectonic, and seismic hazard assessment (SHA). When the catalog has longer time span, the hazard parameters are well estimated (Rydelek and Sacks 1989; Wiemer and Wyss 2000; Woessner and Wiemer, 2005; Ali, 2016).

The initial earthquake catalog in the current study is compiled for the Arabian shield. It initially comprises 3,750 local earthquakes recorded during the period from 1941 to 2019 with magnitudes range from 1 to 6.2 and focal depths range from 0 to 50 km. This catalog is utilized to characterize seismicity of the study area. It is compiled by combining phase readings and information retrieved from regional seismological agencies and reported by the International Seismological Centre (ISC) online bulletin available at (http://earthquake.isc.ac.uk/). In examining the earthquake catalog completeness, the earthquake dataset used in the seismicity studies should use similar magnitude scales. The most recorded events in the study area have been reported by ISC in “ml” magnitude scale. Only few events are reported by other different magnitude scales, such as Md, mb, and/or Ms, which have been removed from our study for consistency. Therefore, a homogenous earthquake data catalog has been prepared using only one magnitude type “ml” (**Table 1**).

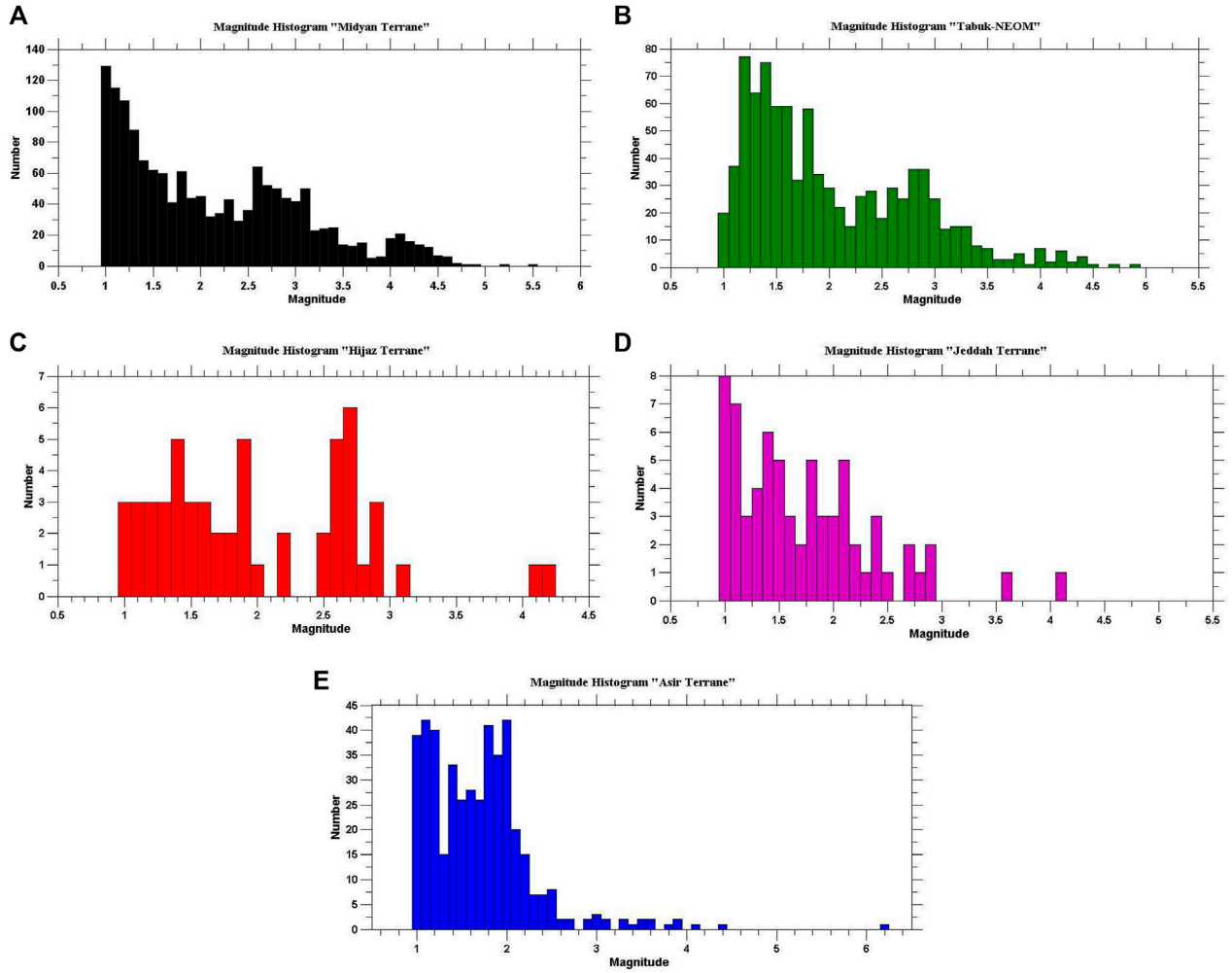

FIGURE 9 | (A–E) Magnitude histograms for the studied regions as represented by the color legend.

The ISC bulletin is one of the main sources of data for regional and global imaging of the Earth's tectonics and structure, and seismic hazard research work. The most important feature of the ISC bulletin is that all events with sufficient data are manually checked and relocated by experienced analysts. Therefore, the latest earthquake information in the database is 2 years behind in real-time. It also presents the event parameters reported by the contributor agencies and centers. The ISC finished rebuilding the entire database in 2020 by utilizing a new location algorithm (Bondár and Storchak, 2011) with the ak135 seismic velocity model (Kennett et al., 1995). Furthermore, previously unavailable hypocenter and station phase readings from the temporary and permanent networks are used to the rebuild bulletin (Storchak et al., 2017; International Seismological Centre, 2021). Therefore, the latest, most recent, and revised international dataset is used in this study. The earthquake parameters in the bulletin are in the IASPEI Seismic Format (available at: http://www.isc.ac.uk/standards/isf/). The overall data processing is given in the flowchart in **Figure 5**. Because the bulletin may contain multiple hypocenters from multiple agencies for an event, the ISC considers that one of them is primary and assigns to it the PRIME flag. A hypocenter determined by the ISC always has the PRIME flag. The parameters reported by the ISC are preferred first. If there is no information from the ISC, the availability of the hypocenter parameters from the European-Mediterranean Seismological Centre (EMSC or CSEM) is searched (see **Appendix A** for the institute abbreviations). The priority of both institutes is high because they use all available data in the study area.

7 METHODS AND DATA ANALYSIS

The ZMAP software package (Wiemer, 2001) available at http://www.earthquake.ethz.ch/ software/zmap has been utilized to perform the statistical analyses on the compiled data set. It includes a set of tools operated by a graphical user interface (GUI) and intended to help scientist in their analyses of catalog data. ZMAP is primarily a tool used to evaluate the quality of catalogs and to address assumptions. It was first published in

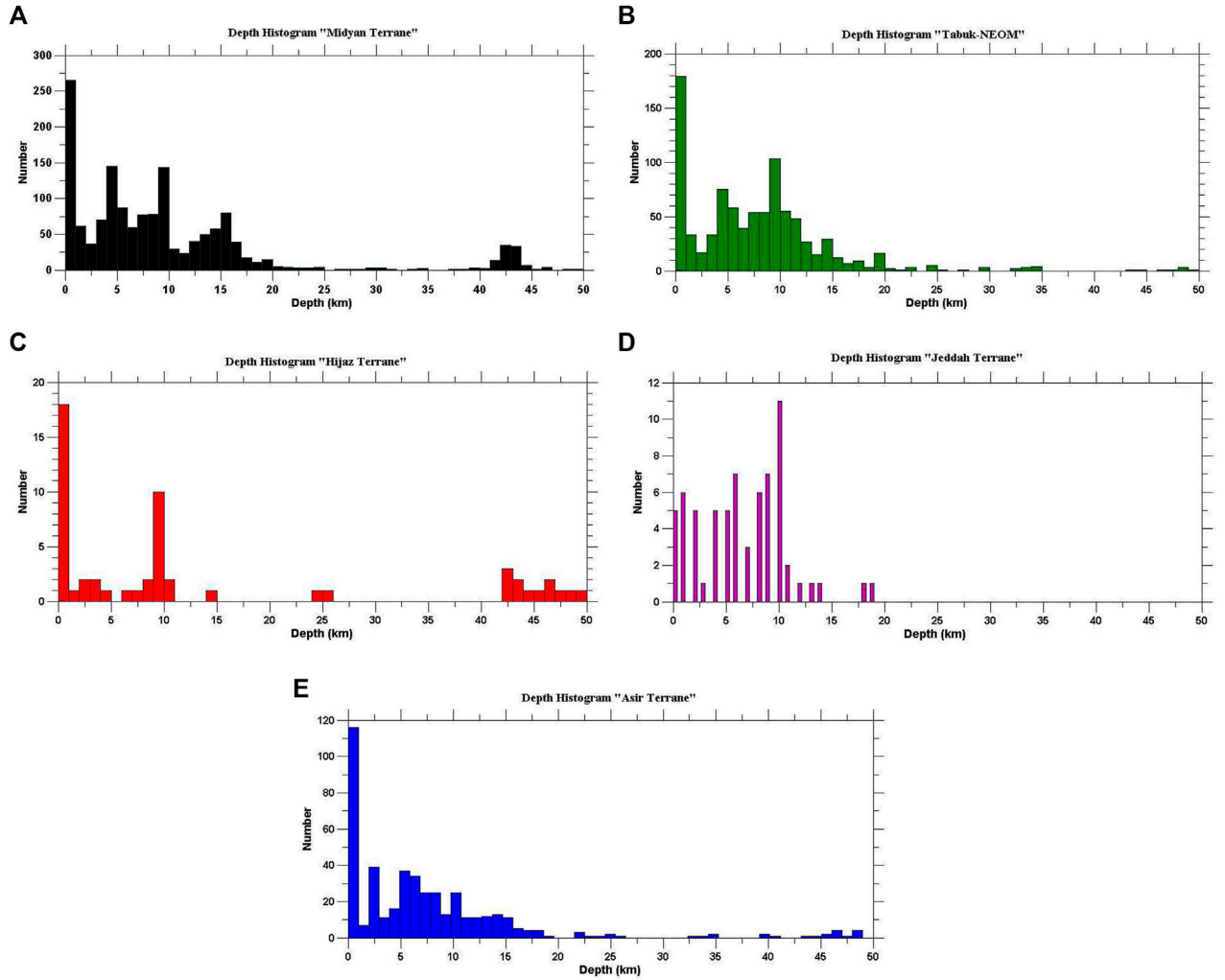

FIGURE 10 | (A–E) Depth histograms for the studied regions as represented by the color legend.

1994 then became well known over the last few years. It includes important features for the catalog quality assessment, such as artifacts, completeness, and contamination of explosion as well as interactive data exploration, stress tensor inversions, mapping transients in seismicity (b-values and rate changes) and fractal dimension analysis. The code of ZMAP is an open source, written in Matlab by the Mathworks, which is a widely used software language in the natural sciences. The ongoing renovation process of Zmap tools, which started as simple graphical retrofits, has evolved to leverage modern MATLAB's new graphics system, improved object-oriented capabilities, updated toolboxes, and has resulted in a version of ZMAP that provides vastly improved usability, speed, and reliability. Nearly every aspect of the ZMAP has been modified and is now compatible with MATLAB R2018a and later. The user interfaces have been modified to provide consistency and a high degree of interactivity.

The statistical analyses have been performed on the whole dataset of the Arabian Shield as a one region before subdividing it into terranes (**Figure 6**). The evolutions among the levels of seismic activities, i.e., the cumulative number of earthquakes plotted against time, are shown in **Figure 6A**. This evolution indicates the sudden increase in the cumulative seismicity curves of the Arabian Shield in 2004 and 2018. The a- and b- values, which may exhibit some differences based on the tectonic characteristics of the investigation area, were calculated for the Arbian Shield using the magnitude–frequency relationship (**Figure 6B**). The obtained a- and b-values were 4.53 and 0.64, respectively. The estimated magnitude of completeness for the whole catalog of the Arabian shield was Mc = 2.4. The magnitude histogram (**Figure 6C**) shows that the average magnitudes are between 1 and 3.4. The depth distribution (**Figure 6D**) shows that the depths of the vast majority of events in the catalog are between 0 and 15 km. The seismic activities between 40 and50 km have also been reported. The predominant depths are about 0–10 km. The time histogram (**Figure 6E**) displays the increase of seismic activity in 2004 and 2018–2019. There are very low activities that have been noticed in the period between 2013 and 2017.

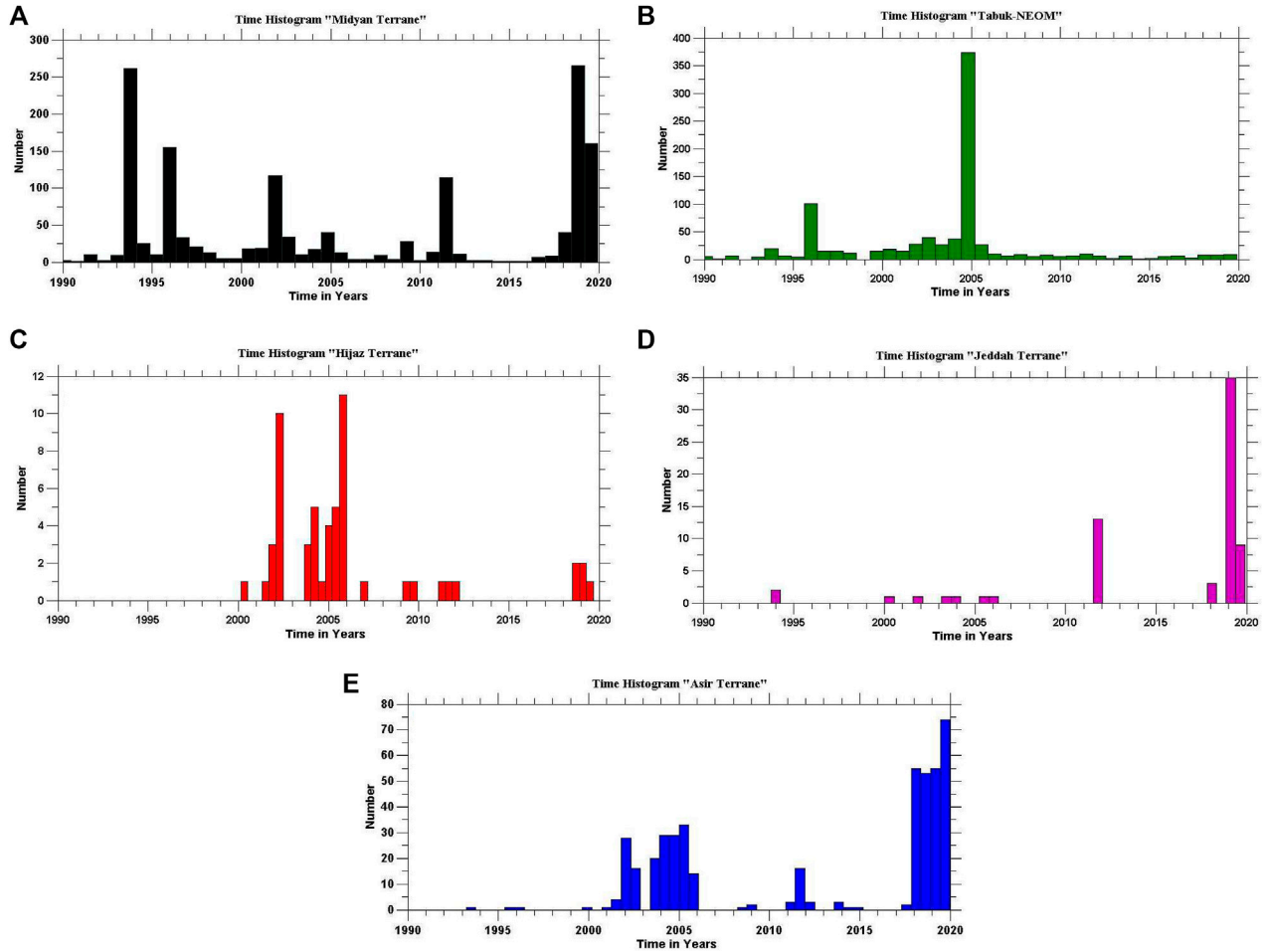

FIGURE 11 | (A–E) Time histograms for the studied regions as represented by the color legend.

In order to ensure a time-independent Poissonian distribution of seismicity, the earthquakes that occurred in clusters, such as foreshocks/aftershocks sequences and swarms, are aimed to be identified and then removed from the catalog. This process called the declustering process, in which earthquake clusters are usually defined by their proximity in time and space. Several approaches can be used for the declustering process (e.g., stochastic, deterministic = linking, and windowing methods). The windowing methods, such as the Gardner and Knopoff (1974) and Reasenberg (1985) are capable of identifying in a straightforward way the foreshock/mainshock/aftershock sequences, simply by applying the windows forward and backward in time from the mainshock. These methods do not distinguish between different generation of aftershocks (i.e., first generation resulting from the mainshock and those associated to previous aftershocks), and it is assumed that all dependent events would occur within the window. Also, they assumed a circular spatial window searching not full consistent with fault extension for larger magnitude earthquakes. We then used the most widely applied deterministic approach (Gardner and Knopoff, 1974), which is based on a windowing algorithm originally conceived for Southern California, but later adopted/modified to be used across the world (Uhrhammer, 1986; Stiphout et al., 2012). This method takes into consideration the tectonic context and related seismicity present in the region (active shallow, stable, and interface/inslab subduction) in order to decluster the catalog.

The distribution of events through time and latitude showing the foreshock, mainshock, aftershock sequences after applying the declustering for the subduction region are presented in **Figure 7**, together with window sizes (distance and time) with respect to the magnitude used by declustering methods. The declustering found a total of 759 (20.24%) clustered events out of 3,750. The map window now displays the declustered catalog containing 2,991 events as blue dots. The individual clusters are displayed as magenta pluses (**Figure 7**). The magnitude histogram of the declustered catalog is shown in **Figure 7C**. It shows a noteworthy difference from the magnitude histogram distributed by the data of the whole catalog (**Figure 6C**), which highlights the importance of the declustering process.

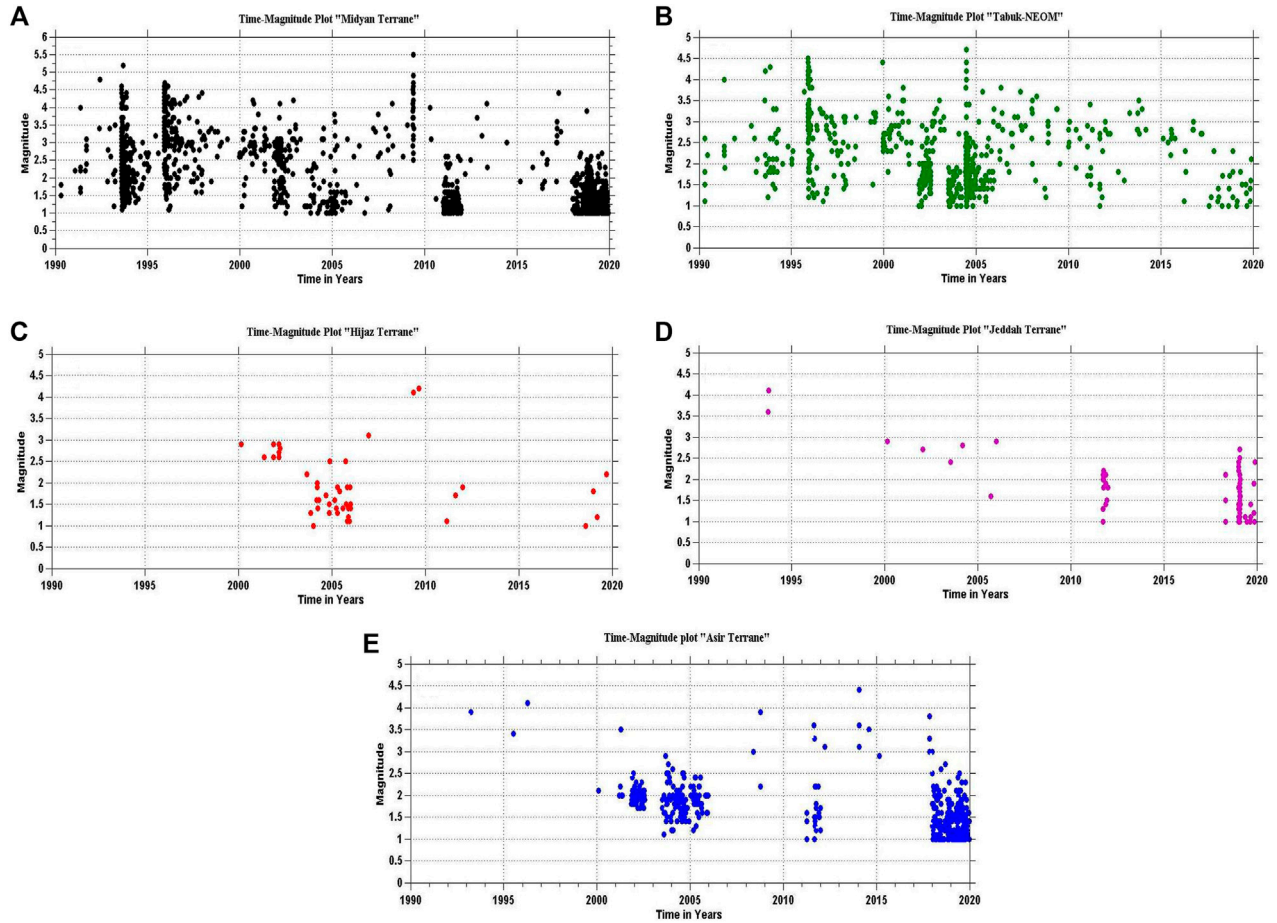

FIGURE 12 | (A–E) Time–magnitude distributions for the studied regions as represented by the color legend.

8 RESULTS

The Arabian Shield has been subdivided into five regions (The Midyan terrane, the Tabuk-Neom area, the Hijaz terrane, the Jeddah terrane, and the Asir terrane). The purpose of this study is to characterize the seismic activities related to these main terrains in the Arabian Shield. Furthermore, to indicate the dominant tectonic regimes of the studied regions and identify their related faulting types as well as characterize the earthquake rate changes and the risk of higher magnitude earthquakes related to each terrane and obtain some seismicity parameters [a- and b-values and magnitude of completeness (Mc)] and seismic hazard parameters (earthquake recurrence and maximum expected magnitude) to be able to perform actions for seismic risk reduction in the studied region.

For this purpose, we estimated the parameters from the deviation of the earthquake frequency–magnitude distribution from the Gutenberg–Richter law in each region (**Figure 8**). The a- and b-values, which may exhibit some differences based on the tectonic characteristics of the investigation areas, were calculated for each source region along with the magnitude–frequency relationship (**Figure 8** and **Table 1**). Among all the investigated areas, the highest b-values are detected in the Hijaz terrane (b = 1.04), while the lowest b-values were recorded in the Midyan terrane (b = 0.53). A reliable estimate of Mc is to define the point of the maximum curvature as the Mc by computing the maximum value of the first derivative of the frequency–magnitude curve. In practice, this matches the magnitude bin with the highest frequency of events in the noncumulative frequency–magnitude distribution (triangle symbols in **Figure 8**). Using the maximum curvature, which simply computes the maximum value of the first derivative of the FMD curve, the higher Mc values of 2.3 and 2.4 are obtained at the Hijaz terrane and Tabuk-Neom, respectively, while the lower values of Mc are of 1.4 for Midyan and Jeddah terranes. The obtained Mc values for all studied regions are given in **Table 1**.

The magnitude histograms illustrated in **Figure 9** shows that Midyan, Tabuk, and Asir Terranes have the higher seismicity at the study area with average magnitudes of 1.0–4.1 at Midyan, 1.0–3.3 at Tabuk, and 1.0–2.2 at Asir Terranes. The depth distributions (**Figure 10**) show that most earthquakes in the catalog occurred in shallow depths. The predominant depth ranges between 0 and 15 km. Hijaz and Jeddah Terranes show lower depth distributions. The yearly seismic rate histograms

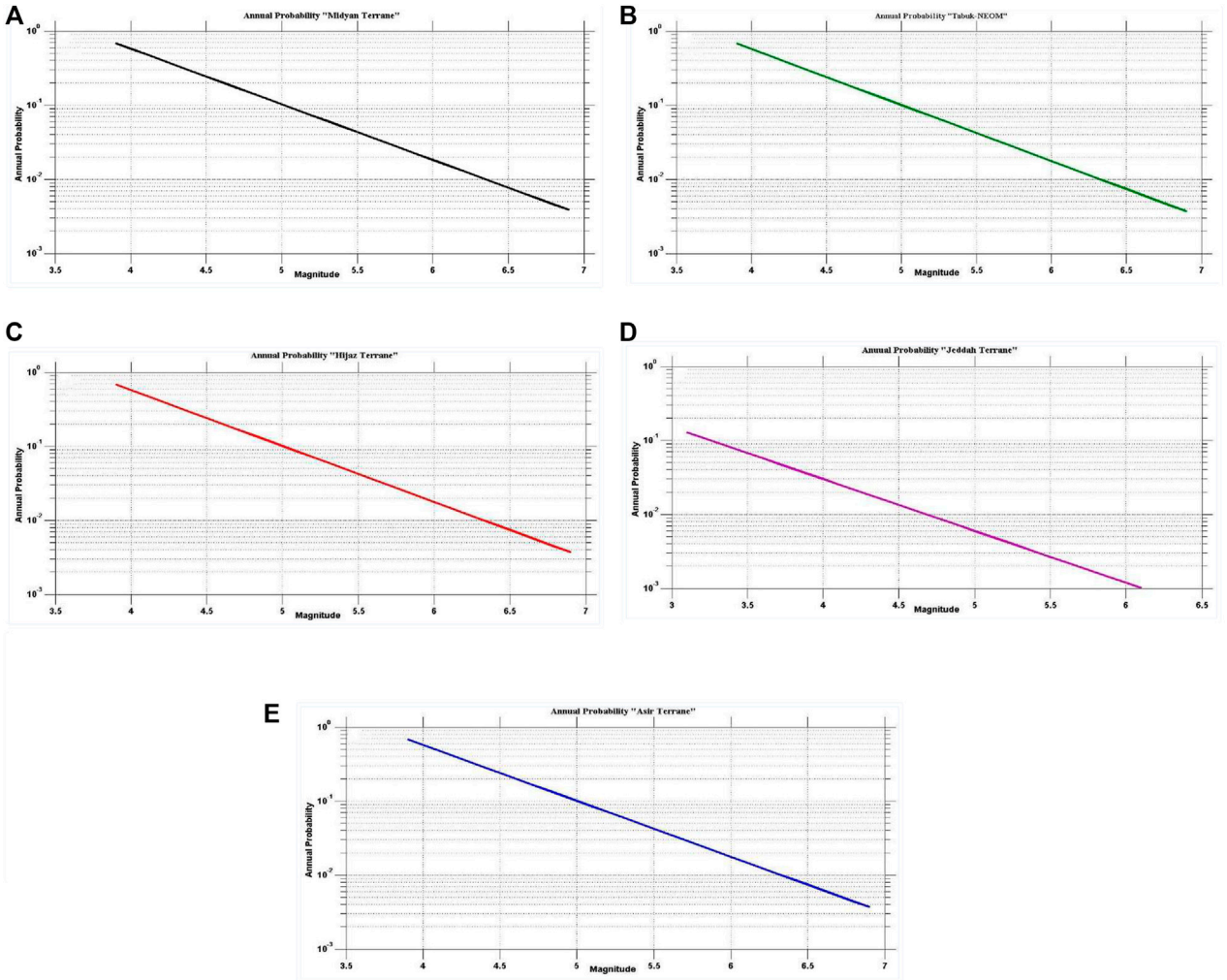

FIGURE 13 | (A–E) Annual probabilities of the earthquake activities in various levels of magnitude for the studied regions as represented by the color legend.

(**Figure 11**) display the higher seismic activity periods in 1993, 1995, 2001–2002, 2011, and 2017–2019 (Midyan), in 2005 (Tabuk), between 2002 and 2006 (Hijaz), in 2011 and between 2019 and 2020 (Jeddah), and between 2001 and2006 and 2017 and 2020 (Asir). The Magnitude rate distribution of the earthquakes (**Figure 12**) reveals an important increase in the number of large magnitude earthquakes in the period between 1993 and2009 in Midyan terrain, in 1996 and 2004 in Tabuk. Two events above magnitude 4.0 unlike the normal moderate activity with magnitudes below 3.0 are recorded in Hijaz terrane. The same for the Jeddah terrane, where most of the seismicity are below 3.0, except in 1994, where two events with magnitudes above 3.5 are reported. A random slight increase in magnitude is observed at Asir terrane from time to time.

The probability of occurrence of earthquakes of various magnitudes in certain time intervals is of the highest rate in Midyan terrane and lowest in Jeddah terrane (**Figure 13**), while the returned periods were found to be higher in Jeddah terrane and lowest in Midyan terrane (**Figure 14**). The maximum expected magnitudes (Mmax) are found to be 6.0 for Midyan terrane, 5.4 for Tabuk-Neom, 4.7 for Hijaz terrane, 4.8 for Jeddah terrane, and 7.7 for Asir terrane. The average recurrence intervals of earthquakes with the Mmax are ~7, ~20, ~6, ~120, and ~200 years for each seismic terrane, respectively.

9 DISCUSSION AND CONCLUSION

In the context of tectonic plate movements, complex structural patterns within the Arabian Plate related to the collision between Arabian and Eurasian plates have been interpreted. The slowing of the convergence or the onset of collision between Arabia and Eurasia, as well as the change in Africa–Eurasia motion may be reflected by a stepping of the locus of extension from the spreading axis to off axis dikes and temporarily correlated with the onset of volcanism within the western Arabian margin (Aldaajani et al., 2021).

Several geophysical studies indicate that the Arabian Shield is an active seismic region (Al-Noury and Ali, 1986; Al-Haddad

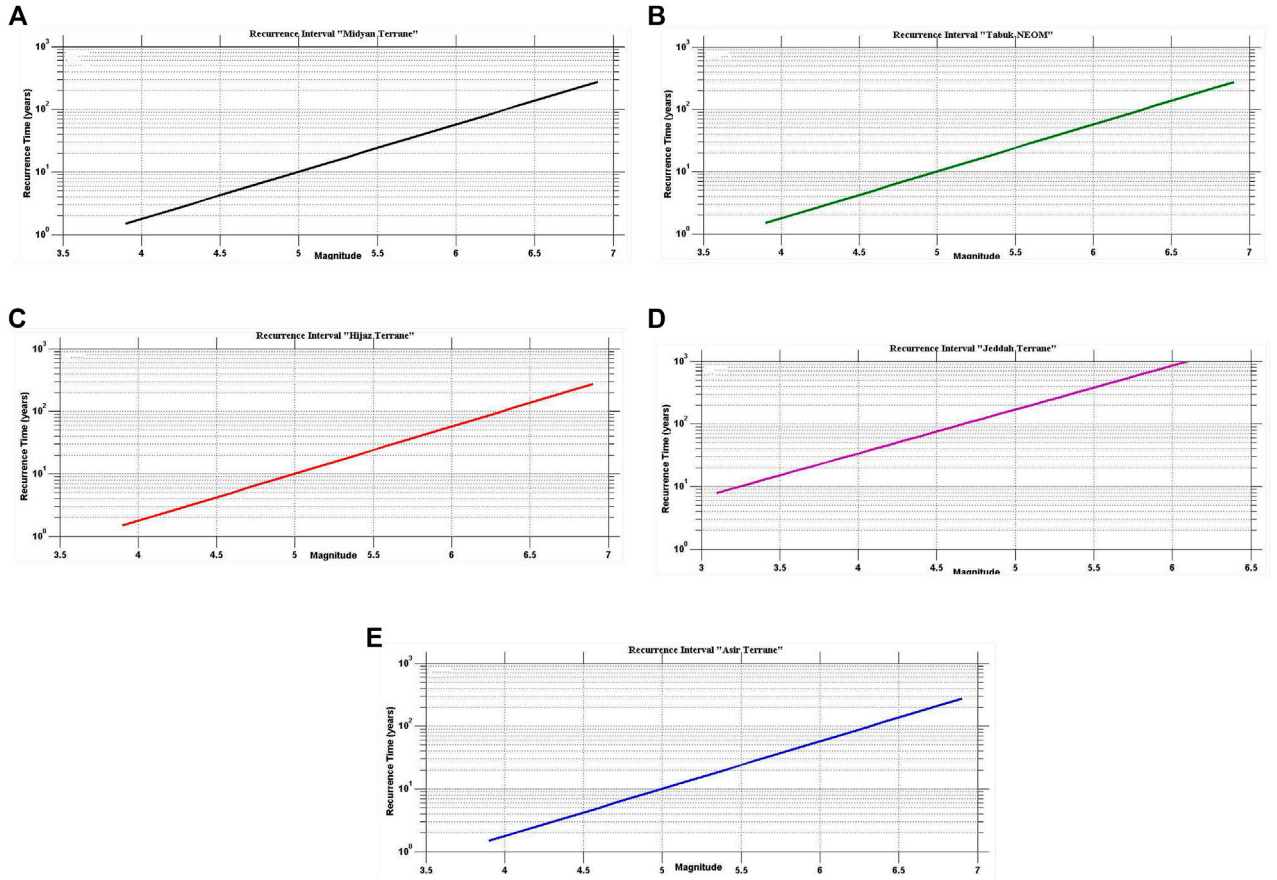

FIGURE 14 | (A–E) The recurrence interval for all earthquake magnitudes as represented by the color legend.

et al., 1994; Al-Amri, 2013; Youssef, 2015). The rapid economic expansion in the region has resulted in industrial development and intensive urbanization, with large engineering structures and projects already constructed, under construction, or being planned, such as dams for irrigation and power, desalination plants, and nuclear power plants.

The most recently compiled focal mechanism solutions of 122 earthquakes with $3.7 \leq ml \leq 7.1$ and depth ranges between 0 and 30 km demonstrate a dominant normal faulting mechanism with a minor component of strike-slip motion and the two nodal planes trending NW-SE. This type of mechanism presents the tectonic movement of the region and the NW-SE trend is consistent with the common trending faults. The dominantly extensional tectonic regime with nearly horizontal NE-SW trending delineates the influence of NE extension in the Red Sea. This stress system reactivated the preexisting lineaments of the Najd fault system, which was active during the Precambrian, and was reactivated several times during the geological history of the region (Agar, 1987; Stern, 1994). The above results get on well with the geological observations (Roobol, 2007) that exhibit that the Red Sea passive margin is undergoing extension by rotational normal faulting dipping both toward and away from the Red Sea that cause thinning of the Arabian Shield.

In order to determine the earthquake occurrences and earthquake recurrence characteristics in the study area, an initial earthquake dataset containing 3,750 seismic events recorded between 1941 and 2019 with magnitudes of 1.0 and 6.2 and depths between 0 and 50 km was examined. The statistical analyses have been performed on the whole dataset and the results demonstrate the sudden increase in the cumulative seismicity curves of the Arabian Shield in 2004 and 2018. The obtained a- and b-values were 4.53 and 0.64, respectively. The estimated magnitude of completeness was Mc = 2.4. The average magnitudes were estimated between 1 and 3.4. The predominant depths are about 0–10 km, and seismic activities in depths between 40 and 50 km with exceedingly low strain rates were also noticed. These activities could be within the lithospheric mantle where Volcanic fields in the mantle and lower-crustal zones are located. An increase of seismic activity in 2004 and 2018–2019 was displayed, and very low activities were noticed in the period between2013 and 2017.

In the current study all inadequate data of the catalog, as well as the aftershocks have been taken off, and each earthquake cluster has been replaced by an equivalent event using the declustering technique represented by Gardner and Knopoff (1974). Finally, a declustered earthquake catalog includes 2,991 earthquakes has been used to characterize the seismicity of the

study area. Keeping in view the prevalent tectonics and the geological, geophysical, and seismological data, the study area is represented by five zones (terranes) include Midyan terrane, Tabuk-Neom, Hijaz terrane, Jeddah terrane and Asir terrane.

The distributions of spatial magnitudes along the study area denote higher seismic activity records at the northwestern part of Arabian Shield, especially at Midyan and Tabuk-Neom with average magnitudes of 1.0–4.1 and 1.0–3.3, respectively, as well as at the southeastern Saudi Arabia at Asir terrane with an average magnitude of 1.0–2.2. Low seismic activities have been observed at Hijaz and Jeddah terranes. The temporal migrations of seismicity along the depth axis indicate that the seismic activity of the study area is concentrated in the upper crust zone in a shallow depth between 0 and 15 km.

In the current study, the maximum likelihood technique was applied to specify the seismicity of the areas under study and to calculate their associated seismicity parameters [Gutenberg–Richter (GR) recurrence parameters (a- and b-values) and the Magnitudes of completeness (Mc)]. Compared with the least-square regression method, this method gives more reasonable results (Aki, 1965). The ZMAP software has been used to compute Mc, a- and b-values. The results showed that the a-values varied between 2.70 and 4.35, and the b-values varied between 0.50 and 1.04.

The variations of the defined a- and b- values through the study regions not only reflect the geodynamic processes such as seafloor spreading and continental rift but also assess the seismic hazard that threatens the megaprojects in the regions such as the Red Sea Development and Neom. The highest b-value was determined in the Hijaz terrane (b = 1.04), which suggests that it is associated with a decreased risk of higher magnitude earthquakes. The lowest b-value was estimated in the Midyan terrane (b = 0.53) that indicates the higher risk of larger magnitude earthquakes. Since b-value is inversely related to stress (Woessner and Wiemer, 2005), so the Hijaz terrane is associated with low stress regime. This indicates the faults of this source zone are capable to generate numerous smaller magnitude earthquakes of short return periods, which agrees with the estimated maximum magnitude of ml = 4.7. In contrast, the Midyan terrane indicates high stress regime that may have high hazard of large magnitude earthquakes of large return periods, which is confirmed by the estimated maximum magnitude of ml = 6.0. The higher Mc values of 2.3 and 2.4 are obtained at the Hijaz terrane and Tabuk-Neom, respectively, while the lower values of Mc are of 1.4 for Midyan and Jeddah terranes. The lower value of Mc at the Midyan terrane demonstrates appropriate station distribution and high earthquake rates. However, at the Jeddah terrane the seismic activities are poorly detected (with only 68 events over magnitude 1.0) that probably leads to the small value of Mc. Mc thresholds in the Hijaz terrane and Tabuk-Neom are with higher values, where the station distribution is very poor.

The probability of occurrence and return periods for earthquakes of various magnitudes in each terrane indicate that the regions related to the Najd strike-slip fault system are probably the regions for large earthquake occurrences.

The results of the current study demonstrate the influence of tectonic activities, geodynamic processes, thickness of the crust, the active volcanic field in the lithospheric mantle, and the multiple directions of the faults and their densities and stresses on the locations and depths of the seismic activities in each terrane of the Arabian Shield. These results are consistent with the previous studies that have been done in the study area and surrounding regions, such as Al-Amri et al., 2004; El-Hadidy et al., 2015; Zahran et al., 2016; Alzahrani et al., 2022.

DATA AVAILABILITY STATEMENT

The original contributions presented in the study are included in the article/Supplementary Material. Further inquiries can be directed to the corresponding author.

AUTHOR CONTRIBUTIONS

SA gathered, retrieved, processed, analyzed, and interpreted the data, created and edited the figures, and was a contributor in writing and editing the manuscript. KA brought the idea of the research, gathered the structure, tectonic, and seismicity of the study area, plotted the study region map, and was a contributor in writing and editing the manuscript. All authors read and approved the final version of the manuscript.

FUNDING

This study was financed by the Researchers Supporting Project number (RSP-2021/351), King Saud University, Riyadh, Saudi Arabia. Funds are received for open access publication fees.

ACKNOWLEDGMENTS

Sincere thanks and gratitude to the Researchers Supporting Project number (RSP-2021/351), King Saud University, Riyadh, Saudi Arabia, for funding this research article. The authors are grateful to the reviewers and the handling editor for their constructive comments and suggestions.

REFERENCES

Agar, R. A. (1987). The Najd Fault System Revisited; a Two-Way Strike-Slip Orogen in the Saudi Arabian Shield. *J. Struct. Geology.* 9, 41–48. doi:10.1016/0191-8141(87)90042-3

Aki, K. (1965). Maximum Likelihood Estimates of B in the Formula Log N=a-bM and its Confidence Limits. *Bull. Earthq. Res. Inst. Univ. Tokyo* 43, 237–239.

Al-Amri, A. M., Punsslan, B. T., Khalil, A., and Uy, E. A. (2004). *Seismic hazard Assessment of Western Saudi Arabia and the Red Sea Region*. Japan: IISEE, 95–112.

Al-Amri, A. M. (2013). "Seismotectonics and Seismogenic Source Zones of the Arabian Platform," in *Lithosphere Dynamics and Sedimentary Basins: The Arabian Plate and Analogues*. Editors K. Al Hosani, F. Roure, R. Ellison, and S. Lokier (Springer Frontiers in Earth Sciences), 295–316. doi:10.1007/978-3-642-30609-9-1510.1007/978-3-642-30609-9_15

Al-Haddad, M., Siddiqi, G. H., Al-Zaid, R., Arafah, A., Necioglu, A., and Turkelli, N. (1994). A Basis for Evaluation of Seismic hazard and Design Criteria for Saudi Arabia. *Earthquake Spectra* 10, 231–258. doi:10.1193/1.1585773

Al-Malki, M. A., and Al-Amri, A. M. (2013). "Seismic Zones Regionalization and hazard Assessment of SW Arabian Shield and Southern Red Sea Region," in *Lithosphere Dynamics and Sedimentary Basins: The Arabian Plate and Analogues* (Springer), 317–331. doi:10.1007/978-3-642-30609-9_16

Al-Noury, S., and Ali, S. (1986). Seismic Risk Analysis of Western Arabia. *Eng. Geology.* 23, 95–108. doi:10.1016/0013-7952(86)90032-3

Aldaajani, T. Z., Almalki, K. A., and Betts, P. G. (2021). Plume versus Slab-Pull: Example from the Arabian Plate. *Front. Earth Sci.* 9, 494. doi:10.3389/feart.2021.700550

Ali, S. M., and Akkoyunlu, M. F. (2022). Statistical Analysis of Earthquake Catalogs for Seismic hazard Studies Around the Karliova Triple Junction (Eastern Turkey). *J. Afr. Earth Sci.* 186, 104436. doi:10.1016/j.jafrearsci.2021.104436

Ali, S. M., and Shanker, D. (2017). Study of Seismicity in the NW Himalaya and Adjoining Regions Using IMS Network. *J. Seismol.* 21, 317–334. doi:10.1007/s10950-016-9603-7

Ali, S. M. (2016). Statistical Analysis of Seismicity in Egypt and its Surroundings. *Arab J. Geosci.* 9, 52. doi:10.1007/s12517-015-2079-x

Alzahrani, H., Abdelrahman, K., Qaysi, S., and Baras, M. (2022). Seismicity of the Neom Megaproject Area, Northwestern Saudi Arabia. *J. King Saud Univ. - Sci.* 34, 101659. doi:10.1016/j.jksus.2021.101659

Ambraseys, N. N., and Adams, R. D. (1988). *The Seismicity of Saudi Arabia and Adjacent Areas: Part B. ICST/ KACST Project*. ESEE Rep. no. 88/11. London: Dept. of Civil Engineering, Imperial College of Science and Technology.

Ambraseys, N. N., Melville, C. P., and Adams, R. D. (1994). *The Seismicity of Egypt, Arabia and the Red Sea: A Historical Review*. Cambridge: Cambridge University Press.

Ambraseys, N. N., and Melville, C. P. (1989). Evidence for Intraplate Earthquakes in Northwestern Arabia. *Bull. Seism Soc. Am.* 79, 1279–1281.

Ambraseys, N. N., and Melville, C. P. (1988). *The Seismicity of Saudi Arabia and Adjacent Areas: Part A. ICST/ KACST Project*. ESEE Rep. no. 88/11. London: Dept. of Civil Engineering, Imperial College of Science and Technology.

ArRajehi, A., McClusky, S., Reilinger, R., Daoud, M., Alchalbi, A., Ergintav, S., et al. (2010). Geodetic Constraints on Present-Day Motion of the Arabian Plate: Implications for Red Sea and Gulf of Aden Rifting. *Tectonics* 29 (3), TC3011 (1–10). doi:10.1029/2009tc002482

Beydoun, Z. R. (1999). Evolution and Development of the Levant (Dead Sea Rift) Transform System: A Historical-Chronological Review of a Structural Controversy. *Geol. Soc. Lond. Spec. Publ.* 164 (1), 239–255. doi:10.1144/gsl.sp.1999.164.01.12

Bondár, I., and Storchak, D. (2011). Improved Location Procedures at the International Seismological Centre. *Geophys. J. Int.* 186, 1220–1244. doi:10.1111/j.1365-246X.2011.05107.x

Brown, G. F. (1970). A Discussion on the Structure and Evolution of the Red Sea and the Nature of the Red Sea, Gulf of Aden and Ethiopia Rift junction - Eastern Margin of the Red Sea and the Coastal Structures in Saudi Arabia. *Phil. Trans. R. Soc. Lond. A.* 267, 75–87. doi:10.1098/rsta.1970.0024

Davidson, I., Al-Kadasi, M., Al-Kihrbash, A., Baker, J., Blakey, S., Bosence, D., et al. (1994). Structural Evolution of the southeastern Red Sea Margin, Republic of Yemen. *Geol. Soc. Am. Bull.* 106, 1474–1493.

Efron, B. (1979). Bootstrap Methods: Another Look at the Jackknife. *Ann. Statist.* 7, 1–26. doi:10.1214/aos/1176344552

El-Hadidy, S. Y., Zahran, H. M., El-Hadidy, M., and Sami, M. (2015). "Seismicity and Seismotectonic Settings of Western Saudi Arabia with Special Emphasis of 5.1 Baish-Jizan Earthquake 2014," in Workshop on Imaging and Active Tectonics of the Red Sea Region, Kingdom of Saudi Arabia, March 10-13, 2015 (King Abdulaziz University of Science and Technology KAUST).

El-Isa, Z. H., and Shanti, A. A. (1989). Seismicity and Tectonics of the Red Sea and Western Arabia. *Geophys. J.* 97, 449–457. doi:10.1111/j.1365-246x.1989.tb00515.x

Frankel, A. (1995). Mapping Seismic hazard in the Central and Eastern United States. *Seismol. Res. Lett.* 66 (4), 8–21. doi:10.1785/gssrl.66.4.8

Frohlich, C., Gan, W., and Herrmann, R. B. (2015). Two Deep Earthquakes in Wyoming. *Seismol. Res. Lett.* 86, 810–818. doi:10.1785/0220140197

Gardner, J. K., and Knopoff, L. (1974). Is the Sequence of Earthquakes in Southern California, with Aftershocks Removed, Poissonian? *Bull. Seismol. Soc. Am.* 64 (5), 1363–1367. doi:10.1785/bssa0640051363

Genna, A., Nehlig, P., Le Goff, E., Guerrot, C., and Shanti, M. (2002). Proterozoic Tectonism of the Arabian Shield. *Precambr. Res.* 117, 21–40. doi:10.1016/s0301-9268(02)00061-x

Ghebreab, W. (1998). Tectonics of the Red Sea Region Reassessed. *Earth Sci. Rev.* 45, 1–44. doi:10.1016/S0012-8252(98)00036-1

Girdler, R. W. (1991). The Afro-Arabian Rift System-An Overview. *Tectonophysics* 197, 139–153. doi:10.1016/0040-1951(91)90038-t

Gutenberg, R., and Richter, C. F. (1944). Earthquake Magnitude, Intensity, Energy, and Acceleration. *Bull. Seismol Soc. Am.* 32, 163–191.

Hafiez, H. E. A., and Toni, M. (2020). Magnitude of Completeness for the Northern Stations of the Egyptian National Seismological Network. *Arab J. Geosci.* 13 (12), 458–461. doi:10.1007/s12517-020-05461-0

International Seismological Centre (ISC) (2021). On-line Bulletin. Available at: http://www.isc.ac.uk/iscbulletin/search/catalogue/. doi:10.31905/D808B830

Jamali, F., Aghda, S. M. F., and Aliyari, A. (2006). *Evaluation of Seismic Sources for hazard Assessment in the Fujairah Emirate (UAE)*. London, UK: The Geological Society of London. IAEG2006, 305 (1–6).

Johnson, P. R. (1998). *Tectonic Map of Saudi Arabia and Adjacent areasMinistry of Petroleum and Mineral Resources*. Jiddah, Saudi Arabia: Deputy Ministry for Mineral Resources. Technical Report USGS TR-98-3 (IR 948).

Kennett, B. L. N., Engdahl, E. R., and Buland, R. (1995). Constraints on Seismic Velocities in the Earth from Traveltimes. *Geophys. J. Int.* 122, 108–124. doi:10.1111/j.1365-246x.1995.tb03540.x

Kijko, A. (2004). Estimation of the Maximum Earthquake Magnitude, M max. *Pure Appl. Geophys.* 161, 1655–1681. doi:10.1007/s00024-004-2531-4

Klinger, Y., Rivera, L., Haessler, H., and Maurin, J.-C. (1999). Active Faulting in the Gulf of Aqaba: New Knowledge from the Mw 7.3 Earthquake of 22 November 1995. *Bull. Seismol Soc. Am.* 89, 1025–1036. doi:10.1785/bssa0890041025

Kröner, A. (1985). Ophiolites and the Evolution of Tectonic Boundaries in the Late Proterozoic Arabian-Nubian Shield of Northeast Africa and Arabia. *Precambr. Res.* 27, 277–300. doi:10.1016/0301-9268(85)90016-6

Leonard, T., Papasouliotis, O., and Main, I. G. (2001). A Poisson Model for Identifying Characteristic Size Effects in Frequency Data: Application to Frequency-Size Distributions for Global Earthquakes, "starquakes", and Fault Lengths. *J. Geophys. Res.* 106 (B7), 13473–13484. doi:10.1029/2000jb900429

Manakou, M. V., and Tsapanos, T. M. (2000). Seismicity and Seismic hazard Parameters Evaluation in the Island of Crete and the Surrounding Area Inferred from Mixed Data Files. *Tectonophysics* 321, 157–178. doi:10.1016/s0040-1951(00)00075-5

Michael, A. J. (2014). How Complete Is the ISC-GEM Global Earthquake Catalog? *Bull. Seismol. Soc. Am.* 104, 1829–1837. doi:10.1785/0120130227

Mignan, A., Werner, M. J., Wiemer, S., Chen, C. C., and Wu, Y. M. (2011). Bayesian Estimation of the Spatially Varying Completeness Magnitude of Earthquake Catalogs. *Bull. Seismol. Soc. Am.* 101, 1371–1385. doi:10.1785/0120100223

Mignan, A., and Woessner, J. (2012). *Estimating the Magnitude of Completeness for Earthquake Catalogs*. Community Online Resource for Statistical Seismicity Analysis. ETH Zurich: Swiss Seismological Service, 45. Available at: http://www.corssa.org. doi:10.5078/corssa-00180805

Mogi, K. (1962). Magnitude–frequency Relationship for Elastic Shocks Accompanying Fractures of Various Materials and Some Related Problems in Earthquakes. *Bull. Earthq Res. Inst. Univ. Tokyo* 40, 831–883.

Petersen, M. D., Bryant, W. A., Cramer, C. H., Cao, T., Reichle, N. S., Frankel, A. D., et al. (1996). *Probabilistic Seismic hazard Assessment for the State of California*. Open-File Report 96–08, USGS Open File Report 96–706. California, USA: California Dept. of Conservation Division of Mines and Geology. doi:10.3133/ofr96706

Prieto, G. A., Froment, B., Yu, C., Poli, P., and Abercrombie, R. (2017). Earthquake Rupture below the Brittle-Ductile Transition in continental Lithospheric Mantle. *Sci. Adv.* 3, e1602642. doi:10.1126/sciadv.1602642

Reasenberg, P. (1985). Second-order Moment of central California Seismicity, 1969-1982. *J. Geophys. Res.* 90, 5479–5495. doi:10.1029/jb090ib07p05479

Reilinger, R., McClusky, S., Vernant, P., Lawrence, S., Ergintav, S., Cakmak, R., et al. (2006). GPS Constraints on continental Deformation in the Africa-Arabia-Eurasia continental Collision Zone and Implications for the Dynamics of Plate Interactions. *J. Geophys. Res.* 111, B05411 (1–26). doi:10.1029/2005jb004051

Roobol, J. (2007). "Cenozoic Faults in Western Saudi Arabia," in 7th meeting of the Saudi society for geosciences, Riyadh, Saudi Arabia (King Saud University).

Rydelek, P. A., and Sacks, I. S. (1989). Testing the Completeness of Earthquake Catalogues and the Hypothesis of Self-Similarity. *Nature* 337, 251–253. doi:10.1038/337251a0

Scholz, C. H. (1968). The Frequency-Magnitude Relation of Microfracturing in Rock and its Relation to Earthquakes. *Bull. Seismol Soc. Am.* 58, 399–415. doi:10.1785/bssa0580010399

Schorlemmer, D., Wiemer, S., and Wyss, M. (2005). Variations in Earthquake-Size Distribution across Different Stress Regimes. *Nature* 437 (7058), 539–542. doi:10.1038/nature04094

Sharland, P. R., Archer, R., Casey, D. M., Davies, R. B., Hall, S. H., Heward, A. P., et al. (2001). *Arabian Plate Sequence Stratigraphy*, 2. Bahrain: GeoArabia Special Publication, 371.

Stern, R. J. (1994). Arc Assembly and continental Collision in the Neoproterozoic East African Orogen: Implications for the Consolidation of Gondwanaland. *Annu. Rev. Earth Planet. Sci.* 22, 319–351. doi:10.1146/annurev.ea.22.050194.001535

Stern, R. J., and Johnson, P. (2010). Continental Lithosphere of the Arabian Plate: a Geologic, Petrologic, and Geophysical Synthesis. *Earth-Science Rev.* 101, 29–67. doi:10.1016/j.earscirev.2010.01.002

Stiphout, T. v., Zhuang, J., and Marsan, D. (2012). "Theme V -Models and Techniques for Analysing Seismicity,". Technical report in *Community Online Resource for Statistical Seismicity Analysis*. Available at: http://www.corssa.org.

Stoeser, D. B., and Camp, V. E. (1985). Pan-African Microplate Accretion of the Arabian Shield. *Geol. Soc. Am. Bull.* 96, 817–826. doi:10.1130/0016-7606(1985)96<817:pmaota>2.0.co;2

Storchak, D. A., Harris, J., Brown, L., Lieser, K., Shumba, B., Verney, R., et al. (2017). Rebuild of the Bulletin of the International Seismological Centre (ISC), Part 1: 1964-1979. *Geosci. Lett.* 4 (32), 1–14. doi:10.1186/s40562-017-0098-z

Uhrhammer, R. (1986). Characteristics of Northern and Central California Seismicity. *Earthquake Notes* 57.1, 21.

Walpersdorf, A., Hatzfeld, D., Nankali, H., Tavakoli, F., Nilforoushan, F., Tatar, M., et al. (2006). Difference in the GPS Deformation Pattern of North and Central Zagros (Iran). *Geophys. J. Int.* 167 (3), 1077–1088. doi:10.1111/j.1365-246x.2006.03147.x

Wells, D. L., and Coppersmith, K. J. (1994). New Empirical Relationships Among Magnitude, Rupture Length, Rupture Width, Rupture Area, and Surface Displacement. *Bull. Seismol Soc. Am.* 84, 974–1002.

Wiemer, S. (2001). A Software Package to Analyze Seismicity: ZMAP. *Seismol. Res. Lett.* 72, 373–382. doi:10.1785/gssrl.72.3.373

Wiemer, S., and Wyss, M. (2000). Minimum Magnitude of Completeness in Earthquake Catalogs: Examples from Alaska, the Western United States, and Japan. *Bull. Seismol. Soc. Am.* 90, 859–869. doi:10.1785/0119990114

Woessner, J., and Wiemer, S. (2005). Assessing the Quality of Earthquake Catalogues: Estimating the Magnitude of Completeness and its Uncertainty. *Bull. Seismol. Soc. Am.* 95, 684–698. doi:10.1785/0120040007

Youssef, S. E.-H. (2015). "Seismicity and Seismotectonic Setting of the Red Sea and Adjacent Areas," in *The Red Sea*. Editors N. M. A. Rasul and I. C. F. Stewart (Berlin Heidelberg: Springer Earth System Sciences), 151–159. doi:10.1007/978-3-662-45201-1_8

Zahran, H. M., Sokolov, V., Roobol, M. J., Stewart, I. C. F., El-Hadidy Youssef, S., and El-Hadidy, M. (2016). On the Development of a Seismic Source Zonation Model for Seismic hazard Assessment in Western Saudi Arabia. *J. Seismol.* 20, 747–769. doi:10.1007/s10950-016-9555-y

Author Disclaimer: The views expressed on this paper are those of the authors and do not necessarily reflect the views of the organizations that the authors represent.

Conflict of Interest: The authors declare that the research was conducted in the absence of any commercial or financial relationships that could be construed as a potential conflict of interest.

Publisher's Note: All claims expressed in this article are solely those of the authors and do not necessarily represent those of their affiliated organizations, or those of the publisher, the editors, and the reviewers. Any product that may be evaluated in this article, or claim that may be made by its manufacturer, is not guaranteed nor endorsed by the publisher.

APPENDIX A

The ISC contributor institutes mentioned in this study are given below. The ISS and GUTE catalogs are used for the events in the period of 1900–1964.

Code Institute

ISC International Seismological Centre

ISS International Seismological Summary [for 1900–1964]

GUTE Gutenberg and Richter (1954) [for 1900–1952]

CSEM European-Mediterranean Seismological Centre - EMSC (France)

ISK B.U. Kandilli Observatory and Earthquake Research Institute (Turkey)

DDA General Directorate of Disaster Affair (Turkey), until September 2017

AFAD Disaster and Emergency Management Presidency (Turkey), since October 2017

ATH National Observatory of Athens (Greece)

THE Dept. of Geophysics, Aristotle University of Thessaloniki (Greece)

MOS Geophysical Survey of Russian Academy of Sciences (Russia)

TEH Tehran University (Iran)

TAB Tabriz Seismological Observatory (Iran)

TIF Institute of Earth Sciences/ National Seismic Monitoring Center (Georgia)

SOF National Institute of Geophysics, Geology, and Geography (Bulgaria)

BUC National Institute for Earth Physics (Romania)

SIGU Subbotin Institute of Geophysics, National Academy of Sciences (Ukraine)

IPER Institute of Physics of the Earth, Academy of Sciences, Moscow (Russia)

NSSP National Survey of Seismic Protection (Armenia)

AZER Republican Seismic Survey Centre of Azerbaijan National Academy of Sciences (Azerbaijan)

NSSC National Syrian Seismological Centre (Syria)

THR International Institute of Earthquake Engineering and Seismology (Iran)

frontiers in Earth Science

ORIGINAL RESEARCH
published: 23 March 2022
doi: 10.3389/feart.2022.849079

Interpretation of Magnetic Anomalies by Simple Geometrical Structures Using the Manta-Ray Foraging Optimization

Ubong C. Ben[1], Stephen E. Ekwok[1], Anthony E. Akpan[1], Charles C. Mbonu[2], Ahmed M. Eldosouky[3], Kamal Abdelrahman[4] and David Gómez-Ortiz[5]*

[1]Department of Geophysics, University of Calabar, Calabar, Nigeria, [2]Department of Physics, University of Uyo, Uyo, Nigeria, [3]Geology Department, Faculty of Science, Suez University, Suez, Egypt, [4]Department of Geology and Geophysics, College of Science, King Saud University, Riyadh, Saudi Arabia, [5]Department of Biology and Geology, Physics and Inorganic Chemistry, ESCET, Universidad Rey Juan Carlos, Móstoles, Spain

In this paper, a geophysical strategy based on the recently proposed Manta-Ray Foraging (MRF) Optimization algorithm is adapted and presented for the blind computation of depth/shape defining parameters from magnetic anomalies due to buried geo-bodies. The model parameters deciphered are the coefficient of amplitude (K), buried structure's origin (x_0), the depth (z), magnetization angle (α), and a shape factor (q). After detailed and piecewise design, the new inversion tool is originally trial-tested on anomaly data generated synthetically. The uncorrupted version of the test data is first analyzed, then - it is corrupted with noise varied at 5, 10, 15, and 20% corruption levels. Thereafter, it is experimented with magnetic profiles taken from exploration fields in the United States, Peru, and Egypt. From the evaluation of results obtained, the new procedure is observed as exhibiting outstanding stability and flexibility especially with noisy dataset and notable efficiency in the quantitative resolution of magnetic inversion problems. The results obtained for the field cases are also mostly consistent especially when compared with background results from similar studies conducted with other methods; further affirming the new tool as reliable for the geophysical investigation of buried minerals.

Keywords: shapes, anomaly, optimization, manta ray minerals, interpretation, magnetics

OPEN ACCESS

Edited by:
Mourad Bezzeghoud, Universidade de Évora, Portugal

Reviewed by:
Khalid ESSA, Cairo University, Egypt
Arkoprovo Biswas, Banaras Hindu University, India
Salah Mehanee, Cairo University, Egypt

****Correspondence:***
Ahmed M. Eldosouky
dr_a.eldosoky@yahoo.com

Specialty section:
This article was submitted to Solid Earth Geophysics, a section of the journal Frontiers in Earth Science

Received: *05 January 2022*
Accepted: *28 February 2022*
Published: *23 March 2022*

Citation:
Ben UC, Ekwok SE, Akpan AE, Mbonu CC, Eldosouky AM, Abdelrahman K and Gómez-Ortiz D (2022) Interpretation of Magnetic Anomalies by Simple Geometrical Structures Using the Manta-Ray Foraging Optimization. Front. Earth Sci. 10:849079. doi: 10.3389/feart.2022.849079

INTRODUCTION

Magnetic, gravity, electromagnetic, DC resistivity and self-potential techniques have successful applications in mineral exploration (e.g., Biswas et al., 2014; Portniaguine & Zhdanov, 2000a; Mehanee & Zhdanov, 2004; Pellerin & Wannamaker, 2005; Essa et al., 2021; Mehanee, 2022a; Mehanee, 2022b). Synonymous with other conventional geophysical methods, optimal interpretations require that magnetic field data be analyzed in ways generally deemed best for the recovery of characteristic parameters mirroring those of the features causing the anomalies (Klein et al., 2016; Balkaya et al., 2017; Xie et al., 2019; Ben et al., 2021c). Generally, geologic structures are extensively classified into four geometrical categories: spheres, thin sheets, infinitely long cylinders, and geological contacts (Ben et al., 2021a). These simple geometric models conveniently approximate structures that are commonly in during magnetic data interpretation. Geophysical inversion aims at unraveling parameters characteristic of geologic structures through numerical adjustments to these

already defined models (Essa & Elhussein, 2020; Essa et al., 2020). The notably sought-for parameters are usually those defining anomaly position (in space), depth, and those characterizing the anomaly shape (Ekinci et al., 2021; Essa et al., 2021; Mehanee, 2022b).

A review of published literature reveals that several strategies have been priorly employed for magnetic inversion. An adept number of them take advantage of computational approaches such as those consistent with classical/numerical theories. Gay (1965) using conventional curve fitting theories developed standard curves for common geologic structures. Abo-Ezz & Essa (2016) introduced a linear least-squares method for the deciphering of buried geologic bodies from magnetic anomaly profiles. Araffa et al. (2018) employed Euler deconvolution to delineate subsurface structural features of basement complex from magnetic data. Ouyang & Chen (2020) iteratively modeled magnetic anomalies using the Fourier transform technique. Duong et al. (2021) interpreted magnetic data at low latitude areas using Marquardt algorithm and continuous wavelet transform. Some of other deterministic methods experimented and reported in literature for magnetic anomalies include fair function minimization procedures (Asfahani & Tlas, 2012; Abbas & Fedi, 2013), simplex algorithm (Pan et al., 2009; Abdelrahman et al., 2019), regularized inversion and image focusing (Portniaguine & Zhdanov, 2000b) and Hilbert Transform (Dondurur and Pamukçu, 2003). However, these inversion techniques sometimes generate poor solutions mostly accrued to causatives such as recursive noise, window size incompatibility and the number of data points considered in the interpretation out of the entire magnetic data profile. Furthermore, the majority of them rely heavily on a series of initializations derived from subjective historical geologic deductions. This pre-knowledge is not always available and even if they are, their reputability can sometimes be disputed.

With recent advancements in machine intelligence and with increased efforts to address the aforementioned challenges, interpretative heuristic methodologies are increasingly being introduced for magnetic anomaly interpretations. Some of these methodologies are based on; genetic algorithm, particle swarm, differential evolution, ant colony optimization, and genetic-price algorithm. Liu et al. (2015) optimized interpretation of surface and subsurface magnetic measurements using ant colony optimization. Biswas & Acharya (2016) deployed VFSA for the interpretation and modeling of magnetic anomaly over a vertically magnetized rod-like structure. Biswas et al. (2017) developed an approach to the estimation model parameters from the total gradient of magnetic data based on Very Fast simulated Annealing (VFSA). Agarwal et al. (2018) developed a grey-wolf optimer based

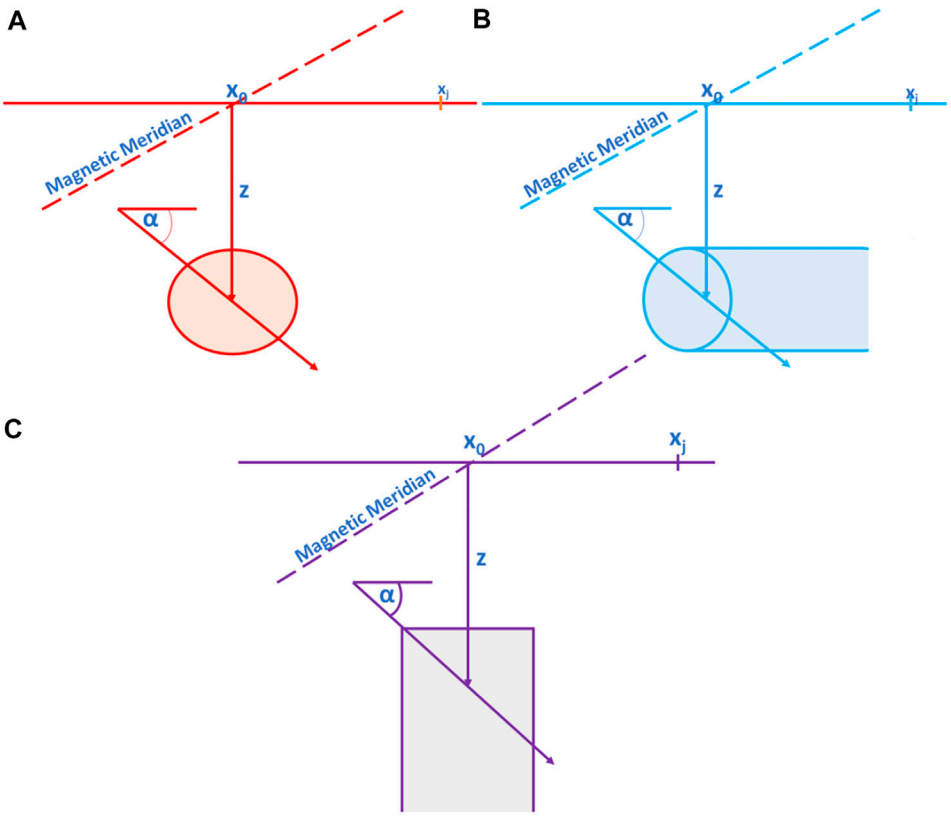

FIGURE 1 | Schematic cross-sections showing configurations of simple geometrical shaped models and their parameters; **(A)** Sphere **(B)** Horizontal cylinder **(C)** Thin sheet.

TABLE 1 | Characteristic inclination parameter for vertical, horizontal and total magnetic field anomalies due to thin sheets and horizontal cylinders (after Gay, 1963, Gay, 1965).

Magnetic Field	Inclination Parameter	
	Thin sheet	Horizontal cylinder
Vertical	I_T-§	I_T-90
Horizontal	I_T-§-90	I_T-180
Total	$2I_T$-§-90	$2I_T$-180

methodology for the inversion of magnetic datasets from surface and airborne surveys. Ekinci et al. (2019) in their comparative study analyzed the performance of differential evolution against particle swarm optimization for magnetic parameterization through direct search. Essa & Elhussein (2020) emphasized the employment of particle swarm optimization for the inferring of residual magnetic anomalies. Di Maio et al. (2020) introduced a hybrid genetic-price heuristic for the inverse modeling of magnetic anomalies due to simple geological structures. Gobashy et al. (2020) introduced the Whale Optimization Algorithm for the assessment of model parameters from magnetic anomalies over mineralization structures. Balkaya & Kaftan (2021) conducted inverse modeling of intrusive structures using differential search algorithm. Essa et al. (2021) applied the variance analysis method for magnetic profile interpretation. Mehanee et al. (2021) carried out magnetic modeling using a R-parameter imaging approach. Balkaya & Kaftan (2021) interpreted magnetic anomalies caused by dyke-shaped bodies using differential search algorithm. Du et al. (2021) proposed a new method to conduct lp norm magnetic inversion of 2D data using adaptive differential evolution technique. The most obvious advantage of meta-heuristics techniques is that unlike their analytical strategies, improvements in directions referencing the feasible solution are not influenced by the gradients of the minimized objective function (Kombe & Muguthu, 2019; Elaziz et al., 2020; Hayyolalam & Pourhaji Kazem, 2020).

Noting the meritoriousness of the aforementioned, especially in interpretative resolvability of buried structures, the reader may be puzzled as to why a new optimizer-based procedure is still developed to solve problems that previous optimizers have already solved. A geophysical interpretation of the infamous No Free Lunch Theorem of Optimization (Salcedo-Sanz et al., 2018; Gharehchopogh & Gholizadeh, 2019; Gupta & Deep, 2019) presents an appropriate response to this question. This is that, while the majority of the previously proposed methodologies based on intelligent optimization algorithms have greatly improved anomaly interpretation quality, analytical perfection has yet to be achieved, particularly in terms of convergence and computation complexity. The continuous pursuit of analytical perfection necessitates the testing of new optimizers. This is also the primary motivation for this research. In this research paper, we present a new interpretative methodology for describing geophysical anomalies over different geometrically-shaped geologic bodies. The methodology is based on the manta-ray foraging (MRF) optimization algorithm.

The MRF algorithm–originally introduced by Zhao et al. (2020) leverages the foraging actions of manta rays for resolving physical optimization problems. This is accomplished by imitating the chain, cyclone, and saumasault foraging techniques–three of the manta ray's most efficient foraging strategies. Ensuing experimentations in other fields such as pharmacy and engineering, the optimization technique was found to outperform existing metaheuristic algorithms especially in the aspects of computing cost, performance, and solution accuracy (Elaziz et al., 2020; Hemeida et al., 2020; Xu et al., 2020; Ghosh et al., 2021; Hassan et al., 2021; Houssein et al., 2021), the method has been recommended for the resolution of structural problems such as those in geophysics (Elaziz et al., 2020; Xu et al., 2020; Ghosh et al., 2021; Houssein et al., 2021). It is worthy to note the efforts of Ben et al. (2021b) with vertically dipping dykes and Ben et al. (2021a) with gravity anomalies. Howbeit, to the best of the authors' knowledge, and at the time of preparation of the initial drafting of this research paper, no study in published literature has explicitly employed MRF algorithm for the modeling of magnetized subsurface materials of geometric structure. The new method presents a couple of merits. First, unlike deterministic schemes, iterative computations are independent of the gradient of the objective function, technically limiting immature convergence. Also, the wild function injected during the cyclone foraging stage of the algorithm design allows initial models to parametrize from anywhere within a size-independent range (as would be seen in the examples)—reducing reliance on subjectivity. Most importantly, the superiority of the MRF tool actually lies with its foraging character. With MRF algorithm, the search agents are allowed to switch intelligently and at any point between the strategies of chain foraging and cyclone foraging. The chain foraging behavior allows significant local search while the

TABLE 2 | Definitions of A, B and C parameters.

Parameter	Sphere (total mag. Field)	Sphere (vertical mag. Field)	Spheres (horizontal mag. Field)	Horizontal cylinders; thin sheets (FHD); geological contacts (SHD), (all fields)	Thin sheets; geological contacts (FHD) (all fields)
A	$3\sin^2\alpha - 1$	$2\sin\alpha$	$-\cos\alpha$	$\cos\alpha$	$\frac{\cos\alpha}{z}$
B	$-3z\sin(2\alpha)$	$-3z\cos\alpha$	$-3z\sin\alpha$	$2z\sin\alpha$	$\sin\alpha$
C	$3\cos^2\alpha - 1$	$-\sin\alpha$	$2\cos\alpha$	$-\cos\alpha$	0

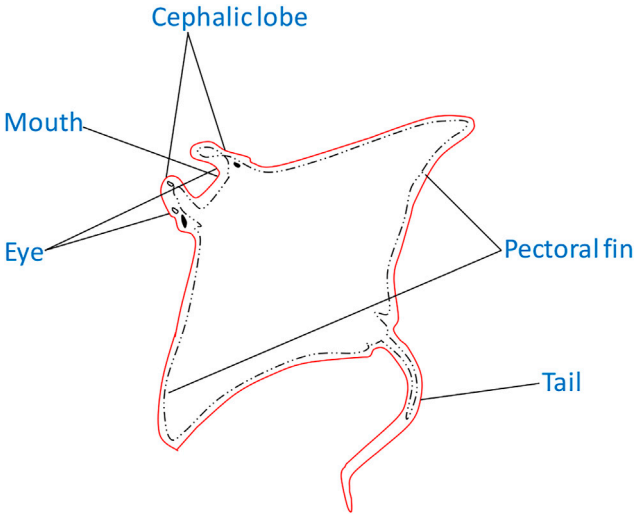

FIGURE 2 | Anatomical structure of a conventional Manta ray.

cyclone foraging behavior concurrently assures non-deteororation of global search during the process; a mutualization of the two as allowed by the new technique ensures comparatively quality solutions through thorough exploration of the whole domain of the geophysical problem.

The paper begins with a magnetic inversion problem layout and a step-by-step architecture of the MRF-based inversion technique. The approach is then trial-tested through applications to synthetic models that have been contaminated with varying degrees of Gaussian random noise (0, 5, 10, 20, and 20%) as well as anomalies from multiple/interfering models. The methodology's performance with real-world anomalies is gauged using field profiles taken from geologically-contrast exploration mining areas. The resultant parameter values are then compared against drilling results and those obtained using other traditional approaches and documented in literature. Finally, we conclude the paper with a review of the adaptability and performance of MRF optimization method as an inversion tool for magnetic anomalies as well as its gains and limitations with respect to previous techniques.

Initialize population, T and individual manta rays $y^4_i(t) = y^4_i + rand().(LB-UB)$ for i=1,2,...,N and t=1
Calculate fitness for each individual and obtain y^4_{best}
while stopping criterion is not satisfied? **do**
  for i = 1,2,3,....N do
    if rand() < 0.5 then #*Cyclone Foraging*
      if t/T < rand() **then**
        $y^4_i(t+1) = \begin{cases} y^4_{best}(t) + rand().(y^4_{best}(t) - y^4_i(t)) + \mu.(y^4_{best}(t) - y^4_i(t)) & i=1 \\ y^4_{best}(t) + rand().(y^4_{i-1}(t) - y^4_i(t)) + \mu.(y^4_{best}(t) - y^4_i(t)) & i=2,3,\ldots,T \end{cases}$
      else
    else #*Chain Foraging*
      $y^4_i(t+1) = \begin{cases} y^4_i(t) + r.(y^4_{best}(t) - y^4_i(t)) + w.(y^4_{best}(t) - y^4_i(t)) & i=1 \\ y^4_i(t) + r.(y^4_{i-1}(t) - y^4_i(t)) + w.(y^4_{best}(t) - y^4_i(t)) & i=2,3,\ldots,T \end{cases}$
      end if
    Calcute fitness for *ith* individual $f(y^4_i(t+1))$
    if $f(y^4_i(t+1)) < f(y^4_{best})$ **then**
      $y^4_{best} = y^4_i(t+1)$
    end if
  end for
  #*Somersault Foraging*
  for i = 1...N **do**
    $y^4_i(t+1) = y^4_i(t) + P.(rand_1().y^4_i(t) - rand_2().y^4_i(t), \quad i = 1, 2, \ldots, N$
  Calculate fitness for ith individual $f(y_i(t+1))$
    if $f(y^4_i(t+1)) < f(y^4_{best})$ **then**
      $y^4_{best} = y_i(t+1)$
    end if
  end for
end while
return y^4_{best}

FIGURE 3 | Pseudocode of the MRF algorithm.

TABLE 3 | Estimated parameters for the example involving synthetically generated noise-free models.

Type of model	Parameters	True	Estimated				
			Noise free	5% noise	10% noise	15% noise	20% noise
Sphere	K ($nT.m^3$)	11000.000	11001.300	11615.407	11907.531	12006.877	12294.040
	α (^{0})	60.000	60.000	60.983	61.217	59.745	60.022
	z (m)	11.000	11.000	11.629	11.892	12.105	12.205
	x_0(m)	0.000	0.000	0.001	0.001	0.000	0.000
	q	2.500	2.500	2.503	2.498	2.502	2.492
	Time elapsed		31s	33s	35s	35s	37s
Horizontal Cylinder	K ($nT.m^2$)	400.000	401.021	402.573	387.476	376.085	421.741
	α (^{0})	35.000	34.998	34.861	33.904	31.653	30.002
	z (m)	5.000	5.000	5.388	5.142	5.271	5.300
	x_0(m)	0.000	0.000	0.000	0.002	- 0.007	0.003
	q	2.000	2.000	2.000	1.986	2.002	2.007
	Time elapsed		30s	32s	32s	34s	36s
Thin Sheet	K (nT.m)	550.000	550.000	550.041	545.703	543.681	558.039
	α (0)	30.000	30.000	30.584	29.628	28.518	29.711
	z (m)	9.000	9.000	8.927	8.887	8.700	8.768
	x_0(m)	0.00	0.002	0.004	0.010	0.012	0.016
	q	1.00	1.005	1.002	1.005	1.009	1.015
	Time Elapsed		32s	34s	35s	37s	40s

METHODOLOGY

Geophysical Inversion and the Magnetic Anomaly Problem

In geophysical exploration, magnetic data inversion is generally initiated by transforming so-called ill-posed problems to optimization models constructed such that the parameters of the model explained by observation data are good descriptions of the subsurface anomaly (Mehanee et al., 1998; Liu et al., 2015; Essa & Elhussein, 2020; Mbonu et al., 2021). The process of finding a solution to an inverse problem normally begins with the supposition of a good initial model. This initial model commonly made from drilling data or reports from previous geophysical expositions is progressively smoothened in stepwise iterative runs until a subjectively suitable fit between the measured and estimated data is acquired. The smoothening is executed by making meta-heuristic forward adjustments to the parameters of the model (Gharehchopogh & Gholizadeh, 2019; Wang & Li, 2019; Hayyolalam & Pourhaji Kazem, 2020). In this research, the model parameters of interest are amplitude coefficient (K) related to the composition of the body, depth (z), location of the origin (x_o), angle of magnetization (α), and a shape factor (q) whose value is unique for each different structural shape (**Figure 1**)

For this study, we employ the general formula for magnetic anomaly profile -T (x_j) over simple-geometrically shaped structures meticulously extrapolated from the inductive analysis of mathematical expressions for horizontal, vertical, and total magnetic anomaly of spheres (Prakasa Rao & Subrahmanyam, 1988), horizontal cylinders (Rao et al., 1973) and thin sheets (Gay, 1963). The formula (**Equation 1**) is given as (Mehanee et al., 2021):

$$T(x_j) = K\frac{Az^2 + B(x_j - x_0) + C(x_j - x_0)^2}{\left[(x_j - x_0)^2 + z^2\right]^q}, \quad j = 1, 2, 3, 4, \ldots \quad (1)$$

where z is depth to the buried anomaly, K the amplitude coefficient and, α the angle of magnetization normally in the plane of the principle profile coinciding with the *x*-direction. This is illustrated by Prakasa Rao and Subrahmanyam, 1988) for spheres and compiled by Gay (1965) for horizontal cylinders and thin sheets (**Table 1**). x_0 indicates the coordinate of the center of the structure, §-the dip, I_T the effective inclination of the geomagnetic field in the vertical plane normal to the body's strike while q is the shape factor taken as 2.5 for spheres, 2.0 for infinitely-long horizontal cylinders, and 1.0 for thin geologic sheets (Mehanee et al., 2021). FHD and SHD are the first and second derivatives of the anomaly respectively while A, B, and C constants are defined in **Table 2**;

The five controlling model parameters (K, z, *α*, xo, and q) are computationally obtained by strategically introducing procedures outlined in the succeeding section on the objective function expressed in **Equation 2** (Essa & Elhussein, 2020). Puzzling of optimal parameters for the geophysical model of interest is carried out such that the misfit between the true and estimated data (calculated using the objective function - **Equation 2**) is minimized (Mehanee et al., 1998; Ouadfel & Taleb-Ahmed, 2016).

$$\frac{\sum_{i=1}^{S}\left(T_i^m - T_i^c\right)^2}{S} \quad (2)$$

where T_i^m and T_i^c are respectively the magnetic anomaly from observed data and that estimated using the proposed methodology.

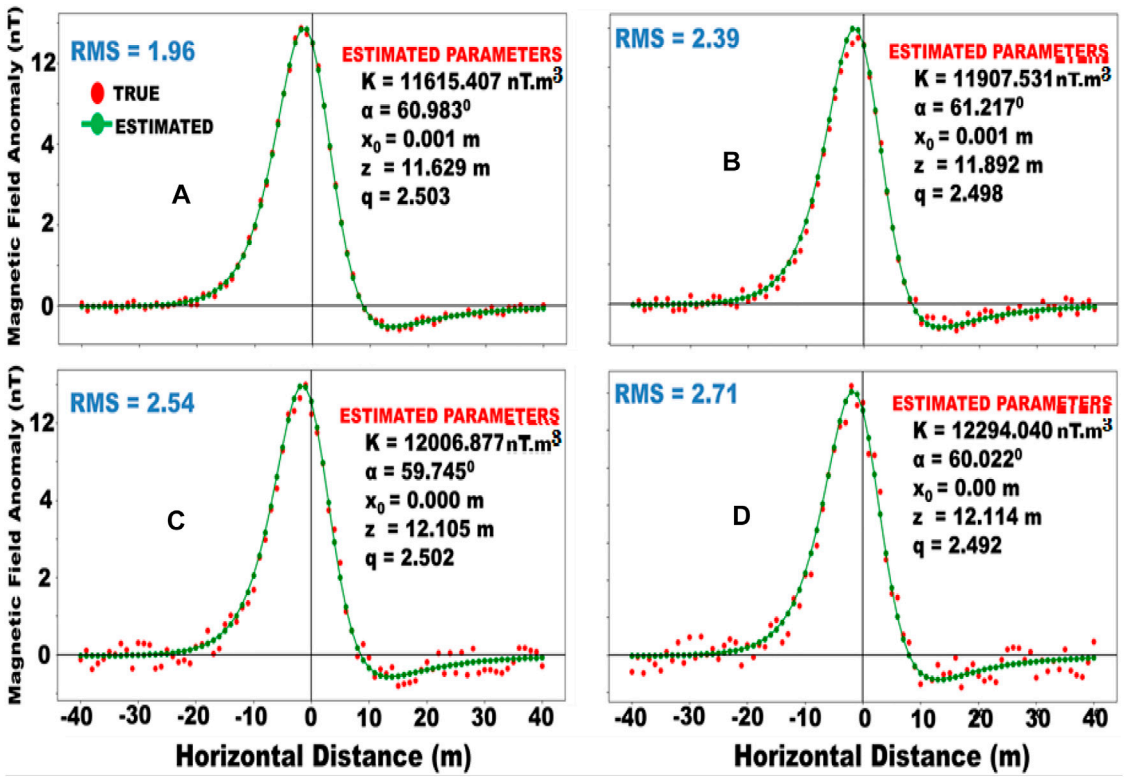

FIGURE 4 | Synthetically generated noisy and estimated (MFR) magnetic anomalies for a sphere model with K = 11,000 nT.m3, z = 11 m, q = 2.5, α = 600, xo = 0 m with **(A)** 5% **(B)** 10% **(C)** 15% **(D)** 20% gaussian random error.

Manta Ray Foraging Optimization Algorithm

The MRF optimization algorithm (which is the backbone of our new methodology) is designed based on the foraging strategies of marine-living Manta rays (**Figure 2**). The foraging strategies include chain, cyclone, and somersault techniques (Ghosh et al., 2021). For our geophysical case, the iterating vectoral positions of the Manta-rays (search agents) represents the probable positions of physical parameters sought-for. The position of the plankton itself (also vectoral) points to the geoscientific optimization problem's solution. For the chain foraging strategy, the agents identify and frame a head-tail formation (also referred to as foraging chain) towards a potential plankton. As a result, any plankton lost by one Manta-ray will not escape the next; thereby improving the overall rate of exploitation. In the cyclone style of foraging, the manta rays swim towards the food in design spirals such that while maintaining its foraging chain-line, each agent is concurrently advancing towards its target food. Alternatively, the solution to the magnetic problem is placed as a pivot in the summersault foraging technique; such that the agents recurrently translate about this pivot before moving into new positions. The result of this is that the new positions are not purely random but rather, circumvents of the best position found (at least up to that point). These numerical constructs for these foraging strategies as adapted from Zhao et al. (2020) and remodeled for our geophysical case are described below; Chain foraging: **Equation 3**

$$T\left(x_j\right)_i^D = \begin{cases} T\left(x_j\right)_i^D(t) + r.\left(T\left(x_j\right)_{best}^D(t) - T\left(x_j\right)_i^D(t)\right) + w.\left(T\left(x_j\right)_{best}^D(t) - T\left(x_j\right)_i^D(t)\right) & i=1 \\ T\left(x_j\right)_i^D(t) + r.\left(T\left(x_j\right)_{i-1}^D(t) - T\left(x_j\right)_i^D(t)\right) + w.\left(T\left(x_j\right)_{best}^D(t) - T\left(x_j\right)_i^D(t)\right) & i=2,3,\ldots,N \end{cases} \quad (3)$$

$$w = 2.rand().\sqrt{|\log(r)|} \quad (4)$$

where $T\left(x_j\right)(t)$ is the *i*th search agent's position at a time t. *rand*() –a vector randomly generated within 0 and 1; w- the coefficient of weight, N is the maximum iterations allowed; while $T\left(x_j\right)_{best}^D(t)$ points to the healthiest pool of planktons representing the optimum vectoral position of the sought geomagnetic parameters. The exponentiation factor D represents the dimension of the position. For the study, D = 4 since we are dealing with four parameters **Equation 4**.

Cyclone foraging:

$$T\left(x_j\right)_i^D(t+1) = \begin{cases} T\left(x_j\right)_{best}^D(t) + rand().\left(T\left(x_j\right)_{best}^D(t) - T\left(x_j\right)_i^D(t)\right) + \mu.\left(T\left(x_j\right)_{best}^D(t) - T\left(x_j\right)_i^D(t)\right) & i=1 \\ T\left(x_j\right)_{best}^D(t) + rand().\left(T\left(x_j\right)_{i-1}^D(t) - T\left(x_j\right)_i^D(t)\right) + \mu.\left(T\left(x_j\right)_{best}^D(t) - T\left(x_j\right)_i^D(t)\right) & i=2,3,\ldots,N \end{cases} \quad (5)$$

where μ, known as the cyclone foraging's coefficient of weight, is generated stochastically using **Equation 6**;

$$\mu = 2e^{rand()\frac{T-t+1}{T()}}.\sin 2\pi rand() \quad (6)$$

It is noteworthy to add that after executing **Equation 5** for our structural problem, we uncomfortably observe that the optimizing parameters for our geophysical structure tend to vacillate around a certain position in a loose loop-like manner. To resolve this particularity, we force each of our agents to find new positions far from its current best position in the search space by randomly injecting a wild function q^D_{rand} with the whole search taken as the reference position (Ben et al., 2021b). q^D_{rand} was constructed numerically using **Equation 7**.

$$q^D_{rand} = LB^D + rand().\ (UB^D - LB^D) \tag{7}$$

as such, **Equation 7** became;

$$T(x_j)^D_i(t+1) = \begin{cases} q^D_{rand}(t) + rand().q^D_{rand}(t) - T(x_j)^D_i(t)) + \mu\ .\ (q^D_{rand}(t) - T(x_j)^D_i(t)) & i=1 \\ q^D_{rand}(t) + rand().(T(x_j)^D_{i-1}(t) - T(x_j)^D_i(t)) + \mu\ .\ (q^D_{rand}(t) - T(x_j)^D_i(t)) & i=2,3,\ldots,N \end{cases} \tag{8}$$

This strategy that the algorithm extensively performs global search; substantially improving general exploration. **Equation 8**.

Summersault foraging:

$$T(x_j)^D_i(t+1) = T(x_j)(t) + P.(rand().T(x_j)^D_i(t) - rand().T(x_j)^D_i(t),\ \ i = 1, 2, \ldots, N \tag{9}$$

where the term P - a constant known as the somersault factor determines the range at which the Manta rays somersault. **Equation 9**.

Generally, the chain strategy encourages individual positioning based on short-term historical positioning and current global best. The cyclone foraging strategy makes each individual update its position with respect to both its preceding neighbor and the reference position while the summersault foraging technique enforces thorough adaptive search.

For exhaustive details about the adoption of the MRF algorithm for optimization scenarios, the readers are referred to Zhao et al. (2020). In our new method, we start by initiating a random population of Manta-rays in the search domain (designed around the upper bound (UB) and lower bound (LB) of our magnetic model parameters) with each agent position in the space representing characteristic parameters of the geologic structure. In our geophysical case, the selection of bounds are done based on priori geological knowledge such as information from maps, geophysical data and drilling reports. At each iterative step, the individuals are coerced to update these positions based on the referential position and the individual out front. This reference position depends on t/T which decreases from 1/T to 1 (Xu et al., 2020; Mbonu & Ben, 2021). With t/T less than rand (), exploitation is implemented else, exploration is performed. Based on this, our MRF optimization algorithm allows the individuals to decide and when necessary, switch between chain and cyclone foraging behaviors. Then through somersault foraging, the agents adaptively update their positions within the space and with respect to the most optimal position so far found.

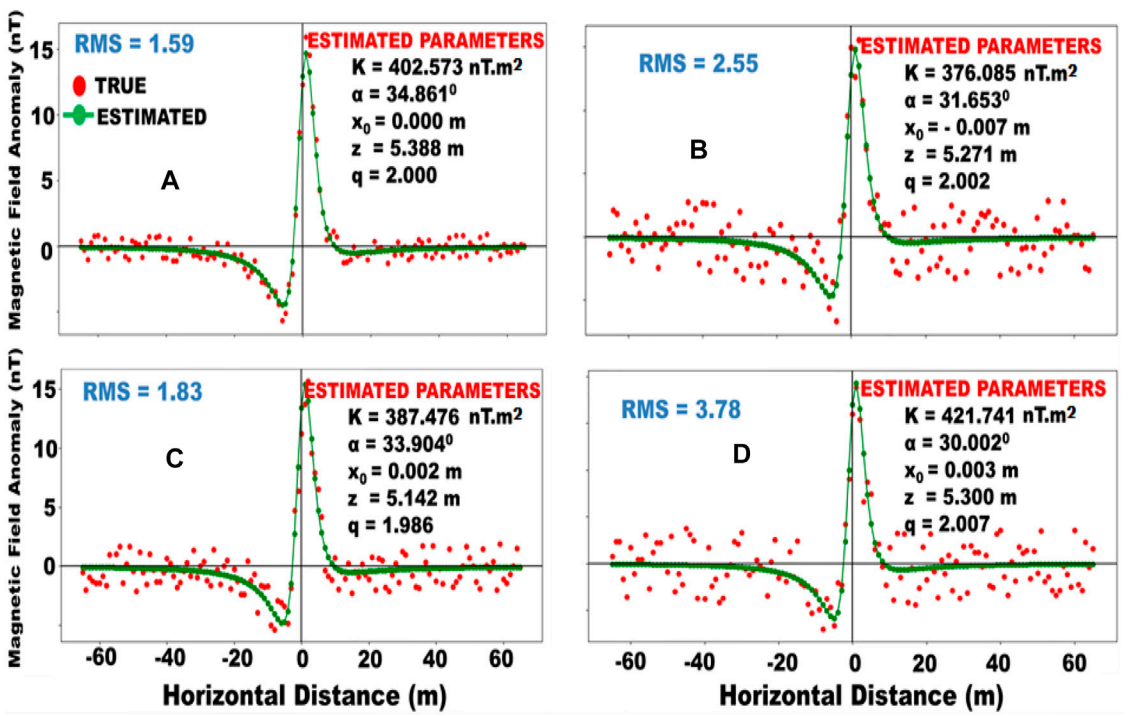

FIGURE 5 | Synthetically generated noisy and estimated (MFR) magnetic anomalies for a horizontal cylinder model with K = 400 nT.m2, z = 5 m, α = 35, q = 2, xo = 0 m, with **(A)** 5% **(B)** 10% **(C)** 15% **(D)** 20% gaussian random error.

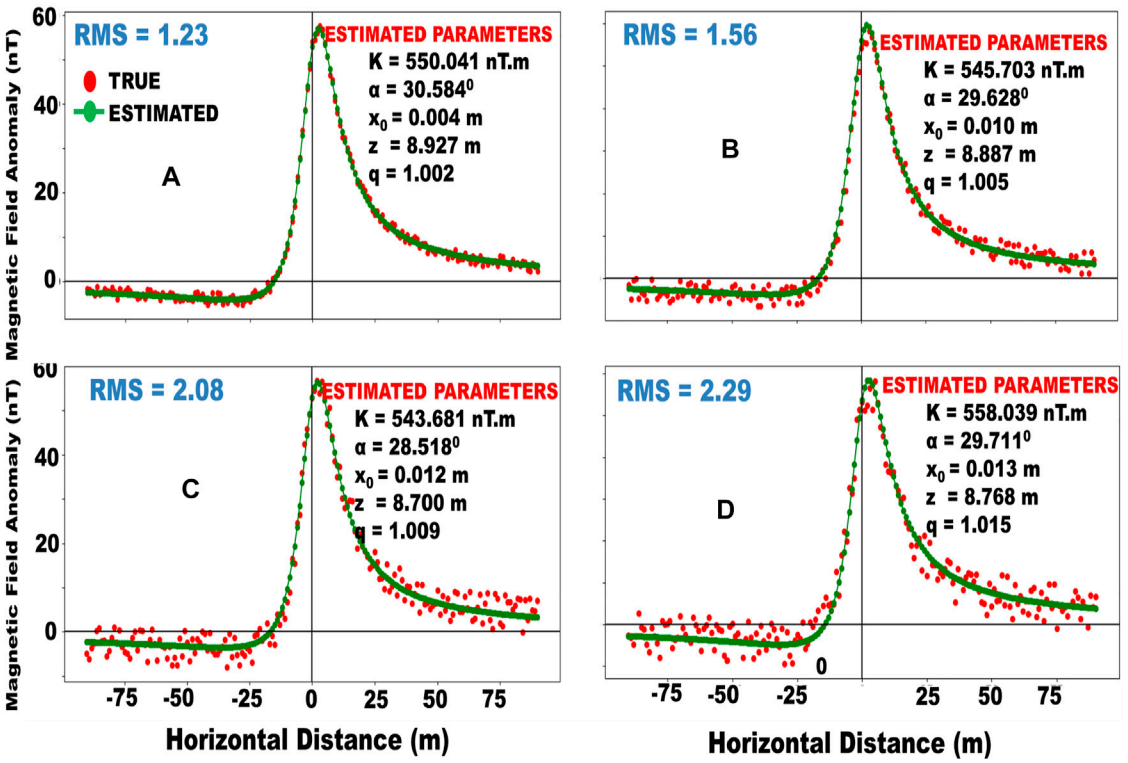

FIGURE 6 | Synthetically generated noisy and estimated (MFR) magnetic anomalies for a thin sheet model with K = 550 nT m, z = 9 m, α = 30, q = 1, xo = 0 m, with **(A)** 5% **(B)** 10% **(C)** 15% **(D)** 20% gaussian random error.

It is noteworthy to add that these calculations and updates explained are interactively performed step-wise until the stopping criterion is met. After each step, the quality is assessed. This is done by gauging the misfit between the measured and estimated anomalies. The misfit is calculated using the root mean technique (Abdelrahman et al., 2012; Mehanee, 2014).

Eventually, convergence is achieved and the four required model parameters are returned. The pseudo-code for the whole optimization process is shown in **Figure 3**.

Algorithm Configuration/Processing Time

The algorithm for this study is designed using the PYTHON programming language and implemented on the virtual studio code IDLE. The IDLE is installed on a PC operating with a Windows 10 operating system and a core i7 processor. The duration of the compilation process is found to depend on the complexity of the anomaly. For simple structures, the iteration process rounds off in 30–50 s. However, there was a 20% increase in processing time for multi-model cases such as those in *Conclusion* Section and Section 5.3. Howbeit, in all cases, the process is found to completely round off in less than 100 s.

RESULTS AND DISCUSSION

The goal of this study is to assess the effectiveness of the MRF optimization technique in modelling magnetic anomalies over geometric geological structures. To monitor this performance, the tool is tested on synthetic and then on field magnetic data.

Synthetic Examples

The proposed method is subjected to controlled experiments using data generated synthetically for idealized spheres, horizontal cylinders, and thin sheet models. First, analysis is done on the synthetic anomaly constructed such that it is noise-free; then the data is consciously corrupted with different levels of noise and reanalyzed.

Noise-Free Models

The MFRO technique is employed to noise-free synthetic anomalies due to geometric interpretative models consisting of: a sphere with K = 11,000 nT m^3, z = 11 m, q = 2.5, α = 60°, x_o = 0 m, and profile length = 80 m; a horizontal cylinder with K = 400 nT m^2, z = 5 m, α = 35, q = 2, x_o = 0 m, and profile length = 120 m, and a thin sheet with K = 550 nT m, z = 9 m, α = 30, q = 1, x_o = 0 m, and profile length = 180 m. The magnetic field anomalies due to these models are computed using **Equation 1**.

The proposed methodology is initiated with 80 initial models and broad search space. For the sphere, we set the range for K to be from 5,000 to 300,000 nT m^3, z from 3 to 15 m, α from -90° to 90°, q from 0 to 3, and x_o from−30 to 30 m. For the horizontal cylinder model, we set K from 100 to 9,000 nT m^2, z from 3 to 15 m, α from -90° to 90°, q from 0 to 3, and x_o from−30 to 30 m. For the thin sheet model, we set K from 100 to 20,000 nT m, z

from 0 to 30 m, α from -90° to 90°, q from 0 to 3, and x_o from−30 to 30 m. A total of 800 repetitive iterations are allowed for each algorithm run. MFRO has very extensive and strong search ability. Impressively, the best model parameters are arrived at in under a quarter of that number of iterations.

From the result obtained (**Table 3**), it is observed that the output for each of the five considered parameters (K, z, α, q, x_o) agree with those originally used to design the three models (with very negligible errors).

Noisy Models

It is well recognized that geophysical data from real buried anomalies are scarcely (if ever) pure. More also, due to the heterogeneity of the earth, it is often very difficult to understand what degree of noise is muddled up in such data. Hence, to delineate the method's efficiency, all the synthetic test data were tweaked to simulate non-ideal geologic scenarios. For this research, the non-ideal geologic scenarios are simulated by contaminating the error-free synthetic anomalies with 5, 10, 15 and 20% white gaussian noise. The noise is generated using a combination of the rand () function and the *SCIPY* library in PYTHON. The noise percentage are computed using **Equation 10** (Mehanee, 2022b).

$$Percentage\ of\ Noise = \frac{||T_n - T||}{||T_n||} \text{x}100 \tag{10}$$

where T_n and T are vectors of the noisy and noise-free anomaly data respectively.

The proposed methodology is once again employed for the estimation of the model-describing parameters. For this, **Equation 2** is re-adopted as the cost function and bounds consistent with the noiseless cases are re-selected. After each iteration session, the convergence and level of misfit are meticulously analyzed.

At the end of the optimization process, it is observed that the algorithm estimates (**Table 3**; **Figures 4–6**) and the true parameter values are to an appreciable level, consistent. However, it is noticed from the results in **Table 3** that the M parameter tends to exhibit more sensitivity with increasing levels of noise. This sensitivity - which would only have likelihood of affecting interpretation when dealing with extremely complicated and deep-seated surface structures is not unrelated to the fact the K is a multiplier factor in **Equation 2**; it can easily be handled by flexibly narrowing ranges for UB and LB. Also, results indicate the misfit after acceptable convergence and the RMS error at the end of the run as marginally upsurging with increasing levels of noise. Nevertheless, this does not wholly affect the general inversion process as parameter results consistently remain attractive even to 20% noise level (**Table 3**). It can thus be concluded that the new methodology is inherently stable and exhibits admirable adeptness in handling noisy anomalies.

Figures 4–6 are plots illustrating the performance of the new technique with synthetic data generated for the three geometric models.

Applicability in Multi-Model Cases

We now seek to assess the new procedure's performance with anomalies from complicated and interfering subsurface structures. To simulate this scenario, we once again generate model data synthetically but, in this scenario, from multiple source bodies (with multifarious parameters) placed at proximity. For the sake of this example, we adopt a horizontal cylinder model with K = 55,000 nT m^2, z = 15 m, α = 25, q = 2, x_o = 30 m, and a thin sheet model with K = 75 nT m, z = 9 m, α = -15, q = 2, x_o = 120 m. The profile length is 400 m. The magnetic field anomaly generated is as shown in **Figure 7**.

We then apply steps consistent with the proposed methodology (as with those in the two preceding sections). However, in this case, the structures are modeled together with parameter bounds as displayed in **Table 4** selected. From results (**Figure 7**; **Table 4**), the parameters can be observed as being well recuperated from and showing admirable consistency with the actual field anomaly confirming the congruency of the methodology.

Comparative Analysis of MRF Optimization With Other Inversion Techniques

In this section, we compare the optimization performance of MRF with those from other methods commonly used for geophysical inversion. In our analysis, we are concerned with the convergence rate, quality/depth of exploration, and accuracy.

For the analysis, three common inversion techniques were selected namely; PSO, SA, and GA.

Particle Swarm Optimization

PSO originally introduced by Kennedy & Eberhart (1995) mimics the behavior of swarms in nature. These swarms may be fish schools or bird flocks. Members of the swarms represent exploring search agents. The technique achieves optimization by updating the positions and velocities of the swarm members based on the positions and velocities of their in-swarm neighbors their movement history. These updates are made using **Equations 11**, **12**;

$$v_i(t+1) = \omega v_i(t) + c_1 r_1 \left(p_i - xi(t)\right) + c_2 r_2 \left(p_g - x_i(t)\right) \tag{11}$$

$$x_i(t+1) = x_i(t) + v_i(t+1) \tag{12}$$

where ω is the inertia constant, c_1 and c_2 are respectively cognitive and social coefficients, pi is the personal optimum of xi, and pg is the global best. For this study, values of 0.729, 2.041, 0.948 were assigned for the inertia weight (ω) and the cognitive and social coefficients.

Simulated Annealing

SA is an optimization procedure the mimics the cooling of metals. The value for the cost function corresponds to energy levels in a melted metal while model parameters are depicted by its molecules' position. For any given parameter set with error ε_0, a new set is methodically generated using random walk. If $\varepsilon < \varepsilon_0$, the new set is discarded, and another is generated. Alternatively, if $\varepsilon \geq \varepsilon_0$, then the set is accepted with a probability defined by Boltzmann's distribution (**Equation 13**):

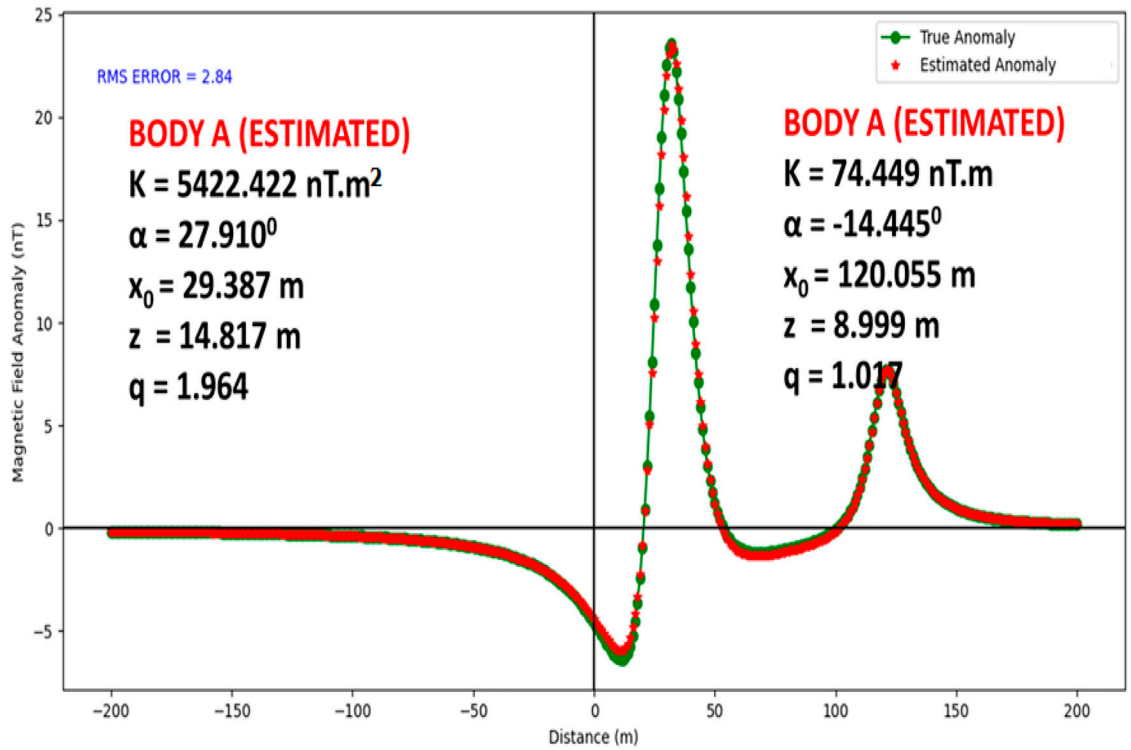

FIGURE 7 | Synthetic and predicted magnetic anomalies of multimodel example consisting of a cylinder model K = 55,000 nT.m2, z = 15 m, α = 25, q = 2.0, xo = 30 m, and a thin sheet model with K = 75 nT m, z = 9 m, α = -15, q = 2, xo = 120 m.

$$f(\Delta E) = e^{\frac{-\Delta\varepsilon}{kT}} \tag{13}$$

where $\Delta\varepsilon = \varepsilon - \varepsilon_0$, T is the temperature while k is the Boltzmann constant. This step is repeated iteratively until an equilibrium state is arrived at. This is a penultimate state where the new set possesses minimum energy at fixed temperature. A generalization of the strategy introduced by Kirkpatrick et al. (1983) adopts a controlled cooling scheme (annealing) where the temperature is gradually (but strategically) reduced with minimum error gauged at each temperature until it arrives at a global minima. For this comparative study, the temperature was reduced by multiplying the previous value by a coefficient less than unity (0.85).

TABLE 4 | Selected ranges of model parameters and numerical results for the synthetic multimodal anomaly example.

Model parameter	Range selected	Result
Anomaly 1		
K (nT.m^2)	1,000–20,000	5422.422
α (^{0})	-90—90	27.910
z (m)	1–300	14.817
x_0(m)	-3—3	29.387
q	0—3	1.964
Anomaly 2		
K (nT.m)	0—200	74.449
α (^{0})	–90—90	–14.445
z (m)	1–20	120.055
x_0(m)	–3—3	8.999
q	0—3	1.017
Elapsed time	55s	

Genetic Algorithm

GA is a search heuristic inspired by the theory of natural evolution. The algorithm reflects the process of natural selection where the fittest individuals are selected to reproduce for the next generation. A generational GA is initialized by a randomly generated population (set containing probable solutions), then the fitness (the objective function) of each individual is evaluated. Then, a new population is generated from the original one; this is aided by some GA operators: selection, crossover, and mutation. To form this new population, two solutions from the original population are selected considering their fitness. They are crossed over with the crossover probability to generate two new offspring who are then mutated with a mutation probability. The mutation guides against local minima. After obtaining the new generation, the steps are repeated. The algorithm terminates after reaching a finite number of generations; and the individual with the best fitness value returned as the solution to the problem. For this study, a crossover probability of 0.7 and a mutation probability of 0.1 was used for producing 800 generations.

TABLE 5 | Parameter results from inversion of sphere model anomaly using MRF, PSO, SA and GA techniques.

	True	MRF	PSO	SA	GA
K (nT.m^3)	11000.000	11001.300	11035.231	11374.306	10585.321
α (^{0})	60.000	60.000	59.783	61.621	61.218
z (m)	11.000	11.000	11.032	10.532	10.824
x_0 (m)	0.000	0.000	0.000	−0.010	0.007
q	2.500	2.500	2.498	2.552	2.531
RMS	—	3.22×10^{-5}	1.05×10^{-3}	5.85×10^{-2}	7.23×10^{-2}
Elapsed Time	—	30s	27s	22s	41s

Procedures consistent with PSO, SA, and GA were concurrently implemented on the synthetic sphere model constructed in *Synthetic Examples* Section. More also, bounds consistent with those used for MRF optimization were adopted. The results obtained are shown in **Table 5**. From the table, it can be observed that with an RMS of 3.22×10^{-5}, MRF optimization technique produced results of greater quality than its comparative counterparts. **Figure 8** shows the convergence character for the four techniques after 800 iterations. From the plots, it is observed that while all the methods achieved minimum errors in less than 250 iterations, MRF clearly boasted the fastest convergence. This advantage is accrued to the somersault foraging behavior of the procedure (as earlier explained in *Manta Ray Foraging Optimization Algorithm* Section). Notably, SA and GA did not achieve convergence even after 800 iterations. More too, from **Figure 9**, the MRF presented the greater error variability compared to GA, SA, and PSO. The superior interquartile curve indicates that the MRF algorithm possesses greater exploration capabilities than GA, SA, and PSO. This is expected as the MRF optimization algorithm allows for intelligent/situational switching between cyclone and chain foraging strategies. The chain foraging strategy favors local search while the cyclone foraging technique allows for extensive global exploration.

Case Studies

The performance of the new technique is further investigated using three field cases.

The Pima Copper Mine Anomaly

The Pima mine is an open pit, "complex" porphyry copper deposit located off the northeast flanks of the Sierrita Mountains at about 30 km south of Arizona, United States. At full production, the mine can produce up to 50,000 tons of copper per day (Hamel, 1979; Cox et al., 2006; Biswas et al., 2017).

Stratigraphically, the mine is fixated in an east-north-eastly striking and south-eastly dipping Paleozoic to Mesozoic sedimentary sequence intermediately intruded by quartz monzonite porphyry believed to be of Tertiary age (Abbas & Fedi, 2013). These Paleozoic sediments notably observed to be dolomites, limestones, and sandstones have historically been anti-frigidly metamorphized into calco-silicate skarns, marble, and quartzite and then, unconformably overlain by marginally recrystallized and hydrothermally altered Mesozoic to Triassic clastic (Cox et al., 2006). The intrusions have characteristically resulted in mineralization of high grade in the Paleozoic rocks and ore dissemination in the relatively younger Mesozoic sediments. Structurally, the area is dominated by east-west post-mineralization faults in the western part of the mine, and

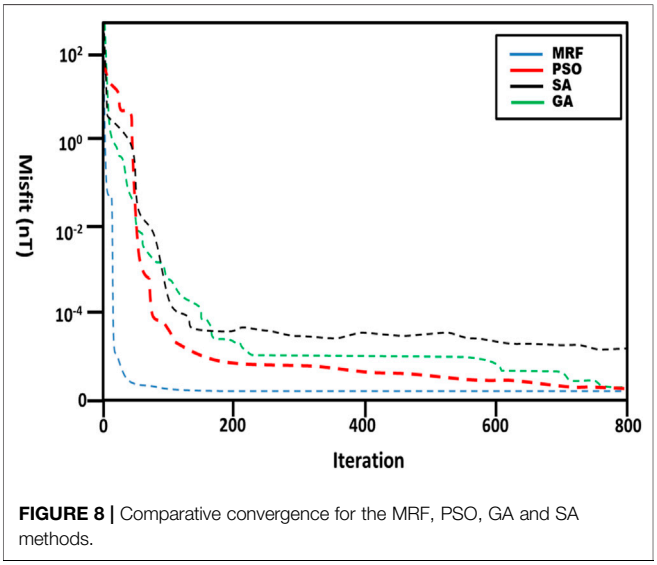

FIGURE 8 | Comparative convergence for the MRF, PSO, GA and SA methods.

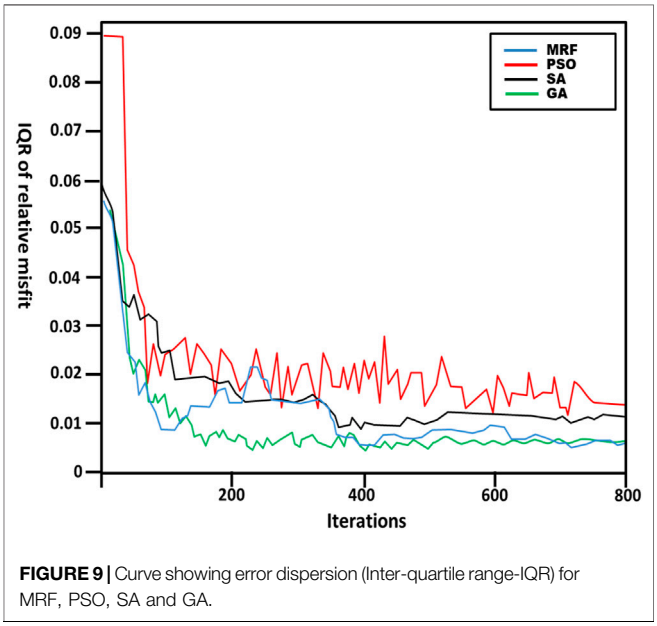

FIGURE 9 | Curve showing error dispersion (Inter-quartile range-IQR) for MRF, PSO, SA and GA.

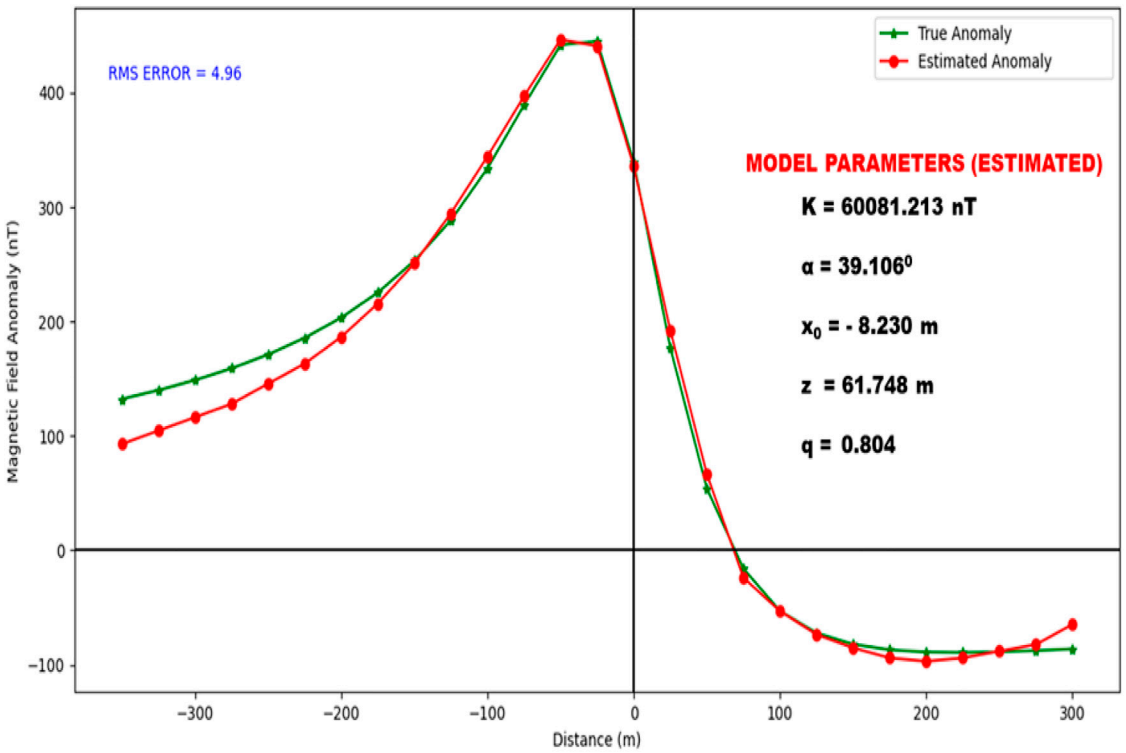

FIGURE 10 | Magnetic anomaly profile over the Pima copper mine anomaly, Arizona using the MRF algorithm.

TABLE 6 | Numerical results for Pima copper mine Anomaly.

Model parameters	Selected ranges	Result	Error	Time elapsed (s)
K (nT.m)	1,000–20,000	60081.313	4.96	33
α (^{0})	−90—90	39.106		
z (m)	0–500	61.748		
x_0(m)	−12–12	−8.230		
q	0–3	0.804		

strong shearing and faulting of low angle truncating the ore body at depth (Hamel, 1979; Barter & Kelly, 1982; Abbas & Fedi, 2013).

Figure 10 (red line with round markers) is a magnetic anomaly profile over a buried ore body retrieved from magnetic survey data taken across the Pima mine (Gay, 1963). The profile was digitized with a sampling interval of 25 m. In this research, the new method attempts at deciphering the parameters characterizing the geologic feature whose structure (initially unknown) can take any of the three studied geometric shapes. We initialize the algorithm using bounds indicated in **Table 6**. The algorithm is set to terminate after 1,000 iterations. At the end of the MRF optimization session, the misfit was monitored using the RMSE technique (**Figure 10**). The results obtained are displayed in **Table 6**.

TABLE 7 | Comparative analysis of parameter results for the Pima copper mine anomaly.

Model parameters	Gay (1963)	Venkata Raju (2003)	Abdelrahman et al. (2003b)	Tarantola (2005)	Mehanee et al. (2021)	Drilling information	Present study
K (nT.m)	—	—	80,550	39190.00	46,424.38	—	60081.31
α (^{0})	−50.00	−51.00	—	−44.70	−55.11	—	39.11
z (m)	70.00	76.81	68.00	64.10	71.00	64	61.75
x_0 (m)	—	—	—	—	—	—	−8.23
q	1.00	—	—	1.0	1.00	—	0.80

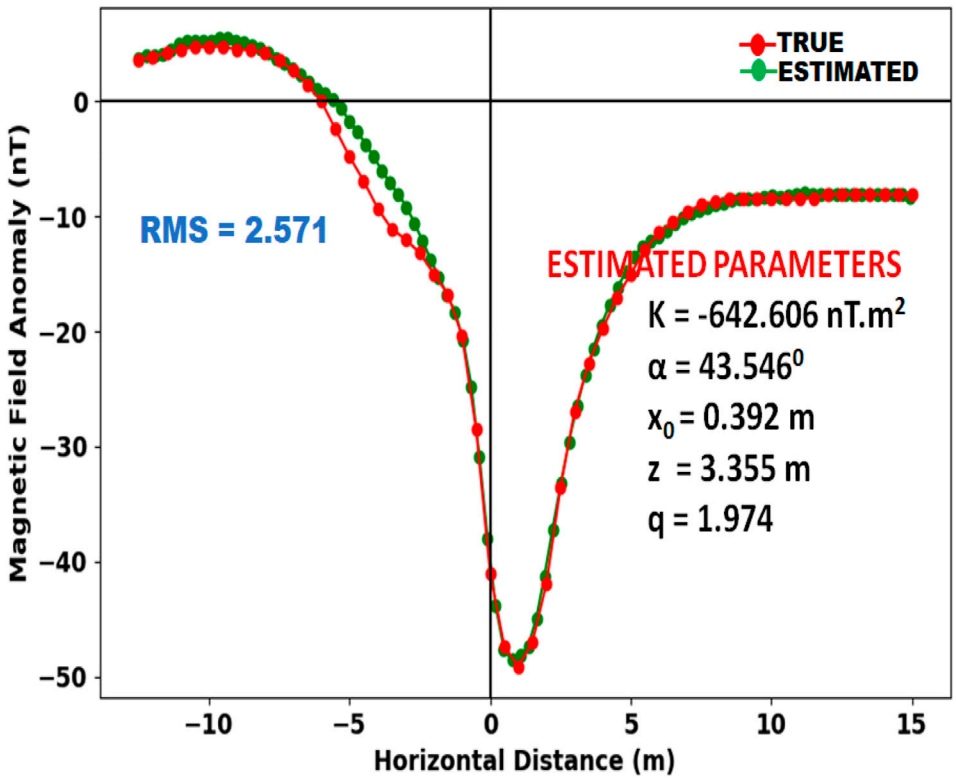

FIGURE 11 | Magnetic anomaly profile over the Parniaba field anomaly using the MRF algorithm.

TABLE 8 | Numerical results for the Parnaiba anomaly.

Model parameters	Selected ranges	Result	Error	Time elapsed (s)
K (nT.m^2)	–5,000–5,000	642.606	2.571	34
α (^{0})	–90–90	43.546		
z (m)	0–200	3.35		
x_0 (m)	–10–10	0.39		
q	0–3	1.97		

Results from analysis suggest that the investigated structure's shape compares appositely with that of a perfect thin sheet model. The parameters characterizing the model are estimated as K = 6,081.213 nT m, α = 39.106, x_o = -8.230 m and z = 61.748 m. More also, the obtained RMSE of 2.14 indicates that the actual and estimated data fits excellently.

We now attempt to compare these results with those from similar studies. Notably, the Pima anomaly has been widely interpreted in literature. Initially Gay (1963) used classical curve matching techniques to interpret the buried geologic feature as a sheet-like structure inclined at about -50° at a depth of 21.34 m. Venkata Raju, 2003) employed a LIMAT

TABLE 9 | Comparative analysis of parameter results for the Parnaiba anomaly.

Model parameters	Silva (1989)	Abdelrahman et al. (2019)	Abdelrahman et al. (2003a)	Tlas and Asfalhani (2011)	Tlas and Asfalhani (2015)	Present study
K (nT.m^2)	—	–717.90	–215.60	–552.30	–4007.6	642.606
α (^{0})	—	33.30	52.58	46.83	41.3	43.546
z (m)	3.50	3.50	2.23	3.36	3.4	3.35
x_0 (m)	—	—	—	—	—	0.39
q	—	—	—	2.00	2.00	1.97

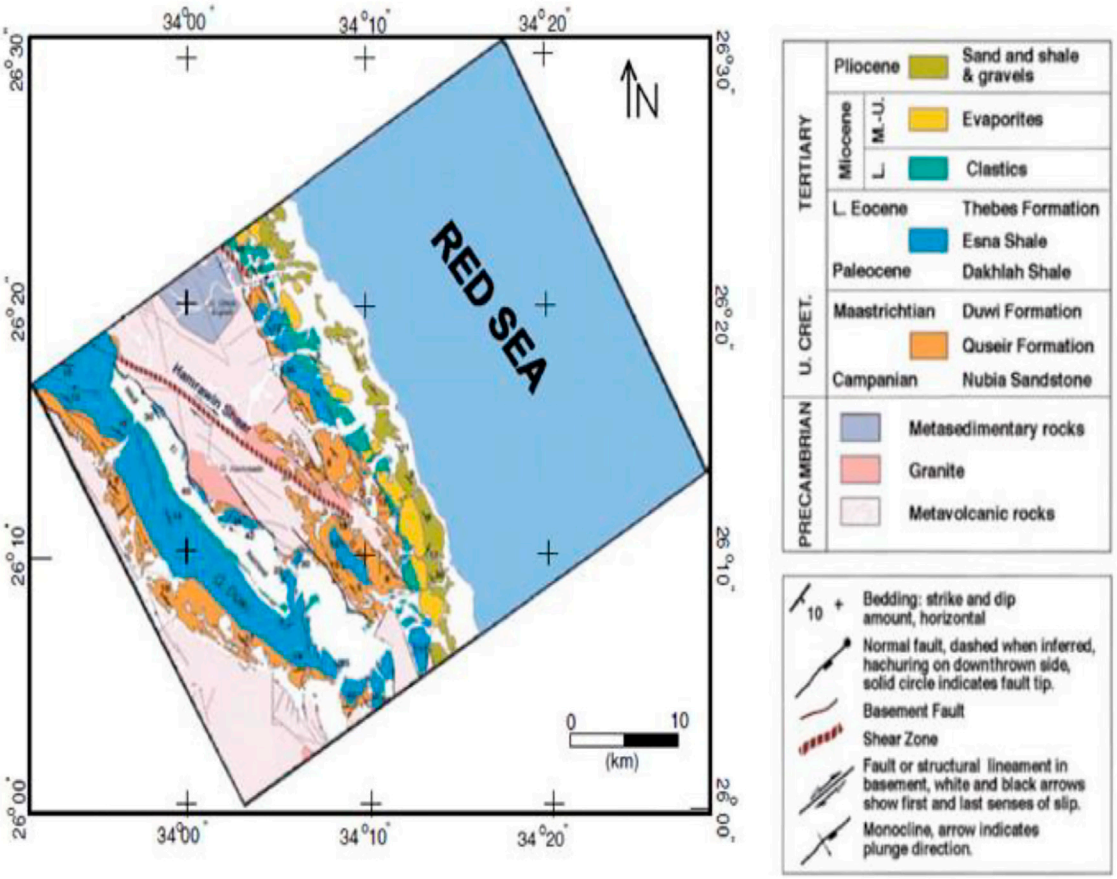

FIGURE 12 | Geologic map of the Quseir area, Egypt showing the Hamrawein shear (modified after Essa and Elhussein, 2018).

computer program for least-squares magnetic inversion over the Pima anomaly. After adequate smoothening of the initial solution using Marquarst's algorithm, he interpreted the anomaly as a thin sheet of depth -76.81 m. Recently, the buried anomaly was interpreted as between a thin sheet and dyke like structure using the simplex algorithm (Tlas & Asfahani, 2015). After calculations, Tlas & Asfahani (2015) gave the depth of the Pima copper anomaly as 64.1 m. Mehanee et al., 2021) employed an R-Parameter imaging method to pin-point the anomaly to a sheet-like structure buried at depth of 71 m. Petrophysical information reports the drilling depth as 64 m (Biswas, 2018). Considering these findings (**Table 7**), it can be concluded that results from our new methodology comparably agree acceptably with previous studies.

The Parnaiba Anomaly

In our second field case, we analyze crustal anomaly in the Parnaiba basin.

The Parnaíba basin is a 500,000 km-square wide Paleozoic basin structurally situated between the São Francisco and Amazonian cratons (Cordani et al., 2013; Daly et al., 2018) in north-east Brazil and widely regarded by explorationists as one of the world's most promising modern onshore gas basin. Priori regional studies report that the basin which is characterized by Neoproterozoic structures mapped to the Brazilian Orogenic Cycle (Mckenzie & Tribaldos, 2018) is accrued with 3–5 km of sediments in the main depo-center of its Phanerozoic-aged sedimentary rocks (Solon et al., 2018). These rocks overlie the Neoproterozoic structures of the Brazilian Orogenic Cycle. Oregenically, the crustal masses of this basin are convicted to be resultant from the massive splitting of the Rodinia believed to have occurred before the development of the trending Brazilian fold belts around 900 Ma (Cioccari & Mizusaki, 2019; Jurandyr Luciano Sanches Ross, 2020). Basement inliers were then formed with the surrounding of these classical cratonic fragments by Neoproterozoic fold belts during the amalgamation process of the Gondwana supercontinent. These inliers were further reworked thermally and contracted into cratonic nuclei during the Brazilian orogeny. However, the inclusive geo-magmatism widely observed in greater portions of the Parnaíba Basin has been associated with events of distention events and faults remobilization that followed the rupturing of the Pangea and the opening of the Atlantic Ocean (Cioccari & Mizusaki, 2019). Macedo Filho et al., 2019) reports that these magmatic occurrences in the basin as well as their associated geothermal gradients may have generated the much-acclaimed hydrocarbons in the sedimentary sequences of the Parnaíba Basin.

Figure 11 (red line with round markers) shows the vertical magnetic anomaly resulted from a 26 m-long profile over a

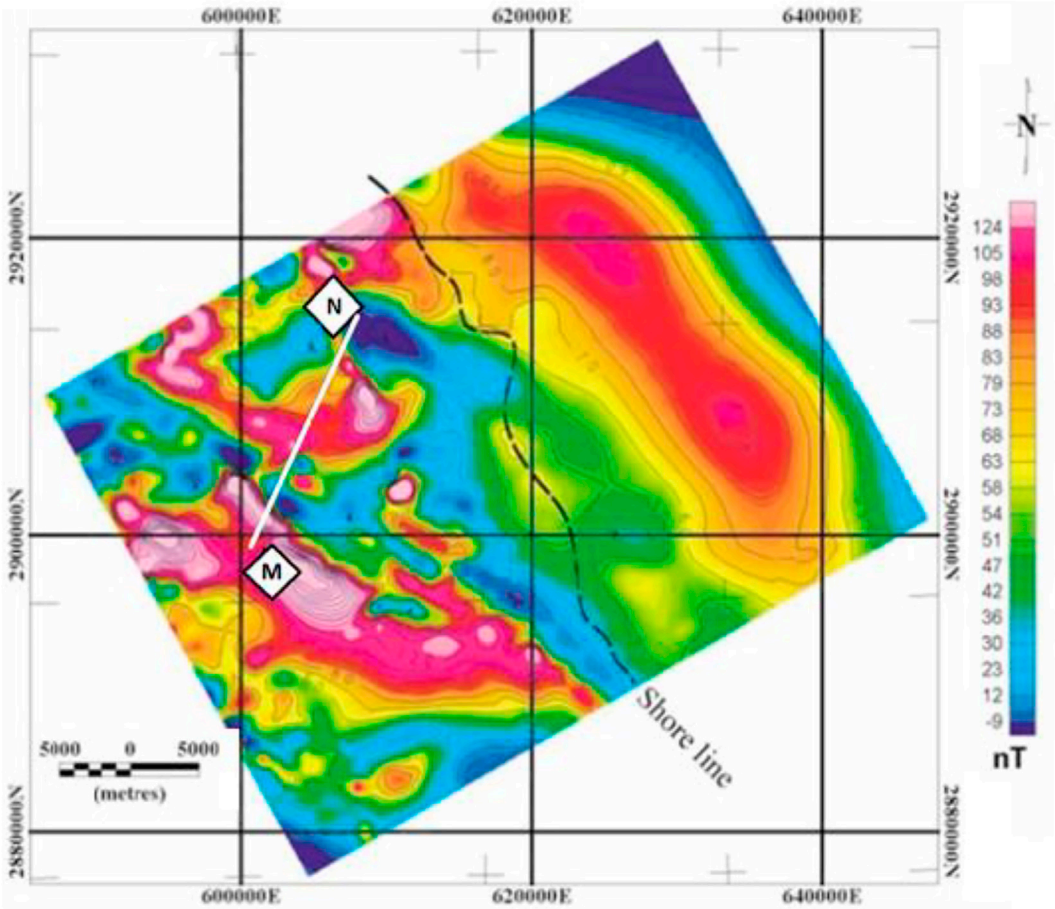

FIGURE 13 | Magnetic intensity map of the Hamrawein field area showing Profile MN (redrawn after Essa and Elhussein, 2018).

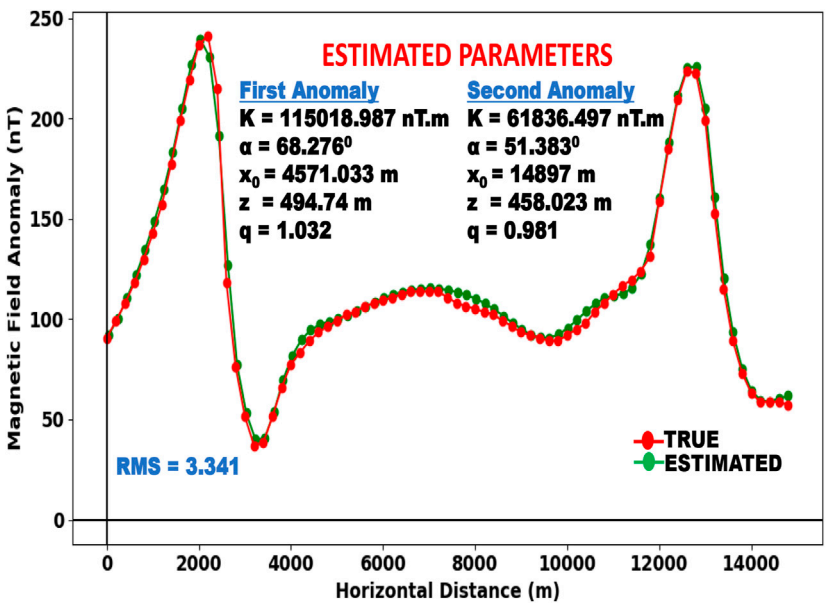

FIGURE 14 | Magnetic anomaly profile over the Hamrawein field anomaly using the MRF algorithm.

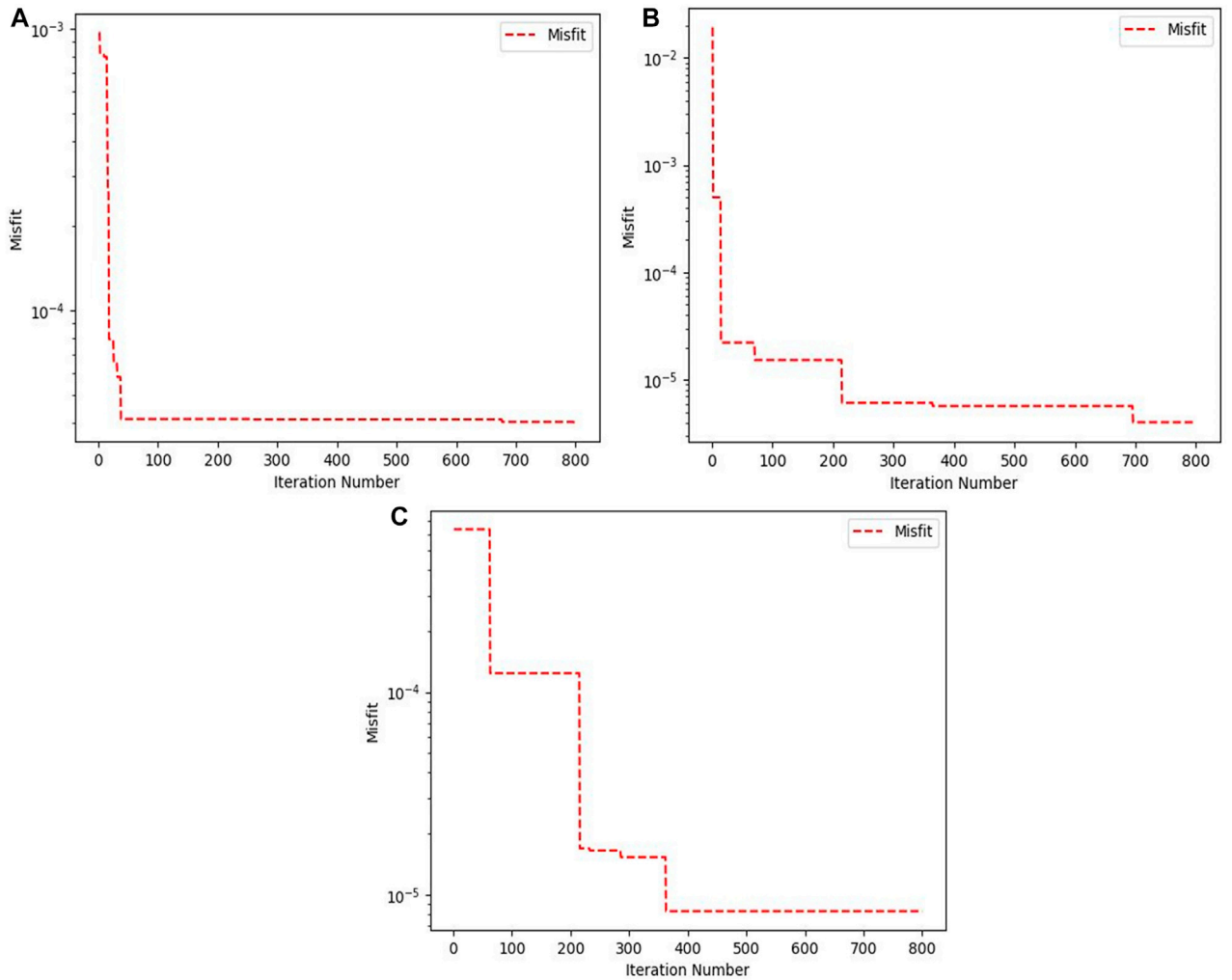

FIGURE 15 | Convergence behavior of the investigated case studies **(A)** Pima anomaly, **(B)** Parnaiba anomaly and **(C)** Hamrawein anomaly.

Mesozoic diabase intruded into the Paleozoic sediment of the Parnaiba basin. The profile was sampled at an interval of 0.5 m. The uniqueness of this anomaly problem lies in the fact that the oxidization of magnetite resultant from extensive weathering of the upper part of the buried structure has led to the loss of most of its magnetism (Silva, 1989). As a result of this geological peculiarity, we expect the magnetic anomaly to be largely affected by random noise at gross levels. This field case is also a test of the stability of the method in the presence of such peculiarity.

The anomaly depth, magnetic angle, amplitude coefficient, anomaly origin, and shape factor are estimated using MRF algorithm are guided by UB-LB outlined in **Table 8**. This magnetic anomaly is inverted with the cylinder model considered as the priori anomaly causative.

After each iterating round, the misfit between sample data and those from the estimated parameters are calculated (**Figure 11**). The obtained results are displayed in **Table 8**.

Comparatively, it can be observed that depth to the center of the anomaly estimated using our new method (z = 3.355 m) agrees with previous reports from similar studies by Silva (1989); Abdelrahman et al., 2019), Tlas and Asfahani, 2011), and Tlas and Asfahani, 2015). Silva (1989) obtained a depth of 3.5 m after converting the problem from non-linear to linear using the M-fitting technique; Abdelrahman et al., 2019 using the least square minimization method reported that the cylinder is buried at a depth of 3.5 m. On the other hand, Tlas & Asfahani (2011) and Tlas & Asfahani (2015) estimated the depth to the center of the cylinder as 3.36 and 3.4 m by respectively employing the deconvolution technique and simplex algorithm. Furthermore, the obtained values of K and RMSE confirm the algorithm's stability in the presence of contamination.

The results obtained using the present technique as well as those reported from the previous studies are displayed in **Table 9**.

The Hamrawein Field Anomaly

In our final case study, we will be analyzing a multi-model anomaly from Hamrawein field–an Egyptian mining field situated around the western throat of the Red Sea in North Africa. This geologic region is

TABLE 10 | Numerical Results for the Hamrawein field anomaly.

Model parameters	Selected ranges	Result
First Anomaly		
K (nT.m)	100–500,000	110531.368
α (^{0})	−90—90	65.031
z (m)	100–1,000	446.832
x_o (m)	0–15,000	2377.424
q	0–3	0.921
Second Anomaly		
K (nT.m)	100–500,000	49713.438
α (^{0})	−90—90	57.382
z (m)	100–1,000	399.963
x_o (m)	0–15,000	13629.462
q	0–3	0.873
Elapsed time	90s	

a constituted part of the East-African rift system believed to have been structurally architected from the anti-clockwise rotational divergence of the Arabian plate from the African tectonic Plate with the central Mediterranean Sea as the pole of rotation (Noweir & Fheel, 2015). The field is petrologically dominated with volcanic rocks such as pillow tholeiitic basalts overly genetically on layers of ultramafic and gabbroic strata. These layers of strata are unevenly covered with volcanic and sedimentary rocks of calco-alkaline geochemistry (Salem et al., 2005; Smith & Salem, 2005). **Figure 12** is a geological map of Qusier area showing the Hamrawein field.

Figures 13, **14** show a 15 km magnetic anomaly profile (MN) extracted from a magnetic map designed from an extensive high definition aeromagnetic survey data originally carried out by Salem et al. (1999). For this study, the profile is digitized at a 200 m interval. From priori geologic studies, we can ascertain that the profile is characterized by two prominent anomalies. However, the structure or characteristics of these anomalies cannot be distinctly defined initially and as such could be interpreted broadways as a combination of any of the simple shapes. This situation normally renders inherent non-uniqueness around solutions for the anomaly.

Fudging in the peculiarity of this problem and to resolve this technical complication, we run the algorithm for all possible dual-combinable shapes. The least RMSE error of 3.341 is achieved and accepted for model shapes with q values of 1.032 and 0.981 respectively which proximate synonymously with models of thin sheet structure. Then too, our algorithm eliminants K = 115,018.987 nT m, z = 494.74 m, α = 68.276° and x_o = 4571.033 m as optimal model parameters for the first buried structure while the parameters of the second structure are computed to be K = 61,836.497 nT m, z = 458.023 m, α = 51.383° and x_o = 14897 m (**Table 10**). From **Figure 14**, it can be observed that the fit between the observed and estimated anomalies is consistently excellent.

Table 11 compares results obtained in this present study with those obtained from similar studies reported in literature. Salem et al., 2005) modified the enhanced local wavenumber method and used it to interpret the two subsurface anomalies as thin sheet structures buried at depths of 555.7 and 441.2 m respectively. Salem et al., 2005) did heterological computation of the anomaly using analytic signal derivative but reported depths of 540 and 447 m respectively. Salem (2011) on the other hand conducted his analysis of the Hamrawein anomaly using both total gradient (TG) and local wave number (LW) methods. The LG methodology outputted depths of 486.5 and 440.4 m while the LW method out-turned 432.6 and 422.8 m as respective depths to the two anomalies. Essa & Elhussein, 2018 and Essa & Elhussein (2020) used particle swarm optimization (PSO) to carry out magnetic inversion for the area. While the former employed robust PSO for this task and reported the subsurface structures as thin sheets with depths of 623.05 and 494.14 m, the latter who emphasized the use of the optimization technique to infer second moving average residual magnetic anomalies also interpreted the structures as thin sheets but emplaced them at depths of 604 and 500 m respectively. Comparing results from this study with these previous findings, it can be generally deduced that resolutions using this new methodology stand in good agreement with those from previous reports. **Figure 15** shows the convergence behavior of the investigated case studies (Pima, Parnaiba, and Hamrawein anomalies).

Evaluation of results obtained using this new methodology has revealed that the technique exhibits admirable stability in the presence of noise, remarkable flexibility especially when confronted with interfering anomalies, and great pervasiveness in the quantitative resolution of magnetic inversion problems. The consistency of the results obtained from the analysis of the field

TABLE 11 | Comparative analysis of results for the Hamrawein field anomaly.

Model parameters	Salem et al. (2005)	Salem et al. (2005)	Salem (2011)	Essa & Elhussein (2018)	Mehanee et al. (2021)	Present study
First Anomaly						
K (nT.m)	—	—	127595.3	507.64	102046.00	115.02
α (^{0})	—	—	—	57.04	70.49	68.27
z (m)	555.7 ± 10	540 ± 30	486.5	623.05	480.00	494.74
x_o(m)	4526.00 ± 7	4530 ± 10	—	4255.98	4550.00	4571.03
q	1.44	-	1.0	0.89	1.00	1.03
Second anomaly						
K (nT.m)	—	—	83746.7	427.38	56549.52	61836.497
α (^{0})	—	—	—	37.21	55.04	51.383
z (m)	441.2 ± 3	477 ± 25	440.4	494.14	400.00	458.023
x_o (m)	14858.00 ± 17	14850 ± 21	—	14823.96	15200.00	148973.295
q	1.20	1.2 ± 01	1.0	0.93	1.00	0.981

examples when compared with background results from other similar studies conducted with other methods further affirms the reliability of the new methodology. While this consistency is continuous for shape and depth parameters, **Tables 6**, **8**, **10** show that there are significant variations in the amplitude parameter for all field cases. This large variation could be attributed to two main reasons. The first, which is the mathematical role of K in the forward model (**Equation 1**) has already been explained in *Synthetic Examples* Section. Ambiguity makes up the second reason. The K parameter—directly related to the magnetic susceptibility is a physical property that points to the type of materials making up the buried anomaly. As has been explained severally in literature (Clark, 1996; Crowther, 2003; Marques et al., 2014; Teixeira et al., 2018; César de Mello et al., 2020), magnetic susceptibility is a very non-unique rock property and could sometimes range up to factors of 10^4. It is therefore not surprising to find authors reporting different values for K. Howasmuch, it will be rather skewed to conduct appraisal of this parameter based on these literature reports alone. The efficiency of the new method in the estimation of K would only be assessed without bias if the result were gauged against laboratory findings for cores harvested from these field sites. Unfortunately, this information is not available for any of the three field cases. Nonetheless, the new technique still exhibited comparative edge over other well-known and conventional techniques especially on the grounds of convergence rate, and quality of the anomaly parameters (depth and shape) resolved.

CONCLUSION

In this study, we have introduced and investigated the applicability and the performance of the Manta Ray Foraging Optimization algorithm in elucidating distinctive physical parameters of simple geometrically shaped geologic structures (spheres, horizontal cylinders, and thin sheets). This new inversion technique has been demonstrated successfully on synthetically generated magnetic anomalies corrupted with different levels of Gaussian noise (0, 5, 10, 15, 20%), applied to cases of anomalies from multiple and intercalating structures, and finally experimented on heterologous field cases taken from mining sites in Brazil, United States, and Egypt.

Generally, the test examples (real and synthetic) treated in this research work have all affirmed the MRF-based algorithm's suitability for the inverse modeling of magnetic anomalies caused by conventional geometrically shaped structures. Furthermore, the examples enabled us in the evaluation of the new technique's strengths with regards to geophysical optimization and extendedly, as compared with existing methods. First, considering reports so far published and even that from the comparative study in this work, it has been observed that amongst stochastic geophysical optimization techniques, the proposed algorithm presents one of the best convergence rates. This rate, however, has no effect on its optimization abilities, as the misfits calculated at the culmination of the procedure still fell within acceptable levels. Most significantly, the method was able to address the reoccurring challenge of immature convergence and local optima (commonly resulting in poor solutions) encountered by conventional intelligent methods such as DE, PSO, GA, and ACO. This is enabled by the search agents' propensity to transition between chain and cyclone foraging strategies. The chain strategy contributes to the algorithm's local search ability, whereas the cyclone foraging behavior is significantly dedicated to the algorithm's global search capacity; a combination of these two, as permitted by our new method, enables extensive exploration of the entire problem domain and practically, greatly improved the quality of solutions. It should however be added that while the algorithm converge in fewer iterations, it took a longer time to complete an iteration. This is but a limitation of this method. As a recommendation, this temporal cost could be improved through modifications (e.g., binary-MRF, quantum-MRF, Chaotic-MRF) and hybridization (e.g., PSO-MRF, GA-MRF, ACO-MRF) of the technique. Considering these gains, and the significantly lower computational effort required to attain them (gauging the limitation), MRF has been proven to positively outperform conventional optimizers in the resolution of geophysical optimization problems with respect to geometrically shaped magnetic anomalies.

Hereto, the novel methodology can be recommended for ore/mineral exploration as well as reconnaissance studies aimed at efficiently resolving subsurface structures from magnetic field data. As a recommendation for future studies, the method can be further developed for the interpretation of other potential field data such as resistivity and self-potential data.

DATA AVAILABILITY STATEMENT

The original contributions presented in the study are included in the article/Supplementary Material, further inquiries can be directed to the corresponding author.

AUTHOR CONTRIBUTIONS

UB, SE, AA, and CM prepared data, applied methodology, writing the first draft of the manuscript. AE, KA, and DG-O revised the manuscript, methodology, and editing the manuscript.

FUNDING

We declare all sources of funding received for the research being submitted. Researchers Supporting Project number (RSP-2022/351), King Saud University, Riyadh, Saudi Arabia.

ACKNOWLEDGMENTS

Deep thanks and gratitude to the Researchers Supporting Project number (RSP-2022/351), King Saud University, Riyadh, Saudi Arabia for funding this research article. The authors wish to thank the management of the University of Calabar for providing the facilities used for this research.

REFERENCES

Abbas, M. A., and Fedi, M. (2013). "Automatic DEXP Imaging of Potential fields Independent of the Structural Index," in 75th European Association of Geoscientists and Engineers Conference and Exhibition 2013 Incorporating SPE EUROPEC 2013, European Association of Geoscientists & Engineers, London, United Kingdom. doi:10.3997/2214-4609.20130120

Abdelrahman, E.-S. M., Abo-Ezz, E. R., and Essa, K. S. (2012). Parametric Inversion of Residual Magnetic Anomalies Due to Simple Geometric Bodies. *Exploration Geophys.* 43, 178–189. doi:10.1071/EG11026

Abdelrahman, E.-S. M., El-Araby, H. M., El-Araby, Tarek., and Essa, Khalid. (2003a). A Numerical Approach to Depth Determination from Magnetic Data. *Kuwait J. Sci. Eng.* 29, 121–134.

Abdelrahman, E.-S. M., El-Araby, T. M., and Essa, K. S. (2003b). A Least-Squares Minimisation Approach to Depth, index Parameter, and Amplitude Coefficient Determination from Magnetic Anomalies Due to Thin Dykes. *Exploration Geophys.* 34, 241–248. doi:10.1071/eg03241

Abdelrahman, E. M., Abdelazeem, M., and Gobashy, M. (2019). A Minimization Approach to Depth and Shape Determination of Mineralized Zones from Potential Field Data Using the Nelder-Mead Simplex Algorithm. *Ore Geology. Rev.* 114, 103123. doi:10.1016/j.oregeorev.2019.103123

Abo-Ezz, E. R., and Essa, K. S. (2016). A Least-Squares Minimization Approach for Model Parameters Estimate by Using a New Magnetic Anomaly Formula. *Pure Appl. Geophys.* 173, 1265–1278. doi:10.1007/s00024-015-1168-9

Agarwal, A., Chandra, A., Shalivahan, S., and Singh, R. K. (2018). Grey Wolf Optimizer: a New Strategy to Invert Geophysical Data Sets. *Geophys. Prospecting* 66, 1215–1226. doi:10.1111/1365-2478.12640

Araffa, S. A. S., El-bohoty, M., Abou Heleika, M., Mekkawi, M., Ismail, E., Khalil, A., et al. (2018). Implementation of Magnetic and Gravity Methods to Delineate the Subsurface Structural Features of the Basement Complex in central Sinai Area, Egypt. *NRIAG J. Astron. Geophys.* 7, 162–174. doi:10.1016/j.nrjag.2017.12.002

Asfahani, J., and Tlas, M. (2012). Fair Function Minimization for Direct Interpretation of Residual Gravity Anomaly Profiles Due to Spheres and Cylinders. *Pure Appl. Geophys.* 169, 157–165. doi:10.1007/s00024-011-0319-x

Balkaya, Ç., Ekinci, Y. L., Göktürkler, G., and Turan, S. (2017). 3D Non-linear Inversion of Magnetic Anomalies Caused by Prismatic Bodies Using Differential Evolution Algorithm. *J. Appl. Geophys.* 136, 372–386. doi:10.1016/j.jappgeo.2016.10.040

Balkaya, Ç., and Kaftan, I. (2021). Inverse Modelling via Differential Search Algorithm for Interpreting Magnetic Anomalies Caused by 2D Dyke-Shaped Bodies. *J. Earth Syst. Sci.* 130. doi:10.1007/s12040-021-01614-1

Barter, C. F., and Kelly, J. L. (1982). *Geology of the Twin Buttes mineral deposit, Pima Mining District, Pima County, Arizona. Advances in Geology of the Porphyry Copper Deposits*. Tucson: University of Arizona Press, 407–432.

Ben, U. C., Akpan, A. E., Enyinyi, E. O., and Awak, E. (2021b). Novel Technique for the Interpretation of Gravity Anomalies over Geologic Structures with Idealized Geometries Using the Manta ray Foraging Optimization. *J. Asian Earth Sci. X* 6, 100070. doi:10.1016/j.jaesx.2021.100070

Ben, U. C., Akpan, A. E., Mbonu, C. C., and Ebong, E. D. (2021a). Novel Methodology for Interpretation of Magnetic Anomalies Due to Two-Dimensional Dipping Dikes Using the Manta Ray Foraging Optimization. *J. Appl. Geophys.* 192, 104405. doi:10.1016/j.jappgeo.2021.104405

Ben, U. C., Akpan, A. E., Mbonu, C. C., and Ufuafuonye, C. H. (2021c). Integrated Technical Analysis of Wind Speed Data for Wind Energy Potential Assessment in Parts of Southern and central Nigeria. *Clean. Eng. Technology* 2, 100049. doi:10.1016/j.clet.2021.100049

Biswas, A., and Acharya, T. (2016). A Very Fast Simulated Annealing Method for Inversion of Magnetic Anomaly over Semi-infinite Vertical Rod-type Structure. *Model. Earth Syst. Environ.* 2, 1–10. doi:10.1007/s40808-016-0256-x

Biswas, A. (2018). Inversion of Source Parameters from Magnetic Anomalies for Mineral/Ore Deposits Exploration Using Global Optimization Technique and Analysis of Uncertainty. *Nat. Resour. Res.* 27, 77–107. doi:10.1007/s11053-017-9339-2

Biswas, A., Mandal, A., Sharma, S. P., and Mohanty, W. K. (2014). Delineation of Subsurface Structures Using Self-Potential, Gravity, and Resistivity Surveys from South Purulia Shear Zone, India: Implication to Uranium Mineralization. *Interpretation* 2, T103–T110. doi:10.1190/INT-2013-0170.1

Biswas, A., Parija, M. P., and Kumar, S. (2017). Global Nonlinear Optimization for the Interpretation of Source Parameters from Total Gradient of Gravity and Magnetic Anomalies Caused by Thin Dyke. *Ann. Geophys.* doi:10.4401/ag-7129

César de Mello, D., Demattê, J. A. M., Silvero, N. E. Q., Di Raimo, L. A. D. L., Poppiel, R. R., Mello, F. A. O., et al. (2020). Soil Magnetic Susceptibility and its Relationship with Naturally Occurring Processes and Soil Attributes in Pedosphere, in a Tropical Environment. *Geoderma* 372, 114364. doi:10.1016/j.geoderma.2020.114364 10.1016/j.geoderma.2020.114364

Cioccari, G. M., and Mizusaki, A. M. P. (2019). Sistemas Petrolíferos Atípicos Nas Bacias Paleozoicas Brasileiras - Uma Revisão. *Geociencias* 38, 367–390. doi:10.5016/geociencias.v38i2.13173

Clark, A. J. (1996). "Magnetic Susceptibility Survey," in *The Experimental Earthwork Project, 1960–1992. 118–121*. Editors M. G. Bell, P. J. Fowler, and S. W. Hilson (York: Council for British Archaeology Research Report).

Cordani, U. G., Pimentel, M. M., Araújo, C. E. G. d., and Fuck, R. A. (2013). The Significance of the -Transbrasiliano-Kandi Tectonic Corridor for the Amalgamation of West Gondwana. *Braz. J. Geol.* 43, 583–597. doi:10.5327/Z2317-48892013000300012

Cox, D. P., Force, E. R., Wilkinson, W. H., More, S. W., Rivera, J. S., and Wooden, J. L. (2006). *The Ajo Mining District, Pima County, Arizona-evidence for Middle Cenozoic Detachment Faulting, Plutonism, Volcanism, and Hydrothermal Alteration*. Reston, VA: U.S. Geological Survey. doi:10.3133/pp1733

Crowther, J. (2003). Potential Magnetic Susceptibility and Fractional Conversion Studies of Archaeological Soils and Sediments*. *Archaeometry* 45 (4), 685–701. doi:10.1046/j.1475-4754.2003.00137.x

Daly, M. C., Fuck, R. A., Julià, J., Macdonald, D. I. M., and Watts, A. B. (2018). Cratonic basin Formation: a Case Study of the Parnaíba Basin of Brazil. *Geol. Soc. Lond. Spec. Publications* 472, 1–15. doi:10.1144/SP472.20

Di Maio, R., Milano, L., and Piegari, E. (2020). Modeling of Magnetic Anomalies Generated by Simple Geological Structures through Genetic-Price Inversion Algorithm. *Phys. Earth Planet. Interiors* 305, 106520. doi:10.1016/j.pepi.2020.106520

Dondurur, D., and Pamukçu, O. A. (2003). Interpretation of Magnetic Anomalies from Dipping dike Model Using Inverse Solution, Power Spectrum and Hilbert Transform Methods. *J. Balkan Geophys. Soc.*

Du, W., Cheng, L., and Li, Y. (2021). Lp Norm Smooth Inversion of Magnetic Anomaly Based on Improved Adaptive Differential Evolution. *Appl. Sci.* 11, 1072. doi:10.3390/app11031072

Duong, T. Q. C., Dương, Đ. H., Phạm, N. N., Nguyễn, H. T., and Danh, A. (2021). Interpretation for Magnetic Data at Low Latitude Areas Using Continuous Wavelet Transform and Marquardt Algorithm. *Sci. Tech. Dev. J. - Nat. Sci.* 5, first. doi:10.32508/stdjns.v5i2.957

Ekinci, Y. L., Balkaya, Ç., Göktürkler, G., and Özyalın, Ş. (2020). Gravity Data Inversion for the Basement Relief Delineation through Global Optimization: A Case Study from the Aegean Graben System, Western Anatolia, Turkey. *Geophys. J. Int.* 224, 923–944. doi:10.1093/gji/ggaa492

Ekinci, Y. L., Balkaya, Ç., and Göktürkler, G. (2019). Parameter Estimations from Gravity and Magnetic Anomalies Due to Deep-Seated Faults: Differential Evolution versus Particle Swarm Optimization. *Turkish J. Earth Sci.* doi:10.3906/yer-1905-3

Elaziz, M. A., Hosny, K. M., Salah, A., Darwish, M. M., Lu, S., Sahlol, A. T., et al. (2020). New Machine Learning Method for Image-Based Diagnosis of COVID-19. *PLoS ONE* 15, e0235187. doi:10.1371/journal.pone.0235187

Essa, K. S., and Elhussein, M. (2020). Interpretation of Magnetic Data Through Particle Swarm Optimization: Mineral Exploration Cases Studies. *Nat. Resour. Res.* 29, 521–537. doi:10.1007/s11053-020-09617-3

Essa, K. S., and Elhussein, M. (2018). PSO (Particle Swarm Optimization) for Interpretation of Magnetic Anomalies Caused by Simple Geometrical Structures. *Pure Appl. Geophys.* 175, 3539–3553. doi:10.1007/s00024-018-1867-0

Essa, K. S., Mehanee, S. A., Soliman, K. S., and Diab, Z. E. (2020). Gravity Profile Interpretation Using the R-Parameter Imaging Technique with Application to Ore Exploration. *Ore Geology. Rev.* 126, 103695. doi:10.1016/j.oregeorev.2020.103695

Essa, K. S., Mehanee, S., and Elhussein, M. (2021). Magnetic Data Profiles Interpretation for Mineralized Buried Structures Identification Applying the

Variance Analysis Method. *Pure Appl. Geophys.* 178, 973–993. doi:10.1007/s00024-020-02553-6

Gay, S. P. (1963). Standard Curves for Interpretation of Magnetic Anomalies over Long Tabular Bodies. *Geophysics* 28, 161–200. doi:10.1190/1.1439164

Gay, S. P. (1965). Standard Curves for Magnetic Anomalies over Long Horizontal Cylinders. *Geophysics* 30, 818–828. doi:10.1190/1.1439656

Gharehchopogh, F. S., and Gholizadeh, H. (2019). A Comprehensive Survey: Whale Optimization Algorithm and its Applications. *Swarm Evol. Comput.* 48, 1–24. doi:10.1016/j.swevo.2019.03.004

Ghosh, K. K., Guha, R., Bera, S. K., Kumar, N., and Sarkar, R. (2021). S-shaped versus V-Shaped Transfer Functions for Binary Manta ray Foraging Optimization in Feature Selection Problem. *Neural Comput. Applic.* doi:10.1007/s00521-020-05560-9

Gobashy, M., Abdelazeem, M., and Abdrabou, M. (2020). Minerals and Ore Deposits Exploration Using Meta-Heuristic Based Optimization on Magnetic Data. *Contrib. Geophys. Geod.* 50, 161–199. doi:10.31577/congeo.2020.50.2.1

Gupta, S., and Deep, K. (2019). A Novel Random Walk Grey Wolf Optimizer. *Swarm Evol. Comput.* 44, 101–112. doi:10.1016/j.swevo.2018.01.001

Hamel, J. V. (1979). "Pima Mine Slope Failure, Arizona, U.S.A," in *Developments in Geotechnical Engineering*, 633–649. doi:10.1016/B978-0-444-41508-0.50026-0

Hassan, M. H., Houssein, E. H., Mahdy, M. A., and Kamel, S. (2021). An Improved Manta ray Foraging Optimizer for Cost-Effective Emission Dispatch Problems. *Eng. Appl. Artif. Intelligence* 100, 104155. doi:10.1016/j.engappai.2021.104155

Hayyolalam, V., and Pourhaji Kazem, A. A. (2020). Black Widow Optimization Algorithm: A Novel Meta-Heuristic Approach for Solving Engineering Optimization Problems. *Eng. Appl. Artif. Intelligence* 87, 103249. doi:10.1016/j.engappai.2019.103249

Hemeida, M. G., Alkhalaf, S., Mohamed, A.-A. A., Ibrahim, A. A., and Senjyu, T. (2020). Distributed Generators Optimization Based on Multi-Objective Functions Using Manta Rays Foraging Optimization Algorithm (MRFO). *Energies* 13, 3847. doi:10.3390/en13153847

Houssein, E. H., Emam, M. M., and Ali, A. A. (2021). Improved Manta ray Foraging Optimization for Multi-Level Thresholding Using COVID-19 CT Images. *Neural Comput. Applic* 33, 16899–16919. doi:10.1007/s00521-021-06273-3

Jurandyr Luciano Sanches Ross (2020). *Brazilian Relief, Planation Surfaces and Morphological Levels*. William Morris Davis – Revista de Geomorfologia. doi:10.48025/issn2675-6900.v1n1.p264-285.2020

Kennedy, J., and Eberhart, R. (1995). "Particle Swarm Optimization," in IEEE International Conference on Neural Networks - Conference Proceedings. doi:10.4018/ijmfmp.2015010104

Kirkpatrick, S., Gelatt, C. D., and Vecchi, M. P. (1983). Optimization by Simulated Annealing. *Science* 220, 671–680. doi:10.1126/science.220.4598.671

Klein, C. E., Segundo, E. H. V., Mariani, V. C., and dos S. Coelho, L. (2016). Modified Social-Spider Optimization Algorithm Applied to Electromagnetic Optimization. *IEEE Trans. Magn.* 52, 1–4. doi:10.1109/TMAG.2015.2483059

Kombe, E. Y., and Muguthu, J. (2019). Wind Energy Potential Assessment of Great Cumbrae Island Using Weibull Distribution Function. *Jenrr*, 1–8. doi:10.9734/jenrr/2019/v2i229734

Liu, S., Hu, X., Liu, T., Xi, Y., Cai, J., and Zhang, H. (2015). Ant colony Optimisation Inversion of Surface and Borehole Magnetic Data under Lithological Constraints. *J. Appl. Geophys.* 112, 115–128. doi:10.1016/j.jappgeo.2014.11.010

Macêdo Filho, A. A., Archanjo, C. J., Hollanda, M. H. B. M., and Negri, F. A. (2019). Mineral Chemistry and crystal Size Distributions of Mafic Dikes and Sills on the Eastern Border of the Parnaíba Basin, NE Brazil. *J. Volcanology Geothermal Res.* 337, 69–80. doi:10.1016/j.jvolgeores.2019.03.021

Marques, J., Siqueira, D. S., Camargo, L. A., Teixeira, D. D. B., Barrón, V., and Torrent, J. (2014). Magnetic Susceptibility and Diffuse Reflectance Spectroscopy to Characterize the Spatial Variability of Soil Properties in a Brazilian Haplustalf. *Geoderma* 219-220, 63–71. doi:10.1016/j.geoderma.2013.12.007

Mbonu, C. C., and Ben, U. C. (2021). *Assessment of Radiation hazard Indices Due to Natural Radioactivity in Soil Samples from Orlu*. Imo State, Nigeria: Heliyon. doi:10.1016/j.heliyon.2021.e07812

Mbonu, C. C., Essiett, A., and Ben, U. C. (2021). Geospatial Assessment of Radiation hazard Indices in Soil Samples from Njaba, Imo State, South-Eastern Nigeria. *Environ. Challenges* 4, 100117. doi:10.1016/j.envc.2021.100117

Mckenzie, D., and Rodríguez Tribaldos, V. (2018). Lithospheric Heating by Crustal Thickening: a Possible Origin of the Parnaíba Basin. *Geol. Soc. Lond. Spec. Publications* 472, 37–44. doi:10.1144/SP472.5

Mehanee, S. A. (2022b). A New Scheme for Gravity Data Interpretation by a Faulted 2-D Horizontal Thin Block: Theory, Numerical Examples and Real Data Investigation. *IEEE Trans. Geosci. Remote Sensing*, 1. doi:10.1109/TGRS.2022.3142628

Mehanee, S. A. (2014). An Efficient Regularized Inversion Approach for Self-Potential Data Interpretation of Ore Exploration Using a Mix of Logarithmic and Non-logarithmic Model Parameters. *Ore Geology. Rev.* 57, 87–115. doi:10.1016/j.oregeorev.2013.09.002

Mehanee, S. A. (2022a). Simultaneous Joint Inversion of Gravity and Self-Potential Data Measured along Profile: Theory, Numerical Examples, and a Case Study from Mineral Exploration with Cross Validation from Electromagnetic Data. *IEEE Trans. Geosci. Remote Sensing* 60, 1–20. doi:10.1109/TGRS.2021.3071973

Mehanee, S., Essa, K. S., and Diab, Z. E. (2021). Magnetic Data Interpretation Using a New R-Parameter Imaging Method with Application to mineral Exploration. *Nat. Resour. Res.* 30, 77–95. doi:10.1007/s11053-020-09690-8

Mehanee, S., Golubev, N., and Zhdanov, M. S. (1998). Weighted Regularized Inversion of Magnetotelluric Data. *SEG Annu. Meet.* 1998. doi:10.1190/1.1820468

Mehanee, S., and Zhdanov, M. (2004). A Quasi-Analytical Boundary Condition for Three-Dimensional Finite Difference Electromagnetic Modeling. *Radio Sci.* 39 (6), a–n. doi:10.1029/2004RS003029

Noweir, M. A., and Fheel*, A. S. (2015). *Structural Evolution of Extensional Phanerozoic Rift Blocks: El Hamrawein Area, Northwest Red Sea, Eastern Desert*. Egypt. doi:10.1190/ice2015-2212373

Ouadfel, S., and Taleb-Ahmed, A. (2016). Social Spiders Optimization and Flower Pollination Algorithm for Multilevel Image Thresholding: A Performance Study. *Expert Syst. Appl.* 55, 566–584. doi:10.1016/j.eswa.2016.02.024

Ouyang, F., and Chen, L. (2020). Iterative Magnetic Forward Modeling for High Susceptibility Based on Integral Equation and Gauss-Fast Fourier Transform. *Geophysics* 85, J1–J13. doi:10.1190/geo2018-0851.1

Pan, J., Wang, X., Zhang, X., Xu, Z., Zhao, P., Tian, X., et al. (2009). 2D Multi-Scale Hybrid Optimization Method for Geophysical Inversion and its Application. *Appl. Geophys.* 6, 337–348. doi:10.1007/s11770-009-0034-x

Pellerin, L., and Wannamaker, P. E. (2005). Multi-dimensional Electromagnetic Modeling and Inversion with Application to Near-Surface Earth Investigations. *Comput. Electronics Agric.* 46, 71–102. doi:10.1016/j.compag.2004.11.017

Portniaguine, O., and Zhdanov, M. S. (2000b). 3-D Magnetic Inversion with Data Compression and Image Focusing. *Geophysics* 67 (5), 1532–1541.

Portniaguine, O., and Zhdanov, M. S. (2000a). 3-D Magnetic Regularized Inversion with Data Compression and Image Focusing. *SEG Tech. Program Expanded Abstr.* doi:10.1190/1.1816073

Prakasa Rao, T. K. S., and Subrahmanyam, M. (1988). Characteristic Curves for the Inversion of Magnetic Anomalies of Spherical Ore Bodies. *Pure Appl. Geophys. PAGEOPH*. doi:10.1007/bf00876915

Rao, B. S. R., Radhakrishna Murthy, I. V., and Visweswara Rao, C. (1973). A Computer Program for Interpreting Vertical Magnetic Anomalies of Spheres and Horizontal Cylinders. *Pageoph* 110, 2056–2065. doi:10.1007/BF00876569

Salcedo-Sanz, S., Cornejo-Bueno, L., Prieto, L., Paredes, D., and García-Herrera, R. (2018). Feature Selection in Machine Learning Prediction Systems for Renewable Energy Applications. *Renew. Sustainable Energ. Rev.* 90, 728–741. doi:10.1016/j.rser.2018.04.008

Salem, A., Elsirafi, A., and Ushijima, K. (1999). *Design and Application of High-Resolution Aeromagnetic Survey over Gebel Duwi Area and its*

Offshore Extension. Egypt: Memoirs of the Graduate School of Engineering, Kyushu University.

Salem, A. (2011). Multi-deconvolution Analysis of Potential Field Data. *J. Appl. Geophys.* 74, 151–156. doi:10.1016/j.jappgeo.2011.04.001

Salem, A., Ravat, D., Smith, R., and Ushijima, K. (2005). Interpretation of Magnetic Data Using an Enhanced Local Wavenumber (ELW) Method. *Geophysics* 70, L7–L12. doi:10.1190/1.1884828

Silva, J. B. C. (1989). Transformation of Nonlinear two-dimensional Problems into Linear Ones Applied to the Magnetic Field of a Prism. *Geophysics* 54, 114–121. doi:10.1190/1.1442568

Smith, R. S., and Salem, A. (2005). Imaging Depth, Structure, and Susceptibility from Magnetic Data: The Advanced Source-Parameter Imaging Method. *Geophysics* 70, L31–L38. doi:10.1190/1.1990219

Solon, F. F., Fontes, S. L., and La Terra, E. F. (2018). Electrical Conductivity Structure across the Parnaíba Basin, NE Brazil. *Geol. Soc. Lond. Spec. Publications* 472, 109–126. doi:10.1144/SP472.19

Tarantola, A. (2005). "Inverse Problem Theory and Methods for Model Parameter Estimation," in *Inverse Problem Theory and Methods for Model Parameter Estimation*. doi:10.1137/1.9780898717921

Teixeira, D. D. B., Marques, J., Siqueira, D. S., Vasconcelos, V., Carvalho, O. A., Martins, É. S., et al. (2018). Mapping Units Based on Spatial Uncertainty of Magnetic Susceptibility and clay Content. *Catena* 164, 79–87. doi:10.1016/j.catena.2017.12.038

Tlas, M., and Asfahani, J. (2011). Fair Function Minimization for Interpretation of Magnetic Anomalies Due to Thin Dikes, Spheres and Faults. *J. Appl. Geophys.* 75, 237–243. doi:10.1016/j.jappgeo.2011.06.025

Tlas, M., and Asfahani, J. (2015). The Simplex Algorithm for Best-Estimate of Magnetic Parameters Related to Simple Geometric-Shaped Structures. *Math. Geosci.* 47, 301–316. doi:10.1007/s11004-014-9549-7

Venkata Raju, D. C. (2003). LIMAT: A Computer Program for Least-Squares Inversion of Magnetic Anomalies over Long Tabular Bodies. *Comput. Geosciences*. doi:10.1016/S0098-3004(02)00108-5

Wang, J.-S., and Li, S.-X. (2019). An Improved Grey Wolf Optimizer Based on Differential Evolution and Elimination Mechanism. *Sci. Rep.* 9. doi:10.1038/s41598-019-43546-3

Xie, W., Wang, Y.-C., Liu, X.-Q., Bi, C.-C., Zhang, F.-Q., Fang, Y., et al. (2019). Nonlinear Joint PP-PS AVO Inversion Based on Improved Bayesian Inference and LSSVM. *Appl. Geophys.* 16, 64–76. doi:10.1007/s11770-019-0750-9

Xu, H., Song, H., Xu, C., Wu, X., and Yousefi, N. (2020). Exergy Analysis and Optimization of a HT-PEMFC Using Developed Manta Ray Foraging Optimization Algorithm. *Int. J. Hydrogen Energ.* 45, 30932–30941. doi:10.1016/j.ijhydene.2020.08.053

Zhao, W., Zhang, Z., and Wang, L. (2020). Manta ray Foraging Optimization: An Effective Bio-Inspired Optimizer for Engineering Applications. *Eng. Appl. Artif. Intelligence* 87, 103300. doi:10.1016/j.engappai.2019.103300

Conflict of Interest: The authors declare that the research was conducted in the absence of any commercial or financial relationships that could be construed as a potential conflict of interest.

Publisher's Note: All claims expressed in this article are solely those of the authors and do not necessarily represent those of their affiliated organizations, or those of the publisher, the editors and the reviewers. Any product that may be evaluated in this article, or claim that may be made by its manufacturer, is not guaranteed or endorsed by the publisher.

frontiers in Earth Science

ORIGINAL RESEARCH
published: 23 March 2022
doi: 10.3389/feart.2022.870299

A Novel Method for Estimating Model Parameters From Geophysical Anomalies of Structural Faults Using the Manta-Ray Foraging Optimization

Ubong C. Ben[1], Stephen E. Ekwok[1], Ogiji-Idaga M. Achadu[2], Anthony E. Akpan[1], Ahmed M. Eldosouky[3], Kamal Abdelrahman[4] and David Gómez-Ortiz[5]*

[1]Department of Physics, University of Calabar, Calabar, Nigeria, [2]Department of Geology, University of Calabar, Calabar, Nigeria, [3]Geology Department, Faculty of Science, Suez University, Suez, Egypt, [4]Department of Geology and Geophysics, College of Science, King Saud University, Riyadh, Saudi Arabia, [5]Department of Biology and Geology, Physics and Inorganic Chemistry, ESCET, Universidad Rey Juan Carlos, Madrid, Spain

The Manta-Ray Foraging Optimization has been adapted and implemented in computing model parameters from potential field anomalies originating from two-dimensional dipping faults. The inversion technique was originally demonstrated on magnetic anomalies from uncorrupted–then, corrupted synthetic datasets. Thereafter, it was experimented on profiles taken from mining fields in the United States, and Australia. The results obtained showed that the design procedure is admirably stable and flexible, especially when dealing with noisy data. It is also notably efficient in the quantitative resolution of geophysical inverse problems. The consistency in results obtained from analysis of deep-seated and shallow field examples, even when compared against background results, is also impressive. The new technique has also exhibited notable superiorities over other well-known and conventional techniques, especially on the grounds of convergence rate, cost, and quality of resolved anomaly parameters. Consequently, it is recommended for interpretation of other structures and modeling of other geophysical data like self-potential and resistivity data.

Keywords: manta-ray, optimization, magnetics, gravity, Fault

OPEN ACCESS

Edited by:
Mourad Bezzeghoud,
Escola de Ciência e Tecnologia,
Universidade de Évora, Portugal

Reviewed by:
Serdar Ekinci,
Batman University, Turkey
Qiang Guo,
China Jiliang University, China
Kittisak Jermsittiparsert,
Dhurakij Pundit University, Thailand

****Correspondence:***
Ahmed M. Eldosouky
dr_a.eldosoky@yahoo.com

Specialty section:
This article was submitted to Solid Earth Geophysics, a section of the journal Frontiers in Earth Science

Received: *06 February 2022*
Accepted: *28 February 2022*
Published: *23 March 2022*

Citation:
Ben UC, Ekwok SE, Achadu O-IM, Akpan AE, Eldosouky AM, Abdelrahman K and Gómez-Ortiz D (2022) A Novel Method for Estimating Model Parameters From Geophysical Anomalies of Structural Faults Using the Manta-Ray Foraging Optimization. Front. Earth Sci. 10:870299. doi: 10.3389/feart.2022.870299

INTRODUCTION

In magnetics and gravity prospecting, signals of interest typically include those originating from buried rock units, as well as those from neighboring formations. The interpretational focus, however, is mostly on geologic structures that are of economic end-importance. Faults, ores, contacts, and dykes are examples of such structures. Notably, attention on the interpretation of anomalies due to faults for mineral prospecting has been appreciated among geophysicists lately. This is unrelated to the fact that over the years–in addition to immense improvements in geophysical data interpretation measures; faults have proven as good traps and caps over hydrocarbon pools. They have also been known to exert a strong influence on the regional and local direction of mineralization (Li et al., 2020).

Several techniques that ensure economically friendly and accurate acquisition and processing of potential field data have been developed and accepted for different exploration problems. However, for optimal interpretability and also to ensure the suitability of the acquired data for structural

imaging of the subsurface, the data must undergo geophysical inversion (Abo-Ezz & Essa, 2016). Geophysical inversion is a step-by-step modeling approach that aims to unravel the features of buried geologic structures by establishing similarities between them and to already well-defined models (Essa & Munschy 2019). Over the years, various inversion techniques have been designed for the deciphering/computation of these characteristic physical parameters. Some of these procedures are united by adept functional exploitation of computational approaches including Euler deconvolution (Mota et al., 2020), Werner deconvolution (Cerovský & Pašteka 2003), model layering (Pilkington 2006), and parametric curves (Abdelrahman et al., 2012). Others employ procedures consistent with fair function minimization and Depth From Extreme Points (DEXP) (Abbas and Fedi 2013), simplex algorithm (Pan et al., 2009), and linear least squares (Melo & Barbosa 2018). However, experience has shown that results obtained from these conventional inversion approaches usually lead to the generation of large amounts of invalid solutions. The invalid solutions are caused by many factors including noise sensitiveness and poor window size compatibility (Li et al., 2020). Another cause is improper filtering of noise from signals of interest. Also, there is a characteristic over-dependence of initializations on subjective priori geologic information which may not be reliable or sufficiently reputable.

With recent improvements in machine intelligence, these classical magnetic inversion methods are gradually being substituted with more dependable, accurate, and reliable metaheuristic techniques. Some of the intelligent techniques employed for geophysical inversion include ant colony optimization - ACO (Gupta et al., 2013); genetic algorithm (Sen & Mallick 2018), particle swarm optimization- PSO (Guo et al., 2020; Essa 2021; Essa et al., 2021); neural networks method (Yadav et al., 2021); differential evolution-DEA (Garabito and Cruz 2019; Ekinci Y. L. et al., 2021); simulated annealing (Pan et al., 2009) and genetic price algorithm (Kaftan 2017). These intelligent algorithms, which mostly work by the functional imitation of the normal behavior of objects from nature; have generally upset most of the challenges posed by the classical algorithms. The most obvious advantage of these techniques is that they are conditioned to be zero-ordered. This implies that any performance enhancements made in a direction towards feasible solutions are not related to the derivatives of the function minimized/maximized.

The performance of the above-mentioned intelligence-based methodologies have generally been applausive. This is especially in terms of optimized structural resolvability and improvements in interpretation quality. Howbeit, these methodologies are still short of analytical perfection, particularly in terms of convergence and computational cost (Hemeida et al., 2020; Ben et al., 2021b; Mbonu et al., 2021; Turgut 2021). Continual pursuit of this analytical perfection necessitates continual development and deployment of new optimizers and hence, the motivation for this study. In this research paper, we present a new way of parameterizing magnetic and gravity anomalies generated by dipping fault structures based on the Manta-Ray Foraging Optimization (MRFO) algorithm.

The MRFO algorithm—a relatively recent metaheuristic technique, leverages the bio-inspired foraging strategies of Manta-Rays for the resolution of optimization problems (Hemeida et al.., 2020). The MRFO approach has previously been tested and proven to be effective with contextual and engineering challenges such as Covid-19 thresholding, arrhythmia classification, energy minimization, wind turbine control, fractional-order proportional–integral–derivative controller design as well as magnetic levitation system (Ekinci et al., 2021b; Ekinci et al., 2021c; Feng et al., 2021; Houssein et al., 2021; Rezk et al., 2021). From the results of those applications, MRFO optimization technique was reported as superior to existing heuristic algorithms in several ways, such as better accuracy, enhanced performance, and lower computational cost. Resultantly, the scholars strongly recommended the method for inversion situations. Up to the initial draft of this manuscript, a total of two geophysical inversion studies using the MRFO technique has been reported in published literature. Ben et al. (2021b) employed the technique for the modeling of dipping dykes; Ben et al. (2021c) interpreted gravity anomalies over geometric geological structures such as spheres, cylinders, sheets, and, horizontal faults using the MRFO strategy. Barnhart and Lohman (2010), Amoruso et al. (2013), and, Qureshi & Nalaye (1978) have however explained problems associated with interpreting faults without regards to the angle of dip–especially for fault structures in highly deformed regions, e.g zones of folding. The novelty of this study lies in the pioneering application of the MRFO algorithm to non-horizontal fault problems. The parameters sought in this study are those defining the character, location, and position of the subsurface feature. The new method presents a couple of merits. First, unlike deterministic schemes, iterative computations are independent of the gradient of the objective function, technically limiting immature convergence. Also, the wild function injected during the cyclone foraging stage of the algorithm design allows initial models to parameterize from anywhere within a size-independent range (as would be seen in the examples)—reducing reliance on subjectivity. Most importantly, the superiority of the MRF tool actually lies with its foraging character. With MRFO algorithm, the search agents are allowed to switch intelligently and at any point between the strategies of chain foraging and cyclone foraging. The chain foraging behavior allows significant local search while the cyclone foraging behavior concurrently assures non-deterioration of global search during the process; a mutualization of the two as allowed by the new technique ensures comparatively quality solutions through a thorough exploration of the whole domain of the geophysical problem.

The layout of the present paper is described as follows. First, the 2-D potential field problem with respect to dipping faults is introduced. Next, the proposed inversion methodology based on MRFO is strategically constructed. The technique is then experimented on synthetically constructed models corrupted with random noise at varying levels and further, with two real case studies. The obtained parameter values are then compared with published results previously reported for similar anomalies but obtained using other conventional techniques. Additionally,

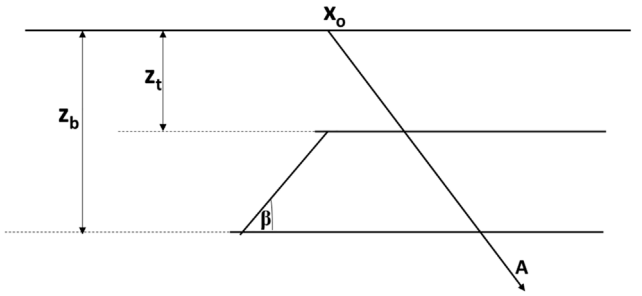

FIGURE 1 | A dipping fault model.

to understand uncertainties in the obtained solutions, appraisals are conducted using Markov Chain Monte Carlo sampling procedure. The MCMCprocedure adopted employs the simulated-annealing without cooling scheme. Finally, the study concludes with a brief assessment of the applicability and effectiveness of MRFO as a tool for inversion of gravity and magnetic field anomalies.

METHODOLOGY

Forward Modeling Problem

Assume a standard Cartesian coordinate system whose ordinate represents the strike of a dipping fault buried at depth z, and whose abscissa indicates the profile direction (**Figure 1**). The magnetic -T and gravity G anomalies- (collectively depicted as P later in the paper for inclusiveness and generality) (**Eq. 1** and **Eq. 2**); of the two-dimensional fault at any point x_k can be expressed as (Essa, 2013; Abdelrahman et al., 2019):

$$G(x_k, A, x_o, z, \beta) = A\left[\pi + \tan^{-1}\left(\frac{x_k - x_o}{z_t} + \cot\beta\right) - \tan^{-1}\left(\frac{x_k - x_o}{z_b} + \cot\beta\right)\right], \quad (1)$$

$$T(x_k, A, x_o, z_t, z_b, \beta) = A\left[\sin\beta\left(\tan^{-1}\frac{x_k - x_o}{z_t} - \tan^{-1}\frac{x_k - x_o}{z_b}\right) + \frac{\cos\beta}{2}\left(\ln\frac{(x_k - x_o)^2 - z_b^2}{(x_k - x_o)^2 - z_t^2}\right)\right], \quad (2)$$

where z_t is depth to the top and z_b is depth to the bottom of the structure from the observation plane, β and A are respectively, the dip angle, and amplitude coefficient that has a direct relationship with thickness of fault, density contrast of the gravity anomaly case and inclination of the geomagnetic field in the vertical plane perpendicular to the strike of the fault.

These five controlling model parameters were determined in this research, by constraining the cost function—*obj* (**Eq. 3**) using the MRFO procedure. Acceptable values were determined by lessening disparities between the calculated and actual data (Essa et al., 2018; Ekinci et al., 2019).

$$objective\ function = \frac{\sum_{i=1}^{S}\left(P_i^m - P_i^c\right)^2}{S}, \quad (3)$$

where P_i^m and P_i^c are respectively the potential field anomaly from observed data and those estimated using the proposed methodology.

Manta-Ray Foraging Optimization Algorithm

Manta-Rays, one of the ocean's biggest creatures, are commonly found in tropical environments. As manta-rays are naturally toothless (**Figure 2**), their diet is normally limited to microscopic aquatic creatures -planktons (Alturki et al., 2020). Due to the dependence of plankton on ebbs and tides, the occurrence of planktons in large concentrations is often erratic and infrequent. For that reason, finding the best strategies for assuring consistent food availability is essential for Manta-Ray survival (Izci et al., 2020). Interestingly, Manta-Rays have developed and honed several clever foraging tactics that are so effective they rarely face food scarcity. The MRFO algorithm, which provides the basis of our new methodology, is premised on these distinct foraging strategies, specifically the chain, somersault, and cyclone techniques (Turgut, 2021). Herewith, vectorial positions of each foraging Manta-ray depict probable positions of the required potential field parameter; and that of the planktons indicate the optimum solution to the geoscientific problem. The accompanying sections discuss these foraging approaches as well as the numerical constructs designed for our novel geophysical methodology.

Chain Foraging

Manta-Rays implement the chain foraging method by first, locating prospective plankton and then, advancing toward it via a foraging chain (technically a head-tail formation). As a result, the neighbor would immediately take up any plankton

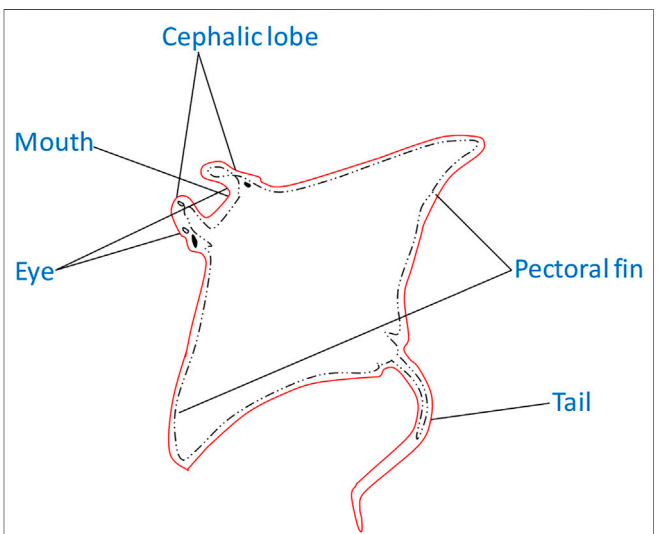

FIGURE 2 | Simplified anatomy of a Manta-Ray.

that is missed by one agent and improve overall opportunities for exploitation. The denser the concentration of plankton at a specific position, the stronger that position (Ghosh et al., 2021; Houssein et al., 2021). To achieve this strategy a premise equating the original best position to the current optimal solution is employed. This comparative position was subsequently utilized to update the location of each agent and its immediate predecessor. For our dipping fault problem, the strategy was implemented using **Eq. 4** (Houssein et al., 2021).

$$P(\mathrm{x}_k) = \begin{cases} \mathrm{P}(\mathrm{x}_k)_i^4(t) + \boldsymbol{r}.\left(\mathrm{P}(\mathrm{x}_k)_{best}^4(t) - \mathrm{P}(\mathrm{x}_k)_i^4(t)\right) + \boldsymbol{w}.\left(\mathrm{P}(\mathrm{x}_k)_{best}^4(t) - \mathrm{P}(\mathrm{x}_k)_i^4(t)\right) \boldsymbol{i} = 1 \\ \mathrm{P}(\mathrm{x}_k)_i^4(t) + \boldsymbol{r}.\left(\mathrm{P}(\mathrm{x}_k)_{i-1}^4(t) - \mathrm{P}(\mathrm{x}_k)_i^4(t)\right) + \boldsymbol{w}.\left(\mathrm{P}(\mathrm{x}_k)_{best}^4(t) - \mathrm{P}(\mathrm{x}_k)_i^4(t)\right) \boldsymbol{i} = 2, 3, \ldots, \boldsymbol{T} \end{cases}, \tag{4}$$

$$\boldsymbol{w} = 2.\boldsymbol{rand}().\sqrt{\left|\log(\boldsymbol{r})\right|}, \tag{5}$$

where $\mathrm{P}(\mathrm{x}_k)(t)$ is search agent's *i*th position (the potential field parameters) at t, T the maximum iteration number; w the weight coefficient (**Eq. 5**); *rand*()-a vector randomly generated between 0 and 1 while $\mathrm{P}(\mathrm{x}_k)_{best}^4(t)$ the optimal geophysical parameter position vector is technically located in the healthiest plankton cluster.

The *i*th individual's position is determined by positions $\mathrm{P}(\mathrm{x}_k)_{i-1}^4(t)$ of the (i-1)$^{\text{th}}$ search agent and $\mathrm{P}(\mathrm{x}_k)_{best}^4(t)$ of the food (the target solution of our geophysical problem).

Cyclone Foraging

If a group of Manta-Rays, as detailed above, identify and create a foraging chain to lucrative plankton in deep water, they will glide towards them in spirals. The spirals are similar to the one employed in the Water Optimization Algorithm (Gharehchopogh & Gholizadeh 2019). For MRFO, however, the approaching Manta-Ray swarm maintains their line while whirling, such that while an individual follows the one in front, it is still going towards the target food.

We use the following equations to numerically describe this method in a form that is specific to our potential field problem (Zhao et al., 2020).

$$\mathrm{P}(\mathrm{x}_k)_i^4(\boldsymbol{t}+1) = \begin{cases} \mathrm{P}(\mathrm{x}_k)_{best}^4(t) + \boldsymbol{rand}().\left(\mathrm{P}(\mathrm{x}_k)_{best}^4(\boldsymbol{t}) - \mathrm{P}(\mathrm{x}_k)_i^4(\boldsymbol{t})\right) + \boldsymbol{w}.\left(\mathrm{P}(\mathrm{x}_k)_{best}^4(\boldsymbol{t}) - \mathrm{P}(\mathrm{x}_k)_i^4(\boldsymbol{t})\right) \boldsymbol{i} = 1 \\ \mathrm{P}(\mathrm{x}_k)_{best}^4(t) + \boldsymbol{rand}().\left(\mathrm{P}(\mathrm{x}_k)_{i-1}^4(\boldsymbol{t}) - \mathrm{P}(\mathrm{x}_k)_i^4(\boldsymbol{t})\right) + \boldsymbol{w}.\left(\mathrm{P}(\mathrm{x}_k)_{best}^4(\boldsymbol{t}) - \mathrm{P}(\mathrm{x}_k)_i^4(\boldsymbol{t})\right) \boldsymbol{i} = 2, 3, \ldots, \boldsymbol{T} \end{cases}, \tag{6}$$

where w is asymptotically generated by **Eq. 7** as weight coefficient for cyclone foraging.

$$w = 2e^{rand()\frac{T-t+1}{T}}\sin 2\pi rand(), \tag{7}$$

However, after completing this stage successfully, the estimations for the required fault parameters failed to converge repeatedly and instead become unstable; fluctuating about a central position inside the search space. Convergence was obliged by nudging each agent to new positions that differed from their current ones but remained within the problem domain. This was strategized by injecting a wild random function into each structural parameter's bound (Houssein et al., 2021; Ghosh et al., 2021). This local strategy allowed comprehensive global search by MRFO and significantly increased overall exploration. The numerical construct for this stage is expressed as shown in **Eq. 8**. It was generically implemented using **Eq. 9** (Rezk et al., 2021).

$$\boldsymbol{q}_{\boldsymbol{rand}}^4 = \boldsymbol{LB}^4 + \boldsymbol{rand}().\left(\boldsymbol{UB}^4 - \boldsymbol{LB}^4\right), \tag{8}$$

$$\mathrm{P}(\mathrm{x}_k)_i^4(t+1) = \begin{cases} \boldsymbol{q}_{\boldsymbol{rand}}^4(t) + \boldsymbol{rand}().\boldsymbol{q}_{\boldsymbol{rand}}^4(t) - \mathrm{P}(\mathrm{x}_k)_i^4(t)) + \boldsymbol{\mu}.\left(\boldsymbol{q}_{\boldsymbol{rand}}^4(t) - \mathrm{P}(\mathrm{x}_k)_i^4(t)\right) \boldsymbol{i} = 1 \\ \boldsymbol{q}_{\boldsymbol{rand}}^4(t) + \boldsymbol{rand}().\left(\mathrm{P}(\mathrm{x}_k)_{i-1}^4(t) - \mathrm{P}(\mathrm{x}_k)_i^4(t)\right) + \boldsymbol{\mu}.\left(\boldsymbol{q}_{\boldsymbol{rand}}^4(t) - \mathrm{P}(\mathrm{x}_k)_i^4(t)\right) \boldsymbol{i} = 2, 3, \ldots, \boldsymbol{T} \end{cases}, \tag{9}$$

where $\boldsymbol{q}_{\boldsymbol{rand}}^4$ is the random function explained earlier.

Somersault Foraging

Here, the search domain is reconstructed such that our ideal geophysical solution (promising planktons) is positioned as a pivot. This is such that, before somersaulting off to other locations, each of our investigative search agents revolves around this pivot. By this, the new positions are not completely random or stray too far, but rather circle about the most promising found up to that time. With increasing iterations, the algorithm is designed such that the somersaulting range is intelligently lowered step-wise until the solutions are obtained. This is achieved numerically using **Eq. 10** (Elattar et al., 2020; Ben et al., 2021b; Feng et al., 2021)

$$\begin{aligned} \mathbf{P}(\mathbf{x}_k)_i^4(\boldsymbol{t}+1) = \mathbf{P}(\mathbf{x}_k)(\boldsymbol{t}) + \boldsymbol{S}.\boldsymbol{rand}_1().\mathbf{P}(\mathbf{x}_k)_i^4(\boldsymbol{t}) \\ - \boldsymbol{rand}_2().\mathbf{P}(\mathbf{x}_k)_i^4(\boldsymbol{t}), \\ \boldsymbol{i} = 1, 2, \ldots, \boldsymbol{N}, \end{aligned} \tag{10}$$

where the term S—a constant known as the somersault factor, determines the Manta-Ray's somersaulting range. $rand_1()$ and $rand_2()$ determined randomly between 0 and 1 were generated using PYTHON's NUMPY library.

Random initialization of the Manta-Ray's population in the search space (designed around the UB and LB) is the first step in our proposed method. Each agent in the domain is made to contain all the fault parameters required. The user-selection of UB and LB for each structural problem is driven by historical geology, geophysical, and petrophysical information. The bounds do not necessarily affect the results but only prevent the agents from completely iterating out into infinity. At each iteration step, the agents update their current positions based on the agent preceding them and their referential position. These positions of reference are determined by t/T, whose value is skillfully decreased from 1/T to 1 for exploratory and exploitative searches (Houssein et al., 2021). Exploitation is done when t/T is smaller than rand(); otherwise, exploration takes place. As a result, the MRFO algorithm enables individuals to determine and, if necessary, transpose between cyclone and chain behaviors. These calculations and updates are carried out iteratively, step by step, until the stopping criterion is met.

The estimated data was assessed after each step by comparing it with the measured data using RMS error technique (**Eq. 3**).

The best positions representing the five required model parameters are returned whenever convergence is achieved. **Figure 3** is a flowchart for the entire optimization procedure discussed above.

Algorithm Configuration/Time Complexity

The algorithm used for this study was designed with PYTHON3 programming package and compiled on the VSCode developer

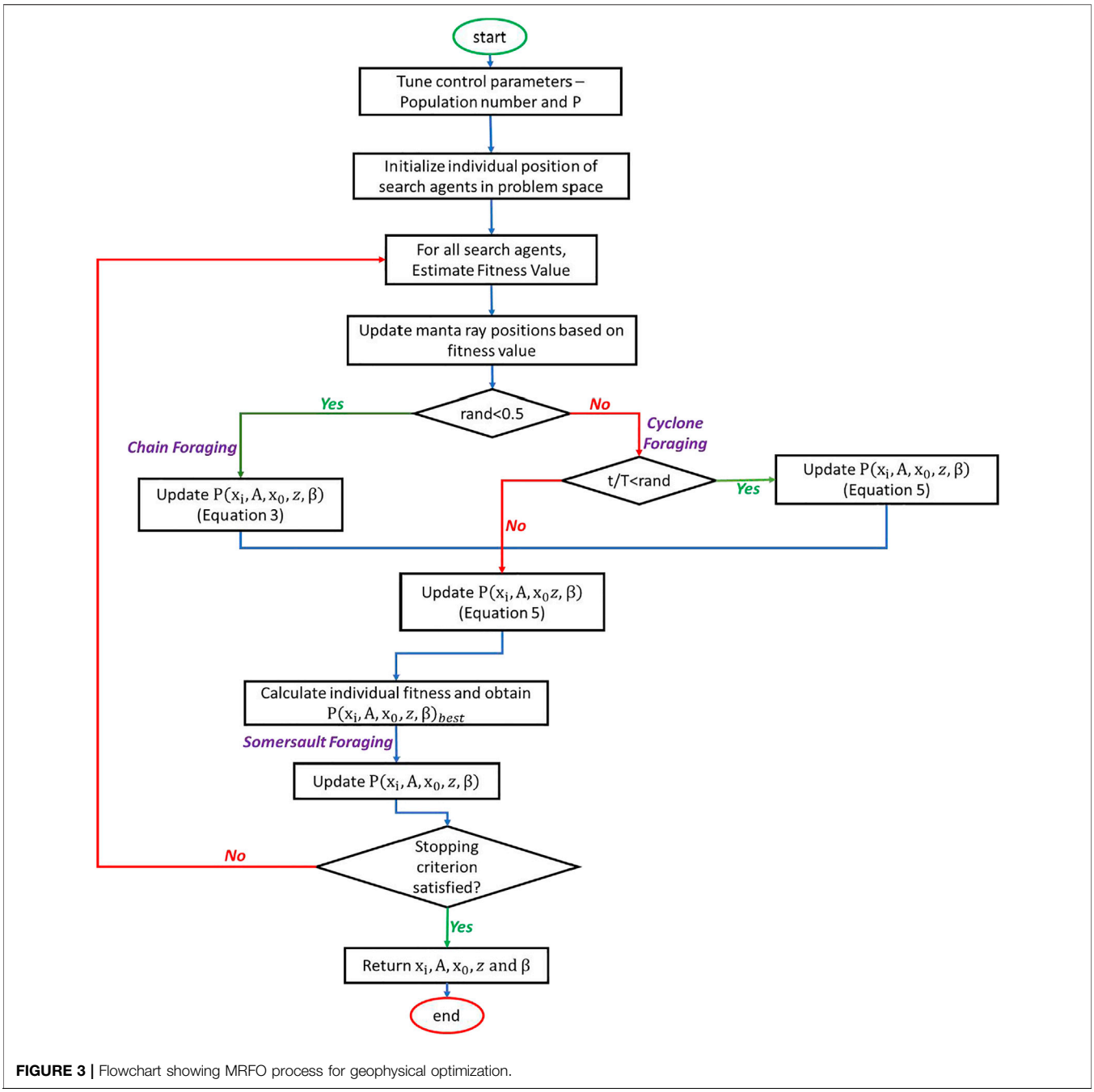

FIGURE 3 | Flowchart showing MRFO process for geophysical optimization.

environment. The compiling environment was installed on a simple PC running on a core i7 processor and a Windows 10 package.

For time complexity, this factor depended-first on the structural feature's complexity; then on the number of iterations allowed. Nonetheless, for all cases in this study, the process rounded up completely in less than 50 s.

Uncertainty Analysis

Arising from the characteristic non-uniqueness, non-linearity, and ill-posedness of geophysical inverse problems; it is mathematically possible for various models constructed from different sets of parameters to fit into similar observed measurements. This situation usually raises considerable uncertainty around ultimately estimated parameters. As a result, uncertainty appraisal has come to be accepted as very vital in inversion studies (Scales & Tenorio 2001).

The Bayesian approach has been reportedly employed in parameter estimations involving considerable stochasticity. The procedure relies on the concept of conditional probability. By combining a priori information with the experimental data's likelihood, prior probability distributions for the required

parameters could be obtained (Tarantola 2005; Biswas et al., 2017; Yusof et al., 2018). For global optimization algorithms like SA, PSO, and, GA, correct sampling has been achieved with the Markov-Chain Monte Carlo algorithm (Yusof et al., 2018; Ekinci et al., 2020). For this investigation, the Metropolis-Hasting algorithm (M–H), a generalized Markov chain Monte Carlo (MCMC) method (Metropolis et al., 1953; Hastings, 1970) was used for parameter sampling. The M-H method suggests various models based on some prior distribution. The likelihood of each proposed model is computed by resolving the forward model problem and then, obtaining the misfit in the data. If there is a likelihood increase, the revised model is accepted. Nonetheless, even if there is an observed decrease in likelihood, the proposed model can still be accepted, although with a probability dependent on the ratio of likelihood between the proposed and the original model. The method, based upon simulated annealing, allowed for the assessment of uncertainty by providing parameter confidence intervals (Ekinci et al., 2020).

PARAMETER TUNING STUDIES

Pluralities of bio-inspired global optimization algorithms have unique control parameters that have a big impact on the algorithm's inversion convergence point. These control features are critical for any algorithm's overall performance. Their selection, however, heavily depends on the problem-at-hand's nature (Kanimozhi & Jacob 2019; Gonzalez et al., 2021). Resultantly and prior to conducting our inversion analysis, we modify model parameters to establish the appropriate control parameters for the Manta-Ray algorithm. The parameter tuning study in our metaheuristic instance is primarily concerned with determining the optimum population of experimenting agents and the Somersault factor–S.

To properly guide the tuning studies, a synthetic magnetic anomaly dataset was theoretically generated using **Eq. 1** with A = 200 nT. Further, z_b = 30 m, z_t = 10 m, $\beta = 40^{\circ}$, x_o = 10 m, and profile length was 160 m. A synthetic gravity anomaly dataset was also generated with A = 50 mGal, z_b = 30 m, z_t = 8 m, $\beta = 40^{o}$, x_o = 0 m, and profile length of 80 m. In both synthetic magnetic and gravity data experiments, broad search spaces (**Table 1**, **2**) are adopted for the model parameters. This was to enable investigation of S's effect on the overall solution. The inversion of both anomalies was then carried out using identical approaches. Thirty independent runs in 500 optimization iterations were permitted with population number = 150. The select population number was arrived at by multiplying the number of unknown model parameters (5) with total independent runs allowed (30). The magnetic and gravitational anomaly problem was thereafter investigated statistically utilizing the mean, standard deviation, and minimum of the RMS. **Tables 3** (magnetic data) and 4 (gravity data) show the findings obtained for various S values.

According to the tables, the best statistical results (boldface) were obtained with an S value of 2. This means that using this value as the S for both gravity and magnetic data would make the whole optimization process more resilient and effective. The huge range in error values between the control producing the best and those producing the worst is another notable/interesting observation. This huge discrepancy could definitely have a significant impact on the solution's correctness in relation to the optimal model parameter resolution. This so emphasizes the critical need for parameter tuning studies during global optimization applications.

TABLE 1 | Search space, actual and estimated parameters uncorrupted synthetic gravity anomaly.

Anomaly parameters	Search Space	Actual (Control)	Estimated
A (mGal)	0–200	50.000	49.974
x_o (m)	−20–20	0.000	0.036
z_b (m)	0–100	30.000	30.278
z_t (m)	0–50	8.000	7.892
β (°)	−180–180	40.000	39.991

TABLE 2 | Bounds, actual and estimated parameters for uncorrupted synthetic magnetic anomaly.

Anomaly parameters	Search bounds	Actual (Control)	Estimated
A (nT)	0–500	200	200.031
x_o (m)	−50 – 50	10	9.931
z_b (m)	0–100	30	30.008
z_t (m)	0–100	10	10.003
β (°)	−180–180	40	39.997

TABLE 3 | Statistical results for RMS values obtained from parameter tuning of MRFO for synthetic magnetic dataset.

S	RMS (nT)		
	Minimum	Mean	Standard deviation
0.5	1.3869	1.7836	0.7548
1	0.5383	0.9471	0.2674
1.5	0.2536	0.4368	0.0734
2	0.0745	0.8352	2.4836×10^{-5}
2.5	0.1338	0.1836	5.3425×10^{-3}
3	0.3846	0.5358	0.2036

SYNTHETIC EXAMPLES

To assess performance, we put the proposed methodology through controlled series of tests using synthetic data simulating an idealized dipping fault. The uncorrupted version synthetic anomaly was examined first; then the clean anomaly was purposefully contaminated with noise and reanalyzed.

Noiseless Anomaly

The MRFO technique was used to investigate the uncontaminated magnetic and gravity field anomalies synthetically generated for a dipping fault structure. The synthetic magnetic anomaly constructed along a 160-m long

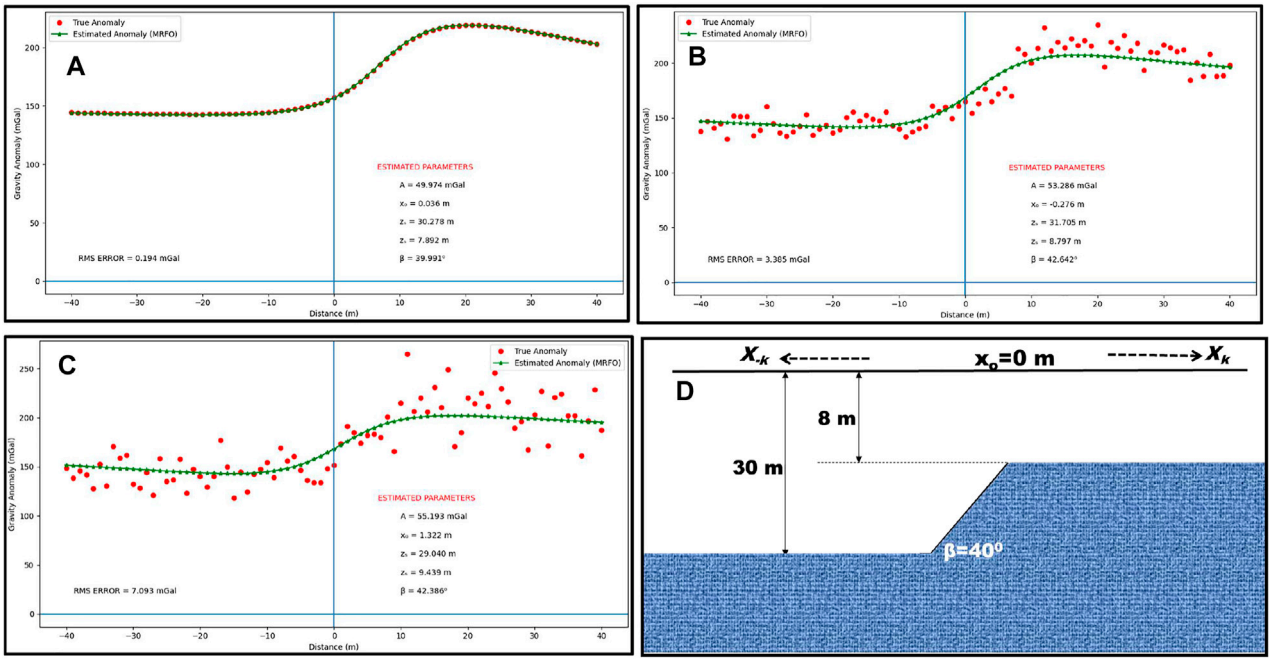

FIGURE 4 | Actual and estimated anomalies (gravity) of a synthetic dipping fault structure with **(A)** 0% **(B)** 5% **(C)** 10% Gaussian noise using MRFO algorithm **(D)** Sketch of the fault model.

profile was sampled at 1 m sampling interval. Model parameters: A = 200 nT, z_b = 30 m, z_t = 10 m, $\beta = 40^{\circ}$, x_o = 10 m was adopted. The synthetic gravity anomaly was produced with A = 50 mGal, z_b = 30 m, z_t = 8m, $\beta = 40^{\circ}$, x_o = 0 m along an 80 m profile. The gravity profile was also sampled at an interval of 1 m. The magnetic and gravity anomalies were computed with **Eqs 1**, **2** respectively.

The search space was populated with 150 initial models/vectors and a broad range of parameter boundaries. For the magnetic case, A-values were set to be in the range of 0–500 nT, and β from -180° to 180°, z_b ranged from 0 to 100 m z_t from 0 to 100 m while x_o stretched between—50 and 50 m. On the other hand, for the gravity anomaly, A was set to vary between 100 and 2000 mGal, β from −180° to 180°, z_b ranged from 0 to 100 m, z_t from 0 to 50 m, and x_o from—20 to 20 m. A total of 500 repetitive iterations were allowed for each run. MFRO has comprehensive and powerful search capabilities. Convergence was attained in less than 100 steps; and good approximations of the five model parameters (A, x_o, z_b, x_t) determined to be in good agreement with their known values were obtained (**Figures 4A**, **5A**; **Table 1**, **2**). Furthermore, a careful evaluation of the histogram generated after uncertainty appraisal analysis (**Figures 6**, **7**) reveals the estimates within highly acceptable confidence intervals.

Noisy Anomaly

To imitate non-ideal subsurface conditions, the previously modeled synthetic dataset was contaminated with varying degrees of Gaussian random noise (5 percent and 10 percent). Using a customized version of the SCIPY library, the Gaussian noise generation process was automated and then individually added data. These various amounts of noise were added to evaluate the suggested methodology's efficacy in the presence of external interferences. These interferences may be from a host material or even signals from neighboring geologic intercalations (Balkaya & Kaftan 2021; Essa & Abo-Ezz 2021). **Eq. 11** was used for calculating the noise percentage.

$$\textbf{Noise percentage} = \frac{\boldsymbol{P}_{\mathbf{n}} - \mathbf{P}}{\mathbf{P}_{\mathbf{n}}}, \tag{11}$$

where P and P_n respectively represent the clean and contaminated anomalies.

With **Eq. 3** used as the cost function, and parameter bounds identical to those used in the noiseless anomaly, cases were re-adopted; the anomalies were reanalyzed with MRFO. The misfit and their convergence were examined after each iteration.

The MRFO algorithm-estimated model parameters were found to be remarkably consistent (**Figures 4B**,C, **5B**,C; **Tables 4**, **5**). **Figures 4D**, **5D** show the Sketches of the fault models. However, based on the results, A appeared to be more sensitive to increasing noise. This sensitivity, which is likely to alter interpretations when dealing with exceedingly sophisticated and deep-seated problems, may be explained by the fact that A is a multiplier factor (**Eqs 1**, **2**). In any case, it could be easily handled by shortening the lower-upper bound range. Further, the results show that the after-convergence misfit and RMS error increase somewhat with the noise level. Nonetheless, this does not affect the inversion process because the resulted parameters continuously remained appealing even to a 10% noise level (**Tables 5**, **6**). It can therefore be inferred that the new technique is intrinsically stable and demonstrates

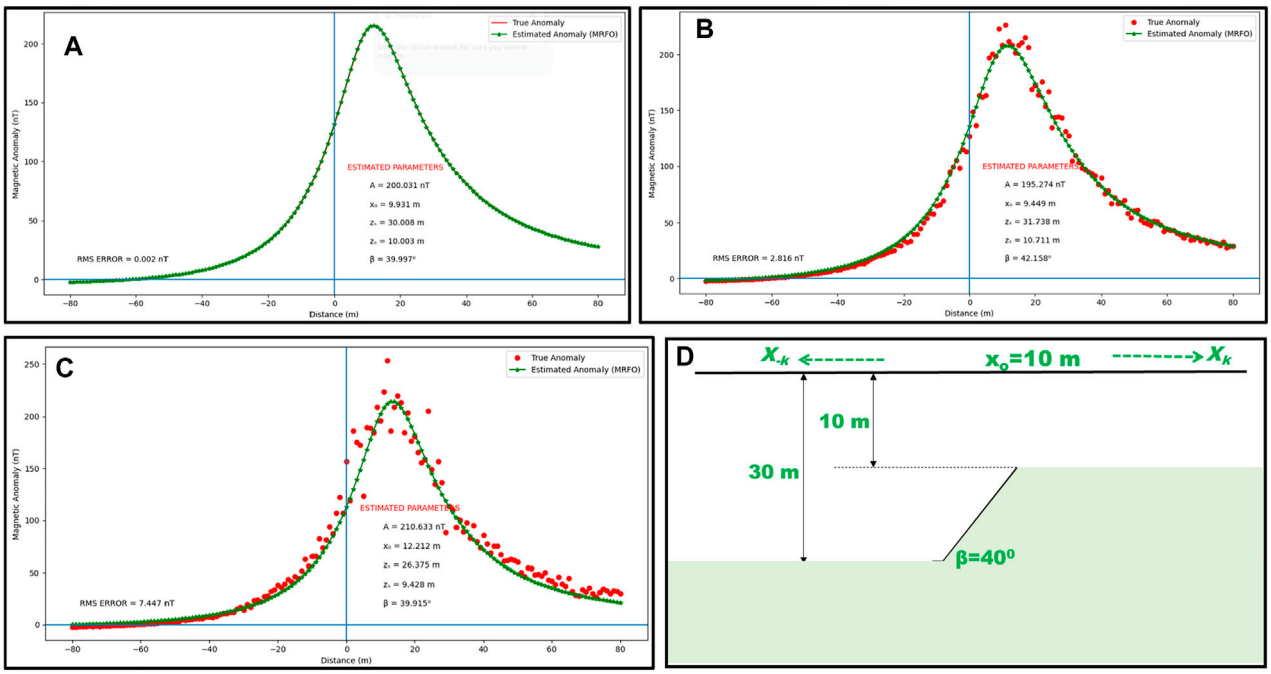

FIGURE 5 | Actual and estimated anomalies (magnetic) of a synthetic dipping fault structure with **(A)** 0% **(B)** 5% **(C)** 10% Gaussian noise using MRFO algorithm **(D)** Sketch of the fault model.

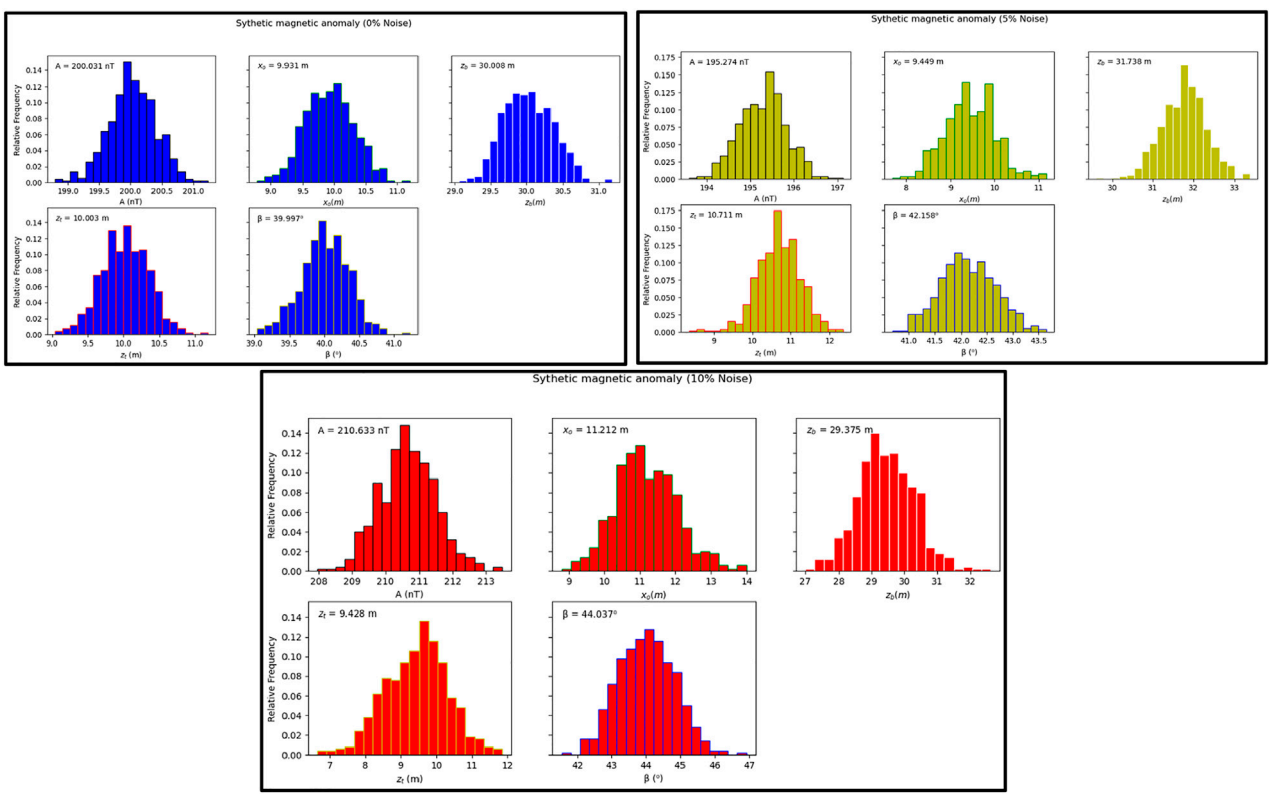

FIGURE 6 | Produced histograms after uncertainty appraisal using MCMC algorithm (synthetic magnetic anomaly). Estimated values indicated on upper-left part of the charts.

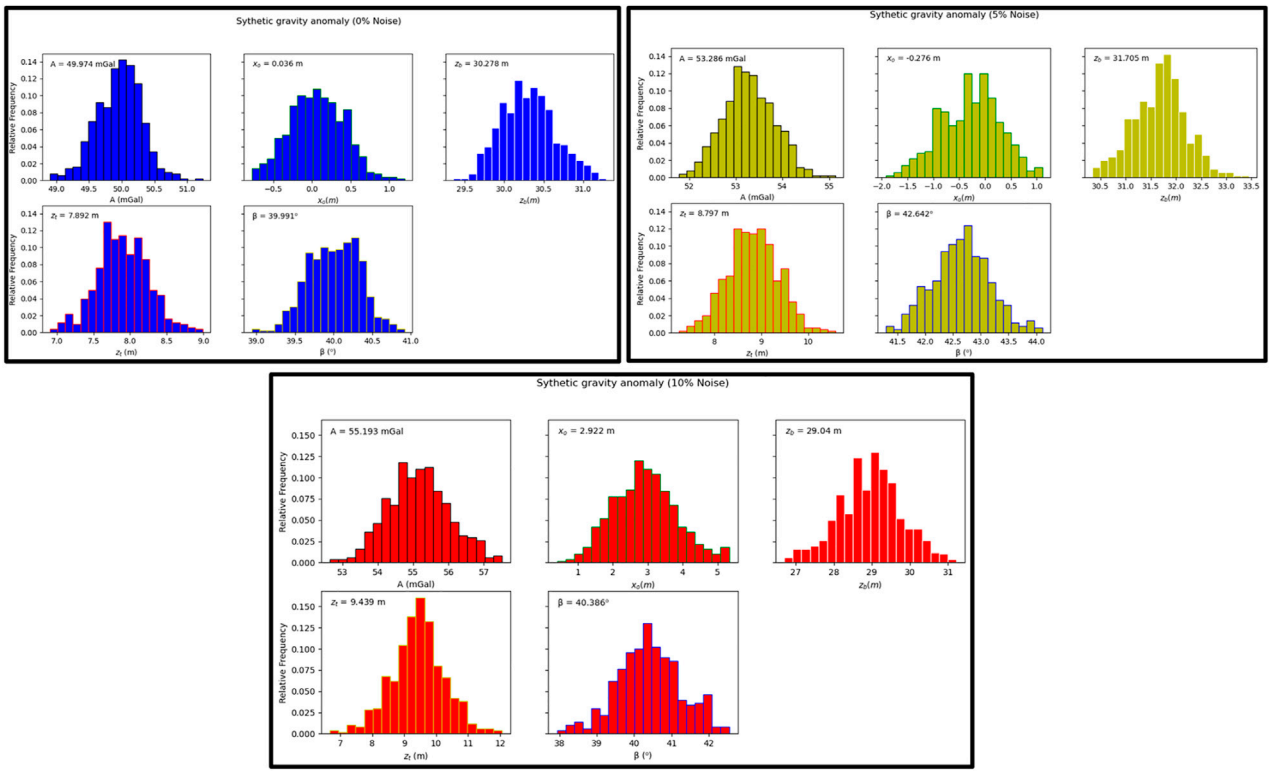

FIGURE 7 | Produced histograms after uncertainty appraisal using MCMC algorithm (synthetic gravity anomaly). Estimated values indicated on upper-left part of the chart.

TABLE 4 | Statistical results for RMS values obtained from parameter tuning of MRFO for synthetic gravity dataset.

S	RMS (mGal)		
	Minimum	Average	Standard deviation
0.5	0.4729	0.8468	0.0658
1	0.0374	0.0846	0.0173
1.5	0.0383	0.0519	0.0052
2	0.0063	0.0094	3.7841×10^{-8}
2.5	0.0327	0.0682	7.3081×10^{-5}
3	0.0472	0.0773	0.0401

TABLE 5 | Search bound, actual and estimated parameters synthetic gravity anomaly corrupted with random noise.

Model parameter	Percentage of noise and observed results	
—	5%	10%
A (mGal)	53.286	55.193
x_o (m)	–0.276	2.922
z_b (m)	31.705	29.040
z_t (m)	8.797	9.439
β (°)	42.642	40.386

commendable proficiency in handling corrupt anomaly data. **Figures 6**, **7** show the MCMC appraisal histogram for all noisy cases. Careful consideration of the generated histograms shows all estimated parameters as well-placed within excellent probability regions affirming the effectiveness of the algorithm's sampling operation.

FIELD CASES

It is generally understood that the strength and credibility of any new geophysical procedure depend on its practical applicability in the exploration of ores and minerals. The developed MRFO

TABLE 6 | Search space, actual and estimated parameters for synthetic magnetic anomaly corrupted with random noise.

Model parameter	Percentage of noise added and observed results	
—	5%	10%
A (nT)	195.274	210.633
x_o (m)	9.449	11.212
z_b (m)	31.738	29.375
z_t (m)	10.711	9.428
β (°)	42.158	44.037

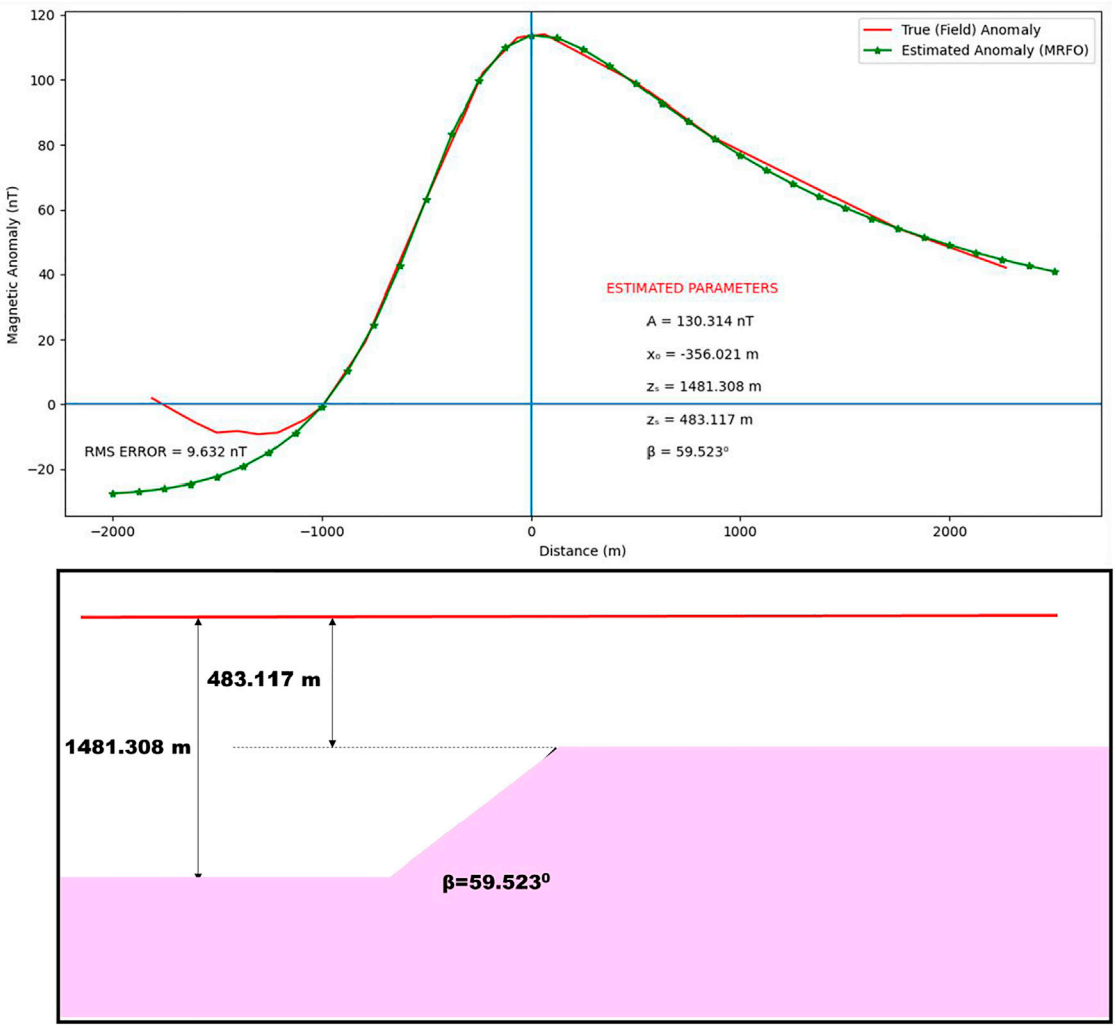

FIGURE 8 | Total magnetic anomaly of Lanchlan anomaly, Australia inverted using the MRFO procedure.

algorithm is as such, experimented against two real examples. The examples are taken from mining fields in the United States of America and Australia. The parameters reflecting the physical characteristics of the subsurface anomalies are estimated using the technique, and then subsequently compared against results from previous investigations for similar examples (published in the literature).

Lachlan Anomaly, Australia

In the first implementation of our new methodology with real-life anomalies, we seek at interpreting a total magnetic anomaly observed over the Molong anticlinorium; a major structural division of the Lachlan fold belt in New South Wales, Australia. The Lachlan fold belt is a middle Paleozoic accretionary orogen widely explored for its rich gold deposits. Orogenically, the belt was massively affected by the Benambrian Orogeny. The event is also believed to have resulted in the development of the Wagga-Omeo zone during the Late Ordovician to Early Silurian period. This was followed by the Middle Devonian Tabberabberan Orogeny which brought an end to the precratonic evolution; before it was being converted to a neo-craton at the last stage of the Carboniferous Kanimblan Orogeny. Structurally, the Silurian rocks which make up the belt fold characteristically to a syncline with a slight dip in the northwest direction (Wang et al., 2019). **Figure 8** is an east-west profile constructed from aeromagnetic data acquired over the anticlinorium with a flight height of about 200 m across the synclinal structure's western limb. The anomaly, buried at depth, was believed to be due to the abrupt thinning of the 1000 m thick tuff of the Douro volcanic against a fault (Ekinci et al., 2020). For this study, the 4 km long profile was digitized after every 125 m interval.

The MRFO technique was employed for parameterizing the subsurface structure, which is considered to be a dipping fault based on past geologic information. The parameter ranges indicated in **Table 7** are used to initialize the algorithm, and the maximum iterations allowed were pegged at 500. Finally, the RMS approach is used to monitor the difference between

TABLE 7 | Recovered parameter results and comparative analysis for Lanchlan Anomaly, Australia.

Model parameters	Search Space	Estimated (MRFO)	Qureshi & Nalaye (1978)	Ekinci et al. (2020)
A (nT)	0–1000	130.314	—	—
x_o (m)	−1500–1500	356.021	—	—
z_b (m)	1–4000	1481.308	1105	1149.84
z_t (m)	1–1000	483.117	115	135.81
β (°)	−180–180	59.523	49	138.27

the real and calculated data. The obtained results are displayed in **Table 7**.

The inversion result shows that the target structure is fault-like with an origin at approximately -356.021 m and an amplitude coefficient of 130.314 nT. The fault was inclined at 59.523° and is buried at 483.117 m to the top and 1481.308 m to the bottom of the fault. After 150 iterations, which lasted only 120 s, the iterations converged. This demonstrates that the MRFO algorithm performs admirably in terms of speed, complexity, and cost. Furthermore, the 9.632 nT misfit calculated implies that the actual and projected data fit together perfectly.

Several workers have shown interest in the Lachlan anomaly because of its economic potential, as evidenced by relevant literature. Qureshi & Nalaye (1978) decomposed the anomaly into symmetric and antisymmetric parts. Thereafter, after independently analyzing these two parts, they reported the buried feature as a fault dipping at an angle of 49° They also resulted 115 m as depth to the structure's top and 1105 m as depth to its bottom. Ekinci et al. (2020) alternatively inverted the anomaly using a fault model via differential evolution algorithm. Their experimentation resulted 1149.84 and 135.81 m as respective depths to the fault's bottom and top and 138.27° as dipping angle. It must be added that Ekinci et al. (2020) designed their forward models assuming non-coplanar relationships between the dislocated fault slabs. More too, their dipping angle was constructed to be strongly affected by the general strike and regional direction of magnetization. These factors are believed to have added up to the large dipping angle obtained from their study. However, the β-parameter from this study shows better favorability as it is compatible with observed dips for other structures in the region (35^0–80^0) as documented by the Geological Survey of South Wales (Qureshi & Nalaye, 1978). Nonetheless, analysis of these reports (**Table 7**) reveals that results from our new methodology still agree impressively with findings from similar studies in literature.

Garber Oil Field Anomaly, Oklahoma United States

Discovered in 1916, the Garber field which is situated on a dominant regional feature is one of Oklahoma's most prominent hydrocarbon fields (Kirkland et al., 1995; Gouin, 1956). The field is characterized by minor faults which dominate its surroundings and numerous anticlinal folds. In addition to these features, it is structurally deformed by the major Nemaha fault. In 1965, workers reported a fault structure suspected to be deep-seated from a geophysical contour map developed for the region (Ferris 1987). The suspected fault is the interpretative focus of this field example.

Gravity data was digitized across a 20-km-long profile over the fault structure. The sampling was carried out at 500 m intervals. To decipher the parameters defining the buried dipping fault structure, we followed the steps outlined in the proposed methodology. First, we initialized the algorithm with parameters based on the bounds shown in **Table 7**, as consistent with the previous field example. The maximum iteration number was then set to 500. The RMS error was used to monitor the disparity between the digitized gravity data and those calculated from MRFO-generated parameters (**Figure 9**). **Table 8** shows the results that were obtained.

According to results from the inversion process, the targeted source can be inferred as a fault-like structure inclined at an angle of 126.135°. Its origin is at a horizontal distance of 16.924 km on the profile. The depth to the structure's top and bottom is calculated to be 6.083 and 14.537 km respectively. The iterations converged after about 180 iterations, which took about 150 s, confirming the superiority of the algorithm in cost management and time complexity. More too, it is observed from the obtained error of 1.857 mGal that the measured and the computed data fit excellently (**Figure 9**).

Table 8 shows how the results obtained using our proposed methodology compare to those obtained using other methodologies and published in the literature. Using the least-squares inversion approach, Qureshi & Nalaye (1978) reported that the anomaly is a fault; with its top at a depth of 9.25 km and its bottom at a depth of 15.55 km. Murty et al. (2001) generalized an interpretation technique based on angular value decomposition. They then investigated the Garber field anomaly using the constructed tool. From results obtained after their analysis, they also pinpointed the anomaly to a fault structure. However, they reported the source structure as being relatively thinner and also as being buried at shallower top and bottom depths of 8.86 and 15.07 km. Using a comparative approach, Ekinci et al. (2019) recently employed the robust PSO and DE algorithms for the intelligent investigation of the Garber anomaly. They also confirmed that the anomaly-causing

TABLE 8 | Comparative analysis of parameter results for Garber Oil Field Anomaly, United States

Model parameters	Search Space	Estimated (MRFO)	Qureshi & Nalaye (1978)	Radhakrishna et al. (2001)	Ekinci et al. (2019)-PSO	Ekinci et al. (2019)-DE
A (mGal)	0–500	241.968	—	—	—	—
x_o (km)	0–20	16.924	—	—	—	—
z_b (km)	1–60	14.537	15.55	15.07	10.77	13.76
z_t (km)	1–30	6.083	9.25	8.86	5.62	5.10
β (°)	−180–180	126.135	—	—	108.41	141.13

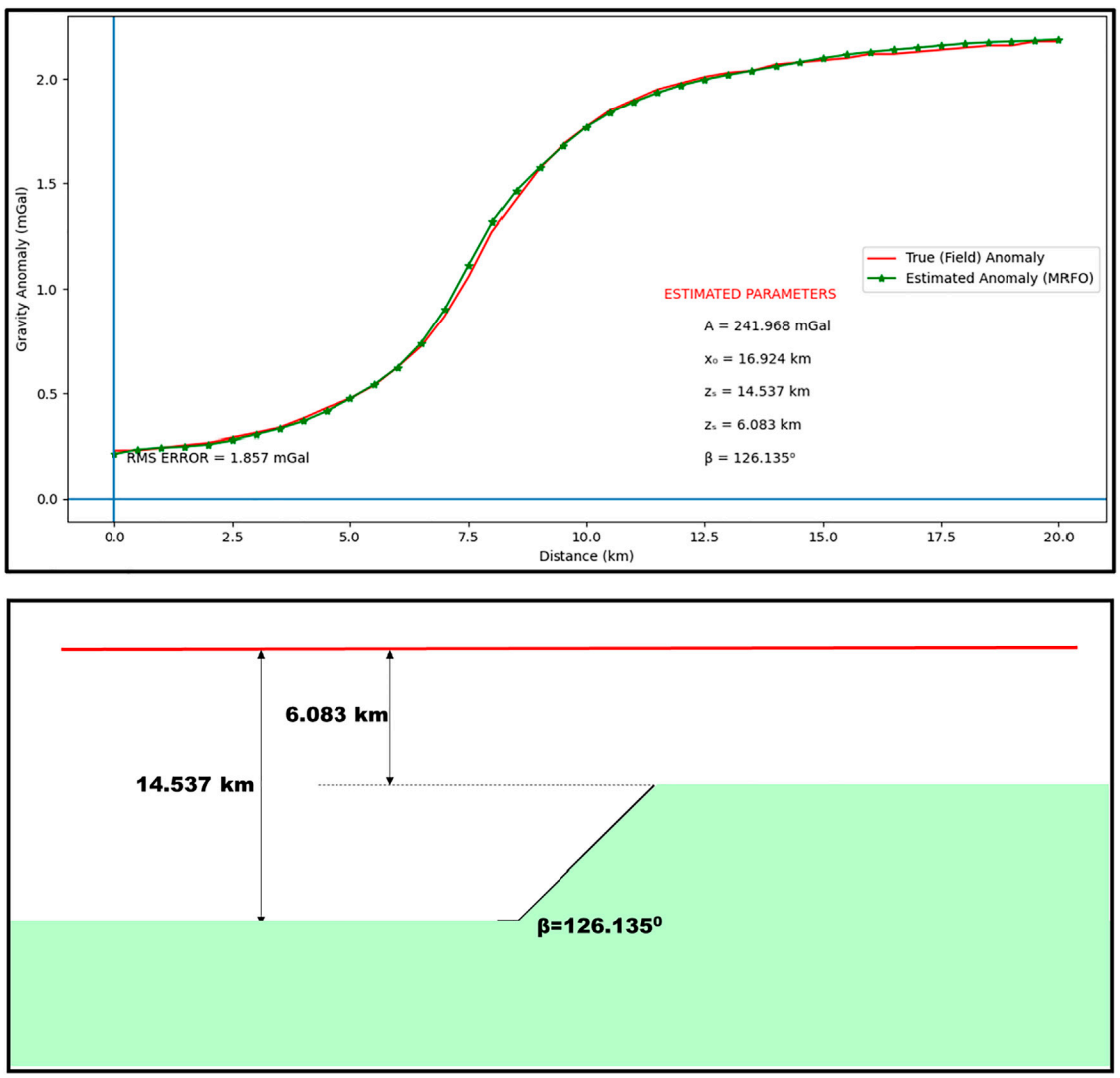

FIGURE 9 | Total gravity anomaly of Garber anomaly, Oklahoma inverted using the MRFO procedure.

structure was fault-like; howbeit, the fault was calculated as stretching from depth 5.62–10.77 km using PSO. DE resulted 5.10 and 13.76 km for the same respectively. These results indicate that findings obtained using our new methodology are consistent (**Table 8**) with existing information about this same anomaly, present in relevant literature.

DISCUSSION OF RESULTS

In both synthetic and actual examples, MRFO-based inversion proved to be an accurate and dependable technique for modeling potential field anomalies detected across geo-structures such as dipping faults (**Figures 10**, **11**). Furthermore, the MRFO

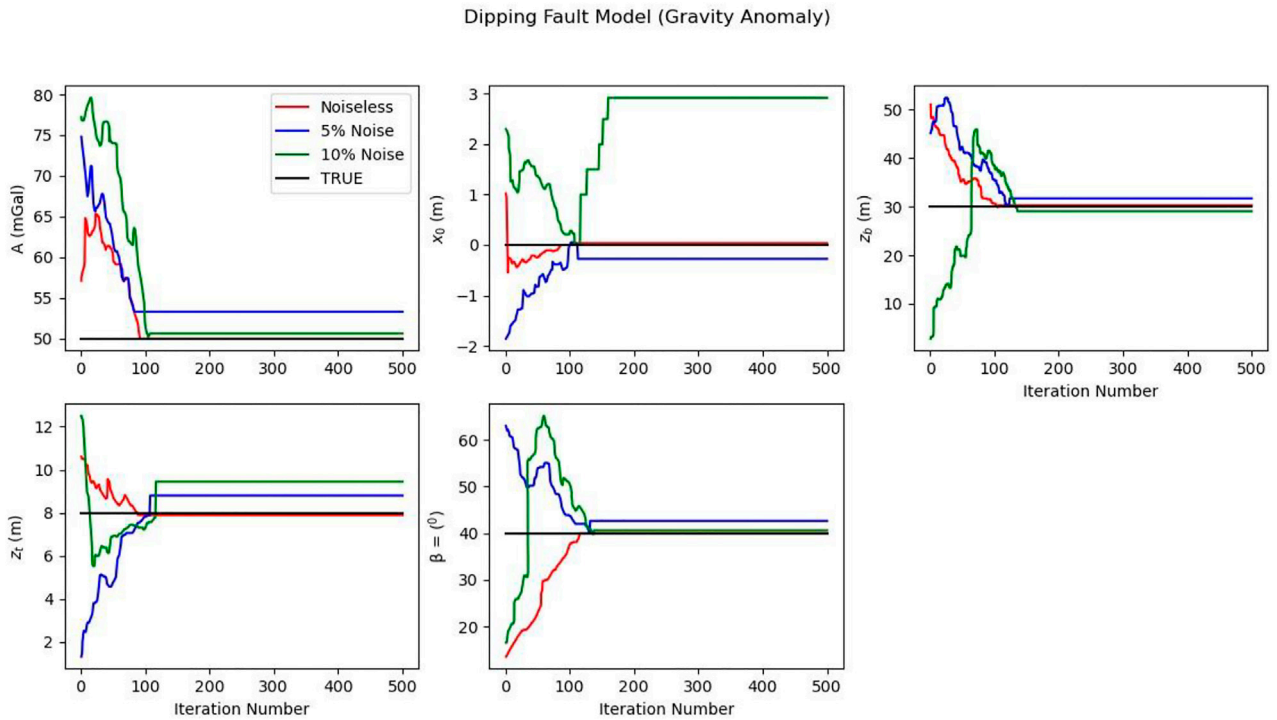

FIGURE 10 | Change in model parameters with iteration (Gravity Anomaly).

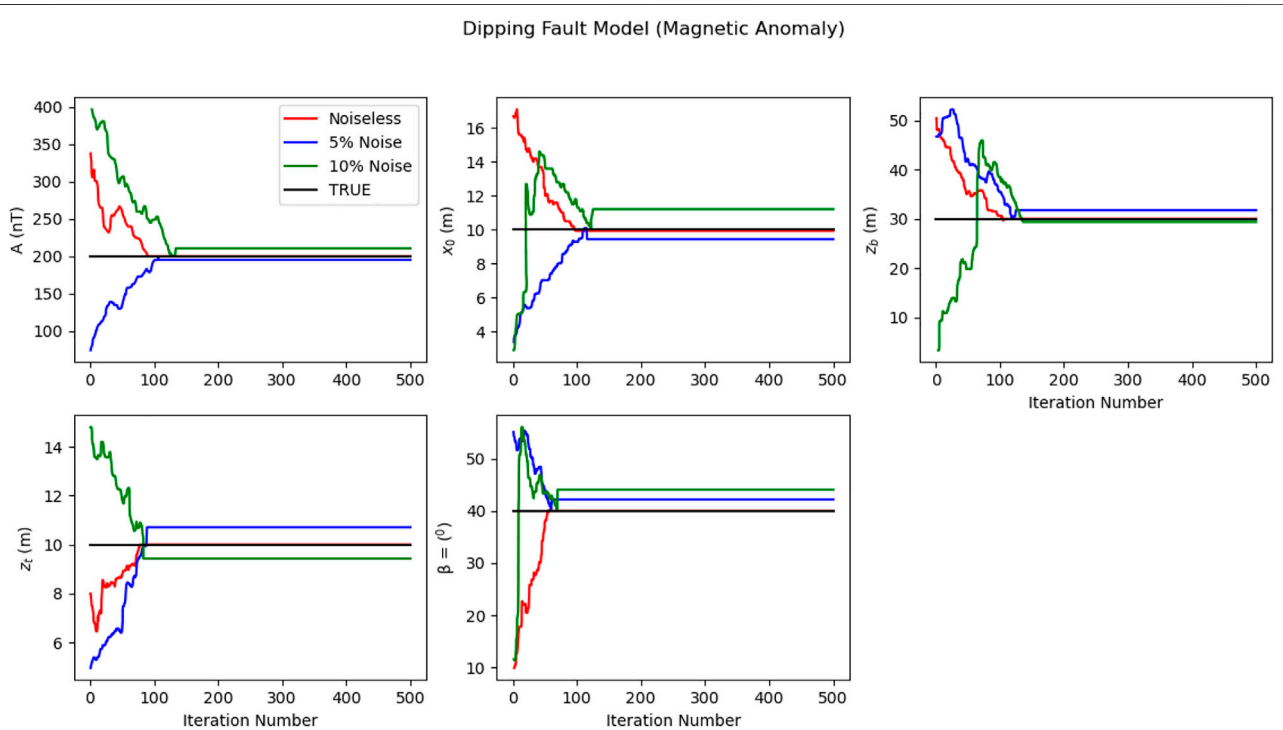

FIGURE 11 | Change in model parameters with iteration (Magnetic Anomaly).

algorithm's fast convergence rate suggests that it is a better-performing method for geophysical inversion. Surprisingly, this speed has no effect on optimization capability because the errors recorded at the end of the method are were still within acceptable ranges. Notably, the algorithm appears to overcome unpopular/recurring problems of immature convergence and local optima that regularly limits intelligent techniques such as ACO, PSO, and GA (Mehanee & Essa 2015; Roshan & Kumar Singh 2017; Chopard and omassini 2018; Izci et al., 2020; Hua et al., 2021). This is accomplished by the search agents' capacity to intelligently switch between chain and cyclone foraging techniques when necessary. The chain foraging method is often responsible for improving the algorithm's local search; whereas the cyclone strategy is mostly concerned with enhancing the algorithm's global search for solutions. By mutually combining the two–as the proposed methodology permits, a thorough exploration of the entire domain of the problem can be achieved. Noting these gains, as well as the comparatively lesser computational efforts required for the achievement of the gains, MRFO has been found to effectively supersede all other well-known optimizers in the resolution of the geophysical optimization problem. This is with respect to structural anomalies due to shallow and deep-seated dipping faults.

CONCLUSION

The feasibility of adapting the MRFO technique for the solution of geophysical inverse problems has been investigated. The procedure was structured towards obtaining precise estimates of five separate model parameters describing buried dipping fault. The parameters of interest were amplitude coefficient, origin, inclination, and depth from the surface to the top and bottom of the structural feature. The experimental data set consisted of synthetic potential field data that were later polluted with 5 and 10% random noise, as well as real profile anomalies extracted from mining fields in Australia and the United States. The algorithm execution rate was impressive-finding solutions with excellent RMS well before the maximum iterations allowed. Even so, analysis of the algorithm's performance and generated results reveal that the technique is outstanding, stable, and flexible, even in the presence of noise. The consistency of the results produced from the analysis of the field instances, when compared to control data generated from earlier research, further confirms that the procedure is accurate and reliable for the resolution of potential field problems. Resultantly, the approach is recommended for modeling potential field data and even alternative geophysical data such as self-potential, resistivity, and electromagnetics.

DATA AVAILABILITY STATEMENT

The raw data supporting the conclusion of this article will be made available by the authors, without undue reservation.

AUTHOR CONTRIBUTIONS

Conceptualization, AE; Data curation, UB; Formal analysis, O-IA and DG-O; Funding acquisition, KA; Investigation, UB, SE, and AA; Methodology, AA; Software, UB; Validation, O-IA; Visualization, SE and AE; Writing – review and editing, AE and AA.

ACKNOWLEDGMENTS

Deep thanks and gratitude to the Researchers Supporting Project number (RSP-2022/351), King Saud University, Riyadh, Saudi Arabia for funding this research article. The authors wish to thank the management of the University of Calabar for providing the facilities used for this research.

REFERENCES

Abbas, M. A., and Fedi, M. (2013). "Automatic DEXP Imaging of Potential fields Independent of the Structural Index," in 75th European Association of Geoscientists and Engineers Conference and Exhibition 2013 Incorporating SPE EUROPEC 2013: Changing Frontiers. doi:10.3997/2214-4609.20130120

Abdelrahman, E.-S., Gobashy, M., Abo-Ezz, E., and El-Araby, T. (2019). A New Method for Complete Quantitative Interpretation of Gravity Data Due to Dipping Faults. *Contrib. Geophys. Geodesy* 49, 133–151. doi:10.2478/congeo-2019-0007

Abdelrahman, E.-S. M., Abo-Ezz, E. R., and Essa, K. S. (2012). Parametric Inversion of Residual Magnetic Anomalies Due to Simple Geometric Bodies. *Exploration Geophys.* 43, 178–189. doi:10.1071/EG11026

Abo-Ezz, E. R., and Essa, K. S. (2016). A Least-Squares Minimization Approach for Model Parameters Estimate by Using a New Magnetic Anomaly Formula. *Pure Appl. Geophys.* 173, 1265–1278. doi:10.1007/s00024-015-1168-9

Alturki, F. A., Omotoso, H. O., Al-Shamma'a, A. A., Farh, H. M. H., and Alsharabi, K. (2020). Novel Manta Rays Foraging Optimization Algorithm Based Optimal Control for Grid-Connected PV Energy System. *IEEE Access* 8, 187276–187290. doi:10.1109/access.2020.3030874

Amoruso, A., Barba, S., Crescentini, L., and Megna, A. (2013). Inversion of Synthetic Geodetic Data for Dip-Slip Faults: Clues to the Effects of Lateral Heterogeneities and Data Distribution in Geological Environments Typical of the Apennines (Italy). *Geophys. J. Int.* 192, 745–758. doi:10.1093/gji/ggs042

Balkaya, Ç., Ekinci, Y. L., Göktürkler, G., and Turan, S. (2017). 3D Non-linear Inversion of Magnetic Anomalies Caused by Prismatic Bodies Using Differential Evolution Algorithm. *J. Appl. Geophys.* 136, 372–386. doi:10.1016/j.jappgeo.2016.10.040

Balkaya, Ç., and Kaftan, I. (2021). Inverse Modelling via Differential Search Algorithm for Interpreting Magnetic Anomalies Caused by 2D Dyke-Shaped Bodies. *J. Earth Syst. Sci.* 130. doi:10.1007/s12040-021-01614-1

Barnhart, W. D., and Lohman, R. B. (2010). Automated Fault Model Discretization for Inversions for Coseismic Slip Distributions. *J. Geophys. Res.* 115. doi:10.1029/2010JB007545

Ben, U. C., Akpan, A. E., Enyinyi, E. O., and Awak, E. (2021c). Novel Technique for the Interpretation of Gravity Anomalies over Geologic Structures with Idealized Geometries Using the Manta ray Foraging Optimization. *J. Asian Earth Sci. X* 6, 100070. doi:10.1016/j.jaesx.2021.100070

Ben, U. C., Akpan, A. E., Mbonu, C. C., and Ebong, E. D. (2021b). Novel Methodology for Interpretation of Magnetic Anomalies Due to Two-Dimensional Dipping Dikes Using the Manta Ray Foraging Optimization. *J. Appl. Geophys.* 192, 104405. doi:10.1016/j.jappgeo.2021.104405

Ben, U. C., Akpan, A. E., Mbonu, C. C., and Ufuafuonye, C. H. (2021a). Integrated Technical Analysis of Wind Speed Data for Wind Energy Potential Assessment in Parts of Southern and central Nigeria. *Clean. Eng. Tech.* 2, 100049. doi:10.1016/j.clet.2021.100049

Biswas, A., Parija, M., and Kumar, S. (2017). Global Nonlinear Optimization for the Interpretation of Source Parameters from Total Gradient of Gravity and Magnetic Anomalies Caused by Thin Dyke. *Ann. Geophys.* 60. doi:10.4401/ag-7129

Cerovský, I., and Pašteka, R. (2003). Imaging and Clustering of Depth Estimations for Werner and 2D-Euler Deconvolution. *Contrib. Geophys. Geodesy* 33, 2.

Chopard, B., and omassini, M. (2018). "Particle Swarm Optimization," *Natural Computing Series* (Cham: Springer). doi:10.1007/978-3-319-93073-2_6

Ekinci, S., Izci, D., and Hekimoğlu, B. (2021b). Optimal FOPID Speed Control of DC Motor via Opposition-Based Hybrid Manta Ray Foraging Optimization and Simulated Annealing Algorithm. *Arab J. Sci. Eng.* 46, 1395–1409. doi:10.1007/s13369-020-05050-z

Ekinci, S., Izci, D., and Kayri, M. (2021c). An Effective Controller Design Approach for Magnetic Levitation System Using Novel Improved Manta Ray Foraging Optimization. *Arab J. Sci. Eng.* doi:10.1007/s13369-021-06321-z

Ekinci, Y. L., Balkaya, Ç., and Göktürkler, G., 2020. Global Optimization of Near-Surface Potential Field Anomalies through Metaheuristics, 155, 188. doi:10.1007/978-3-030-28909-6_7

Ekinci, Y. L., Balkaya, Ç., Göktürkler, G., and Özyalln, Ş. (2021a). Gravity Data Inversion for the Basement Relief Delineation through Global Optimization: A Case Study from the Aegean Graben System, Western Anatolia, Turkey. *Geophys. J. Int.* 224 (2), 923–944. doi:10.1093/gji/ggaa492

Ekinci, Y. L., Balkaya, Ç., and Göktürkler, G. (2019). Parameter Estimations from Gravity and Magnetic Anomalies Due to Deep-Seated Faults: Differential Evolution versus Particle Swarm Optimization. *Turkish J. Earth Sci* 28 (6), 860–881. doi:10.3906/yer-1905-3

Elattar, E. E., Shaheen, A. M., Elsayed, A. M., and El-Sehiemy, R. A. (2020). Optimal Power Flow with Emerged Technologies of Voltage Source Converter Stations in Meshed Power Systems. *IEEE Access* 8, 166963–166979. doi:10.1109/ACCESS.2020.3022919

Essa, K. S., and Abo-Ezz, E. R. (2021). Potential Field Data Interpretation to Detect the Parameters of Buried Geometries by Applying a Nonlinear Least-Squares Approach. *Acta Geod Geophys* 56, 387–406. doi:10.1007/s40328-021-00337-5

Essa, K. S. (2021). Evaluation of the Parameters of the Fault-like Geologic Structure from the Gravity Anomalies Applying the Particle Swarm. *Environ. Earth Sci.* 80. doi:10.1007/s12665-021-09786-1

Essa, K. S. (2013). Gravity Interpretation of Dipping Faults Using the Variance Analysis Method. *J. Geophys. Eng.* 10, 015003. doi:10.1088/1742-2132/10/1/015003

Essa, K. S., Mehanee, S. A., and Elhussein, M. (2021). Gravity Data Interpretation by a Two-Sided Fault-like Geologic Structure Using the Global Particle Swarm Technique. *Phys. Earth Planet. Interiors* 311, 106631. doi:10.1016/j.pepi.2020.106631

Essa, K. S., and Munschy, M. (2019). Gravity Data Interpretation Using the Particle Swarm Optimisation Method with Application to mineral Exploration. *J. Earth Syst. Sci.* 128. doi:10.1007/s12040-019-1143-4

Essa, K. S., Nady, A. G., Mostafa, M. S., and Elhussein, M. (2018). Implementation of Potential Field Data to Depict the Structural Lineaments of the Sinai Peninsula, Egypt. *J. Afr. Earth Sci.* 147, 43–53. doi:10.1016/j.jafrearsci.2018.06.013

Fedi, M., and Florio, G. (2013). Determination of the Maximum-Depth to Potential Field Sources by a Maximum Structural index Method. *J. Appl. Geophys.* 88, 154–160. doi:10.1016/j.jappgeo.2012.10.009

Feng, J., Luo, X., Gao, M., Abbas, A., Xu, Y. P., and Pouramini, S. (2021). Minimization of Energy Consumption by Building Shape Optimization Using an Improved Manta-Ray Foraging Optimization Algorithm. *Energ. Rep.* 7, 1068–1078. doi:10.1016/j.egyr.2021.02.028

Ferris, C. (1987). Gravity Anomaly Resolution at the Garber Field. *Geophysics* 52, 1570–1579. doi:10.1190/1.1442275

Garabito, G., and Cruz, J. C. R. (2019). Application of Very Fast Simulated Annealing and Differential Evolution in the Search for FO-CRS Wavefield Attributes. *Geophysics* 84, O81–O92. doi:10.1190/geo2018-0193.1

Gharehchopogh, F. S., and Gholizadeh, H. (2019). A Comprehensive Survey: Whale Optimization Algorithm and its Applications. *Swarm Evol. Comput.* 48, 1–24. doi:10.1016/j.swevo.2019.03.004

Ghosh, K. K., Guha, R., Bera, S. K., Kumar, N., and Sarkar, R. (2021). S-shaped versus V-Shaped Transfer Functions for Binary Manta ray Foraging Optimization in Feature Selection Problem. *Neural Comput. Applic* 33, 11027–11041. doi:10.1007/s00521-020-05560-9

Gonzalez, S., Salvi, D., Baeza, D., Antonacci, F., and Sarti, A. (2021). A Data-Driven Approach to Violin Making. *Sci. Rep.* 11. doi:10.1038/s41598-021-88931-z

Gouin, F. (1956). Surface Criteria of Southern Oklahoma Oil Fields. *Pet. Geology. South. Okla*, 14–35. doi:10.1306/sv16348c1

Guo, Q., Ba, J., Luo, C., and Xiao, S. (2020). Stability-enhanced Prestack Seismic Inversion Using Hybrid Orthogonal Learning Particle Swarm Optimization. *J. Pet. Sci. Eng.* 192, 107313. doi:10.1016/j.petrol.2020.107313

Gupta, D. K., Gupta, J. P., Arora, Y., and Shankar, U. (2013). Recursive Ant colony Optimization: A New Technique for the Estimation of Function Parameters from Geophysical Field Data. *Near Surf. Geophys.* 11, 325–340. doi:10.3997/1873-0604.2012062

Hemeida, M. G., Ibrahim, A. A., Mohamed, A.-A. A., Alkhalaf, S., and El-Dine, A. M. B. (2021). Optimal Allocation of Distributed Generators DG Based Manta Ray Foraging Optimization Algorithm (MRFO). *Ain Shams Eng. J.* 12, 609–619. doi:10.1016/j.asej.2020.07.009

Houssein, E. H., Emam, M. M., and Ali, A. A. (2021). Improved Manta ray Foraging Optimization for Multi-Level Thresholding Using COVID-19 CT Images. *Neural Comput. Applic* 33, 16899–16919. doi:10.1007/s00521-021-06273-3

Hua, Y., Sui, X., Zhou, S., Chen, Q., Gu, G., Bai, H., et al. (2021). A Novel Method of Global Optimisation for Wavefront Shaping Based on the Differential Evolution Algorithm. *Opt. Commun.* 481, 126541. doi:10.1016/j.optcom.2020.126541

Hastings, W. K. (1970). Monte Carlo Sampling Methods Using Markov Chains and Their Applications. *Biometrika* 57 (1), 97–109. doi:10.1093/biomet/57.1.97

Izci, D., Ekinci, S., Eker, E., and Kayri, M. (2020). "Improved Manta Ray Foraging Optimization Using Opposition-Based Learning for Optimization Problems," in HORA 2020 - 2nd International Congress on Human-Computer Interaction, Optimization and Robotic Applications, Proceedings. doi:10.1109/HORA49412.2020.9152925

Kaftan, İ. (2017). Interpretation of Magnetic Anomalies Using a Genetic Algorithm. *Acta Geophys.* 65, 627–634. doi:10.1007/s11600-017-0060-7

Kanimozhi, V., and Jacob, T. P. (2019). Artificial Intelligence Based Network Intrusion Detection with Hyper-Parameter Optimization Tuning on the Realistic Cyber Dataset CSE-CIC-Ids2018 Using Cloud Computing. *ICT Express* 5, 211–214. doi:10.1016/j.icte.2019.03.003

Kirkland, D. W., Denison, R. E., and Rooney, M. A. (1995). Diagenetic Alteration of Permian Strata at Oil fields of South central Oklahoma, USA. *Mar. Pet. Geology.* 12 (6), 629–644. doi:10.1016/0264-8172(95)98089-N

Li, J., Li, J., Li, W., Jian, X., and Wu, X. (2020). Multi-scale Apparent Magnetization Inversion Imaging Method Based on the Theoretical Pseudo-gravity Anomalies. *Chaos, Solitons & Fractals* 131, 109480. doi:10.1016/j.chaos.2019.109480

Mbonu, C. C., Essiett, A. A., and Ben, U. C. (2021). Geospatial Assessment of Radiation hazard Indices in Soil Samples from Njaba, Imo State, South-Eastern Nigeria. *Environ. Challenges* 4, 100117. doi:10.1016/j.envc.2021.100117

Mehanee, S. A., and Essa, K. S. (2015). 2.5D Regularized Inversion for the Interpretation of Residual Gravity Data by a Dipping Thin Sheet: Numerical Examples and Case Studies with an Insight on Sensitivity and Non-uniqueness. *Earth Planet. Sp* 67. doi:10.1186/s40623-015-0283-2

Melo, F. F., and Barbosa, V. C. F. (2018). Correct Structural index in Euler Deconvolution via Base-Level Estimates. *Geophysics* 83, J87–J98. doi:10.1190/geo2017-0774.1

Metropolis, M. N., Rosenbluth, A. W., Rosenbluth, M. N., Teller, A. H., and Teller, E. (1953). Equation of State Calculations by Fast Computing Machines. *J. Chem. Phys.* 21 (6), 1087–1092.

Mosegaard, K., and Tarantola, A. (2002). 16 Probabilistic Approach to Inverse Problems. *Int. Geophys.* doi:10.1016/S0074-6142(02)80219-4

Mota, E. S. A., Medeiros, W. E., and Oliveira, R. G. (2020). Can Euler Deconvolution Outline Three- Dimensional Magnetic Sources? *Geophys. Prospecting* 68 (7), 2271–2291. doi:10.1080/20909977.2020.1743019

Murthy, I. R., Swamy, K. V., and Rao, S. J. (2001). Automatic Inversion of Magnetic Anomalies of Faults *Comput. Geosci.* 27 (3), 315–325.

Pan, J., Wang, X., Zhang, X., Xu, Z., Zhao, P., Tian, X., et al. (2009). 2D Multi-Scale Hybrid Optimization Method for Geophysical Inversion and its Application. *Appl. Geophys.* 6, 337–348. doi:10.1007/s11770-009-0034-x

Pilkington, M. (2006). Joint Inversion of Gravity and Magnetic Data for Two-Layer Models. *Geophysics* 71 (3), L35–L42. doi:10.1190/1.2194514

Qureshi, I. R., and Nalaye, A. M. (1978). A Method for the Direct Interpretation of Magnetic Anomalies Caused by Two-dimensional Vertical Faults. *Geophysics* 43, 179–188. doi:10.1190/1.1440819

Rezk, H., Mazen Alhato, M., Alhaider, M., and Bouall鑄ue, S. (2021). Fractional-Order Control of a Wind Turbine Using Manta Ray Foraging Optimization. *Comput. Mater. Continua* 68, 185–199. doi:10.32604/cmc.2021.016175

Roshan, R., and Singh, U. K. (2017). Inversion of Residual Gravity Anomalies Using Tuned PSO. *Geosci. Instrum. Method. Data Syst.* 6, 71–79. doi:10.5194/gi-6-71-2017

Russell, B. (2019). Machine Learning and Geophysical Inversion - A Numerical Study. *The Leading Edge* 38, 512–519. doi:10.1190/tle38070512.1

Scales, J. A., and Tenorio, L. (2001). Prior Information and Uncertainty in Inverse Problems. *Geophysics* 66, 389–397. doi:10.1190/1.1444930

Selem, S. I., Hasanien, H. M., and El-Fergany, A. A. (2020). Parameters Extraction of PEMFC's Model Using Manta Rays Foraging Optimizer. *Int. J. Energ. Res* 44, 4629–4640. doi:10.1002/er.5244

Sen, M. K., and Mallick, S. (2018). Genetic Algorithm with Applications in Geophysics. *Genet. Algorithm Appl. Geophys.*, 487–533. doi:10.1007/978-3-319-66532-0_7

Tarantola, A. 2005. *Inverse Problem Theory and Methods for Model Parameter Estimation*. Society for Industrial and Applied Mathematics. doi:10.1137/1.9780898717921

Turgut, O. E. (2021). A Novel Chaotic Manta-ray Foraging Optimization Algorithm for Thermo- Economic Design Optimization of an Air-Fin Cooler. *SN Appl. Sci* 3, 3. doi:10.1007/s42452-020-04013-1

Wang, D.-s., Wang, Z., Wang, Z.-q., Wang, G., Guo, X.-q., and Wu, Y.-d. (2019). Characteristics of Tectonic Deformation of the Melange Zone in the Lachlan Orogen along Eastern Coast of Australia. *China Geology.* 3, 1–16. doi:10.31035/cg2018131

Xie, W., Wang, Y.-C., Liu, X.-Q., Bi, C.-C., Zhang, F.-Q., Fang, Y., et al. (2019). Nonlinear Joint PP-PS AVO Inversion Based on Improved Bayesian Inference and LSSVM. *Appl. Geophys.* 16, 64–76. doi:10.1007/s11770-019-0750-9

Yadav, A., Yadav, K., and Anirbid Sircar, Anirbid. (2021). Feedforward Neural Network for Joint Inversion of Geophysical Data to Identify Geothermal Sweet Spots in Gandhar, Gujarat, India. *Energ. Geosci.* 2, 189–200. doi:10.1016/j.engeos.2021.01.001

Yusof, M. A., Agi, A., Gbadamosi, A., Junin, R., and Abbas, A. (2018). Uncertainty Analysis of Hydrocarbon in Place Calculation Using 3D Seismic and Well Data during Appraisal Stage - Case Study of Goldie Field, Offshore Sarawak. *J. Nat. Gas Sci. Eng.* 57, 238–265. doi:10.1016/j.jngse.2018.06.038

Zhao, W., Zhang, Z., and Wang, L. (2020). Manta ray Foraging Optimization: An Effective Bio-Inspired Optimizer for Engineering Applications. *Eng. Appl. Artif. Intelligence* 87, 103300. doi:10.1016/j.engappai.2019.103300

Zhdanov, M. S. (2002). *Geophysical Inverse Theory and Regularization Problems*. Amsterdam, Netherlands: Elsevier Science, Vol. 36.

Conflict of Interest: The authors declare that the research was conducted in the absence of any commercial or financial relationships that could be construed as a potential conflict of interest.

Publisher's Note: All claims expressed in this article are solely those of the authors and do not necessarily represent those of their affiliated organizations, or those of the publisher, the editors and the reviewers. Any product that may be evaluated in this article, or claim that may be made by its manufacturer, is not guaranteed or endorsed by the publisher.

frontiers in Earth Science

ORIGINAL RESEARCH
published: 28 March 2022
doi: 10.3389/feart.2022.847984

Geometry of the Magma Chamber and Curie Point Depth Beneath Hawaii Island: Inferences From Magnetic and Gravity Data

Ahmed Mohamed[1]*, *Mohamed Al Deep*[2], *Kamal Abdelrahman*[3] and *Ahmed Abdelrady*[4]

[1]Geology Department, Faculty of Science, Assiut University, Assiut, Egypt, [2]Geomagnetic and Geoelectric Department, National Research Institute of Astronomy and Geophysics, Helwan, Egypt, [3]Department of Geology and Geophysics, College of Science, King Saud University, Riyadh, Saudi Arabia, [4]Department of Water Management, Faculty of Civil Engineering and Geoscience, Delft University of Technology, Delft, Netherlands

This study used land gravity and airborne magnetic data to investigate the depth to the magmatic chamber and map the heat flow distribution beneath the active volcanoes of Hawaii Island using the Curie point depth (CPD) and gravity modeling. Obtaining some of the ground-based geophysical measurements was problematic due to accessibility limitations; therefore, this study used available data. The CPD and magnetic data were used to map the depth to the bottom of the magnetic layer by calculating the depth to the Curie isotherm (540°C) beneath Hawaii Island. The spectral peak method was used to calculate the depths to the shallow and deep magnetic sources for the entire island, and the CPD was calculated using the centroid method. A two-dimensional density model for two Earth layers was constructed using forward modeling of the gravity data. A large plume of dense intrusive material was observed beneath the three adjacent volcanoes of Mauna Loa, Mauna Kea, and Kilauea, and two small chambers were found to be located beneath the Kohala and Hualalai volcanoes. Based on the gravity modeling results, the depth to the magma layer varied from 0.5 to 10 km, and the heat flow was higher close to the volcanic eruption zones. The current study is informative and cost effective for the world's most active volcanic areas.

Keywords: magmatic chamber, gravity inversion, Curie depth point, geothermal gradient, heat flow, Hawaii Island

OPEN ACCESS

Edited by:
Amin Beiranvand Pour, INOS University Malaysia Terengganu, Malaysia

Reviewed by:
Özkan Kafadar, Kocaeli University, Turkey
Saada Saada, Suez University, Egypt

***Correspondence:**
Ahmed Mohamed
ahmedmohamed@aun.edu.eg

Specialty section:
This article was submitted to Solid Earth Geophysics, a section of the journal Frontiers in Earth Science

Received: *03 January 2022*
Accepted: *28 January 2022*
Published: *28 March 2022*

Citation:
Mohamed A, Al Deep M, Abdelrahman K and Abdelrady A (2022) Geometry of the Magma Chamber and Curie Point Depth Beneath Hawaii Island: Inferences From Magnetic and Gravity Data. Front. Earth Sci. 10:847984. doi: 10.3389/feart.2022.847984

INTRODUCTION

The structural complexity of volcanic islands and their difficult accessibility make geophysical imaging problematic. Moreover, geophysical modeling generally suffers from nonuniqueness in its solutions. This study uses two geophysical techniques to overcome these problems and reduce modeling errors. Despite the accessibility limitations, geophysical modeling techniques of potential data have been used extensively in different geologic settings to provide reliable results on structures and geometries (Green, 1975; Guillen and Menichetti, 1984; Camacho et al., 1997; Li and Oldenburg, 1998; Camacho et al., 2000; Boulanger and Chouteau, 2001; Montesinos et al., 2006; Cella wt al., 2007; Camacho et al., 2011; Marcotte et al., 2014; Barnoud et al., 2016). **Figure 1** shows the location and topography of the Hawaiian Island arch system.

Geophysical and structural measurements are used extensively to delineate the three-dimensional (3-D) shape of granitoid plutons (Miller and Tauch, 1989; Vigneresse, 1995a, b; Eguíluz et al., 1999)

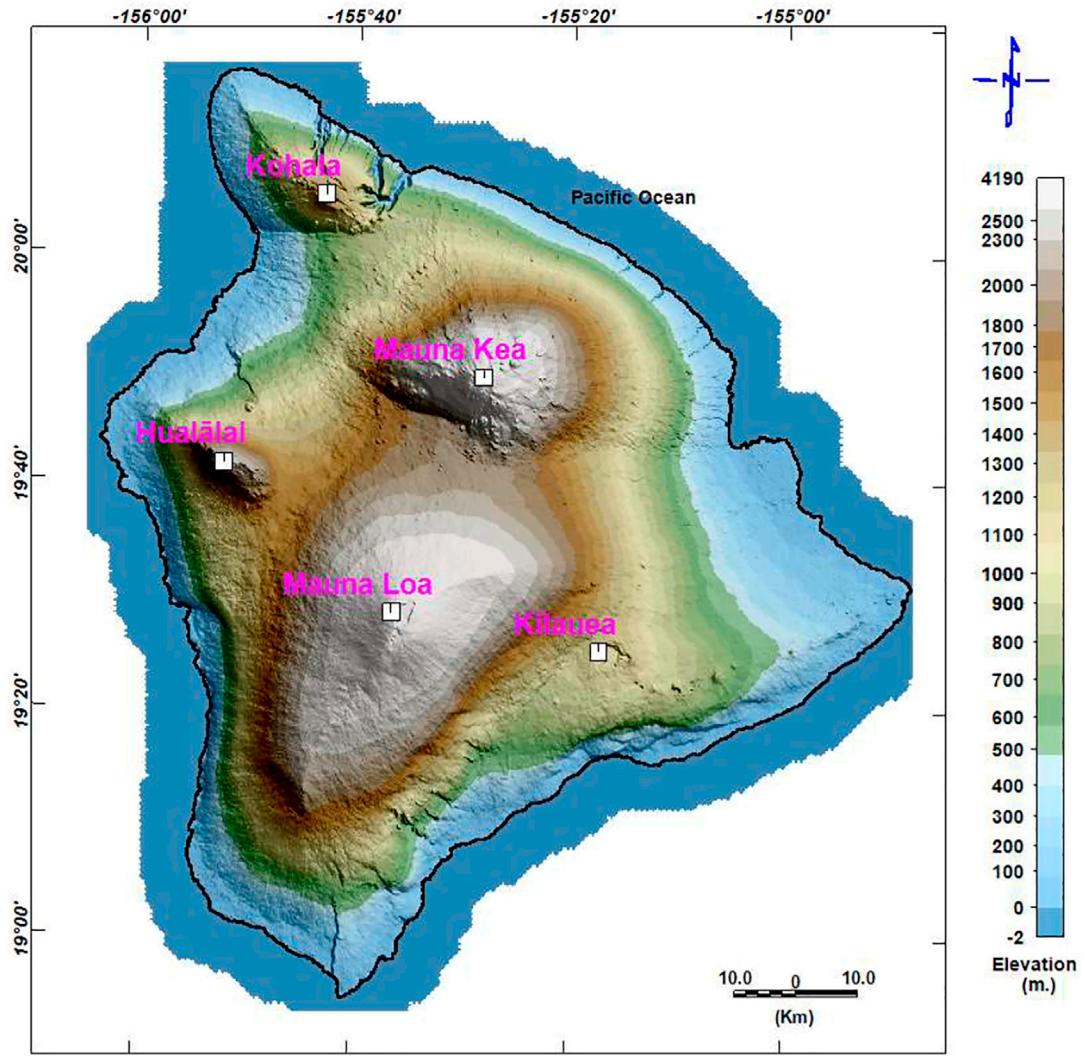

FIGURE 1 | Topography of Hawaii Island. Mauna Loa and Mauna Kea are the highest peaks.

in different areas. Most previous studies include horizontal map views of intrusions in their results. However, scientific studies assume the widespread concept of the inverted teardrop when considering pluton 3-D geometries (Vigneresse, 1995b) based on structural extrapolations to depth. Most field-based studies use extrapolations to depth without direct evidence to obtain a reasonable approximation when geophysical techniques are employed.

Aeromagnetic datasets are widely used to estimate the Curie point depth (CPD) and assess geothermal resources (Chiozzi et al., 2005; Trifonova et al., 2009; Hsieh et al., 2014). The CPD is considered at the surface at a high temperature of ~540°C, as measured *in situ* from holes drilled through the crust and into the still-molten lens of tholeiitic basalt in Kilauea (Zablocki and Tilling, 1976). The CPD surface indicates the bottom of the magnetic layer; this is where paramagnetic minerals are formed from ferromagnetic minerals when they reach the Curie point temperature (Nagata, 1961) or the depth at which nonmagnetic rocks are formed from magnetic rocks (Ravat et al., 2007). Iron sulfides and iron–titanium oxide are the most common ferromagnetic minerals (Rajaram, 2007).

Castro and Brown (1987) have used high-resolution sampling of the 1950 and 1972 flows in Kilauea to identify the intraflow variations of very young basalt flows. The paleomagnetic directions of these samples are different from the direction of Hawaii's geomagnetic field. This shallow inclination anomaly was attributed to the recording mechanism of subaerial basalts (Castro and Brown, 1987); however, it has since been identified as the nondipole field effect (Cox, 1975). Another paleomagnetic study has identified the lavas in the main part of the Pohue Bay flow and those of the Hawaiian cones to have similar paleomagnetic properties with relatively similar ages (Jurado-Chichay et al., 1993). That study could have identified both younger lava flows, which later utilized the main tube, and an earlier subset of cones, which were formed before the Pohue Bay eruption.

Magnetic data have been analyzed extensively to estimate both the depth to the magnetic basement (Spector and Grant, 1970; Hahn et al., 1976; Garcia-Abdeslem and Ness, 1994) and the Curie isotherm (Blakely, 1988; Okubo and Matsunaga, 1994). According to Spector and Grant (1970), the depth factor controls the shape of the readily averaged power spectrum. Their statement has resulted in a wide interpretation of the average two-dimensional (2-D) power spectrum of magnetic data. Moreover, the depth to the source can be calculated from the slope of the log radially averaged power spectrum.

The thermal structure of the crust in different geologic environments has been widely investigated using magnetic data (Spector and Grant, 1970; Bhattacharyya B. K. and Leu L.-K., 1975, 1977; Byerly and Stolt, 1977; Okubo et al., 1985; Blakely, 1995; Tanaka et al., 1999; Chiozzi et al., 2005; Ross et al., 2006; Trifonova et al., 2009; Gabriel et al., 2011, 2012; Bansal et al., 2013, 2016; Hsieh et al., 2014; Nwankwo and Shehu, 2015; Nwankwo and Abayomi, 2017); the resulting geomagnetic anomalies above the CPD have been used to delineate magnetic structures (Bhattacharyya and Leu, 1975a, b; Byerly and Stolt, 1977; Blakely and Hassanzadeh, 1981; Blakely, 1988; Chiozzi et al., 2005; Trifonova et al., 2009; Hsieh et al., 2014; Idárraga-García and Vargas, 2018; Mohamed Al Deep, 2021).

Flinders et al. (2013) used land and marine gravity data and a 3-D gravity model to calculate the average densities, volumes, and percentages of olivine in the intrusive materials and cumulate cores below the volcanoes in Hawaii. They used an isosurface density of 2.85 g cm^{-3} to delineate intrusive material, which equated to over 60% of dikes with a density of 2.95 g cm^{-3}. Furthermore, they defined cumulate cores using an isosurface density of 3.00 g cm^{-3}, which corresponded to ~35% olivine (density: 3.2–3.3 g cm^{-3}) in the intrusive complex (density: 2.85 g cm^{-3}).

The Hawaiian Islands were formed during the past 70 Ma as the Pacific lithospheric plate moved north and then west relative to a melting anomaly. This phenomenon is represented by the hotspot hypothesis, which accounts for the formation of a volcanic chain on the ocean floor. Wilson (1963a, c) proposed that the islands of Hawaii were formed when the seafloor moved over lava sources in the asthenosphere; they limited this theory to the volcanoes and the ridge of the Hawaiian Islands. Subsequently, Wilson's theory was expanded by Christofferson (1968) to include the Emperor Seamounts. Morgan (1972a, b) suggested that the Hawaiian hotspot and others are thermal plumes of material rising from the deep mantle. Clague and Dalrymple (1987) tested and validated this hypothesis based on a study of the geologic evolution of the Hawaiian–Emperor volcanic chain. In terms of geology, tholeiitic basalts account for >95% of the islands' rocks (Clague and Darlrymple, 1989).

Geophysical data collected from the ground and from the airborne were commonly employed in groundwater investigations and subsurface geology (e.g., Meneisy and Al Deep, 2020; Mohamed and Abu El Ella, 2021; Al Deep et al., 2021). On the other hand, Global data from the Earth Gravitational Model and the Earth Magnetic Anomaly Grid have been widely used for crustal studies and the depth to the bottom of the magnetic layer (e.g., Idárraga-García and Vargas, 2018; Mohamed and Al Deep, 2021), whereas gravity data from the Gravity Recovery and Climate Experiment mission have been successfully applied for estimating mass transport and distribution in the Earth's fluid (e.g., Mohamed et al., 2017; Mohamed, 2019; Mohamed, 2020a; Mohamed, 2020b; Mohamed, 2020c; Taha et al., 2021; Mohamed and Gonçalvès, 2021; Mohamed et al., 2021; Mohamed et al., 2022).

The current study aims to characterize the morphology of the magmatic chamber beneath Hawaii Island using gravity and magnetic potential fields. Delineating the geometrical border of the magmatic chamber beneath the island of Hawaii and estimating the CPD, geothermal gradient, and heat flow of the area require the techniques of gravity inversion and spectral analysis of magnetic data. Our method of estimating the CPD to determine the maximum depth to the magnetized rocks calculates the depth to the upper surface of the magma chamber indirectly. Additionally, a two-layer 2-D geological model using the contrast in density between the average density of the solidified rocks and the magma layer is applied using gravity modeling techniques.

GEOLOGIC SETTING OF HAWAII ISLAND

Hawaii Island comprises five major shield volcanoes (**Figure 2**): Mauna Kea (MK), Kohala (Ko), Kilauea (Ki), Mauna Loa (ML), and Hualalai (Hu) (Langenheim and Clague, 1987). Except for some minimal erosion to the northern sides of Ko and MK, these volcanoes have suffered little erosion (Langenheim and Clague, 1987). They progress in age from the southeast end (with its still-active volcanoes) to the northwest end (with its volcanoes dating from 75 to 80 Ma) (Clague and Dalrymple, 1987).

The ML volcano is the largest on Earth at 97-km long, 48-km wide, and an estimated volume of 70–80 million km^3 (Robinson and Eakins, 2006). Its shield-shaped dome rises to 4,167 m above sea level (**Figures 1**, **2**), and its slopes are dotted with a few cinder cones. The caldera of Mokuaweoweo is located on the summit (Macdonald, 1977). ML formed over a period of ~0.5 million year. During recent years, lava younger than 1,000 year has poured from fissures and a cone on the volcano's floor and rim, filling depressions and covering about 40% of its surface area (Lockwood and Lipman, 1987). A few weak explosions have occurred. The surface of ML originates mostly from the Holocene (Stearns and Macdonald, 1946; Lipman and Swenson, 1984). Stearns and Macdonald (1946) divided the volcano's rocks into Pliocene Ninole basalt, Pleistocene Kahuku basalt, and Pleistocene and Holocene Kau basalt (the most recent).

At 4,205 m above sea level, MK is Hawaii's highest volcano (**Figures 1**, **2**). There have been no eruptions over the past 3,600 years (Porter, 1979a). The configurations of cinder cones indicate the location of less-defined southerly, easterly, and westerly rifts. The volcano's rocks were divided into two volcanic series by Stearns and Macdonald (1946). The older (Hamakua) series forms a major part of the mountain and represents the shield stage and part of the post-shield stage. The upper part of the mountain (above 3,353 m) comprises a plateau resulting from the Laupahoehoe series filling of a caldera

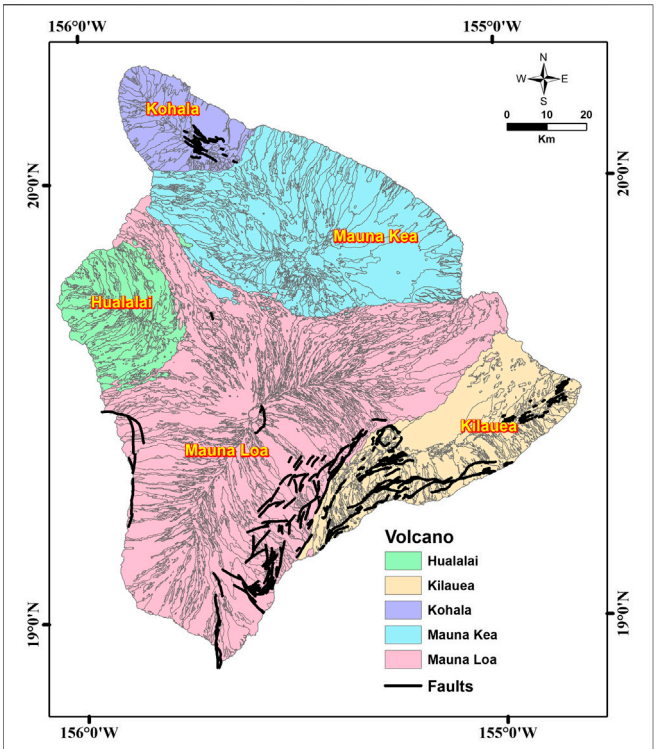

FIGURE 2 | Rock compositions of Hawaii Island and the faults in the southern part (source: Stearns and Macdonald, 1946; Wolfe and Morris, 1996a; Wolfe et al., 1997; Kauahikaua et al., 2002; Swanson, 2005).

in the Hamakua volcanic series, which represents the rest of the post-shield stage. Porter (1979a, 1979b) redefined the volcano's two rocks to include glacial deposits; additionally, they were elevated to a group ranking of volcanic and glacial formations.

The last eruptions of the Hu volcano in 1800–1801 occurred from five separate vents (Moore et al., 1987) (**Figures 1**, **2**). The volcano has an approximate diameter of 27 km and a well-defined NW-striking rift zone; its less-well-defined N- and SE-trending rift zones are characterized by widespread cinders and spatter cones (Langenheim and Clague, 1987). Its subaerial surface is represented by the Pleistocene Waawaa Trachyte Member, with short flows of hawaiite and a few flows of alkali basalt lava (Moore et al., 1987). According to detailed mapping and C-14 dating, the volcano's Holocene lava flows have been divided into four groups: 10–5, 5–3, 3–1, and <1 ka (Moore et al., 1987).

Based on K–Ar analysis, Ko is the oldest Pleistocene (McDougall and Swanson, 1972) and longest inactive volcano in the islands (Lipman, 1980) (**Figures 1**, **2**). It was formed over northwesterly and southwesterly rifts and a weak southwesterly rift (Langenheim and Clague, 1987). Its last eruption was ~60,000 years ago, and it is considered to be extinct. The volcano's rocks represent two volcanic series (Stearns and Macdonald, 1946): the older Pololu series (Pololu basalt) (Langenheim and Clague, 1987) of shield-stage tholeiitic basalt and caldera-filling postshield-stage alkalic basalt (Stearns and Macdonald, 1946) and the younger Hawi series (Hawi Volcanics) (Langenheim and Clague, 1987) of differentiated alkalic lava of the postshield stage (Stearns and Macdonald, 1946).

The Ki volcano has an area of 2,500 km^2 and rests on the southeast slope of ML (**Figures 1**, **2**). Lava flows from ML pass over the slopes of Ki. The Ki volcano is the youngest in Hawaii and remains very active (Clague and Dalrymple, 1987). Around 70% of its surface is younger than 500 years, and about 90% is younger than 1,100 years (Holcomb, 1987). At the base of a fault escarpment on its mobile south flank, Ki's older rocks of Hilina basalt are between 100 and 30 kyr old (Easton, 1987). The most recent Puna basalts of the Pleistocene and Holocene (Easton, 1987) represent the younger rocks and are separated from the older ones by Pahala ash.

DATA

The land and airborne potential field data used in this study are described below.

Gravity anomaly data

Gravity measurements from the study area were collected as datasets on the deep magmatic structures of the Hawaiian volcanoes. A complete Bouguer anomaly map was constructed from the corrected observed gravity data to build a realistic model for Hawaii relative to the ground surface. The gravity data, which were collected by Kauahikaua (2017), did not contain base station time series records, and there was no time channel for the data points. Therefore, it was assumed that the instrumental drift had been completed. A free air anomaly map was constructed, and a complete Bouguer anomaly map was compiled for use in the gravity inversion calculation.

The first step of the data processing involved calculating the theoretical gravity for the study area by **Eq. 1**. Provided the data projection was in the WGS84, the same datum was used.

$$G_n = a_1 \frac{\left(1 + a_2 \left(\sin \phi\right)^2\right)}{\sqrt{\left(1 + a_3 \left(\sin \phi\right)^2\right)}} \quad (1)$$

The subtraction of theoretical gravity from the observed data resulted in latitude-corrected data. The formula below (**Eq. 2**) was used for the latitude correction calculations:

$$G_l = G_{obseved} - G_n \quad (2)$$

where G_n is the theoretical gravity, ϕ is the latitude, and a_1, a_2, and a_3 are constants that are equal to 9780326.7714, 0.00193185138639, and −0.00669437999013, respectively.

The second step involved the calculation of the free air anomaly (G_{fair}) assuming that the elevation of the ground above or below the datum was without any representation of the density variation. Therefore, this was excluded from this study's modeling. The free air correction was calculated and subtracted from the latitude correction for the WGS84 data using the following equations:

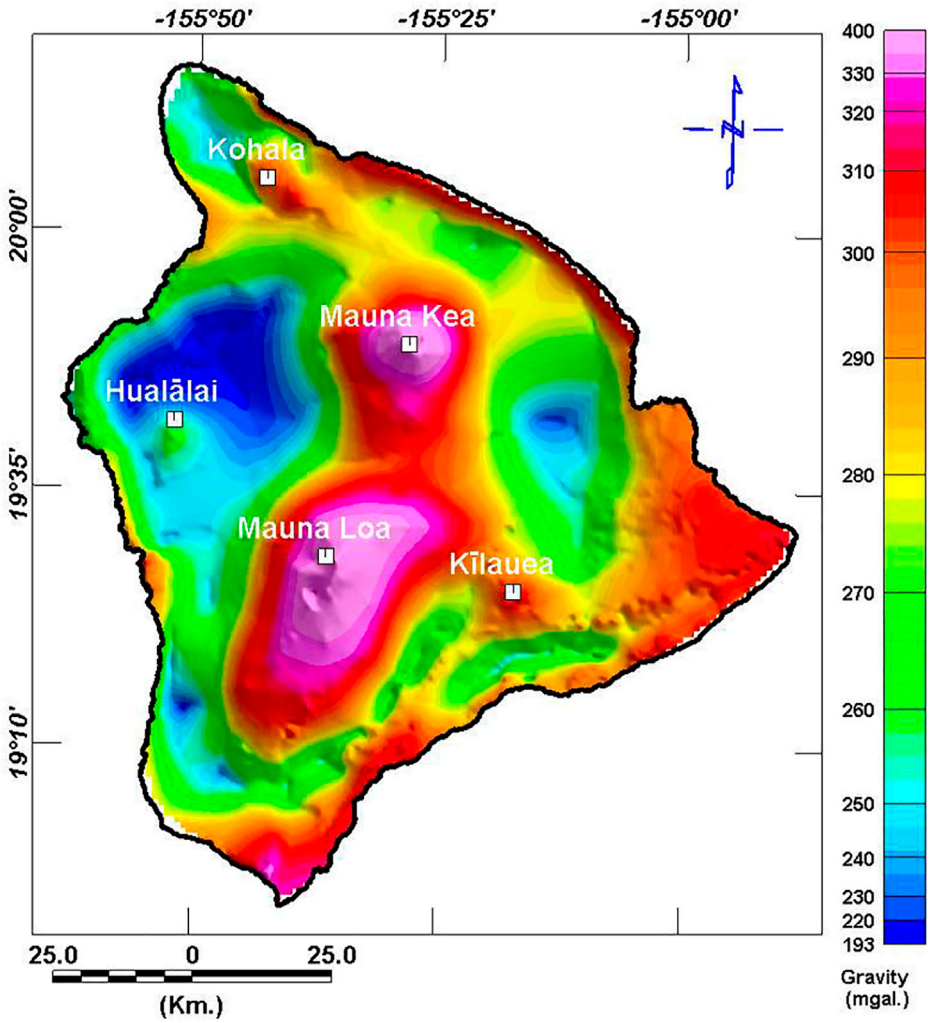

FIGURE 3 | Complete Bouguer gravity anomaly map of Hawaii Island.

$$\delta gh = -\left(3.083293357 + 0.004397732 * cos^2\,\phi\right) * h + 7.2125 * 10{-}7 * h^2 \quad (3)$$

$$G_{fair} = G_n - \delta gh \quad (4)$$

where δgh is the free air correction, h is the elevation of the gravity sensor above the datum, and ϕ is the latitude.

A simple Bouguer anomaly map was constructed by subtracting the Bouguer correction, which replaces the air above a datum by the mean density of land. The complete Bouguer correction calculates the terrain correction for the gravity stations and then applies the complete Bouguer correction to the simple Bouguer-corrected data. The terrain correction used topography data obtained from the Shuttle Radar Topography Mission (NASA, 2013).

The final complete Bouguer anomaly (**Figure 3**) was calculated according to **Eq. 5**:

$$G_B = G_{fair} - 0.0419088 * [D * Hs + (Dw - D) * Hw + (Di - Dw) * Hi] - G_c \quad (5)$$

where G_B is the complete Bouguer anomaly, D is the Bouguer density of the Earth in that area (~2.73 g cm^{-3}), Hs is the station elevation (meters), Dw is the Bouguer density of water (~1.027 g cm^{-3}), Hw is the water depth (meters), Di is the Bouguer density of ice (~0.917 g cm^{-3}), Hi is the ice thickness (meters), and G_c is the correction of the Earth's curvature.

Magnetic anomaly data

The available magnetic data for Hawaii Island comprise four aeromagnetic datasets. The United States Geological Survey's Hawaii-78-Hawaii data are the only data available with complete coverage of the island; they were collected along the north–south lines by aircraft instruments at a height of 305 m, and magnetic field values and locations were recorded (Godson et al., 1981). The data were collected along longitudinal lines with a spacing of 1.6 km and include latitude, longitude, altitude, and magnetic field values. Some variations in magnetic measurements are caused by rocks with high proportions of magnetic minerals; these anomalies reflect variations in the amount/type of magnetic material and the

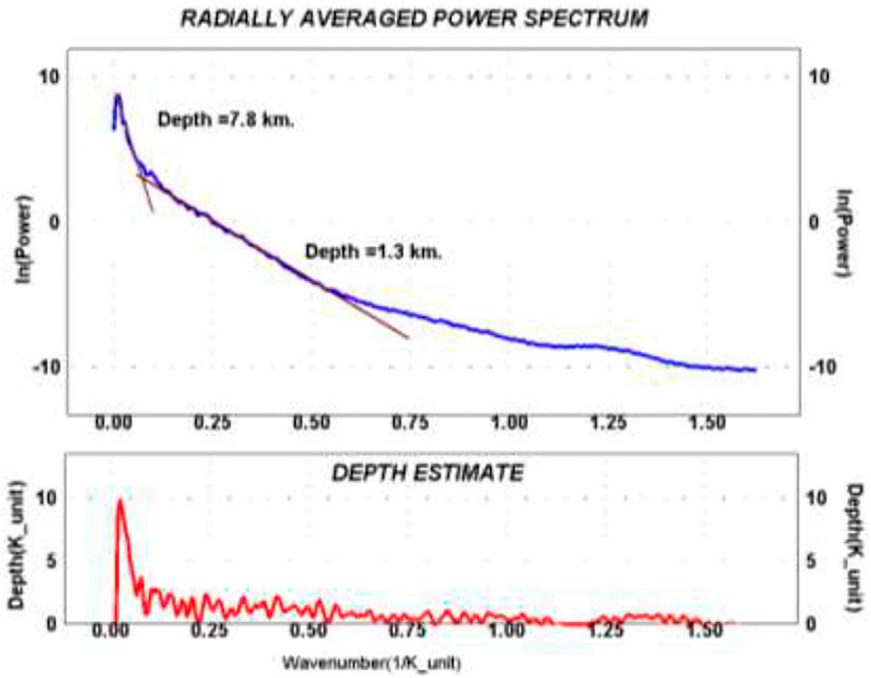

FIGURE 4 | Calculated depth from the averaged 2-D power spectrum to magnetic sources that may relate to volcanic cycles with high magnetite content.

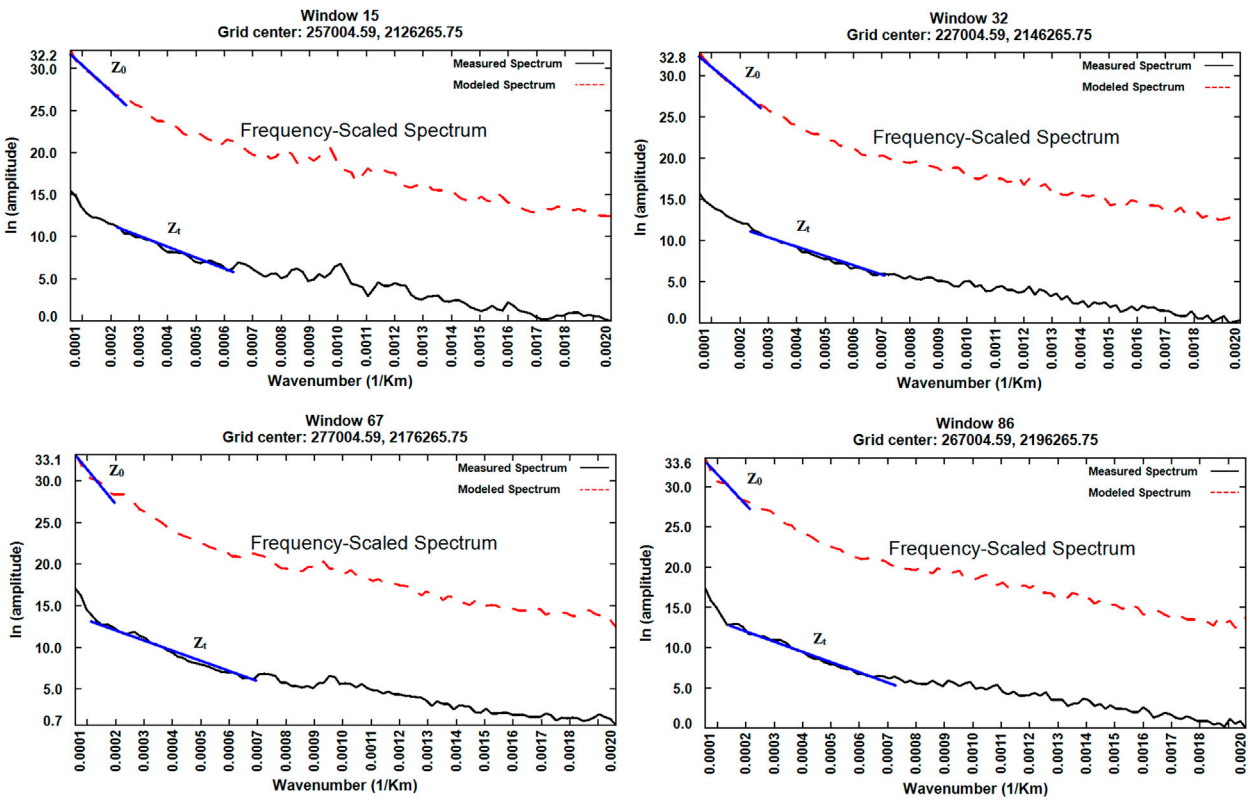

FIGURE 5 | Examples of spectra for the estimation of the depth of the top bound (Z_t) and the depth of the centroid (Z_0) of magnetic sources for different windows.

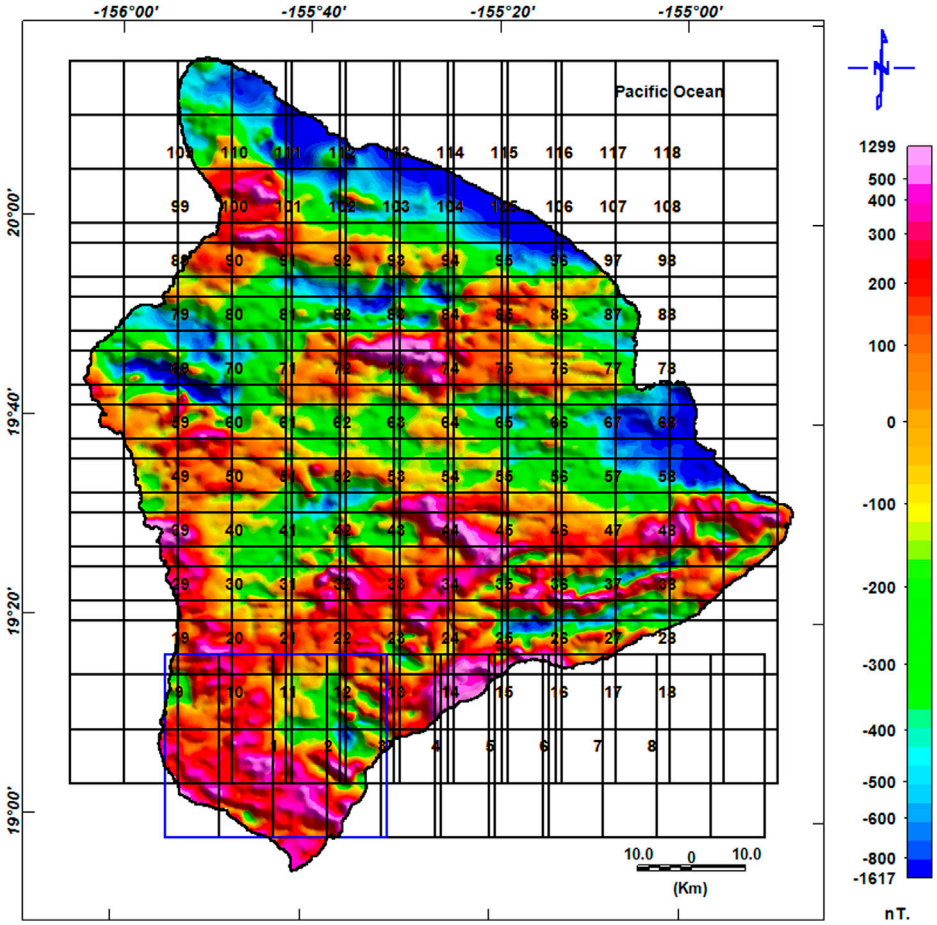

FIGURE 6 | Windows used to calculate the Curie point depth.

shape/depth of the rock bodies. The features and patterns of the aeromagnetic anomalies in the Hawaii-78-Hawaii dataset were processed to map the CPD and estimate the geothermal activity in the active volcanic zones based on the high resolution and consistency of the data along the flight lines.

Hildenbrand et al. (1993) used this dataset as well as other data that were obtained along lines normal to the rifts of ML and Ki at a flight height of 90 m (Flanigan et al., 1986). By merging the two datasets, they produced the most comprehensive dataset for the entire island. This is the only difference in our data reduction, as we used aeromagnetic data that provided complete coverage (Hawaii-78-Hawaii) of the island.

The complete dataset was gridded with 0.5-km spacing using the minimum curvature technique, and the dataset was continued upward to 305 m using the Geosoft 8.4 software (Geosoft Oasis Montaj, 2015). The shifted anomalies were adjusted using a reduction-to-pole transformation, while spectral and centroid techniques were used to delineate the shallow and deep sources and define the CPD, which denotes the interface between the magma layer and the overlying magmatic layer. The terrain effect was calculated using a spectral inversion process, which was subsequently removed to estimate the terrain-corrected magnetic field used in the current study.

RESULTS

Identifying the upper surface of the magmatic chamber from magnetic data

Calculating the CPD to determine the maximum depth to the magnetized rocks allows the upper surface of the magma chamber to be delineated indirectly. The rocks in Iki lava lake in Hawaii cannot contain any magnetization above the Curie temperature (540°C) (Zablocki and Tilling, 1976). Thus, for magnetite (the most abundant magnetic mineral), residual magnetism appears below the Curie point of ~540°C. In this case, the magma beneath Hawaii Island is basic, reflecting higher temperatures of 1,100°C to 1,300°C. The CPD denotes the depth to the bottom of the magnetized rocks, i.e., the depth to the upper surface of the magmatic chamber. As the CPD calculation involves the power spectrum, we calculated the 2-D radial power spectrum for the entire area to provide an overview of the depth distribution in that vicinity.

The spectral peak and centroid methods are commonly used spectral techniques for estimating the depth to the bottom of a magnetic layer (Ravat et al., 2007). The spectral peak method (Spector and Grant, 1970) was used by Shuey et al. (1977) and Connard et al. (1983). The present study also used this method to

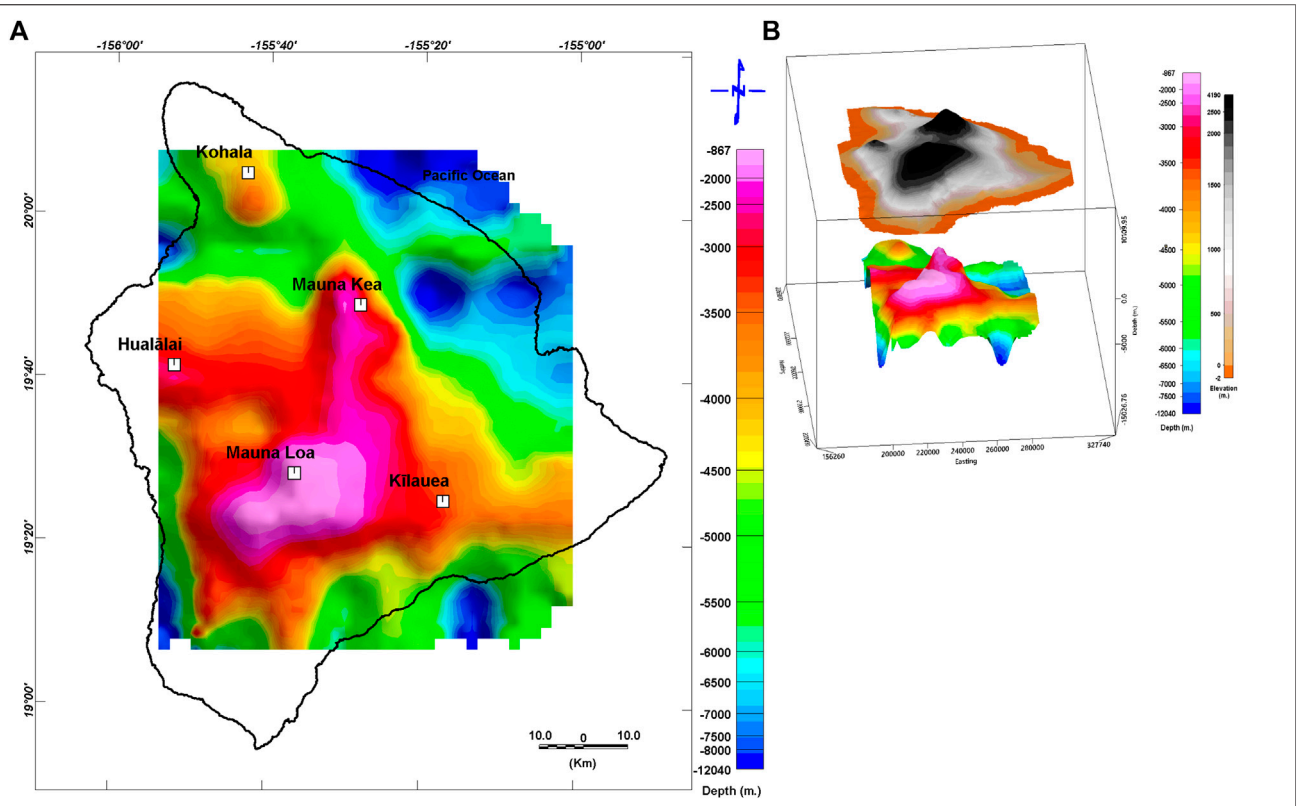

FIGURE 7 | (A) The calculated Curie point depth. **(B)** Three-dimensional representation of the upper surface of the magma chamber, which is correlated with the actual topography of Hawaii Island.

allocate depth to the top of the magnetized sources along with the centroid method (Bhattacharyya B. K. and Leu L. K., 1975, 1977; Okubo et al., 1985; Tanaka et al., 1999) to determine the centroid of rectangular parallelepiped sources or the depth to the centroid.

Spectral peak method (two-dimensional power spectrum)

The Spector and Grant (1970) equation (after Blakely, 1995) was used to estimate the depths to the bottom and top of the collective magnetic sources from their averaged power spectra:

$$|F(k)|^2 = 4\pi^2 C_m^2 |\theta_m|^2 |\theta_f|^2 C M_0^2 e^{-2|k|z_t} \left(1 - e^{-|k|(Z_b - Z_t)}\right)^2 S^2(a, b) \quad (6)$$

where F is Fourier power spectrum, k is wavenumber (cycles km^{-1}), C_m is a constant, θ_m is a magnetization direction factor, θ_f is a magnetic field direction factor, M_o is the magnetization, Z_b is depth to the bottom of the magnetic sources, Z_t is depth to the top of the ensemble of magnetic sources, and $S^2(a, b)$ is the horizontal dimensions of sources factor.

Figure 4 reveals that the azimuthally averaged log power spectrum, which was calculated using the Geosoft 8.4 software (Geosoft Oasis Montaj, 2015), has two segments reflecting the deeper and shallower sources of the magnetic field. The depth to each zone was calculated from the slope of each segment of the spectrum using **Eq. 7**:

$$h = -\frac{s}{4\pi} \quad (7)$$

where h is the depth, and s is the slope of the log power (energy) spectrum.

The depth of the deeper sources with wavenumbers between 0.0 and 0.0001 cycle km^{-1} (**Figure 4**) was calculated at 7.8 km below the flight height, whereas the depth to the shallower sources with wavenumbers between 0.0001 and 0.0007 cycle km^{-1} was calculated at 1.3 km below the flight height (i.e., 305 m).

Centroid method

Bhattacharyya and Leu (1977) proposed a technique for calculating the centroid of rectangular parallelepiped sources. Tanaka et al. (1999) calculated the CPD map for East and Southeast Asia by dividing the region into subregional data over about 40,000 km^2. Blakely (1988) divided the magnetic data map over the Nevada area into subregions with approximate areas of 14,400 km^2 and estimated the CPD of the state of Nevada. The CPD in Bulgaria was calculated by Trifonova et al. (2009) using six subregions with a 300-km edge. Hsieh et al. (2014) divided the integrated magnetic anomaly data of Taiwan into square subregions (250 × 250 km^2) and calculated

TABLE 1 | A sample of the calculated CPD with a 40 × 40 km^2 window, the estimated geothermal gradient, and heat flow. The data misfit using the RMSE is also shown.

Window No.	UTM		Root mean square error (RMSE)	Curie point depth (CPD) (km)	Geothermal gradient (°C/km)	Heat flow (mW/m^2)
	X	Y				
1	224,571.3	2,116,266	1.8	3.8	142.1	355.3
10	217,004.6	2,126,266	0.37	4	135	337.5
11	227,004.6	2,126,266	0.99	3.5	154.3	385.7
15	267,004.6	2,126,266	1.02	8.2	65.9	164.6
20	217,004.6	2,136,266	1.42	2.4	225	562.5
24	257,004.6	2,136,266	1.26	3.9	138.5	346.2
26	277,004.6	2,136,266	1.15	4.8	112.5	281.3
28	197,004.6	2,146,266	0.91	5	108	270
32	237,004.6	2,146,266	0.65	1.6	337.5	843.8
34	257,004.6	2,146,266	0.3	3.1	174.2	435.5
38	197,004.6	2,156,266	0.12	5.4	100	250
40	217,004.6	2,156,266	0.12	2.9	186.2	465.5
41	227,004.6	2,156,266	0.09	0.93	581.2	1453
43	247,004.6	2,156,266	0.08	2.6	207.7	519.2
47	287,004.6	2,156,266	0.25	4.1	131.7	329.3
49	207,004.6	2,166,266	0.34	3.6	150	375
53	247,004.6	2,166,266	0.43	2.5	216	540
57	287,004.6	2,166,266	0.67	5.8	93.1	232.8
59	207,004.6	2,176,266	0.88	2.9	186.2	465.5
63	247,004.6	2,176,266	0.59	3.7	145.9	364.9
67	287,004.6	2,176,266	0.58	7	77.1	192.9
71	227,004.6	2,186,266	0.75	3.7	145.9	364.9
75	267,004.6	2,186,266	0.69	6.5	83.1	207.7
81	227,004.6	2,196,266	0.73	5.1	105.9	264.7
83	247,004.6	2,196,266	0.54	4.9	110.2	275.5
86	277,004.6	2,196,266	0.35	8	67.5	168.8
88	197,004.6	2,206,266	0.27	7.8	69.2	173.1
91	227,004.6	2,206,266	0.31	5.7	94.7	236.8
92	237,004.6	2,206,266	0.43	4.5	120	300
94	257,004.6	2,206,266	0.44	5.4	100	250
99	207,004.6	2,216,266	0.5	5.1	105.9	264.7
101	227,004.6	2,216,266	0.86	4.9	110.2	275.5
103	247,004.6	2,216,266	0.8	7.4	73	182.4
105	267,004.6	2,216,266	0.79	7.7	70.1	175.3
108	197,004.6	2,226,266	0.34	6.3	85.7	214.3
111	227,004.6	2,226,266	0.02	5.1	105.9	264.7
113	247,004.6	2,226,266	0.25	12.4	43.5	108.8

the 2-D fast Fourier transform power spectrum for each region to estimate the CPD map. The Curie temperature depths in northern Italy (the Alps and the Po Plain) were calculated by Speranza et al. (2016) by creating windows with a 100-km edge and a 50% overlap between the aeromagnetic data and data from the Earth Magnetic Anomaly Grid two over the study area. Yang et al. (2017) calculated the CPD of Southeast Tibet via a spectral analysis of satellite data magnetic anomalies. Finally, Blakely (1995) presented the power spectral density of the total magnetic field [$\boldsymbol{\phi_{\Delta T}}$ ($\mathbf{k_x}$; $\mathbf{k_y}$)], as follows:

$$\phi\Delta T\left(k_x,k_y\right)=\phi M\left(k_x,k_y\right)*4\pi^2C_M^2|\theta M|^2\left|\theta_f\right|^2e^{-2|k|Z_t}\left(1-e^{-2|k|\left(Z_b-Z_t\right)}\right)^2 \quad (8)$$

Equation (8) was reduced to **Eq. (9)**. Assuming that **M (x; y)** is the layer's magnetization and a random function of **x, y**, this indicates that the power-density spectra of the magnetization $\boldsymbol{\phi_M}$ ($\mathbf{k_x}$, $\mathbf{k_y}$) is a constant. Then, the averaged power spectrum of $\boldsymbol{\phi}$ (|**k**|) can be written as:

$$\phi\left(|k|\right)=Ae^{-2|k|Z_t}\left(1-e^{-2|k|\left(Z_b-Z_t\right)}\right)^2 \quad (9)$$

where A is a constant. The depth to the top of the ensemble of magnetic sources ($\mathbf{Z_t}$) was derived from the slope of the high wavenumber segment of a radially averaged power spectrum $\ln\left(P\left(k\right)^{\frac{1}{2}}\right)$, as follows:

$$\ln\left(P\left(k\right)^{\frac{1}{2}}\right)=A-|k|\,Z_t \quad (10)$$

Additionally, the centroid depth ($\boldsymbol{Z_0}$) could be estimated from the low wavenumber segment of the spectrum (Tanaka et al., 1999):

$$\ln\left(P\left(k\right)^{1/2}/k\right)=B-|k|\,Z_0 \quad (11)$$

where $\boldsymbol{B}$ is a constant. Finally, $\mathbf{Z_b}$ could be calculated from the following formula (Okubo et al., 1985):

$$Z_b=2Z_0-Z_t \quad (12)$$

According to Blakely (1996), the window size was suggested to be five times that of the CPD. Therefore, the current study applied a moving window to subset the data into

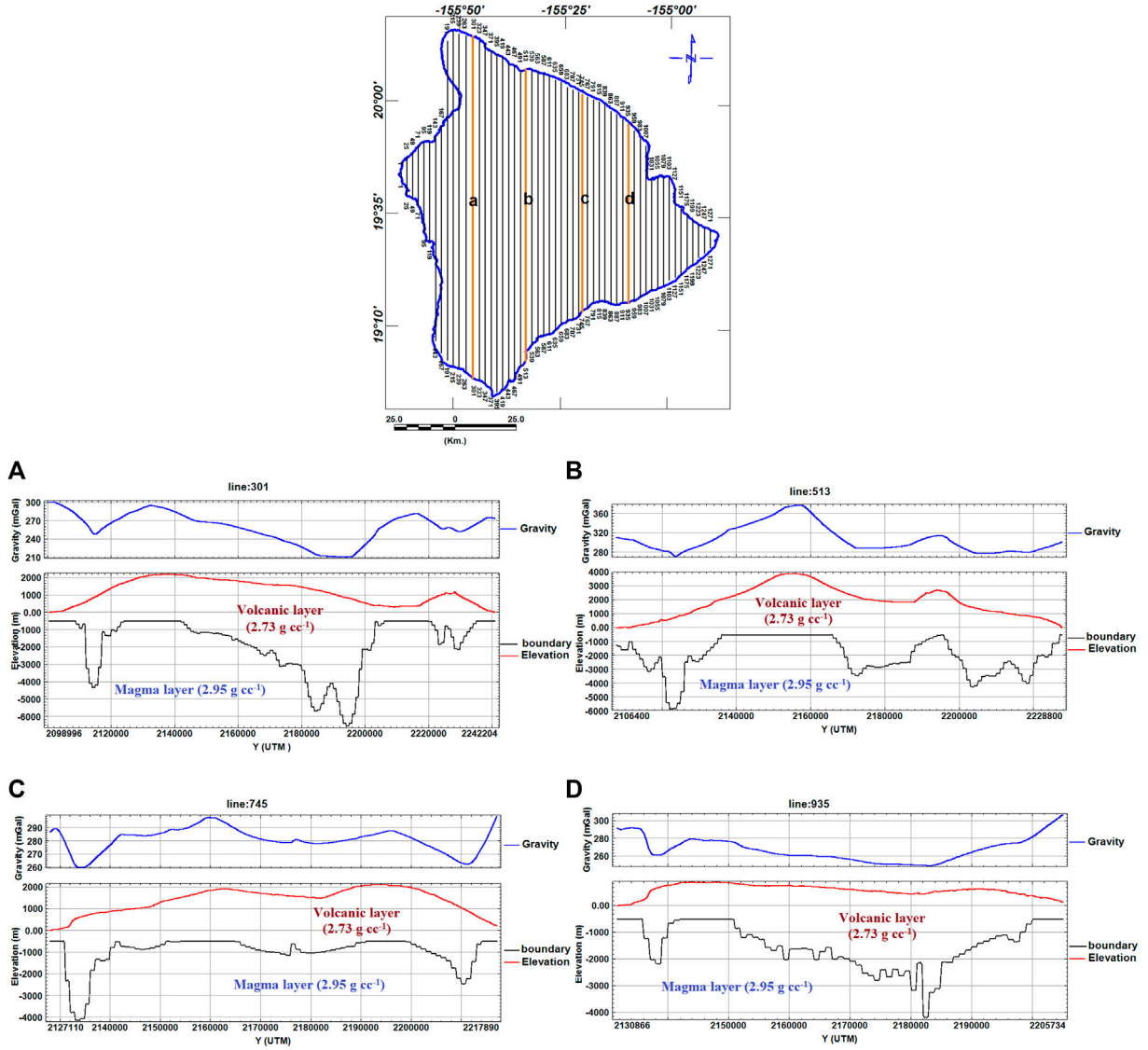

FIGURE 8 | Location map of the north–south parallel profiles used to calculate the density inversion model. The orange lines refer to selected 2-D modeled profiles **(A–D)**.

TABLE 2 | Pillow lava layers intercalated by hyaloclastite from the Hilo borehole and their densities [Source: (Moore, 2001)].

Lithologic zone	Depth range (m.)	Density (g/cc)
Hyaloclastite	Intercalated	2.3 to 2.7 Avg. 2.5
1st pillow lava	1,983–2,136	3.01 ± 0.10
2nd pillow lava	2,234–2,470	2.67 ± 0.13
3rd pillow lava	2,640–2,790	2.89 ± 0.17
4th pillow lava	2,918–3,097	2.97 ± 0.08

square regions with a 40-km edge and an overlap of 25% to generate adequate wavelengths for the power spectrum calculation.

An example of the azimuthally averaged power spectrum for some selected windows is given in **Figure 5** while **Figure 6** contains a location map of each spectral window. **Figure 7** shows the estimated depth to the bottom of the magnetized layer, which varies from 0.93 to 12.4 km below the ground surface when using a 40 × 40 km^2 window. Based on the window of 40 × 40 km^2, the surface of the magmatic plume was more correlated to the distribution of volcanoes on the surface of the island. Moreover, a large plume was observed beneath the ML, Ki, and MK volcanoes, underneath which uprising magma may be accumulating. **Table 1** presents the calculated CPD (using a 40 × 40 km^2 window), the calculated geothermal gradient, and the heat flow. The misfit was also calculated (**Table 1**) using the root mean square errors (RMSEs) of the match between the observed and modeled spectra.

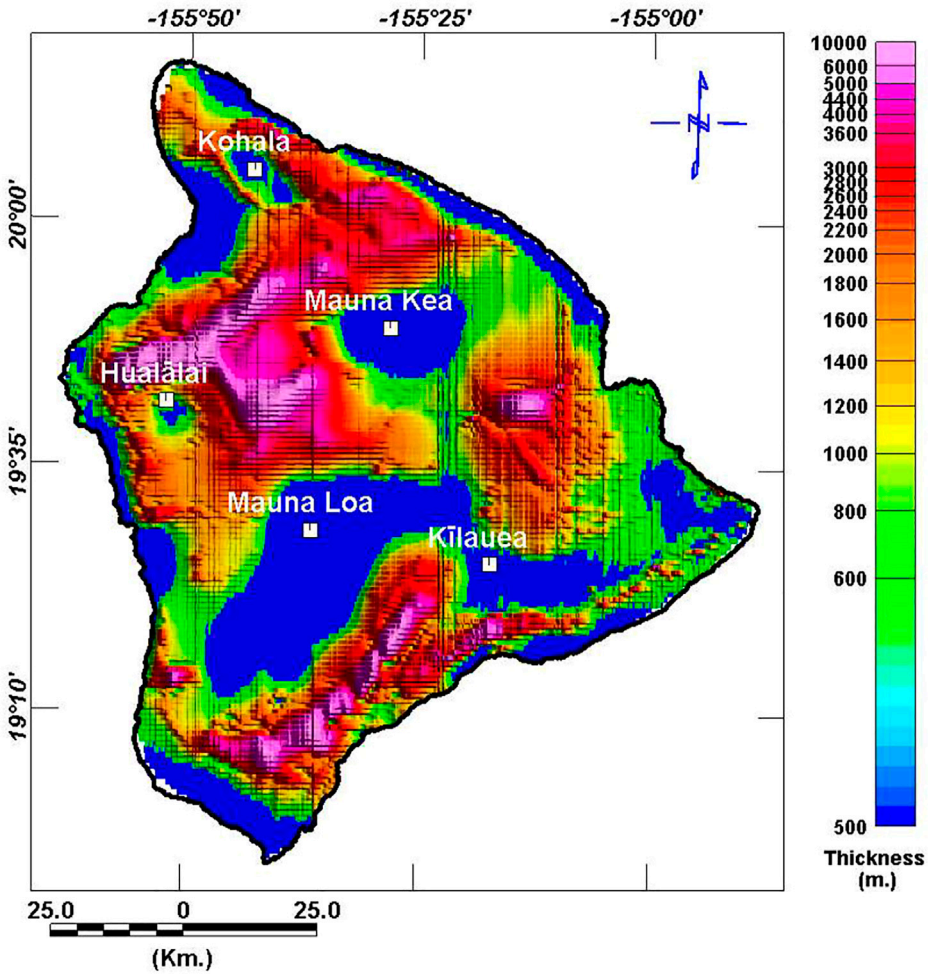

FIGURE 9 | Thickness of the first layer based on the north–south parallel profiles in **Figure 8**.

Morphology of the Magmatic Chamber from the Gravity Data

To construct a more realistic model for Hawaii Island, this section used the 2-D technique of gravity field modeling. The objective was to propose a comprehensive density model of the crust below the island.

Gravity inversion

The gravity data modeling was carried out along profiles (**Figure 8**) on the complete Bouguer anomaly map using the Intrepid 4.5 geophysics software (Intrepid Geophysics, 2013). This calculation method applies the algorithm presented by Murthy and Rao (1993). **Equation 13** provides the gravity anomaly $\Delta g(\mathbf{0})$ at any point $\mathbf{P(0)}$ of a 2-D body of the polygonal cross section:

$$\Delta g(\mathbf{0}) = 2Gd_c \sum_{k=1}^{N} p_k \left[\sin i_k \ln\left(r_k + \frac{1}{r_k} \right) - \cos i_k \left(\theta_{k+1} - \theta_k \right) \right] \tag{13}$$

where **G** is the universal gravitational constant, $\mathbf{r_k}$ is the length of the line from the surface to the first point (vertex), $\mathbf{r_{k+1}}$ is the length to the next point, and $\boldsymbol{\theta_k}$ and $\boldsymbol{\theta_{k+x}}$ are the angles to the body vertices. The term r_k is defined by **Eq. 14**:

$$r_k = \sqrt{x_k^2 + z_k^2},\ r_{k+1} = \sqrt{x_{k+1}^2 + z_{k+1}^2} \tag{14}$$

where z_k is the depth to vertex **k**, and z_{k+1} is the depth to the next vertex of the assumed polygonal body.

This study constructed a 2-D density model for two Earth layers by forward modeling the gravity data along selected profiles (**Figure 8**). The two-layer model was constructed based on the density contrast properties of these layers and the assumption that the second layer (magma) was denser. The interface between the two layers was assumed to comprise a sequence of polygonal bodies, and a density contrast value of 0.22 g cc^{-1} between the two layers was also assumed.

Two-dimensional density models were operated along the profiles (with 1-km line spacing) using the GRAVINV module in the Intrepid 4.5 geophysics software (Intrepid Geophysics,

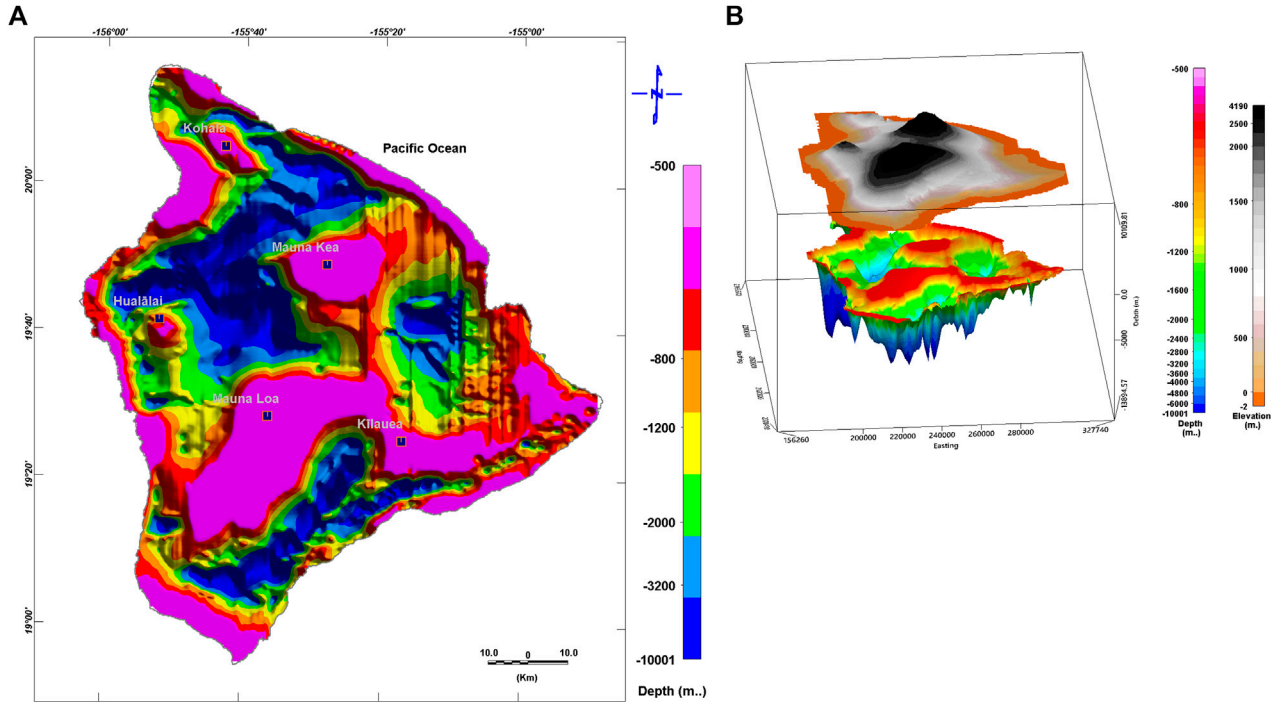

FIGURE 10 | (A) Calculated depth to the magma using density variation inversion. **(B)** Three-dimensional representation of the magma's upper surface correlated with the actual topography of Hawaii Island. The generated model was influenced by the edge effect.

2013). Each model contained two layers. The first (top) volcanic layer had a density of 2.73 g cc^{-1}, which was averaged for 1,600 core samples obtained at depths between 889 and 3,097 m below sea level near the city of Hilo (Moore, 2001). The densities of the borehole samples are summarized in **Table 2**. The second magmatic layer was assumed to have a high density of 2.95 g cc^{-1}. As shown in **Figures 9**, **10**, a complete two-layer solution for the gravity modeling was provided along the north–south profiles, which were interpolated across the island of Hawaii. **Figure 9** shows the thickness of the first layer based on the north–south parallel profiles in **Figure 8**, which equals the depth of the second (magma) layer in **Figure 10**. **Figure 10** depicts very steep vertical rising magmatic plumes, which resemble those calculated by the magnetic method. The Z_t value varied from 500 m to over 10 km. Compared with the actual volcanic activity conditions on Hawaii Island, these calculated depths were very reasonable. However, the edge effect meant that the outer rim of the model could not be considered.

GEOTHERMAL GRADIENT AND HEAT FLOW

The geothermal gradient (dt/dz) from the Earth's surface to the CPD was estimated using **Eq. (15)** (Tanaka et al., 1999):

$$dt/dz = 540^{\circ}\mathrm{C}/Z_b \tag{15}$$

The heat flow (q) was calculated using **Eq. 16** (Okubo et al., 1985):

$$q = h\,(dt/dz) = h(540^{\circ}\mathrm{C}/Z_b) \tag{16}$$

This study used h = 2.5 W/m°C as the value for igneous rocks (Springer, 1999). As can be seen in **Table 1**, the dt/dz varied from 43.5 to 581.1 °C km^{-1}. **Figure 11** presents the estimated heat flow, which ranges between 108.8 and 1,453 mW/m^2 close to the volcanic eruption zone of ML. As geological constraints strongly influence CPDs (Ross et al., 2006), in the volcanic zones, the CPDs are shallower than 10 km (Obande et al., 2014). According to **Table 1** and **Figure 11**, Hawaii Island has high geothermal potential energy proximal to the volcanic eruption zones with shallower CPDs as well as high geothermal gradient and heat flows. The data in **Table 1** show window no. 213 to have the lowest heat flow, while the flow is highest in window no. 141.

DISCUSSION AND CONCLUSION

Investigating the morphology of the magmatic chamber beneath Hawaii Island as an example of an island arc system enhances the current understanding of plate tectonics theory. However, the growth and movement directions of these magmatic diapirs require a time-lapse investigation. Herein, we utilized the available potential data to better understand the morphology of the magmatic chamber, estimate the CPD, and calculate the heat flow.

This study successfully applied airborne geophysical data to characterize the morphology of the magmatic chamber beneath

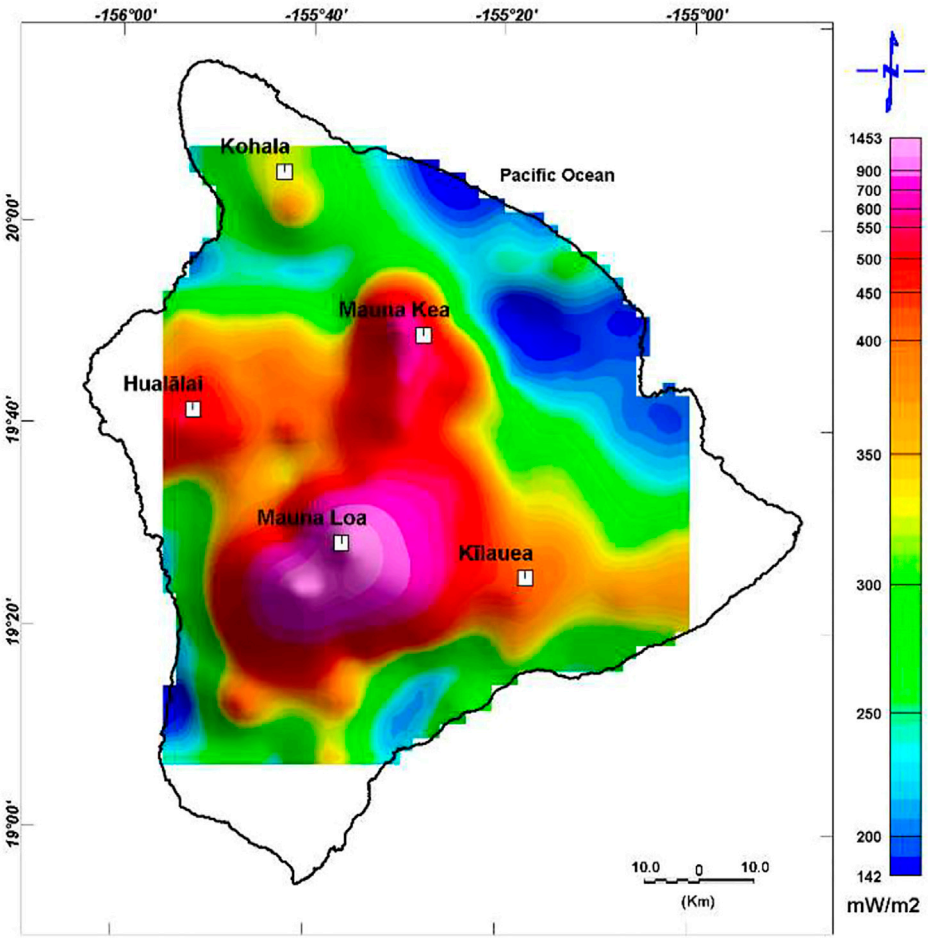

FIGURE 11 | Heat flow map of Hawaii Island, which corresponds with the active volcanoes in the area.

Hawaii Island and estimate the depths to the deeper sources; these varied from 7.8 km below the flight height to shallower sources estimated to be 1.3 km deep. The Curie point is located from shallow depths (<1 km) at and proximal to the ML volcano to 12 km close to the northeastern part of the MK volcano region below the ground surface.

The results of the gravity data inversion revealed the existence of very steep vertical rising magmatic plumes, reflecting the dense intrusive material of basaltic and ultramafic rocks underlying the volcanoes. The results corresponded well with those calculated using the magnetic method. The depth to the top of the second (magma) layer varied from 500 m to about 10 km. An inverse relation was identified between the heat flow and the CPD, whereby a decrease in heat flow corresponded with an increase in the CPD. The highest value of 1,453 mW/m^2 occurred at the shallowest CPD (0.93 km) in window no. 141, while the lowest value of 108.8 mW/m^2 was correlated with the highest CPD (12.4 km) in window no. 213. According to Jessop et al. (1976), these anomalous geothermal conditions are related to heat flows of between 80 and 100 mW/m^2.

The results of this study are in good agreement with the previous 3-D gravity models used by Kauahikaua et al. (2000), who studied the magmatic structures within basaltic volcanoes and defined the structures related to seismic hazards and landslides on the island of Hawaii. Their results revealed the existence of dense cumulates and intrusions beneath the summits of every volcano.

Information on the magmatic properties of subsurface rocks was provided by Hildenbrand et al. (1993), who applied the spectral depth technique to aeromagnetic data. Two shallow magnetic zones were identified at a depth of 1 km. Additionally, using the spectral inversion of the magnetic data, they defined a deep magnetic horizon at 10.5 km below the flight height. The results of the current study correspond well with those of Hildenbrand et al. (1993), as our interpretation revealed shallow and deep magnetic sources to be located at 1.3 and 8 km below the flight height, respectively. Based on the CPD estimations, the bottom of the magnetized layer varied between 0.93 and 12.4 km in depth, while the gravity inversion technique indicated a depth of 0.5–10 km below the ground surface.

The existence of large magmatic plumes of dense cumulates and intrusions beneath the summits of the MK, ML, and Ki active volcanoes in this study was confirmed by the presence of

higher-velocity regions near the active volcanoes containing dense intrusive materials, such as olivine cumulates (Thurber, 1984; Hill and Zucca, 1987; Okubo et al., 1997). However, a 3-D P-wave velocity model run by Park et al. (2007) for the southeastern part of Hawaii Island produced higher crustal seismic velocity values of 7.0–7.4 km/s. These higher values indicate the dominance of dense olivine cumulates mixed with extrusive and intrusive basaltic rocks in the high-velocity regions underlying the summits and rift regions of the active areas of Ki and ML. In the study of Park et al. (2007), the lower-velocity regions south of the Hilina and along the Kao'iki fault zones were attributed to thick accumulations of volcaniclastic sediments.

Using more than one geophysical dataset provides adequate confidence in the calculated results to overcome the problem of nonuniqueness. The calculated upper surface of the magma chamber delineated about five diapirs, three of which (ML, MK, and Ki) were grouped in one large plume of dense basic and ultrabasic materials. Compared with other studies, the integrated approach presented herein provides an in-depth understanding of the geometry of the magmatic chamber using an indirect CPD estimation to calculate the depth to the chamber's upper surface. Finally, the new gravity model for Hawaii Island, which incorporates advanced software, corresponds well with the results of the magnetic data.

KEY POINTS

Estimates the depth to the bottom of the magnetized rocks based on calculating the Curie point depth beneath Hawaii Island.

Characterizes the morphology of the magmatic chamber beneath Hawaii Island using the gravity inversion technique.

Estimates the geothermal gradient and heat flow associated with the active volcanoes of Hawaii Island.

DATA AVAILABILITY STATEMENT

The aeromagnetic field data (Hawaii-78-Hawaii, Godson et al., 1981) can be found at http://mrdata.usgs.gov/geophysics/surveys/geophysics2/HI/HI_1071.jpg and http://mrdata.usgs.gov/geophysics/surveys/geophysics2/HI/HI_1071.zip. The gravity measurements for Hawaii Island (Kauahikaua, 2017) can be found at https://doi.org/10.5066/F7V1230Q.

AUTHOR CONTRIBUTIONS

All authors listed have made a substantial, direct, and intellectual contribution to the work and approved it for publication.

ACKNOWLEDGMENTS

The authors would like to thank especially the staff members of U.S. Geological Survey and Hawaiian Volcano Observatory for providing the aeromagnetic field data (Hawaii-78-Hawaii, Godson et al., 1981) and making it available online. Deep thanks to Jim Kauahikaua for collecting the gravity measurements for the Hawaii Island that were published in Kauahikaua (2017) and making it available online. Deep thanks and gratitude also to the Researchers Supporting Project number (RSP-2021/351), King Saud University, Riyadh, Saudi Arabia for funding this research article.

REFERENCES

Al Deep, M., Araffa, S. A. S., Mansour, S. A., Taha, A. I., Mohamed, A., and Othman, A. (2021). Geophysics and Remote Sensing Applications for Groundwater Exploration in Fractured Basement: A Case Study from Abha Area, Saudi Arabia. *Journal of African Earth Sciences* 184 (1), 104368.

Bansal, A. R., Anand, S. P., Rajaram, M., Rao, V. K., and Dimri, V. P. (2013). Depth to the Bottom of Magnetic Sources (DBMS) from Aeromagnetic Data of central India Using Modified Centroid Method for Fractal Distribution of Sources. *Tectonophysics* 603, 155–161. doi:10.1016/j.tecto.2013.05.024

Bansal, A. R., Dimri, V. P., Kumar, R., and Anand, S. P. (2016). "Curie Depth Estimation from Aeromagnetic for Fractal Distribution of Sources," in *Fractal Solutions for Understanding Complex Systems in Earth Sciences*. Editor V. P. Dimri (Switzerland: Springer International Publishing), 19–31. doi:10.1007/978-3-319-24675-8_2

Barnoud, A., Coutant, O., Bouligand, C., Gunawan, H., and Deroussi, S. (2016). 3-D Linear Inversion of Gravity Data: Method and Application to Basse-Terre Volcanic Island, Guadeloupe, Lesser AntillesGeophysical Journal International. *Geophys. J. Int.* 205 (1), 562–574. doi:10.1093/gji/ggw030

Bhattacharyya, B. K., and Leu, L.-K. (1975a). Analysis of Magnetic Anomalies over Yellowstone National Park: Mapping of Curie point Isothermal Surface for Geothermal Reconnaissance. *J. Geophys. Res.* 80, 4461–4465. doi:10.1029/jb080i032p04461

Bhattacharyya, B. K., and Leu, L. K. (1977). Spectral Analysis of Gravity and Magnetic Anomalies Due to Rectangular Prismatic Bodies. *Geophysics* 42, 41–50. doi:10.1190/1.1440712

Bhattacharyya, B. K., and Leu, L. K. (1975b). Spectral Analysis of Gravity and Magnetic Anomalies Due to Two-dimensional Structures. *Geophysics* 40, 993–1013. doi:10.1190/1.1440593

Blakely, R. J. (1995). *Potential Theory in Gravity and Magnetic Applications*. Cambridge: Cambridge University Press.

Blakely, R. J. (1996). *Potential Theory in Gravity and Magnetic Applications*. Cambridge: Cambridge University Press, 464.

Blakely, R. J. (1988). Curie Temperature Isotherm Analysis and Tectonic Implications of Aeromagnetic Data from Nevada. *J. Geophys. Res.* 93 (B10), 11817–11832. doi:10.1029/JB093iB10p11817

Blakely, R. J., and Hassanzadeh, S. (1981). Estimation of Depth to Magnetic Source Using Maximum Entropy Power Spectra, with Application to the Peru-Chile Trench. *Geol. Soc. Am. Mem.* 154, 667–682. doi:10.1130/mem154-p667

Boulanger, O., and Chouteau, M. (2001). Constraints in 3D Gravity Inversion. *Geophys. Prospect.* 49, 265–280. doi:10.1046/j.1365-2478.2001.00254.x

Byerly, P. E., and Stolt, R. H. (1977). An Attempt to Define the Curie point Isotherm in Northern and central Arizona. *Geophysics* 42, 1394–1400. doi:10.1190/1.1440800

Camacho, A. G., Fernández, J., and Gottsmann, J. (2011). A New Gravity Inversion Method for Multiple Subhorizontal Discontinuity Interfaces and Shallow Basins. *J. Geophys. Res.* 116, B02413. doi:10.1029/2010JB008023

Camacho, A. G., Montesinos, F. G., and Vieira, R. (1997). A Three-Dimensional Gravity Inversion Applied to São Miguel Island (Azores). *J. Geophys. Res.* 102 (B4), 7717–7730. doi:10.1029/96jb03667

Camacho, A. G., Montesinos, F. G., and Vieira, R. (2000). Gravity Inversion by Means of Growing Bodies. *Geophysics* 65 (1), 95–101. doi:10.1190/1.1444729

Castro, J., and Brown, L. (1987). Shallow Paleomagnetic Directions from Historic Lava Flows, Hawaii. *Geophys. Res. Lett.* 14 (12), 1203–1206. doi:10.1029/gl014i012p01203

Cella, F., Fedi, M., Florio, G., Grimaldi, M., and Rapolla, A. (2007). Shallow Structure of the Somma-Vesuvius Volcano from 3D Inversion of Gravity Data. *J. Volcanology Geothermal Res.* 161, 303–317. doi:10.1016/j.jvolgeores.2006.12.013

Chiozzi, P., Matsushima, J., Okubo, Y., Pasquale, V., and Verdoya, M. (2005). Curie-point Depth from Spectral Analysis of Magnetic Data in central-southern Europe. *Phys. Earth Planet. Interiors* 152, 267–276. doi:10.1016/j.pepi.2005.04.005

Christofferson, E. (1968). The Relationship of Sea-Floor Spreading in the Pacific to the Origin of the Emperor Seamounts and the Hawaiian Island Chain (abst.,). *Am. Geophys. Union Trans.* 49, 214.

Clague, D. A., and Dalrymple, G. B. (1987). Chapter I. The Hawaiian-Emperor Volcanic Chain. Part I. Geologic Evolution. *USGS Profesisonal Paper* 1350, 5–54.

Clague, D. A., and Dalrymple, G. B. (1989). "Tectonic, Geochronologayn, and Origin of the Hawaiian-Emperorv Olcanic Chain," in *The Eastern Pacific Ocean and Hawaii, the Geology of North America*. Editors E. K. Winterer, D . M. Hussonga, and R. W. Decker (Boulder, Colo: Geological Society of America), 188–217.

Connard, G., Couch, R., and Gemperle, M. (1983). Analysis of Aeromagnetic Measurements from the Cascade Range in central Oregon. *Geophysics* 48, 376–390. doi:10.1190/1.1441476

Cox, A. (1975). The Frequency of Geomagnetic Reversals and the Symmetry of the Nondipole Field. *Rev. Geophys.* 13 (3), 35–52. doi:10.1029/rg013i003p00035

Easton, R. M. (1987). Volcanism in Hawaii. Stratigraphy of Kilauea Volcano. *U.S. Geol. Surv. Prof. Pap.* 1350, 243–260.

Eguíluz, L., Apraiz, A., and Abalos, B. (1999). Structure of the Castillo Granite, Southwest Spain: Variscan Deformation of a Late Cadomian Pluton. *Tectonophysics* 18 (6), 1041–1063.

Flanigan, V. J., Long, C. K., Rohret, D. H., and Mohr, P. J. (1986). *Aeromagnetic Map of the Rift Zones of Kilauea and Mauna Loa Volcanoes, Island of Hawaii, Hawaii, U.S. Geol. Surv*. Reston, VA: Misc. Field Invest. Map. MF–1845A.

Flinders, A. F., Ito, G., Garcia, M. O., Sinton, J. M., Kauahikaua, J., and Taylor, B. (2013). Intrusive dike Complexes, Cumulate Cores, and the Extrusive Growth of Hawaiian Volcanoes. *Geophys. Res. Lett.* 40, 3367–3373. doi:10.1002/grl.50633

Gabriel, G., Bansal, A. R., Dressel, I., Dimri, V. P., and Krawczyk, C. M. 2011. Curie Depths Estimation in Germany: Methodological Studies for Derivation of Geothermal Proxies Using New Magnetic Anomaly Data. 218(1):494–507. 10.1093/gji/ggz166

Gabriel, G., Dressel, I., Vogel, D., and Krawczyk, C. M. (2012). Depths to the Bottom of Magnetic Sources and Geothermal Prospectivity in Southern Germany. *First Break* 30, 39–47. doi:10.3997/1365-2397.2012001

Garcia-Abdeslem, J., and Ness, G. E. (1994). Inversion of the Power Spectrum from Magnetic Anomalies. *Geophysics* 59, 391–401.

Geosoft Oasis Montaj, v.8.2.4 (2015). *Geosoft Software for the Earth Sciences*. Toronto, Canada: Geosoft Inc.

Godson, R. H., Zablocki, C. J., Pierce, H. A., Frayser, J. B., Mitchell, C. M., and Sneddon, R. A. (1981). *Aeromagnetic Map of the Island of Hawaii: USGS Geophysical Investigation Map GP-946, Scale 1:250,000*. Data available online at https://catalog.data.gov/dataset/airborne-geophysical-survey-hawaii-78-hawaii.

Green, W. R. (1975). Inversion of Gravity Profiles by Use of a Backus-gilbert Approach. *Geophysics* 40 (5), 763–772. doi:10.1190/1.1440566

Guillen, A., and Menichetti, V. (1984). Gravity and Magnetic Inversion with Minimization of a Specific Functional. *Geophysics* 49 (8), 1354–1360. doi:10.1190/1.1441761

Hahn, A., Kind, E. G., and Mishra, D. C. (1976). Depth Estimation of Magnetic Sources by Means of Fourier Amplitude Spectra*. *Geophys. Prospect* 24, 287–306. doi:10.1111/j.1365-2478.1976.tb00926.x

Hildenbrand, T. G., Rosenbaum, J. G., and Kauahikaua, J. P. (1993). Aeromagnetic Study of the Island of Hawaii. *J. Geophys. Res.* 98 (B3), 4099–4119. doi:10.1029/92jb02483

Hill, D. P., and Zucca, J. J. (1987). Geophysical Constraints on the Structure of Kilauea and Mauna Loa Volcanoes and Some Implications for Seismomagmatic Processes. *U.S. Geol. Surv. Prof. Pap.* 1350, 903–917.

Holcomb, R. T. (1987). Volcanism in Hawaii. Eruptive History and Long-Term Behavior of Kilauea Volcano. *U.S. Geol. Surv. Prof. Pap.* 1350, 261–350.

Hsieh, H.-H., Chen, C.-H., Lin, P.-Y., and Yen, H.-Y. (2014). Curie point Depth from Spectral Analysis of Magnetic Data in Taiwan. *J. Asian Earth Sci.* 90, 26–33. doi:10.1016/j.jseaes.2014.04.007

Idárraga-García, J., and Vargas, C. A. (2018). Depth to the Bottom of Magnetic Layer in South America and its Relationship to Curie Isotherm, Moho Depth and Seismicity Behavior. *Geodesy and Geodynamics* 9 (1), 93–107.

Intrepid Geophysics (2013). *Intrepid Geophysics, 110/3 Male Street, Brighton Vic 3186 Australia*. Data available online at www.intrepid-geophysics.com.

Jessop, A. M., Hobart, M. A., and Sclater, J. G. (1976). The Wsorld Heat Flow Data Collection 1975. *Can.Earth Phys. Branch, Geotherm. Ser.* 5, 125.

Jurado-Chichay, Z., Urrutia-Fucugauchi, J., and Rowland, S. K. (1993). A Paleomagnetic Study of the Pohue Bay Flow and its Associated Coastal Cones, Mauna Loa Volcano, Hawaii: Constraints on Their Origin and Temporal Relationships. *Phys. Earth Planet. Interiors* 97, 269–277.

Kauahikaua, J., Cashman, K. V., Clague, D. A., Champion, D., and Hagstrum, J. T. (2002). Emplacement of the Most Recent Lava Flows on Hualalai Volcano, Hawaii. *Bull. Volcanology* 64, 229–253.

Kauahikaua, J. (2017). *Gravity Data for Island of Hawai`i.Csv. Geospatial Data Presentation Form: Tabular Data*. Reston, VA: USGS. doi:10.5066/F7V1230Q

Kauahikaua, J., Hildenbrand, T., and Webring, M. (2000). Deep Magmatic Structures of Hawaiian Volcanoes, Imaged by Three-Dimensional Gravity Models. *Geology* 28 (10), 883–886. doi:10.1130/0091-7613(2000)028<0883:dmsohv>2.3.co;2

Langenheim, V. A. M., and Clague, D. A. (1987). Chapter 1. The Hawaiian-Emperor Volcanic Chain. Part II. Stratigraphic Framework of Volcanic Rocks of the Hawaiian Islands. *USGS Profesisonal Paper* 1350.

Li, Y., and Oldenburg, D. W. (1998). 3-D Inversion of Gravity Data. *Geophysics* 63 (1), 109–119. doi:10.1190/1.1444302

Lipman, P. W., and Swenson, A. (1984). Generalized Geologic Map of the Southwest Rift Zone of Mauna Loa Volcano, Hawaii. *United States Geological Survey Miscellaneous Investigations Map 1-1312*, Scale 1: 100,000.

Lipman, P. W. (1980). The Southwest Rift Zone of Mauna Loa: Implications for Structural Evolution of Hawaiian Volcanoes. *Am. J. Sci.* 280-A, 752–776.

Lockwood, J. P., and Lipman, P. W. (1987). Holocene Eruptive History of Mauna Loa Volcano, Hawaii. *USGS Prof. paper* 1350, 509–535.

Macdonald, G. A., 1977. Geologic Map of the Mauna Loa Quadrangle, Hawaii. *United States Geological Survey*,Geologic Quadrangle Map, GQ-897, scale I: 24,000.

Marcotte, D., Shamsipour, P., Coutant, O., and Chouteau, M. (2014). Inversion of Potential fields on Nodes for Large Grids. *J. Appl. Geophys.* 110, 90–97. doi:10.1016/j.jappgeo.2014.09.003

McDougall, I., and Swanson, D. A. (1972). Potassium-Argon Ages of Lavas from the Hawi and Pololu Volcanic Series, Kohala Volcano, Hawaii. *Geol. Soc. America Bull.* 83, 3731–3738. doi:10.1130/0016-7606(1972)83[3731:paolft]2.0.co;2

Meneisy, A. M., and Al Deep, M. (2020). Investigation of Groundwater Potential Using Magnetic and Satellite Image Data at Wadi El Amal, Aswan, Egypt. *Egypt. J. Remote Sens. Space Sci.*. doi:10.1016/j.ejrs.2020.06.006

Miller, H. G., and Tuach, J. (1989). Gravity and Magnetic Signatures of the Ackley Granite Suite, southeastern Newfoundland: Implications for Magma Emplacement. *Can. J. Earth Sci.* 26, 2697–2709. doi:10.1139/e89-229

Mohamed, A. (2019). Hydro-Geophysical Study of the Groundwater Storage Variations Over the Libyan Area and its Connection to the Dakhla Basin in Egypt. *J. African Earth Sci.* 157, 103508. doi:10.1016/j.jafrearsci.2019.05.016

Mohamed, A. (2020a). Gravity Based Estimates of Modern Recharge of the Sudanese Area. *J. African Earth Sci.* 163, 103740. doi:10.1016/j.jafrearsci.2019.103740

Mohamed, A. (2020b). Gravity Applications in Estimating the Mass Variations in the Middle East: A Case Study from Iran. *Arab J Geosci.* 13, 364. doi:10.1007/s12517-020-05317-7

Mohamed, A. (2020c). Gravity Applications to Groundwater Storage Variations of the Nile Delta Aquifer. *J. Appl. Geophys.* 182, 104177. doi:10.1016/j.jappgeo.2020.104177

Mohamed, A., Abdelrahman, K., and Abdelrady, A. (2022). Application of Time-Variable Gravity to Groundwater Storage Fluctuations in Saudi Arabia. *Front. Earth Sci.* 10, 873352. doi:10.3389/feart.2022.873352

Mohamed, A., and Abu El Ella, E. M. (2021). Magnetic Applications to Subsurface and Groundwater Investigations: A Case Study from Wadi El Assiuti, Egypt. *Int. J. Earth Sci.* 12, 77–101. doi:10.4236/ijg.2021.122006

Mohamed, A., and Al Deep, M. (2021). Depth to the Bottom of the Magnetic Layer, Crustal Thickness, and Heat Flow in Africa: Inferences from Gravity and Magnetic Data. *J. African Earth Sci.* 179, 104204.

Mohamed, A., and Gonçalvès, J. (2021). Hydro-Geophysical Monitoring of the North Western Sahara Aquifer System's Groundwater Resources Using Gravity Data. *J. African Earth Sci.* 178, 104188. doi:10.1016/j.jafrearsci.2021.104188

Mohamed, A., Ragaa Eldeen, E., and Abdelmalik, K. (2021). Gravity Based Assessment of Spatio-Temporal Mass Variations of the Groundwater Resources in the Eastern Desert, Egypt. *Arab. J. Geosci.* 14, 500. doi:10.1007/s12517-021-06885-y

Mohamed, A., Sultan, M., Ahmed, M., Yan, E., and Ahmed, E. (2017). Aquifer Recharge, Depletion, and Connectivity: Inferences from GRACE, Land Surface Models, and Geochemical and Geophysical Data. *Geol. Soc. Am.* 129, 534–546. doi:10.1130/B31460.1

Mohamed, A., and Al Deep, M. (2021). Depth to the Bottom of the Magnetic Layer, Crustal Thickness, and Heat Flow in Africa: Inferences from Gravity and Magnetic Data. *J. Afr. Earth Sci.* 179, 104204. doi:10.1016/j.jafrearsci.2021.104204

Montesinos, F. G., Arnoso, J., Benavent, M., and Vieira, R. (2006). The Crustal Structure of El Hierro (Canary Islands) from 3-D Gravity Inversion. *J. Volcanology Geothermal Res.* 150, 283–299. doi:10.1016/j.jvolgeores.2005.07.018

Moore, J. G. (2001). Density of basalt Core from Hilo Drill Hole, Hawaii. *J. Volcanology Geothermal Res.* 112 (1), 221–230. doi:10.1016/S0377-0273(01)00242-6

Moore, R. B., Clague, D. A., Rubin, M., and Bohrson, W. A. (1987). Chapter 20. Hualalai Volcano: A Preliminary Summary of Geologic, Petrologic, and Geophysical Data. *USGS Profesisonal Paper* 1350.

Morgan, W. J. (1972a). Deep Mantle Convection Plumes and Plate Motions. *Am. Assoc. Pet. Geologists Bull.* 56, 203–213. doi:10.1306/819a3e50-16c5-11d7-8645000102c1865d

Morgan, W. J. (1972b). Plate Motions and Deep Mantle Convection. *Geol. Soc. America Memoir* 132, 7–22. doi:10.1130/mem132-p7

Nagata, T. (1961). *Rock Magnetism*. Tokyo: Maruzen Company Ltd, 350.

Nasa, J. P. L. (2013) Topography Mission Global 1 Arc Second [Data Set]. *NASA EOSDIS Land Processes DAAC*. doi:10.5067/MEaSUREs/SRTM/

Nwankwo, L. I., and Shehu, A. T. (2015). Evaluation of Curie-point Depths, Geothermal Gradients and Near-Surface Heat Flow from High-Resolution Aeromagnetic (HRAM) Data of the Entire Sokoto Basin, Nigeria. *J. Volcanology Geothermal Res.* 305, 45–55. doi:10.1016/j.jvolgeores.2015.09.017

Nwankwo, L. I., and Sunday, A. J. (2017). Regional Estimation of Curie-point Depths and Succeeding Geothermal Parameters from Recently Acquired High-Resolution Aeromagnetic Data of the Entire Bida Basin, north-central Nigeria. *Geoth. Energ. Sci.* 5, 1–9. doi:10.5194/gtes-5-1-2017

Obande, G. E., Lawal, K. M., and Ahmed, L. A. (2014). Spectral Analysis of Aeromagnetic Data for Geothermal Investigation of Wikki Warm Spring, north-east Nigeria. *Geothermics* 50, 85–90. doi:10.1016/j.geothermics.2013.08.002

Okubo, P. G., Benz, H. M., and Chouet, B. A. (1997). Imaging the Crustal Magma Sources beneath Mauna Loa and Kilauea Volcanoes, Hawaii. *Geol* 25, 867–870. doi:10.1130/0091-7613(1997)025<0867:itcmsb>2.3.co;2

Okubo, Y., Graf, R. J., Hansen, R. O., Ogawa, K., and Tsu, H. (1985). Curie point Depths of the Island of Kyushu and Surrounding Areas, Japan. *Geophysics* 50 (3), 481–494. doi:10.1190/1.1441926

Okubo, Y., and Matsunaga, T. (1994). Curie point Depth in Northeast Japan and its Correlation with Regional thermal Structure and Seismicity. *J. Geophys. Res.* 99, 363–437. doi:10.1029/94jb01336

Park, J., Morgan, J. K., Zelt, C. A., Okubo, P. G., Peters, L., and Benesh, N. (2007). Comparative Velocity Structure of Active Hawaiian Volcanoes from 3-D Onshore-Offshore Seismic Tomography. *Earth Planet. Sci. Lett.* 259, 500–516. doi:10.1016/j.epsl.2007.05.008

Porter, S. C. (1979a). Hawaiian Glacial Ages. *Quat. Res.* 12, 161–187. doi:10.1016/0033-5894(79)90055-3

Porter, S. C. (1979b). Quaternary Stratigraphy and Chronology of Mauna Kea, Hawaii: A 380,000-yr Record of Mid-Pacific Volcanism and Ice-Cap Glaciation. *Geol. Soc. America Bull. Part* 90, 980–1093. doi:10.1130/gsab-p2-90-980

Radhakrishna Murthy, I. V., and Rama Rao, P. (1993). Inversion of Gravity and Magnetic Anomalies of Two-Dimensional Polygonal Cross Sections. *Comput. Geosciences* 19 (9), 1213–1228. doi:10.1016/0098-3004(93)90026-2

Rajaram, M. (2007). "Encyclopedia of Geomagnetism and Paleomagnetism," in *Encyclopedia of Geomagnetism and Paleomagnetism*. Editors D. Gubbins and E. Herrero-Bervera (Dordrecht: Springer). doi:10.1007/978-1-4020-4423-6

Ravat, D., Pignatelli, A., Nicolosi, I., and Chiappini, M. (2007). A Study of Spectral Methods of Estimating the Depth to the Bottom of Magnetic Sources from Near-Surface Magnetic Anomaly Data. *Geophys. J. Int.* 169, 421–434. doi:10.1111/j.1365-246x.2007.03305.x

Robinson, J. E., and Eakins, B. W. (2006). Calculated Volumes of Individual Shield Volcanoes at the Young End of the Hawaiian Ridge. *J. Volcanology Geothermal Res.* 151 (1), 309–317. doi:10.1016/j.jvolgeores.2005.07.033

Ross, H. E., Blakely, R. J., and Zoback, M. D. (2006). Testing the Use of Aeromagnetic Data for the Determination of Curie Depth in California. *Geophysics* 71, L51–L59. doi:10.1190/1.2335572

Shuey, R. T., Schellinger, D. K., Tripp, A. C., and Alley, L. B. (1977). Curie Depth Determination from Aeromagnetic Spectra. *Geophys. J. Int.* 50, 75–101. doi:10.1111/j.1365-246X.1977.tb01325.x

Spector, A., and Grant, F. S. (1970). Statistical Models for Interpreting Aeromagnetic Data. *Geophysics* 35 (2), 293–302. doi:10.1190/1.1440092

Speranza, F., Minelli, L., Pignatelli, A., Gilardi, M., and Gilardi, M. (2016). Curie Temperature Depths in the Alps and the Po Plain (Northern Italy): Comparison with Heat Flow and Seismic Tomography Data. *J. Geodynamics* 98, 19–30. doi:10.1016/j.jog.2016.03.012

Springer, M. (1999). Interpretation of Heat-Flow Density in the Central Andes. *Tectonophysics* 306 (3), 377–395. doi:10.1016/s0040-1951(99)00067-0

Stearns, H. T., and Macdonald, G. A. (1946). Geology and Groundwater Resources of the Island of Hawaii: Hawaii Division of Hydrogeology. *Bulletin* 9, 363.

Swanson, D. A. (2005). *Age Determination by D.A. Swanson on Basis of Detailed Tephra Stratigraphic Studies for Lava-Flow Units Shown*. Wolfe and Morris.

Taha, A. I., Al Deep, M., and Mohmed, A. (2021). Investigation of Groundwater Occurrence Using Gravity and Electrical Resistivity Methods: A Case Study from Wadi Sar. *Arab. J. Geosci.* 14, 334. doi:10.1007/s12517-021-06628-z

Tanaka, A., Okubo, Y., and Matsubayashi, O. (1999). Curie point Depth Based on Spectrum Analysis of Magnetic Anomaly Data in East and Southeast Asia. *Tectonophysics* 306 (3e4), 461e470. doi:10.1016/S0040-1951(99)00072-4

Thurber, C. H. (1984). Seismic Detection of the summit Magma Complex of Kilauea Volcano, Hawaii. *Science* 223, 165–167. doi:10.1126/science.223.4632.165

Trifonova, P., Zhelev, Z., Petrova, T., and Bojadgieva, K. (2009). Curie point Depths of Bulgarian Territory Inferred from Geomagnetic Observations and its Correlation with Regional thermal Structure and Seismicity. *Tectonophysics* 473, 362–374. doi:10.1016/j.tecto.2009.03.014

Vigneresse, J. L. (1995a). Control of Granite Emplacement by Regional Deformation. *Tectonophysics* 249, 173–186. doi:10.1016/0040-1951(95)00004-7

Vigneresse, J. L. (1995b). Crustal Regime of Deformation and Ascent of Granitic Magma. *Tectonophysics* 249, 187–202. doi:10.1016/0040-1951(95)00005-8

Wilson, J. T. (1963a). A Possible Origin of the Hawaiian Islands. *Can. J. Phys.* 41, 863–870. doi:10.1139/p63-094

Wilson, J. T. (1963c). Evidence from Islands on the Spreading of Ocean Floors. *Nature* 197, 536–538. doi:10.1038/197536a0

Wolfe, E. W., and Morris, J. (1996a). *Geologic Map of the Island of Hawaii: USGS Miscellaneous Investigations Series Map I-2524-A*, Scale 1:100000, 3 Sheets.

Wolfe, E. W., Wise, W. S., and Dalrymple, G. B. (1997). The Geology and Petrology of Mauna Kea Volcano, Hawaii-A Study of Postshield Volcanism. *U.S. Geol. Surv. Prof. Paper* 1557, 129.

Yang, K., Xing, J., Gong, W., Li, C., and Wu, X. (2017). Curie Point Depth from Spectral Analysis of Magnetic Data in the Southeast Tibet. *Earth* 6 (5), 88–96. doi:10.11648/j.earth.20170605.15

Zablocki, C. J., and Tilling, R. I. (1976). Field Measurements of Apparent Curie Temperatures in a Cooling Basaltic Lava lake, Kilauea Iki, Hawaii. *Geophys. Res. Lett.* 3 (8), 487–490. doi:10.1029/gl003i008p00487

Conflict of Interest: The authors declare that the research was conducted in the absence of any commercial or financial relationships that could be construed as a potential conflict of interest.

Publisher's Note: All claims expressed in this article are solely those of the authors and do not necessarily represent those of their affiliated organizations, or those of the publisher, the editors, and the reviewers. Any product that may be evaluated in this article, or claim that may be made by its manufacturer, is not guaranteed or endorsed by the publisher.

frontiers | Frontiers in Earth Science

ORIGINAL RESEARCH
published: 07 April 2022
doi: 10.3389/feart.2022.873352

Application of Time-Variable Gravity to Groundwater Storage Fluctuations in Saudi Arabia

Ahmed Mohamed[1]*, *Kamal Abdelrahman*[2] *and Ahmed Abdelrady*[3]

[1]*Department of Geology, Faculty of Science, Assiut University, Asyut, Egypt,* [2]*Department of Geology and Geophysics, College of Science, King Saud University, Riyadh, Saudi Arabia,* [3]*Department of Water Management, Faculty of Civil Engineering and Geoscience, Delft University of Technology, Delft, Netherlands*

In the Middle East, water shortage is becoming more and more serious due to the development of agriculture and industry and the increase in population. Saudi Arabia is one of the most water-consuming countries in the Middle East, and urgent measures are needed. Therefore, we integrated data from Gravity Recovery and Climate Experiment (GRACE), and other relevant data to estimate changes in groundwater storage in Saudi Arabia. The findings are as follows: 1) Average annual precipitation (AAP) was calculated to be 76.4, 90, and 72 mm for the entire period, Period I (April 2002 to March 2006) and Period II (April 2006 to July 2016), respectively. 2) The average TWS variation was estimated to be −7.94 ± 0.22, −1.39 ± 1.35, and −8.38 ± 0.34 mm/yr for the entire period, Period I and Period II, respectively. 3) The average groundwater storage was estimated to be +1.56 ± 1.35 mm/yr during Period I. 4) The higher average groundwater depletion rate was calculated to be −6.05 ± 0.34 mm/yr during Period II. 5) Both soil texture and surface streams in the study area promote lateral flow and carry surface water to the Arabian Gulf and the Red Sea. 6) During Period II, average annual recharge rates were estimated to be +9.48 ± 2.37 and +4.20 ± 0.15 km^3 for Saudi Arabia and the Saq aquifer, respectively. 7) This integrated approach is an informative and cost-effective technique to assess the variability of groundwater resources in large areas more efficiently.

Keywords: Saudi Arabia, Saq aquifer, time-variable gravity, rainfall, groundwater, depletion, recharge

OPEN ACCESS

Edited by:
Ahmed M. Eldosouky, Suez University, Egypt

Reviewed by:
Omid Memarian Sorkhabi, University of Isfahan, Iran
Ebong D. Ebong, University of Calabar, Nigeria
Mohammed Hassoup, Sohag University, Egypt
Salem Barbary, Nuclear Materials Authority, Egypt

***Correspondence:**
Ahmed Mohamed
ahmedmohamed@aun.edu.eg

Specialty section:
This article was submitted to Solid Earth Geophysics, a section of the journal Frontiers in Earth Science

Received: *10 February 2022*
Accepted: *04 March 2022*
Published: *07 April 2022*

Citation:
Mohamed A, Abdelrahman K and Abdelrady A (2022) Application of Time-Variable Gravity to Groundwater Storage Fluctuations in Saudi Arabia. Front. Earth Sci. 10:873352. doi: 10.3389/feart.2022.873352

INTRODUCTION

Water sustainability is a critical issue globally, given its importance for humans and ecosystems (United Nations, 2013; Bernauer and Böhmelt, 2020). Water sustainability is affected by anthropogenic water use and climatic conditions (United Nations, 2014; Wada et al., 2010). Globally, irrigation accounts for about 70% of water extraction and 90% of water consumption, with heavy groundwater withdrawal in arid regions (Siebert et al., 2010; Gerten et al., 2020).

Due to hot and arid climatic conditions, the water shortage has become a severe problem in the Arab region. Therefore, recognizing the impacts of climate change, population growth, economic development, and land management is a key strategy for achieving water security in this region (Trondalen, 2009). In addition, desertification is affecting the Middle East region, particularly Iraq, Syria, Jordan, and Iran.

Several methods have been applied to evaluate the hydrological behavior of aquifers using *in situ* observation techniques, such as modeling and chemical methods (de Vries and Simmers, 2002; Milewski et al., 2009; Scanlon et al., 2012). However, it is difficult to estimate the spatial and temporal

variations of groundwater storage on a large scale using a relatively small number of scattered point measurements in these conventional methods. Moreover, the results of these methods are often questionable because they require significant efforts and resources to obtain. To solve these problems, several studies have been conducted to analyze and integrate the outputs of the Gravity Recovery and Climate Experiment (GRACE) and compare them with many climate models and *in situ* data (Wahr et al., 1998; Rodell and Famiglietti, 2001; Wahr et al., 2004; Syed et al., 2008; Longuevergne et al., 2010).

Many studies have been conducted to estimate the hydrological components and settings of large basins and transboundary aquifers in recent years. For example, Yeh et al. (1998), Yeh et al. (2006), and Rodell et al. (2007) applied GRACE, Global Land Data Assimilation System (GLDAS) data, and *in situ* observations to partition the water budget of the Mississippi River basin and obtained reasonable results. Wang et al. (2014) compared monthly total water storage variations obtained from GRACE with those estimated from water budget equations for 16 Canadian basins. In addition, some studies have combined GRACE and climate data with other relevant datasets to estimate changes in groundwater storage and evaluate rates of recharge, discharge, and depletion in aquifer systems in the Arab region (Mohamed et al., 2014; Mohamed et al., 2015; Ahmed and Abdelmohsen, 2018; Mohamed, 2019; Mohamed, 2020a; Mohamed, 2020b; Mohamed, 2020c; Mohamed, 2020d; Mohamed et al., 2021; Mohamed and Gonçalvès, 2021; Taha et al., 2021). On a continental scale, other global gravity field datasets from the Earth Gravitational model have been used to investigate the crustal structures (Mohamed and Al Deep, 2021). However, on a smaller scale, airborne and ground-based geophysical data have been used for groundwater studies, subsurface geology (Meneisy and Al Deep, 2020; Al Deep et al., 2021; Mohamed and Ella, 2021), magma chamber geometry (Mohamed et al., 2022), as well as for land subsidence due to groundwater over-pumping (Othman, 2019; Othman and Abotalib, 2019).

The GRACE satellites provide vertically integrated terrestrial water storage (ΔTWS) changes from regional to global scale. These TWS values are expressed in terms of groundwater storage (ΔGWS), surface water storage (ΔSWS), soil moisture storage (ΔSMS), and snow water equivalent (ΔSWE). However, GRACE cannot distinguish between the contributions from these components, due to the low horizontal resolution of GRACE data and the absence of its vertical resolution (Ahmed et al., 2016; Mohamed et al., 2017). To overcome this weakness, outputs of land surface models were integrated with GRACE data to enhance the horizontal resolution of the data, and to isolate individual components from the GRACE-derived ΔTWS estimates.

Fallatah et al. (2017) calculated the Saq aquifer's depletion rates and found the governing factors that influence these depletions. However, Fallatah et al. (2019) went farther and calculated the modern recharge to the Saq aquifer, rather than only the depletion rates.

It is worth noting that the current work differs from those previous studies, where our current study aims to 1) provide the best estimate of the groundwater storage variability in the Saudi Arabia region and locally for the Saq aquifer using the spherical harmonics (SH) and mass concentration (mascon) GRACE-derived ΔTWS solutions and other climate datasets; and 2) quantify the modern recharge to the Saudi Arabia region and to the Saq aquifer. This aquifer is one of the most important aquifers in Saudi Arabia's northern region. Findings were evidenced by results of land subsidence and water quality degradation. Conducting this study for this arid environment is important for agricultural activities, irrigation, and domestic use.

GEOLOGICAL AND HYDROGEOLOGICAL SETTING

According to Tariki, (1947), Saudi Arabia is divided into two geological zones. The western zone is represented by Precambrian crystalline igneous and metamorphic rocks (**Figure 1**), sloping southeast, east, and northeast. The eastern zone consists of sedimentary rocks that dip eastward and overlay crystalline basement rocks (**Figure 1**). These sedimentary rocks are composed of Paleozoic, Mesozoic, Tertiary, and Recent deposits. The sedimentary basin can be divided into the Nejd and Hassa regions. In the eastern part of the Nejd region, sedimentary rocks of early Paleozoic to early Eocene are distributed, with alternating clastic and calcareous facies. Outcrop rocks in the Hassa region are represented by Tertiary and younger sequences, including lower to middle Eocene and Miocene to Pliocene. Most of the Eocene rocks are calcareous. The Miocene and Pliocene are formed by continental deposits, with some exceptions of intercalating marine strata.

The Arab world is one of the driest places on the planet. Due to a lack of surface water; the region relies heavily on groundwater supplies, and excessive water stress in the region is met with variable degrees of aquifer depletion and mining. As a result, numerous groundwater supplies are in the risk of depletion (Khater, 2010).

Climate change is considered as one of the most urgent environmental issues facing humanity. Environmental changes are expected from accelerated global climate change, which may affect groundwater sustainability. Several important initiatives are underway in Arabic countries to introduce integrated water resource management to address water scarcity (Khater, 2010). In the Arab region, groundwater is being consumed in large quantities due to the expansion of cultivation, urbanization, and industrialization. Climate change will likely impact the dynamics of groundwater availability and sustainability in the Arab world.

Saudi Arabia has two sources of groundwater: non-renewable groundwater comes from deep fossil aquifers, and renewable groundwater comes from shallow aquifers. These two sources account for 40% of Saudi Arabia's water supply. The deep sandstone aquifer is of sedimentary origin and stores fossil

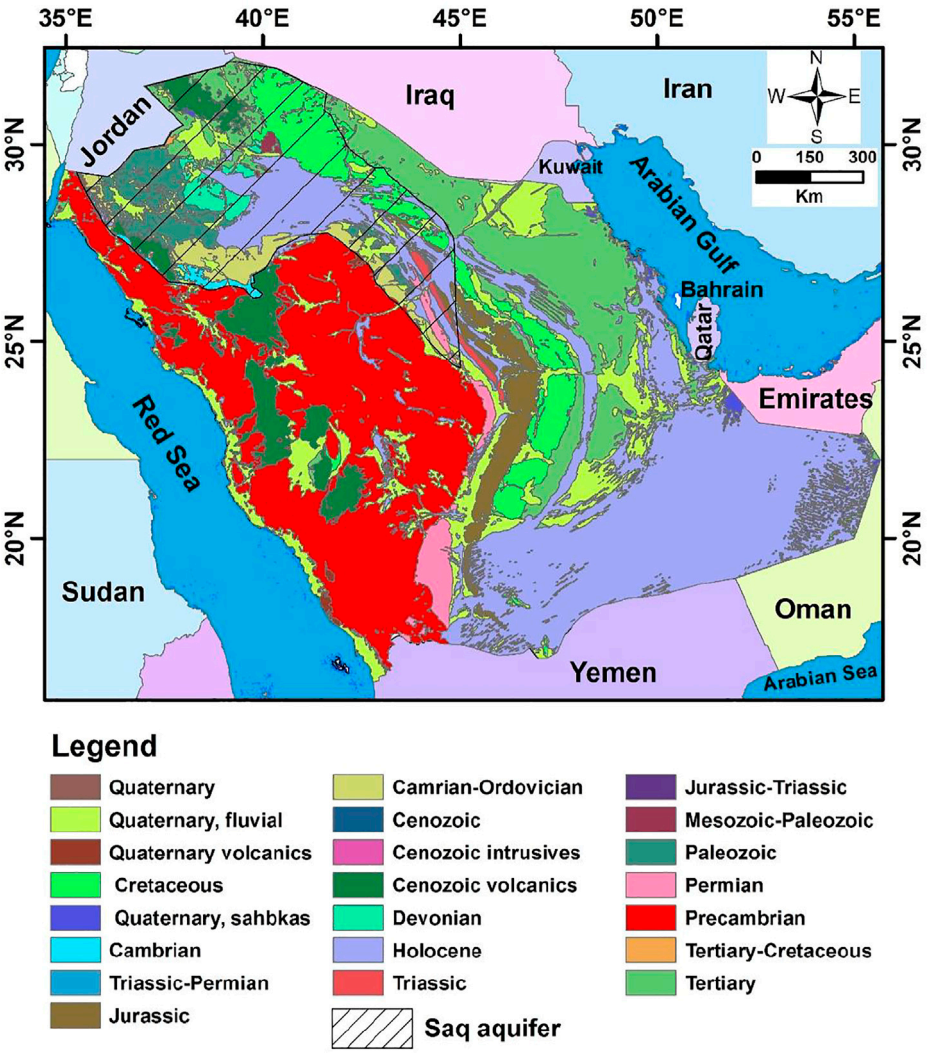

FIGURE 1 | Saudi Arabia's geological map. The aerial distribution of the Saq aquifer is also shown.

water (DeNicola et al., 2015). Renewable groundwater is found in shallow and deep layers in alluvial valleys. However, the shallow aquifers are depleted due to high water extraction compared to recharge. Fossil groundwater is stored in six major sedimentary paleo-aquifers located in the eastern and central parts of the country (**Figure 2**). It is confined in sand and limestone formations of a thickness of about 300 m. One of these, the Saq aquifer (**Figure 1**), extends more than 1,200 km northward in the eastern part of the country (FAO, 2008).

DATA AND METHODOLOGY

The GRACE satellite is a joint US–German mission launched in 2002 and consists of twin satellites that measure spatial and temporal changes in the Earth's gravitational field (Tapley et al., 2004). Changes in the Earth's gravity field are mainly due to changes in water content.

Data from GRACE are processed at three different centers: The Jet Propulsion Laboratory (JPL), the Center for Space Research at the University of Texas at Austin (CSR-UTA), and German Research Centre for Geosciences (GFZ). These centers provide the monthly GRACE solutions using the RL05 spherical harmonic (SH) data (Tapley et al., 2004) as follows: 1) Removing the atmosphere and ocean signals. 2) The C20 from GRACE has a large uncertainty (Cheng et al., 2011), probably due to tidal and other aliasing, so it is replaced by the C20 obtained from satellite laser ranging. In addition, the first-order calculated coefficients (Swenson et al., 2008) are added. 3) Corrections for glacial isostatic adjustments (Geruo et al., 2013). 4) Minimization of correlation errors using a de-striping filter. 5) Minimization of random errors using a 300-km Gaussian filter.

We rescaled the GRACE-derived ΔTWS time series to minimize the effects of smoothing and truncation (Long et al., 2015) using a scale factor of 1.26 averaged from the NCAR-CLM4.0 model (Landerer and Swenson, 2012). As a

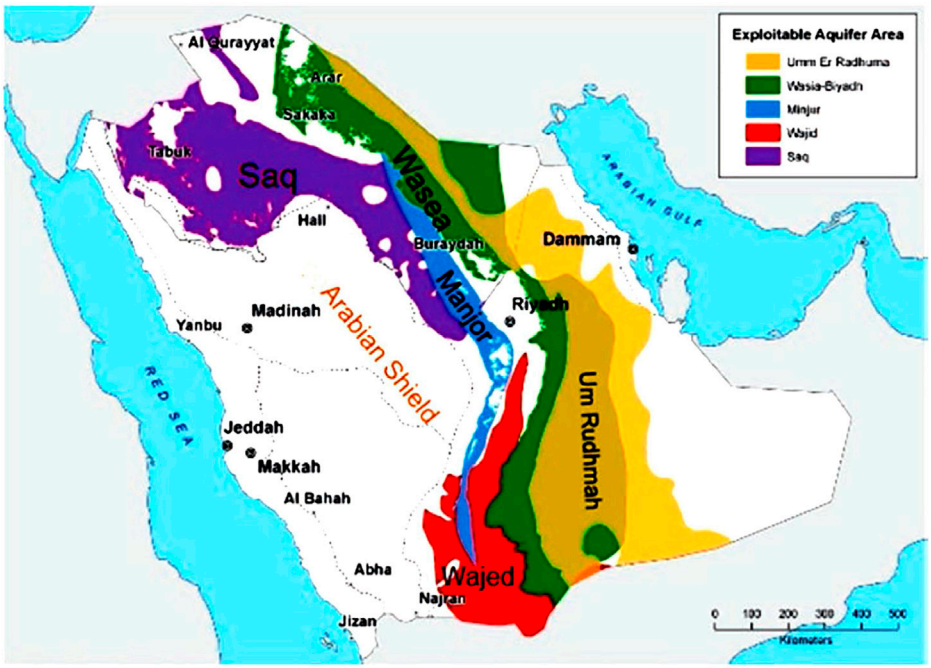

FIGURE 2 | Aquifers in the Arabian Shield and their locations.

result, the bi-monthly GRACE (CSR-SH and JPL-SH) solutions show relatively similar results, with minor differences being within the error range of GRACE. However, due to the significant noise reduction in the signals (Sakumura et al., 2014), the mean of the two rescaled solutions were used in the calculations.

The second GRACE source is the mascon solutions (release 06, version 1; CSR-M and JPL-M). These solutions provide high spatial resolution and minimum error because they capture all signals within the noise levels of GRACE. There is no need for spectral de-striping or smoothing filtering for these solutions. Moreover, these solutions do not require any scaling factor (Luthcke et al., 2013; Save et al., 2016; Wiese et al., 2016).

We used the monthly spherical harmonic (CSR-SH and JPL-SH) and mascon (CSR-M and JPL-M) GRACE solutions for the study area throughout the period. Next, we calculated the secular trend of the ΔTWS data by simultaneously fitting a trend term and a seasonal term to each TWS time series. Finally, the errors associated with the calculated trend values were estimated.

Monthly trends of non-groundwater components, such as soil moisture storage and surface water storage dam capacity data, are necessary to separate the ΔGWS variations in the study area. Therefore, these components must be removed from the GRACE-derived TWS variations. Due to the lack of data from the gauge stations in the study area, we used the land surface model (e.g., CLM) of GLDAS (Rodell et al., 2004), which can be downloaded from the Goddard Earth Sciences Data and Information Services Center (GES DISC). The CLM model of the land surface provides both monthly SMS and SWE data. The average of the monthly ΔSMS data of the LSM was used.

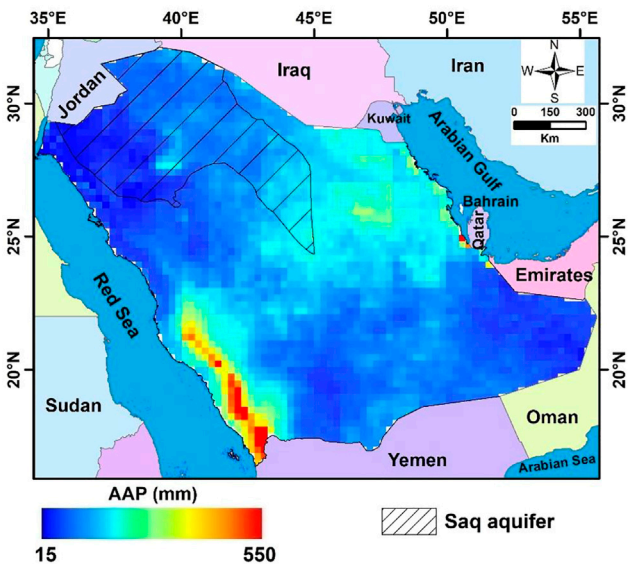

FIGURE 3 | Average annual precipitation (mm) obtained from Tropical Rainfall Measuring Mission (TRMM) data collected across the study area from April 2002 to July 2016.

This study used annual data of surface water reservoirs of dams constructed in Saudi Arabia. These reservoirs may affect the water budget calculated from the GRACE signals and the ΔGWS values in the target area. Therefore, the SWS trend was calculated and removed from the ΔTWS trend.

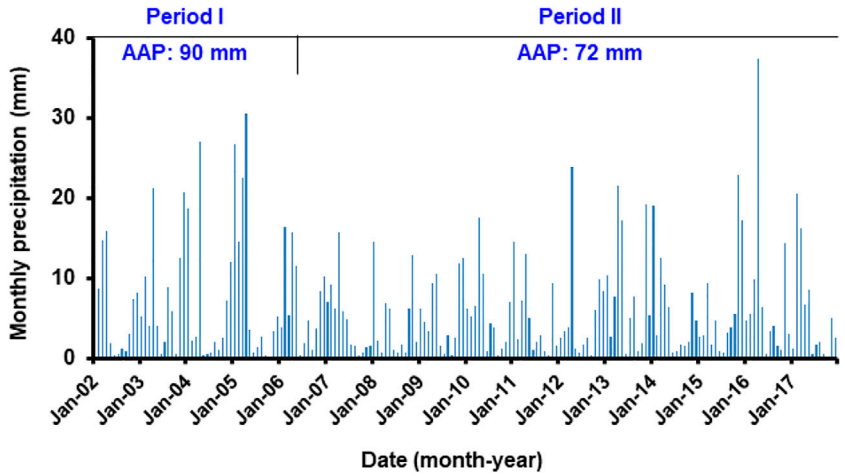

FIGURE 4 | Monthly precipitation (mm) across the Saudi Arabia throughout the two periods.

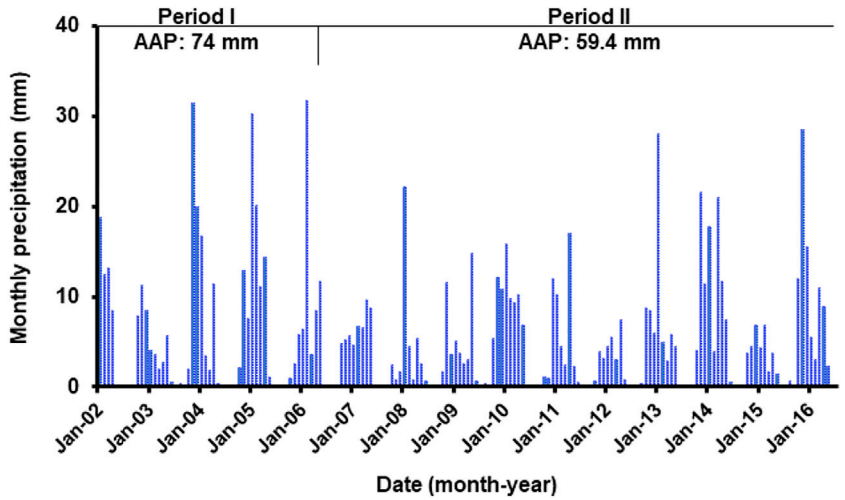

FIGURE 5 | Monthly precipitation (mm) over the Saq aquifer throughout the two periods.

In order to estimate changes in ΔGWS in the study area, it is necessary to remove the non-groundwater contribution from the changes in ΔTWS. The average of the non-groundwater outputs from the GLDAS CLM model was used, and **Eq. 1** was applied (e.g., Rodell et al., 2009; Mohamed et al., 2017).

$$\mathbf{\Delta TWS = \Delta GWS + \Delta SMS + \Delta SWS + \Delta SWE} \quad (1)$$

where ΔSMS, ΔSWS, and ΔSWE are variations in soil moisture, surface water, and snow water equivalent, respectively. ΔSWE is negligible.

Because climatic variability is thought to be one of the primary drivers of changes in ΔGWS, and continuous ground-based rainfall data are not available in the study area, monthly rainfall data from the Tropical Rainfall Measuring Mission (TRMM; http://disc.sci.gsfc.nasa.gov/) were employed (Kummerow, 1998; Huffman et al., 2007; Huffman et al., 2010). First, the rainfall data (April 2002 to July 2016) were processed to create total monthly rainfall images. Second, a monthly rainfall time series was generated by averaging the rainfall rates of all the grid points lying within the study area. Third, the average annual precipitation (AAP) (**Figure 3**) of the study area was calculated. Finally, the TRMM data were used to study the effect of rainfall on the changes in ΔGWS during the study period in Saudi Arabia.

RESULTS AND DISCUSSION

Analysis of Rainfall Data

Figures 4, **5** depict the temporal fluctuations of the observed mean monthly rainfall over Saudi Arabia and the Saq aquifer, respectively. In the Middle East, two climatic periods have been

TABLE 1 | GRACE-estimated ΔTWS components over Saudi Arabia.

Component		Units	Entire time period	Period I (04/2002–03/2006)	Period II (04/2006–07/2016)
GRACE total (ΔTWS)	CSR-M	mm/yr	−7.43 ± 0.20	−2.83 ± 1.37	−7.19 ± 0.31
		km^3/yr	−15.97 ± 0.43	−6.08 ± 2.95	−15.46 ± 0.67
	JPL-M	mm/yr	−8.80 ± 0.10	−3.38 ± 0.59	−8.63 ± 0.13
		km^3/yr	−18.92 ± 0.21	−8.23 ± 1.27	−18.55 ± 0.28
	CSR-SH	mm/yr	−7.58 ± 0.36	+2.14 ± 2.26	−8.57 ± 0.57
		km^3/yr	−16.29 ± 0.77	+4.60 ± 4.86	−18.42 ± 1.23
	JPL-SH	mm/yr	−7.95 ± 0.36	−1.49 ± 2.16	−9.12 ± 0.58
		km^3/yr	−17.09 ± 0.77	−3.20 ± 4.64	−19.61 ± 2.41
	AVG	mm/yr	−7.94 ± 0.22	−1.39 ± 1.35	−8.38 ± 0.34
		km^3/yr	−17.07 ± 0.92	−2.99 ± 5.63	−18.01 ± 0.73
ΔSMS		mm/yr	−2.60 ± 0.01	−2.95 ± 0.003	−2.46 ± 0.008
		km^3/yr	−5.59 ± 0.02	−6.34 ± 0.01	−5.29 ± 0.02
Dams		mm/yr	-	-	+0.13 ± 0.03
		km^3/yr			+0.28 ± 0.06
ΔGWS		mm/yr	−5.33 ± 0.22	+1.56 ± 1.35	−6.05 ± 0.34
		km^3/yr	−11.46 ± 0.47	+3.35 ± 2.90	−13.00 ± 0.73
D		mm/yr	-	-	−10.46 ± 1.05
		km^3/yr			−22.48 ± 2.25
R		mm/yr	-	-	+4.41 ± 1.10
		km^3/yr			+9.48 ± 2.37
AAP		mm/yr	76.4	90	72
		km^3/yr	164.24	193.47	154.78

CSR-M, Mascon solution from the Center for Space Research; JPL-M, Jet Propulsion Laboratory mascon solution; CSR-SH and JPL-SH, Monthly GRACE spherical harmonic solutions; ΔTWS, Changes in Terrestrial Water Storage; ΔGWS: Changes in groundwater storage; ΔSMS, Variation in Soil Moisture Storage; AAP, Average Annual Precipitation; D, Artificial withdrawal; R, Recharge.

TABLE 2 | GRACE-estimated ΔTWS components over the Saq aquifer.

Component		Units	Entire time period	Period I (04/2002–03/2006)	Period II (04/2006–07/2016)
GRACE total (ΔTWS)	CSR-M	mm/yr	−11.44 ± 0.20	−5.11 ± 0.12	−11.47 ± 0.30
	JPL-M	mm/yr	−11.60 ± 0.15	−2.88 ± 0.04	−12.36 ± 0.18
	CSR-SH	mm/yr	−10.92 ± 0.41	1.61 ± 0.38	−12.00 ± 0.64
	JPL-SH	mm/yr	−11.48 ± 0.45	−1.51 ± 0.47	−13.19 ± 0.71
	AVG	mm/yr	−11.36 ± 0.26	−1.97 ± 0.67	−12.25 ± 0.39
ΔSMS		mm/yr	−2.41 ± 0.02	−3.14 ± 0.01	−2.10 ± 0.02
ΔGWS		mm/yr	−8.95 ± 0.27	+1.17 ± 0.67	−10.16 ± 0.39
D		mm/yr	−21.39	−21.39	−21.39
		km^3/yr	−8.00	−8.00	−8.00
R		mm/yr	+12.44 ± 0.27	+22.56 ± 0.67	+11.23 ± 0.39
		km^3/yr	+4.65 ± 0.10	+8.44 ± 0.65	+4.20 ± 0.15
AAP		mm/yr	63.3	74.0	59.4

CSR-M, Mascon solution from the Center for Space Research; JPL-M, Jet Propulsion Laboratory mascon solution; CSR-SH and JPL-SH, Monthly GRACE spherical harmonic solutions; ΔTWS, Changes in Terrestrial Water Storage; ΔGWS, Changes in groundwater storage; ΔSMS, Variation in Soil Moisture Storage; AAP, Average Annual Precipitation; D, Artificial withdrawal; R, Recharge.

defined based on the drought that occurred in 2007 (Mohamed, 2020b). As a result, we used the AAP to determine the two climatic periods that have dominated Saudi Arabia: Period I was from April 2002 to March 2006, and the AAP rate was as high as 90 mm/yr (**Figure 4**). Period II was from April 2006 to July 2016, after the onset of drought, and the AAP rate was as low as 72 mm/yr (**Figure 4**). In Saudi Arabia, the AAP rate was 76.4 mm/yr during the entire period (**Table 1**). In the southwestern mountainous highlands, the AAP rate was as high as 550 mm/yr (**Figure 3**). The Saq aquifer receives a minimum annual precipitation rate of 63.3 mm throughout the entire period (**Table 2**). Period I has a slightly higher precipitation rate of 74.0 mm/yr, whereas period II has a slightly lower rate of 59.4 mm/yr (**Figure 5**). **Figure 6** shows the temporal variation of the SMS time series estimated from GLDAS in Saudi Arabia that ranged between −2.95 ± 0.003 mm/yr for Period I and −2.46 ± 0.008 mm/yr for Period II (**Table 1**). Soil moisture of the Saq aquifer varied from −3.14 ± 0.01 mm/yr estimated for Period I to −2.10 ± 0.02 mm/yr estimated for Period II (**Table 2**).

Temporal Variations in ΔTWS

The secular trends of GRACE-derived TWS were calculated from the monthly SH (CSR-SH and JPL-SH) and mascon (CSR-M and JPL-M) solutions in Saudi Arabia. Their spatial distributions and

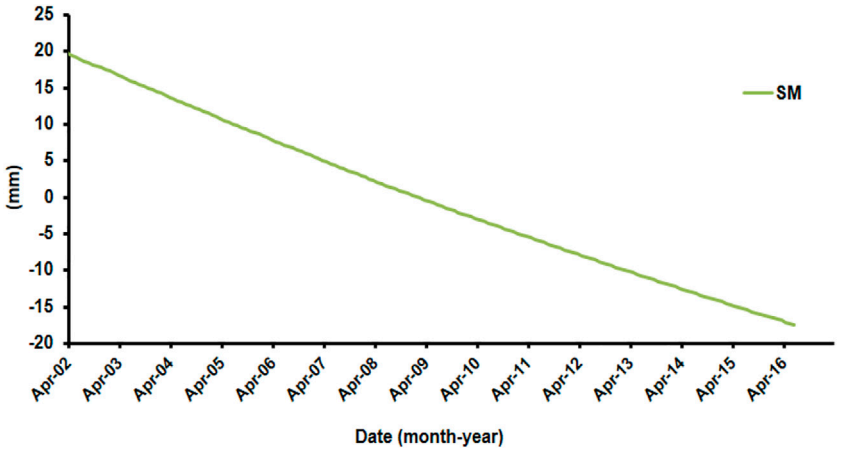

FIGURE 6 | GLDAS-derived soil moisture (ΔSMS) across the whole study area throughout the investigated period.

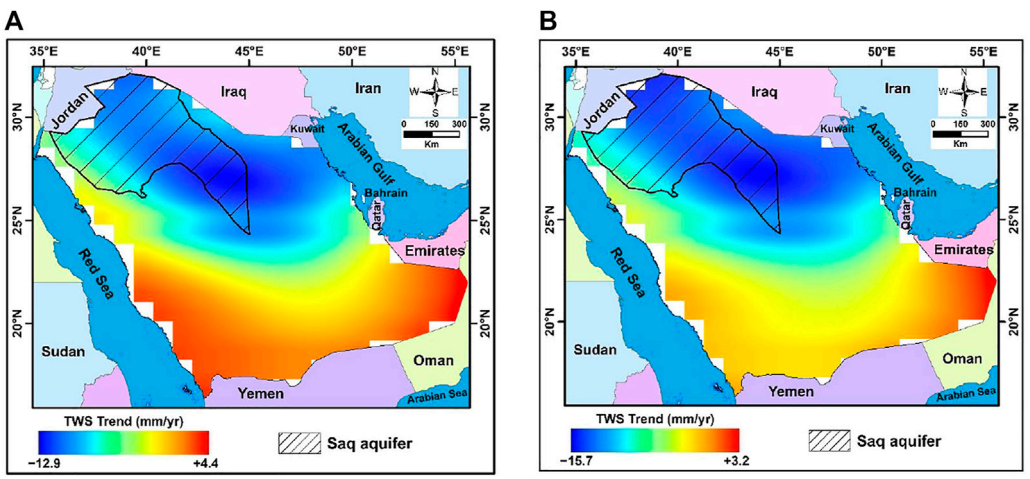

FIGURE 7 | Secular Color-coded GRACE-derived ΔTWS trend map throughout the investigated period from averaging of the monthly CSR spherical harmonic solution **(A)**, and JPL spherical harmonic solution **(B)** over the Saudi Arabia. Also showing the location of the Saq aquifer.

average values are shown in **Figures 7**, **8** during the entire period. The figures show that Saudi Arabia had a general negative GRACE-derived TWS trend during the entire period (April 2002 to July 2016). The southern part of Saudi Arabia shows a positive TWS rate (+4.4 mm/year; **Figure 7A**), while the northern part shows a high TWS depletion rate (−18.1 mm/year; **Figure 8B**). A closer look at **Figures 7A,B** shows that the trend images extracted from the CSR-SH and JPL-SH solutions are similar. The images are also identical in spatial distribution but with small differences in magnitude. These values indicate that the trends of TWS vary from −12.9 and −15.7 to +4.4 and +3.2 from the CRS-SH and JPL-SH solutions, respectively throughout the entire period over the entire study area.

Figures 8A,B shows the secular trends of GRACE-estimated TWS from the mascon solutions. Their spatial distributions show a similar pattern to those estimated from the monthly spherical harmonic solutions in the study area. The results show that the TWS trends remain positive in the southeast. However, the northeastern area shows negative TWS trends. In the northern and central parts of Saudi Arabia, the TWS trend show highly negative values. The CSR-M and JPL-M solutions show quite different spatial distributions. However, their magnitudes are somewhat similar. The TWS trends of JPL-M and CRS-M range from −18.1 and −16.7 to +1.1 and +3.8 mm/yr, respectively, throughout the entire period (**Figure 8**).

The secular trends in TWS derived from GRACE (**Figure 8**) demonstrate that the Saq aquifer is experiencing a significant negative TWS trend for the entire period. Using JPL-SH and CRS-SH, the TWS trend shows values ranging from −13.7 and −12.9 mm/yr to −7.75 and −7.35 mm/yr, respectively (**Figures 7A,B**). The aquifer depletion appears to be localized over its southern part. **Figures 8A,B** reveals that over the Saq aquifer,

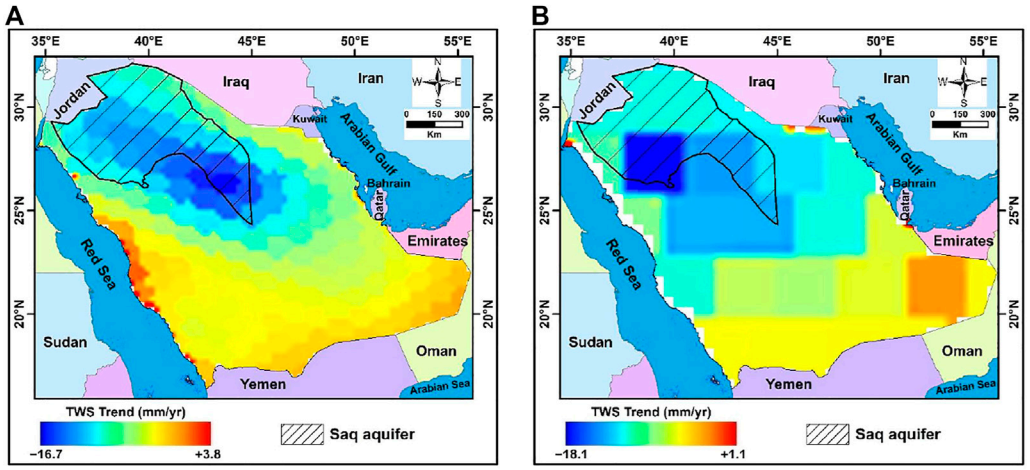

FIGURE 8 | Secular Color-coded GRACE-derived ΔTWS trend map throughout the entire period from averaging of the CRS mascon solution **(A)**, and JPL mascon solution **(B)** over the Saudi Arabia. Also showing the location of the Saq aquifer.

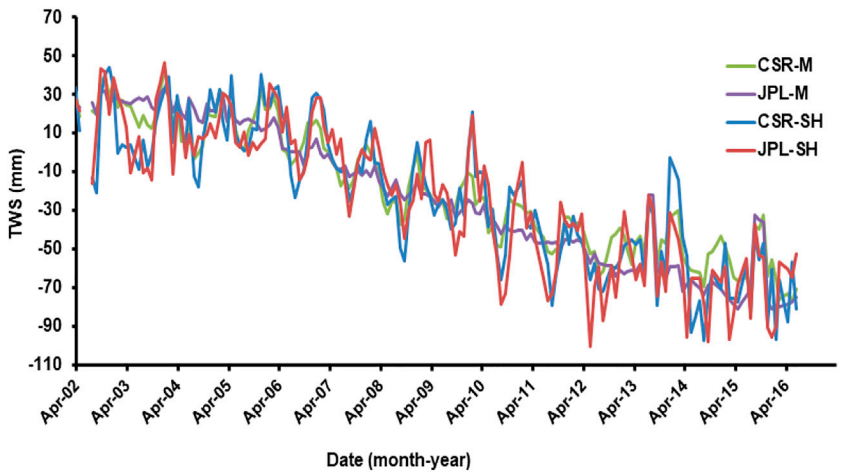

FIGURE 9 | Time series for the terrestrial water storage obtained from various GRACE sources over the Saudi Arabia.

TWS depletion values range from −16.8 and −18.1 to −7.8 and −9.0 mm/yr, using CRS-M and JPL-M, respectively.

Figure 9 shows the temporal variation of the TWS time series and secular trends in Saudi Arabia from different solutions (CSR-M, JPL-M, CSR-SH, and JPL-SH). The average values of monthly SH and mascon solutions are shown in **Figure 10**. **Figures 9**, **10** show that these solutions and their averages are in good agreement in the study area. In addition, a good correlation was achieved between the different data and their averages in the study area, varying between 0.92 and 0.96 (**Figure 11**).

The time series of ΔTWS (**Figure 10**) for the entire period, showing two distinct trends with different slope values, based on a linear regression analysis of the average of all TWS solutions. The first trend that characterizes Period I shows slightly negative signals and is calculated to be −1.39 ± 1.35 mm/yr (**Figure 10**; **Table 1**). In contrast, the second trend that characterizes Period II shows highly negative signals and is calculated to be −8.38 ± 0.34 mm/yr (**Figure 10**; **Table 1**). The entire period shows negative signals estimated to be −7.94 ± 0.22 mm/yr (**Table 1**). A closer inspection at **Figure 12** reveals that over the Saq aquifer, the TWS has a lower negative value of −1.97 ± 0.67 mm/yr during Period I and a higher negative value of −12.25 ± 0.39 mm/yr during Period II. The entire period shows negative signals estimated to be −11.36 ± 0.26 mm/yr (**Table 2**).

Temporal Variations in ΔGWS

The non-groundwater components, represented by ΔSMS, were subtracted from the ΔTWS trend value to estimate ΔGWS (**Table 1**; **Figure 13**). The variation in groundwater storage in Saudi Arabia shows values ranging from −0.43 ± 0.59 to +5.09 ± 2.26 mm/yr, with an average value of +1.56 ± 1.35 mm/yr for Period I. The GRACE-estimated GWS values for the Saq aquifer vary from

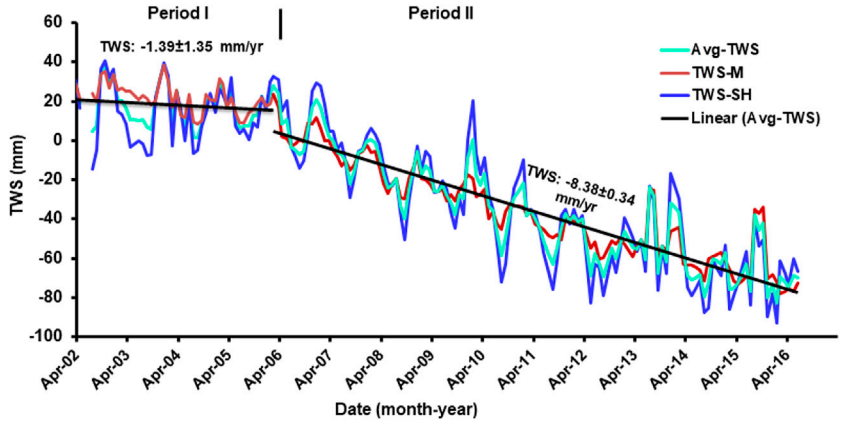

FIGURE 10 | Time series for terrestrial water storage from averaging of the monthly GRACE spherical harmonic solutions (TWS-SH) and mascon solutions (TWS-M) and their averaging (Avg-TWS) across the Saudi Arabia.

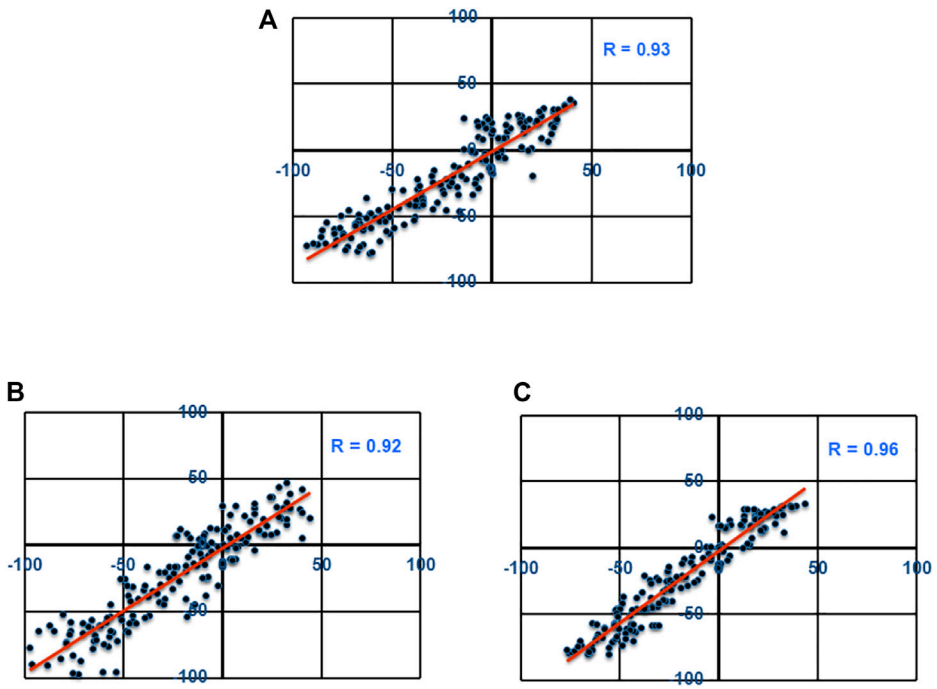

FIGURE 11 | Correlation coefficients (R) between ΔTWS data from averaging of the monthly GRACE spherical harmonic solutions and averaging of the mascon solutions **(A)**, monthly CSR spherical harmonic solution and monthly JPL spherical harmonic solution **(B)**, CSR and JPL mascon solutions **(C)** over the Saudi Arabia throughout the investigated period.

−1.97 ± 1.33 to +4.76 ± 2.4 mm/yr, with an average value of +1.17 ± 0.67 mm/yr throughout period I (**Table 2**; **Figure 14**). However, the depletion in groundwater storage show higher rates ranging from −6.66 ± 0.58 to −4.72 ± 0.31 mm/yr, with an average value of −5.92 ± 0.34 mm/yr for Period II over the entire study area. The temporal variations in surface water reservoirs, represented by the constructed dams, are estimated to be +0.13 ± 0.03 mm/yr (**Table 1**) for Period II. We also subtracted this trend from the GRACE-derived TWS trend. As a result, the depletion rate of the aquifer is estimated to be −6.05 ± 0.34 mm/yr for Period II (**Table 1**). This higher depletion is caused by a large amount of groundwater extraction for anthropogenic activity and a decrease in rainfall throughout the study area after the start of the 2007 drought. This is also supported by the GRACE-calculated GWS over the Saq aquifer, which reveals a larger depletion rate during Period II, estimated at −10.16 ± 0.39 mm/yr (**Table 2**; **Figure 14**).

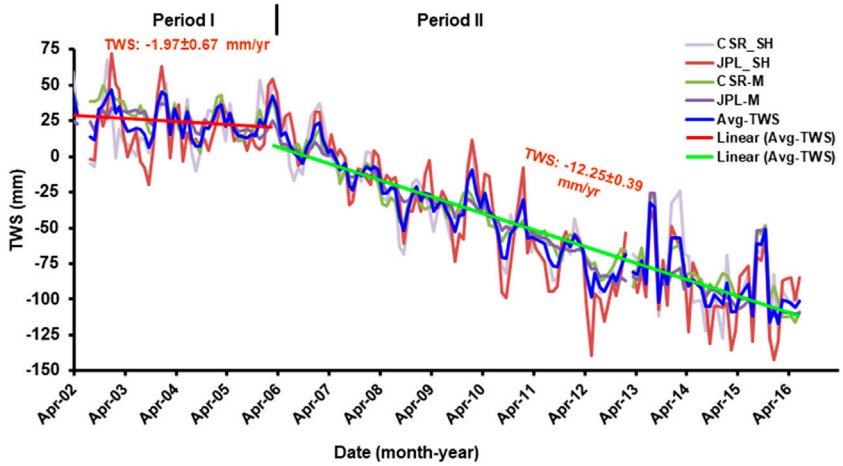

FIGURE 12 | Time series for terrestrial water storage variation from various GRACE sources over the Saq aquifer and their averaging (Avg-TWS).

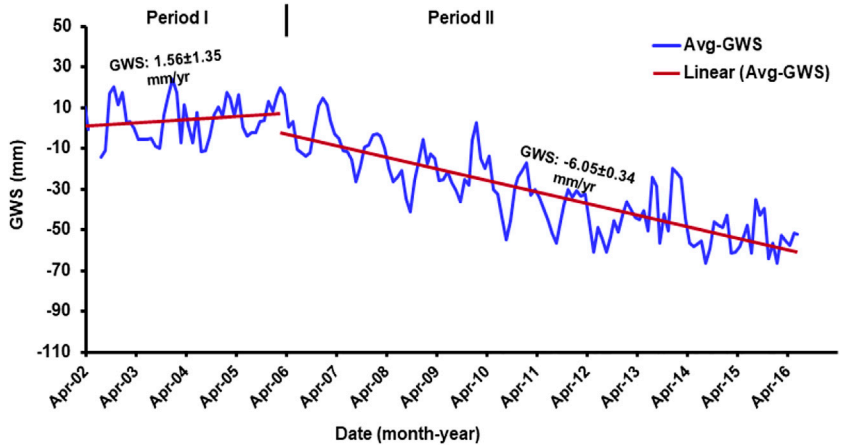

FIGURE 13 | Time series for the averaging groundwater storage variations from the monthly spherical harmonic and Mascon solutions over the whole study area.

Surface Water Flow

Figure 15 shows an elevation map of Saudi Arabia created from ETOPO1 Global Relief Model. It can be seen that there is a difference in altitude from less than 100 m in a zone extending parallel to the Arabian Gulf and near the Emirates to more than 2,500 m in the southern part of the mountainous area near the Red Sea. More than half of Saudi Arabia is occupied by the Arabian–Nubian Shield, stretching parallel to the Red Sea coastal area. This area has highlands ranging from 500 to 2,900 m with dissected wadis, faults, and fissures. The mountainous highlands of southwestern Saudi Arabia receive substantial precipitation (**Figure 3**), which flows into the Arabian Gulf to the east. These streams may recharge the fractured basal aquifers in the southwest and the unconsolidated sands of Rub' al Khali near the Saudi–Omani and the Saudi–UAE borders. This is evident from the positive GRACE signals in southern Saudi Arabia. However, small areas can be cultivated in the narrow valleys of the fractured basement. Moreover, the sandy soil of Rub' al Khali cannot be cultivated because the terrain is covered with sand sheets and dunes up to 250 m high, interspersed by plains of gypsum and gravel. The reddish-orange color of the sand is due to the presence of feldspar.

Sediment Thickness

We extracted sediment thickness data from NOAA National Geophysical Data Center (Divins, 2003) and created a sediment thickness map for Saudi Arabia (**Figure 16**). It can be seen that the sediment thickness varies from 0 m in the Red Sea Hills to about 300 m in wadis that dissected those hills. Groundwater aquifers are present in the northern, eastern, and southeastern parts of the study area. The thickness of sediments in northern and eastern Saudi Arabia varies from about 1,000 m near the Red Sea Hills to more than 4,000 m downstream of the eastern border and more than 6,000 m in the eastern part of Rub' al Khali. In this region, the aquifers are quite thick and are subject to intense

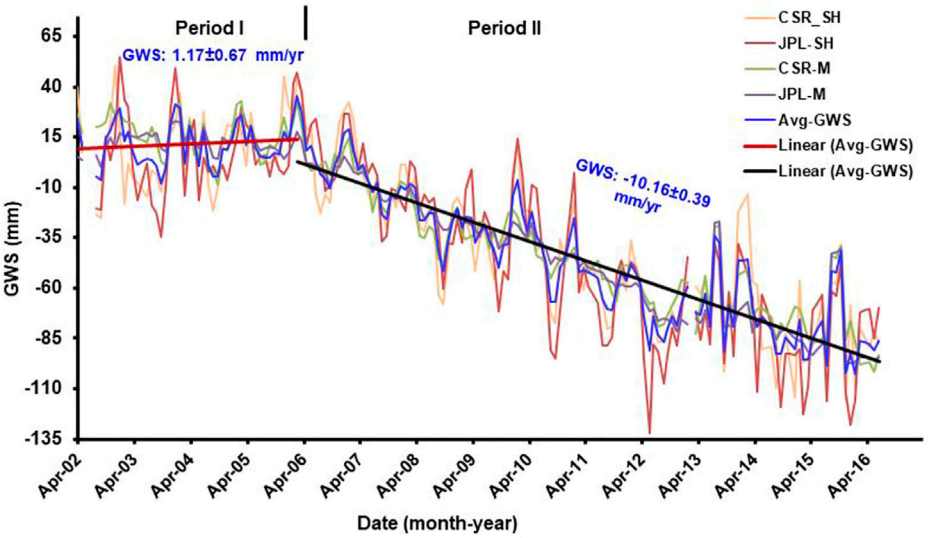

FIGURE 14 | Time series for groundwater storage variation estimated from the different GRACE sources over the Saq aquifer and their averaging (Avg-GWS).

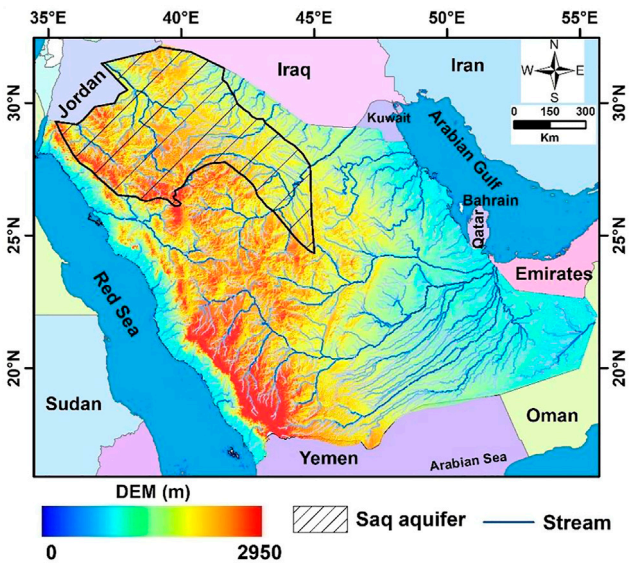

FIGURE 15 | A map of the ground surface elevation based on a Digital Elevation Model (DEM) of the entire study area. The Saq aquifer's distribution and the area's stream networks are also shown.

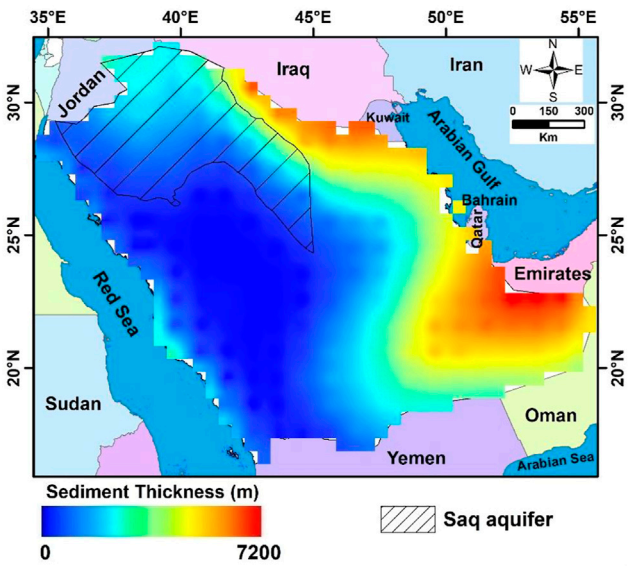

FIGURE 16 | Sediment thickness map (m) in the study area.

exploitation due to low precipitation and subsequent poor recharge. According to the soil map of the Arabian Peninsula developed by De Pauw (2002), the shallow stony soils overlying the western mountainous highlands may be suitable for lateral flow rather than vertical recharge of deep aquifers.

Recharge Rate

The recharge mechanism is highly dependent on topography and soil composition (Wehbe et al., 2018). Most of the Arabian Peninsula is covered with thin and poorly developed soils, rich in gypsum, lime, and salts. These soils indicate that the area is dominantly arid, and most of the area is covered with sand dunes. Moreover, annual precipitation is less than 100 mm/yr (**Figure 3**) throughout Saudi Arabia, except for some parts of the Red Sea highlands. These indicate that Saudi Arabia receives little recharge over the entire area, except for a few areas with higher precipitation rates of good conditions.

Over-exploitation and agricultural development are primarily controlling the GWS variation during the study period in the Saq aquifer, assuming that the aquifer receives a low rate of

precipitation. The groundwater in the Saq aquifer flows eastward following the slope from the low-sediment thickness area near the Red Sea Hills (**Figure 16**) to the higher-sediment thickness area near the Arabian Gulf. Natural discharge in the Arabian Gulf could occur in inland sabkhas close to the Gulf (Sultan et al., 2008). The unconfined zone in the recharge domains near to the Red Sea hilly area was thought to provide modern recharge to the Saq aquifer.

Eq. 2 was used to calculate the average recharge rate (R_n)

$$\mathbf{R_n = \Delta GWS + Discharge} \quad (2)$$

The average groundwater extraction rate (8.00 km^3/yr; −21.39 mm/yr: Abunayyan, 2008) for each period was added to its GWS trend to compute the annual recharge value for the Saq aquifer (using **Eq. 2**). The natural discharge rate was considered to be insignificant.

During the investigated period, the recharge rate for the Saq aquifer was estimated to be +4.65 ± 0.10 km^3/yr (+12.44 ± 0.27 mm/yr). During periods I and II, the Saq aquifer appears to be receiving modern recharge rates of +8.44 ± 0.65 km^3/yr (+22.56 ± 0.67 mm/yr) and +4.20 ± 0.15 km^3/yr (+11.23 ± 0.39 mm/yr), respectively (**Table 2**).

These recharge rates were computed using the aquifer average discharge rate of 8.00 km^3/yr (Abunayyan, 2008). Our findings are consistent with those calculated for the Saq aquifer by Fallatah et al. (2019), who showed that the Saq aquifer received a modern recharge rate of +11.85 ± 0.22 mm/yr (+5.21 ± 0.10 km^3/yr) using GRACE data during the period of April 2002 to December 2016.

The observed TWS depletion across the whole study area and the Saq aquifer is mostly due to increased anthropogenic activities and groundwater extraction that cannot be compensated for by groundwater flow and/or recharge rate.

Saudi Arabia is the world's largest country without running surface water and has one of the world's highest water use rates. Providing additional supplies of potable water for the Kingdom's growing population and economy has long been a national priority for the desert kingdom. The total estimated volume of the average annual recharge rate for the country was obtained by adding the available groundwater withdrawal rate for Period II, averaged for the years of 2007–2017 (− 22.48 ± 2.25 km^3/yr; −10.46 ± 1.05 mm/yr; FAO, 2022) to the to the GRACE-derived ΔGWS rate using **Eq. 2**. For the groundwater withdrawal values, a ten percent error estimate was used. The average annual recharge was estimated to be +4.41 ± 1.10 mm/yr (+9.48 ± 2.37 km^3/yr) for the Saudi Arabia (**Table 1**). However, the country is experiencing severe water shortages, according to the scarcity index (Smakhtin, et al., 2004), and the majority of the country's areas have been intensively exploited to over-exploited groundwater. The majority of this recharge rate happens in inaccessible areas like the unconsolidated sands of the Rub' al Khali in southern Saudi Arabia and narrow wadies in the basement rocks that cover most of eastern Saudi Arabia. Saudi Arabia should build more water desalination plants and more dams for water collection in the wadies to meet rising demand due to the country's growing population. Moreover, the country should increase water transfer efficiency and reduce waste. Furthermore, more wastewater treatment plants should be built to produce grey water, which can be utilized to irrigate crops and be reused in industrial processes.

Uncertainty Estimates

The uncertainty of the monthly variation of ΔGWS and its trend is calculated using **Eq. 3** according to independent error sources. Finally, we applied a Student's t-test to analyze the calculated trend data of ΔGWS.

$$\mathbf{\sigma GWS} = \sqrt{(\boldsymbol{\sigma}_{\mathbf{TWS}})^2 + (\boldsymbol{\sigma}_{\mathbf{SMS}})^2} \quad (3)$$

where (σ_{GWS}), (σ_{TWS}), and (σ_{SMS}) represent the errors associated with GWS, TWS, and SMS, respectively. The error in ΔGWS was estimated from the errors associated with TWS and SMS using **Eq. 3**.

CONSEQUENCES OF HEAVY GROUNDWATER EXTRACTION

Several locally reported data were addressed in this section to demonstrate the effects of excessive groundwater pumping.

Land Subsidence

The Saq sandstone aquifer is widely exposed in central and northern Saudi Arabia (**Figure 1**). The aquifer has a large subsurface extension with an area of about 31 × 10^4 km^2 and a thickness of 250–700 m (UN-ESCWA and BGR, 2013). The main Saq aquifer accounts for 65% of the production, especially in central Saudi Arabia. In central and northern Saudi Arabia, groundwater levels are declining due to increased anthropogenic activities and massive extraction of groundwater. As a result, fractured cavities are formed underground, which are considered to have a serious impact on the stability of the ground, such as the occurrence of sinkholes and associated cracks and land subsidence. Othman and Abotalib, (2019) found that intense extraction of fossil groundwater causes land subsidence, collapse features, and ground fracturing in central Saudi Arabia. However, the massive extraction of groundwater cannot be balanced by the small amount of recharge in the mountainous highlands.

Degradation of Water Quality

The concentration of different types of salts in the water determines the water's quality. Excessive groundwater extraction from an aquifer can lead to water quality degradation. As a result, it may be incompatible with a wide range of applications. The average groundwater level in six piezometric wells in the Saq aquifer decreased from 597 to 526 m above mean sea level between 2002 and 2013. (Al-Naeem, 2014). The total groundwater salinity of the aquifer is impaired in the unconfined zone due to excessive extraction, which causes more mineralized water from lower depths to rise to the surface (Al-Naeem, 2014). Over-irrigation and runoff losses from irrigated regions cause saline drainage water to percolate deeply, resulting in water quality degradation. The significant positive correlation (R^2 = 0.914–0.998) between borehole depth

and water salinity in both the confined and unconfined zones of the Saq aquifer demonstrates that groundwater quality deteriorates with depth because salinity is higher at deeper depths than at shallower depths (Al-Naeem, 2014).

CONCLUSION

During the study period (April 2002 to July 2016), two different climatic periods were recognized based on the analysis of the rainfall in Saudi Arabia: Period I (April 2002 to March 2006) with a higher average annual precipitation (AAP) of 90 mm/yr and Period II (April 2006 to July 2016) with a lower AAP of 72 mm/yr. The integrated outputs showed that Saudi Arabia was subjected to groundwater depletion after the drought and heavy groundwater extraction starting in 2007. The ΔGWS rate was calculated to be +1.56 ± 1.35 mm/yr for Period I, while higher ΔGWS depletion rate was estimated to be −6.05 ± 0.34 mm/yr for Period II over the Saudi Arabia, with an overall depletion rate of −5.33 ± 0.22 mm/yr during the entire period. The average annual recharge for the Saudi Arabia was estimated to be +9.48 ± 2.37 km^3 (+4.41 ± 1.10 mm/yr) during Period II. The Saq aquifer was presumably recharged at a rate of +4.65 ± 0.10 km^3 (+12.44 ± 0.27 mm/yr) during the entire investigated period (April 2002-July 2016), using an annual groundwater extraction rate of 8 km^3 from the aquifer as a constant. However, it does not appear that water abstraction in the aquifer is balanced by groundwater flow and recharge from the highlands. Moreover, the Saq aquifer received only 63.3 mm/yr of rainfall over the entire period. In arid areas, the combined GRACE and GLDAS datasets provide a more precise assessment of water mass fluctuations.

DATA AVAILABILITY STATEMENT

The raw data supporting the conclusions of this article will be made available by the authors, without undue reservation.

AUTHOR CONTRIBUTIONS

All authors listed have made a substantial, direct, and intellectual contribution to the work and approved it for publication.

ACKNOWLEDGMENTS

Deep thanks and gratitude to the Researchers Supporting Project number (RSP-2021/351), King Saud University, Riyadh, Saudi Arabia for funding this research article.

REFERENCES

A, G., Wahr, J., and Zhong, S. (2013). Computations of the Viscoelastic Response of a 3-D Compressible Earth to Surface Loading: an Application to Glacial Isostatic Adjustment in Antarctica and Canada. *Geophys. J. Int.* 192 (2), 557–572. doi:10.1093/gji/ggs030

Abunayyan, B. R. G. M. (2008). *Investigations for Updating the Groundwater Mathematical Model(s) of the Saq Overlying Aquifers Ministry of Water and Electricity* 1. Riyadh, Saudi Arabia: Abunayyan Trading Corporation. BRGM Geosciences for a sustainable Earth.

Ahmed, M., and Abdelmohsen, K. (2018). Quantifying Modern Recharge and Depletion Rates of the Nubian Aquifer in Egypt. *Surv. Geophys.* 39, 729–751. doi:10.1007/s10712-018-9465-3

Ahmed, M., Sultan, M., Yan, E., and Wahr, J. (2016). Assessing and Improving Land Surface Model Outputs over Africa Using GRACE, Field, and Remote Sensing Data. *Surv. Geophys.* 37 (3), 529–556. doi:10.1007/s10712-016-9360-8

Al Deep, M., Araffa, S. A. S., Mansour, S. A., Taha, A. I., Mohamed, A., and Othman, A. (2021). Geophysics and Remote Sensing Applications for Groundwater Exploration in Fractured Basement: A Case Study from Abha Area, Saudi Arabia. *J. Afr. Earth Sci.* 184 (1), 104368. doi:10.1016/j.jafrearsci.2021.104368

Al-Naeem, A. A. (2014). Effect of Excess Pumping on Groundwater Salinity and Water Level in Hail Region of Saudi Arabia. *Research Journal of Environmental Toxicology* 8, 124–135.

Bernauer, T., and Böhmelt, T. (2020). International Conflict and Cooperation over Freshwater Resources. *Nat. Sustain.* 3, 350–356. doi:10.1038/s41893-020-0479-8

Cheng, M., Ries, J. C., and Tapley, B. D. (2011). Variations of the Earth's Figure axis from Satellite Laser Ranging and GRACE. *J. Geophys. Res.* 116, B01409. doi:10.1029/2010JB000850

De Pauw, E. (2002). *An Agroecological Exploration of the Arabian Peninsula*. Beirut: International Center for Agricultural Research in the Dry Areas.

de Vries, J. J., and Simmers, I. (2002). Groundwater Recharge: an Overview of Processes and Challenges. *Hydrogeology J.* 10, 5–17. doi:10.1007/s10040-001-0171-7

DeNicola, E., Aburizaiza, O. S., Siddique, A., Siddique, A., Khwaja, H., and Carpenter, D. O. (2015). Climate Change and Water Scarcity: the Case of Saudi Arabia. *Ann. Glob. Health* 81 (3), 342–353. doi:10.1016/j.aogh.2015.08.005

Divins, D. (2003). *Total Sediment Thickness of the World's Oceans and Marginal Seas*. Boulder, CO: NOAA National Geophysical Data Center.

Fallatah, O. A., Ahmed, M., Cardace, D., Boving, T., and Akanda, A. S. (2019). Assessment of Modern Recharge to Arid Region Aquifers Using an Integrated Geophysical, Geochemical, and Remote Sensing Approach. *J. Hydrol.* 569, 600–611. doi:10.1016/j.jhydrol.2018.09.061

Fallatah, O. A., Ahmed, M., Save, H., and Akanda, A. S. (2017). Quantifying Temporal Variations in Water Resources of a Vulnerable Middle Eastern Transboundary Aquifer System. *Hydrol. Process.* 2017, 1–11. doi:10.1002/hyp.11285

FAO (2008). *AQUASTAT Country Profile – Saudi Arabia*. Rome, Italy: Food and Agriculture Organization of the United Nations.

FAO (2022). AQUASTAT Database. AQUASTAT (Accessed 02 25, 2022).

Gerten, D., Heck, V., Jägermeyr, J., Bodirsky, B. L., Fetzer, I., Jalava, M., et al. (2020). Feeding Ten Billion People Is Possible within Four Terrestrial Planetary Boundaries. *Nat. Sustain.* 3 (3), 200–208. doi:10.1038/s41893-019-0465-1

Huffman, G. J., Adler, R. F., Bolvin, D. T., and Nelkin, E. J. (2010). "The TRMM Multi-Satellite Precipitation Analysis (TMPA)," in *Chapter 1 in Satellite Applications for Surface Hydrology*. Editors F. Hossain and M. Gebremichael (Springer-Verlag), 3–22. doi:10.1007/978-90-481-2915-7_1

Huffman, G. J., Bolvin, D. T., Nelkin, E. J., Wolff, D. B., Adler, R. F., Gu, G., et al. (2007). The TRMM Multisatellite Precipitation Analysis (TMPA): Quasi-Global, Multiyear, Combined-Sensor Precipitation Estimates at fine Scales. *J. Hydrometeorology* 8, 38–55. doi:10.1175/jhm560.1

Khater, A. R. (2010). *Regional Technical Report on the Impacts of Climate Change on Groundwater in the Arab Region*. Regional Bureau for Science and Technology. in Arab States. Technical Document Published by UNESCO Cairo Office.

Kummerow, C. (1998). Beamfilling Errors in Passive Microwave Rainfall Retrievals. *J. Appl. Meteorol.* 37, 356–370. doi:10.1175/1520-0450(1998)037<0356:beipmr>2.0.co;2

Landerer, F. W., and Swenson, S. C. (2012). Accuracy of Scaled GRACE Terrestrial Water Storage Estimates. *Water Resour. Res.* 48 (4). doi:10.1029/2011WR011453.W04531

Long, D., Longuevergne, L., and Scanlon, B. R. (2015). Global Analysis of Approaches for Deriving Total Water Storage Changes from GRACE Satellites. *Water Resour. Res.* 51, 2574–2594. doi:10.1002/2014wr016853

Longuevergne, L., Scanlon, B. R., and Wilson, C. R. (2010). GRACE Hydrological Estimates for Small Basins: Evaluating Processing Approaches on the High Plains Aquifer, USA. *Water Resour. Res.* 46, W11517. doi:10.1029/2009WR008564

Luthcke, S. B., Sabaka, T. J., Loomis, B. D., Arendt, A. A., McCarthy, J. J., and Camp, J. (2013). Antarctica, Greenland and Gulf of Alaska Land-Ice Evolution from an Iterated GRACE Global Mascon Solution. *J. Glaciol.* 59, 613–631. doi:10.3189/2013JoG12J147

Meneisy, A. M., and Al Deep, M. (2021). Investigation of Groundwater Potential Using Magnetic and Satellite Image Data at Wadi El Amal, Aswan, Egypt. *Egypt. J. Remote Sensing Space Sci.* 24, 293–309. doi:10.1016/j.ejrs.2020.06.006

Milewski, A., Sultan, M., Yan, E., Becker, R., Abdeldayem, A., Soliman, F., et al. (2009). A Remote Sensing Solution for Estimating Runoff and Recharge in Arid Environments. *J. Hydrol.* 373, 1–14. doi:10.1016/j.jhydrol.2009.04.002

Mohamed, A. (2020d). Time-lapse Gravity Monitoring of Groundwater of the Sinai Peninsula. *Int. J. Earth Sci. Geophys.* 6 (2). doi:10.35840/2631-5033/1840

Mohamed, A., Al Deep, M., Abdelrahman, K., and Abdelrady, A. (2022). Geometry of the Magma Chamber and Curie Point Depth Beneath Hawaii Island: Inferences From Magnetic and Gravity data.. *Frontiers in Earth Science, section Solid Earth Geophysics* 10, 847984 doi:10.3389/feart.2022.847984

Mohamed, A., and Al Deep, M. (2021). Depth to the Bottom of the Magnetic Layer, Crustal Thickness, and Heat Flow in Africa: Inferences from Gravity and Magnetic Data. *J. Afr. Earth Sci.* 179, 104204. doi:10.1016/j.jafrearsci.2021.104204

Mohamed, A., and Ella, E. M. A. E. (2021). Magnetic Applications to Subsurface and Groundwater Investigations: a Case Study from Wadi El Assiuti, Egypt. *Ijg* 12, 77–101. doi:10.4236/ijg.2021.122006

Mohamed, A., and Gonçalvès, J. (2021). Hydro-geophysical Monitoring of the North Western Sahara Aquifer System's Groundwater Resources Using Gravity Data. *J. Afr. Earth Sci.* 178, 104188. doi:10.1016/j.jafrearsci.2021.104188

Mohamed, A. (2020b). Gravity Applications in Estimating the Mass Variations in the Middle East: a Case Study from Iran. *Arab J. Geosci.* 13, 364. doi:10.1007/s12517-020-05317-7

Mohamed, A. (2020c). Gravity Applications to Groundwater Storage Variations of the Nile Delta Aquifer. *J. Appl. Geophys.* 182, 104177. doi:10.1016/j.jappgeo.2020.104177

Mohamed, A. (2020a). Gravity Based Estimates of Modern Recharge of the Sudanese Area. *J. Afr. Earth Sci.* 163, 103740. doi:10.1016/j.jafrearsci.2019.103740

Mohamed, A. (2019). Hydro-geophysical Study of the Groundwater Storage Variations over the Libyan Area and its Connection to the Dakhla basin in Egypt. *J. Afr. Earth Sci.* 157, 103508. doi:10.1016/j.jafrearsci.2019.05.016

Mohamed, A., Ragaa Eldeen, E., and Abdelmalik, K. (2021). Gravity Based Assessment of Spatio-Temporal Mass Variations of the Groundwater Resources in the Eastern Desert, Egypt. *Arab. J. Geosci.* 14, 500. doi:10.1007/s12517-021-06885-y

Mohamed, A., Sultan, M., Ahmed, M., Yan, E., and Ahmed, E. (2017). Aquifer Recharge, Depletion, and Connectivity: Inferences from GRACE, Land Surface Models, and Geochemical and Geophysical Data. *Geol. Soc. America Bull.* 129, 534–546. doi:10.1130/B31460.1

Mohamed, A., Sultan, M., Ahmed, M., and Yan, E. (2014). *Quantifying Modern Recharge to the Nubian Sandstone Aquifer System: Inferences from GRACE and Land Surface Models*. San Francisco, CA: American Geophysical Union.

Mohamed, A., Sultan, M., Yan, E., Ahmed, M., Sturchio, N., and Ahmed, E. (2015). *Towards a Better Understanding of the Hydrologic Setting of the Nubian Sandstone Aquifer System: Inferences from Groundwater Flow Models, Cl-36 Ages, and GRACE Data*. San Francisco, CA: American Geophysical Union.

Othman, A., and Abotalib, A. Z. (2019). Land Subsidence Triggered by Groundwater Withdrawal under Hyper-Arid Conditions: Case Study from Central Saudi Arabia. *Environ. Earth Sci.* 78 (7), 243. doi:10.1007/s12665-019-8254-8

Othman, A. (2019). "Measuring and Monitoring Land Subsidence and Earth Fissures in Al- Qassim Region, Saudi Arabia: Inferences from InSAR," in *Advances in Remote Sensing and Geo Informatics Applications. CAJG 2018. Advances in Science, Technology & Innovation (IEREK Interdisciplinary Series for Sustainable Development)*. Editors H. El-Askary, S. Lee, E. Heggy, and B. Pradhan (Cham: Springer). doi:10.1007/978-3-030-01440-7_66

Rodell, M., Chen, J., Kato, H., Famiglietti, J. S., Nigro, J., and Wilson, C. R. (2007). Estimating Groundwater Storage Changes in the Mississippi River basin (USA) Using GRACE. *Hydrogeol. J.* 15, 159–166. doi:10.1007/s10040-006-0103-7

Rodell, M., Chen, J., Kato, H., Famiglietti, J. S., Nigro, J., and Wilson, C. R. (2007). Estimating Groundwater Storage Changes in the Mississippi River basin (USA) Using GRACE. *Hydrogeol J.* 15 (1), 159–166. doi:10.1007/s10040-006-0103-7

Rodell, M., and Famiglietti, J. S. (2001). An Analysis of Terrestrial Water Storage Variations in Illinois with Implications for the Gravity Recovery and Climate Experiment (GRACE). *Water Resour. Res.* 37, 1327–1339. doi:10.1029/2000wr900306

Rodell, M., Houser, P. R., Jambor, U., Gottschalck, J., Mitchell, K., Meng, C.-J., et al. (2004). The Global Land Data Assimilation System. *Bull. Amer. Meteorol. Soc.* 85, 381–394. doi:10.1175/BAMS-85-3-381

Sakumura, C., Bettadpur, S., and Bruinsma, S. (2014). Ensemble Prediction and Intercomparison Analysis of GRACE Time-Variable Gravity Field Models. *Geophys. Res. Lett.* 41, 1389–1397. doi:10.1002/2013GL058632

Save, H., Bettadpur, S., and Tapley, B. D. (2016). High-resolution CSR GRACE RL05 Mascons. *J. Geophys. Res. Solid Earth* 121, 7547–7569. doi:10.1002/2016JB013007

Scanlon, B. R., Longuevergne, L., and Long, D. (2012). Ground Referencing GRACE Satellite Estimates of Groundwater Storage Changes in the California Central Valley, USA. *Water Resour. Res.* 48, 1–9. doi:10.1029/2011WR011312

Siebert, S., Burke, J., Faures, J. M., Frenken, K., Hoogeveen, J., Döll, P., et al. (2010). Groundwater Use for Irrigation - a Global Inventory. *Hydrol. Earth Syst. Sci.* 14, 1863–1880. doi:10.5194/hess-14-1863-2010

Smakhtin, V., Revenga, C., and Döll, P. (2004). A Pilot Global Assessment of Environmental Water Requirements and Scarcity. *Water Int.* 29, 307–317. doi:10.1080/02508060408691785

Sultan, M., Sturchio, N., Al Sefry, S., Milewski, A., Becker, R., Nasr, I., et al. (2008). Geochemical, Isotopic, and Remote Sensing Constraints on the Origin and Evolution of the Rub Al Khali Aquifer System, Arabian Peninsula. *J. Hydrol.* 356, 70–83. doi:10.1016/j.jhydrol.2008.04.001

Swenson, S., Chambers, D., and Wahr, J. (2008). Estimating Geocenter Variations from a Combination of GRACE and Ocean Model Output. *J. Geophys. Res.* 113, B08410. doi:10.1029/2007jb005338

Syed, T. H., Famiglietti, J. S., Rodell, M., Chen, J., and Wilson, C. R. (2008). Analysis of Terrestrial Water Storage Changes from GRACE and GLDAS. *Water Resour. Res.* 44, W02433. doi:10.1029/2006WR005779

Taha, A. I., Al Deep, M., and Mohamed, A. (2021). Investigation of Groundwater Occurrence Using Gravity and Electrical Resistivity Methods: a Case Study from Wadi Sar, Hijaz Mountains, Saudi Arabia. *Arab. J. Geosci.* 14, 334. doi:10.1007/s12517-021-06628-z

Tapley, B. D., Bettadpur, S., Watkins, M., and Reigber, C. (2004). The Gravity Recovery and Climate experiment: Mission Overview and Early Results. *Geophys. Res. Lett.* 31. doi:10.1029/2004GL019920

Tariki, A. H. (1947). *Geology of Saudi Arabia, MSc Thesis*. Austin, Texas: University of Texas at Austin.

Trondalen (2009). "Climate Changes, Water Security and Possible Remedies for the Middle East. From Potential Conflict to Co-operation Potential," in *The United Nations World Water Development Report 3, Water in a Changing World*. The United Nations Educational, Scientific and Cultural Organization, 7: University of Texas at Austin.

UN-ESCWA; BGR (2013). *United Nations economic and social commission for western Asia; Bundesanstaltfu¨ r Geowissenschaften und Rohstoffe*. Beirut, Lebanon: Inventory of Shared Water Resources in Western Asia.

Wada, Y., Van Beek, L. P. H., Van Kempen, C. M., Reckman, J. W. T. M., Vasak, S., and Bierkens, M. F. P. (2010). Global Depletion of Groundwater Resources. *Geophys. Res. Lett.* 37 (20). doi:10.1029/2010gl044571

Wahr, J., Molenaar, M., and Bryan, F. (1998). Time Variability of the Earth's Gravity Field: Hydrological and Oceanic Effects and Their Possible Detection Using GRACE. *J. Geophys. Res.* 103, 30. doi:10.1029/98jb02844

Wahr, J., Swenson, S., Zlotnicki, V., and Velicogna, I. (2004). Time-Variable Gravity From GRACE: First Results. *Geophys. Res. Lett.* doi:10.1029/2004GL019779

Wang, S., Huang, J., Li, J., Rivera, A., McKenney, D. W., and Sheffield, J. (2014). Assessment of Water Budget for Sixteen Large Drainage Basins in Canada. *J. Hydrol.* 512, 1–15. doi:10.1016/j.jhydrol.2014.02.058

Wehbe, Y., Temimi, M., Ghebreyesus, D. T., Milewski, A., Norouzi, H., and Ibrahim, E. (2018). Consistency of Precipitation Products over the Arabian Peninsula and Interactions with Soil Moisture and Water Storage. *Hydrological Sci. J.* 63 (3), 408–425. doi:10.1080/02626667.2018.1431647

Wiese, D. N., Landerer, F. W., and Watkins, M. M. (2016). Quantifying and Reducing Leakage Errors in the JPL RL05M GRACE Mascon Solution. *Water Resour. Res.* 52, 7490–7502. doi:10.1002/2016WR019344

Yeh, P. J.-F., Irizarry, M., and Eltahir, E. A. B. (1998). Hydroclimatology of Illinois: A comparison of Monthly Evaporation Estimates Based on Atmospheric Water Balance With Estimates Based on Soil Water Balances. *J. Geophys. Res.* 103 (D16), 19823–19837.

Yeh, P. J-F., Swenson, S., Famiglietti, J. S., and Rodell, M. (2006). Remote Sensing of Groundwater Storage Changes in Illinois Using the Gravity Recovery and Climate Experiment (GRACE). *Water Resour. Res.* 42, W12203. doi:10.1029/2006wr005374

Conflict of Interest: The authors declare that the research was conducted in the absence of any commercial or financial relationships that could be construed as a potential conflict of interest.

Publisher's Note: All claims expressed in this article are solely those of the authors and do not necessarily represent those of their affiliated organizations, or those of the publisher, the editors and the reviewers. Any product that may be evaluated in this article, or claim that may be made by its manufacturer, is not guaranteed or endorsed by the publisher.

frontiers | Frontiers in Environmental Science

ORIGINAL RESEARCH
published: 26 April 2022
doi: 10.3389/fenvs.2022.852591

Integrated Monitoring for the Rock Mass State During Large-Scale Subsoil Development

Oleg Bazaluk[1], Kanay Rysbekov[2], Marzhan Nurpeisova[2], Vasyl Lozynskyi[3], Guldana Kyrgizbayeva[2]* and Turar Turumbetov[4]*

[1]Belt and Road Initiative Institute for Chinese-European Studies (BRIICES), Guangdong University of Petrochemical Technology, Maoming, China, [2]Mining and Metallurgical Institute Named After O.A. Baikonurov, Satbayev University, Almaty, Kazakhstan, [3]Department of Mining Engineering and Education, Dnipro University of Technology, Dnipro, Ukraine, [4]Department of Cartography and Geoinformatics, Al Farabi Kazakh National University, Almaty, Kazakhstan

The purpose of this study was to develop a methodology for integrated monitoring of the rock mass state, which ensures the industrial and environmental safety of the Central Kazakhstan region. As a result of the research, a methodology for maintaining an integrated system of geodynamic monitoring has been developed. The results of predicting the physical–mechanical properties and stress–strain state of the rock mass are presented. Based on the data obtained, graphical–analytical dependences between the most important quantitative characteristics of the rock properties in the studied deposits are presented. The scientific novelty of the presented research lies in determining the pattern of changes in the structural peculiarities and strength properties of rocks with the depth of their occurrence, which makes it possible to predict the stress–strain state of the rock mass. The authors propose a new method for creating a geodynamic test site. The geodynamic test site created in the fields of Central Kazakhstan is a reliable basis for the organization of long-term monitoring for the earth's surface deformation processes during large-scale development of the field, which improves the productivity and accuracy of observations. The results obtained can be used to improve the level of industrial safety at mines and minimize environmental risks caused by the subsoil development.

Keywords: deposits, fracturing, rocks, stress–strain state, mining operations, monitoring, mass stability, deposits

OPEN ACCESS

Edited by:
Biswajeet Pradhan, University of Technology Sydney, Australia

Reviewed by:
Jianwei Cheng, China University of Mining and Technology, China
Izabela Jonek-Kowalska, Silesian University of Technology, Poland

****Correspondence:***
Vasyl Lozynskyi
lvg.nmu@gmail.com
Guldana Kyrgizbayeva
g.kyrgizbayeva@satbayev.university

Specialty section:
This article was submitted to Environmental Informatics and Remote Sensing, a section of the journal Frontiers in Environmental Science

Received: *11 January 2022*
Accepted: *14 March 2022*
Published: *26 April 2022*

Citation:
Bazaluk O, Rysbekov K, Nurpeisova M, Lozynskyi V, Kyrgizbayeva G and Turumbetov T (2022) Integrated Monitoring for the Rock Mass State During Large-Scale Subsoil Development. Front. Environ. Sci. 10:852591. doi: 10.3389/fenvs.2022.852591

INTRODUCTION

Mining of mineral resources is considered an important issue for energy-saving and resource-saving sustainability (Golik et al., 2018). The energy sector of industry development needs more mineral resources for energy generation that is mined out from the earth's subsoil. At the same time, the innovative development of mining technologies is also driven by the need for saturation of the long-term demand for raw materials (Zhironkin and Cehlár, 2021; Zhironkin and Szurgacz, 2021).

Large-scale mining operations conducted in highly stressed hard-rock mass are characterized by significant geomechanical and geodynamic processes associated with a change in the stress state, deformation, and displacement of mine rocks. These processes entail not only catastrophic technical-and-economic consequences but sometimes also lead to human losses. Technogenic earthquakes occurred in Germany, United States, Poland, and Czech Republic (Field, 2007; Burmin and Shumlianska, 2017; Adushkin, 2018; Gerasymenko et al., 2020; Sach et al., 2020; Amemoutou

et al., 2021). In Russia, this problem is acute in the mines of the Verkhnekamensk potassic salt deposits and the Khibiny apatite-nepheline mines (Viktorov et al., 2005; Rebetskiy et al., 2017). All this is a direct consequence of the change in the geodynamic regime of the geological environment under the influence of large-scale mining operations (Pavlychenko and Kovalenko, 2013; Buzylo et al., 2018). Moreover, this is convincingly confirmed by the results of many years of scientific research into the Zhezkazgan natural–technical system, which is formed by mines, dressing mills with tailing dumps, and copper-smelting plants in Karaganda, Balkhash, Zhezkazgan, and Satpayev (Bekbergenov et al., 2020). The corresponding infrastructure in Central Kazakhstan is a powerful subject of anthropogenic impact on the environment, providing great opportunities for researching a wide range of environmental problems (Ryl'nikova et al., 2016; Mikhailova and Uzbekov, 2018a).

In recent years, objects with a complex geological structure and a large depth of occurrence have been increasingly included in the development and operation of ore deposits. This requires special conditions for mining and development of these objects. K.I. Satpayev (1962) wrote about this in his study "Zhezkazgan copper ore region and its mineral resources", creating a metallogenic prediction map of Kazakhstan. And at present, the mineral resource base of Central Kazakhstan is expanding.

Rational development of mineral deposits presupposes the complete extraction of reserves while performing a minimum volume of overburden operations with geomechanical substantiation of the required degree of the rock mass stability (Stupnik et al., 2014; Babets et al., 2017; Abdiev et al., 2020; Zhanakova et al., 2020; Bazaluk et al., 2021). Masloboev et al. (2021) discussed the minimization of artificial impacts on the environment, and new technological solutions have been developed for mining enterprises. Waloski et al. (2021) indicate that from the point of view of the stability of underground structures, the most critical features of the rock mass are rock and rock mass strength as well as discontinuity surfaces. Moreover, the influence of cutting is considered an important issue in mining (Łukasz, 2020). The main initial information is the geological knowledge of the deposit (Aitkazinova et al., 2016; Petlovanyi et al., 2019), knowledge of the parameter values of the physical–mechanical and strength properties of rocks (Malanchuk et al., 2021), as well as the elements of the occurrence, structural-tectonic peculiarities of the rock mass, and fractures in rocks (Dychkovskyi et al., 2018; Lozynskyi et al., 2020). This makes it possible to determine the mass stress state in the mining process.

The geomechanical processes are studied at individual mines, and there is an experience in this direction. The dynamics of the mining complex development in Kazakhstan and in the world over the past century has led to a qualitatively new situation, when the "local" geomechanical fields induced by human technogenic activity are no longer small in comparison with the global geodynamic processes of the Earth's tectonic activity (Begalinov et al., 2020a; Zeylik et al., 2021). Therefore, it is necessary to consider mines and pits as unique natural laboratories, where it is possible to study in detail the relationship between geomechanical and geodynamic processes using mining-geophysical and satellite geodetic methods.

In Kazakhstan, such studies, to a large extent, are conducted only during the development of oil and gas resources (Karatayev and Clarke, 2014), where both technogenic consequences and natural geodynamic peculiarities of the region are taken into account (Sarybayev et al., 2015; Moldabayev et al., 2019). At the same time, such studies on ore deposits have not been widely developed.

During large-scale and long-term mining of ore deposits, along with geomechanical deformation processes, geodynamic processes also develop (Mikhailova and Uzbekov, 2018b; Ursul and Ursul, 2018; Begalinov et al., 2020b). In this regard, the past decade has been marked by major achievements in the field of industrial and environmental safety, as evidenced by the increased number of publications on this topic (Mora and Keipi, 2006; Bondarenko et al., 2012; Oparin, 2015; Haiko et al., 2019). Special attention is paid to sustainable development because the environment is one of the essential state-level and international challenges (Rakhmangulov et al., 2017; Rozin, 2021).

The scope of application of modern mining requires an advanced study and constant monitoring of geomechanical processes occurring in the inner part of the earth, based on monitoring the state of the open-pit slopes, which provides a systematic approach to solving all components of the problems, comprehensive accounting, and analysis of all natural and technogenic factors (Dryzhenko et al., 2017; Cheskidov et al., 2019). Surface mining, in the broadest sense of the word monitoring, is the observation of the environment, presented as a dynamic, constantly changing system, and which is aimed at its control, study, prediction, and protection (Aitkazinova et al., 2014; Kyrgizbayeva et al., 2015; Nurpeissova et al., 2020). At the same time, sustainability of the open-pit mining and technical system is one of its key goals in the changing conditions of the external and internal environment (Rakhmangulov et al., 2021).

A prerequisite for the safe and environmentally sustainable development of surface mining is the improvement of the system for monitoring and observing the deformations of the open-pit slopes, slopes, and dumps using the modern methods of geodesy and high-precision deformation measurements (Malanchuk et al., 2020; Moshynskyi et al., 2020). The stability of the open-pit sides is characterized by the stability coefficient, the value of which shows the relative excess in the rock mass strength in comparison with the shearing stresses (Du and Xing, 2017). At the stage of open-pit design, in order to determine and substantiate the parameters of its slopes and benches, the stability coefficient is calculated taking into account the geological and hydrogeological conditions of the adjacent rock mass (Bitimbaev et al., 2017; Stupnik et al., 2019; Sobko et al., 2020). The choice of the optimal parameters of the slopes and local benches of open pits affects the safety of mining operations and the economic efficiency of the enterprise (Kharisov, 2018).

In general, minerals are mainly mined by the surface mining method, which accounts for up to 75% of the extracted mineral products from the subsoil, and this level will be maintained in the future (Cherniaiev, 2017; Ali Elbeblawi et al., 2021). At the same

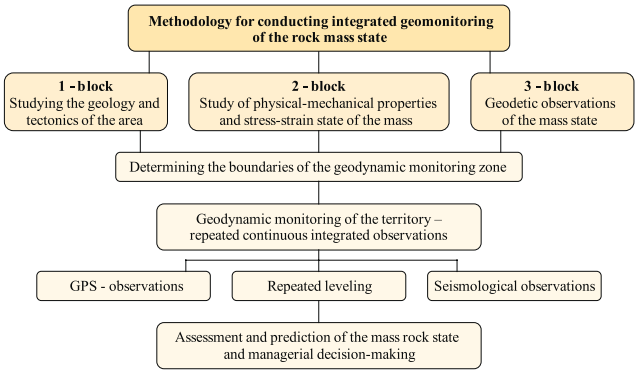

FIGURE 1 | Scheme of an integrated methodology for conducting geomonitoring.

FIGURE 2 | Sampling at the Saryoba deposit: **(A)** cores from wells; **(B)** monolithic samples.

time, an increase in the depth, size, and production capacity of open pits can be traced to the tendency of their development (Dagdelen and Traore, 2018; Whittle et al., 2018; Babets et al., 2021). Under these conditions, the task of ensuring the stability of the open-pit slopes becomes especially urgent (Stacey et al., 2003). In this regard, it becomes necessary to conduct geomechanical monitoring and improve its geodetic observation methods to ensure the long-term stability of the open-pit slopes.

Modern methods of monitoring the geomechanical state of the open-pit slopes are very diverse (Fleurisson, 2012). Among the equipment most commonly used for monitoring the safety situation in open pits are laser scanning (Rysbekov et al., 2019), electronic total stations and Global Positioning System (GPS) technology (Kim et al., 2003), and big data (Krichevsky, 2016; Jiang et al., 2018). During geodetic monitoring of objects located in the industrial zone of the Maykain mine in Kazakhstan, such geodetic instruments as satellite technologies, electronic total stations, and leveling lasers have been successfully used (Krylova, 1978; Nurpeisova et al., 2016; Nurpeisova and Kurmanbaev, 2016).

The technical level of traditional geodetic observations during geomechanical monitoring does not always meet the requirements of mining enterprises. Since this requires a lot of working time and there is no possibility of promptly obtaining the necessary infomation about the deformation state of the rock mass. Therefore, the use of modern geodetic instruments in geomonitoring, such as electronic total stations, GPS technologies, and laser scanners, as well as the improvement of methods of working with them, are closely related to an increase in the level of innovative directions. All this confirms the importance of improving the methodology for conducting geomechanical monitoring using modern geodetic instruments as the basis for solving a scientific–technical problem.

METHODS

Analysis of the state of the methodology for conducting geodetic observations on the territory of the developed field is primarily associated with the lack of effective methods for determining the values of deformations. This necessitates the improvement of the methodology for geodetic observations of rock deformations using modern instruments. Geodetic observations make it possible to reveal the mass deformations, which is essential for assessing the geomechanical situation in the area of field mining. But they do not provide a complete picture of deformation processes in the course of time. This can be performed only when using the proposed integrated methodology for conducting geomonitoring of the state of the near-side masses (**Figure 1**).

Based on the above, the purpose is set, the idea is substantiated and the structure of the integrated monitoring conducted in Central Kazakhstan is formulated.

According to the 1-block of the recommended methodology (**Figure 1**), the engineering-geological and mining-technical conditions of the giant Saryoba copper deposit located in Central Kazakhstan have been studied in detail. The parameters for studying the geology and tectonics in the area are the numerical data of surveying the deposit. The East Saryoba ore bodies are represented by stratified, rounded, and banded deposits with a very variable thickness and nonuniform distribution of useful components. The thickness of commercial ore bodies ranges from 0.1 to 20 m and averages 3–8 m for the East Saryoba deposit. The reserves of B + C1 + C2 categories have been explored and approved in quantities that make it possible to classify the ore field as a large industrial facility.

According to the 2-block of the recommended methodology (**Figure 1**), the structural peculiarities on the outcrops and the physical–mechanical properties of the rocks in the Saryoba deposit mass have been studied. The rock samples, including minerals, are taken for the purpose of laboratory determination of indicators of physical–mechanical properties that significantly influence the displacement process. In practice, the laboratory method is mainly used to study the physical–mechanical properties of rocks on samples made from cores from geological exploration wells (**Figure 2A**). In the presence of mine workings (trenches, pitholes, shafts, crossdrifts, etc.), samples are taken from rocks in the form of monoliths (**Figure 2B**). The parameters for studying the physical–mechanical properties and stress–strain state of the rock mass are depth of rock occurrence, compression strength,

tension strength, density, adhesion, internal friction angle, and rock hardness according to Prof. M. M. Protodiakonov scale. It should be noted that the main part of the East Saryoba deposit reserves (up to 90%) is represented by flat-dipping and nearly level bedding with a dip angle of up to 25°. The East Saryoba deposit is mined using the pillar-and-panel system with the division of ore bodies into panels—mining units.

To compare the results obtained at the studied object of the Saryoba deposit with the data of other mines, a combined graph of the relationship of rock properties is compiled. Assessment and reliability of determining the dependencies are made according to the formulas of mathematical statistics:

$$\sigma = \pm \sqrt{\frac{\sum (x_i - \bar{x})}{n-1}}, \text{MPa} \quad (1)$$

$$V = \frac{\sigma}{\bar{x}} \cdot 100 \quad (2)$$

$$m_v = \frac{V \cdot \sqrt{0.5 + \left(\frac{V}{100}\right)}}{\sqrt{n}} \quad (3)$$

where σ is the standard; x_1 is the characteristic value; $\bar{x}$ is the characteristic value arithmetic mean; n is the number of observations; V is the coefficient of variation; mv is the reliability of calculating the coefficient of variation.

If the condition **Eq. 3** $m_v < V$ is satisfied, then the results can be considered reliable and the number of initial data for determining the statistical means is sufficient.

According to the 3-block of the recommended methodology (**Figure 1**), geodetic observation of the rock mass state is necessary. When performing geodetic observations of the mass state and determining the mining allotment boundaries, the spatial contours of the mineral deposit are taken into account: position of the site for construction, as well as operation of underground structures; boundaries of safe mining and blasting operations; zones of protection from the harmful effects of mining operations; zones of rock displacement; contours of protecting pillars under natural objects, buildings and structures; spacing out of the open-pit sides and cuts, as well as other factors influencing the state of the subsoil and the earth's surface as a result of the process of geological exploration and the subsoil use. Mining of minerals is permissible only within the subsoil site boundaries provided for use in accordance with the standard procedure. To date, various methods and ways of controlling the rock mass stress–strain state have been developed. Among the main ones are unloading VNIMI method, core disking, etc. To determine the stress state of the rock masses in the Karatau deposit (1995–2000), the Akbakai deposit (2012–2015), the authors have studied the core materials of geological exploration wells and the disking method. When conducting the geotechnological studies of the mine rock stability with the issuance of recommendations for managing the rock pressure in the Akzhal mine of Nova Zinc LLP (2007–2018), a "Seismic-acoustic method for predicting the stress–strain state of a rock mass", developed by the authors for determining the mass disturbance, is used in the Saryoba deposit (2020–2021).

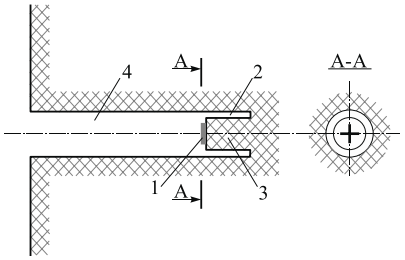

FIGURE 3 | Stresses measurement scheme: 1, strain gauge; 2, annular slot; 3, core; 4, well.

The seismic-acoustic method for predicting the rock mass stress–strain state includes setting a sensor of seismic-acoustic signals emitted by natural sources in the rock mass, after which the parameters of these signals are determined. Seismic-acoustic signals are recorded by a sensor in wells drilled near mine workings at different horizons. This method is characterized by simplicity and speed of measurement with high reliability of results. The scheme of the seismic-acoustic method implementation for predicting the rock mass stress–strain state is presented in **Figure 3**.

The stress measurement scheme works according to the method of unloading the core at the end of the well (4). To do this, a special disk fixed on a rod is used to grind the end of the well and the strain gauge (1) is firmly pressed onto the end. The cable from the strain gauge is passed into a hollow drill rod and, with the help of a crown, is inserted into the annular slot (2). As a result, elastic expansion of the core (3) occurs, which is fixed by a measuring strain gauge in three directions, the results of which are shown in **Table 2**. After measuring the deformations, the core is broken off and is sent to the laboratory in a special package to determine the elastic characteristics of the rocks (E and μ).

RESULT AND DISCUSSION

State of the Current Development of the Problem and Formulating a Research Task

In the ore field of the Saryoba deposit, 11 ore deposits are identified, in which 109 ore bodies are explored. The largest deposits are confined to the Taskuduk horizon. Their strike is north-eastern, the length is up to 3,200 m, the thickness is from 0.5 to 17 m, and the size of the dip is up to 1,400 m (**Figure 4**).

The geological structure of the area involves rocks of several geological systems—from the pre-Cambrian rocks to the Anthropocene. The thick (up to 3,000 m) Middle Paleozoic stratum of terrigenous and carbonate deposits transgressively overlies pre-Cambrian and Lower Paleozoic formations through basal conglomerates. The Zhezkazgan formation of deposits is assigned to the Upper Paleozoic, which includes from bottom to top:

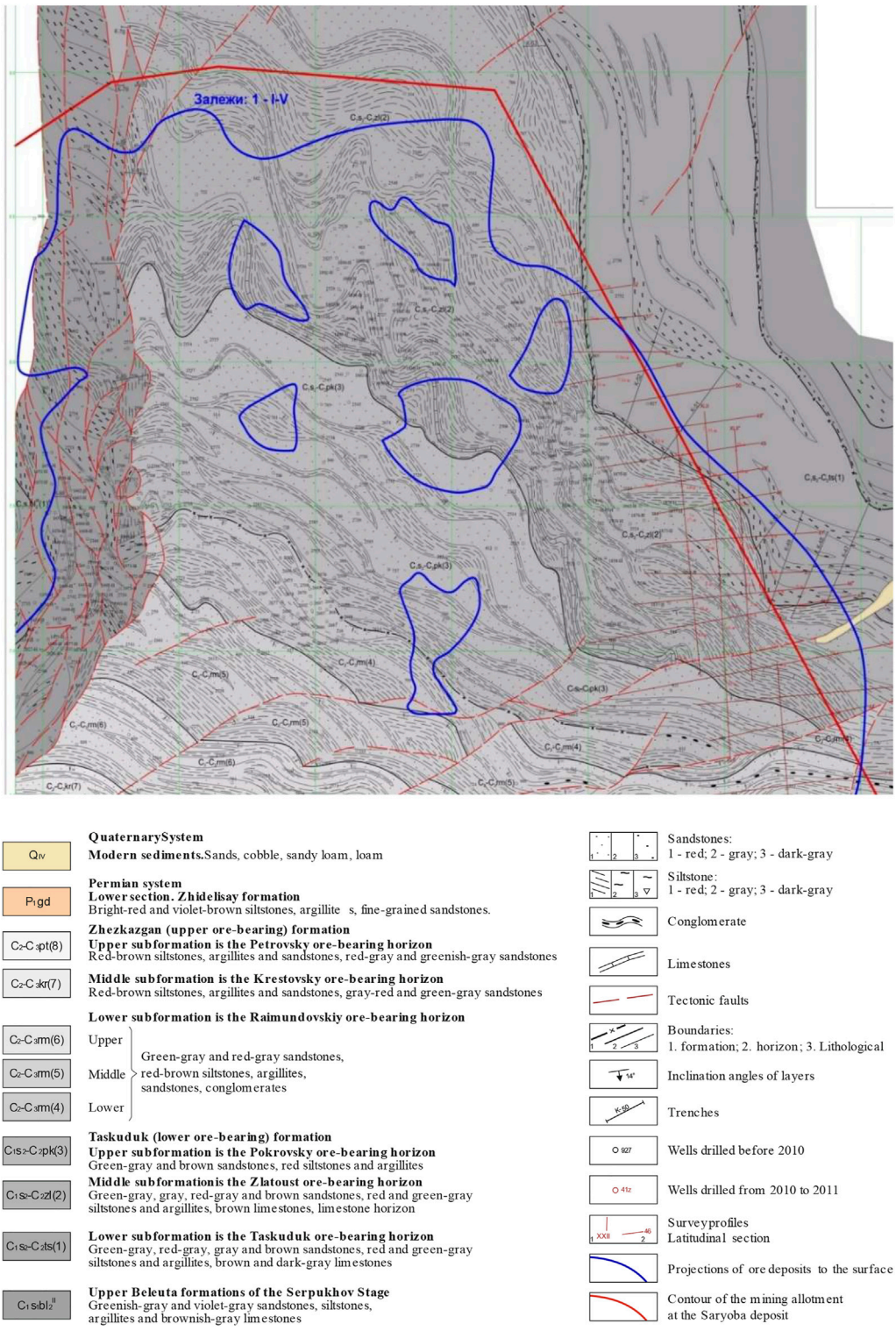

FIGURE 4 | Geological map of the Taskuduk horizon at the Saryoba deposit.

A) Zhezkazgan ore-bearing stratum of argillo-arenaceous deposits, subdivided into the Taskuduk and Zhezkazgan formations with a total thickness of 650–680 m;

B) Zhidelisay formation, consisting of alternating layers of red argillites and sandstones with a total thickness of 300 m;

TABLE 1 | Physical-mechanical properties of rocks from the Saryoba deposit.

Depth of rocks occurrence, m	Name of the rock	Strength, MPa		Density (γ), g/mm^3	Adhesion (K), MPa	Internal friction angle (ρ), deg.	Rock hardness, f*
		Compression, σ_{compr}	Tension, σ_{tens}				
51.0	Massive limestone	110	13.0	2.60	25	30	7.6
53.0	Gray sandstones	112	13.6	2.60	27	30	7.8
53.5	Siltstones	126	14.0	2.62	30.4	30	7.7
54.0	Limestones	128	14.2	2.62	36.5	30	7.9
84.0	Limestones	135	14.3	2.67	36.8	31	8.3
112.0	Sandstones	135	15.3	2.68	38.8	31	8.6
115.6	Red limestone	137	16.8	2.65	42.7	32	8.2
153.0	Massive limestones	139	15.5	2.71	34	32	8.2
155.0	Gray limestones	174.0	16.0	2.67	46.8	31	8.8
170.8	Massive limestone	143	15.8	2.72	34.8	31	9.0
201.0	Gray limestones	151.3	16.2	2.69	40.0	31	9.1
221.0	Limestones	158.1	16.5	2.69	42.0	32	9.1
248.1	Gray-red limestones	154.5	12.3	2.70	43.5	32	9.2
258.5	Siltstones	157.6	14.0	2.70	45.0	33	9.1
260.8	Siltstones	163.1	14.5	2.71	45.2	33	9.0
265.3	Sandstones	166.1	15.2	2.71	46.0	34	9.0
310.5	Conglomerates	173.1	17.2	2.72	46.0	34	9.1
315.8	Limestones	172.6	17.0	2.73	47.2	34	9.1
345.2	Siltstones	170.0	16.0	2.73	47.5	35	9.1
345.5	Limestones	171.4	16.8	2.71	47.0	35	9.2
355.0	Limestones	172.1	17.0	2.72	47.5	36	9.4
355.4	Sandstones	173.5	17.2	2.72	48.5	35	9.3
425.1	Red limestone	174.5	17.3	2.73	48.8	36	9.5
425.7	Massive limestones	175.1	17.5	2.73	48.7	36	9.6
505.2	Gray limestones	178.0	16.4	2.73	49.2	37	9.8
505.6	Massive limestones	180.1	16.5	2.74	49.5	37	9.9
545.0	Gray limestones	171.4	16.8	2.74	49.8	38	10.0
545.5	Limestones	175.1	17.0	2.74	50.0	39	10.1
550.1	Gray-red limestones	186.1	17.5	2.75	50.5	38	10.0
550.5	Massive limestones	183.4	17.2	2.75	50.0	38	10.2

*f is rock hardness according to Professor Protodiakonov scale.

C) Red stratum, overlain uniformly by the Kengir formation, represented by interbedded layers of gray and dark gray marls and dolomitic limestones with a total thickness of 500 m.

The first two formations are ore-bearing, and the main attention in the area is paid to their study. Therefore, we have thoroughly studied the Taskuduk formation, which is currently being developed.

Pre-ore and post-ore disjunctive faults are present at the Saryoba deposit, which greatly complicates their detailed survey and development. In the studied area, the south-western part of the ore field (**Figure 3**) is complicated by high-order folds and faults, the largest of which is the Saryoba transpressional fault of submeridional strike. Its length is more than 10 km with a width of 250–400 m, the main plane dips to the west at an angle of 25–30°. The Saryoba transpressional fault divides the ore field into two almost equal parts. West Saryoba deposit is located in the western half, and East Saryoba is located in the eastern half.

Studying the Physical–Mechanical Properties and Stress–Strain State of the Mass

The results of testing the physical–mechanical properties of rocks from the Saryoba deposit are given in **Table 1**. It should be noted that the table includes only data on the average values of core samples from each horizon. Samples for studying the physical–mechanical properties of rocks to a depth of 100 m are taken from the outcropped benches of the open-pit sides, the rest are taken from the cores of drilled exploration and production wells.

In the studied area, the south-western part of the ore field (**Figure 4**) is complicated by high-order folds and faults, the largest of which is the Saryoba transpressional fault of submeridional strike. Its length is more than 10 km with a width of 250–400 m, the main plane dips to the west at an angle of 25–30°. The Saryoba transpressional fault divides the ore field into two almost equal parts. The West Saryoba deposit is located in the western half, and East Saryoba is located in the eastern half.

Analysis of the results of studying the physical–mechanical properties of rocks makes it possible to determine graphical-analytical dependences of changes in the strength properties of mass rocks with the depth of their occurrence and promptly make changes in the horizontally calculated stability of mine workings (**Figure 5**).

Similar dependencies have also been obtained for a number of fields in Kazakhstan, namely for the Akzhal field, Akbakai, and Sayak deposits, etc. To find the general patterns of variability in the strength and structural properties of rocks, data from a number of deposits have also been generalized and graphical-analytical

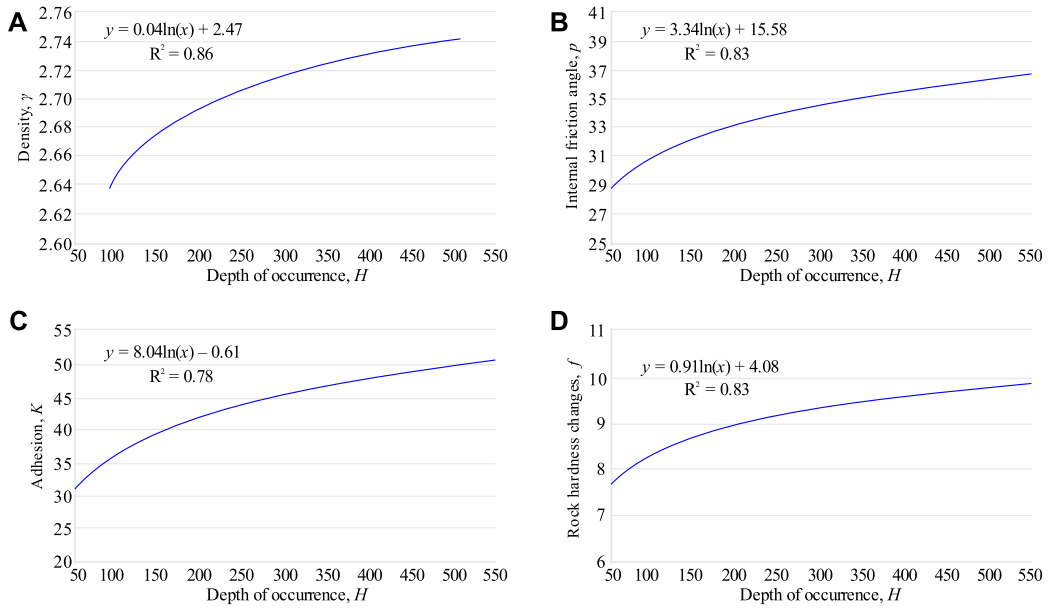

FIGURE 5 | Dependence of the massive limestone strength properties with the depth of its occurrence (H): **(A)** density changes, g; **(B)** changes in the internal friction angle, p; **(C)** adhesion changes, K; **(D)** rock hardness changes, f.

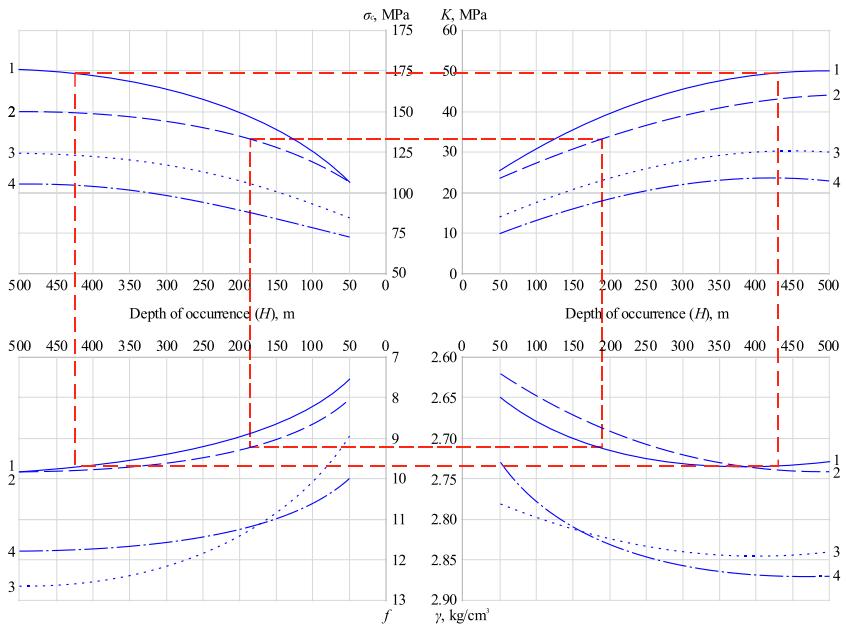

FIGURE 6 | Dependences of the rock properties on changes in the depth of their occurrence: 1, Saryoba deposit; 2, Akzhal field, 3, Sayak deposit, 4, Akbakai deposit; σc, compression strength of rocks, MPa; K, adhesion, MPa; f, rock hardness; γ, density, kg/cm^3.

dependences have been determined between the average density, adhesion, compression, hardness of rocks, and the depth of their occurrence. The curves of changes in the properties of rocks are drawn according to the averaged group indicators for the depth intervals every 5 m. To compare the results obtained at the studied object with the data of other mines, a combined graph of the relationship of rock properties has been compiled (**Figure 6**).

The curves of changes in the rock properties are drawn according to averaged indicators in a depth every 50 m. Assessment and reliability of determining the dependencies are made according to the formulas of mathematical statistics. The deviation of the calculated curves from the empirical ones ranges from 5 to 8%, and most of the curves coincide with each other. The analysis of the data also shows

TABLE 2 | Results of measuring the natural stresses in the Saryoba deposit.

Depth from the daylight surface, *H*, m	Average stress values, MPa*			Sum of horizontal stresses, ($\sigma_x + \sigma_y$), MPa
	σ_x	σ_y	$\sigma_z = \sigma H$	σ_x
60	5.2	3.3	60	5.2
60	5.0	3.2	60	5.0
120	7.8	4.4	120	7.8
120	6.3	5.7	120	6.3
180	9.1	6.6	180	9.1
180	10.5	5.1	180	10.5
240	12.1	7.1	240	12.1
240	14.0	5.1	240	14.0
240	13.7	5.3	240	13.7
300	12.2	10.4	300	12.2
300	14.0	9.0	300	14.0
300	13.8	8.8	300	13.8
260	8.6	6.3	260	8.6
280	9.0	6.5	280	9.0
300	10.2	7.3	300	10.2
460	14.8	10.4	460	14.8
460	17.1	8.6	460	17.1
460	18.5	7.3	460	18.5
500	20.1	10.1	500	20.1
500	20.5	10.6	500	20.5
500	20.7	10.7	500	20.7

*σ_x is average value of the normal stress acting in the meridional direction; σ_y is average value of the normal stress acting in the latitudinal direction; σ_z is average value of the stress acting in the vertical direction.

that the strength properties of rocks change noticeably with the depth of their occurrence.

Based on the research performed, quantitative and qualitative characteristics of the rock properties in a number of deposits, including the Saryoba deposit, have been obtained. These characteristics will be used to solve a number of technical problems in open pits and underground mines, to assess the stability of benches and open-pit slopes, design pillars and limiting floor pillars, as well as to generalize the results of instrumental observations and understand the physical nature of the displacement process.

Studying the Physical–Mechanical Properties and Stress–Strain State of the Mass

The results of measuring the natural stresses in the Saryoba deposit according to the geodetic observation (3-block) are given in **Table 2**.

When analyzing **Table 2** and the results of determining the natural stresses obtained for other mines, one cannot fail to notice the following peculiarities of the horizontal stresses distributed in the rock mass. Firstly, the horizontal stresses exceed vertical ones in terms of their values. Secondly, at equal depths from the daylight surface in hard rocks, horizontal stresses have higher values than in relatively weak rocks. Thirdly, the vertical stresses are on average close to the value of σH, regardless of the rock strength. Thus, all types of stresses change with depth, especially the sum of values of horizontal stresses ($\sigma_x + \sigma_y$) changes according to a certain pattern, and this is clearly seen from **Figure 7**.

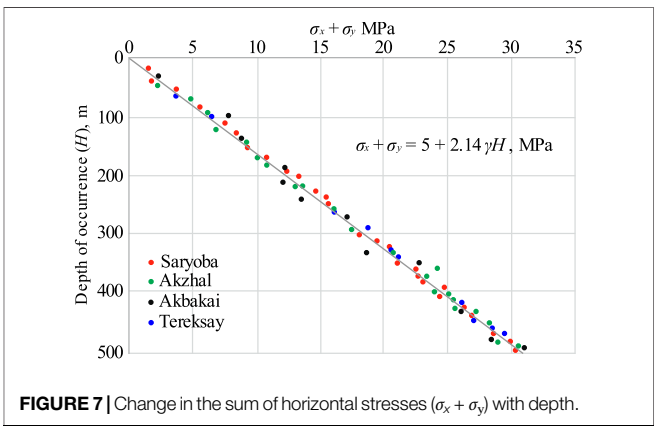

FIGURE 7 | Change in the sum of horizontal stresses ($\sigma_x + \sigma_y$) with depth.

According to **Figure 7**, the correlation between stress and depth is straight-line. The correlation coefficient of the relationship is $R = 0.92$. Accordingly, the correlation relationship can be determined by the following formula:

$$Y = a + bX \tag{4}$$

where Y is the sum of principal horizontal stresses, (σ_x+σ_y); x is the mining depth, H; a and b are parameters of equations.or

$$\sigma_x + \sigma_y = 5 + 0.06 \cdot H, \text{MPa} \tag{5}$$

If to focus on **Formula (4)**, then normal stresses are also related to the bulk density of rocks. Then, **Formula (5)** has the following form:

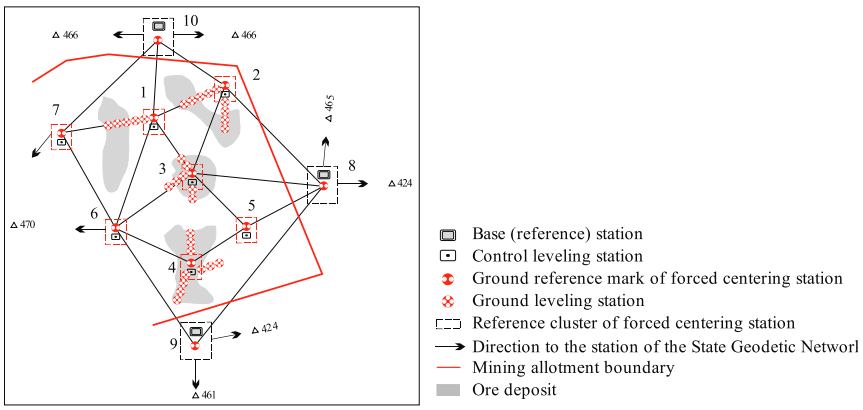

FIGURE 8 | Scheme of the observational network at the geodynamic test.

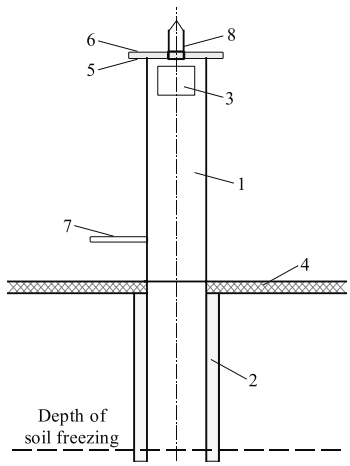

FIGURE 9 | Ground-based FCS construction: 1, metal pipe; 2, concreted lower part; 3, window for setting the device; 4 is earth surface; 5, first metal platform; 6, station center; 7, second metal platform; 8, sighting mark.

$$\sigma_x + \sigma_y = 5 + 2.14\gamma H, \text{MPa} \quad (6)$$

where γ is average bulk density 2.8 t/m^3; H is the depth of the daylight surface, m.

The graphical-analytical dependences obtained as a result of the performed research make it possible to give a qualitative and quantitative assessment of changes in the properties of rocks. There is a stable correlation between the indicators. With some known indicators, it seems possible to determine others using graphs, thereby opening up the possibility of predicting the properties of rocks within the deposits. The initial data for this are the names of the rocks, their depth of occurrence, and individual characteristics, such as the specific density of rocks and others, the determination of which does not require labor-intensive laboratory studies.

Based on the research performed, quantitative and qualitative characteristics of the rock properties in a number of deposits, including the West Saryoba deposit, have been obtained. These characteristics will be used to solve a number of technical problems in open pits and underground mines, in assessing the stability of benches and open-pit sides, in calculating the pillars and limiting floor pillars, as well as to generalize the results of instrumental observations and understand the physical nature of the displacement process.

According to the 3-block of the recommended methodology, to conduct observations of the rock mass state, especially when prospecting a giant copper field, occupying a large area and consisting of several deposits, occurring in various deep horizons, it is necessary to create a high-precision geodetic substantiation. To provide a huge area, the classic option of creating geodetic networks in the fields is rather labor-intensive. It requires large financial costs for the organization and production of observations. In this regard, it is proposed to replace extended leveling lines with local geodetic constructions in the form of profile lines and check "clusters" of geodetic and leveling stations. The complex application of ground and space geodetic methods allows monitoring observations to cover the entire territory of the field, as well as to increase the efficiency of observations and reduce capital costs for their implementation.

Thus, during large-scale and long-term field development, along with geomechanical deformation processes, geodynamic processes can also develop. Therefore, when mining the deep-seated ore bodies, a geodynamic test site is created, where repeated geodetic observations are conducted (Nurpeisova et al., 2019; Nurpeisova et al., 2021).

Accordingly, for a differentiated study of geodynamic and geomechanical processes of mining the fields that occupy a large area and are intended for deep seams, it is proposed to create cluster arms at the field, consisting of base (reference), control (initial), and deformation geodetic and leveling stations. All the focal stations are located in accordance with ore veins and connected to the stations of the State Geodetic Network (**Figure 8**).

Instrumental observations have confirmed the labor intensity of field work, especially the transfer of a set of instruments (the instrument itself, a tripod, rods, etc.) from one station to another. In this regard, in order to install instruments and increase the speed of measuring operations, firstly, a permanent forced

centering station (FCS) has been developed and patented, which is arranged at the control station during geomechanical monitoring. Then, the device is transferred to geodetic centers for setting new instruments and signals.

A schematic representation of the ground-based FCS construction is given in **Figure 9**, which shows a ground-based permanent geodetic station of forced centering of instruments, containing a support protruding above the ground (4) with a height of 1.25 m and buried to a depth of 2.25 m below the depth of soil freezing. On the upper surface, there is a center with the given coordinates (6) for setting the device. The support is made of a metal pipe (1) with a concreted lower part and filled with local soil material. At the upper pipe end, there is a metal platform (5) with a universal socket and a window for setting the device (3) and sighting mark (8). On the side surface of the metal pipe, at a distance of 1 m from the upper platform, a second metal platform is set for the high-elevation reference mark (7), and the lower end of the pipe is equipped with an anchor.

The purpose of the invention is to improve the accuracy of centering, as well as to increase the efficiency of measurements in the absence of a tripod at the stations of setting and observation. The new device allows for quick and accurate centering, as well as eliminates the need for tripods.

Thus, on the basis of the performed GPS measurements, mine surveying services and observation stations of mines in Central Kazakhstan have been provided with control stations, the coordinates of which are determined with high accuracy. Observations of the absolute deformations of the sides at the studied objects have been conducted on the profile lines of the observation station with devices of a new generation.

The planned coordinates and preliminary heights of these stations have been determined by the satellite method using a geodetic satellite receiver Leica GS16 3.75G. The final heights of the reference marks have been determined by the method of geometric leveling of the II class using a Trimble Dini03 digital leveling laser and barcode rails. The coordinates of stations and reference marks of the geodynamic test site will be presented after their adjustment in a single system of coordinates and the Baltic height.

CONCLUSION

Based on the performed analysis in the field of studying geomechanical and geodynamic processes, as well as means of observing the deformations, an integrated methodology for conducting geomonitoring with the use of modern high-precision geodetic instruments and developed methods for their control has been developed and substantiated. The research results of geomechanical and geodynamic processes will allow for the strategic and operational management of mining operations to ensure maximum safety and economic efficiency. The practical use of the results is possible for Central Kazakhstan deposits. In the future, the research will be continued to study the possibility of applying the results obtained to other Zhilandinskaya Group deposits.

The scientific novelty of the presented research is in determining the pattern of changes in the structural peculiarities and strength properties of rocks with the depth of their occurrence, which makes it possible to predict the stress–strain state of the rock mass.

The geological, structural, and tectonic peculiarities of a giant copper deposit in Kazakhstan are presented. The possibility of predicting the physical–mechanical properties and stress–strain state of the rock mass has been substantiated. The results obtained have been compared with the results of similar works by other authors, and they make it possible to conclude that the obtained regression equations are quite reliable (correlation coefficient $R = 0.92$).

The modern approach to the formulation and implementation of observations of geodynamic and geomechanical processes in solid mineral deposits has been analyzed. A new "cluster" method for constructing geodetic observation systems at a geodynamic test site has been substantiated, which makes it possible to perform monitoring control coverage of mining operations, as well as to increase the efficiency of observations and reduce the costs of their implementation.

In order to set high-precision electronic and laser devices during the geomonitoring of the earth's surface, a method has been developed for setting permanent forced centering stations, which make it possible to ensure the speed and accuracy of centering, as well as to exclude the use of tripods. It is proposed to conduct surveys using modern geodetic instruments, such as satellite technologies, and electronic and digital geodetic instruments.

DATA AVAILABILITY STATEMENT

The original contributions presented in the study are included in the article/Supplementary Material, further inquiries can be directed to the corresponding authors.

AUTHOR CONTRIBUTIONS

Conceptualization, KR, MN and GK; methodology, KR and GK; software, VL and TT; validation, KR and GK; formal analysis, VL and TT; investigation, MN and GK; resources, OB and VL; data curation, KR and MN; writing-original draft preparation, KR, MN and GK; writing-review and editing, KR, MN, GK and VL; visualization, OB, VL and TT; supervision, KR and MN; project administration, OB and KR; funding acquisition, OB. All authors have read and agreed to the published version of the manuscript.

FUNDING

This study was carried out as part of the project "Belt and Road Initiative Institute for Chinese-European studies (BRIICES)" and was funded by the Guangdong University of Petrochemical Technology.

ACKNOWLEDGMENTS

The authors express their gratitude to the reviewers for valuable recommendations that have been taken into account to significantly

improve the quality of this paper. The research has been carried out in the framework of the implementation of a research project supported by the Science Committee of the Ministry of Education and Science of the Republic of Kazakhstan (grant No. AP08857097).

REFERENCES

Abdiev, A., Mambetova, R., Abdiev, A., and Abdiev, S. (2020). Development of Methods for Assessing the Mine Workings Stability. *E3s Web Conf.* 201, 01040. doi:10.1051/e3sconf/202020101040

Adushkin, V. V. (2018). Technogenic Tectonic Seismicity in Kuzbass. *Russ. Geology. Geophys.* 59 (5), 571–583. doi:10.1016/j.rgg.2018.04.010

Aitkazinova, S. K., Nurpeisova, M. B., Kirgizbaeva, G. M., and Milev, I. (2014). Geomechanical Monitoring of the Massif of Rocks at the Combined Way of Development of fields. *Int. Multidisciplinary Scientific GeoConference Surv. Geology. Mining Ecol. Manag.* 2 (2), 79–292.

Aitkazinova, S., Soltabaeva, S., Kyrgizbaeva, G., Rysbekov, K., and Nurpeisova, M. (2016). Methodology of Assessment and Prediction of Critical Condition of Natural - Technical Systems. *Scientific Geoconference Surv. Geology. Mining Ecol. Manag. SGEM* 2, 3–10. doi:10.5593/sgem2016/b22/s09.001

Ali Elbeblawi, M. M., Abdelhak Elsaghier, H. A., Mohamed Amin, M. T., and Elrawy Abdellah, W. R. (2021). Surface Mining Methods and Systems. *Top. Mining, Metall. Mater. Eng.*, 289–333. doi:10.1007/978-981-16-3568-7_8

Amemoutou, A., Martínez-Garzón, P., Kwiatek, G., Rubinstein, J. L., and Bohnhoff, M. (2021). Earthquake Source Mechanisms and Stress Field Variations Associated with Wastewater-Induced Seismicity in Southern Kansas, USA. *J. Geophys. Res. Solid Earth* 126 (7), e2020JB021625. doi:10.1029/2020jb021625

Babets, D. V., Sdvyzhkova, O. O., Larionov, M. H., and Tereshchuk, R. M. (2017). Estimation of Rock Mass Stability Based on Probability Approach and Rating Systems. *Naukovyi Visnyk Natsionalnoho Hirnychoho Universytetu* (2), 58–64.

Babets, Y., Terekhov, Y., Mormul, T., Melnikova, I., and Komirna, V. (2021). Environmental and Economic Assessment of the Possibilities to Increase the Land Preservation Level in Terms of Open-Pit Mining. *E3s Web Conf.* 280, 11002. doi:10.1051/e3sconf/202128011002

Bazaluk, O., Petlovanyi, M., Zubko, S., Lozynskyi, V., and Sai, K. (2021). Instability Assessment of Hanging Wall Rocks during Underground Mining of Iron Ores. *Minerals* 11 (8), 858. Available from: https://doi.org10.3390/min11080858. doi:10.3390/min11080858

Begalinov, A., Khomiakov, V., Serdaliyev, Y., Iskakov, Y., and Zhanbolatov, A. (2020). Formulation of Methods Reducing Landslide Phenomena and the Collapse of Career Slopes during Open-Pit Mining. *E3s Web Conf.* 168, 00006. doi:10.1051/e3sconf/202016800006

Begalinov, A., Almenov, T., Zhanakova, R., and Bektur, B. (2020). Analysis of the Stress Deformed State of Rocks Around the Haulage Roadway of the Beskempir Field (Kazakhstan). *Min. Miner. Depos.* 14 (3), 28–36. doi:10.33271/mining14.03.028

Bekbergenov, D., Jangulova, G., Kassymkanova, K.-K., and Bektur, B. (2020). Mine Technical System with Repeated Geotechnology within New Frames of Sustainable Development of Underground Mining of Caved Deposits of the Zhezkazgan Field. *Geodesy and Cartography* 46 (4), 182–187. doi:10.3846/gac.2020.10571

Bitimbaev, M. Z., Krupnik, L. A., Krupnik, L. A., Aben, E. K., and Aben, K. K. (2017). Adjustment of Backfill Composition for mineral Mining under Open Pit Bottom. *Gornyi Zhurnal* (2), 57–61. doi:10.17580/gzh.2017.02.10

Bondarenko, V., Symanovych, G., and Koval, O. (2012). The Mechanism of Over-coal Thin-Layered Massif Deformation of Weak Rocks in a Longwall. *Geomechanical Process. During Underground Mining*, 41–44. doi:10.1201/b13157-8

Burmin, V. Y., and Shumlianska, L. O. (2017). Spatial Distribution of Earthquake Hypocenters in the Crimea-Black Sea Region. *J. Seismol* 22 (2), 391–405. doi:10.1007/s10950-017-9712-y

Buzylo, V., Pavlychenko, A., Savelieva, T., and Borysovska, O. (2018). Ecological Aspects of Managing the Stressed-Deformed State of the Mountain Massif during the Development of Multiple Coal Layers. *E3s Web Conf.* 60 (60), 00013. doi:10.1051/e3sconf/20186000013

Cherniaiev, O. V. (2017). Systematization of the Hard Rock Non-metallic mineral Deposits for Improvement of Their Mining Technologies. *Naukovyi Visnyk Natsionalnoho Hirnychoho Universytetu* (5), 11–17.

Cheskidov, V., Kassymkanova, K.-K., Lipina, A., and Bornman, M. (2019). Modern Methods of Monitoring and Predicting the State of Slope Structures. *E3s Web Conf.* 105, 01001. doi:10.1051/e3sconf/201910501001

Dagdelen, K., and Traore, I. (2018). Open Pit Transition Depth Determination through Global Analysis of Open Pit and Underground Mine Production Scheduling. *Adv. Appl. Strateg. Mine Plann.*, 287–296. doi:10.1007/978-3-319-69320-0_19

Dryzhenko, A., Moldabayev, S., Shustov, A., Adamchuk, A., and Sarybayev, N. (2017). Open Pit Mining Technology of Steeply Dipping mineral Occurences by Steeply Inclined Sublayers. *Int. Multidisciplinary Scientific GeoConference Surv. Geology. Mining Ecol. Manag. SGEM* 17 (13), 599–606. doi:10.5593/sgem2017/13/s03.076

Du, W., and Xing, Z.-g. (2017). Study on the Weight Coefficient Influence of Surface Water on the Stability of Open-Pit Dump. Comparative Analysis of 6 Degree Seismic Simulation. *Vibroengineering Proced.* 11 (11), 85–90. doi:10.21595/vp.2017.18535

Dychkovskyi, R., Vladyko, O., Vladyko, O., Maltsev, D., and Cáceres Cabana, E. (2018). Some Aspects of the Compatibility of mineral Mining Technologies. *Rudarsko-geološko-naftni zbornik* 33 (4), 73–82. doi:10.17794/rgn.2018.4.7

Field, E. H. (2007). Overview of the Working Group for the Development of Regional Earthquake Likelihood Models (RELM). *Seismological Res. Lett.* 78 (1), 7–16. doi:10.1785/gssrl.78.1.7

Fleurisson, J.-A. (2012). Slope Design and Implementation in Open Pit Mines: Geological and Geomechanical Approach. *Proced. Eng.* 46, 27–38. doi:10.1016/j.proeng.2012.09.442

Gerasymenko, O. O., Shumlyanska, L. O., Nadezhka, L. I., Pivovarov, S. P., Ganiev, O. Z., Ostapchuk, N. M., et al. (2020). Neural Network Modeling in the Problem of Localization Earthquake of Ukraine. *Geofizicheskiy Zhurnal* 42 (2), 86–98. doi:10.24028/gzh.0203-3100.v42i2.2020.201743

Golik, V. I., Komashchenko, V. I., Komashchenko, V. I., Morkun, V. S., Morkun, N. V., and Hryshchenko, S. M. (2018). Energy Saving in Mining Production. *Sci. Innov.* 14 (3), 29–39. doi:10.15407/scine14.03.029

Haiko, H., Saik, P., and Lozynskyi, V. (2019). The Philosophy of Mining: Historical Aspect and Future Prospect. *Philos. Cosmology* 22, 76–90. doi:10.29202/philcosm/22/6

Jiang, S., Lian, M., Lu, C., Gu, Q., Ruan, S., and Xie, X. (2018). Ensemble Prediction Algorithm of Anomaly Monitoring Based on Big Data Analysis Platform of Open-Pit Mine Slope. *Complexity* 2018, 1–13. doi:10.1155/2018/1048756

Karatayev, M., and Clarke, M. L. (2014). Current Energy Resources in Kazakhstan and the Future Potential of Renewables: A Review. *Energ. Proced.* 59, 97–104. doi:10.1016/j.egypro.2014.10.354

Kharisov, T. F. (2018). Problem of Assessment of the Safety Factor of the Open-Pit Sides. *Problemy nedroispolzovaniya* 3 (18), 108–118.

Kim, D., Langley, R. B., Bond, J., and Chrzanowski, A. (2003). Local Deformation Monitoring Using GPS in an Open Pit Mine: Initial Study. *GPS Solutions* 7 (3), 176–185. doi:10.1007/s10291-003-0075-1

Krichevsky, S. (2016). New Model of Evolution of Technologies and Prospects of Research with Using Big Data. *Philos. cosmology* (17), 118–135.

Krylova, L. Y. (1978). Exploration Significance of Iodine Distribution in the Bedrock and Weathering Crust of the Maykain deposit. *Int. Geology. Rev.* 20 (3), 357–361. doi:10.1080/00206817809471394

Kyrgizbayeva, G., Nurpeisov, M., and Sarybayev, O. (2015). The Monitoring of Earth Surface Displacements during the Subsoil Development. *New Dev. Mining Eng.* 2015, 161–167. doi:10.1201/b19901-30

Lozynskyi, V., Medianyk, V., Saik, P., Rysbekov, K., and Demydov, M. (2020). Multivariance Solutions for Designing New Levels of Coal Mines. *Rudarsko-geološko-naftni zbornik* 35 (2), 23–31. doi:10.17794/rgn.2020.2.3

Łukasz, B. (2020). Interpretation of the Results of Mechanical Rock Properties Testing with Respect to Mining Methods. *Acta Montanistica Slovaca* 25, 81–93. doi:10.46544/AMS.v25i1.8

Malanchuk, Z., Moshynskyi, V., Malanchuk, Y., Korniienko, V., and Koziar, M. (2020). Results of Research into the Content of Rare Earth Materials in Man-Made Phosphogypsum Deposits. *Key Eng. Mater.* 844 (844), 77–87. doi:10.4028/www.scientific.net/kem.844.77

Malanchuk, Z., Zaiets, V., Tyhonchuk, L., Moshchych, S., Gayabazar, G., and Dang, P. T. (2021). Research of the Properties of Quarry Tuff-Stone for Complex Processing. *E3s Web Conf.* 280 (280), 01003. doi:10.1051/e3sconf/202128001003

Masloboev, V., Makarov, D., Makarov, D., and Klyuchnikova, E. (2021). Sustainable Development of the Mining Complex of the Murmansk Region: Minimization of Man-Made Impacts on the Environment. *Sustainable Dev. Mountain Territories* 13 (2), 188–200. doi:10.21177/1998-4502-2021-13-2-188-200

Mikhailova, N. N., and Uzbekov, A. N. (2018). Tectonic and Technogenic Earthquakes in central Kazakhstan. *News Natl. Acad. Sci. Republic Kazakhstan, Ser. Geology. Tech. Sci.* 3 (429), 146–155.

Mikhailova, N. N., and Uzbekov, A. N. (2018). Tectonic and Technogenic Earthquakes in Central Kazakhstan. *News Natl. Acad. Sci. Republic Kazakhstan* (429), 137–145.

Moldabayev, S., Adamchuk, A., Sarybayev, N., and Shustov, A. (2019). Improvement of Open Cleaning-Up Schemes of Border Mineral Reserves. *Mineral. Reserves. Int. Multidisciplinary Scientific GeoConference* 19, 331–338. doi:10.5593/sgem2019/1.3/s03.042

Mora, S., and Keipi, K. (2006). Disaster Risk Management in Development Projects: Models and Checklists. *Bull. Eng. Geol. Environ.* 65 (2), 155–165. doi:10.1007/s10064-005-0022-1

Moshynskyi, V., Malanchuk, Z., Tsymbaliuk, V., Malanchuk, L., Zhomyruk, R., and Vasylchuk, O. (2020). Research into the Process of Storage and Recycling Technogenic Phosphogypsum Placers. *Min. Miner. Depos.* 14 (2), 95–102. doi:10.33271/mining14.02.095

Nurpeisova, M. B., and Kurmanbaev, O. S. (2016). Laws of Devolopment of Geomechanical Processes in the Rock Mass Maykain Mine. *News Natl. Acad. Sci. Republic Kazakhstan, Ser. Geology. Tech. Sci.* 6 (420), 109–115.

Nurpeisova, M. B., Sarybaiev, O. A., and Kurmanbaiev, O. S. (2016). Study of Regularity of Geomechanical Processes Development while Developing Deposits by the Combined Way. *Naukovyi Visnyk Natsionalnoho Hirnychoho Universytetu* (4), 30–36.

Nurpeisova, M., Donenbaeva, N., and Bek, A. (2019). Devepolment of Geodetic Methods of Monitoring of Open-Pit Sides Stability. *Biosci. Biotechnol. Res. Commun.*, 67–78.

Nurpeisova, M. B., Umirbaeva, A. B., Fedorov, E. V., and Miletenko, N. A. (2021). Assessment of Deformed and Radiological State Territory Based on Integrated Monitoring. *Eurasian Mining*, 83–87. doi:10.17580/em.2021.01.17

Nurpeissova, M., Bekbassarov, S., Bek, A., Kyrgizbaeva, G., Turisbekov, S., and Ormanbekova, A. (2020). The Geodetic Monitoring of the Engineering Structures Stability Conditions. *J. Eng. Appl. Sci.* 12 (11), 9151–9163. doi:10.3923/jeasci.2017.9151.9163

Oparin, V. N. (2015). Sovremennye Dostizheniya Geotekhniki Dlya Postroeniya Monitoringovykh Sistem Geomekhaniko-Geodinamicheskoy Bezopasnosti Na Gornodobyvayushchikh Predpriyatiyakh. *Fiziko-tekhnicheskie problemy razrabotki poleznykh iskopaemy* (2), 6–15.

Pavlychenko, A., and Kovalenko, A. (2013). The Investigation of Rock Dumps Influence to the Levels of Heavy Metals Contamination of Soil. *Annu. Scientific-Technical Collection*, 237–238. doi:10.1201/b16354-43

Petlovanyi, M., Lozynskyi, V., Saik, P., Sai, K., and Sai, K. (2019). The Influence of Geology and Ore deposit Occurrence Conditions on Dilution Indicators of Extracted Reserves. *Rudarsko-geološko-naftni zbornik* 34 (1), 83–91. doi:10.17794/rgn.2019.1.8

Rakhmangulov, A., Burmistrov, K., and Osintsev, N. (2021). Sustainable Open Pit Mining and Technical Systems: Concept, Principles, and Indicators. *Sustainability* 13 (3), 1101. doi:10.3390/su13031101

Rakhmangulov, A., Sladkowski, A., Sladkowski, A., Osintsev, N., and Muravev, D. (2017). Green Logistics: Element of the Sustainable Development Concept. Part 1. *Naše more* 64 (3), 120–126. doi:10.17818/nm/2017/3.7

Rebetskiy, Yu. L., Sim, L. A., and Kozyrev, A. A. (2017). O Vozmozhnom Mekhanizme Generatsii Izbytochnogo Gorizontal'nogo Szhatiya Rudnykh Uzlov Kol'skogo Poluostrova (Khibiny, Lovozero, Kovdor). *Geology. Ore Deposits* 59 (4), 263–280. doi:10.7868/s0016777017040049

Rozin, V. (2021). From Engineering and Technological Process to Post-Cultural Technology. *Fhi* 15, 99–109. doi:10.29202/fhi/15/9

Ryl'nikova, M. V., Yun, A. B., Terent'yeva, I. V., and Esina, E. N. (2016). Vospolnenie Vybyvayushchikh Moshchnostey Rudnikov Na Stadii Dorabotki Balansovykh Zapasov Mestorozhdeniya-Uslovie Ekologicheski Sbalansirovannogo Razvitiya Zhezkazganskogo Regiona. *Mine Surv. Bull.* (5), 6–10. doi:10.3846/gac.2020.10571

Rysbekov, K., Huayang, D., Huayang, D., Kalybekov, T., Sandybekov, M., Idrissov, K., et al. (2019). Application Features of the Surface Laser Scanning Technology when Solving the Main Tasks of Surveying Support for Reclamation. *Min. Miner. Depos.* 13 (3), 40–48. doi:10.33271/mining13.03.040

Sach, V. J., Buchner, E., and Schmieder, M. (2020). Enigmatic Earthquake-Generated Large-Scale Clastic Dyke in the Biberach Area (SW Germany). *Sediment. Geology.* 398, 105571. doi:10.1016/j.sedgeo.2019.105571

Sarybayev, O., Nurpeisova, M., Kyrgizbayeva, G., and Toleyov, B. (2015). Rosk Mass Assessment for Man-Made Disaster Risk Management. *New Dev. Mining Eng.* 2015, 403–409. doi:10.1201/b19901-70

Satpaev, K. I. (1962). Osnovnye Rezul'taty Kompleksnogo Geologicheskogo Izucheniya I Voprosy Genezisa Dzhezkazgana. *Geologiya rudnykh mestorozhdenii* 3, 1–14.

Sobko, B., Lozhnikov, O., and Drebenshtedt, C. (2020). Investigation of the Influence of Flooded Bench Hydraulic Mining Parameters on Sludge Pond Formation in the Pit Residual Space. *E3s Web Conf.* 168, 00037. doi:10.1051/e3sconf/202016800037

Stacey, T. R., Xianbin, Y., Armstrong, R., and Keyter, G. (2003). New Slope Stability Considerations for Deep Open Pit Mines. *J. South. Afr. Inst. Mining Metall.* 103 (6), 373–389.

Stupnik, M., Kolosov, V., Kalinichenko, V., and Pismennyi, S. (2014). Physical Modeling of Waste Inclusions Stability during Mining of Complex Structured Deposits. *Progressive Tech. Coal, Coalbed Methane, Ores Mining*, 25–30. doi:10.1201/b17547

Stupnik, M., Kolosov, V., Pysmennyi, S., and Kostiantyn, K. (2019). Selective Mining of Complex Stuctured Ore Deposits by Open Stope Systems. *E3s Web Conf.* 123, 01007. doi:10.1051/e3sconf/201912301007

Ursul, A., and Ursul, T. (2018). Environmental Education for Sustainable Development. *Fhi* 9, 115–125. doi:10.29202/fhi/9/12

Viktorov, S. D., Iofis, M. A., and Odintsev, V. N. (2005). Razrushenie Gornykh Porod I Risk Tekhnogennykh Katastrof. *Gornyi Zhurnal* 4, 30–35.

Waloski, R., Korzeniowski, W., Bołoz, Ł., and Rączka, W. (2021). Identification of Rock Mass Critical Discontinuities while Borehole Drilling. *Energies* 14, 2748. doi:10.3390/en14102748

Whittle, D., Brazil, M., Grossman, P. A., Rubinstein, J. H., and Thomas, D. A. (2018). Combined Optimisation of an Open-Pit Mine Outline and the Transition Depth to Underground Mining. *Eur. J. Oper. Res.* 268 (2), 624–634. doi:10.1016/j.ejor.2018.02.005

Zeylik, B., Arshamov, Y., Baratov, R., and Bekbotayeva, A. (2021). New Technology for mineral Deposits Prediction to Identify Prospective Areas in the Zhezkazgan Ore Region. *Min. Miner. Depos.* 15 (2), 134–142. doi:10.33271/mining15.02.134

Zhanakova, R., Pankratenko, A., Almenov, T., and Bektur, B. (2020). Rational Selection of the Form of Support for the Formation of Genetic Composition of Rocks in the Conditions of the Beskempir Field. *NATIONAL ACADEMY SCIENCES REPUBLIC KAZAKHSTAN Inst.itute of Plant Biology and Biotechnology* 1, 106–113. doi:10.32014/2020.2518-170x.13

Zhironkin, S., and Cehlár, M. (2021). Coal Mining Sustainable Development: Economics and Technological Outlook. *Energies* 14, 5029. doi:10.3390/en14165029

Zhironkin, S., and Szurgacz, D. (2021). Mining Technologies Innovative Development: Economic and Sustainable Outlook. *Energies* 14, 8590. doi:10.3390/en14248590

Conflict of Interest: The authors declare that the research was conducted in the absence of any commercial or financial relationships that could be construed as a potential conflict of interest.

Publisher's Note: All claims expressed in this article are solely those of the authors and do not necessarily represent those of their affiliated organizations, or those of the publisher, the editors and the reviewers. Any product that may be evaluated in this article, or claim that may be made by its manufacturer, is not guaranteed or endorsed by the publisher.

frontiers | Frontiers in Earth Science

ORIGINAL RESEARCH
published: 30 June 2022
doi: 10.3389/feart.2022.921521

The Tectonic Map and Structural Provinces of the Late Neoproterozoic Egyptian Nubian Shield: Implications for Crustal Growth of the Arabian–Nubian Shield (East African Orogen)

Zakaria Hamimi[1,2], *Wael Hagag*[1], *Harald Fritz*[3], *Haitham Baggazi*[4] *and Samir Kamh*[5]*

[1]Geology Department, Faulty of Science, Benha University, Benha, Egypt, [2]Department of Geological Sciences, Faculty of Science, Galala University, New Galala City, Egypt, [3]Department of Earth Sciences, University of Graz, Graz, Austria, [4]Structural Geology and Remote Sensing Department, Faculty of Earth Sciences, King Abdulaziz University, Jeddah, Saudi Arabia, [5]Geology Department, Faculty of Science, Tanta University, Tanta, Egypt

OPEN ACCESS

Edited by:
Ahmed M. Eldosouky,
Suez University, Egypt

Reviewed by:
Mohamed Abdelkareem,
South Valley University, Egypt
Islam Abou El-Magd,
National Authority for Remote Sensing and Space Sciences, Egypt
Nivaldo Destro,
Petrobras, Brazil

***Correspondence:**
Samir Kamh
skamh@science.tanta.edu.eg

Specialty section:
This article was submitted to Structural Geology and Tectonics, a section of the journal Frontiers in Earth Science

Received: 16 April 2022
Accepted: 13 May 2022
Published: 30 June 2022

Citation:
Hamimi Z, Hagag W, Fritz H, Baggazi H and Kamh S (2022) The Tectonic Map and Structural Provinces of the Late Neoproterozoic Egyptian Nubian Shield: Implications for Crustal Growth of the Arabian–Nubian Shield (East African Orogen). Front. Earth Sci. 10:921521. doi: 10.3389/feart.2022.921521

The Late Neoproterozoic Egyptian Nubian Shield (ENS) has attracted increasing attention since the establishment of the Egyptian Geological Survey and Mining Authority (EGSMA (1896)), which conducted the first mapping. In the last three decades, rapid improvements in analytical techniques, along with field-oriented studies, have made it possible for the interpretation of the ENS as an integral part of the juvenile Arabian–Nubian Shield (ANS) as a portion of the East African Orogen (EAO). However, a consistent tectonic map of the ENS does not exist. Presentation of such a map is the main objective of the present work where Landsat-based lithological discrimination is combined with the systematic structural investigation and careful reassessment of previously published geological maps. Our interpretation of this map indicates that in accordance with previous work, the basement units of the Eastern Desert (ED) can be divided into three structural domains: Northern, Central, and South-Eastern Desert provinces. The proposed provinces are ascribed to three different plate tectonic far-field boundary conditions. The earliest magmatic, metamorphic, and tectonic history was set off by the approximate north–south convergence of the Gabgaba-Gebeit, Jiddah-Asir terranes, and Eastern Desert-Midyan terranes along the Yanbo-Onib-Sol-Hamid-Gerf-Allaqi-Heiani (YOSHGAH) suture between c. 800 and 620 Ma. The second event between c. 640 and 580 Ma was correlated with the Nabitah Orogeny when the Ad Dawadimi-Ar Rayn terranes in the eastern Arabian Shield accreted to the earlier consolidated arc terranes (Afif and Tathlith terranes). During this period, east–west convergence between northwestern Saudi Arabia and the Central Eastern Desert (CED) in Egypt caused a pronounced strike-slip deformation associated with the displacement along the wider Najd Fault system. The third orogenic phase, which was younger than c. 580 Ma, was controlled by the evolution and retreat of the Cadomian Arc. The northern portions of the ENS and the northern

Arabian Shield experienced extension whereas extensive post-orogenic magmatism was related to mantle delamination and associated crustal thinning.

Keywords: Egyptian Nubian Shield, tectonic map, structural provinces, far-field stresses, flow fields, remote sensing

INTRODUCTION

The Late Neoproterozoic Egyptian Nubian Shield (ENS), which includes the Eastern Desert (ED) and Sinai, is a contiguous part of the Arabian–Nubian Shield (ANS), a northern continuation of the East African Orogen (EAO) (**Figure 1**). The ANS was formed by the accretion of island arc tectonic terranes sutured along megashear zones decorated by ophiolites. The late orogenic evolution was characterized by transcurrent plate motion that developed a complex pattern of post-accretional strike-slip and extensional shear zones. The Eastern Desert (ED) is one of these tectonic terranes that demonstrated a conspicuous window of the Neoproterozoic tectonic, magmatic, and metamorphic evolution of the ANS. The Late Neoproterozoic belt of the ED was dominated by ophiolitic nappes, arc-related volcano-sedimentary sequences, and post-amalgamation molasse sediments, which all were accompanied by emplacement of various magmatic suites. From the tectonic prospective, the ED was subdivided into exhumed high-grade metamorphosed gneiss domes ("infrastructure") mantled by lower-grade metamorphosed volcano-sedimentary suites ("suprastructure"). The tectonically and magmatically related exhumation of gneissic domes was associated with the deposition of post-amalgamation molasse sediments. The rock classification and tectonic evolution of the Egyptian basement in ED were strongly premised on the infrastructural-suprastructural orogenic model (Akaad and Noweir, 1980; El-Gaby et al., 1988; Abdel Khalek et al., 1992; Khudeir and Asran, 1992). Ophiolitic nappes, arc-related metavolcanics, and volcaniclastic–metasediments constituted the suprastructural rocks (or "Tier-2" of Bennet and Mosley, 1987). These rocks were thrusted during the Neoproterozoic on the gneisses-migmatites and their remobilized equivalents that represented the infrastructural rocks (or Tier-1 of Bennet and Mosley, 1987; Abdel Khalek et al., 1992). Such a two-tier model suggested a sub-horizontal and penetrating sole thrust (infrastructure–suprastructure transition and ED decollement of Stern, 2017) that separated the lower and upper ED crustal layers.

Remarkable differences in the lithology and structural architecture of the exposed ED basement led Stern and Hedge (1985) and El-Gaby et al. (1988) to subdivide ED into three tectonic provinces: North Eastern Desert (NED), Central Eastern Desert (CED), and South Eastern Desert (SED) (**Figure 2A**). The NED province comprises voluminous granitic intrusions with some exposures of island arc metavolcanics, metasediments, and Hammamat Molasse sediments. In contrast, the CED province is dominated by arc metavolcanics, metasediments, and ophiolitic nappes, which were associated with some gneissic domal structures delineated by transcurrent shear zones (Fritz et al., 1996; Bregar et al., 2002). The SED province is generally composed of complex areas of migmatitic gneisses, foliated granodiorites, and high-grade schistose-metasediments (El-Gaby et al., 1988; Hermina et al., 1989). These provinces were believed to be juxtaposed along major shear zones. The Qena-Safaga shear zone separated the NED from CED, and the Idfu-Mersa Alam shear zone separated the CED from SED. Furthermore, the northerly dipping Nugrus-Shait shear zone was considered to be the tectonic boundary between CED and SED (Fowler and Osman, 2009). One of the objectives of the present study is to expand this model and explain the lithological and structural differences using the differences in the plate motions of the involved plates.

The infracrustal-supracrustal orogenic model and tripartite classification of the ED have been generally agreed upon by the scientific community for decades. However, the studies remained descriptive with little potential for clarifying the causes. Structural, tectonic, and isotopic data have newly been released in the form of comprehensive reviews focused on the tectonic evolution of the ED (Greiling et al., 1994; Johnson et al., 2011; Fritz et al., 2013; Stern, 2017; Hamimi et al., 2019; Hamimi and Abd El-Wahed, 2020; El-Kalioubi et al., 2020; Fowler and Hamimi, 2020; Stern and Ali, 2020). In addition, modern platetectonic reconstructions (Collins et al., 2021a; Collins et al., b) provide a far-field tectonic framework for EAO that inspired questions on the credibility of these old basement models and classifications. In the present study we develop a new tectonic map of ENS that incorporates these new studies. The main objective of the present work is the development of such a tectonic map based on intensive field/structural work and processing and analysis of the images of optical sensors by remote sensing techniques (15 Landsat-8 OLI/TIRS images, **Figure 2B**). We also reexamine and upgrade the previous maps published by EGSMA, CONOCO, and other research works and projects. ENS is a typical example of well-exposed crystalline basement rocks suitable to apply Landsat-8 data for geological and structural mapping. The structural succession and distribution of the characteristic rock assemblages extracted from this map are further used to establish a tectonic model of the ED. The differences in structural associations within the different ED domains are explained and the differences in the plate motions of involved plates ("far-field stress") and partitioned deformation along major high strain zones ("local response").

TECTONOSTRATIGRAPHY OF THE ENS

The ENS includes a vast tract of igneous and metamorphic rock complexes (about 100,000 km^2) exposed along the Red Sea Hills in the ED and occupies a triangular area in Southern Sinai (**Figures 2A, B**). It lies in the northwestern part of the ANS and is composed mainly of a juvenile continental crust of the Neoproterozoic age. The Egyptian basement complex comprises

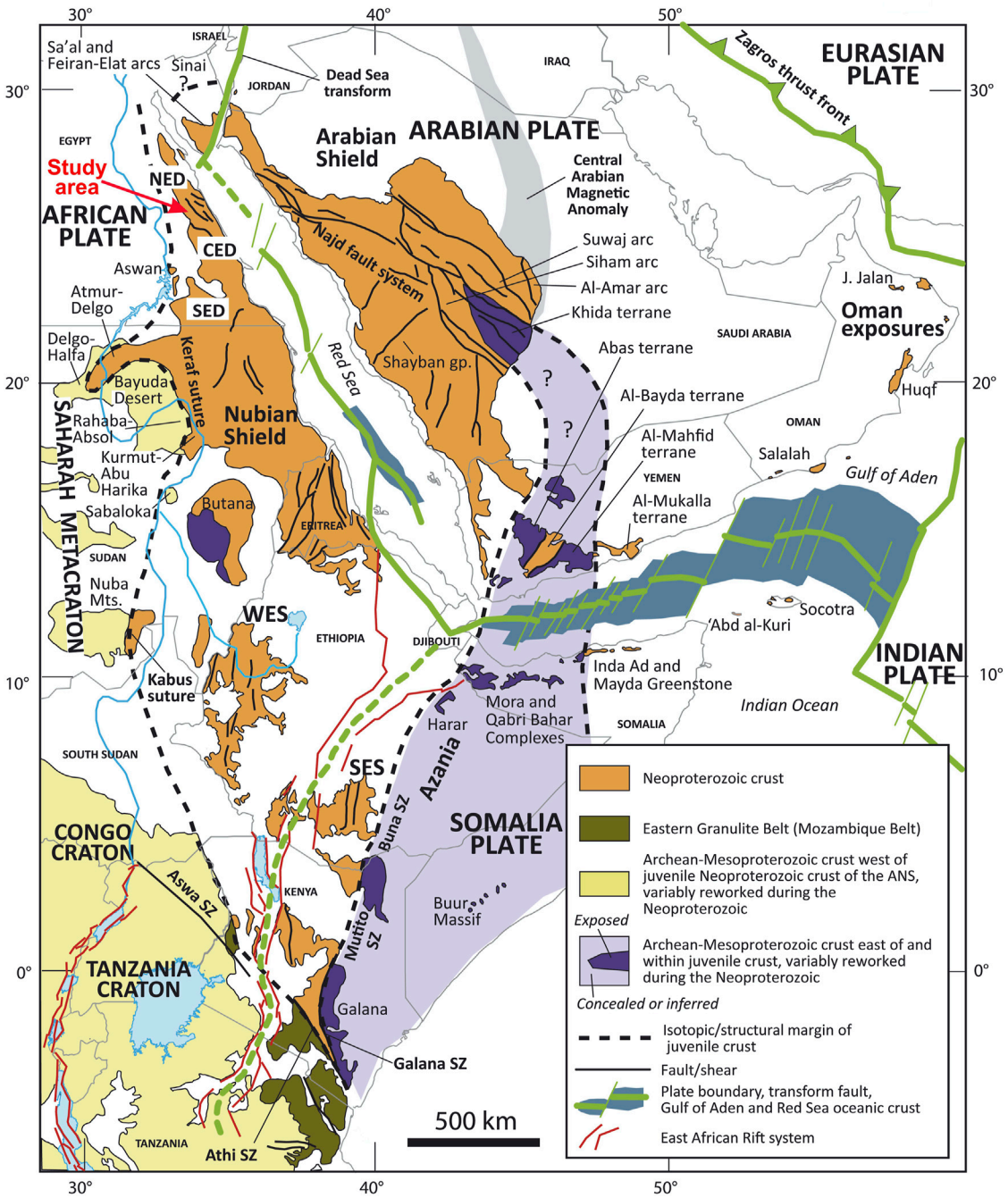

FIGURE 1 | Map of Northeast Africa and the Arabian Peninsula showing the distribution of juvenile Neoproterozoic crust and adjacent regions of Archean-Mesoproterozoic crust (after Fritz et al., 2013) and Cenozoic plate boundaries, Red Sea-Gulf of Aden spreading centers, and the East African Rift system (after Johnson, 2021). CED = Central Eastern Desert; NED = North Eastern Desert; SED = South Eastern Desert; SES = South Ethiopian shield; WES = West Ethiopian shield.

several lithotectonic units; 1) Gneisses and migmatites, 2) Ophiolites and island arc assemblages, 3) Syn-, late-to post-tectonic granitoids, and 4) Dokhan Volcanics and Hammamat Molasse Sediments. The Late Neoproterozoic belt of the ED is covered in the west by Late Paleozoic-Cretaceous sediments, collectively referred to as "Nubian Sandstone".

Gneisses and Migmatites

The gneisses and migmatites constitute the structurally deepest tectonic element of the Egyptian basement (infracrustal rocks or Tier 1, Bennet and Mosley, 1987; Greiling et al., 1994). These rocks are overthrusted by ophiolitic nappes (supracrustal rocks or Tier 2, Bennet and Mosley, 1987; Greiling et al., 1994) along a

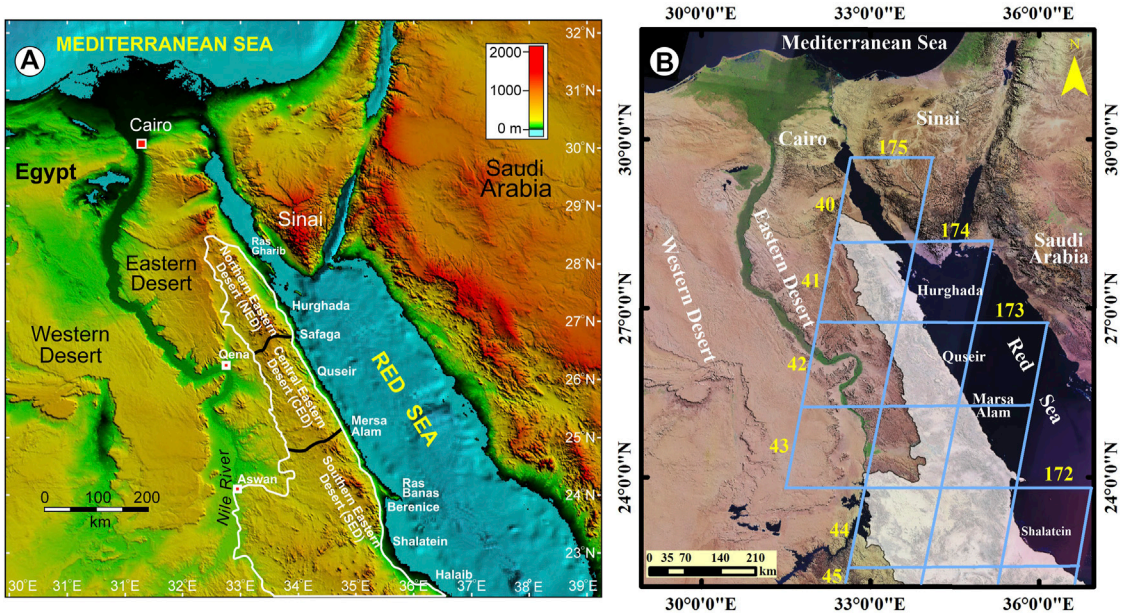

FIGURE 2 | (A) Digital elevation and bathymetric model of the northern Red Sea, Gulf of Suez, and Gulf of Aqaba region (NOAA, 2016), showing outline of Eastern Desert basement rocks (white) and the traditional three-fold subdivisions of the ED into North Eastern Desert (NED), Central Eastern Desert (CED) and South Eastern Desert (SED). **(B)** Satellite image showing the extent of the Eastern Desert basement domains (white polygon) and Path/Raw of the fifteen Landsat-8 (OLI/TIRS) images used in the present study.

major detachment horizon. They are regionally metamorphosed up to the upper amphibolite facies and are mainly represented by schists, gneisses, and migmatites (**Figure 3A**). Earlier, these rocks were considered tectonic windows of "old" continental basement (El-Gaby et al., 1984) forming uplifted regions along the ENS and the entire ANS. The isotopic data of these gneisses rule out a pre-Neoproterozoic formation age. U/Pb zircon ages gave 631 ± 2 Ma at Meatiq (Andersen et al., 2009); 659 ± 5 at Migif-Hafafit (Lundmark et al., 2012); 631 ± 6 Ma at El Shalul (Ali et al., 2012); 725 ± 9 Ma at Beitan (Ali et al., 2015). These data further indicate that a depleted mantle source was the protolith for most of the crust of the ED (Liégeois and Stern, 2010; Augland et al., 2012). We interpreted these rock suites as representing deep-seated metamorphosed roots of arcs, probably delineating sites of individual island arcs. The gneisses and migmatites form conspicuous gneissic domes along the ED at Meatiq, Migif-Hafafit, El Sibai, and El Shalul, where they are structurally overlain by fold/thrust belts of supracrustal rocks. Such domes are bound at their NE and SW margins by NW-trending left-lateral strike-slip faults (e.g., Fritz et al., 1996) and occasionally by NW- and SE-dipping normal faults.

Ophiolites and Island Arc Assemblage

The ED of Egypt contains many remnants of Neoproterozoic oceanic lithosphere in form of ophiolites, obducted during the Pan-African Orogeny (Stern, 1994; Stern et al., 2004). In most cases, the Egyptian ophiolites are variably dismembered forming tectonic melanges. However, local intact ophiolite sequences were documented (Wadi Ghadir ophiolites, El Sharkawi and El Bayoumi, 1979; Gabal Gerf ophiolites, Zimmer et al., 1995). The Egyptian ophiolites include serpentinized ultramafics, metagabbros, and locally observed sheeted dykes (Gerf and Sol Hamed ophiolites; Gahlan, 2006), and mafic-metavolcanics that are sometimes pillowed and associated with ophiolitic metasediments. At their tectonic contacts, sole thrusts, and shear zones, the serpentinites (**Figure 3B**) and metavolcanic rocks are highly deformed and transformed into sheared-serpentinites and talc-schists, and metavolcanic-schists such as chlorite and actinolite schists, respectively. They form imbricate fan structures, thrust duplexes, and antiformal stacks of various scales and concentrate within CED and SED. The majority of ophiolites formed between 750 and 730 Ma in the Allaqi, Gerf, Ghadir, and Fawakhir areas (Zimmer et al., 1995; Ali et al., 2010). Different models have been proposed for the tectonic setting of the ED ophiolites. These include the formation of ophiolitic rocks in fore-arc basins (Gahlan et al., 2015), back-arc basins (Abd El-Rahman et al., 2009), or along mid-ocean ridges (El Gaby et al., 1984). Regardless of their specific setting, the ophiolites formed during the break-up of the Rodinia supercontinent represent the formation of individual basins within the wider Mozambique Ocean (Collins et al., 2021b).

In the Egyptian basement complex, the island arc-related rocks include intrusive as well as extrusive assemblages (Bentor, 1985; Abu El-Ela, 1997). The intrusive suites are represented by gabbro-diorites and tonalites, whereas the extrusive assemblage comprises volcanic rocks (mainly basalts and andesites) and volcano-sedimentary sequences. They have strong calc-alkaline affinity and are regionally deformed and metamorphosed up to the lower amphibolite facies. Like ophiolites, the island arc rocks are proposed to have been formed on the oceanic crust of the Mozambique Ocean (Johnson et al., 2011).

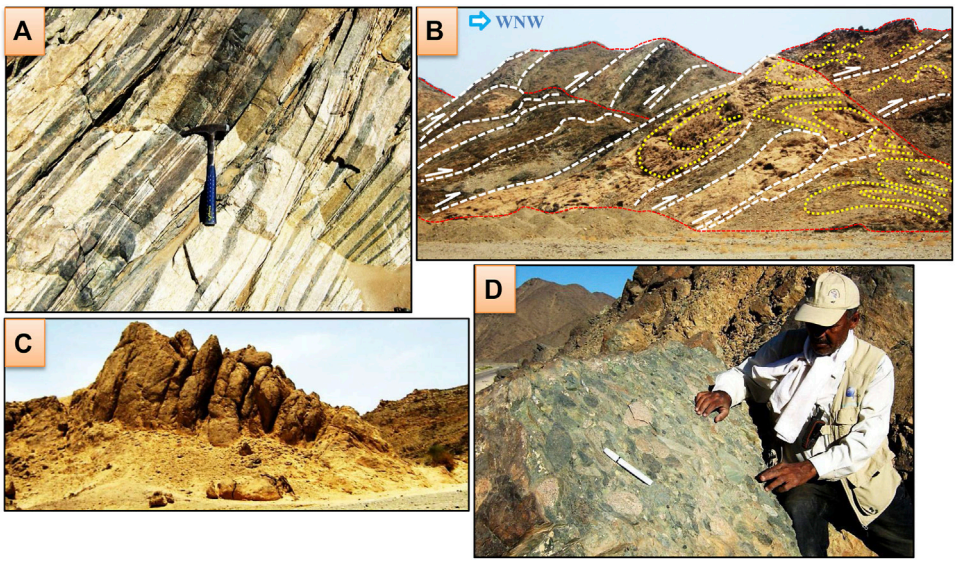

FIGURE 3 | (A) Migmatitic gneisses from the Wadi Kuda (SED). **(B)** Massive serpentinite from the Ghadir area with propagated thrusts (white lines) and thrust-related folds (yellow lines). Red lines define the summits of serpentinite ridges. **(C)** Syn-tectonic granites from the Abu Dabbab area. **(D)** Polymictic conglomerates from the post-amalgamation volcano sedimentary sequence of Wadi Hammamat.

Syn- and Late- to Post-Tectonic Granitoids (Egyptian Granites)

The granitic intrusions of the ENS are classically divided into "older" (gray) to "younger" (pink) granites (Akaad et al., 1979). Most probably, they originated from single or similar magma series that have evolved and fractionated from a mantle-derived magma (Moussa et al., 2008). These intrusions follow a geochemical trend producing earlier phases of calk-alkaline granites while the later phases were represented by alkaline to per-alkaline granites (Hussein et al., 1982; Ali et al., 2013). The older granites (**Figure 3C**) represent the first type, which comprises calc-alkaline granites that range in composition from granodiorite, and tonalite to quartz-diorite. In contrast, the younger granites define the second type with rock compositions including alkali feldspar granites, granites, and granite-adamellites (Ali et al., 2012). The third type of granites that have compositions ranging from alkali feldspar granites up to syenites are considered A-type granites (e.g., Moghazi, 2003). Older granites are syn- to late-tectonic and subduction related (Hassan and Hashad, 1990) representing a pre-collision arc-magmatic phase (Stern, 1994). The younger pink granites and A-type granites specify the late-orogenic to within-plate granitoids (post-tectonic), respectively (El-Bialy and Omar, 2015.

Dokhan Volcanics and Hammamat Molasse Sediments

During the late orogenic history of the ED (~610–590 Ma), a stage of K-rich calc-alkaline volcanic activity evolved resulting in a variety of volcanic rocks (Dokhan Volcanics) ranging in composition from basic-intermediate to acidic volcanics and related pyroclastics and tuffs (Abdel Rahman, 1996; Eliwa et al., 2006). These volcanic rocks are abundant in the NED and CED and rarely recorded in the SED. Dokhan Volcanics erupted before and coeval with the deposition of the Hammamat molasse sediments and are subjected to low-grade metamorphism (Ressetar and Monrad, 1983; Breitkreutz et al., 2010). The tectonic setting of the Dokhan Volcanics is debatable and various origins were proposed covering a wide range of tectonic regimes. These include compressional active continental margin (El-Gaby et al., 1989; Abdel Rahman, 1996) to intermediate (Eliwa et al., 2006) and extensional rift system (Stern et al., 1984).

Hammamat sediments are molasse-type sediments that evolved during the late stages of ENS evolution and the sedimentary environment as well as their composition allows retracing the sedimentary provenance as well as the exhumation history of sediment delivering units. In addition, the sediments act as a time marker for syn- and post-sedimentary tectonics (Fowler and Osman, 2013).

The succession of the Hammamat sediments consists mainly of greywackes and siltstones with polymictic-breccias and conglomerates (**Figure 3D**) at the lower part (El-Gaby et al., 1984; Willis et al., 1988). These sediments were locally subjected to thermal contact metamorphism due to emplacement of the late-to post-tectonic granites (El Gaby and Khudeir, 1988). The petrography and sedimentology of some of these basins, such as Wadi Hammamat, Wadi El Qash, Wadi Kareem, and Wadi Miyah basins have been investigated by Messner (1996) and Fritz and Messner (1999). Hammamat molasse basins are classified according to their location and the structural setting of each basin (Fritz and Messner, 1999; Abd El-Wahed, 2010). These include foreland basins, characterized by thrust-related

structures, such as Wadi Hammamat and Wadi Qash basins. Intermontane basins, markedly developed as pull-apart basins, like Wadi Queih and Wadi Igla basins, and intermontane basins, deformed merely by the strike-slip and extensional shearing, such as Wadi Kareem, Wadi Atawi and Wadi El Miyah basins. Basin formation through general N- to NW-oriented extension was proposed by Hassan and Hashad (1990), Abdeen and Greiling (2005), Shalaby et al. (2006), and Abd El-Wahed (2010). This is in accordance with strain data derived from pebbles (Fowler and Hamimi, 2021a, b) that gave NW-SE major principal strain axes in most of the basins.

LANDSAT-BASED LITHOLOGICAL MAPPING

Data and Methodology

The Landsat-8 data have been widely used for geological mapping and mineral exploration worldwide (Ali and Pour, 2014; Pour and Hashim, 2015; Mwaniki et al., 2015; Safari et al., 2017). In the present study, we obtained fifteen free cloud Landsat-8 level 1T (terrain corrected) images that covered the Neoproterozoic basement of the Eastern Desert of Egypt (**Figure 2B**) through the U.S. Geological Survey Earth Resources Observation and Science Center (EROS) (http://earthexplorer.usgs.gov). **Supplementary Table S1** lists the Landsat-8 characteristics and dataset attributes used in the present study. They were geometrically corrected and georeferenced to the Universal Transverse Mercator (UTM) projection (Zone 36 N), World Geodetic System (WGS) 84 datum, and ellipsoid. The fifteen images were processed using the ENVI 5.3 (ENVI® image processing and analysis software, from ITT Visual Information Solutions) and ArcGIS 10.5 (from ESRI® Environmental Systems Research Institute) packages. One raster image mosaic was made using the seamless mosaic module in ENVI 5.3. Masking of more than 115,350 km^2 of crystalline rocks belt was applied using shapefile in ArcGIS 10.5. Moreover, the atmospheric correction was considered one of the essential steps in the preprocessing phase (Lillesand et al., 2004; Chander et al., 2009; Tyagi and Bhosle, 2011; Abdelmalik, 2018). In the present study, we used the radiometric technique introduced in ENVI 5.3 to calibrate the Landsat-8 OLI images data for reflectance. In addition, the Digital Elevation Model (DEM) of the Shuttle Radar Topography Mission (SRTM) 1 arc-second with a 30 m horizontal spatial resolution was used to extract and visualize the structural elements through their topographical expression using the Geographic Information System (GIS) environment.

Remotely Sensed Data Processing

Mineralogical and chemical composition, vegetation cover and weathering characteristics are important factors for lithological discrimination using remote sensing data (Xiong et al., 2011). The advances in these processing techniques have increased the accuracy of discriminated features. Therefore, image enhancements including color composites (true or false), band ratioing, principal component analysis (PCA), decorrelation stretching, edge enhancements, and image fusion facilitated the differentiation and characterization of various elements in structural geology, mineralization, and rock types (Chen and Campagna, 2009; Gupta, 2013). In ED in Egypt, several studies have shown that appropriate image enhancements of remotely sensed data significantly improved the lithological discrimination and aided in field observations for lithological mapping. These studies pointed out that Landsat-8 with (OLI) sensor is considered one of the most effective data widely and successfully used for lithological mapping and exploration targets (Gabr et al., 2015; Hassan et al., 2015; Sadek et al., 2015; Asran et al., 2017; Aboelkhair et al., 2020; Hamimi et al., 2020). The Landsat-8 data, in combination with other remotely sensed data (e.g., ASTER and Sentinel) have been used to discriminate the exposed lithological units of ENS. These include the northern (Sadek and Hassan, 2009; Mohy et al., 2017), central (Sadek et al., 2015; Khalil et al., 2017; Mohammed et al., 2019), and southern (Zoheir and Emam, 2012; Hassan and Sadek, 2017; Emam et al., 2018; Mohy et al., 2019; Zoheir et al., 2019a, b) Eastern Desert of Egypt.

In the present study, several image processing techniques were applied to the Landsat-8 satellite data to generate a modified geological map with well-emphasized rock units and structural regions, which were verified by field observations of the entire ED. These techniques included color composites, band ratioing, mineral spectral indices, and Principal Component Analysis (PCA).

False Color Composites (FCCs)

Color composites provide color variation images with different color tones that reflect the different spectral characteristics of the exposed rock units, as well as outline the structural features. Depending on the highest values of the Optimum Index Factor (OIF) (Chavez et al., 1982), the color composite of RGB-753 was selected in the present study (**Figure 4A**). This color composite provided a good illustration of the geological and structural features with a clear contrast of the different rock units and obviously traced the trajectories of the major structural elements in the Late Neoproterozoic belt in ED in Egypt. The serpentinites exhibited a mottled dark blue color in the thrust contact with volcaniclastic metasediments, which appeared as dull mixed dark green, dark gray to bluish-green and brown colors. The Hammamat molasse sediments were delineated as dark and light patches of brown areas. The granitic rocks were clearly outlined by brown color tones from light to dark. The image also displayed major fault contacts and shear zones that affected the rock units.

Principal Component Analysis (PCA)

Principal component analysis (PCA) is one of the most effective and powerful image processing tools especially in geological mapping, such as for lithological, mineralogical, and structural applications. It is a multivariate statistical method for displaying the maximum contrast from several spectral bands with just three primary display colors (Vincent, 1997). This technique predicts whether a target is displayed as bright or dark pixels in different principal components based on the magnitude and sign of the

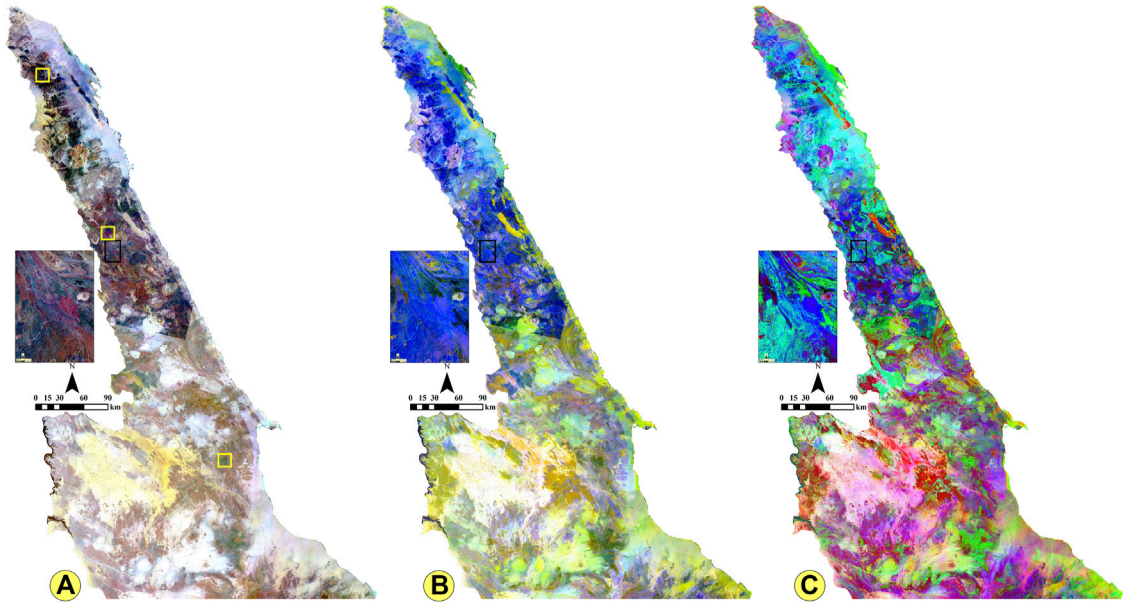

FIGURE 4 | Lithological discrimination using Landsat-8 OLI. **(A)** false color composite FCC RGB-753 discriminates ophiolitic association and related rocks and Hammamat sediments with very dark blue pixels and the syn to late and post-tectonic granitoids with light to dark brown pixels. **(B)** Principal component analysis in PCA RGB (PC2, PC1, PC4) highlights the metavolcanics–metasediments association and clearly displays the sense of shearing and dislocation. **(C)** PCA RGB (PC2, PC3, PC4) promotes the ophiolitic rocks with bright green signature, metavolcanics with blue to violet pixels, Hammamat sediments with cyan color and clearly enhances the foliation, major thrusts, and strike-slip movement. The inset image (outlined in black on the main maps) is an enlarged area for more details. The yellow boxes show the geographic locations of the tested area in the (**Supplementary Figures 1A–C**) from north to south, respectively.

eigenvector loading (Jolliffe, 1986). In the present study, the eigenvector values of the Landsat-8 image were calculated and which displayed the highest amount of information in PC1 with 96.4 and in PC2 with 2.1. Zoheir et al. (2019a) demonstrated that the first three PCA images (PC1, PC2, and PC3), contained the highest topographical and spectral information and were suitable for lithological discrimination.

The RGB color combinations of Landsat-8 PCA were tested and adopted for mapping the lithological units and structural identification of the current study area. The RGB color composite of PC2, PC1, and PC4 exhibited the ophiolitic melange and associated rocks as grayish blue and the metavolcanics, metasediments, Dokhan Volcanics, and Hammamat sediments as blue tones from dark to light (**Figure 4B**). The felsic rocks exhibited light violet younger granites and lemon-yellow older granites. On the other hand, the ophiolitic rocks (serpentines and talc carbonates) were displayed as bright green patches in a distinct view in the RGB color composite of PC2, PC3, and PC4 (**Figure 4C**). The foliated metavolcanics and metasediments exhibited light purple colors whereas the Dokhan Volcanics and Hammamat sediments were displayed in cyan color. The granitoids appeared in light violet to yellowish violet colors.

Band Ratioing and Spectral Mineral Identification

The fact that each material displays a characteristic spectral reflectance curve that distinguishes it from other materials was considered the base for the identification and discrimination of the different minerals and rocks from the remotely sensed data. Huntington (1996) stated that the hydrous mineral phases with OH groups (Mg-O-H, Al-O-H, Si-O-H) and CO_3 acid group possess diagnostic absorption features in the short-wave infrared region (SWIR) (2.0–2.50 μm). Therefore, the spectral signature was used to discriminate among the different minerals and rocks from the satellite images. In the same manner, numerous studies used band-ratio images to discriminate the different rock units based on their specific spectral characteristics. Therefore, band ratioing is considered one of the most important image processing methods for lithological mapping, and many researchers have applied the lithological and structural mapping in the ED in Egypt (e.g., Zoheir and Emam, 2012; Hassan and Ramadan, 2014; Hassan et al., 2015; Sadek et al., 2015; Abdelmalik and Abd-Allah, 2018; Abdelmalik, 2019; Zoheir et al., 2019a, b).

In the present study, Landsat-8 (6/5) was applied to display the ophiolitic and associated rocks as gray pixels, metavolcanics as light gray pixels, and Hammamat sediments as dark pixels and felsic rocks as bright colors (**Figure 5A**). Sultan et al. (1987) and Hassan et al. (2017) used a band ratio of (6/5) as an effective mafic index to enhance the meta-ultramafic and mafic rocks as light gray pixels.

To illustrate the detailed rock differentiation, the false color composites of some different band ratios were used to observe the variation in colors of the exposed rocks and facilitate their discriminations. Two main false color composites in RGB (6/5, 6/7, 4/2 and 6/7, 6/2, 4/2) (**Figures 5B, C**) were selected and processed to differentiate among the different rock units and demarcate the structural features in the study area. Image ratios

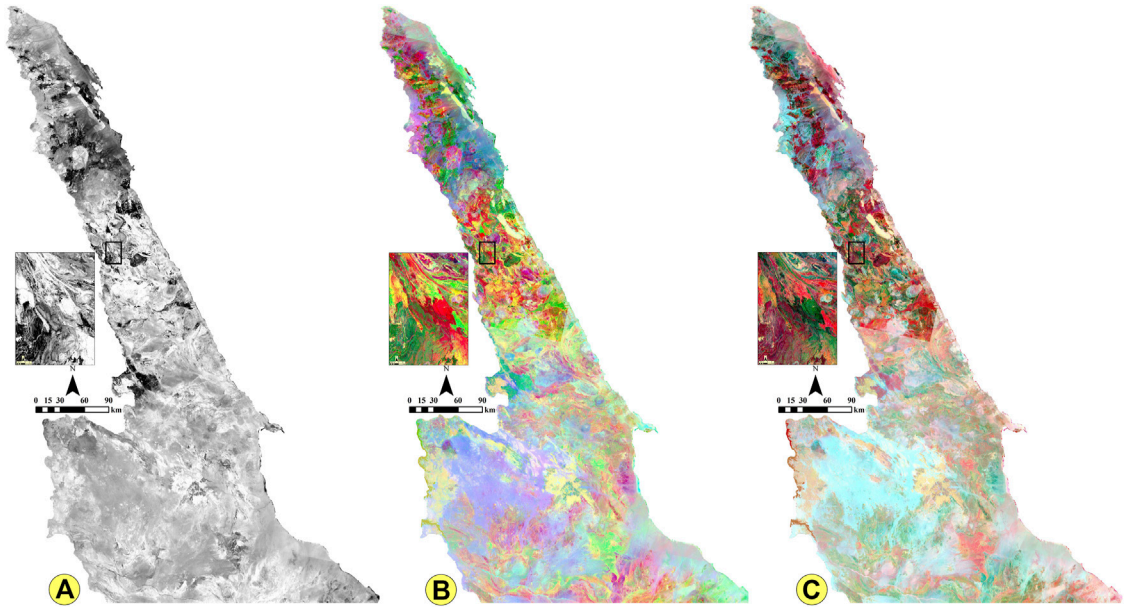

FIGURE 5 | Lithological discrimination using band ratios of Landsat-8 OLI data. **(A)** Gray-scale band ratio BR (6/5) used for mineralogical identification. Ultramafic and mafic rocks appear as light to dark gray pixels where the felsic rocks appear as white pixels. **(B)** Effective band ratio RGB (6/5, 6/7, 4/2) highlights ophiolites as bright green, metavolcanics and metasediments as reddish-yellow, Hammamat sediments, and Dokhan Volcanics as dark green and syn to late/post tectonic granitoids as pale blue and violet signatures. **(C)** Band ratio RGB (6/7, 6/2, 4/2) spectrally discriminates ophiolites as blood red, metavolcanics and metasediments as greenish orange, Hammamat sediments and Dokhan Volcanics as dark brown and syn to late/post tectonic granitoids as light cyan pixels color. The extensional faults, dyke swarms, foliation, thrusts, and strike-slip faults are also enhanced. The inset image is an enlarged area for more details.

of (6/5, 6/7, 4/2) clearly discriminated the ophiolitic melange rocks (massive serpentinite and talc-carbonate schist) and gneisses with bright green and light green colors, respectively, the metagabbro and basic metavolcanics with dark green color and the Dokhan Volcanics with olive green colors (**Figure 5B**). The granitic rocks were shown in bloody red and light purple colors whereas the Hammamat sediments appeared in brownish dark-green colors. In addition, the major structural features (e.g., shear zones, thrusts, and strike-slip faults were obviously demarcated by the variation of in the rock units' colors. The E-W and NW-SE strike-slip faults were clearly visible. On the other hand, image ratios (6/7, 6/2, and 4/2) are represented as the most powerful band ratio introduced in this study as a new band ratio for discriminating the rock units and structural features in more detail. The ophiolitic metaultramafics and related talc-carbonate rocks were obviously delineated with light and red dark purple image signatures (**Figure 5C**). The highly foliated gneisses and the metagabbros appeared as light and dark green colors whereas the metavolcanics and metasediments were displayed in orange green color. The Dokhan Volcanics and Hammamat sediments were shown in dark-brown tones. The vast array of granitic rocks was displayed in light-blue and creamy colors. Moreover, the foliation trajectories, folding, strike-slip faults, and thrusts were delineated by various colors. The aforementioned band ratios were more helpful and satisfactory in detailing lithological/structural mapping of the study area.

To outline the ophiolite assemblage and related rocks, the RGB color composite of PCA (PC2, PC3, and PC4) provided important information about the ultramafic rocks and metavolcanics and metasediments association. The ophiolites appeared as deep blue intercalated with violet patches of metavolcanics and metasediments (**Figure 4C**). The intense foliation in the image delineated the ductile structures, especially in the southern part of the study area. The developed geologic map of ophiolites and related rocks (**Supplementary Figure S1A**) showed that these rocks were mostly distributed in the central and southern parts of the Eastern Desert. Thrust contacts, folding foliation, and strike-slip movement could be clearly observed from the differences in the color tones. The false color composite investigation of Landsat-8 (RGB-652) was performed to extract the felsic rocks in the study area as dark-brown, grayish-brown, and greenish-brown color tones. The granitic windows were well defined and separated from the surrounding rocks (**Supplementary Figure S1B**). Moreover, this composite successfully and clearly enhanced the regional foliation of the foliated rocks such as gneisses and migmatites and outlined the folded rocks as well as the major shear zones. This composite demonstrated the concentration of these rocks in the north Eastern Desert. The extensional features were enhanced by linear structures such as dyke swarms, jointing, and major strike-slip faults.

Finally, image processing of the Landsat-8 OLI data is an effective tool for generating a detailed lithological map, such as rock units and structural provinces, to approximately 115,350 km^2 of the Late Neoproterozoic belt in ED in Egypt. Because of the very large mapped area, some selected large-scale areas are shown in **Supplementary Figure S2A–C** to explore the power of remote sensing in enhancing the lithological contacts. The final modified

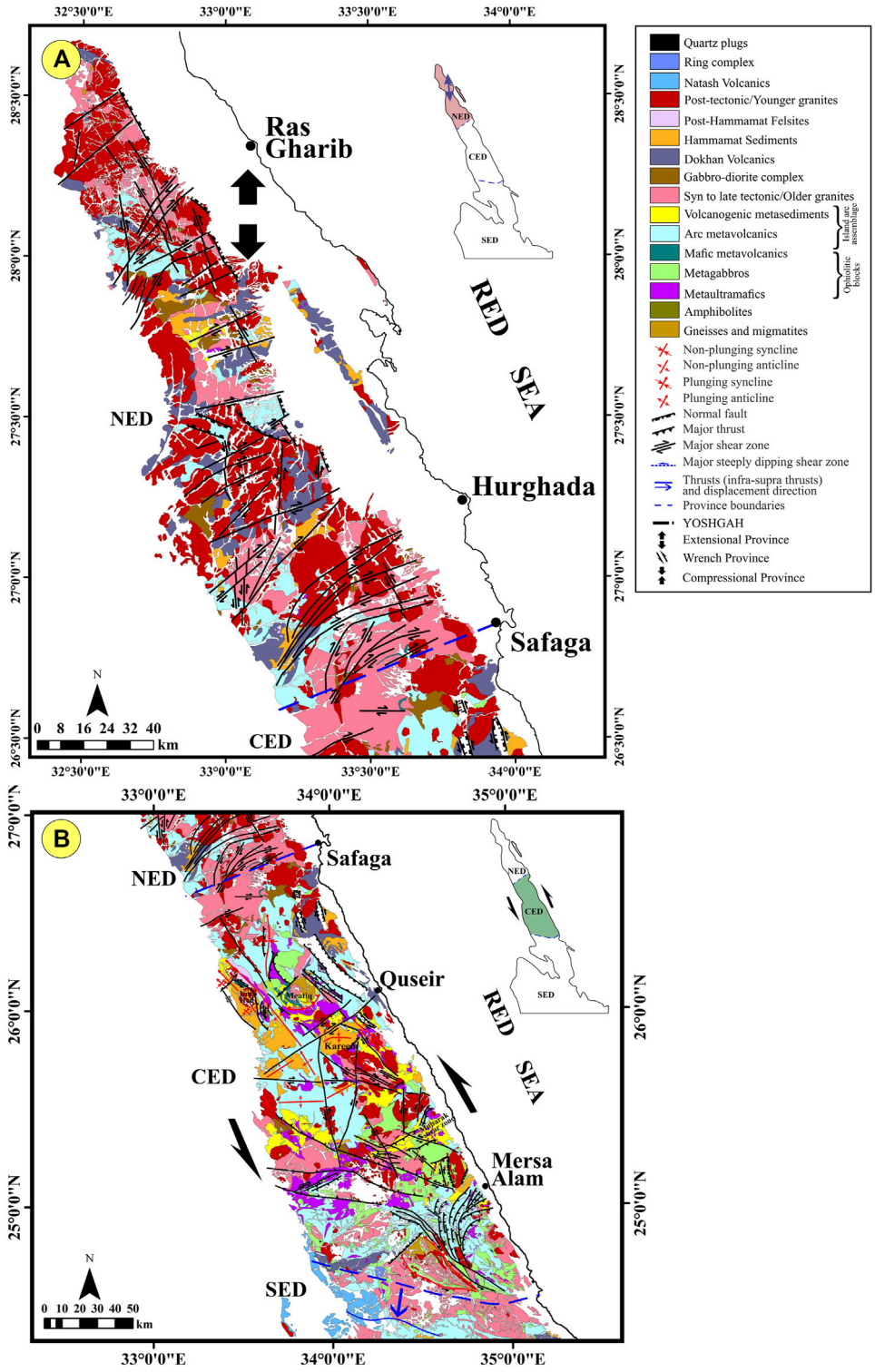

FIGURE 6 | (Continued).

geological maps are shown in **Figures 6A–C**. The output geological map was verified by using intensive fieldwork, observations in many localities in the study area, and correlation with previously published maps. Random stratified samples were used to determine the overall accuracy assessment of the updated geologic map, which attained approximately 96.73% accuracy.

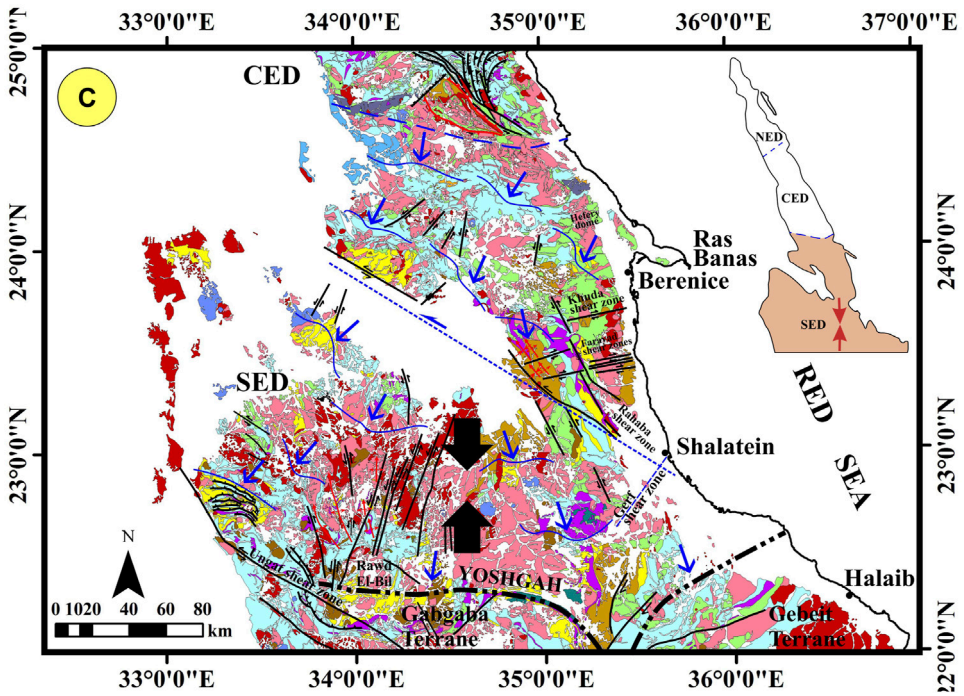

FIGURE 6 | (Continued). The geologic map of the Late Neoproterozoic belt of Egypt. **(A)** NED, **(B)** CED, and **(C)** SED. Discrimination of various lithologies and structural provinces based on image processing of Landsat-8 OLI data and ground intensive field/structural work.

Landsat-Based Structural Mapping

The remote sensing method offers the advantage of providing synoptic overviews of the structural features that extend over large areas. Identification of these structures is very efficient when the remote sensing data are integrated with computer-based GIS and verified by fieldwork. These data can be used to detect large geological structures such as shear and suture zones (e.g., Raharimahefa and Kusky, 2007, 2009). Faults can be demarcated using the topographic features with different orientations on DEM or by using the contrast and textural signatures in the remote sensing data. Homogeneous and kinematically consistent structural assemblages can then be used to define structural provinces, that most probably experienced similar tectonic histories. Zoheir et al. (2019a) recognized nine structural blocks in the Eastern Desert based on the differences in the structural trends. They inferred that the margins of these structural blocks were mostly major faults and shear zones and in some cases well-established or inferred suture zones.

In the present work, the interpretation of the structural provinces were based on the visual inspection of the tonal variation bright colors of the different rock types at band ratios of 6/5, 6/7, and 4/2 (**Figure 7A**). Moreover, the topographical expressions of the rock units, which appeared on the SRTM DEM (with 30 m spatial resolution) (**Figure 7B**) could enhance the tectonic boundaries and structural elements. The interpreted and detected structural elements are shown in **Figure 7C**. Depending on the analysis result of the extracted and previously published structural elements, the architecture ED in Egypt could be divided into three major structural provinces (**Figure 8**). The major and minor brittle and/or ductile structural elements in the study area could be traced as shown in **Figures 7A–C**, **8**. The analysis of these images, allowed us to distinguish the Neoproterozoic ductile and brittle structural assemblages. The traced structural elements overlapped the false color composites of band ratio (6/5, 6/7, 4/2) (**Figure 7A**, as an example). We emphasized that the well-developed foliations were dominant in the transpressional and compressional zones (ductile zone) of CED and SED. The zones accommodated major displacements and formed discontinuities that were considered transitional zones similar to those in CED. The considerable difference in the topography and foliation trajectories in provinces with ophiolite rocks relative to the arc metavolcanic rocks demonstrated distinctive deformation histories. NE-, E-W- and ENE-striking foliation and related close and overturned folds that extended for several kilometers were observed in the study area. The major NW, N-S, NE, ENE, E-W strike-slip faults adequately defined the differences in the color tones and rock units movements (**Figure 7A**).

The ability of remote sensing to extract the detailed structural features and kinematic indicators in the study area was investigated by selecting some examples for reference sites in NED, CED, and SED with small and large-scale areas. Four areas were selected to illustrate how remote sensing enhanced the structural elements (**Figures 9A–H**). **Figures 9A, B** shows ENE folded Hammamat molasse sediments, which exhibited —reddish brown pixels

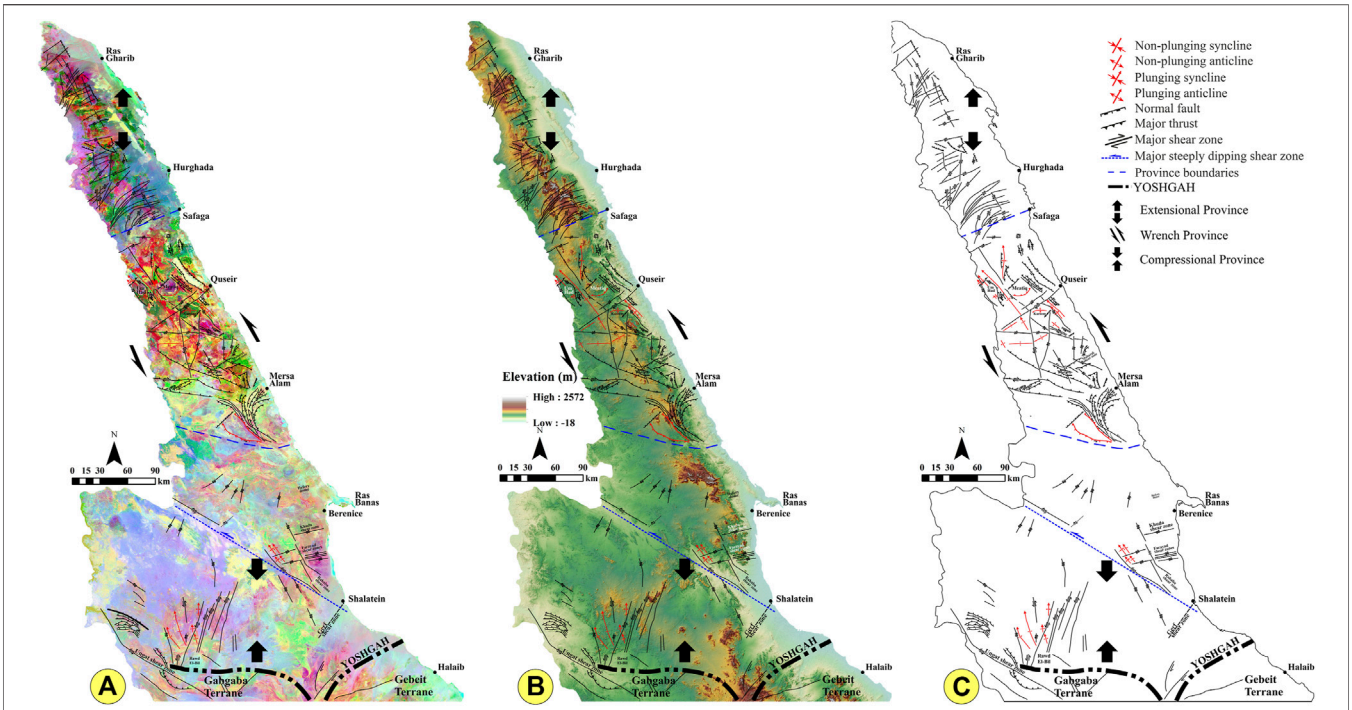

FIGURE 7 | Structural mapping promoted using the processing of Landsat-8 data, Digital Elevation Model (SRTM DEM), and Shaded relief map. The deduced structural elements are draped over **(A)** The landsat-8 band ratio, BR RGB (6/5, 6/7, 4/2), **(B)** SRTM DEM with the 30-m resolution, and Gray topographic Shaded relief map. The delineated structures are represented without a background in **(C)**. The major structural regimes and tectonic provinces were deduced in the present study by the color variation in the processed Landsat, and elevation in DEM.

intruded by granitic rocks (green pixels) and cross-cutting by the NW-trending strike-slip faults at G. El-Uref in NED. **Figures 9C, D** shows small-scale strike-slip faults that affected the sheared metavolcanics and metasediments at Wadi El-Miyah in CED. **Figures 9E, F** presents different folding styles that affected the Hammamat molasse sediments at the Hammamat Basin (Wadi El-Arak) and thrusted ophiolitic rocks along the Atalla shear zone in CED. **Figures 9G, H** shows one of the most complex areas in the Wadi Allaqi in the South Eastern Desert. Compressional structures were conspicuous in this province and hydroxyl mineral zones mimicked the intensive foliation of the sheared rocks, which exhibited obvious ductile structures. The folded ophiolitic rocks were noticeably distributed adjacent to the variably deformed island arc metavolcanics and metasediments. These rocks were overthrust NW of the area. In addition, a series of NNW-oriented folds that are distributed and disrupted by the NE-striking faults was well observed and clearly traced.

THE STRUCTURAL PROVINCES OF THE ENS

In the present study, the new tectonic map of the ENS encompasses a mosaic of three major structural provinces, namely, from south to north, compressional, transpressional/wrench, and extensional (**Figures 6**, **8**). The discrimination of these provinces is based on the compatibility of the structural associations from the hand specimen up to mountain scales that define the predominant tectonic regime. We concentrate on the major tectonic features and locate them onto a plate tectonic frame. For details, the readers are referred to the summary papers by Fritz et al. (1996), Abdeen and Greiling (2005), Abd El-Wahed (2007), Hamimi et al. (2019), Mohammad et al. (2019), Fowler and Hamimi (2020) and Hamimi and Abd El-Wahed (2020). The relative time constraints of the tectonic regimes are derived from the relationship between the rock formation and deformation. In the present study, we distinguish among the following 1) pre-Hammamat structural elements formed earlier than the sedimentation of the Hammamat molasse sediments, which are most likely related to accretion of the arcs and establishment of major decollement that separates infra-from supra-structures; 2) syn-to-late-Hammamat structural elements that evolved through the final collision and subsequent exhumation of metamorphosed arc roots; and 3) late-tectonic features that post-date Hammamat sedimentation and calc-alkaline magmatism (**Figures 6**, **8**).

Compressional Province

In the extreme southern portion of ED in Egypt, a prominent compressional province exists to the north of the Wadi Allaqi Shear Belt (part of the Greater YOSHGAH suture) that juxtaposed the Gabgaba-Gebeit Terranes against the Eastern Desert Terrane. The structures evolved as a consequence of a NNE–SSW contractional phase at c. 750–660 Ma. This province is characterized by WNW-ESE to W-E oriented thrust sequences,

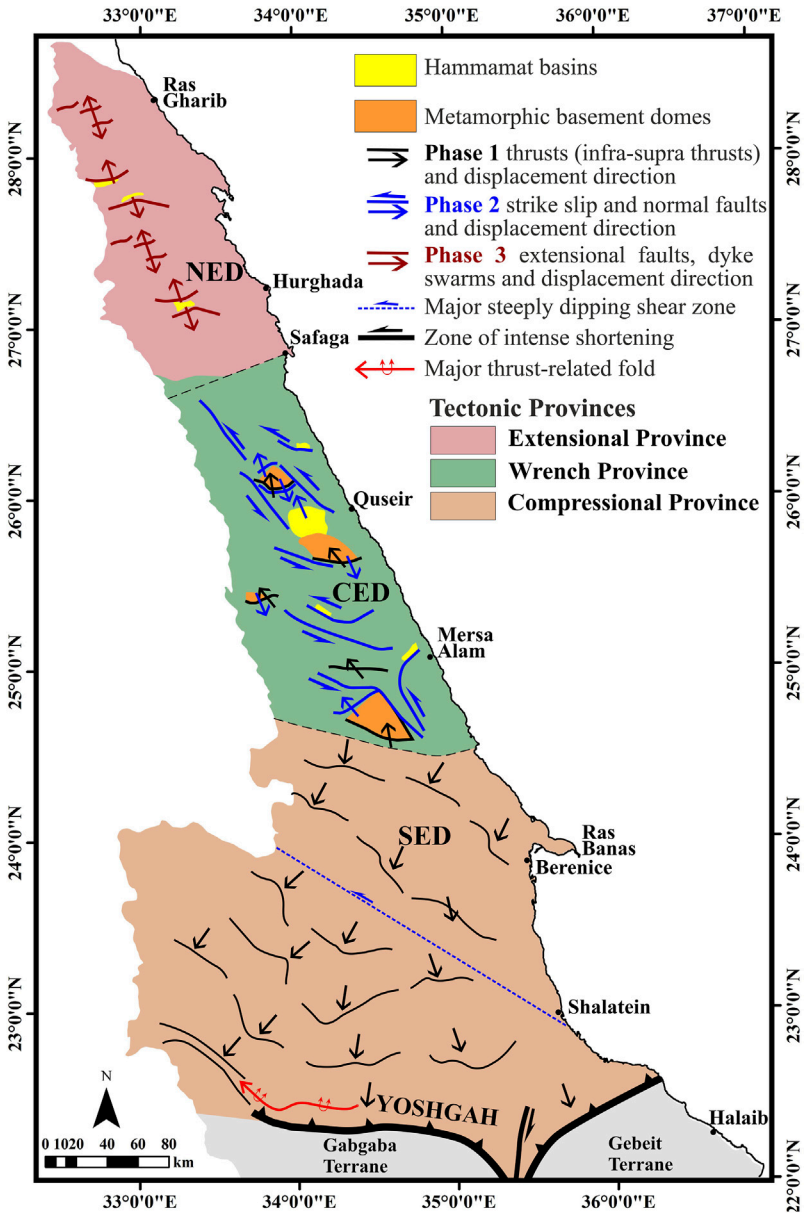

FIGURE 8 | Tectonic map showing structures separated according to the age and occurrences in different tectonic provinces.

which are best exemplified by those recorded to the west of Deneibet El-Koleib and near the Ungat shear zone (**Figures 9G, H**) and emplacement of the Gerf ophiolitic suite. The displacement of the thrusts towards SSW and S is responsible for the formation of well-developed thrust-propagation folds at Gabal Muqsim (**Figure 10**) and Um Shilman. The province extends northward to the Hafafit basement dome but in the present study, an opposite sense of thrusting is shown (top N-NW) along NE-to-ENE-oriented thrusts. Further north, the top N-NW thrusting is preserved in the basement domes. The major decollement between the internal portions of these basement domes and the low-grade metamorphosed envelope of metavolcanics and ophiolite remnants are considered part of this oldest compressional phase. In the current work, we believe that although the earliest structural elements dated back to c. 750 Ma, the SED compressional phase may have continued throughout the Late Neoproterozoic evolution in the ED. We also believe that although the conspicuous NNW-SSE trending Wadi Beitan major structure lies in this province, this structure was related to an earlier convergence between E- and W-Gondwanalands. The N-S shortening may be responsible for the refolding of this structure around the ENE-WSW (to E-W) direction. In this context, the remarkable transpressional shearing along the Wadi Kharit–Wadi Hodein belt (see **Figures 7**, **8**) can be considered as the combination of the YOSHGAH shearing eco and the N-S contraction.

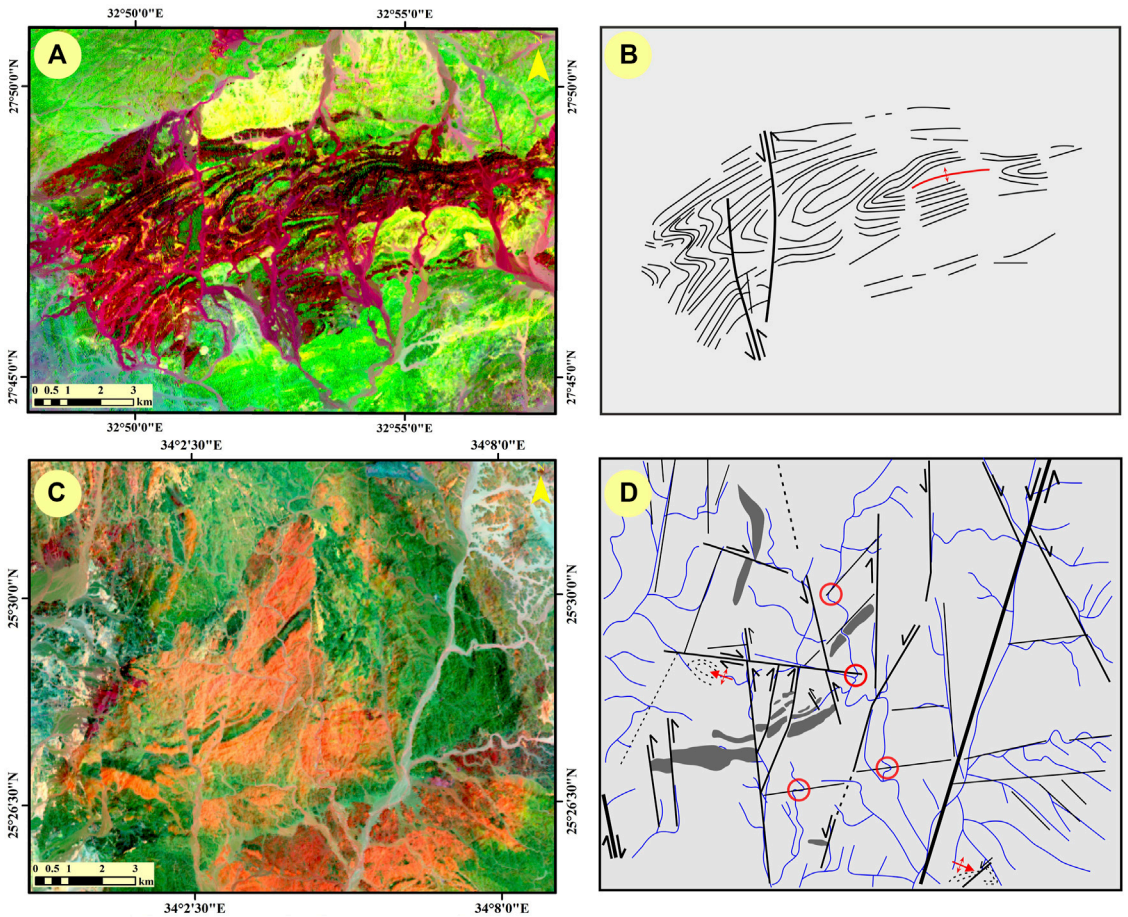

FIGURE 9 | (A,C,E,G) The band ratio BR RGB (6/7, 6/5, 4/2) of the processed Landsat-8 images and **(B,D,F,H)** their structural interpretation of El-Uref (NED), W. El-Arak (CED), W. El-Miyah (CED), and W. El-Allaqi (SED), respectively. Note that the red circles in **(D)** show the offset drainage by the strike-slip faults.

Transpressional/Wrench Province

The transpressional province evolves between Marsa Alam in the south and Safaga in the north. This province includes large parts of the Najd Fault System and a transition zone that abuts the southern compressional domain. The compressional west-east-trending structures of the southern province are progressively overprinted by NW-SE-trending structural elements (**Figure 10**). The structures include NW-trending thrusts and folds in the external, western portions of the orogen such as in the Hammamat basin at the Quseir latitude. The main transcurrent belt is dominated by prominent NNE-SSW trending sinistral strike-slip shear zones. A number of cogenetic structural elements and rock suites evolve during this tectonic phase. The activity of the shear zones is associated with the coeval exhumation of metamorphic domes as evident from the $^{40}Ar/^{39}Ar$ cooling ages of the domes (620–590 Ma) and the ages interpreted to represent a time of sinistral shearing (c. 590 Ma) (Fritz et al., 1996; 2002). The large shear belts adjacent to the Meatiq, Sibai, and Hafafit metamorphic domes, are most prominent, as better shown in the insets of **Figures 4**, **5**, which show an enlargement of the Atalla Shear Belt (**Figures 11A–C**). Between the segments of NNE-trending strike-slip faults, extensional bridges exhumed the domes through W-E trending normal faults. These extensional faults are formed at the margins of the Hafafit, Sibai, and Meatiq domes and indicate a significant component of the orogen parallel NNW-SSE extension. The extensional shearing is locally accompanied by emplacement of the syn-extensional granitoids (e.g., Abu Ziran granitoids to the south of Meatiq: Fritz et al., 2014) and is associated with the formation of the Hammamat molasse basins (e.g., Fritz and Messner, 1999; Abd El-Wahed, 2010; Fowler and Osman, 2013). Hence this structural association is clearly assigned "syn-to-late-Hammamat association".

Extensional Province

North of the Qena-Safaga Shear Belt lies a large extensional province that extends to the northern tip of ENS. This area is the site of voluminous post-orogenic magmatism (e.g., the voluminous granitoids of Gabal Shaeib El-Banat, Gabal Qattar, (**Figure 11D**), and Gabal Gharib, which is considered the result of mantle delamination and associated crustal thinning. Other evidence that supports the extensional regime includes the widespread E-W trending dyke swarms and the E- (to ENE-)

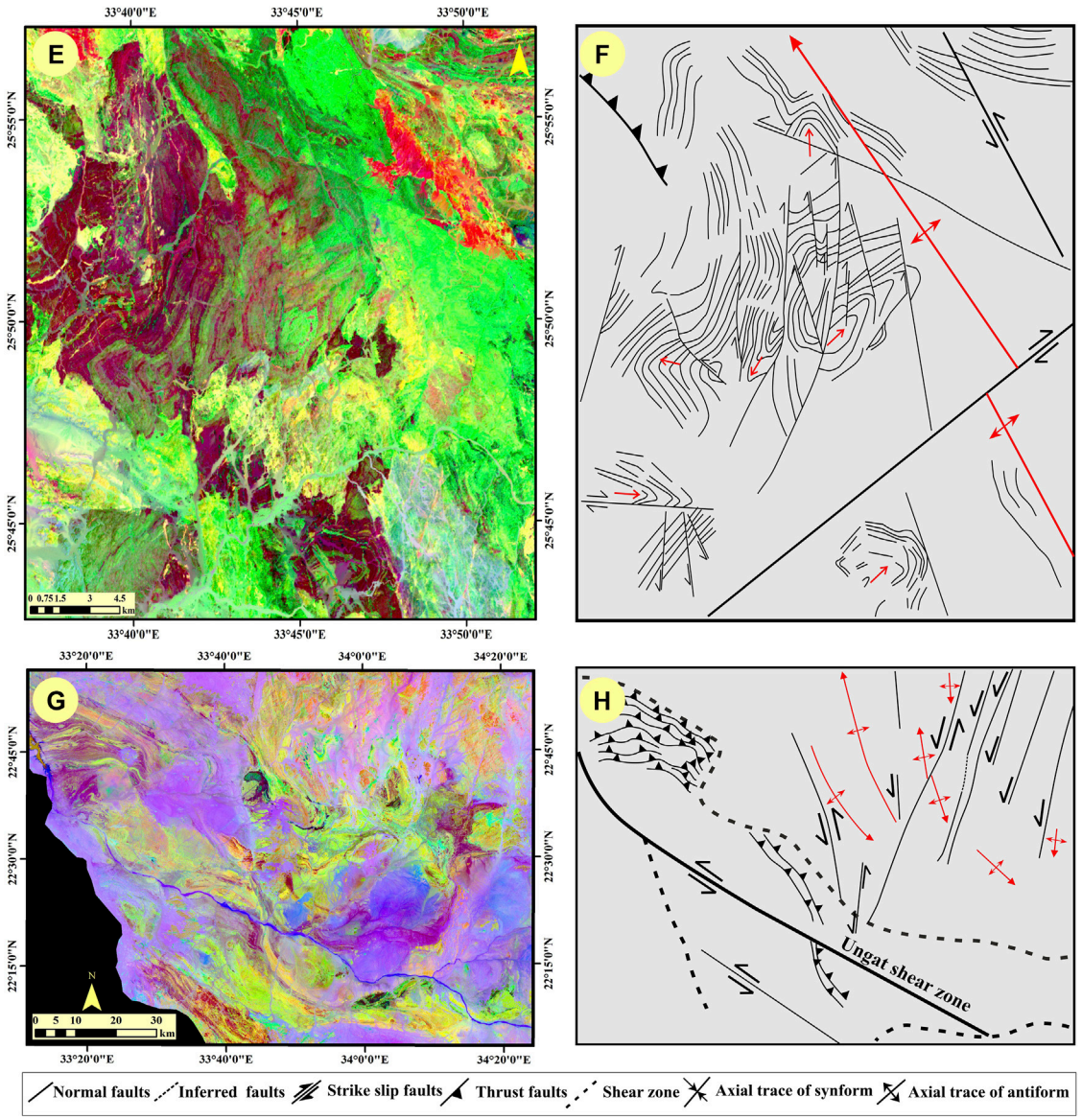

FIGURE 9 | (Continued). **(A,C,E,G)** The band ratio BR RGB (6/7, 6/5, 4/2) of the processed Landsat-8 images and **(B,D,F,H)** their structural interpretation of **(G)**. El-Uref (NED), W. El-Arak (CED), W. El-Miyah (CED), and W. El-Allaqi (SED), respectively. Note that the red circles in **(D)** show the offset drainage by the strike-slip faults.

trending tensile fractures. Voluminous emplacement of the bimodal Dokhan Volcanics nearby the large granitoid masses is additional evidence of a late-stage extensional regime.

DEFORMATION REGIMES AND FLOW FIELDS

Deformation Regimes

Evidently, the deformation styles in the orogens are determined by the relative motion of the plates and changes in the plate motion, which are termed as "far-field boundary conditions". It has been shown that oblique plate convergence has the potential to develop large strike-slip systems within the orogen, as exemplified by the Alpine Fault of New Zealand or the San Andreas Fault System of western North America (e.g., Norris et al., 1990; Titus et al., 2007; Mouslopoulou et al., 2009). Orthogonal convergence is, by contrast, characterized by an absence of large orogen-parallel faults, as seen in the central Himalayan or South American Andean systems (Xu et al., 2012; Armijo et al., 2015; Li et al., 2015; Horton et al., 2016; Hu et al., 2016). In the case of Late Neoproterozoic/Early Cambrian deformation events in the ED of Egypt, we suggest that three different far-field boundary conditions are

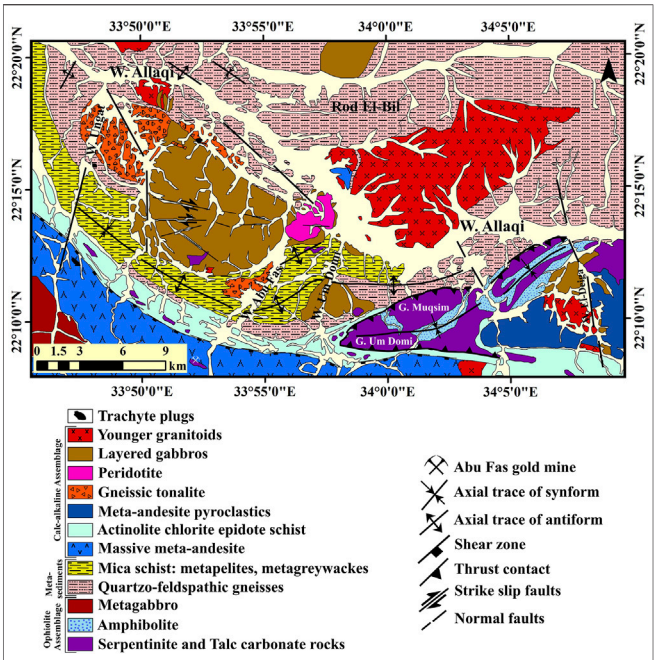

FIGURE 10 | Geological map of Moqsem-Ungat area (modified after Sadek, 1995) showing the c. E-W trending folds and thrusts.

responsible to resolve the aforementioned structural assemblages. The earliest magmatic, metamorphic and tectonic history was released by the c. N-S convergence (recent coordinate system) of the Gabgaba—Gebeit, Jiddah—Asir terranes, and the Eastern Desert—Midyan terranes along the Allaqi-Heiani-Onib-Sol Hamid-Yanbo (YOSHGAH) suture between c. 800 and 620 Ma (**Figure 12**). The second event, between c. 640 and 580 Ma, is believed to be related to the Nabitah Orogeny when the Afif-, Ad Dawadimi-Ar Rayn terranes of Saudi Arabia accreted to the earlier consolidated arc terranes (Afif and Tathlith terranes). E-W shortening in southern Saudi Arabia may have correlated with the N-S trending Hamisana Shear Belt of southern Egypt—northern Sudan. The northwestern Saudi Arabia and CED of Egypt simultaneously experience pronounced strike-slip deformation associated with displacement along wider NFS. This shear deformation offsets parts of the YOSHGAH suture through sinistral shear, namely the Yanbu suture segment. The third orogenic phase, which is younger than c. 580 Ma, is interpreted to be related to the evolution and retreat of the Cadomian Arc (Ballevre et al., 2001; Bandres et al., 2002; Linnemann and Romer, 2002; Stern et al., 2016). The northern portions of ED in Egypt and Saudi Arabia have experienced extension and extensive post-orogenic magmatism.

As a working hypothesis, we suggest that the three different far-field boundary conditions controlled, with overlap, the structural assembly within three different domains in the ED of Egypt. Southern domains were influenced mainly by N-S convergence (**Figure 13**: far-field condition 1) and localized effect of W-E shortening (**Figure 14**: far-field condition 2) as seen in the activity within the Hamisana Shear Belt. The influence of far-field condition 1 diminishes northward but the influence of far-field condition 2 increases. The CED is considered a core area where Najd Fault-related structural elements developed. The far-field condition 3 dominates the northern segment of the ED as evident from extensive late orogenic magmatism and extensional fabrics (**Figure 15**). We relate the classical subdivision of the ED geology into NED, CED, and SED rather to external far-field boundary conditions than to activity of cryptic fault systems that remain proposed but unproven.

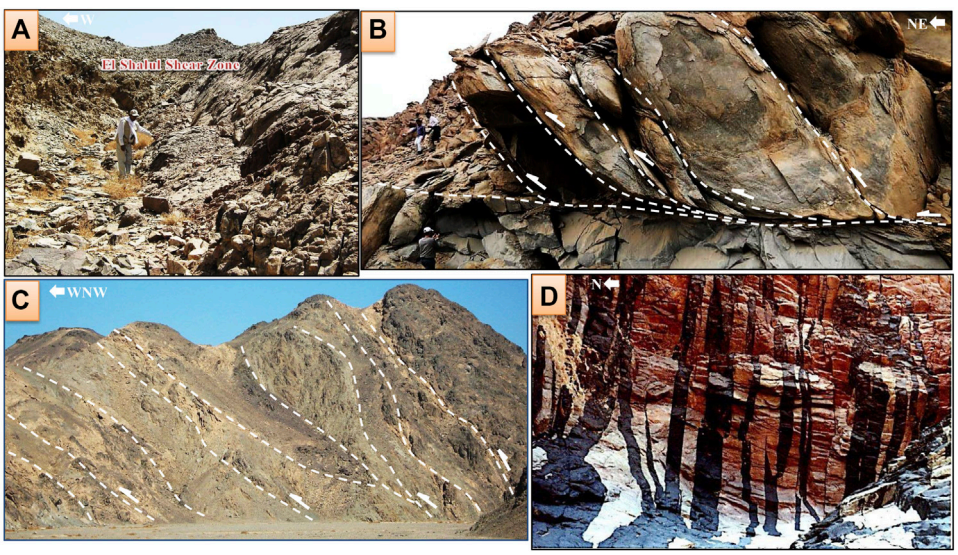

FIGURE 11 | Field photographs indicating a transition from compression to extensional shearing along El Shalul Shear Zone **(A)**, transpressive structures to the SE of Meatiq dome and along the Atalla Shear Zone **(B,C)**, respectively, and remarkable dyke swarms in the extensional province at Wadi El Thelma south Gabal Gattar granitic pluton **(D)**.

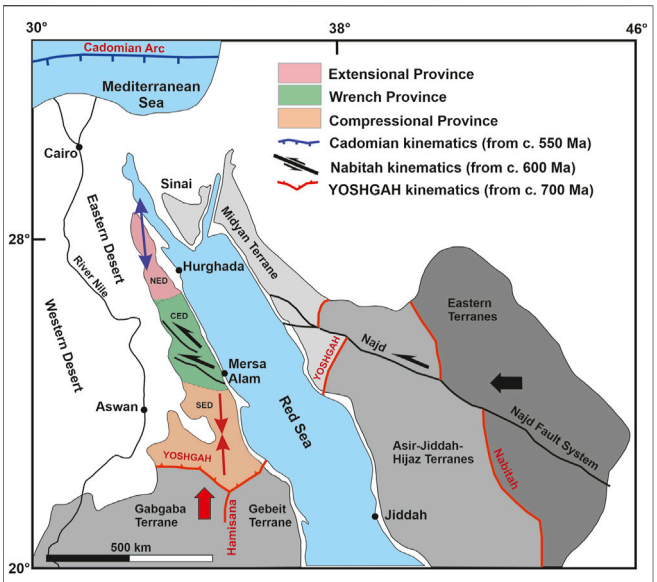

FIGURE 12 | Plate tectonic situation and structural provinces related to different plate kinematics. The earliest event, convergence, and collision between Gabgaba-Gebeit terranes and the Eastern Desert terrane along the YOSHGAH suture released north-south compression (thick red arrow) and related north and south directed thrusts (red double arrow) in the southern compressional province. West—east convergence (thick black arrow) associated with Nabitah Orogeny caused modification of suture and W-E compression in the Hamisana Belt. In the northern portion, this motion is partitioned into large sinistral strike-slip systems of the Najd Fault System leading to transcurrent motion within the CED wrench province (black half arrows). The retreat of the northern Cadomian arc enabled extension in the northern NED extensional province (blue double arrow).

Flow Fields

Far-field boundaries are simple, and associated structural assemblages are, however, complex. This is not only because of the superposition of successive deformation events but because deformation may partition into different components. The shape changes and particle displacement fields that characterize the flow of rock particles and thus the geometry of the structural elements are tensor quantities (second rank tensors). The displacement gradient tensor is related to the shapes of the initial to finite state and from the eigen-quantities of that tensor, the strain may be extracted. The velocity gradient tensor describes the way rock particles flow, the orientation of flow apophyses (eigen-vectors) provides information on the vorticity of the flow (Bobyarchik, 1986). This is expressed as a kinematic vorticity number, the nonlinear ratio between pure and simple shear components (for theory see Tikoff and Fossen, 1993). Conventionally velocity fields and displacement gradient tensors are derived from structural assemblages that are relevant to local situations. In Egypt, these kinds of data are rare. Here we use another approach and derive these quantities from the geometry and motion of plates. Plate motion vectors and plate boundaries, or high-strain deformation zones have shown to be parallel/contain the flow apophyses. Hence, from far-field boundary conditions, the flow fields may be derived when a homogeneous continuum is assumed (Tikoff and Teyssier, 1994). Considering these assumptions, structural associations can be predicted and compared with observed structural elements. Below we display qualitatively the flow fields for the three different far-field boundary conditions suggested for the Neoproterozoic ED of Egypt.

These simple models are applicable for homogeneous continuum and isochoric deformation. A more realistic view has to implement concepts of displacement partitioning and strain compatibility (e.g., Tikoff and Teyssier, 1994; Teyssier and Tikoff, 1999; Jones et al., 2005). The concept of deformation partitioning states that the overall, over-regional geometry of a flow type maintains constant but may partition regionally. As soon as the vorticity in one domain is increased, for example through the activity of a simple shear zone, the vorticity in adjacent domains is reduced to keep the overall flow geometry constant. Hence, the presence or absence of a high-strain shear zone has a strong influence on the geometry of the structural assembly within and outside shear domains. The concept of strain compatibility states that geometries of bodies before and after deformation have to be compatible, common boundaries maintain and voids have to be avoided. This implies that deformation is not only determined by the overall induced stress field but also by the requirement to keep structural domains compatible. As an example, simple and pure shear (or general shear) deformations are not compatible with geometries. In progressive simple shear, the length of the shear zone boundary remains constant whereas this boundary is stretched in pure and general shear. To fulfill the requirements of strain compatibility either a fault has to be introduced between both domains or rock volume has to be removed or added.

YOSHGAH Suturing—First Far-Field Conditions

Structural assemblages that are related to this event dominate the SED. Plate motion of the Gabgaba/Gebeit terranes relative to the Egyptian Eastern Desert terrane was largely orthogonal to the Allaqi–Heiani suture (Hamimi et al., 2019), western segments of the YOSHGAH suture system (**Figures 12**, **13**). Hence minor lateral, suture-parallel motion is predicted and plane strain deformation is considered. The plane containing all relevant features including flow apophyses, instantaneous stretching axes, and strain axes is given by the plate motion vector and the normal trend of the suture zone. Flow apophyses were drawn parallel to the plate motion vector (eigenvector a_2: flow into the orogen) and parallel to the assumed dip of the subduction zone (eigenvector a_1: flow out of the orogen) (**Figure 13A**). The subduction zone dip was taken to be 45°, which corresponds to a general shear deformation with a kinematic vorticity number of c. Wk = 0,7. Schematically drawn flow lines show that expected structures include southward and upward emplacement of units within the Eastern Desert terrane with steepening of structures when approaching the subduction zone. This is in accordance with structural data from the SED which overwhelmingly displays top-to-south displacement (for a summary of data see Fowler and Hamimi, 2020). North-south trending lineaments (**Figure 8**) may represent tear faults accommodating differential shortening or

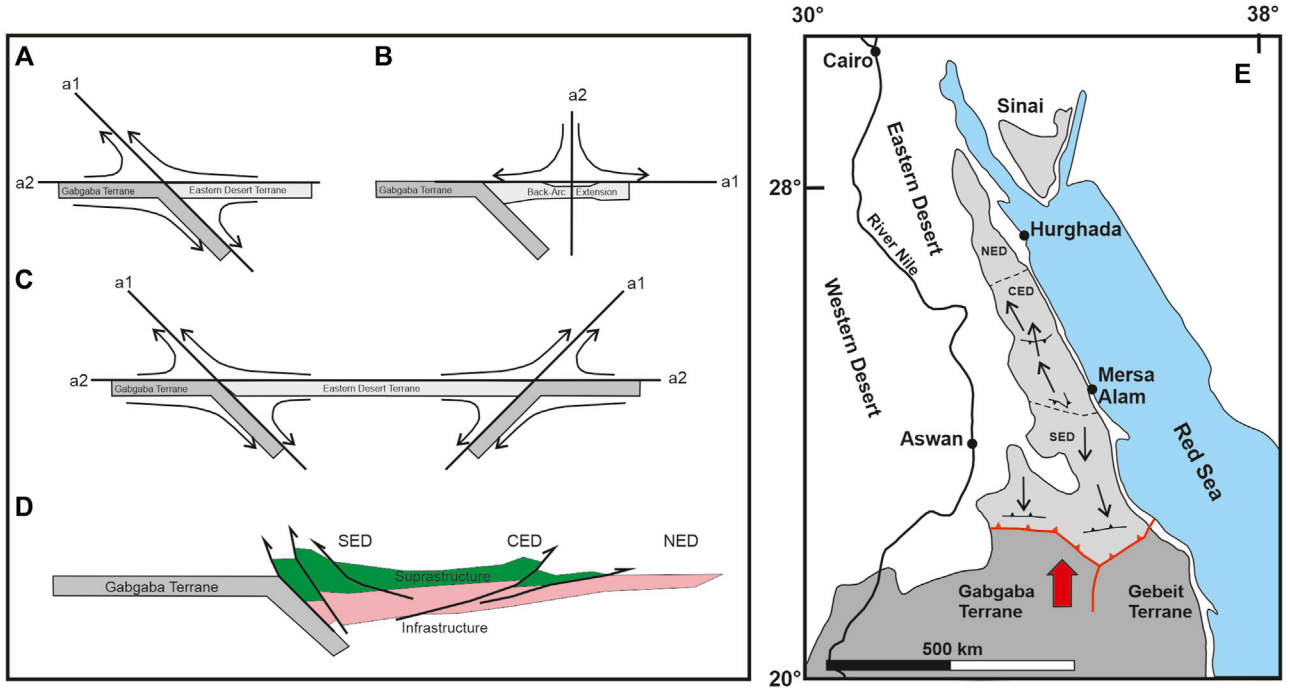

FIGURE 13 | Kinematics and flow fields during first far-field boundary conditions; the N-S compressive event. Flow lines are drawn taking subduction zones and assumed sub-horizontal infra-to supra-structure thrusts as flow apophyses. Individual steps **(A–C)** depict initial subduction along YOSHGAH suture **(A)**, a phase of back-arc extension **(B)**, and final bi-vergent thrusting **(C,D)**. Simplified kinematics on map scale is shown in **(E)**.

younger faults. As seen from **Figure 6C**, the SED is dominated by "Older Granites" and arc-related assemblages. Therefore, we argue that the structural setting described affected mainly the arc that developed in the back of the subduction zone.

The CED differs in that it contains much more ophiolitic assemblages including mafic metavolcanics and ophiolitic melanges. Indeed, most authors favor the existence of back-arc and/or fore-arc basins separating older arc complexes (for discussion, see Fowler and Hamimi, 2020). This implies at least localized north-south extension to serve deposition of sediments between older arc assemblages and, when flow fields are considered, a shift in the flow apophyses. The flow apophyses parallel to the plate motion vector remain in the same orientation but become parallel to the extensional direction. The other one becomes subvertical (Wk = 0), flow is now north-south and subhorizontal fabrics evolve (**Figure 13B**). Phases of north-south convergence and divergence may alternate before the final convergent phase and the closure of intra-arc basins. The sense of displacement in the CED is largely top-to-the north. It remains unclear whether this results from southward subduction in the CED or is the result of thrust and back thrust systems. We are convinced, however, that these structural elements, that is, south and north thrusting are related to the first far field condition and are responsible for the subdivision into tier 1, tier 2, or infra-supra-structure. Ophiolitic fragments and melange were emplaced along flat thrusts over deeper roots of island arcs (**Figure 13D**).

Nabitah Suturing—Second Far-Field Conditions

The structures related to this event evolved in Saudi Arabia as early as c. 680–640 Ma (Stoeser and Stacey, 1988); the major activity in Egypt was between c. 620 and 580 Ma, that is, after suturing of the Nabitah Suture (Collins et al., 2021a). Plate motion instigated activity of the crustal scale NFS, clearest seen in the CED (**Figure 12**). Fault activity falls into the time interval of cooling and exhumation of rocks now exposed in the Egyptian infrastructure domes (Fritz et al., 2002). Concomitantly, it occurred deposition and deformation of Hammamat molasse-type Basins (Abd El-Wahed, 2007; Fowler and Osman, 2013) and emplacement of shear related plutons (Fritz et al., 2014). Older structural elements, such as the infra-supra-structure tectonic boundary were overprinted and refolded.

From the geometry of involved plates and the plate motion vector, two domains are distinguished. Southern Egypt, to the north of the YOSHGAH suture, experienced orthogonal W-E convergence and shortening in the N-S-trending Hamisana Shear Belt (**Figure 12**). This belt is considered to represent a pure shear-dominated deformation zone (De Wall et al., 2001). Northern parts of Saudi Arabia and the CED, considered here in detail, experienced lateral displacement through oblique plate motion.

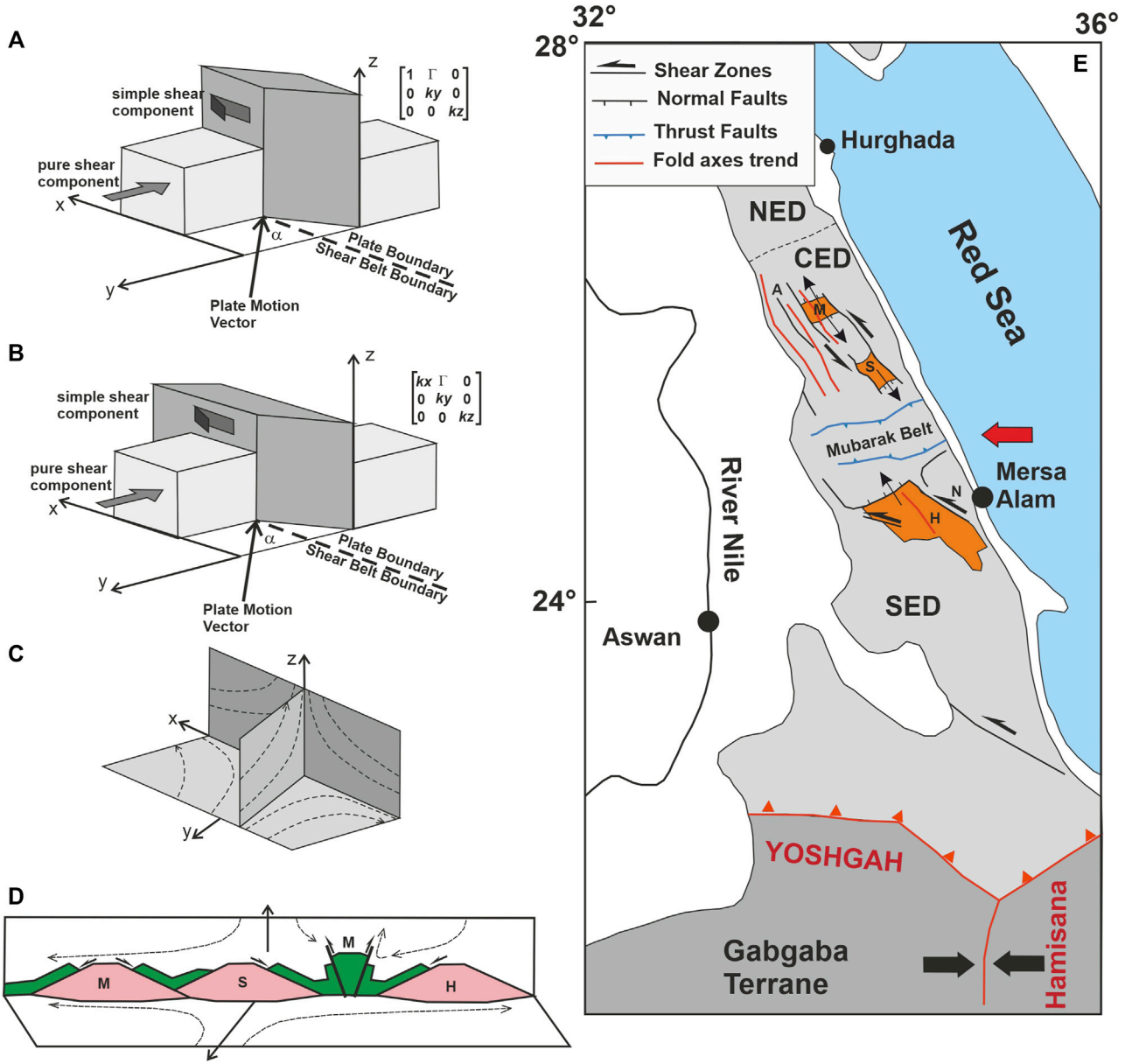

FIGURE 14 | The wrench domain in the CED as a result of the second far-field boundary condition. Schematic crustal blocks, plate motion vectors, and related flow fields along principal sections of flow are shown in **(A–C)**. Also shown are displacement gradient tensor for transpression **(A)** and combined transpression and extrusion **(B,C)**. From the structural inventory present in the CED, namely shear belts with significant N-S extension we argue for a combined transpression/extrusion scenario. N-S extension within the shear belt enabled the exhumation of metamorphic domes (M: Meatiq; S: Sibai; (H): Hafafit) and local convergent structures as given in the sketch **(D)** (M: Mubarak Belt). A summary of the CED structural association is given in **(E)**.

The flow field associated with Najd shearing is 3-dimensional. Full 3-dimensional calculation of flow fields is not only complex but also not very descriptive. Instead, it is convenient to look for special cases, such as transpression, lateral and vertical extrusion, or transtension, or to display flow fields in sections parallel to principal axes of flow (Tikoff and Fossen, 1999). Here we examine three possible strains and displacement scenarios and discuss the role of displacement partitioning. Flow and associated strain geometries during wrench tectonics could be transpressional with subtypes of simple-shear- and pure-shear-dominated transpression, or combined transpression and lateral extrusion. Transpression in the strict sense as originally defined by Sanderson and Marchini (1984) can be ruled out. This is a pseudo-3D geometry that allows length changes in vertical (z) and shear zone perpendicular directions (y), but no change in length parallel to the shear zone boundaries (x) as observed in the CED (**Figure 14**). The diagonal term in the displacement gradient tensor defining stretch parallel to x is 1 (**Figure 14A**).

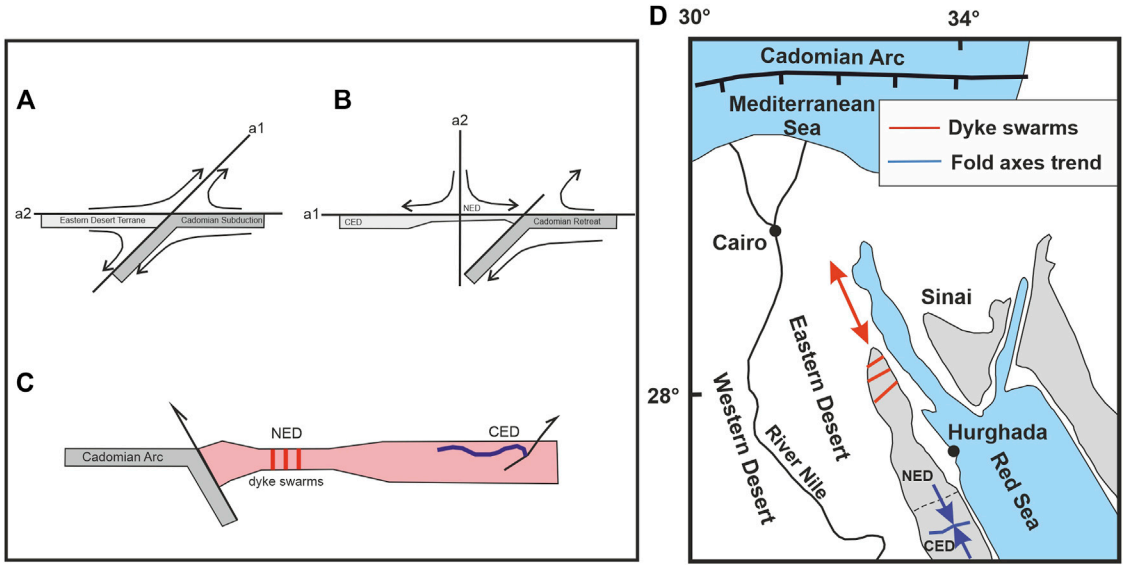

FIGURE 15 | Third far-field boundary condition is connected with the formation and retreat of the Cadomian Arc, **(A)** shows the flow field during initial arc formation and **(B)** flow field during arc retreat and thinning of NED crust. A structural sketch with thinned crust and emplacement of dyke swarms and younger granites is shown in **(C)**. Locally, compressional structures evolve in domains unaffected by crustal thinning. A sketch of map scale structures is given in **(D)** with domains of extension (red arrow) and compression (blue arrow).

Depending on the amount of accumulated strain and convergence angle of plates the long axes of the finite strain ellipsoid may be vertical or horizontal. At small angles of plate convergence up to α = 10° and finite strain ellipse ratios up to 100 (wrench dominated transpression) vertical foliation and horizontal lineation develops; at higher plate convergence angles α > 20° vertical foliation and vertical principal strain axes occur (Teyssier and Tikoff, 1999). Both scenarios are not compatible with the situation in the CED. The angle between the plate motion vector and the average trend of the NFS is 30°–40°. Thus vertical stretch is expected but stretching lineation along CED shear belts is, from field observation, subhorizontal. Hence, a component of lateral extrusion has to be added to fulfill the requirements of the observed vertical foliation and horizontal lineation. For a convergence angle of 30° and an assumed strain of R = 10 (minimum) and R = 1,000 (maximum) at least, 15–20% of lateral extrusion has to be added to reach these conditions (see graphs in Teyssier and Tikoff, 1999). This scenario is compatible with the structural assemblage observed in the CED as it enables vertical foliation, horizontal lineation, and components of horizontal and vertical flow (**Figures 14B, C**). In summary, the central part of the CED containing the NFS is a belt of pure shear dominated transpression combined with lateral extrusion.

Another important concept to explain structural associations within oblique convergent belts is that of displacement partitioning. Thereby, homogeneous flow patterns are decoupled, most probably along zones of strong rheological contrasts. Flow is no longer homogeneous, simple shear component concentrates in distinct shear zones, and the pure shear component in domains outside simple-shear domains. The amount of decoupling, that is, the percentage of slip partitioned on strike-slip faults can be quantified by comparison of structural elements in- and outside-shear belts. In active orogens, measurements used to quantify partitioning are the flow apophyses derived from the plate motion vector and instantaneous stretching axes (stress) as obtained from active faults or borehole break-outs (Tikoff and Teyssier, 1994). This is not applicable in ancient orogens because all other elements except those parallel to flow apophyses change orientation during progressive deformation and strain accumulation.

A conspicuous feature of the CED is that almost all fabric elements are orthogonal to the Najd trend (for details see: Hamimi and Abd El-Wahed, 2020; Fowler and Hamimi, 2020). Fold axes trend parallel the shear zones and extensional faults occupy high angles to shear zones (**Figure 14D**). This could mean almost complete partitioning where the shear belts accommodated almost all of the simple shear components and coaxial fabrics evolved outside the shear domains. However, there are arguments pointing against such a scenario. The NFS itself is much more a broad belt with general shear deformation with much coaxial component than a distinct simple shear zone. Shear zone boundaries are stretched and when the extrusion component exceeds the shear component, horizontal shear may even reverse from sinistral to dextral. Structural elements at a high angle to the shear zones should rotate towards the extensional flow apophyses (a1). Observed normal faults, however, that could represent extensional bridges between branches of shear zones, such as the Nugrus–Hafafit shear extension system, have still high angles to the shear belt. Finally, the NFS in the CED is discontinuous and is transected by thrust belts at high angles to the shear zones. The most prominent of these belts is the W-E-trending Mubarak Belt with steep north- and south-dipping thrusts. In addition to these thrusts, prevalent dextral shear was taken as an argument to interpret the Mubarak Belt as

a conjugate shear system to the NFS (Shalaby et al., 2005; Hamimi and Abd El-Wahed, 2020). Here we offer another explanation for the Mubarak Belt and other high-angle shortening zones within the CED. Transpression and lateral extrusion within the CED were inhomogeneous in space and time; the component of NNW-SSE lateral extrusion was high but discontinuous. This is evident from the $^{40}Ar/^{39}Ar$ hornblende cooling ages related to the shearing and exhumation of infrastructural domes (Fritz et al., 2002). Inner parts of the Sibai Complex exhumed and cooled below ca. 500°C at ca. 620 Ma. The northern Meatiq and the southern Hafafit Complexes cooled much later, at c. 580 Ma. This implies that the Sibai was a cold and rigid block representing a back-stop at the time when Meatiq and Hafafit complex exhumed through N-S extrusion. The extension was blocked by the back-stop and compressional fabric evolved next to the stiff block.

The Cadomian Arc—Third Far-Field Conditions

From c. 590 Ma onwards northern Gondwana destabilized and crustal fragments drifted northwards assembling with today's Europe. The northward motion was accomplished through retreat of the Cadomian arc and extension in the back of the arc. Fragments of Cadomian crust (ca. 560 Ma) and eclogite (560–540 Ma) are now exposed in the northern Arabian Peninsula (Stern et al., 2016) and Anatolia (Canadan et al., 2016). In northern Saudi Arabia and northern Egypt, signs for slab retreat and possible mantle delamination are provided from extensive post-orogenic magmatism (younger granites) that concentrates in the NED (**Figure 6A**). The principal extension direction was approximately NW-SE based on the trend of 590–545 Ma dyke swarm trends in the NED (for a summary, see Abdel-Karim and Azzaz, 1995; Fowler and Hamimi, 2020). Shortly before the onset of retreat NED and CED may have experienced north-south shortening (**Figure 15**). This could explain the west-east-trending fold trends (Fowler and Hamimi, 2020) that post-date Hammamat sedimentation.

THE PRESENT TECTONIC MAP VERSUS THE PREVIOUS MAPS AND CLASSIFICATIONS

Since the establishment of the Egyptian Geological Survey and Mining Authority (EGSMA), the geological mapping was rapidly growing over decades producing a vast literature of published and unpublished maps covering most of (if not all) the Egyptian territory. However, the previously constructed maps of the ENS suffered un-unified scale and map projection. These maps provide geological and structural data on limited and separate areas all over the shield. In addition, there wasn't an attempt to produce a tectonic map expressing such a name and subdivided the shield into tectonic provinces with an attached comprehensive review notes on the tectonic boundaries between the provinces. It also lacked to relate the structural elements that occurred within them to the major tectonic events that deformed the ENS as a prominent part of the entire ANS.

The present study provides the first attempt to construct a tectonic map for the ENS in the ED utilizing the modern techniques of remote sensing and GIS, structural investigation, and re-evaluation of the previously published maps. The produced images and maps (**Figures 4–7** and **Supplementary Figures S1, S2**) indicate that the remote sensing/GIS is a powerful tool in mapping lithological units of the Neoproterozoic basement complex of the ED. Also, remote sensing has successfully extracted detailed structural features and kinematic indicators which are reexamined in detail for some selected reference sites in NED, CED, and SED (**Figures 9A–H**). The final image processing of Landsat-8 OLI and DEM data is a comprehensive geological map (**Figures 6A–C**) with detailed lithology and structural features and a structural map (**Figure 8**). This figure shows the structural architecture of the ED is divided into three major provinces with the tectonic boundaries, major structures, and dominated tectonic regimes.

On the new tectonic map, the Neoproterozoic belt of the ED is subdivided into three structural provinces; Northern, Central, and South Eastern Deserts. These provinces are interpreted in terms of the different far-field boundary conditions between the tectonic plates/terranes. These boundary conditions controlled the assembly of structures within the ED structural provinces with an overlap at their transitions. The southern domain of the ED (SED) was influenced by the N-S convergence between Gabgaba—Gebeit, Jiddah—Asir terranes, and the Eastern Desert—Midyan terranes along the Yanbo-Onib-Sol-Hamid-Gerf-Allaqi-Heiani (YOSHGAH) suture (800–620 Ma). The central domain (CED) is the core of the belt where the Najd Fault-related structural elements developed between c. 640 and 580 Ma. It ascribed to the Nabitah Orogeny when the Ad Dawadimi-Ar Rayn terranes (eastern Arabian Shield) accreted to the earlier arc-related Afif and Tathlith terranes. In the northern segment of the ED (NED), the extensive late orogenic magmatism and extensional fabrics were dominated and controlled by the evolution and retreat of the Cadomian Arc (younger than 580 Ma).

The classical subdivision of the ED into NED, CED, and SED (Stern and Hedge, 1985; El-Gaby et al., 1988) was focusing mainly on the differences in lithology along with the unclear structural boundaries between the three domains. These boundaries follow the route of the main asphaltic roads that were suspected as major shear zones (the Qena-Safaga and Idfu-Mersa Alam shear zones) although they apparently do not cut through the exposed lithological units at their vicinity. The main advantage of the new tectonic map in the present study upon such previous classification and the previously published maps of EGSMA and CONOCO is the integration of the deformation regimes and flow fields (**Figure 12–15**) in the subdivision of the Egyptian Shield into provinces.

In general, the proposed tectonic map will open the door to a serious challenge to modify and even discard some old models and classifications on the ENS and help the better understanding of the lithologic units and affected structures. It will also allow to follow effective methods and approaches for re-evaluating the

local structures and tectonic setting in terms of the given far-field boundary conditions, tectonic regimes, and intraplate flow fields.

CONCLUDING REMARKS

The results obtained from the present study can be summarized as follows:

- A new tectonic map has been developed based on intensive field/structural work, which is integrated with processing and analysis of the optical sensors using remote sensing techniques, and careful re-examination of the previously published geological maps and literature.
- ENS is subdivided into three structural provinces; compressional-, transpressional- and extensional-provinces. The proposed provinces are ascribed to three different far-field boundary conditions.
- The first kinematic event (between c. 800 and 620 Ma) was released by the c. N-S convergence of Gabgaba—Gebeit, Jiddah—Asir terranes and Eastern Desert—Midyan terranes along the YOSHGAH suture. Several lines of evidence illustrate such convergence, the prevailing compressional regime in the vicinity of the Allaqi-Heini belt and the extreme SED in Egypt.
- The second kinematic event (between c. 640 and 580 Ma) was released by the Nabitah Orogeny when the Ad Dawadimi—Ar Rayan terranes of the Eastern Arabian Shield accreted to the earlier consolidated arc terranes (Afif and Tathlith terranes).
- W-E shortening in southern Saudi Arabia may be correlated to the N-S trending of the Hamisana Shear Belt.
- Northwestern Saudi Arabia and the CED of Egypt suffer from pronounced strike-slip deformation associated with the displacement along the wider NFS.
- The third kinematic event (younger than c. 580 Ma) was released by the evolution and retreat of the Cadomian Arc. The main effects of this event are remarkable extension, mantle delamination-related widespread postorogenic magmatism, associated crustal thinning, and E-W trending dyke swarms. It is well represented in the northern sectors of the ENS and the Midyan terrane in the northern Arabian Shield.
- The classical tripartite subdivision of the ED geology into NED, CED, and SED is related to the external far-field boundary conditions instead of the activity of cryptic fault systems that were proposed but have not been proven.

DATA AVAILABILITY STATEMENT

The original contributions presented in the study are included in the article/**Supplementary Material**; further inquiries can be directed to the corresponding author.

AUTHOR CONTRIBUTIONS

ZH, WH, HF, HB, and SK contributed to conceptualization, fieldwork, writing the draft manuscript, data processing, and software manipulation. All authors have read and agreed to the published version of the manuscript.

ACKNOWLEDGMENTS

The authors would like to thank ND, IE, and MA for valuable comments that were significantly improved the original version of the manuscript.

SUPPLEMENTARY MATERIAL

The Supplementary Material for this article can be found online at: https://www.frontiersin.org/articles/10.3389/feart.2022.921521/full#supplementary-material

Supplementary Table S1 | Landsat 8 OLI/TIRS characteristics and the scenes used in the present study (after US Geological Survey, 2016).

Supplementary Figure S1 | (A) Ophiolitic rocks and metavolcanic-metasediments association mapping promoted by the principal component analysis image PCA RGB (PC2, PC4, PC5) of landsat-8 OLI which represents the geographic distribution of serpentinites, ophiolitic metagabbros, mafic and arc metavolcanics and volcaniclastic metasediments in the Egyptian Nubian shield. **(B)** Gneisses and granitoid rocks mapped using the processed false color composite (RGB-753) of Landsat-8 OLI which showed the distribution of the gneisses rock in the South Eastern Desert, syn to late granitoids are mostly presented in the Central and south Eastern desert where the post-tectonic granitoids are dominated in the extensional province at the North Eastern Desert.

Supplementary Figure S2 | Detailed lithological mapping of some selected areas in the ENS in the Eastern Desert using different image processing techniques such as false color composites (FCC), band ratios (BR), principal component analysis (PCA) to Landsat-8 OLI data and the interpreted lithologic map. **(A)** G. Dara (NED), **(B)** G. Meatiq (CED), **(C)** G. Abu Dahr (SED). Note: Gm: gneisses and migmatites; Mu: Metaultramafics; Mg: Metagabbros; Am: Arc metavolcanics; Vom: Volcanogenic metasediments; Og: Older granites; Gd: Gabbro-diorite complex; Dv: Dokhan volcanics; and Yg: Younger granites. The color code of the interpreted maps is shown in Figure 6a and the locations of these selected areas are shown in Figure 4a.

REFERENCES

Abd El-Rahman, Y., Polat, A., Dilek, Y., Fryer, B., El-Sharkawy, M., and Sakran, S. (2009). Geochemistry and Tectonic Evolution of the Neoproterozoic Wadi Ghadir Ophiolite, Eastern Desert, Egypt. *Lithos* 113, 158–178. doi:10.1016/j.lithos.2008.12.014

Abd El-Wahed, M. A. (2007). Late Pan-African Tectonic Evolution and Strain Determination in the Late Neoproterozoic Molasse Sediments, Eastern Desert, Egypt: Evidence for Post-hammamat Compression and Transpression. *Egypt J. Geol.* 51, 1–39.

Abd El-Wahed, M. A. (2010). The Role of the Najd Fault System in the Tectonic Evolution of the Hammamat Molasse Sediments, Eastern Desert, Egypt. *Arab. J. Geosci.* 3, 1–26. doi:10.1007/s12517-008-0030-0

Abdeen, M. M., and Greiling, R. O. (2005). A Quantitative Structural Study of Late Pan-African Compressional Deformation in the Central Eastern Desert (Egypt) during Gondwana Assembly. *Gondwana Res.* 8 (4), 457–471. doi:10.1016/s1342-937x(05)71148-5

Abdel Khalek, M. L., Takla, M. A., Sehim, A., Hamimi, Z., and El Manawi, A. W. (1992). "Geology and Tectonic Evolution of Wadi Beitan Area, South Eastern Desert, Egypt," in *GAW* (Giza, Egypt: Cairo University), 1, 369–393.

Abdel-Karim, A. M., and Azzaz, S. A. (1995). On the Age Dating of the Dyke Swarms of Southwestern Sinai, Egypt. *Arab. Gulf J. Sci. Res.* 13, 41–53.

Abdel-Rahman, A.-F. M. (1996). Pan-African Volcanism: Petrology and Geochemistry of the Dokhan Volcanic Suite in the Northern Nubian Shield. *Geol. Mag.* 133, 17–31. doi:10.1017/s0016756800007226

Abdelmalik, K. W., and Abd-Allah, A. M. A. (2018). Integration of Remote Sensing Technique and Field Data in Geologic Mapping of an Ophiolitic Suture Zone in Western Arabian Shield. *J. Afr. Earth Sci.* 146, 180–190. doi:10.1016/j.jafrearsci.2017.10.006

Abdelmalik, K. W. (2019). Landsat 8: Utilizing Sensitive Response Bands Concept for Image Processing and Mapping of Basalts. *Egypt. J. Remote Sens. Space Sci.* 23, 263–274. doi:10.1016/j.ejrs.2019.04.004

Abdelmalik, K. W. (2018). Role of Statistical Remote Sensing for Inland Water Quality Parameters Prediction. *Egypt. J. Remote Sens. Space Sci.* 21 (2), 193–200. doi:10.1016/j.ejrs.2016.12.002

Aboelkhair, H., Abdelhalim, A., Hamimi, Z., and Al-Gabali, M. (2020). Reliability of Using ASTER Data in Lithologic Mapping and Alteration Mineral Detection of the Basement Complex of West Berenice, Southeastern Desert, Egypt. *Arab. J. Geosci.* 13, 287. doi:10.1007/s12517-020-5227-x

Abu El-Ela, F. F. (1997). Geochemistry of an Island-Arc Plutonic Suite: Wadi Dabr Intrusive Complex, Eastern Desert, Egypt. *J. Afr. Earth Sci.* 24, 473–496. doi:10.1016/s0899-5362(97)00076-6

Akaad, M. K., and Noweir, A. M. (1980). Geology and Lithostratigraphy of the Arabian Desert Orogenic Belt of Egypt between Latitudes 25° 35′ and 26° 30′ N. *Bull. Inst. Appl. Geol. (King Abdel Aziz Univ. Jeddah)* 3 (4), 127–135. doi:10.1016/b978-0-08-024481-5.50016-9

Akaad, M. K., Noweir, A. M., and Kotb, H. (1979). Geology and Petrochemistry of the Granite Association of the Arabian Desert Orogenic Belt of Egypt between 25°35′ and 26°30′. *Delta J. Sci.* 3, 107–151.

Ali, K. A., Azer, M. K., Gahlan, H. A., Wilde, S. A., Samuel, M. D., and Stern, R. J. (2010). Age Constraints on the Formation and Emplacement of Neoproterozoic Ophiolites along the Allaqi-Heiani Suture, South Eastern Desert of Egypt. *Gondwana Res.* 18, 583–595. doi:10.1016/j.gr.2010.03.002

Ali, K. A., Kröner, A., Hegner, E., Wong, J., Li, S.-Q., Gahlan, H. A., et al. (2015). U-pb Zircon Geochronology and Hf-Nd Isotopic Systematics of Wadi Beitan Granitoid Gneisses, South Eastern Desert, Egypt. *Gondwana Res.* 27, 811–824. doi:10.1016/j.gr.2013.11.002

Ali, K., Andresen, A., Manton, W. I., Stern, R. J., Omar, S. A., and Maurice, A. E. (2012). U-pb Zircon Dating and Sr-Nd-Hf Isotopic Evidence to Support a Juvenile Origin of the ~ 634 Ma El Shalul Granitic Gneiss Dome, Arabian-Nubian Shield. *Geol. Mag.* 149, 783–797. doi:10.1017/s0016756811000975

Ali, K. A., Wilde, S. A., Stern, R. J., Moghazi, A.-K. M., and Ameen, S. M. M. (2013). HF Isotopic Composition of Single Zircons from Neoproterozoic Arc Volcanics and Post-collision Granites, Eastern Desert of Egypt: Implications for Crustal Growth and Recycling in the Arabian-Nubian Shield. *Precambrian Res.* 239, 42–55. doi:10.1016/j.precamres.2013.05.007

Ali, S. O. A., and Pour, B. A. (2014). Lithological Mapping and Hydrothermal Alteration Using Landsat 8 Data: a Case Study in Ariab Mining District, Red Sea Hills, Sudan. *Int. J. Basic Appl. Sci.* 3 (3), 199–208. doi:10.14419/ijbas.v3i3.2821

Andersen, A., Abu El-Rus, M. A., Myhre, P. I., Boghdady, G. Y., and Corfu, F. (2009). U-pb TIMS Age Constraints on the Evolution of the Neoproterozoic Meatiq Gneiss Dome, Eastern Desert, Egypt. *Int. J. Earth Sci. Geol. Rundsch)* 98, 481–497.

Armijo, R., Lacassin, R., Coudurier-Curveur, A., and Carrizo, D. (2015). Coupled Tectonic Evolution of Andean Orogeny and Global Climate. *Earth-Science Rev.* 143, 1–35. doi:10.1016/j.earscirev.2015.01.005

Asran, A. M., Emam, A., and El-Fakharani, A. (2017). Geology, Structure, Geochemistry and ASTER-Based Mapping of Neoproterozoic Gebel El-Delihimmi Granites, Central Eastern Desert of Egypt. *Lithos* 282-283, 358–372. doi:10.1016/j.lithos.2017.03.022

Augland, L. E., Andresen, A., and Boghdady, G. Y. (2012). U-pb ID-TIMS Dating of Igneous and Metaigneous Rocks from the El-Sibai Area: Time Constraints on the Tectonic Evolution of the Central Eastern Desert, Egypt. *Int. J. Earth Sci. Geol. Rundsch)* 101, 25–37. doi:10.1007/s00531-011-0653-3

Ballevre, M., Le Goff, E., and Hebert, R. (2001). The Tectonothermal Evolution of the Cadomian Belt of Northern Brittany, France: a Neoproterozoic Volcanic Arc. *Tectonophysics* 331 (1–2), 19–43. doi:10.1016/s0040-1951(00)00234-1

Bandres, A., Eguiluz, L., Ibarguchi, J. I., and Palacios, T. (2002). Geodynamic Evolution of a Cadomian Arc Region: the Northern Ossa-Morena Zone, Iberian Massif. *Tectonophysics* 352 (1-2), 105–120. doi:10.1016/s0040-1951(02)00191-9

Bennett, J. D., and Mosley, P. N. (1987). "Tiered-tectonics and Evolution, Eastern Desert and Sinai, Egypt," in *Current Research in African Earth Sciences*. Editors G. Matheis and H. Schandelmeier (Rotterdam: Balkema), 79–82.

Bentor, Y. K. (1985). The Crustal Evolution of the Arabo-Nubian Massif with Special Reference to the Sinai Peninsula. *Precambrian Res.* 28, 1–74. doi:10.1016/0301-9268(85)90074-9

Bobyarchik, A. R. (1986). The Eigenvalues of Steady State Flow in Mohr Space. *Tectonophysics* 122, 35–52.

Bregar, M., Bauernhofer, A., Pelz, K., Kloetzli, U., Fritz, H., and Neumayr, P. (2002). A Late Neoproterozoic Magmatic Core Complex in the Eastern Desert of Egypt: Emplacement of Granitoids in a Wrench-Tectonic Setting. *Precambrian Res.* 118, 59–82. doi:10.1016/s0301-9268(02)00062-1

Breitkreutz, C., Eliwa, H. A., Khalaf, I. M., El Gameel, K., Buhler, B., Sergeev, S., et al. (2010). Neoproterozoic SHRIMP U-Pb Zircon Ages of Silica-Rich Dokhan Volcanics in the North Eastern Desert, Egypt. *Precambrian Res.* 182, 163–174.

Canadan, O., Koralay, O. E., Topuz, G., Oberhänsli, R., Fritz, H., Collins, A. S., et al. (2016). Late Neoproterozoic Gabbro Emplacement Followed by Early Cambrian Eclogite-Facies Metamorphism in the Menderes Massif (W. Turkey): Implications on the Final Assembly of Gondwana. *Gondwana Res.* 34, 158–173. doi:10.1016/j.gr.2015.02.015

Chander, G., Markham, B. L., and Helder, D. L. (2009). Summary of Current Radiometric Calibration Coefficients for Landsat MSS, TM, ETM+, and EO-1 ALI Sensors. *Remote Sens. Environ.* 113 (5), 893–903. doi:10.1016/j.rse.2009.01.007

Chavez, P., Bauer, B., and Sowers, L. B. (1982). An Automatic Pptimum Kernel-Size Selection Technique for Edge Enhancement. *Remote Sens. Environ.* 12 (1), 23–38. doi:10.1016/0034-4257(82)90005-0

Chen, X., and Campagna, D. J. (2009). "Remote Sensing of Geology," in *The SAGE Handbook of Remote Sensing*. Editors T. A. Warner, M. D. Nellis, and G. M. Foody (Thousand Oaks, CA: Sage), 328–340.

Collins, A. S., Blades, M. L., Merdith, A. S., and Foden, J. D. (2021b). Closure of the Proterozoic Mozambique Ocean Was Instigated by a Late Tonian Plate Reorganization Event. *Commun. Earth Environ.* 2. doi:10.1038/s43247-021-00149-z

Collins, A. S., Blades, M. L., and Merdith, A. S. (2021a). "The Arabian-Nubian Shield within the Neoproterozoic Plate Tectonic Circuit," in *The Geology of the Arabian-Nubian Shield*. Editors Z. Hamimi, A. R. Fowler, J. P. Liégeois, A. S. Collins, M. G. Abdelsalam, and M. A. El-Wahed (Cham, Switzerland: Regional Geology Reviews, Springer Nature Switzerland), 195–202. doi:10.1007/978-3-030-72995-0_8

De Wall, H., Greiling, R. O., and Fouad Sadek, M. (2001). Post-collisional Shortening in the Late Pan-African Hamisana High Strain Zone, SE Egypt: Field and Magnetic Fabric Evidence. *Precambrian Res.* 107, 179–194. doi:10.1016/s0301-9268(00)00141-8

El Kalioubi, B., Fowler, A.-R., and Abdelmalik, K. (2020). "The Metamorphism and Deformation of the Basement Complex in Egypt," in *The Geology of Egypt*. Editors Z. Hamimi, A. El-Barkooky, J. Martínez Frías, H. Fritz, and Y. Abd El-Rahman (Cham, Switzerland: Regional Geology Reviews, Springer Nature Switzerland), 191–251. doi:10.1007/978-3-030-15265-9_6

El-Bialy, M. Z., and Omar, M. M. (2015). Spatial Association of Neoproterozoic Continental Arc I-type and Post-collision A-type Granitoids in the Arabian-Nubian Shield: The Wadi Al-Baroud Older and Younger Granites, North Eastern Desert, Egypt. *J. Afr. Earth Sci.* 103, 1–29. doi:10.1016/j.jafrearsci.2014.11.013

El-Gaby, S., el-Nady, O., and Khudeir, A. (1984). Tectonic Evolution of the Basement Complex in the Central Eastern Desert of Egypt. *Geol. Rundsch.* 73, 1019–1036. doi:10.1007/bf01820886

El-Gaby, S., and Khudeir, A. A. (1988). Low Pressure Metamorphism in Hammamat Sediments at Um Had Area, Central Eastern Desert, Egypt. *Bull. Fac. Assuit Univ.* 17 (2-F), 51–71.

El-Gaby, S., Khudier, A. A., and El Taky, M. (1989). "The Dokhan Volcanics of Wadi Queh Area, Central Eastern Desert, Egypt," in 1st Conf. on Geochem, Alexandria, Egypt, 42–62.

El-Gaby, S., List, F. K., and Tehrani, R. (1988). "Geology, Evolution and Metallogenesis of the Pan-African Belt in Egypt," in *The Pan-African Belt of*

NE Africa and Adjacent Areas, Tectonic Evolution and Economic Aspects. Editors S. El Gaby and R. Greiling (Braunschweig, Wiesbaden: Vieweg), 17–68.

El-Sharkawy, M. A., and El-Bayoumi, R. M. (1979). The Ophiolites of Wadi Ghadir Area Eastern Desert, Egypt. *Ann. Geol. Surv. Egypt* 9, 125–135.

Eliwa, H. A., Kimura, J.-I., and Itaya, T. (2006). Late Neoproterozoic Dokhan Volcanics, North Eastern Desert, Egypt: Geochemistry and Petrogenesis. *Precambrian Res.* 151, 31–52. doi:10.1016/j.precamres.2006.08.005

Emam, A., Hamimi, Z., El-Fakharani, A., Abdel-Rahman, E., Barreiro, J. G., and Abo-Soliman, M. Y. (2018). Utilization of ASTER and OLI Data for Lithological Mapping of Nugrus-Hafafit Area, South Eastern Desert of Egypt. *Arab. J. Geosci.* 11, 756. doi:10.1007/s12517-018-4106-1

Fowler, A.-R., and Hamimi, Z. (2021a). A Review and Synthesis of Strain Studies in the Egyptian Nubian Shield: Materials, Methods, Problems and Prospects. *Precambrian Res.* 355, 106072. doi:10.1016/j.precamres.2020.106072

Fowler, A.-R., and Hamimi, Z. (2021b). "Post-amalgamation Depositional Basins in the Arabian-Nubian Shield: The Hammamat Basins of Egypt," in *The Geology of the Arabian-Nubian Shield. Regional Geology Reviews*. Editors Z. Hamimi, A. R. Fowler, J. P. Liégeois, A. Collins, M. G. Abdelsalam, and M. Abd EI-Wahed (Cham, Switzerland: Regional Geology Reviews, Springer Nature Switzerland), 451–483. doi:10.1007/978-3-030-72995-0_19

Fowler, A.-R., and Hamimi, Z. (2020). "Structural and Tectonic Framework of Neoproterozoic Basement of Egypt: from Gneiss Domes to Transpression Belts," in *The Geology of Egypt. Regional Geology Reviews*. Editors Z. Hamimi, A. El-Barkooky, J. Martínez Frías, H. Fritz, and Y. Abd El-Rahman (Cham, Switzerland: Springer Nature Switzerland), 81–129. doi:10.1007/978-3-030-15265-9_3

Fowler, A., and Osman, A. F. (2013). Sedimentation and Inversion History of Three Molasse Basins of the Western Central Eastern Desert of Egypt: Implications for the Tectonic Significance of Hammamat Basins. *Gondwana Res.* 23, 1511–1534. doi:10.1016/j.gr.2012.08.022

Fowler, A., and Osman, A. F. (2009). The Sha'it-Nugrus Shear Zone Separating Central and South Eastern Deserts, Egypt: A Post-arc Collision Low-Angle Normal Ductile Shear Zone. *J. Afr. Earth Sci.* 53, 16–32. doi:10.1016/j.jafrearsci.2008.07.006

Fritz, H., Abdelsalam, M., Ali, K. A., Bingen, B., Collins, A. S., Fowler, A. R., et al. (2013). Orogen Styles in the East African Orogen: a Review of the Neoproterozoic to Cambrian Tectonic Evolution. *J. Afr. Earth Sci.* 86, 65–106. doi:10.1016/j.jafrearsci.2013.06.004

Fritz, H., Dallmeyer, D. R., Wallbrecher, E., Loizenbauer, J., Hoinkes, G., Neumayr, P., et al. (2002). Neoproterozoic Tectonothermal Evolution of the Central Eastern Desert, Egypt: a Slow Velocity Tectonic Process of Core Complex Exhumation. *J. Afr. Earth Sci.* 34, 137–155. doi:10.1016/s0899-5362(02)00014-3

Fritz, H., Loizenbauer, J., and Wallbrecher, E. (2014). Magmatic and Solid State Structures of the Abu Ziran Pluton: Deciphering Transition from Thrusting to Extension in the Eastern Desert of Egypt. *J. Afr. Earth Sci.* 99, 122–135. doi:10.1016/j.jafrearsci.2013.11.012

Fritz, H., and Messner, M. (1999). Intramontane Basin Formation during Oblique Convergence in the Eastern Desert of Egypt: Magmatically versus Tectonically Induced Subsidence. *Tectonophysics* 315, 145–162. doi:10.1016/s0040-1951(99)00284-x

Fritz, H., Wallbrecher, E., Khudeir, A. A., Abu El Ela, F., and Dallmeyer, D. R. (1996). Formation of Neoproterozoic Metamorphic Complex during Oblique Convergence (Eastern Desert, Egypt). *J. Afr. Earth Sci.* 23, 311–329. doi:10.1016/s0899-5362(97)00004-3

Gabr, S. S., Hassan, S. M., and Sadek, M. F. (2015). Prospecting for New Gold-Bearing Alteration Zones at El-Hoteib Area, South Eastern Desert, Egypt, Using Remote Sensing Data Analysis. *Ore Geol. Rev.* 71, 1–13. doi:10.1016/j.oregeorev.2015.04.021

Gahlan, H. A., Azer, M. K., and Khalil, A. E. S. (2015). The Neoproterozoic Abu Dahr Ophiolite, South Eastern Desert, Egypt: Petrological Characteristics and Tectonomagmatic Evolution. *Min. Pet.* 109, 611–630. doi:10.1007/s00710-015-0397-z

Gahlan, H. A. (2006). *Petrological Characteristics of the Mantle Section in the Proterozoic Ophiolites from the Pan-African Belt*. Ph.D. thesis (Kanazawa, Japan: Kanazawa Univ.), 227.

Greiling, R. O., Abdeen, M. M., Dardir, A. A., El Akhal, H., El Ramly, M. F., El Din Kamal, G. M., et al. (1994). A Structural Synthesis of the Proterozoic Arabian-Nubian Shield in Egypt. *Geol. Rundsch.* 83, 484–501. doi:10.1007/bf01083222

Gupta, R. P. (2013). *Remote Sensing Geology*. Berlin, Heidelberg: Springer-Verlag, 438.

Hamimi, Z., Abd El-Wahed, M. A., Gahlan, H. A., and Kamh, S. Z. (2019). "Tectonics of the Eastern Desert of Egypt: Key to Understanding the Neoproterozoic Evolution of the Arabian-Nubian Shield (East African Orogen)," in *Geology of the Arab World-An Overview*. Editors A. Bendaoud, Z. Hamimi, M. Hamoudi, S. Djemai, and B. Zoheir (Berlin, Germany: Springer Geology), 1–81. doi:10.1007/978-3-319-96794-3_1

Hamimi, Z., Abd El-Wahed, M. A., Hamimi, Z., El-Barkooky, A., Martínez Frías, J., Fritz, H., et al. (2020). "Suture(s) and Major Shear Zones in the Neoproterozoic Basement of Egypt," in *The Geology of Egypt. Regional Geology Reviews* (Cham, Switzerland: Springer Nature Switzerland), 153–189. doi:10.1007/978-3-030-15265-9_5

Hamimi, Z., Hagag, W., Kamh, S., and El-Araby, A. (2020). Application of Remote-Sensing Techniques in Geological and Structural Mapping of Atalla Shear Zone and Environs, Central Eastern Desert, Egypt. *Arab. J. Geosci.* 13, 414. doi:10.1007/s12517-020-05324-8

Hassan, M. A., and Hashad, A. H. (1990). "Precambrian of Egypt," in *The Geology of Egypt*. Editor R. Said (Rotterdam: Balkema), 201–245.

Hassan, S. M., El kazzaz, Y. A., Taha, M. M. N., and Mohammad, A. T. (2017). Late Neoproterozoic Basement Rocks of Meatiq Area, Central Eastern Desert, Egypt: Petrography and Remote Sensing Characterizations. *J. Afr. Earth Sci.* 131, 14–31. doi:10.1016/j.jafrearsci.2017.04.001

Hassan, S. M., and Ramadan, T. M. (2014). Mapping of the Late Neoproterozoic Basement Rocks and Detection of the Gold-Bearing Alteration Zones at Abu Marawat-Semna Area, Eastern Desert, Egypt Using Remote Sensing Data. *Arab. J. Geosci.* 8, 4641–4656. doi:10.1007/s12517-014-1562-0

Hassan, S. M., and Sadek, M. F. (2017). Geological Mapping and Spectral Based Classification of Basement Rocks Using Remote Sensing Data Analysis: The Korbiai-Gerf Nappe Complex, South Eastern Desert, Egypt. *J. Afr. Earth Sci.* 134, 404–418. doi:10.1016/j.jafrearsci.2017.07.006

Hassan, S. M., Soliman, O. S., and Mahmoud, A. S. (2015). Optimized Data Input for the Support Vector Machine Classifier Using ASTER Data. Case Study: Wadi Atalla Area, Eastern Desert, Egypt. *Carpa. J. Earth Environ. Sci.* 10 (1), 15–26.

Hermina, M., Klitzsch, E., and List, F. K. (1989). *Stratigraphic Lexicon and Explanatory Notes to the Geological Map of Egypt 1:500,000*. Cairo, Egypt: Conoco Inc.

Horton, B. K., Fuentes, F., Boll, A., Starck, D., Ramirez, S. G., and Stockli, D. F. (2016). Andean Stratigraphic Record of the Transition from Backarc Extension to Orogenic Shortening: A Case Study from the Northern Neuquén Basin, Argentina. *J. S. Am. Earth Sci.* 71, 17–40. doi:10.1016/j.jsames.2016.06.003

Hu, X., Garzanti, E., Wang, J., Huang, W., An, W., and Webb, A. (2016). The Timing of India-Asia Collision Onset - Facts, Theories, Controversies. *Earth-Science Rev.* 160, 264–299. doi:10.1016/j.earscirev.2016.07.014

Huntington, J. F. (1996). The Role of Remote Sensing in Finding Hydrothermal Mineral Deposits on Earth. *Ciba Found. Symp.* 202, 214–215. doi:10.1002/9780470514986.ch12

Hussein, A. A. A., Ali, M. M., and El Ramly, M. F. (1982). A Proposed New Classification of the Granites of Egypt. *J. Volcanol. Geotherm. Res.* 14, 187–198. doi:10.1016/0377-0273(82)90048-8

Johnson, P. R., Andresen, A., Collins, A. S., Fowler, A. R., Fritz, H., Ghebreab, W., et al. (2011). Late Cryogenian-Ediacaran History of the Arabian-Nubian Shield: a Review of Depositional, Plutonic, Structural, and Tectonic Events in the Closing Stages of the Northern East African Orogen. *J. Afr. Earth Sci.* 61, 167–232. doi:10.1016/j.jafrearsci.2011.07.003

Johnson, P. R. (2021). "The Arabian–Nubian Shield, an Introduction: Historic Overview, Concepts, Interpretations, and Future Issues," in *The Geology of the Arabian-Nubian Shield*. Editors Z. Hamimi, A. R. Fowler, J. P. Liegeois, A. Collins, M. Abdelsalam, and M. Abd EI-Wahed (Cham, Switzerland: Regional Geology Reviews book series (RGR), Springer Nature Switzerland), 785. doi:10.1007/978-3-030-72995-0

Jolliffe, I. T. (1986). *Principal Component Analysis*. Berlin, Germany: Springer-Verlag, 487.

Jones, R. R., Holdsworth, R. E., McCaffrey, K. J. W., Clegg, P., and Tavarnelli, E. (2005). Scale Dependence, Strain Compatibility and Heterogeneity of Three-Dimensional Deformation during Mountain Building: a Discussion. *J. Struct. Geol.* 27, 1190–1204. doi:10.1016/j.jsg.2005.04.001

Khalil, A. E., El-Desoky, H. M., and Salem, S. M. (2017). Contribution of Remote Sensing Techniques to the Recognition of Titanite Occurrences at Gabal El-Degheimi Area, Central Eastern Desert, Egypt. *Egypt. J. Remote Sens. Space Sci.* 20, 41–50. doi:10.1016/j.ejrs.2016.08.003

Khudeir, A. A., and Asran, A. H. (1992). Back-arc Wizr Ophiolites at Wadi Um Gheig District, Eastern Desert, Egypt. *Bull. Fac. Sci. Assiut Univ.* 21, 1–22.

Li, Y., Wang, C., Dai, J., Xu, G., Hou, Y., and Li, X. (2015). Propagation of the Deformation and Growth of the Tibetan-Himalayan Orogen: A Review. *Earth-Science Rev.* 143, 36–61. doi:10.1016/j.earscirev.2015.01.001

Liégeois, J. P., and Stern, R. J. (2010). Sr–Nd Isotopes and Geochemistry of Granite–Gneiss Complexes from the Meatiq and Hafafit Domes, Eastern Desert, Egypt: No Evidence for Pre-neoproterozoic Crust. *Int. J. Earth Sci.* 57, 31–40.

Lillesand, T. M., Kiefer, R. W., and Chipman, J. W. (2004). *Remote Sensing and Image Interpretation*. New York: John Wiley & Sons.

Linnemann, U., and Romer, R. (2002). The Cadomian Orogeny in Saxo-Thuringia, Germany: Geochemical and Nd–Sr–Pb Isotopic Characterization of Marginal Basins with Constraints to Geotectonic Setting and Provenance. *Tectonophysics* 352 (1-2), 33–64. doi:10.1016/s0040-1951(02)00188-9

Lundmark, A. M., Andresen, A., Hassan, M. A., Augland, L. E., Boghdady, G. Y., and Boghdady, G. Y. (2012). Repeated Magmatic Pulses in the East African Orogen in the Eastern Desert, Egypt: An Old Idea Supported by New Evidence. *Gondwana Res.* 22, 227–237. doi:10.1016/j.gr.2011.08.017

Messner, M. (1996). *Basin Analysis of Hammamat Type Molasse Basins, Eastern Desert, Egypt*. Cairo, Egypt: Proc. of the Geol. Surv. Egypt, 125–126.

Moghazi, A. M. (2003). Geochemistry and Petrogenesis of a High-K Calc-Alkaline Dokhan Volcanic Suite, South Safaga Area, Egypt: the Role of Late Neoproterozoic Crustal Extension. *Precambrian Res.* 125, 161–178. doi:10.1016/s0301-9268(03)00110-4

Mohammad, A. T., El Kazzaz, Y. A., Hassan, S. M., and Taha, M. M. N. (2019). Neoproterozoic Tectonic Evolution and Exhumation History of Transpressional Shear Zones in the East African Orogen: Implications from Kinematic Analysis of Meatiq Area, Central Eastern Desert of Egypt. *Int. J. Earth Sci. Geol. Rundsch)* 109, 253–279. doi:10.1007/s00531-019-01801-y

Mohy, H., Basta, F., Saber, S., and El Sobky, A. (2017). Using Landsat 8 and ASTER Data for Lithological Discrimination and Mapping in Wadi Hamad Area, North Eastern Desert, Egypt. *J. Amer. Sci.* 13 (7), 1–13.

Mohy, H., El-Magd, I. A., Basta, F., and Amasha, A. (2019). Utilization of Full-Polarimetric SAR Data (RADARSAT-2), ASTER and Landsat 8 Data in Geological Mapping of the West Gebal Elba Area, Halayeb District, South Eastern Desert, Egypt. *J. Indian Soc. Remote Sens.* 47, 267–278. doi:10.1007/s12524-018-0923-7

Mouslopoulou, V., Nicol, A., Little, T. A., and Begg, J. G. (2009). "Palaeoearthquake Surface Rupture in a Transition Zone from Strike-Slip to Oblique-Normal Slip and its Implications to Seismic Hazard, North Island Fault System, New Zealand," in *Palaeoseismology: Historical and Prehistorical Records of Earthquake Ground Effects for Seismic Hazard Assessment*. Editors K. Reicherter, A. M. Michetti, and P. G. Silva (London: Geological Society, London, Special Publications), 316, 269–292. doi:10.1144/sp316.17

Moussa, E. M. M., Stern, R. J., Manton, W. I., and Ali, K. A. (2008). SHRIMP Zircon Dating and Sm/Nd Isotopic Investigations of Neoproterozoic Granitoids, Eastern Desert, Egypt. *Precambrian Res.* 160, 341–356. doi:10.1016/j.precamres.2007.08.006

Mwaniki, M. W., Moeller, M. S., and Schellmann, G. (2015). A Comparison of Landsat 8 (OLI) and Landsat 7 (ETM+) in Mapping Geology and Visualising Lineaments: A Case Study of Central Region Kenya. *Int. Arch. Photogramm. Remote Sens. Spat. Inf. Sci.* XL-7/W3, 897–903. doi:10.5194/isprsarchives-xl-7-w3-897-2015

NOAA (2016). *World Data Service for Geophysics-Bathymetry and Global Relief Grid Extract. Grid Extract*. Washington, D.C., USA: National Oceanic and Atmospheric Administration, National Centers for Environmental Information. Available at: http://www.ngdc.noaa.gov/mgg/bathymetry/relief.html.

Norris, R. J., Koons, P. O., and Cooper, A. F. (1990). The Obliquely-Convergent Plate Boundary in the South Island of New Zealand: Implication for Ancient Collision Zones. *J. Struct. Geol.* 12 (5/6), 715–725. doi:10.1016/0191-8141(90)90084-c

Pour, A. B., and Hashim, M. (2015). Integrating PALSAR and ASTER Data for Mineral Deposits Exploration in Tropical Environments: a Case Study from Central Belt, Peninsular Malaysia. *Int. J. Image Data Fusion* 6 (2), 170–188. doi:10.1080/19479832.2014.985619

Raharimahefa, T., and Kusky, T. M. (2009). Structural and Remote Sensing Analysis of the Betsimisaraka Suture in Northeastern Madagascar. *Gondwana Res.* 15, 14–27. doi:10.1016/j.gr.2008.07.004

Raharimahefa, T., and Kusky, T. M. (2007). Structural and Remote Sensing Studies of the Southern Betsimisaraka Suture, Madagascar. *Gondwana Res.* 10, 186–197.

Ressetar, R., and Monrad, J. R. (1983). Chemical Composition and Tectonic Setting of the Dokhan Volcanic Formation, Eastern Desert, Egypt. *J. Afr. Earth Sci. (1983)* 1, 103–112. doi:10.1016/0899-5362(83)90002-7

Sadek, M. F., Ali-Bik, M. W., and Hassan, S. M. (2015). Late Neoproterozoic Basement Rocks of Kadabora-Suwayqat Area, Central Eastern Desert, Egypt: Geochemical and Remote Sensing Characterization. *Arab. J. Geosci.* 8, 10459–10479. doi:10.1007/s12517-015-1973-6

Sadek, M. F., and Hassan, S. M. (2009). "Rock Discrimination and Geological Mapping of Basement Rocks at Gabal Gharib Area North Eastern Desert of Egypt with Application of Landsat ETM and Egyptsat-1 Data," in *Remote Sensing for Environmental Monitoring, GIS Applications, and Geology IX*. Editors U. Michel and D. L. Civco (Berlin: Proc. of SPIE), Vol. 4780J. doi:10.1117/12.829752

Sadek, M. S. (1995). Geology, Geochemistry and Structure of Gabal Muqsim Area and Environs, South Eastern Desert, Egypt. *Forschungszentrum Julich* 32.

Safari, M., Maghsoudi, A., and Pour, A. B. (2017). Application of Landsat-8 and ASTER Satellite Remote Sensing Data for Porphyry Copper Exploration: a Case Study from Shahr-E-Babak, Kerman, South of Iran. *Geocarto Int.* 33 (11), 1186–1201. doi:10.1080/10106049.2017.1334834

Sanderson, D. J., and Marchini, W. R. D. (1984). Transpression. *J. Struct. Geol.* 6, 449–458. doi:10.1016/0191-8141(84)90058-0

Shalaby, A., Stüwe, K., Fritz, H., and Makroum, F. (2006). The El Mayah Molasse Basin in the Eastern Desert of Egypt. *J. Afr. Earth Sci.* 45, 1–15. doi:10.1016/j.jafrearsci.2006.01.004

Shalaby, A., Stuwe, K., Makroum, F., Fritz, H., Kebede, T., and Klotzli, U. (2005). The Wadi Mubarak Belt, Eastern Desert of Egypt: a Neoproterozoic Conjugate Shear System in the Arabian?Nubian Shield. *Precambrian Res.* 136, 27–50. doi:10.1016/j.precamres.2004.09.005

Stern, R. J., Ali, K. A., Ren, M., Jarrar, G. H., Romer, R. L., Leybourne, M. I., et al. (2016). Cadomian (~560 Ma) Crust Buried beneath the Northern Arabian Peninsula: Mineral, Chemical, Geochronological, and Isotopic Constraints from NE Jordan Xenoliths. *Earth Planet. Sci. Lett.* 436, 31–42. doi:10.1016/j.epsl.2015.12.026

Stern, R. J., Ali, K., Hamimi, Z., El-Barkooky, A., Martínez Frías, J., Fritz, H., et al. (2020). "Crustal Evolution of the Egyptian Precambrian Rocks," in *The Geology of Egypt. Regional Geology Reviews* (Cham, Switzerland: Springer Nature Switzerland), 131–151. doi:10.1007/978-3-030-15265-9_4

Stern, R. J. (1994). Arc Assembly and Continental Collision in the Neoproterozoic East African Orogen: Implications for the Consolidation of Gondwanaland. *Ann. Revi. Earth Planet. Sci.* 22, 315–319. doi:10.1146/annurev.ea.22.050194.001535

Stern, R. J., Gottfried, D., and Hedge, C. E. (1984). Late Precambrian Rifting and Crustal Evolution in the Northeastern Desert of Egypt. *Geol* 12, 168–172. doi:10.1130/0091-7613(1984)12<168:lprace>2.0.co;2

Stern, R. J., and Hedge, C. E. (1985). Geochronologic and Isotopic Constraints on Late Precambrian Crustal Evolution in the Eastern Desert of Egypt. *Am. J. Sci.* 285, 97–127. doi:10.2475/ajs.285.2.97

Stern, R. J., Johnson, P. R., Kröner, A., and Yibas, B. (2004). "Neoproterozoic Ophiolites of the Arabian-Nubian Shield," in *Precambrian Ophiolites and Related Rocks*. Editor T. M. Kusky (Amsterdam: Elsevier), 95–128. doi:10.1016/s0166-2635(04)13003-x

Stern, R. J. (2017). Neoproterozoic Formation and Evolution of Eastern Desert Continental Crust-The Importance of the Infrastructure Superstructure Transition. *J. Afr. Earth Sci.* 146, 15–27. doi:10.1016/j.jafrearsci.2017.01.001

Stoeser, D. B., and Stacey, J. S. (1988). "Evolution, U-Pb Geochronology, and Isotope Geology of the Pan-African Nabitah Orogenic Belt of the Saudi Arabian Shield," in *The Pan-African Belt of Northeast African and Adjacent Areas*.

Editors S. El-Gaby and R. O. Greiling (Braunschweig/Wiesbaden: Friedrich, Viewig and Sohn), 227–288.
Sultan, M., Arvidson, R. E., Sturchio, N. C., and Guinness, E. A. (1987). Lithologic Mapping in Arid Regions with Landsat Thematic Mapper Data: Meatiq Dome, Egypt. *Geol. Soc. Am. Bull.* 99, 748–762. doi:10.1130/0016-7606(1987)99<748:lmiarw>2.0.co;2
Teyssier, C., and Tikoff, B. (1999). Fabric Stability in Oblique Convergence and Divergence. *J. Struct. Geol.* 21, 969–974. doi:10.1016/s0191-8141(99)00067-x
Tikoff, B., and Fossen, H. (1993). Simultaneous Pure and Simple Shear: the Unifying Deformation Matrix. *Tectonophysics* 217, 267–283. doi:10.1016/0040-1951(93)90010-h
Tikoff, B., and Fossen, H. (1999). Three-dimensional Reference Deformations and Strain Facies. *J. Struct. Geol.* 21, 1497–1512. doi:10.1016/s0191-8141(99)00085-1
Tikoff, B., and Teyssier, C. (1994). Strain Modeling of Displacement-Field Partitioning in Transpressional Orogens. *J. Struct. Geol.* 16, 1575–1588. doi:10.1016/0191-8141(94)90034-5
Titus, S. J., Housen, B., and Tikoff, B. (2007). A kinematic model for the Rinconada fault system in central California based on structural analysis of en echelon folds and paleomagnetism. *J. Struct. Geol.* 29 (6), 961–982. doi:10.1016/j.jsg.2007.02.004
Tyagi, P., and Bhosle, U. (2011). Atmospheric Correction of Remotely Sensed Images in Spatial and Transform Domain. *Int. J. Image Proc.* 5 (5), 564–579.
US Geological Survey (2016). *Landsat 8 (L8) Data User Handbook*. South Dakota: US, EROS Sioux Falls. Version 0.2, 29 March 2016.
Vincent, R. K. (1997). *Fundamentals of Geological and Environmental Remote Sensing*. Upper Saddle River, NJ: Prentice-Hall, 366–470.
Willis, K. M., Stern, R. J., and Clauer, N. (1988). Age and Geochemistry of Late Precambrian Sediments of the Hammamat Series from the Northeastern Desert of Egypt. *Precambrian Res.* 42, 173–187. doi:10.1016/0301-9268(88)90016-2
Xiong, Y., Khan, S. D., Mahmood, K., and Sisson, V. B. (2011). Lithological Mapping of Bela Ophiolite with Remote-Sensing Data. *Int. J. Remote Sens.* 32 (16), 4641–4658. doi:10.1080/01431161.2010.489069
Xu, Z., Ji, S., Cai, Z., Zeng, L., Geng, Q., and Cao, H. (2012). Kinematics and Dynamics of the Namche Barwa Syntaxis, Eastern Himalaya: Constraints from Deformation, Fabrics and Geochronology. *Gondwana Res.* 21 (1), 19–36. doi:10.1016/j.gr.2011.06.010
Zimmer, M., Kröner, A., Jochum, K. P., Reischmann, T., and Todt, W. (1995). The Gabal Gerf Complex: a Precambrian N-MORB Ophiolite in the Nubian Shield, NE Africa. *Chem. Geol.* 123, 29–51. doi:10.1016/0009-2541(95)00018-h
Zoheir, B., El-Wahed, M. A., Pour, A. B., and Abdelnasser, A. (2019a). Orogenic Gold in Transpression and Transtension Zones: Field and Remote Sensing Studies of the Barramiya-Mueilha Sector, Egypt. *Remote Sens.* 11 (2122), 2122. doi:10.3390/rs11182122
Zoheir, B., Emam, A., Abd El-Wahed, M., and Soliman, N. (2019b). Gold Endowment in the Evolution of the Allaqi-Heiani Suture, Egypt: A Synthesis of Geological, Structural, and Space-Borne Imagery Data. *Ore Geol. Rev.* 110, 102938. doi:10.1016/j.oregeorev.2019.102938
Zoheir, B., and Emam, A. (2012). Integrating Geologic and Satellite Imagery Data for High-Resolution Mapping and Gold Exploration Targets in the South Eastern Desert, Egypt. *J. Afr. Earth Sci.* 66-67, 22–34. doi:10.1016/j.jafrearsci.2012.02.007

Conflict of Interest: The authors declare that the research was conducted in the absence of any commercial or financial relationships that could be construed as a potential conflict of interest.

frontiers | Frontiers in Earth Science

ORIGINAL RESEARCH
published: 12 July 2022
doi: 10.3389/feart.2022.937402

Integrated Geophysical Assessment of Groundwater Potential in Southwestern Saudi Arabia

Ahmed Mohamed[1,2]*, *Mohamed Al Deep*[3], *Abdullah Othman*[4], *Ayman I. Taha*[3], *Fahad Alshehri*[2] *and Ahmed Abdelrady*[5]*

[1]Geology Department, Faculty of Science, Assiut University, Assiut, Egypt, [2]Abdullah Alrushaid Chair for Earth Science Remote Sensing Research, Geology and Geophysics Department, College of Science, King Saud University, Riyadh, Saudi Arabia, [3]Geoelectric and Geomagnetism Department, National Research Institute of Astronomy and Geophysics, Helwan, Egypt, [4]Department of Environmental Engineering, Umm Al-Qura University, Makkah, Saudi Arabia, [5]Faculty of Civil Engineering and Geoscience, Delft University of Technology, Delft, Netherlands

Saudi Arabia is seeking fresh groundwater resources to face the increase in anthropogenic activities. The groundwater storage variations and occurrence were investigated and the surface and subsurface structures influencing the groundwater resources in the research area were defined using a combined study of Gravity Recovery and Climate Experiment, aeromagnetic data, and electrical resistivity data with other relevant datasets. Results are: The groundwater storage fluctuation is calculated at –0.34 ± 0.01 mm/yr during the period 04/2002-12/2021. The area is receiving an average annual rainfall rate of 117.6 mm during the period 2002 to 2019. Three structural trends, defined in the directions of NS, NNW, and NNE are cutting the sedimentary cover and the basement rocks. The sedimentary cover ranges from 0 to 1.2 km thick. Vertical electrical sounding results indicate three main geoelectric layers: the surface geoelectrical layer of higher resistivity values (428-9626 Ω. m) is made up of unconsolidated Quaternary sediments; the water-bearing layer of saturated sands with a resistivity range between 5.1 and 153 Ω. m and with depths vary from 1 to 94 m, and highly fractured basement rocks with resistivity values ranging from 813 to 6030 Ω. m. The integrated results are useful in providing a comprehensive image of the study area's surface and subsurface structures, as well as groundwater potential in the southwestern part of Saudi Arabia. Our integrated approach provides a reproducible model for assessing groundwater potential in arid and semiarid areas.

Keywords: gravity data, magnetic data, vertical electrical soundings, satellite data, structural trends, groundwater, saudi arabia

OPEN ACCESS

Edited by:
Ahmed M. Eldosouky, Suez University, Egypt

Reviewed by:
Ebong D. Ebong, University of Calabar, Nigeria
Omid Memarian Sorkhabi, University of Isfahan, Iran

***Correspondence:**
Ahmed Mohamed
ahmedmohamed@aun.edu.eg
Ahmed Abdelrady
A.R.A.Mahmoud@tudelft.nl

Specialty section:
This article was submitted to Solid Earth Geophysics, a section of the journal Frontiers in Earth Science

Received: *06 May 2022*
Accepted: *27 May 2022*
Published: *12 July 2022*

Citation:
Mohamed A, Al Deep M, Othman A, Taha AI, Alshehri F and Abdelrady A (2022) Integrated Geophysical Assessment of Groundwater Potential in Southwestern Saudi Arabia. Front. Earth Sci. 10:937402. doi: 10.3389/feart.2022.937402

INTRODUCTION

Saudi Arabia is the largest arid country in the Middle East, with an area of 2.24×10^6 km^2 in the Arabian Peninsula. Saudi Arabia is an arid country with limited water resources. Due to the increasing demand and unreliable sources of surface water, about 75-85% of water supplies come from groundwater, which is essentially classified as a fossil water resource. Minor natural recharge might occur in the mountainous areas. Therefore, investigating groundwater occurrence plays an important role in the country.

The launch of the Gravity Recovery and Climate Experiment (GRACE) mission opened up new possibilities for monitoring and estimating the terrestrial component of the hydrological cycle, which

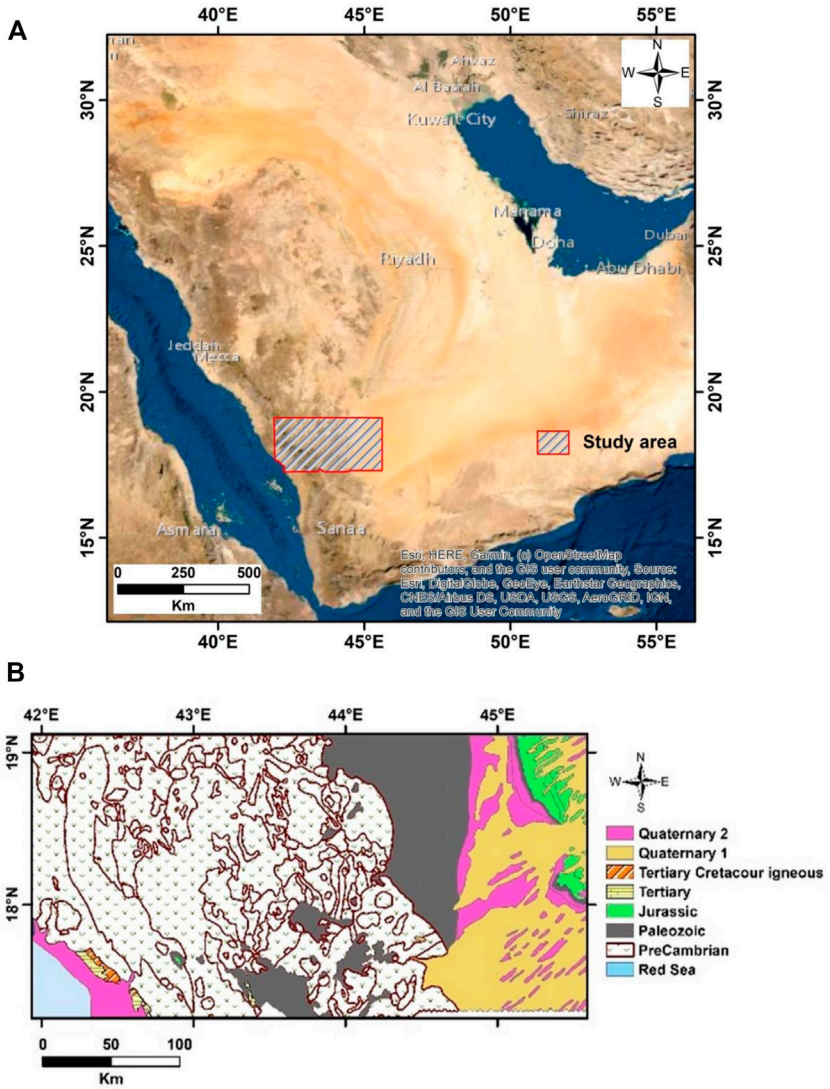

FIGURE 1 | (A) the Location map of the study area, and **(B)** its geology.

includes groundwater resources (Tapley et al., 2004). GRACE anomalies in terrestrial water storage (TWS) are widely employed in hydrological applications ranging from regional to global scales (e.g., Wouters et al., 2014; Frappart et al., 2019). In recent years, several studies were carried out to assess the hydrological settings and components of major basins and large aquifers. For instance, GRACE and Global Land Data Assimilation System (GLDAS) data, with other observed data were used to differentiate the Mississippi River basin's water budget and came up with respectable results (Yeh et al., 1998; Yeh et al., 2006; Rodell et al., 2007). Furthermore, some studies in the Arab world have combined GRACE with other relevant information to quantify groundwater storage variability and estimate aquifer recharge and depletion rates (Mohamed et al., 2014; Mohamed et al., 2015; Fallatah et al., 2017; Mohamed et al., 2017; Fallatah et al., 2019; Mohamed, 2019; Mohamed, 2020a; Mohamed, 2020b; Mohamed, 2020c; Mohamed et al., 2021; Mohamed and Gonçalvès, 2021; Taha et al., 2021; Mohamed et al., 2022b). GRACE can be used to fill the blanks in hydrologically monitoring data (Famiglietti et al., 2011).

It offers global monthly fluctuations in terrestrial water storage (ΔTWS) (Wahr et al., 2004; Syed et al., 2008). GRACE data has a low horizontal resolution, and there is no vertical resolution for GRACE data, which makes this use difficult (e.g., Ahmed et al., 2016). GRACE is unable to distinguish between contributions from TWS's multiple compartments (for example, surface water, groundwater, and soil moisture). The combination of land surface model outputs with GRACE data is now allowing individual elements from GRACE-derived TWS estimates to be extracted and the data's horizontal resolution to be improved.

The magnetic method has been widely applied for delineation of the structural trends of the subsurface structures and estimating the depth of the basement crystalline rocks in many regions (Al-Garni, 2004a; Al-Garni, 2004b; Al-Garni

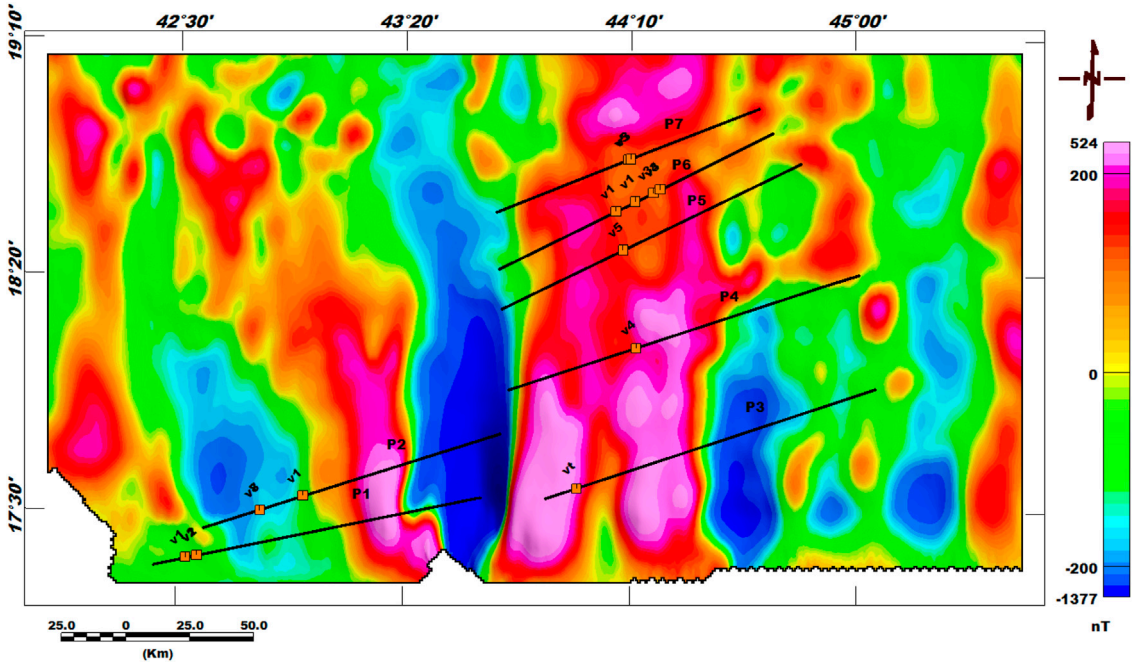

FIGURE 2 | The RTP map of the study area shows the locations of the 2D profiles and the Vertical Electrical Soundings.

et al., 2005; Al-Garni et al., 2006; Sultan et al., 2009; Al-Garni, 2010). The aeromagnetic data is integrated with remote sensing data to investigate groundwater resources (Meneisy and Al Deep, 2020; Mohamed and Ella, 2021). Bakheit et al. (2013) used airborne magnetic data to trace and analyze structural trends to locate the position of tectonic lines and subsurface structures. Eldosouky et al. (2022a) used the analytical signal and the horizontal gradient magnitude to map the structures of Gabal Shilman area. Saada et al. (2022) have applied the regional-residual separation, tilt derivative, and spectral analysis techniques to better understanding the structural features for the east of the Qattara depression area using magnetic and gravity data. Ranganai and Ebinger (2008) assessed the regional groundwater resources using an integrated approach of Landsat images with aeromagnetic data at south-central Zimbabwe Craton.

Separating the deep from the shallow sources of potential field anomalies and recognizing their edges are crucial in geophysics (Eldosouky, 2019; Pham et al., 2021a; Eldosouky and Mohamed, 2021; Eldosouky et al., 2022d). As a result, edge detection is an important analysis direction in pattern recognition for mapping structures, geologic contacts, and ore deposits (Oruç, 2011; Arisoy and Dikmen, 2013; Ibraheem et al., 2018; Eldosouky et al., 2020; Eldosouky and Saada, 2020; Pham et al., 2020; Pham et al., 2021a; Saada et al., 2021a; Pham et al., 2021b; Saada et al., 2021b; Pham et al., 2021c; Pham et al., 2021d; Eldosouky et al., 2021; Eldosouky et al., 2021; Melouah et al., 2021; Eldosouky et al., 2022a; Eldosouky et al., 2022b; Eldosouky et al., 2022c; Sehsah and Eldosouky, 2022).

The geoelectrical resistivity, electromagnetic, seismic refractive, gravity, magnetic, and radioactivity techniques are among the surface geophysical methods utilized in groundwater study. Overburden thickness, aquiferous zones, bedrock architecture, and topography can all be estimated using these methods (Adagunodo et al., 2014; Joel et al., 2016; Adagunodo et al., 2017; Oyeyemi et al., 2017; Adagunodo et al., 2018). The current research is based on the use of electrical resistivity as a geophysical tool for groundwater exploration that is considered the most promising and appropriate technology for groundwater exploration and aids in the identification of the appropriate place for groundwater investigation.

The electrical resistivity method was widely used for issues associated with groundwater exploration (Mousa, 2003; Hosny et al., 2005; Nigm et al., 2008; Mohamaden et al., 2009) in different media by detecting the surface effects produced by the flow of electric current inside the earth and correlation between the electrical properties of geological formations and their fluid content. The aquifer material, pore space volume, fluid quantity, and salinity level all have an impact on electrical resistivity values. Moreover, the water-bearing formations' geometry has been assessed. (Robain et al., 1995; Robain et al., 1996). This electrical resistivity method was employed to identify the saline-freshwater interface zone (Yechieli, 2000; Choudhury et al., 2001), water-related parameters (Kosinski and Kelly, 1981; Frohlich and Kelly, 1988; Troisi et al., 2000) and water quantity (Kessels et al., 1985). Furthermore, contaminated groundwater zones influence the electrical resistivity approach (Karlik and Kaya, 2001). The resistivity technique has been effectively utilized to determine the formations' thickness and groundwater potential (Raju and Reddy, 1998) and to study the groundwater potential and the aquifer system of fractured hard rocks (Chandra et al., 2012; Ologe et al., 2014; Al Deep

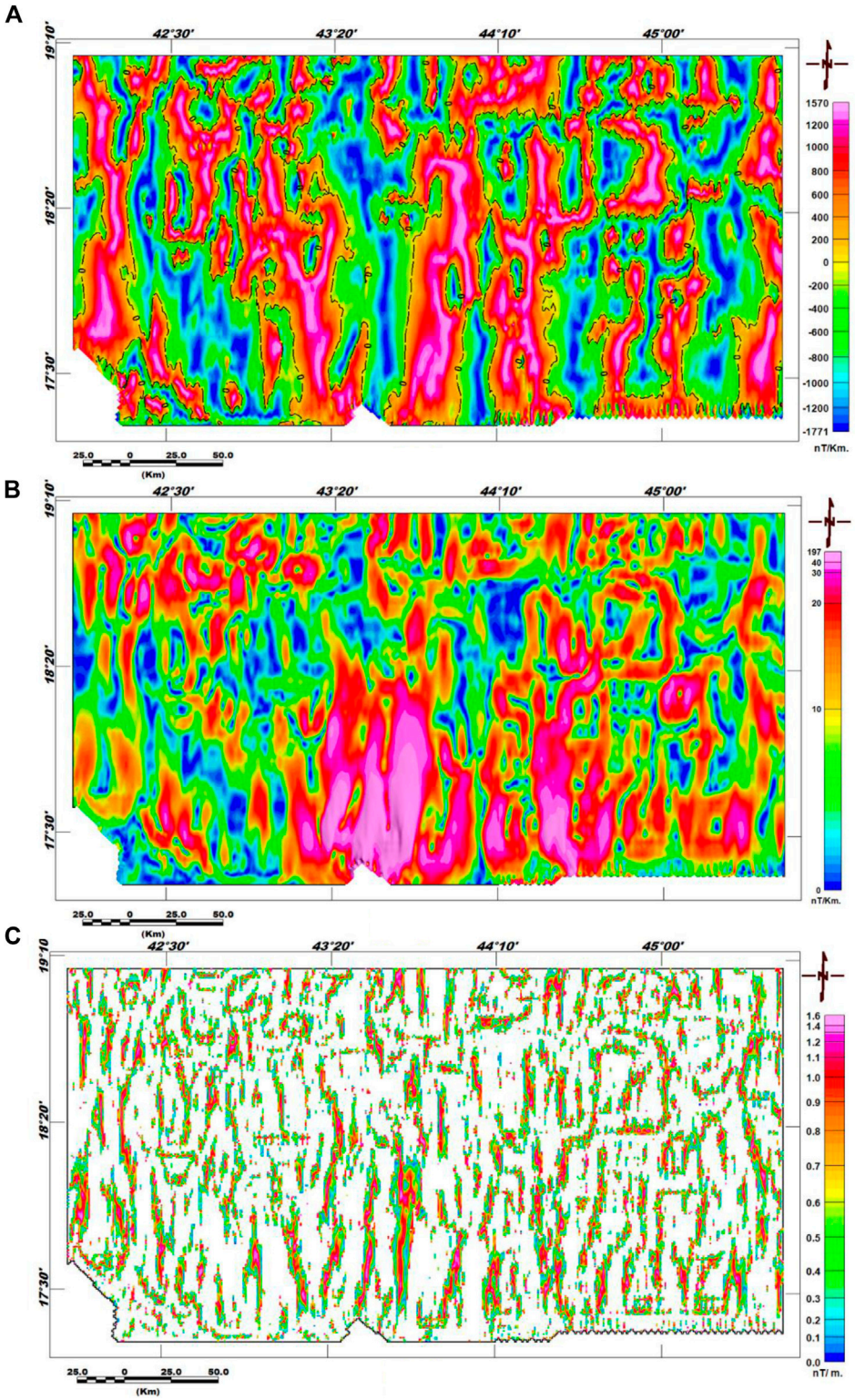

FIGURE 3 | Tilt derivative angle **(A)**, Total horizontal derivative **(B)**, and Enhanced horizontal gradient amplitude **(C)** maps of the study area.

et al., 2021). It has also been combined with borehole data to estimate geohydraulic parameters from Abi's fractured shales and sandstone aquifers (Ebong et al., 2014). In hard rock environments, geoelectrical resistivity techniques have been widely used to delineae shallow subsurface lineamnets and fractures (Ebong et al., 2014; Almadani et al., 2019) and faults

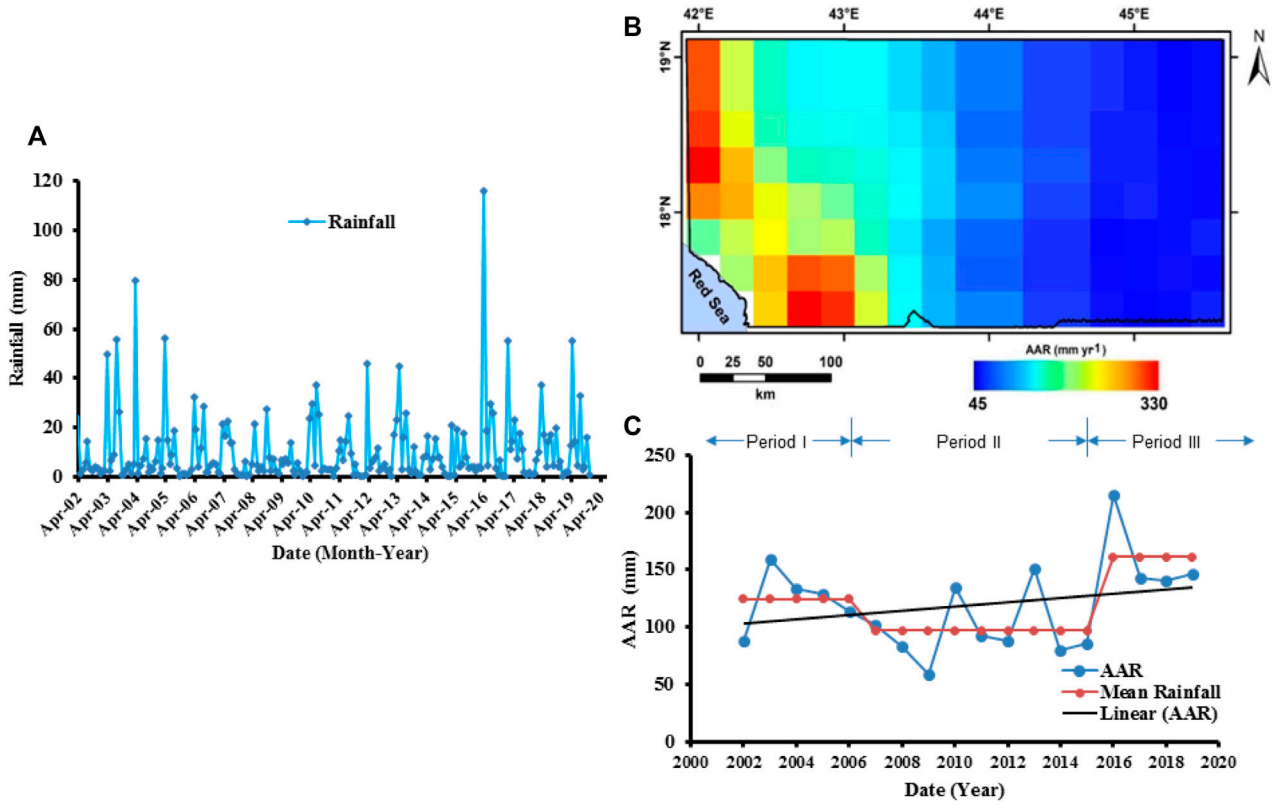

FIGURE 4 | (A) Monthly rainfall rate (mm/month) derived from TRMM data over the area. **(B)** the average annual rainfall (AAR) was taken from TRMM data. **(C)** Annual rainfall rate (mm) for the research area.

(Suzuki et al., 2000; Fazzito et al., 2009), which are the targets of groundwater investigation (Titus et al., 2009). Ebong et al. (2021) have applied vertical electrical sounding (VES) and electrical resistivity tomography techniques to evaluate the geological features and groundwater potential of the Obudu basement complex in southeastern Nigeria. Because of its availability, simplicity, and developments in computer software and other inversion approaches, VES is the most often used groundwater prospecting technique (Kana et al., 2015).

Morsy and Othman (2021) have applied an integrated approach of electrical resistivity and ground-penetrating radar with topographic data to evaluate the groundwater potential zones in the southwestern part of Makkah city. Their results show that the groundwater accumulation is localized in faulted-bounded depressions and wadis. Sharaf (2011) has integrated the resistivity and seismic measurements with test holes drilled in the As Suqah area, Makkah ditrcit. His findings demonstrate that groundwater is found mostly in two water-bearing zones: alluvial deposits and the Haddat Ash Sham and Ash Shumaysi formations' clastic sedimentary rocks. Taha et al. (2021) used gravity and electrical resistivity data to investigate the groundwater resources of wadi Sar in Hijaz mountains on a regional and local scale. Their findings reveal a general downward trend in groundwater storage variation computed at −2.00 ± 0.34 mm/yr from 04/2002 to 07/2017, as well as the presence of a water-bearing layer with low resistivity and variable thickness in fractured basement rocks of Wadi Sar. Despite the fact that similar studies may be conducted in various locations in Saudi Arabia's southwest, no previous studies using our proposed geophysical methodologies have been conducted for the entire study area, which is located between longitudes 41.91° and 45.61° and latitudes 17.26° and 19.12°.

Other satellite and airborne geophysical field datasets have been utilized to explore crustal features at the continental scale (Mohamed and Al Deep, 2021), the geometry of the magma chamber and heat flow (Mohamed et al., 2022a), and land subsidence caused by heavy groundwater withdrawal (Othman, 2019; Othman and Abotalib, 2019).

GRACE and GRACE Follow-On (GRACE-FO) solutions are used in conjunction with other climatic data to track spatial and temporal changes in water storage as a result of climate change and/or anthropogenic activities. The study also aims to investigate the groundwater potential of the study area using airborne magnetic data and electrical resistivity technique. Magnetic data was used to identify structural features and map the depth to underlying crystalline rocks that affect groundwater in the study area, whereas the shallow electrical survey was carried out to investigate the depth of the groundwater and the subsurface geology in the study area.

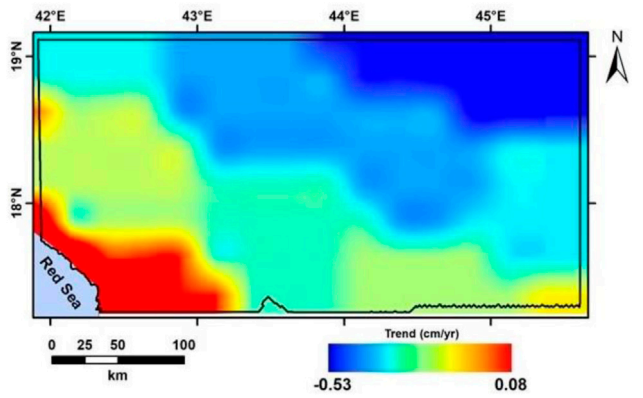

FIGURE 5 | Color-coded ΔTWS trend during the period 04/2002-12/2021from averaging of the CSR-M data.

GEOLOGICAL AND HYDROGEOLOGICAL SETTING

According to Greenwood et al. (1982), there are two primary subdivisions of layered rocks on the southern Arabian Shield south of latitude 22° N. An older ensimatic-arc complex and a younger marginal-arc complex are involved. Greywacke and mafic to intermediate volcanic rocks of the essentially contemporaneous Baish, Bahah, and Jidah groups make up the older arc complex. The younger arc complex is ensimatic in nature and partly superimposed over the older arc complex. The Halaban group, which was located to the east and northeast of the older ensimatic-arc complex, formed part of the younger arc group's ensimatic portion. The Ablah, Samran, and maybe Arafat groups reflect the superimposed parts of the younger arc complex. The Halaban group consists of andesitic and dacitic volcanic rocks as well as related clastic sedimentary rocks.

Based on the distribution of layered rock units of various ages and the orientation of overlying structural features, a number of N to NE-trending belts were delineated in the southern part of the Arabian Shield. Major fault zones run the length of these belts, defining their limits. The majority of these boundary faults go north and dip severely. Folds and other lineations in and around them frequently plunge down dip, both shallowly and steeply. Many of these faults are folded in random locations along their strike (Greenwood et al., 1982).

Our study region is located in the southwestern part of Saudi Arabia (**Figure 1A**). Its geology is shown in **Figure 1B**. The study region's exposed basement rocks are made up of two separate units: Khamis Mushayt Gneiss and pegmatites. The Khamis Mushayt Gneiss rocks, which include banded orthogneiss, migmatite with little paragneiss, and amphibolite, are the major basement unit in the area. There are various aplite and pegmatite dikes in this unit. Quartz, orthoclase, plagioclase, and biotite make up the pegmatite unit. Flat-lying Cambrian-Ordovician sandstones and spatially variable alluvial deposits of pebbles, gravels, sands, and clays overlay these two basement layers in some locations. In the western part of the area, the old Wajid Sandstone rocks appear. After the end of late Proterozoic igneous activity, the Cambrian-Ordovician Wajid Sandstone rocks were deposited.

According to field research, the majority of the aquifer in the researched area is made up of cracked and jointed hard rocks, which are then refilled by precipitation via infiltration. Shallow aquifers with varied porosity and permeability are formed by cracked and jointed hard rocks, affecting the aquifer storage coefficient. Groundwater flow is reduced by fine sediments deposited in joints, cracks, and faults in hard rocks, allowing runoff loss and aquifer recharging. By digging the rocks below, the water from these aquifers is pumped through the drilled wells (Khan, et al., 2022).

MATERIALS AND METHODS

GRACE/FO Data

GRACE is a pair of satellites that measure changes in the Earth's gravitational field in both spatial and temporal variations. It was launched in 2002 as a collaborative US-German project (Tapley et al., 2004). Changes in water content are the primary cause of changes in the Earth's gravity field. There are two sources of the GRACE/FO datasets, represented by the spherical harmonic and mass concentration solutions (mascon). In this study, the mascon products were used in the current study. With improved spatial resolution and minimal inaccuracy, these mascons capture all of the signals detected by GRACE within the GRACE noise limits. Smoothing filtering and/or Spectral de-striping are not required with the mascon solutions. Furthermore, there is no need for a scaling technique for the CSR-M. CSR-M (Save et al., 2016; Save, 2020; released from the Center for Space Research; http://www2.csr.utexas.edu/grace/), and JPL-M (Watkins et al., 2015; Wiese et al., 2016, Wiese et al., 2018; Landerer et al., 2020; released from the Jet Propulsion Laboratory; http://grace.jpl.nasa.gov), two versions of GRACE/FO mascon solutions, are used to calculate the ΔTWS that are available from april 2002 to June 2017 for GARCE and from June 2018 to December 2021 for GRCE/FO. Monthly gravity field fluctuations provided by the JPL-M data are of release 06, and with 0.5 ° × 0.5 ° grids (Watkins et al., 2015; Wiese, et al., 2016; Wiese, et al., 2018; Landerer et al., 2020). A subset of these JPL mascons crosses coasts and includes signals from both land and sea mass changes. As a post-processing step, the Coastal Resolution Improvement filter was used for the entire mascon solution to detect land and ocean mass from individual mascons that cross coastlines (Watkins et al., 2015). Therefore, the scaling factor must apply to the JPL-M to recover the leakage signals. In comparison to the RL05 version, the CSR mascon products of release 06, and with 0.25 ° × 0.5 ° grids (Save et al., 2016; Save 2020) use a freshly designed grid. The hexagonal tiles that cover the shoreline in this new grid are split into two tiles along the coast to reduce signal loss between land and sea. The cubic-spine approach was used to interpolate the missing monthly data. The time series and secular trends of TWS and groundwater storage variations (GWS) were constructed using the two potential solutions, and the TWS trend was produced.

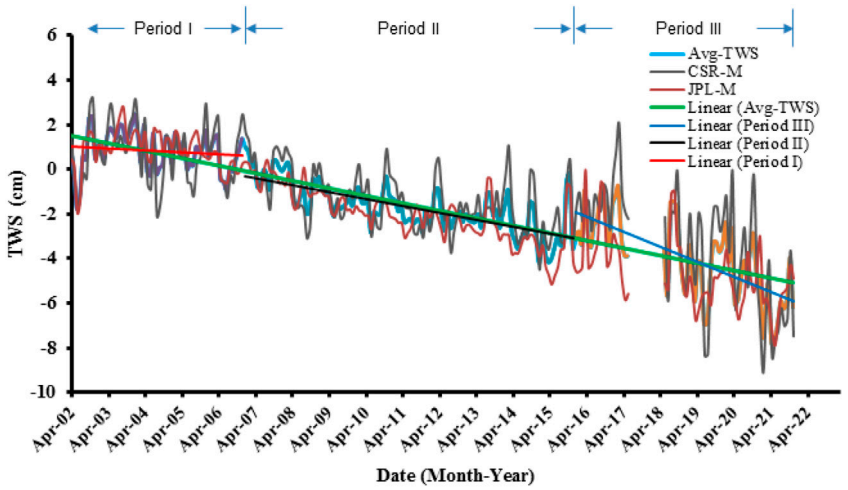

FIGURE 6 | ΔTWS from JPL-M and CSR-M mascon products across the study area, as well as their averaging (Avg-TWS) during the investigated time.

TABLE 1 | TWS components calculated by GRACE and GLDAS.

Component		Entire Time Period	Period I (02/2004-12/2006)	Period II (01/2007-12/2015)	Period III (01/2016-12/2021)
GRACE total (ΔTWS) (cm/yr)	CSR-M	−0.30 ± 0.02	−0.06 ± 0.13	−0.26 ± 0.04	−0.90 ± 0.14
	JPL-M	−0.38 ± 0.01	−0.12 ± 0.08	−0.37 ± 0.03	−0.44 ± 0.09
	AVG	−0.34 ± 0.0.1	−0.09 ± 0.09	−0.31 ± 0.03	−0.67 ± 0.09
ΔSMS (mm/yr)		+0.03 ± 0.02	+0.12 ± 0.19	+0.04 ± 0.04	−0.18 ± 0.14
ΔGWS (cm/yr) *p* value		−0.34 ± 0.01 <0.0001	−0.10 ± 0.08	−0.32 ± 0.03 <0.0001	−0.66 ± 0.09 <0.0001
AAR (mm)		117.6	124.8	97.4	161.3

Mascon products CSR-M, and JPL-M; GWS: groundwater storage change; SMS: soil moisture change; Annual Average Rainfall is abbreviated as AAR.

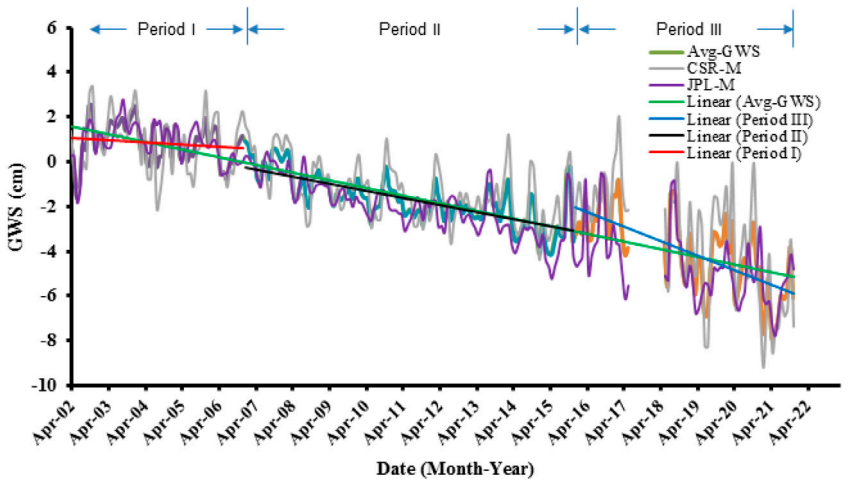

FIGURE 7 | Time series and averaging of ΔGWS from JPL-M and CSR-M mascon products across the study area over the investigated time.

GLDAS, TRMM, and SRTM Data

GLDAS is an observational data assimilation system with satellite and ground-based components. It produces optimal fields of land surface states and fluxes using advanced land surface modelling and data assimilation techniques. For soil moisture storage (ΔSMS), outputs of GLDAS (Rodell et al., 2004; https://disc.gsfc.nasa.gov/datasets) are employed. In this work, the averaging of three GLDAS versions (CLSM, VIC and NOAH)

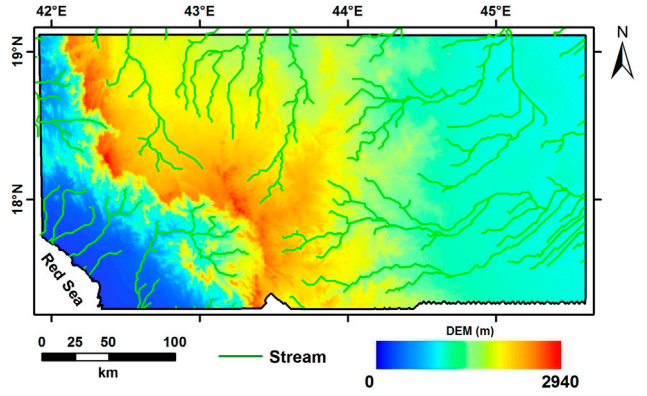

FIGURE 8 | Stream networks were extracted from SRTM 90 over the study area.

was used. To calculate the ΔGWS, the ΔSMS changes are subtracted from the ΔTWS using **Eq 1**

$$\mathbf{\Delta TWS = \Delta GWS + \Delta SMS} \quad (1)$$

The Tropical Rainfall Measuring Mission (TRMM; https://disc.gsfc.nasa.gov/datasets) is a collaborative space mission designed to monitor and analyze tropical rainfall (Kummerow, 1998). TRMM and Shuttle radar topography mission (SRTM) data are used. The monthly TRMM data, covering the January 2002-December 2019 period with a spatial resolution of 0.25° × 0.25°, are used to create the average annual rainfall (AAR) and to generate the monthly rainfall time series and the AAR rate over the study area. A Digital Elevation Model (DEM) was created using SRTM data with a 90 m resolution that was used for the delineation of the stream networks in the area. Landsat eight datasets were used to extract the surface lineaments affecting the area.

Aeromagnetic Data

The total magnetic intensity (TMI) map used in the current study was provided from the Saudi Geological Survey. The TMI map was subjected to different filtering techniques such as the reduction to the pole, tilt derivative, and analytical signal. These filters were used to enhance the image's signal intensity, evaluate the magnetic anomalies qualitatively, and calculate the depth to the magnetic sources. The Geosoft program (Geosoft oasis montaje, V.8.2.4, 2015) was used to handle and analyze the aeromagnetic data. **Figure 2** shows the reduced-to-pole (RTP) magnetic map.

The RTP filter is used to eliminate the skewness of magnetic anomalies induced by non-vertical magnetization directions. The RTP anomalies' maxima are directly over the causal bodies, making explanations easier (Lu et al., 2003). The TMI data were corrected for the RTP in this investigation using the Oasis Montaj Fourier transformation approach (Geosoft oasis montaje, V.8.2.4, 2015). The parameters of the International Geomagnetic Reference Field (IGRF) are as follows: The total magnetic field intensity was 39,582 nT, and the inclination and declination were 25.5 and 1.6, respectively. These characteristics were utilized to produce the RTP map (**Figure 2**) from the TMI field.

The magnetic anomalies' edges and locations were sharpened using the Tilt angle (TDR) derivative (Mushayandebvu et al., 2001). It is applicable in mapping mineral investigations and shallow basement structures (Geosoft oasis montaje, V.8.2.4, 2015). It was defined by Miller and Singh (1994), as the ratio of a vertical to a combined horizontal derivative as in **Eq.2**:

$$\mathbf{TDR} = \mathbf{tan}^{-1}\left[(\partial \mathbf{f}/\partial \mathbf{z})/\mathbf{sqrt}\left[(\partial f/\partial x)^2 + (\partial f/\partial y)^2\right]\right] \quad (2)$$

The potential field is represented by **f**, and the vertical derivative of the field is (**∂f/∂z**). The tilt angle is positive when above the source, at the edge where the vertical derivative is zero and the horizontal derivative is a maximum, and negative when beyond the source region. The tilt angle can be used to trace the pattern of the edges because it produces a zero value over the source edges (Miller and Singh, 1994). The tilt amplitudes are in the range of -π/2 to +π/2.

To detect the borders of the magnetic structures, the total horizontal derivative (THDR) technique was used extensively (Pilkington and Keating, 2004; Cowan et al., 2005; Cooper, 2009). It calculates the potential field's rate of change in horizontal directions (Cordell, 1979). The faulted boundaries may have high gradient zones, which can be identified using horizontal derivative maps. The horizontal gradient approach has the advantage of being less vulnerable to data noise because it only involves the computation of the field's two first-order horizontal derivatives (Phillips, 1998). The horizontal gradient's amplitude (Cordell and Grauch, 1985) is represented as :

$$\mathbf{THDR} = \mathbf{sqrt}\left[(\partial \mathbf{f}/\partial \mathbf{x})^2 + (\partial \mathbf{f}/\partial \mathbf{y})^2\right] \quad (3)$$

The horizontal derivatives of the field in the *x* and *y* directions are (∂f/∂x) and (∂f/∂y), respectively. When applied to field observations, TDR and THDR (**Figure 3**) both operate as an automatic gain control filter.

To detect the magnetic and gravity source edges, Pham et al. (2020) designed a new edge detection filter. The real part (*R*) of an arcsine function (asin) of the ratio of the vertical gradient to the total gradient of the amplitude of the field's horizontal gradient is used to create the new Enhanced Horizontal Gradient Amplitude (EHGA) filter. They tested its usefulness in defining source edges using synthetic and real data, and compared the results to those produced by other methods. Edges produced by the filter are more accurate and have a higher resolution. **Eq 4** gives the EGHA edge detector:

$$\mathbf{EHGA} = \mathbf{R}\left[\mathbf{asin}\left(\mathbf{k}\left(\frac{\mathbf{HGA}_z}{\sqrt{\mathbf{HGA}_x^2 + \mathbf{HGA}_{xy}^2 + \mathbf{HGA}_z^2}} - 1\right) + 1\right)\right] \quad (4)$$

Where HGA is the potential field's entire horizontal gradient amplitude. HGA_x, HGA_y, and HGA_z are the x, y, and z gradients of the HGA. *K* is a positive number decided by the interpreter.

Geoelectrical Data

On the local scale, the use of geophysical techniques for groundwater investigation has increased considerably during

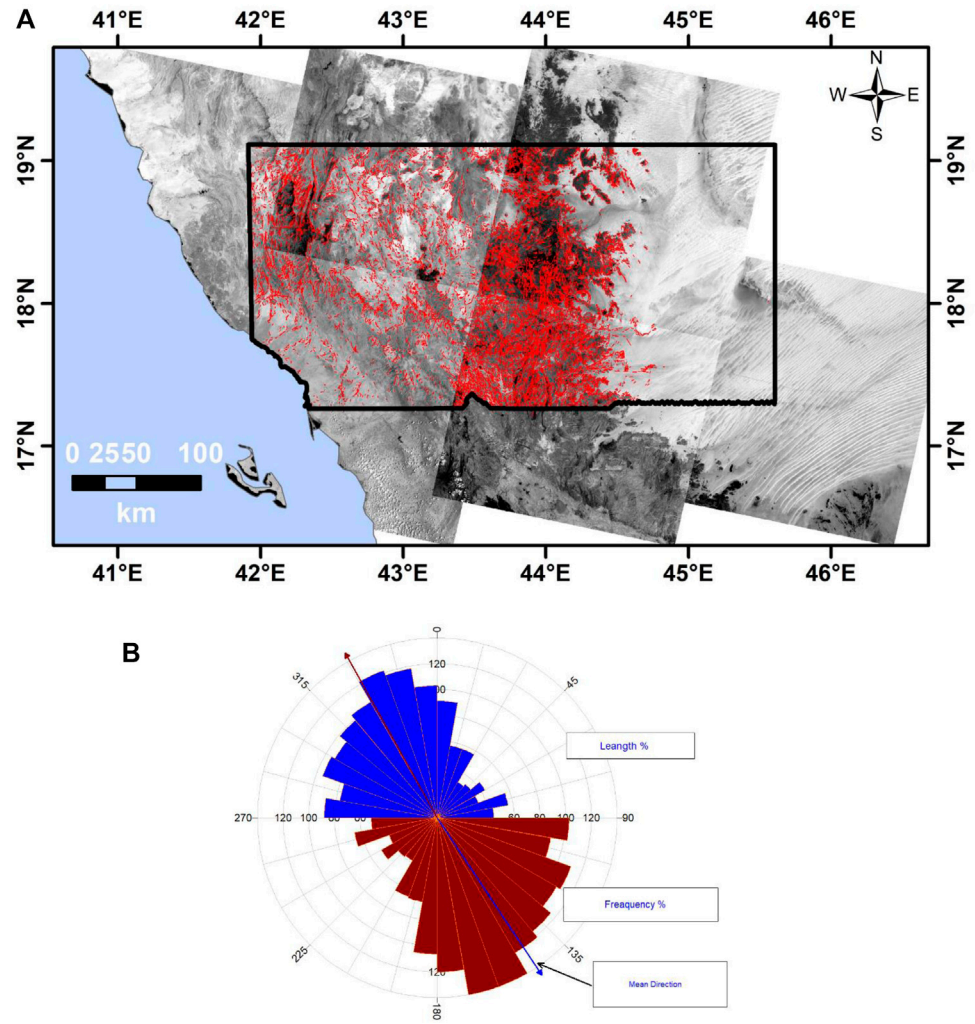

FIGURE 9 | (A) Landsat images with extracted surface lineaments, and **(B)** a rose diagram with the major structural patterns.

the previous decade due to the high advances and developments in electronic technology and numerical modeling solutions (Metwaly et al., 2009; Ndlovu et al., 2010). The electrical resistivity is a common method for groundwater exploration due to its low cost, simple operation, and efficiency.

Electrical resistivities of subsurface materials can be measured using geoelectrical techniques. These measurements provide information on underlying geoelectrical layers, structures, and groundwater occurrence (Van Overmeeren, 1989; Dahlin et al., 1999a; Muchingami et al., 2012). Archie's Law (Archie, 1942) describes the occurrence of fluid in the fluid-bearing formations and suggests that the resistance decreases with increased water content according to an inverse power law as follows:

$$\rho_o = a\rho f\varphi^{-m} \tag{5}$$

Where ρ_o is the fully saturated rock's resistivity, ρ_f is the water filling the pores' resistivity, φ is the porosity, and a and m are empirical parameters (Keller and Frischknecht, 1966).

The cementation exponent is defined by the m parameter, which has values ranging from one to 5. (Glover, 2010). Regarding the soil moisture content, Grellier et al. (2005) demonstrated that Archie's law can be reduced to **Eq 6**:

$$\rho_o = \alpha\rho f\theta_w^{-m} \tag{6}$$

Where θ_w is the medium's gravimetric moisture content, and α is a quantity that includes the medium's bulk density, as in **Eq 7**:

$$\theta = \frac{M}{M_t} \tag{7}$$

Passing an electrical current (I) between two metallic electrodes and measuring the potential difference (V) between them is the electrical resistivity method. The apparent resistivity is calculated using the following equation (ρ_a, **Eq 8**) (Dahlin, 2001):

$$\rho_a = K\Delta V/I \tag{8}$$

K, a geometrical factor, depends only on the position of the electrodes.

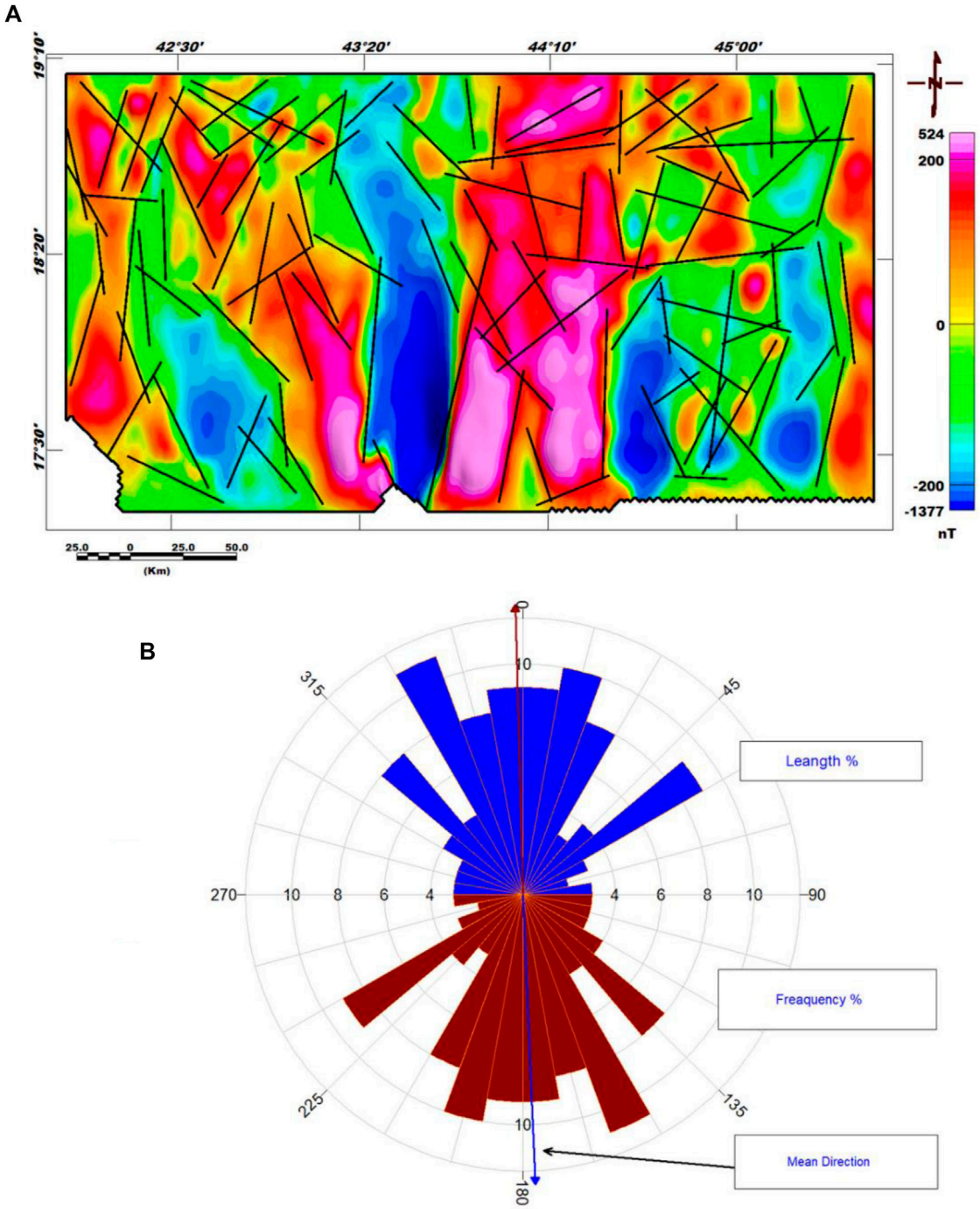

FIGURE 10 | (A) Magnetic lineaments extracted from the RTP map; **(B)** a rose diagram highlighting the major structural patterns.

Twelve vertical electrical resistivity soundings (VESes), with current electrode (AB) separation, ranging between 200 and 500 m, were conducted along eight profiles (**Figure 2**) using a Schlumberger array. The apparent resistivity value depends on the geometrical configuration of the electrode array, as defined by the geometric factor.

The IP2WIN (2005) application was used to process the VESes. The experimental data curve has been divided into smaller curves. Each one is a geoelectrical unit with a known resistivity Ω.m) and thickness (m), and it could represent a geologic layer with different physical attributes than the layers above and below it.

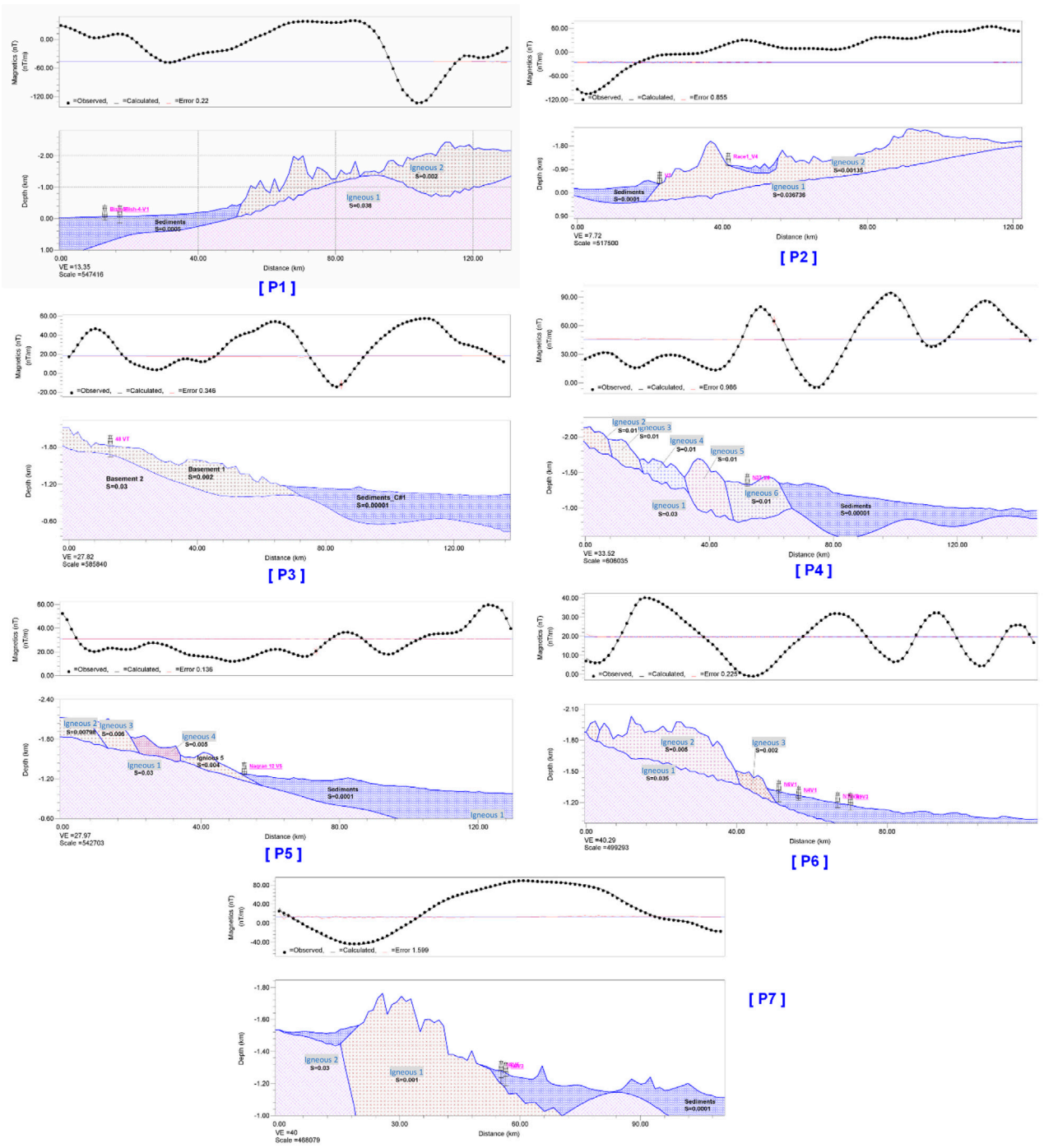

FIGURE 11 | The 2D inverted magnetic models.

RESULTS

The results of the processed TRMM data are shown in **Figure 4**. Analyses of the rainfall data show a general positive AAR trend over the study area estimated at 117.6 mm/yr. The results of the spatial distribution of the secular trend in GRACE-derived ΔTWS data and the monthly ΔTWS time series over the study area are shown in **Figures 5**, **6**. Both the ΔTWS and ΔGWS from the two mascon datasets show a negative trend estimated at −0.34 ± 0.01 cm/yr over the entire period. The RTP, TDR, THDR, and EHGA maps are shown in **Figures 2**, **3**. These maps show that the study area is affected by subsurface structural trends in the directions of NS, NNW, and NNE. The ground surface relief is forming streams (**Figure 8**) taking the surface water away

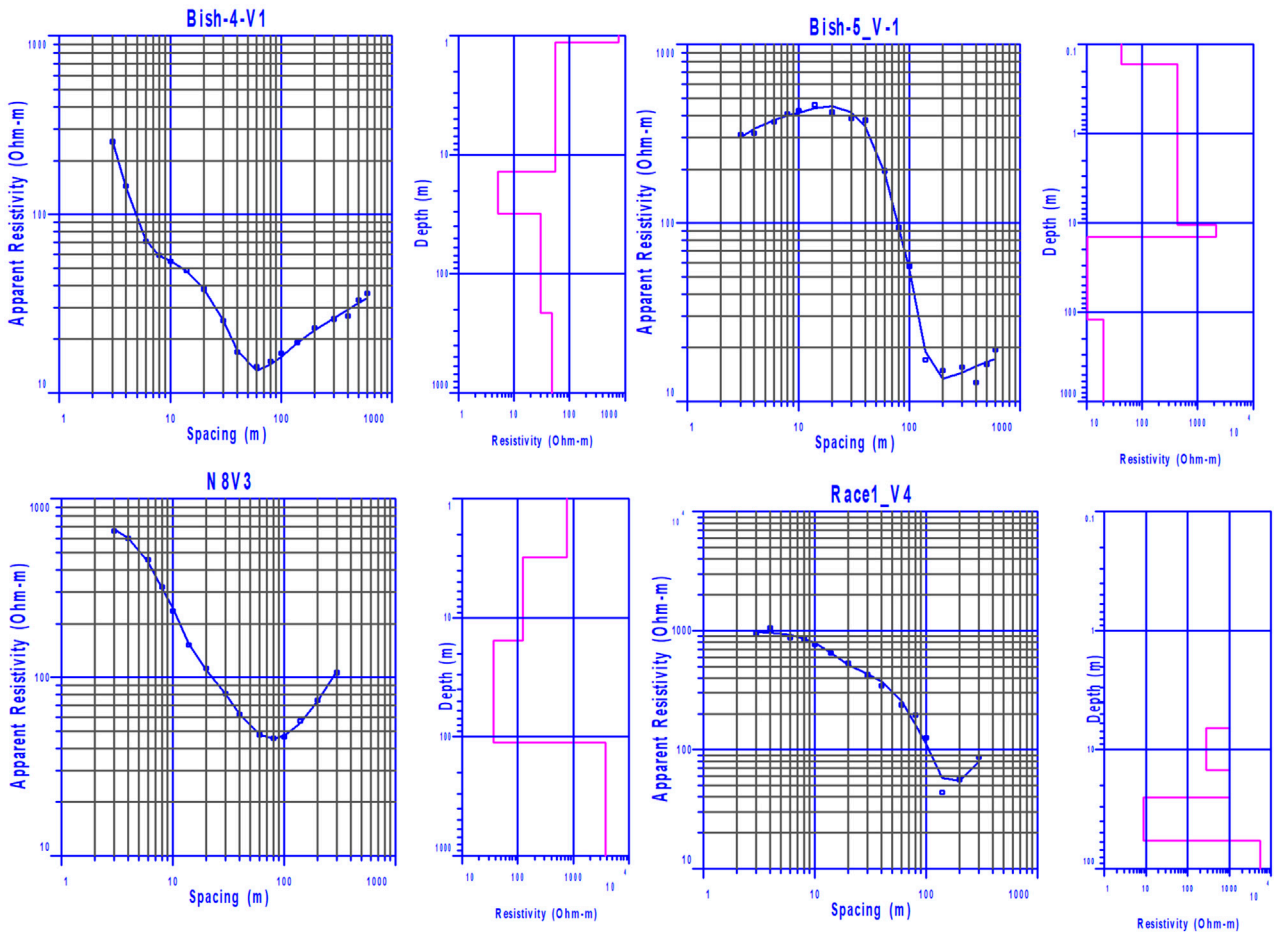

FIGURE 12 | The VES inverted models.

towards the E, N, and W. The surface structures were extracted from the Landsat images (**Figure 9**). Surface and subsurface main trends in the direction of NNW are delineated from the Landsat images (**Figure 9**) and the RTP map (**Figure 10**), respectively. The subsurface geology is represented by two layers (**Figure 11**) of different magnetic susceptibility values reflecting the top sedimentary cover and the lower basement crystalline rocks. The inversion of the resistivity data resulted in three geoelectrical layers (**Figure 12**) with varied physical attributes. Higher resistant unconsolidated Quaternary sediments make up the first geolectrical layer, low resistant sands saturated with water make up the second layer, and low to high resistant fractuted and/or massive basement rocks make up the third one (**Table 2**).

DISCUSSION

In this work, we used a combined method using GRACE satellite data with other airborne and ground-based geophysical data to investigate the groundwater potentialities of the southwestern part of Saudi Arabia. The monthly rainfall rate (**Figure 4A**) is higher in the March to September months and lower in the October to February months. The coastline region had a higher AAR rate of about 300 mm, whilst the eastern parts had lower values of up to 50 mm (**Figure 4B**). The AAR time series (**Figure 4C**) shows a generally positive trend with the AAR of 117.6 mm throughout the period 2002-2019. The AAR rate is one of the most important characteristics of a region's climate, as well as its associated ecosystem types and habitats. The amount of rainfall a region receives has an impact on stream density, water availability, land cover type, and agricultural output. Based on the linear regression analysis of the AAR; three time periods are distinguished (**Figure 4C**). Period I (2002-2006) shows an AAR of 124.8 mm/yr; Period II (2007-2015) shows a minimal AAR of 97.4 mm/yr; Period III (2016-2019) shows the highest AAR of 161.3 mm/yr. Period II is consistent with the onset of the 2007 drought and the dry climatic conditions that affected the Middle East area (Trigo et al., 2010). As a result, the region has suffered from water scarcity and limited water resources since the beginning of that drought (Wolf and Newton 2007; IRIN

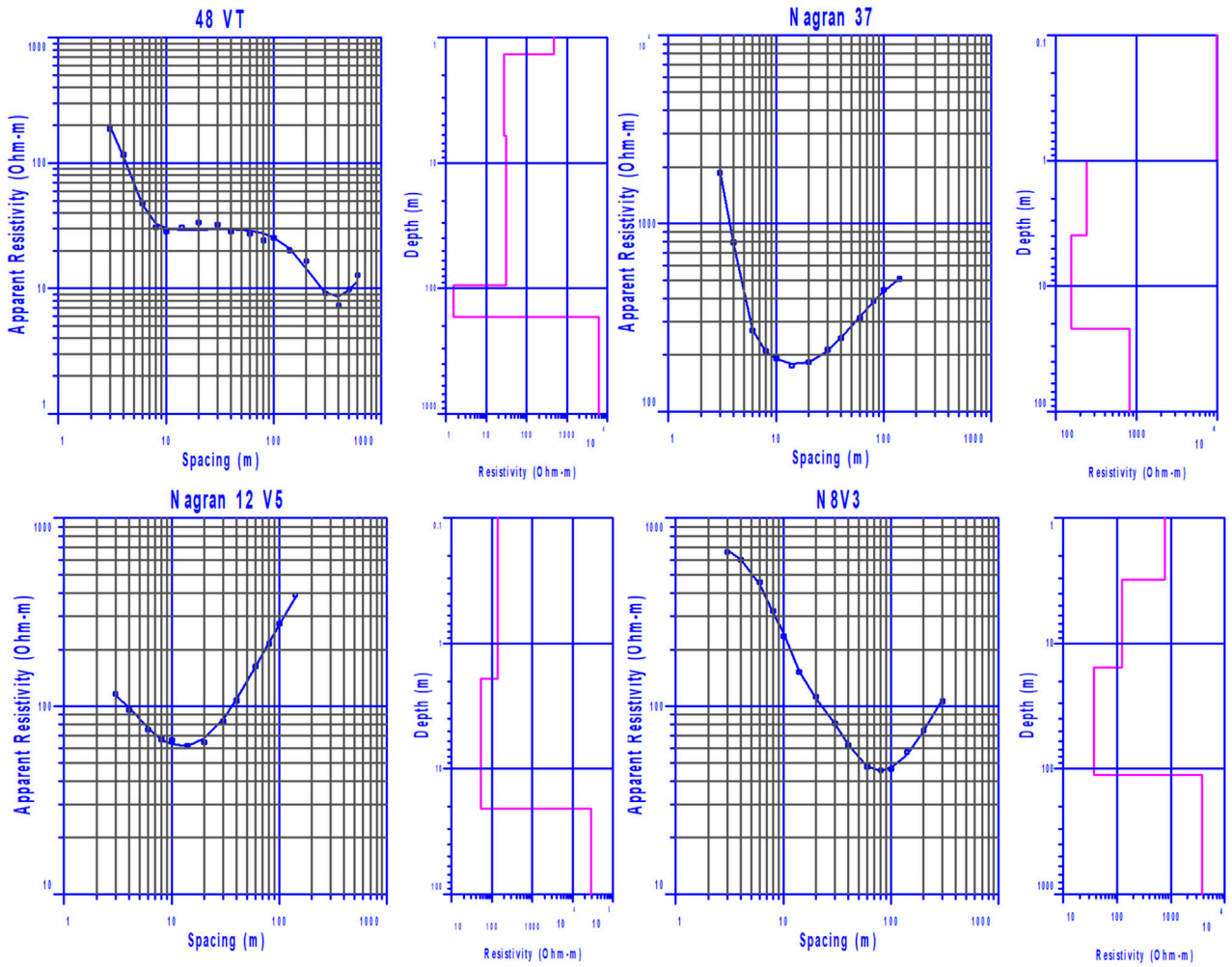

FIGURE 12 | (Continued).

2010; Voss et al., 2013; Mohamed, 2020b). However, the higher AAR rate during Period III indicates that the study area is receiving a substantial precipitation rate.

The research area had an overall negative TWS trend over the entire period (04/2002-12/2021), as shown in **Figure 5**. The southwestern part of the research area has a little positive TWS rate (+0.08 cm/yr), but the northeastern part has a negative TWS rate (−0.5 cm/yr). **Figure 6** shows the monthly time series of TWS fluctuations from the two mascon products, as well as their mean. Witnessing of this figure shows a general depletion in ΔTWS rate estimated at −0.30 ± 0.02, −0.38 ± 0.01, and −0.34 ± 0.01 cm/yr from the CSR-M, JPL-M, and their mean, respectively during the entire period. The ΔTWS time series has three trends throughout the entire study period based on the linear regression analysis of the average (**Figure 6**). Period I shows a slightly negative trend, calculated at −0.09 ± 0.09 cm/yr (**Table 1**). A negative TWS Δtrend is estimated at −0.31 ± 0.03 cm/yr for Period II, whereas Period III shows a highly negative trend, calculated at −0.67 ± 0.09 cm/yr.

The GLDAS-derived ΔSMS for Periods I, II, III, and the entire period are +0.12 ± 0.19, +0.04 ± 0.04, −0.18 ± 0.14 and +0.03 ± 0.02 mm/yr, respectively assuming that large crystalline rocks occupy the majority of the surface area. To estimate the fluctuations in the ΔGWS (**Figure 7**), the non-groundwater component, represented by the ΔSMS, was subtracted from the ΔTWS. During Periods I, II, III, and the entire period, average depletion rates of −0.10 ± 0.08, −0.32 ± 0.03, −0.66 ± 0.09 and −0.34 ± 0.01 cm/yr were obtained for the ΔGWS trend values, respectively. The ΔTWS and ΔGWS trends both follow the same pattern.

Inspection of **Figure 4C** indicates that there is a general increase in the AAP rate during Period III; however, the highest ΔGWS depletion rate (**Figure 7**) is observed in that Period. This is largely attributed to the drainage pattern and the surface material of the study area. Inspection of **Figure 8** shows the stream networks overlay the DEM. It shows higher relief of about 2000-2900 m in the Mountainous area close to the Red Sea coastal area. It decreases north and eastward to low values of about 1,000 m in its eastern part. It shows a steep slope toward

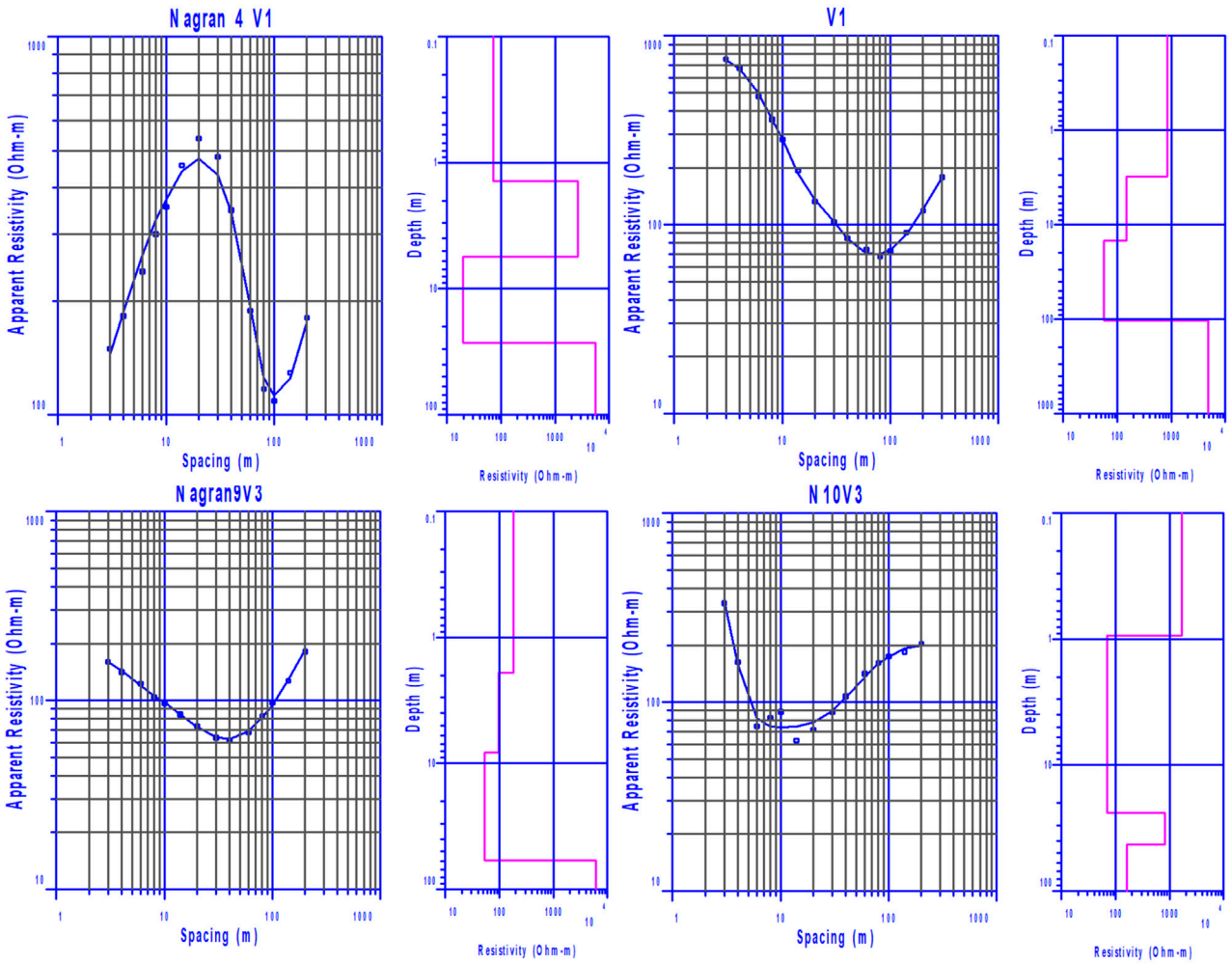

FIGURE 12 | The VES inverted models.

the west at the coastal area. Surface water that may be formed from the substantial rainfall is being drained away from these stream networks toward the east and north. The rest of the surface water drains into the Red Sea's coastline area. This may explain the negative trend in ΔGWS over the study area. Moreover, the eastern and central parts of the area are occupied by massive crystalline rocks that help the surface water drain away north and eastwards. Part of the surface water is drained toward the coastal area which shows a positive TWS value (**Figure 5**).

Witnessing **Figure 2** shows that the magnetic intensity values vary from −1,377 to +524 nT. The lithological changes, basement relief, and/or faulting and folding may be the cause of the variations in the magnetic intensity values. Lower and higher magnetic anomalies are almost arranged in N-S and NNW directions. The enhanced edges of linear features in the TDR map (**Figure 3A**) could be attributable to deep and shallow magnetic sources (Miller and Singh, 1994). The most important advantage of the TDR is its zero contour line that suggests the locations of the subsurface structures caused by sharp changes. The magnetic anomalies are practically aligned in definite orientations, generating structural trends in the NS, NNW, and NNE directions, as seen in the TDR map (**Figure 3A**) and its zero contour line. The edges of the maxima are well-defined in the THDR map (**Figure 3B**), assuming that amplitude enhancement is preserved. It calculates the potential field's rate of change in horizontal directions. The structural trend in the NS direction can be detected from the magnetic anomalies that are oriented in a slightly NS direction, according to the THDR (**Figure 3B**). The EHGA map (**Figure 3C**) reveals that the structural trends are almost in the NS direction, with higher resolution and sharper responses over the edges of the study area's magnetic sources.

The surface geologic features (lineaments) of the study area were mapped using Landsat eight images (**Figure 9A**). The extraction of these lineaments from remote sensing data can be done through automatic extraction (Anwar et al., 2013; Rayan, 2013). Several computer-assisted lineament extraction methods have been proposed. The majority of the methods rely on edge

TABLE 2 | The resistivity (Ω.m) and depth (m) values for the various inverted geoelectrical layers.

Project	Profile No	VES	Elevation (m)	Layer 1 (Weathered rocks)		Layer 2 (Water-Bearing Unit)		Layer 3 (Hard Rocks)	
				Depth (m)	Rho (Ω m)<	Depth (m)	Rho (Ω m)	Depth (m)	Rho (Ω m)<
bish-4	P1	V2	64.6	0:1	766	11:122	11–28	>122	30
bish-5	P1	V1	65	0:14	434	14:121	10	>121	20
Edaby-2	P2	V7	367.5	0:4.5	2133	4.5:12.5	20	>12.5	5,627
Edaby-2	P2	V8	365.2	0:5	1955	5:15	20	>15	5,511
Race 1	P2	V4	1,101	0:25	990	25:58	9	>58	5,434
Race 4	P2	V3	525.6	0:11.5	428	11.5:23	138	23	1,388
Najran 48	P3	Vt	1812	0: 94	467	94:168	1.5	>168	6125
Najran 37	P4	V4	1,325.5	0: 4	9626	4:22	153	>22	813
Najran 12	P5	V5	1,278.1	0: 2	140	2:20.5	53	>20	2779
Najran 4	P6	V1	1,246	0: 5.5	2619	5.5:27	19	>27	5,523
Najran 6	P6	V1	1,303.7	0: 15	828	15:103	56	>103	4,738
Najran 10	P6	V3	1,190	0:1	1,693	1:24	69	>24	814
Najran 9	P6	V3	1,182	0:8	183	8:60	52	>60	6030
Najran 8	P7	V3	1,262	0:18	756	18:78	36	>78	3,738
Najran 8	P7	V5	1,271	0:37	606	37:70	16	>74	1,442

filtering. The PCI Geomatica's LINE module is the most extensively used software for automatic lineament extraction. The predominant trend derived from the analysis of geological lineaments is in the NNW direction (**Figure 9B**). The subsurface trends of fault lines were also analyzed using the trend analysis technique according to their lengths, abundance, and magnitude concerning the azimuth. The magnetic structures have a significant relation with the intensity, direction, and geometry of the magnetic anomaly trends (Hall, 1964). Subsurface tectonics are delineated using magnetic trend patterns (Affleck, 1963). The trend analysis technique was applied to delineate the subsurface trends controlling the groundwater flow pathways in the area. The trend analysis shows that the main structural trends are in NNW, NNE, and NE directions (**Figure 10**). Minor trends are represented in the NS direction. The lineaments could also be interpreted as the edges of geological bodies and directions of structures. The integration of the delineated surface and subsurface structural trends may indicate the continuity of the NNW trend within the basement rocks and the overlying sedimentary deposits. This leads to a connection between the shallow Quaternary and the deeply fractured basement rocks aquifers that may feed the deeper aquifer. The subsurface structural trend and related fractures, on the other hand, are draining groundwater and recharging water away to the north, west, and east. This causes also a depletion in the groundwater storage of the study area, as estimated from the GRACE data at −0.34 ± 0.01 mm/yr during the period 04/2002-12/2021. However, groundwater can be accumulated at the intersection zones of the faults.

The underlying geology was investigated and the thickness of the sediments overlying the crystalline basement rocks was estimated using 2D modeling of magnetic data along profiles. To create 2D models from magnetic data, we used the Geosoft GM-SYS software package. We can optimize the model using the GM-SYS inversion option. Modeling programs require adequate initial estimations of model parameters such as body form, susceptibility, topography, depth, and magnetization of suspected sources to minimise errors of non-unique solution between observed and calculated magnetic fields. The profiles' models are illustrated in **Figure 11**. The geological succession is mostly represented by two rock types, according to these models: (a) the upper sedimentary layer that is composed of Quaternary and/or Paleozoic sediments, and (b) the lower Pre-Cambrian crystalline rocks that are composed of granitic and metamorphic rocks. A two-layer model was applied in the modeling, given that the Quaternary cover is the non-magnetized layer, and the basement is the magnetized layer. The magnetic susceptibility values of 0.00001–0.0005 CGS and 0.001–0.038 CGS units were chosen for the non-magnetized sedimentary and the more magnetized basement rocks, respectively. The thickness of the Quaternary sediments shows wide variations, it varies from 0 to ~1.2 km in the study area. The fewer thickness of the sedimentary cover in that area is suggesting the presence of lower groundwater potential in the upper sedimentary aquifer.

Three geoelectrical units (**Figure 12**; **Table 2**) of known resistivity and thickness values are recognized, which may reflect geologic layers of physical properties that differ from those located above and below. The details of the geoelectrical units are described in the following: The surface geoelectrical layer has different resistivity and thickness values varying from one place to another. The resistivity values of the first layer are varying from 428 Ω m at V3 (Race 4) to 9626 Ω m at V4 (Najran 37), whereas the thickness values are varying from 1 m at VES V1 (bish-4) and VES Vt (Najran 10) to about 94 m at VES 3 (Najran 48). The second geoelectrical layer represents the water-bearing unit in the study area. This layer has resistivity values varying from 5.1 Ω m at V1 (bish-4) to 153 Ω m at V4 (Najran 37), and thickness values varying from 8 m at V7 (Edaby-2) to 107 m at V1 (bish-5). The third geoelectrical layer is represented by low to high resistant basement rocks with resitivity values varying from 20 Ω m at V1 (P1, bish-5) and 30 Ω m at V2 (P1, bish-4) to 6125 Ω m at Vt (P3, Najran 48) and 6030 Ω m at V3 (P6, Najran

9). The lower resistivity values for that layer at particular VES points could result from the presence of fractured basement rocks saturated with water that lowers the resetivity values. In contrast, the higher resistivity values for that layer at certain VES points could indicate the presence of more resistant massive basement rocks. Our current VES interpretation and results are in good agreement with the results of resistivity data at Wadi Sar (Taha et al., 2021), which is located in the northwestern part of the research area. Piezometric wells should be drilled in the wadis of the western portion of the area in the future to test and verify the study's findings, however, this is dependent on budget availability.

CONCLUSION

For the study region, an integrated strategy combining gravity, magnetic, and electrical data with other remote sensing datasets was used. The study area is receiving an average rainfall rate of 117.6 mm/yr forming surface stream networks. Part of the surface water is drained to the Red Sea by the streams, while the rest is drained to the eastern and northern parts of the land. The groundwater shows a depletion trend estimated at −0.34 ± 0.01 mm/yr during the entire period 04/2002-12/2021. The surface trends are in NNW, and the deep trends are in NS, NNW, and NNE directions according to an examination of the structural trends retrieved from Landsat images and magnetic data. The thickness of the sediments varies greatly, ranging from a low of 0 in the mountainous areas to a high of 1.2 km in the valleys. The water-bearing unit has a thickness ranging from 8 to 107 m with low resistivity values of 5.1-153 Ω m. The depth of that unit fluctuates between 1 and 94 m. The average yearly rainfall over the research region is ranging between ~300 mm in the coastal area and up to 50 mm in its eastern parts. The eastern part, as well as the lowlands of the wadies in the west, could be potential areas for agricultural growth and the construction of new villages.

DATA AVAILABILITY STATEMENT

The original contributions presented in the study are included in the article/supplementary material further inquiries can be directed to the corresponding authors.

AUTHOR CONTRIBUTIONS

All authors listed have made a substantial, direct, and intellectual contribution to the work and approved it for publication.

ACKNOWLEDGMENTS

The authors extend their appreciation to the Abdullah Alrushaid Chair for Earth Science Remote Sensing Research for funding.

REFERENCES

Adagunodo, T. A., Adeniji, A. A., Erinle, A. V., Akinwumi, S. A., Adewoyin, O. O., Joel, E. S., et al. (2017). Geophysical Investigation into the Integrity of a Reclaimed Open Dumsite for Civil Engineering Purpose. *Interciencia J.* 42, 324–339.

Adagunodo, T. A., Akinloye, M. K., Sunmonu, L. A., Aizebeokhai, A. P., Oyeyemi, K. D., and Abodunrin, F. O. (2018). Groundwater Exploration in Aaba Residential Area of Akure, Nigeria. *Front. Earth Sci.* 6, 66. doi:10.3389/feart.2018.00066

Adagunodo, T. A., Sunmonu, L. A., and Oladejo, O. P. (2014). "Effect of Constructing High-Rise Buildings without a Geophysical Survey," in *Nigerian J. Phys. Spec. Edition*. Abuja: Nigerian Institute, 91–100.

Affleck, J. (1963). Magnetic Anomaly Trend and Spacing Patterns. *Geophysics* 28 (3), 379–395. doi:10.1190/1.1439188

Ahmed, M., Sultan, M., Yan, E., and Wahr, J. (2016). Assessing and Improving Land Surface Model Outputs over Africa Using GRACE, Field, and Remote Sensing Data. *Surv. Geophys.* 37 (3), 529–556. doi:10.1007/s10712-016-9360-8

AL Deep, M., Araffa, S. A. S., Mansour, S. A., Taha, A. I., Mohamed, A., and Othman, A. (2021). Geophysics and Remote Sensing Applications for Groundwater Exploration in Fractured Basement: A Case Study from Abha Area, Saudi Arabia. *J. Afr. Earth Sci.* 184. doi:10.1016/j.jafrearsci.2021.104368

Al-Garni, M. A. (2004b). Application of Magnetic and Electrical Geophysical Methods in Exploration of Groundwater Resources of Wadi Malakan, Saudi Arabia. *J. King Abdulaziz Univ. Earth Sci.* 16, 67–93. doi:10.4197/Ear.16-1.5

Al-Garni, M. A., Hassanein, H., and Gobashy, M. (2006). Geophysical Investigation of Groundwater in Wadi Lusab, Haddat Ash Sham Area, Makkah Al-Mukarramah, Arab Gulf. *J. Sci. Res.* 24 (2), 83–93.

Al-Garni, M. A., Hassanein, H. I., and Gobashy, M. (2005). Ground-magnetic Survey and Schlumberger Sounding for Identifying the Subsurface Geologic Factors Controlling the Groundwater Flow along Wadi Lusab, Makkah Al-Mukarramah, KSA. *J. Petrophysics Geophys.* 4 (2), 59–74. National research institute, Cairo, Egypt.

Al-Garni, M. A. (2010). Magnetic Survey for Delineating Subsurface Structures and Estimating Magnetic Sources Depth, Wadi Fatima, KSA. *J. King Saud Univ. - Sci.* 22, 87–96. doi:10.1016/j.jksus.2010.02.005

Al-Garni, M. A. (2004a). Schlumberger Sounding and Magnetic Survey in Wadi Al-Damm, Makkah Al-Mukarramah, Saudi Arabia. *J. Petroleum Min. Eng. (JPME)* 7, 45–60.

Almadani, S., Ibrahim, E., Al-Amri, A., Fnais, M., and Abdelrahman, K. (2019). Delineation of a Fractured Granite Aquifer in the Alwadeen Area, Southwest Saudi Arabia Using a Geoelectrical Resistivity Survey. *Arab. J. Geosci.* 12 (15), 449. doi:10.1007/s12517-019-4646-z

Anwar, A., Shawki, N., and Abdoh, G. (2013). Landsat ETM-7 for Lineament Mapping Using Automatic Extraction Technique in the SW Part of Taiz Area, Yemen. *Glob. J. Hum. Soc. Sci. Geogr. geo-science, Environ. Disaster Manag.* 13 (3), 35. VER 1.0.,

Archie, G. E. (1942). The Electrical Resistivity Log as an Aid in Determining Some Reservoir Characteristics. *Trans. AIME* 146, 54–62. doi:10.2118/942054-g

Arisoy, M., and Dikmen, Ü. (2013). Edge Detection of Magnetic Sources Using Enhanced Total Horizontal Derivative of the Tilt Angle. *Bull. Earth Sci. Appl. Res. Cent. Hacet. Univ.* 34, 73–82.

Bakheit, A. A., Abdel Aal, G. Z., El-Haddad, A. E., and Ibrahim, M. A. (2013). Subsurface Tectonic Pattern and Basement Topography as Interpreted from Aeromagnetic Data to the South of El-Dakhla Oasis, Western Desert, Egypt. *Arabian J. Geoscience* 7, 2165–2178. doi:10.1007/s12517-013-0896-3

Chandra, S., Nagaiah, E., Reddy, D. V., Rao, V. A., and Ahmed, S. (20122012). Exploring Deep Potential Aquifer in Water Scarce Crystalline Rocks. *J. Earth Syst. Sci.* 121, 1455–1468. doi:10.1007/s12040-012-0238-y

Choudhury, K., Saha, D. K., and Chakraborty, P. (2001). Geophysical Study for Saline Water Intrusion in a Coastal Alluvial Terrain. *J. Appl. Geophys.* 46 (3), 189–200. doi:10.1016/s0926-9851(01)00038-6

Cooper, G. R. (2009). Balancing Images of Potential-Field Data. *Geophysics* 74, L17–L20. doi:10.1190/1.3096615

Cordell, L., and Grauch, V. J. S. (1985). "Mapping Basement Magnetization Zones from Aeromagnetic Data in the San Juan Basin, New Mexico," in *The Utility of Regional Gravity and Magnetic Anomaly Maps*. Editor W. J. Hinze (Oklahoma, USA: Society of Exploration Geophysicists. Society of Exploration Geophysicists), 181–197. doi:10.1190/1.0931830346.ch16

Cordell, L. (1979). "Gravimetric Expression of Graben Faulting in Santa Fe Country and the Espanola Basin, New Mexico," in *Guidebook to Santa Fe Country*. Editor R. V. Ingersoll (Socorro: New Mexico Geological Society), 59–64.

Cowan, D., Cooper, G. R. J., and Cooper, G. (2005). Separation Filtering Using Fractional Order Derivatives. *Explor. Geophys.* 36, 393–396. doi:10.1071/eg05393

Dahlin, T. (2001). The Development of Electrical Imaging Techniques. *Comput. Geosci.* 27 (9), 1019–1029. doi:10.1016/S0098-3004(00)00160-6

Dahlin, T., Bjelm, L., and Svensson, C. (1999a). Use of Electrical Imaging in Site Investigations for a Railway Tunnel through the Hallandsås Horst, Sweden. *Q. J. Eng. Geol. Hydrogeology* 32, 163–172. doi:10.1144/gsl.qjeg.1999.032.p2.06

Ebong, E. D., Abong, A. A., Ulem, E. B., and Ebong, L. A. (2021). Geoelectrical Resistivity and Geological Characterization of Hydrostructures for Groundwater Resource Appraisal in the Obudu Plateau, Southeastern Nigeria. *Nat. Resour. Res.* 30, 2103–2117. doi:10.1007/s11053-021-09818-4

Ebong, E. D., Akpan, A. E., and Onwuegbuche, A. A. (2014). Estimation of Geohydraulic Parameters from Fractured Shales and Sandstone Aquifers of Abi (Nigeria) Using Electrical Resistivity and Hydrogeologic Measurements. *J. Afr. Earth Sci.* 96, 99–109. doi:10.1016/j.jafrearsci.2014.03.026

Eldosouky, A. M. (2019). Aeromagnetic Data for Mapping Geologic Contacts at Samr El-Qaa Area, North Eastern Desert, Egypt. *Arab. J. Geosci.* 12, 2. doi:10.1007/s12517-018-4182-2

Eldosouky, A. M., El-Qassas, R. A. Y., Pham, L. T., Abdelrahman, K., Alhumimidi, M. S., El Bahrawy, A., et al. (2022c). Mapping Main Structures and Related Mineralization of the Arabian Shield (Saudi Arabia) Using Sharp Edge Detector of Transformed Gravity Data. *Minerals* 12, 71. doi:10.3390/min12010071

Eldosouky, A. M., Elkhateeb, S. O., Mahdy, A. M., Saad, A. A., Fnais, M. S., Abdelrahman, K., et al. (2022a). Structural Analysis and Basement Topography of Gabal Shilman Area, South Eastern Desert of Egypt, Using Aeromagnetic Data. *J. King Saud. Univ. – Sci.* 34 (2), 1018–3647. doi:10.1016/j.jksus.2021.101764

Eldosouky, A. M., and Mohamed, H. (2021). Edge Detection of Aeromagnetic Data as Effective Tools for Structural Imaging at Shilman Area, South Eastern Desert, Egypt. *Arab. J. Geosci.* 14, 13. doi:10.1007/s12517-020-06251-4

Eldosouky, A. M., Pham, L. T., Abdelrahman, K., Fnais, M. S., and Gomez-Ortiz, D. (2022d). Mapping Structural Features of the Wadi Umm Dulfah Area Using Aeromagnetic Data. *J. King Saud. Univ. – Sci.* 34 (2), 1018–3647. doi:10.1016/j.jksus.2021.101803

Eldosouky, A. M., Pham, L. T., El-Qassas, R. A. Y., Hamimi, Z., and Oksum, E. (2021). "Lithospheric Structure of the Arabian-Nubian Shield Using Satellite Potential Field Data," in *The Geology of the Arabian-Nubian Shield. Regional Geology Reviews*. Editors Z. Hamimi, A. R. Fowler, J. P. Liégeois, A. Collins, M. G. Abdelsalam, and M. Abd EI-Wahed (Cham: Springer), 139–151. doi:10.1007/978-3-030-72995-0_6

Eldosouky, A. M., Pham, L. T., and Henaish, A. (2022b). High Precision Structural Mapping Using Edge Filters of Potential Field and Remote Sensing Data: A Case Study from Wadi Umm Ghalqa Area, South Eastern Desert, Egypt. *Egypt. J. Remote Sens. Space Sci.* 25 (2), 501–513. doi:10.1016/j.ejrs.2022.03.001

Eldosouky, A. M., Pham, L. T., Mohmed, H., and Pradhan, B. (2020). A Comparative Study of THG, AS, TA, Theta, TDX and LTHG Techniques for Improving Source Boundaries Detection of Magnetic Data Using Synthetic Models: A Case Study from G. Um Monqul, North Eastern Desert, Egypt. *J. Afr. Earth Sci.* 170, 103940. doi:10.1016/j.jafrearsci.2020.103940

Eldosouky, A. M., and Saada, S. A. (2020). Source Edge Detection (SED) of Aeromagnetic Data: Synthetic Examples and a Case Study from Haimur Area, South Eastern Desert, Egypt. *Arab. J. Geosci.* 13, 626. doi:10.1007/s12517-020-05653-8

Fallatah, O. A., Ahmed, M., Cardace, D., Boving, T., and Akanda, A. S. (2019). Assessment of Modern Recharge to Arid Region Aquifers Using an Integrated Geophysical, Geochemical, and Remote Sensing Approach. *J. Hydrology* 569, 600–611. doi:10.1016/j.jhydrol.2018.09.061

Fallatah, O. A., Ahmed, M., Save, H., and Akanda, A. S. (2017). Quantifying Temporal Variations in Water Resources of a Vulnerable Middle Eastern Transboundary Aquifer System. *Hydrol. Process* 31, 4081–4091. doi:10.1002/hyp.11285

Famiglietti, J. S., Lo, M., Ho, S. L., Bethune, J., Anderson, K. J., Syed, T. H., et al. (2011). Satellites Measure Recent Rates of Groundwater Depletion in California's Central Valley. *Geophys Res. Lett.* 38, LO3403. doi:10.1029/2010GL046442

Fazzito, S. Y., Rapalini, A. E., Cortés, J. M., and Terrizzano, C. M. (2009). Characterization of Quaternary Faults by Electric Resistivity Tomography in the Andean Precordillera of Western Argentina. *J. S. Am. Earth Sci.* 28 (3), 217–228. doi:10.1016/j.jsames.2009.06.001

Frappart, F., Papa, F., Güntner, A., Tomasella, J., Pfeffer, J., Ramillien, G., et al. (2019). The Spatio-Temporal Variability of Groundwater Storage in the Amazon River Basin. *Adv. Water Resour.* 124, 41–52. doi:10.1016/j.advwatres.2018.12.005

Frohlich, R. K., and Kelly, W. E. (1988). Estimates of Specific Yield with the Geoelectric Resistivity Method in Glacial Aquifers. *J. Hydrology* 97 (1–2), 33–44. doi:10.1016/0022-1694(88)90064-9

Geosoft oasis montaje, V.8.2.4 (2015). *Geosoft Software for the Earth Sciences*. Toronto, Canada: Geosoft Inc.

Glover, P. W. J. (2010). A Generalized Archie's Law for N Phases. *Geophysics* 75 (6), 85–91. doi:10.1190/1.3509781

Greenwood, W.,R., Stoeser, D. B., Fleck, R. J., and Stacey, J. S. 1982. Late Proterozoic Island-Arc Complexes and Tectonic Belts in the Southern Part of the Arabian Shield, Kingdomof Saudi Arabia: Saudi Arabian Deputy Ministry for Mineral Resources Open-File Report USGSOF-02-8, 46.

Grellier, S., Bouye, J. M., Guerin, R., Robain, H., and Skhiri, N. (2005). "Electrical Resistivity Tomography (ERT) Applied to Moisture Measurements in Bioreactor: Principles, *In Situ* Measurements and Results," in *Proc. International Workshop on Hydro-Physico-Mechanics of Landfills* (Grenoble, France).

Hall, D. H. (1964). Magnetic and Tectonic Regionalization on Texada Island, British Columbia. *Geophysics* 29 (4), 565–581. doi:10.1190/1.1439394

Hosny, M. M., El-Deen, E. Z. Z., Abdallah Abdel Rahman, A. A., and Barseim, M. S. (2005). Geoelectrical Study on the Groundwater Occurrence in the Area Southwest of Sidi Barrani, Northwestern Coast, Egypt. Egypt. *Geophys. Soc. J.* 3, 109–118.

Ibraheem, I. M., Elawadi, E. A., and El-Qady, G. M. (2018). Structural Interpretation of Aeromagnetic Data for the Wadi El Natrun Area, Northwestern Desert, Egypt. *J. Afr. Earth Sci.* 139, 14–25. doi:10.1016/j.jafrearsci.2017.11.036

Integrated Regional Information Networks (2010). Syria: Drought Pushing Millions into Poverty. Available at: http://www.irinnews.org/Report/90442/SYRIA-Drought-pushing-millionsinto-poverty. (Accesses on April, 2022).

IPI2WIN program 2005. version 3.1 2: 17. 10. 08 (1990–2008) Copyright al 1990 (2010). *Bobachev A.A, Programs Set for VEs Data Interpretation*. Russia: Dep. Of Geophysics, geological fac. Moseeow state VnV. Fussow. 119899.

Joel, E. S., Olasehinde, P. I., De, D. K., and OmejeAdewoyin, M. O. O. (2016). Estimation of Aquifer Transmissivity from Geo-Physical Data. A Case Study of Covennat University and Environs, Southwestern Nigeria. *Sci. Int.* 28, 3379–3385.

Kana, J. D., Djongyang, N., Raïdandi, D., Njandjock Nouck, P., Nouayou, R., Tabod, T. C., et al. (2015). Geophysical Investigation of Low Enthalpy Geothermal Potential and Ground Water Reservoirs in the Sudano-Sahelian Region of Cameroon. *J. Afr. Earth Sci.* 110, 81–91. doi:10.1016/j.jafrearsci.2015.06.007

Karlik, G., and Kaya, M. A. (2001). Investigation of Groundwater Contamination Using Electric and Electromagnetic Methods at an Open Waste Disposal Site: a Case Study from Isparta, Turkey. *Environ. Geol.* 40, 725–731. doi:10.1007/s002540000232

Keller, G. V., and Frischknecht, F. C. (1966). *Electrical Methods in Geophysical Prospecting*. Oxford: Pergamon Press.

Kessels, W., Flentge, I., and Kolditz, H. (1985). Dc Geoelectric Sounding to Determine Water Content in the Salt Mine Asse (FRG). *Geophys. Prospect.* 33, 446–456. doi:10.1111/j.1365-2478.1985.tb00444.x

Khan, M. Y. A., ElKashouty, M., Subyani, A. M., Tian, F., and Gusti, W. (2022). GIS and RS Intelligence in Delineating the Groundwater Potential Zones in Arid

Regions: a Case Study of Southern Aseer, Southwestern Saudi Arabia. *Appl. Water Sci.* 12, 3. doi:10.1007/s13201-021-01535-w

Kosinski, W. K., and Kelly, W. E. (1981). Geoelectric Soundings for Predicting Aquifer Properties. *Ground Water* 19, 163–171. doi:10.1111/j.1745-6584.1981.tb03455.x

Kummerow, C. (1998). Beamfilling Errors in Passive Microwave Rainfall Retrievals. *J. Appl. Meteor.* 37, 356–370. doi:10.1175/1520-0450(1998)037<0356:beipmr>2.0.co;2

Landerer, F. W., Flechtner, F. M., Save, H., Webb, F. H., Bandikova, T., Bertiger, W. I., et al. (2020). Extending the Global Mass Change Data Record: GRACE Follow-On Instrument and Science Data Performance. *Geophys. Res. Lett.* 47, e2020GL088306. doi:10.1029/2020gl088306

Lu, H., Golay, X., Pekar, J. J., and van Zijl, P. C. M. (2003). Functional Magnetic Resonance Imaging Based on Changes in Vascular Space Occupancy. *Magn. Reson. Med.* 50, 263–274. doi:10.1002/mrm.10519

Melouah, O., Eldosouky, A. M., and Ebong, W. D. (2021). Crustal Architecture, Heat Transfer Modes and Geothermal Energy Potentials of the Algerian Triassic Provinces. *Geothermics* 96 (2021), 0375–0505. doi:10.1016/j.geothermics.2021.102211

Meneisy, A. M., and Al Deep, M. (2020). Investigation of Groundwater Potential Using Magnetic and Satellite Image Data at Wadi El Amal, Aswan, Egypt. *Egypt. J. Remote Sens. Space Sci.* 24, 293–309. doi:10.1016/j.ejrs.2020.06.006

Metwaly, M., El-Qady, G., Massoud, U., El-Kenawy, A., Matsushima, J., and Al-Arifi, N. (2009). Integrated Geoelectrical Survey for Groundwater and Shallow Subsurface Evaluation: Case Study at Siliyin Spring, El-Fayoum, Egypt. *Int. J. Earth Sci. Geol. Rundsch* 99, 1427–1436. doi:10.1007/s00531-009-0458-9

Miller, H. G., and Singh, V. (1994). Potential Field Tilt-A New Concept for Location of Potential Field Sources. *J. Appl. Geophys.* 32, 213–217. doi:10.1016/0926-9851(94)90022-1

Mohamaden, M. I. I., Abu Shagar, S., and Abdallah, G. A. (2009). Geoelectrical Survey for Groundwater Exploration at the Asyuit Governorates, Nile Valley. *Egypt JKAU Mar. Sci.* 20, 91–108. doi:10.4197/mar.20-1.7

Mohamed, A., Abdelrahman, K., and Abdelrady, A. (2022b). Application of Time-Variable Gravity to Groundwater Storage Fluctuations in Saudi Arabia. *Front. Earth Sci.* 10, 873352. doi:10.3389/feart.2022.873352

Mohamed, A., Al Deep, M., Abdelrahman, K., and Abdelrady, A. (2022a). Geometry of the Magma Chamber and Curie Point Depth beneath Hawaii Island: Inferences from Magnetic and Gravity Data. *Front. Earth Sci. Sect. Solid Earth Geophys.* 10, 847984. doi:10.3389/feart.2022.847984

Mohamed, A., and Al Deep, M. (2021). Depth to the Bottom of the Magnetic Layer, Crustal Thickness, and Heat Flow in Africa: Inferences from Gravity and Magnetic Data. *J. Afr. Earth Sci.* 179, 104204. doi:10.1016/j.jafrearsci.2021.104204

Mohamed, A., and Ella, E. (2021). Magnetic Applications to Subsurface and Groundwater Investigations: a Case Study from Wadi El Assiuti, Egypt. *Int. J. Geosciences* 12, 77–101. doi:10.4236/ijg.2021.122006

Mohamed, A., and Gonçalvès, J. (2021). Hydro-geophysical Monitoring of the North Western Sahara Aquifer System's Groundwater Resources Using Gravity Data. *J. Afr. Earth Sci.* 178, 104188. doi:10.1016/j.jafrearsci.2021.104188

Mohamed, A. (2020b). Gravity Applications in Estimating the Mass Variations in the Middle East: a Case Study from Iran. *Arab. J. Geosci.* 13, 364. doi:10.1007/s12517-020-05317-7

Mohamed, A. (2020c). Gravity Applications to Groundwater Storage Variations of the Nile Delta Aquifer. *J. Appl. Geophys.* 182, 104177. doi:10.1016/j.jappgeo.2020.104177

Mohamed, A. (2020a). Gravity Based Estimates of Modern Recharge of the Sudanese Area. *J. Afr. Earth Sci.* 163, 103740. doi:10.1016/j.jafrearsci.2019.103740

Mohamed, A. (2019). Hydro-geophysical Study of the Groundwater Storage Variations over the Libyan Area and its Connection to the Dakhla Basin in Egypt. *J. Afr. Earth Sci.* 157, 103508. doi:10.1016/j.jafrearsci.2019.05.016

Mohamed, A., Ragaa Eldeen, E., and Abdelmalik, K. (2021). Gravity Based Assessment of Spatio-Temporal Mass Variations of the Groundwater Resources in the Eastern Desert, Egypt. *Arab. J. Geosci.* 14, 500. doi:10.1007/s12517-021-06885-y

Mohamed, A., Sultan, M., Ahmed, M., Yan, E., and Ahmed, E. (2017). Aquifer Recharge, Depletion, and Connectivity: Inferences from GRACE, Land Surface Models, and Geochemical and Geophysical Data. *Geol. Soc. Am. Bull.* 129, 534–546. doi:10.1130/B31460.1

Mohamed, A., Sultan, M., Ahmed, M., and Yan, E. (2014). *Quantifying Modern Recharge to the Nubian Sandstone Aquifer System: Inferences from GRACE and Land Surface Models*. San Francisco: American Geophysical Union, Fall Meeting. abstract id. G23A-0465.

Mohamed, A., Sultan, M., Yan, E., Ahmed, M., Sturchio, N., and Ahmed, E. (2015). San Francisco: American Geophysical Union, 476. Fall Meeting 2015, abstract id. A11E-0095.Towards a Better Understanding of the Hydrologic Setting of the Nubian Sandstone Aquifer System: Inferences from Groundwater Flow Models, Cl-36 Ages, and GRACE Data.

Morsy, E. A., and Othman, A. (2021). Delineation of Shallow Groundwater Potential Zones Using Integrated Hydrogeophysical and Topographic Analyses, Western Saudi Arabia. *J. King Saud Univ. - Sci.* 33 (7), 101559. doi:10.1016/j.jksus.2021.101559

Mousa, D. A. (2003). The Role of 1-D Sounding and 2-D Resistivity Inversions in Delineating the Near-Surface Lithologic Variations in Tushka Area, South of Egypt. *Geophys. Soc. J.* 1, 57–64.

Muchingami, I., Hlatywayo, D. J., Nel, J. M., and Chuma, C. (2012). Electrical Resistivity Survey for Groundwater Investigations and Shallow Subsurface Evaluation of the Basaltic-Greenstone Formation of the Urban Bulawayo Aquifer. *Phys. Chem. Earth, Parts A/B/C* 50-52, 44–51. doi:10.1016/j.pce.2012.08.014

Mushayandebvu, M. F., van Driel, P., Reid, A. B., and Fairhead, J. D. (2001). Magnetic Source Parameters of Two-dimensional Structures Using Extended Euler Deconvolution. *Geophysics* 66, 814–823. doi:10.1190/1.1444971

Ndlovu, S., Mpofu, V., Manatsa, D., and Muchuweni, E. (2010). Mapping Groundwater Aquifers Using Dowsing, Slingram Electromagnetic Survey Method and Vertical Electrical Sounding Jointly in the Granite Rock Formation: a Case of Matshetshe Rural Area in Zimbabwe. *J. Sustain. Dev. Afr.* 12 (5), 199–208.

Nigm, A. A., Elterb, R. A., Nasr, F. E., and Thobaity, H. M. (2008). Contribution of Ground Magnetic and Resistivity Methods in Groundwater Assessment in Wadi Bany Omair. Holy Makkah Area, Saudi Arabia, Egyptian. *Geophys. Soc. J.* 6 (1), 67–79.

Ologe, O., Bankole, S. A., and Adeoye, T. O. (2014). Geo-Electric Study for Groundwater Development in Ikunri Estate, Kogi West, Southwestern Nigeria. *Ilorin J. Sci.* 1 (1), 154–166.

Oruç, B. (2011). Edge Detection and Depth Estimation Using a Tilt Angle Map from Gravity Gradient Data of the Kozaklı-Central Anatolia Region, Turkey. *Pure Appl. Geophys* 168, 1769–1780. doi:10.1007/s00024-010-0211-0

Othman, A., and Abotalib, A. Z. (2019). Land Subsidence Triggered by Groundwater Withdrawal under Hyper-Arid Conditions: Case Study from Central Saudi Arabia. *Environ. Earth Sci.* 78 (7), 243. doi:10.1007/s12665-019-8254-8

Othman, A. (2019). "Measuring and Monitoring Land Subsidence and Earth Fissures in Al-Qassim Region, Saudi Arabia: Inferences from InSAR," in *Advances in Remote Sensing and Geo Informatics Applications*. Editors H. El-Askary, S. Lee, E. Heggy, and B. Pradhan (Cham: Springer), 287–291. CAJG 2018. Advances in Science, Technology & Innovation (IEREK Interdisciplinary Series for Sustainable Development). doi:10.1007/978-3-030-01440-7_66

Oyeyemi, K. D., Aizebeokhai, A. P., Adagunodo, T. A., Olofinnade, O. M., Sanuade, O. A., and Olaojo, A. A. (2017). Subsoil Characterization Using Geoelectrical and Geotechnical Investigations: Implications for Foundation Studies. *Int. J. Civ. Eng. Technol.* 8, 302–314.

Pham, L. T., Eldosouky, A. M., Oksum, E., and Saada, S. A. (2020). A New High-Resolution Filter for Source Edge Detection of Potential Field Data. *Geocarto Int.*, 1–18 doi:10.1080/10106049.2020.1849414

Pham, L. T., Kafadar, O., Oksum, E., and Eldosouky, A. M. (2021b). An Improved Approach for Detecting the Locations of the Maxima in Interpreting Potential Field Data. *Arab. J. Geosci.* 14, 43. doi:10.1007/s12517-020-06399-z

Pham, L. T., Oksum, E., Do, T. D., Nguyen, D. V., and Eldosouky, A. M. (2021c). On the Performance of Phase-Based Filters for Enhancing Lateral Boundaries of

Magnetic and Gravity Sources: a Case Study of the Seattle Uplift. *Arab. J. Geosci.* 14, 129. doi:10.1007/s12517-021-06511-x

Pham, L. T., Oksum, E., Vu, M. D., Vo, Q. T., Du Le-Viet, K., and Eldosouky, A. M. (2021a). An Improved Approach for Detecting Ridge Locations to Interpret the Potential Field Data for More Accurate Structural Mapping: a Case Study from Vredefort Dome Area (South Africa). *J. Afr. Earth Sci.* 175, 104099. doi:10.1016/j.jafrearsci.2020.104099

Pham, L. T., Vu, M. D., and Thi Le, S. (2021d). Performance Evaluation of Amplitude- and Phase-Based Methods for Estimating Edges of Potential Field Sources. *Iran. J. Sci. Technol. Trans. Sci.* 45 (4), 1327–1339. doi:10.1007/s40995-021-01122-3

Phillips, J. D. (1998). *Processing and Interpretation of Aeromagnetic Data for the Santa Cruz Basin Patahonia Mountains Area*. South-Central Arizona: U.S. Geological Survey. Open-File Report 02-98.

Pilkington, M., and Keating, P. (2004). Contact Mapping from Gridded Magnetic Data–A Comparison of Techniques. *ASEG Ext. Abstr.* 35 (4), 4. doi:10.1071/ASEG2004ab113

Raju, N. J., and Reddy, T. V. K. (1998). Fracture Pattern and Electrical Resistivity Studies for Groundwater Exploration. *Environ. Geol.* 34, 175–182. doi:10.1007/s002540050269

Ranganai, R. T., and Ebinger, C. J. (20082008). Aeromagnetic and Landsat TM Structural Interpretation for Identifying Regional Groundwater Exploration Targets, South-Central Zimbabwe Craton. *J. Appl. Geophys.* 65, 73–83. doi:10.1016/j.jappgeo.2008.05.009

Rayan, T. (2013). Automatic Extraction and Geospatial Analysis of Lineaments and Their Tectonic Significance in Some Areas of Northern Iraq Using Remote Sensing Techniques and GIS. *Int. J. Enhanc. Res. Sci. Technol. Eng.* 2 (2), 1. doi:10.13140/RG.2.2.20851.99363

Robain, H., Braun, J. J., Albouy, Y., and Ndam, J. (1995). "An Electrical Monitoring of an Elementary Watershed in the Rain Forest of Cameroon," in Proceedings of 1st Environmental and Engineering Geophysics meeting (Torino, Italy. European Association of Geoscientists and Engineers), 411–414.

Robain, H., Descloitres, M., Ritz, M., and Atangana, Q. Y. (1996). A Multiscale Electrical Survey of a Lateritic Soil System in the Rain Forest of Cameroon. *J. Appl. Geophys.* 34, 237–253. doi:10.1016/0926-9851(95)00023-2

Rodell, M., Chen, J., Kato, H., Famiglietti, J. S., Nigro, J., and Wilson, C. R. (2007). Estimating Groundwater Storage Changes in the Mississippi River Basin (USA) Using GRACE. *Hydrogeol. J.* 15, 159–166. doi:10.1007/s10040-006-0103-7

Rodell, M., Houser, P. R., Jambor, U., Gottschalck, J., Mitchell, K., Meng, C.-J., et al. (2004). The Global Land Data Assimilation System. *Bull. Amer. Meteor. Soc.* 85 (3), 381–394. doi:10.1175/bams-85-3-381

Saada, A. S., Eldosouky, A. M., Abdelrahm, K., Al-Otaibi, N., Ibrahim, E., and Ibrahim, A. (2021b). New Insights into the Contribution of Gravity Data for Mapping the Lithospheric Architecture. *J. King Saud. Univ. - Sci.* 33, 1018–3647. doi:10.1016/j.jksus.2021.101400

Saada, A. S., Mickus, K., Eldosouky, A. M., and Ibrahim, A. (2021a). Insights on the Tectonic Styles of the Red Sea Rift Using Gravity and Magnetic Data. *Mar. Pet. Geol.* 133, 105253. doi:10.1016/j.marpetgeo.2021.105253

Saada, S. A., Eldosouky, A. M., Kamel, M., Khadragy, A. E., Abdelrahman, K., Fnais, M. S., et al. (2022). Understanding the Structural Framework Controlling the Sedimentary Basins from the Integration of Gravity and Magnetic Data: A Case Study from the East of the Qattara Depression Area, Egypt. *J. King Saud Univ. - Sci.* 34 (2), 101808. doi:10.1016/j.jksus.2021.101808

Save, H., Bettadpur, S., and Tapley, B. D. (2016). High-resolution CSR GRACE RL05 Mascons. *J. Geophys. Res. Solid Earth* 121, 7547–7569. doi:10.1002/2016JB013007

Save, H. (2020). *CSR GRACE and GRACE-FO RL06 Mascon Solutions V02*. doi:10.15781/cgq9-nh24

Sehsah, H., and Eldosouky, A. M. (2022). Neoproterozoic Hybrid Forearc – MOR Ophiolite Belts in the Northern Arabian-Nubian Shield: No Evidence for Back-Arc Tectonic Setting. *Int. Geol. Rev.* 64, 151–163. doi:10.1080/00206814.2020.1836523

Sharaf, M. A. M. (2011). Geological and Geophysical Exploration of the Groundwater Aquifers of as Suqah Area, Makkah District, Western Arabian Shield, Saudi Arabia. *Arab. J. Geosci.* 4, 993–1004. doi:10.1007/s12517-010-0187-1

Sultan, S. A., Mekhemer, H. M., Santos, F. A. M., and Abd Alla, M. (2009). Geophysical Measurements for Subsurface Mapping and Groundwater Exploration at the Central Part of the Sinai Peninsula, Egypt. *Arabian J. Sci. Eng.* 34, 103–119.

Suzuki, K., Toda, S., Kusunoki, K., Fujimitsu, Y., Mogi, T., and Jomori, A. (2000). "Case Studies of Electrical and Electromagnetic Methods Applied to Mapping Active Faults beneath the Thick Quaternary," in *Developments in Geotechnical Engineering*. Editors Y. Kanaori, K. Tanaka, and M. Chigira (Amstredam: Elsevier), 84, 29–45.

Syed, T. H., Famiglietti, J. S., Rodell, M., Chen, J., and Wilson, C. R. (2008). Analysis of Terrestrial Water Storage Changes from GRACE and GLDAS. *Water Resour. Res.* 44, W02433. doi:10.1029/2006WR005779

Taha, A. I., Al Deep, M., and Mohamed, A. (2021). Investigation of Groundwater Occurrence Using Gravity and Electrical Resistivity Methods: a Case Study from Wadi Sar, Hijaz Mountains, Saudi Arabia. *Arab. J. Geosci.* 14, 334. doi:10.1007/s12517-021-06628-z

Tapley, B. D., Bettadpur, S., and Watkins, M. (2004). The Gravity Recovery and Climate Experiment : Mission Overview and Early Results. *Geophys Res. Lett.* 31, L09607. doi:10.1029/2004gl019920

Titus, R., Witthüser, K., and Walters, B. (2009). "Groundwater and Mining in the Bushveld Complex," in Proceedings of the international mine water conference (Pretoria, South Africa. International Mine Water Association), 178–184.

Trigo, R. M., Gouveia, C. M., and Barriopedro, D. (2010). The Intense 2007–2009 Drought in the Fertile Crescent: Impacts and Associated Atmospheric Circulation. *Agric. For. Meteorology* 150, 1245–1257. doi:10.1016/j.agrformet.2010.05.006

Troisi, S., Fallico, C., Straface, S., and Migliari, E. (2000). Application of Kriging with External Drift to Estimate Hydraulic Conductivity from Electrical-Resistivity Data in Unconsolidated Deposits Near Montalto Uffugo, Italy. *Hydrogeology J.* 8, 356–367. doi:10.1007/s100400000083

Van Overmeeren, R. A. (1989). Aquifer Boundaries Explored by Geoelectrical Measurements in the Coastal Plain of Yemen: A Case of Equivalence. *Geophysics* 54, 38–48. doi:10.1190/1.1442575

Voss, K. A., Famiglietti, J. S., Lo, M., De Linage, C., Rodell, M., and Swenson, S. C. (2013). Groundwater Depletion in the Middle East from GRACE with Implications for Transboundary Water Management in the Tigris-Euphrates-Western Iran Region. *Water Resour. Res.* 49, 904–914. doi:10.1002/wrcr.20078

Wahr, J., Swenson, S., Zlotnicki, V., and Velicogna, I. (2004). Time-variable Gravity from GRACE: First Results. *Geophys Res. Lett.* 31, L11501. doi:10.1029/2004gl019779

Watkins, M. M., Wiese, D. N., Yuan, D.-N., Boening, C., and Landerer, F. W. (2015). Improved Methods for Observing Earth's Time Variable Mass Distribution with GRACE Using Spherical Cap Mascons. *J. Geophys. Res. Solid Earth* 120, 2648–2671. doi:10.1002/2014jb011547

Wiese, D. N., Landerer, F. W., and Watkins, M. M. (2016). Quantifying and Reducing Leakage Errors in the JPL RL05M GRACE Mascon Solution. *Water Resour. Res.* 52, 7490–7502. doi:10.1002/2016wr019344

Wiese, D. N., Yuan, D.-N., Boening, C., Landerer, F. W., and Watkins, M. M. (2018). *JPL GRACE Mascon Ocean, Ice, and Hydrology Equivalent Water Height Release 06 Coastal Resolution Improvement (CRI) Filtered Version 1.0. Ver. 1.0*. CA, USA: PO.DAAC. doi:10.5067/TEMSC-3MJC6

Wolf, A. T., and Newton, J. T. (2007). *Case Study Transboundary Dispute Resolution: The Tigris-Euphrates Basin, Transboundary Freshwater Dispute Database (TFDD)*. Corvallis, OR: Oregon State University. Available at http://www.transboundarywaters.orst.edu/.

Wouters, B., Bonin, J. A., Chambers, D. P., Riva, R. E. M., Sasgen, I., and Wahr, J. (2014). GRACE, Time-Varying Gravity, Earth System Dynamics and Climate Change. *Rep. Prog. Phys.* 77, 116801. doi:10.1088/0034-4885/77/11/116801

Yechieli, Y. (2000). Fresh-Saline Ground Water Interface in the Western Dead Sea Area. *Ground Water* 38, 615–623. doi:10.1111/j.1745-6584.2000.tb00253.x

Yeh, P. J.-F., Irizarry, M., and Eltahir, E. A. B. (1998). Hydroclimatology of Illinois: A Comparison of Monthly Evaporation Estimates Based on Atmospheric Water Balance and Soil Water Balance. *J. Geophys. Res.* 103 (D16), 19823–19837. doi:10.1029/98jd01721

Yeh, P. J.-F., Swenson, S. C., Famiglietti, J. S., and Rodell, M. (2006). Remote Sensing of Groundwater Storage Changes in Illinois Using the Gravity Recovery and Climate Experiment (GRACE). *Water Resour. Res.* 42, W12203. doi:10.1029/2006wr005374

Conflict of Interest: The authors declare that the research was conducted in the absence of any commercial or financial relationships that could be construed as a potential conflict of interest.

Publisher's Note: All claims expressed in this article are solely those of the authors and do not necessarily represent those of their affiliated organizations, or those of the publisher, the editors and the reviewers. Any product that may be evaluated in this article, or claim that may be made by its manufacturer, is not guaranteed or endorsed by the publisher.

frontiers | Frontiers in Earth Science

TYPE Methods
PUBLISHED 11 August 2022
DOI 10.3389/feart.2022.956817

OPEN ACCESS

EDITED BY
Ahmed M. Eldosouky,
Suez University, Egypt

REVIEWED BY
Ya-Juan Xue,
Chengdu University of Information Technology, China
Abdelnasser Mohamed,
National Research Institute of Astronomy and Geophysics, Egypt

*CORRESPONDENCE
Shuyan Wang,
350634682@qq.com

SPECIALTY SECTION
This article was submitted to Solid Earth Geophysics,
a section of the journal
Frontiers in Earth Science

RECEIVED 30 May 2022
ACCEPTED 04 July 2022
PUBLISHED 11 August 2022

CITATION
Yu C, Wang S and Cheng L (2022), Application of high-resolution processing in seismic data based on an improved synchrosqueezing transform. *Front. Earth Sci.* 10:956817.
doi: 10.3389/feart.2022.956817

Application of high-resolution processing in seismic data based on an improved synchrosqueezing transform

Chen Yu[1], Shuyan Wang[2]* and Lifang Cheng[3]

[1]China Earthquake Networks Center, Beijing, China, [2]China Academy of Electronics and Information Technology, China Electronics Technology Group Corporation, Beijing, China, [3]School of Geophysics and Information Technology, China University of Geosciences, Beijing, China

This study proposes a high-resolution processing technique for seismic data based on the improved synchrosqueezing transform (SST). The SST rearranges the complex spectrum of the wavelet transform along the frequency axis. However, the energy is not concentrated in the position with the faster frequency change rate. To overcome these problems, the proposed method first transformed the seismic signal into an analytical one *via* Hilbert transformation and then determined the phase correction value (x0(t)) before and after the transformation. This was achieved using the instantaneous frequency attribute (ω(t)) of the analytical signal and a specific frequency (ω0) selected as the dominant frequency of the input data to adjust the change rate of the signal frequency before the SST falls close to zero, which can improve the time–frequency resolution after compression transformation. The essence of this method only adjusts the phase of the signal before and after transformation, without affecting the inverse expression of the SST. The one- and two-dimensional model data results show that the proposed method can better identify the time–frequency distribution characteristics of seismic signals and improve their resolution and the focusing effect in the time–frequency domain. The proposed method shows good prospects for application in gas reservoir detection and identification.

KEYWORDS

improved synchrosqueezing transform, generalized Fourier transform, time–frequency analysis, seismic data, high resolution

Highlights

1) A new high-resolution processing technique for seismic data.
2) The improved synchrosqueezing transform based on the generalized Fourier transform.
3) The phase correction value is calculated using the instantaneous frequency of seismic data.
4) Both synthetic signal and actual data results show remarkable improvement.
5) The new method has a good application prospect in resource exploration.

1 Introduction

With the deepening of exploration and development of oil and gas fields, exploration and development are becoming increasingly difficult. Considering that seismic signals are typical non-stationary signals in nature, the time–frequency analysis technology in modern signal processing can obtain the change process of seismic signals in the time and frequency domains at the same time and extract effective time–frequency characteristics for lithology and fluid interpretation. This study proposes a time–frequency analysis method to improve the time–frequency resolution of seismic data (Li et al., 2004; Wu and Liu, 2009; Han and Van der Baan, 2013).

At present, Fourier transform (FT) is still the most commonly used time–frequency transform method in signal analysis. With the gradual deepening of research on non-stationary signals, researchers have proposed a series of signal analysis techniques aimed at the problems existing in FT, among which the short-time Fourier transform (STFT) (Potter and Steinberg, 1950; Potter et al., 1966) and wavelet transform (WT) (Morlet et al., 1982a; 1982b) are the two primary methods (Abry et al., 1993; Sinha et al., 2005; Daubechies, 2004; Gao et al., 2006; Chen and Gao, 2007). In order to improve the time–frequency resolution of STFT, Kodera et al. (1976) first proposed the time–frequency spectrum rearrangement technique and later generalized it to any bilinear time–frequency or time-scale representation by Auger and Flandrin (1995). Since this method has no accurate inverse transformation, mathematically, it did not receive widespread attention in the years soon after its development. Recently, with the increasing difficulty of exploration and development, the time–frequency spectrum rearrangement method has attracted extensive attention in the field of seismic exploration (Odegard et al., 1997; Han, 2013; Shang, 2014; Kahoo and Siahkoohi, 2009; Pedersen et al., 2003).

The synchrosqueezing transform (SST) is similar to the time–frequency spectrum rearrangement method, which was proposed by Daubechies et al. (2011). In essence, it recalculates a position close to the real coordinates of the time–frequency energy spectrum so as to rearrange the energy according to it. In recent years, SST has been applied in the rearrangement of various original time–frequency representations, including the continuous wavelet transform (CWT) (Daubechies et al., 2011), wave packet transforms (Wang and Gao, 2017), STFT (Oberlin et al., 2014), S transform (Huang et al., 2016), and generalized S transform (Wang et al., 2018). In addition, some new techniques based on the notion of the SST have been proposed, such as the high-order synchrosqueezed transform (Liu W. et al., 2018), concentration of frequency and time (ConceFT) (Daubechies et al., 2016), synchroextracting transform (Yu et al., 2017), and others (Li and Liang, 2012; Thakur et al., 2013; Liu N. et al., 2018; Xue et al., 2019).

Most of the abovementioned methods have been used in seismic signal processing (Huang et al., 2016; Wang and Gao, 2017; Wang et al., 2018). In addition to this, Herrera et al. (2014) applied the SST to time–frequency analysis of seismic signals for the first time and compared it with CWT and complete ensemble empirical mode decomposition (CEEMD) in detail, which verified the superiority of this method in the time–frequency analysis of seismic signals. Herrera et al. (2015) adopted the technology of P- and S-wave separation based on the SST and verified the method through an example. Siahsar et al. (2016) developed a random noise elimination technique based on the SST and verified the effectiveness of the algorithm through a test case as well. The SST based on the STFT was introduced in seismic data analysis by Wu and Zhou (2018). The method reassigns the STFT values to different points to produce a concentrated time–frequency map.

In these studies, Li and Liang (2012) found that the resolution of the SST could be further improved by adding a phase factor to the traditional SST process *via* the notion of the generalized Fourier transform (GFT). For signals whose frequency content changes rapidly with time, this method can increase the resolution in order to identify the time–frequency distribution characteristics. Therefore, this method may provide an opportunity for improving the processing of seismic data through time–frequency analysis techniques. The key to this method is obtaining the phase factor, which is related to the instantaneous frequency of the signal. For stationary signals, the instantaneous frequency is a constant, while for non-stationary signals, the instantaneous frequency is a function of time t. As a seismic wave propagates in the underground medium, energy absorption, attenuation, and scattering occur, leading to a complicated time–frequency relationship in seismic waves. Therefore, accurately obtaining the instantaneous frequency of actual seismic data is key to high-resolution processing in the field of petroleum exploration.

In this study, we attempted to calculate the phase factor using the instantaneous frequency of seismic data, extracted by using a complex signal analysis technique based on the Hilbert transform, and present a high-resolution processing technique for seismic data based on the improved SST. In order to prove the feasibility of this approach, synthetic 1D- and 2D-models and actual seismic data from the Tuha Basin, in the Xinjiang autonomous region of China, were tested as an example. This study is divided into five sections. Section 1 contains the introductory content; Section 2 describes the theory and method of the improved SST; Sections 3 and 4 show the calculation results for the method to model data and real seismic data; and Section 5 discusses the results.

2 Materials and methods

The approach proposed in this study is to adjust the frequency change rate of a signal by some reversible means and map it to a

specific frequency, ω0, before performing the SST. In order to achieve the aforementioned process, it is necessary to find a reversible transformation, which can have a certain influence on the frequency change rate of the signal but will not affect the accuracy of the time spectrum or the effect of the inverse transformation. We attempted to obtain the phase factor using the instantaneous frequency of seismic data, extracted by a complex signal analysis technique based on the Hilbert transform. In the following sections, we briefly describe the theory of SST and GFT and illustrate the improved SST proposed in this study.

2.1 Brief recap of the SST and GFT

The CWT of a signal s(t) is (Daubechies and Maes, 1996)

$$W_s(a,b) = \int s(t)\frac{1}{\sqrt{a}}\psi^*\left(\frac{t-b}{a}\right)dt, \tag{1}$$

where ψ^* is the complex conjugate of the mother wavelet, and b is a time shift factor, which is scaled by a. According to the scaling and shifting method, the signal is analyzed at a multi-scale by the CWT (Kahoo and Siahkoohi, 2009).

Based on Parseval's theorem in the Fourier domain, the CWT of a signal s(t) can be rewritten into the expression of the frequency domain as follows:

$$W_s(a,b) = \frac{1}{2\pi}\int S(\xi)\sqrt{a}\Psi^*(a\xi)\exp(ib\xi)d\xi. \tag{2}$$

In order to facilitate the derivation, the seismic signal is assumed to be only a harmonic wave $s(t) = A\cos(\omega t)$. The Fourier pair $S(\xi) = \pi A[\delta(\xi-\omega)+\delta(\xi+\omega)]$ can be inserted into Eq. 2 as follows:

$$\begin{aligned} W_s(a,b) &= \frac{A}{2}\sqrt{a}\int[\delta(\xi-\omega)+\delta(\xi+\omega)]\Psi^*(a\xi)\exp(ib\xi)d\xi \\ &= \frac{A}{2}\sqrt{a}\Psi^*(a\omega)\exp(ib\omega). \end{aligned} \tag{3}$$

Theoretically, if the FT coefficient of the wavelet $\Psi^*(\xi)$ is concentrated around the central frequency $\xi = \omega_0$, then $W_s(a,b)$ will be concentrated around the scale $a = \omega_0/\omega$. However, in practice, the energy of the wavelet coefficients often diffuses along the scale a direction, which generates the smearing effect in the time–frequency representation (Daubechies et al., 2011). Daubechies and Maes (1996) found that smearing has little effect along the time b axis. For this reason, the instantaneous frequency $\omega_s(a,b)$ can be calculated by taking the partial derivatives for all $W_s(a,b) \neq 0$:

$$\omega_s(a,b) = -i(W_s(a,b))^{-1}\frac{\partial}{\partial_b}W_s(a,b). \tag{4}$$

Eq. 4 expresses the mapping between the time-scale and time–frequency domains, i.e., $(b,a) \rightarrow (b,\omega_s(a,b))$. Every point (b,a) can be mapped to $(b,\omega_s(a,b))$ using this equation. If the sum of every wavelet coefficient at point (b,a) is converted to $(b,\omega_s(a,b))$, the smearing problem can be improved. Because a and b are discrete values, we can define a scale step $(\Delta a)_k = a_k - a_{k-1}$ and frequency step $(\Delta w)_k = w_k - w_{k-1}$. Therefore, the time–frequency spectrum after SST is expressed as follows:

$$T_s(\omega_l,b) = (\Delta\omega)^{-1}\sum_{a_k:\ |\omega(a_k,b)-\omega_l|<\Delta\omega/2} W_s(a_k,b)a_k^{-3/2}(\Delta a)_k, \tag{5}$$

Eq. 5 is the new time–frequency representation of the signal $T_s(a_l,b)$ according to synchrosqueezing along the frequency axis only (Li and Liang, 2012). The inverse transformation of the SST can be obtained by integrating both sides of Eq. 2 as follows:

$$\begin{aligned} \int_0^\infty W_s(a,b)a^{-3/2}da &= \frac{1}{2\pi}\int_{-\infty}^{\infty}\int_0^\infty S(\xi)\Psi^*(a\xi)\exp(ib\xi)a^{-1}dad\xi \\ &= \left(\int_0^\infty \Psi^*(a\xi)\frac{d\xi}{\xi}\right)*\left(\frac{1}{2\pi}\int_0^\infty S(\xi)\exp(ib\xi)d\xi\right). \end{aligned} \tag{6}$$

By taking $C_\varphi = \int \Psi^*(\xi)\frac{d\xi}{\xi}$, the inverse transformation of the SST can be obtained as follows:

$$s(t) = \mathrm{Re}\left[C_\varphi^{-1}\sum_l T_s(\omega_l,b)\Delta\omega\right]. \tag{7}$$

This study adopts a generalized Fourier transform to complete the aforementioned process. The GFT of a signal s(t) is expressed as follows (Detka and El-Jaroudi, 1996):

$$S_G(\omega) = \int_{-\infty}^{+\infty} s(t)\exp\left(-j2\pi(\omega t + x_0(t))\right)dt, \tag{8}$$

where $x_0(t)$ is a real-valued function of t, which is used to represent the phase change of the signal. On expanding this equation, it can be found that the GFT of $s(t)$ is equivalent to the standard FT of $s(t)\exp(-j2\pi x_0(t))$. Therefore, the inverse GFT of $S_G(\omega)$ is

$$s(t) = \exp\left(j2\pi x_0(t)\right)\int_{-\infty}^{+\infty} S_G(\omega)\exp\left(j2\pi\omega t\right)d\omega. \tag{9}$$

By taking $S_G(\omega) = \delta(\omega-\omega_0)$, Eq. 9 can be rewritten as $s(t) = \exp(i2\pi(\omega_0 t + x_0(t)))$. It can be found that signal $s(t)$ can be mapped to a specific point ω_0 through GFT, and the instantaneous frequency of the signal $s(t)$ is

$$\omega(t) = \omega_0 + \frac{dx_0(t)}{dt}. \tag{10}$$

Eq. 10 shows that the key to mapping the instantaneous frequency $\omega(t)$ of the original signal to the specific frequency ω_0 is to determine the function $x_0(t)$.

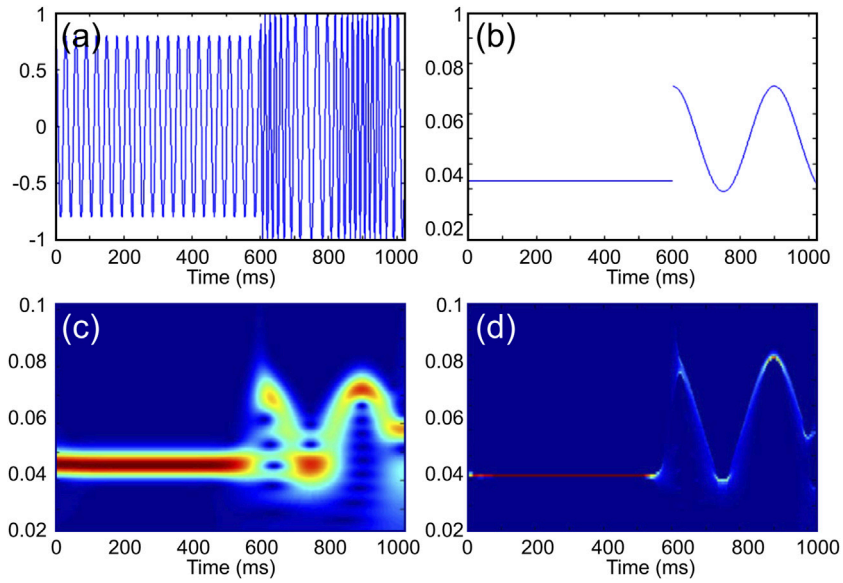

FIGURE 1
Examples of time–frequency representations of the continuous wavelet transform (CWT) and synchrosqueezing transform (SST). **(A)** Signal $s(t)$= $s_1(t)$ +$s_2(t)$ is defined by $s_1(t)$ = 0.7cos(πt/15) for 0 ≤ t ≤ 600 ms and by $s_2(t)$ = cos(πt/10+2πsin(πt/150)) for 601 ≤ t ≤ 1,024 ms; **(B)** instantaneous frequency for its two components (left), $\omega(t)$ = 1/30 for 0 ≤ t ≤ 600 ms and $\omega(t)$ = (π/10+2πcos(πt/150)*(π/150))/(2π); **(C)** example of a continuous wavelet transform of $s(t)$, with a Morlet wavelet [this is plotted with MATLAB, with the "jet" colormap; red indicates higher amplitude]; and **(D)** example of the synchrosqueezing transform(SST) (this is plotted with MATLAB, with the "jet" colormap; red indicates higher amplitude).

2.2 Improved SST for seismic data

In this study, ω_0 is the dominant frequency of input data.

Based on the aforementioned expressions, we introduced GFT into the SST and provided the detailed derivation process. The improved SST needs to be calculated in a complex domain. First, the real value signal needs to be transformed into an analytical signal using a Hilbert transform (HT):

$$p(t) = s(t) + iH(s(t)). \tag{11}$$

According to Eq. 10, $x_0(t)$ is calculated based on the instantaneous frequency $\omega(t)$ of the actual input data. The instantaneous frequency is mathematically defined as the derivative of the signal phase. Taner et al. (1979) introduced a complex signal analysis technique into seismic data processing for the first time and proposed the instantaneous attribute with geological significance. The instantaneous frequencies are extracted by complex signal analysis *via* the Hilbert transform, which is a signal-value function with time as the variable. The instantaneous frequency is expressed as follows:

$$\omega_n = \frac{\mathrm{d}}{\mathrm{d}t}\left(\arctan\frac{\tilde{s}(t)}{s(t)}\right), t = u_n, \tag{12}$$

where $\tilde{s}(t)$ is the Hilbert transform result of the actual seismic data $s(t)$, and u_n represents the time point corresponding to the maximum envelope of the complex signal. Furthermore, the following calculation was completed:

$$q(t) = p(t)\exp(-i2\pi x_0(t)). \tag{13}$$

Since $x_0(t)$ is the function that controls the phase change of the original signal $s(t)$, the instantaneous frequency of the analytical signal $q(t)$ does not change significantly with time during the whole period using Eq. 13. In order to reduce the negative frequency effect of $q(t)$, it is necessary to perform HT on it, as expressed using the following equation:

$$r(t) = q(t) + iH(q(t)). \tag{14}$$

According to SST's implementation steps, CWT of $r(t)$ is performed. Furthermore, the CWT coefficient of the original signal can be obtained using the following equation:

$$W_z(a,b) = W_r(a,b)\exp(i2\pi x_0(t)), \tag{15}$$

where $W_r(a,b)$ is the CWT of $r(t)$. According to Eq. 4, we can observe that $\omega_s(a,b) = \omega_z(a,b)$, which means that the instantaneous frequency of $W_z(a,b)$ obtained after the aforementioned processing is consistent with that calculated using the original data.

According to Eq. 14, the moduli of $W_z(a,b)$ and $W_r(a,b)$ are equal; therefore, the aforementioned processing does not change the energy of the original signal. Based on Eq. 14, the SST of $s(t)$, $T_y(\omega_l,b)$ can be obtained by processing $W_z(a,b)$ in Eq. 5. This

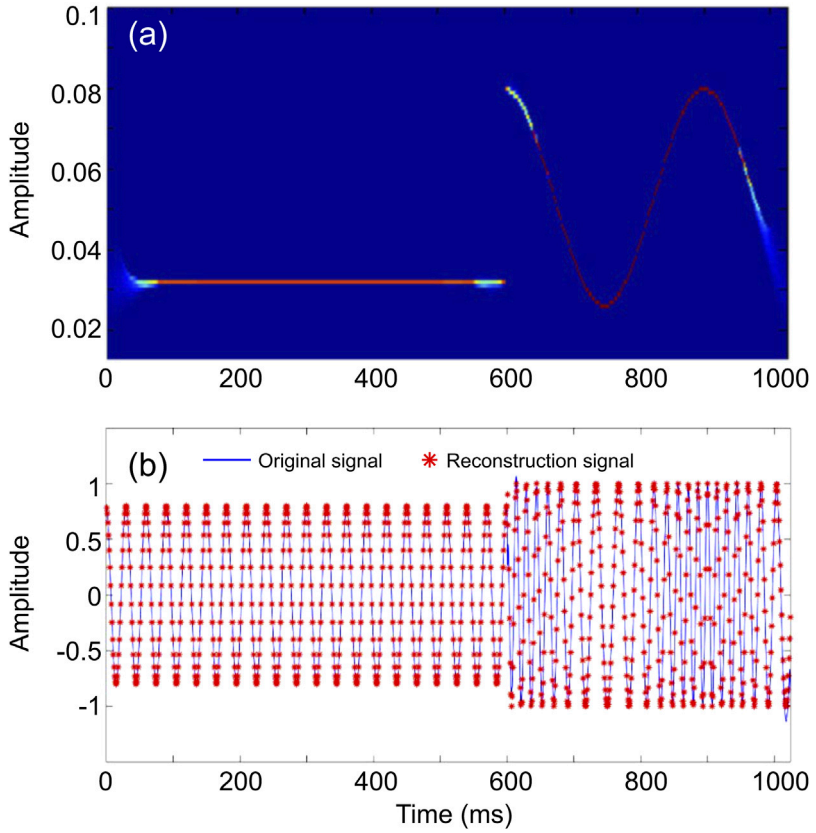

FIGURE 2
Results of the improved synchrosqueezing transform (SST) of s(t), shown in Panel 1. **(A)** Results of the improved SST for the signal (this is plotted with MATLAB, with the "jet" colormap; red indicates higher amplitude); **(B)** comparison between the original signal and reconstructed signal by the improved SST [this is plotted with MATLAB, the blue solid line represents the original signal s(t); the red asterisk represents the reconstructed signal].

processing of the SST will allow the transfer of $r(t)$ features to their results, and $r(t)$ itself is obtained by HT and phase-related processing; therefore, the transmission of the features of $r(t)$ can achieve the purpose of improving the SST. In essence, the aforementioned processing allows the adjustment of the signal phase before and after the transformation so that it does not affect the expression of the inverse SST. Therefore, the improved inverse SST using the proposed method can be expressed as follows:

$$s(t) = \mathrm{Re}\left[C_{\varphi}^{-1}\sum_{l} T_y(\omega_l, b)\Delta\omega\right]. \tag{16}$$

3 Results

3.1 1-D synthetic data

In this section, we present how, in order to test the feasibility of the improved method, the improved SST was performed on the cosine non-stationary model (Figures 2A,B) and compared it with the CWT-based SST results (Figure 1D).

We constructed a non-stationary cosine signal. The signal was a stable frequency cosine wave in the range of 0–600 ms and a modulated signal whose frequency varied with the cosine wave in the range of 600–1,000 ms. Figure 1A displays this signal in the time domain, and its theoretical frequency is shown in Figure 1B. Figures 1Cand D illustrate the CWT and SST of the signal, respectively.

It can be seen from Figures 1C,D that the energy focus of CWT is poor and that energy cluster bonding occurs in some places. The SST obviously has higher focusing ability and time–frequency resolution. After further observation, it is not difficult to recognize that the time-frequency spectrum of SST is close to the theoretical frequency of the signal in the range of 0–560 ms. However, in the area of frequency mutation, i.e., around 600 ms, it cannot effectively distinguish between the two very different frequencies but shows a certain smoothing trend. However, the CWT has a better effect at the

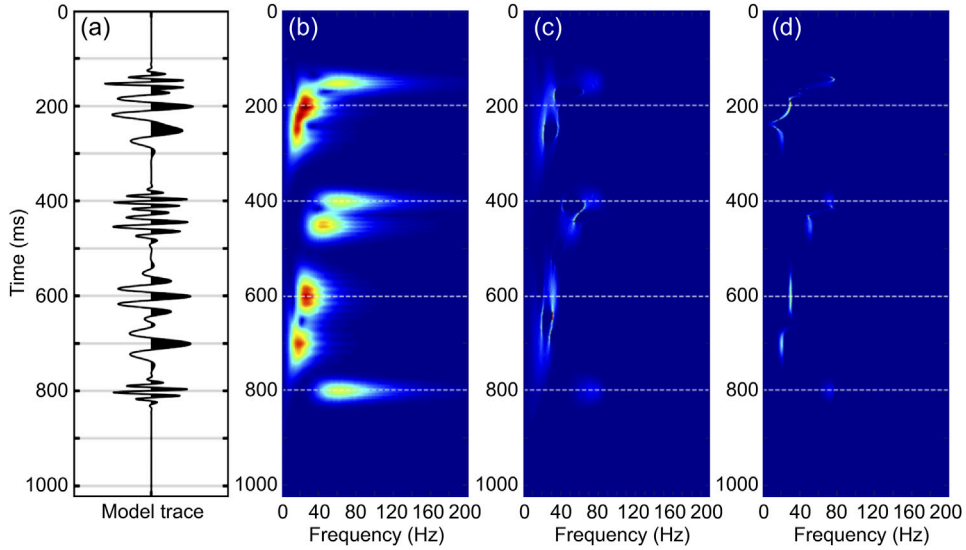

FIGURE 3
Application of the synthetic seismic trace. **(A)** Original synthetic seismic trace with noise; the signal is composed of two 20 Hz zero-phase Morlet wavelets, with scale = 1 at 250 and 700 ms; two 30 Hz zero-phase Morlet wavelets, with scale = 2 at 200 and 600 ms; three 50 Hz Morlet wavelets, with phase = π/2 and scale = 2 at 150, 400, and 800 ms; and a 40 Hz Morlet wavelet, with phase = π/2 and scale = 2 at 450 ms; **(B)** time–frequency spectra of synthetic seismic trace using the continuous wavelet transform (CWT); **(C)** time–frequency spectra of the synthetic seismic trace using the CWT-based synchrosqueezing transform (SST); and **(D)** time–frequency spectra of synthetic seismic trace using our improved SST. [**(B–D)** are plotted with MATLAB, with the "jet" colormap; red indicates higher amplitude].

frequency mutation, showing no smoothness and a real frequency jump. Similarly, when the signal frequency changes at 600–1,000 ms, the energy of SST still diverges slightly in the scale direction.

As shown in Figure 2A, the improved SST effectively reduced the smearing effect of energy on the time axis at the frequency fluctuation, especially at the frequency mutation near 600 ms, which is closer to the theoretical time spectrum than the method in Figure 1. Figure 2B shows the waveform comparison between the original signal and the reconstructed signal. The blue color indicates the original waveform, and the red color indicates the reconstructed data using the inverse transform of the improved SST. The improved SST can reconstruct the model signal accurately without affecting its inverse transformation effect and thus provides a new technical method for threshold denoising in the time–frequency domain and seismic signal reconstruction.

The frequency component of the model is relatively simple compared with actual data; therefore, we further tested the improved method with irregular synthetic data, which is more similar to the real seismic data (Figure 3A). The synthetic trace in Figure 3A is composed of a set of Morlet wavelets with different frequencies, amplitudes, scales, and time delays.

Figures 3B–D show the time–frequency map of CWT, SST, and improved SST, respectively, with the same color scale. Although CWT can recognize the signal components in different frequency bands, the resolution of the time spectrum was obviously insufficient. The distribution of energy groups was not concentrated, and many high-frequency interference components existed (Figure 3B). The results of SST were greatly improved from those of CWT, and the energy distribution was clearly more concentrated. However, it is not difficult to see that if the signal components of two different frequencies are close in time; their time spectra will be entangled with each other, such as at 400–600 ms, or false frequency components will appear. For example, the wavelet frequency of 30 Hz near 600 ms (approximately 550 ms–650 ms) in the time domain extends to nearly 800 ms in the time–frequency representation, and the energy is not concentrated near 600 ms (Figure 3C). The improved SST (Figure 3D) had the best time–frequency focusing effect and could better identify the time–frequency distribution characteristics of the signal. Specifically, the two wavelets at 400 and 450 ms can be more clearly identified on the time spectrum without entanglement. The energy groups of the two sub-waves at 600 and 700 ms were remarkably more concentrated and more easily identified in the time spectrum.

3.2 2-D horizontal layered model

In this section, to test the lateral resolution and the sensitivity of the proposed improved SST in detecting thin reservoirs, we first applied the improved SST to a 2-D horizontal layered model and compared the results to those of the CWT, CWT-based SST

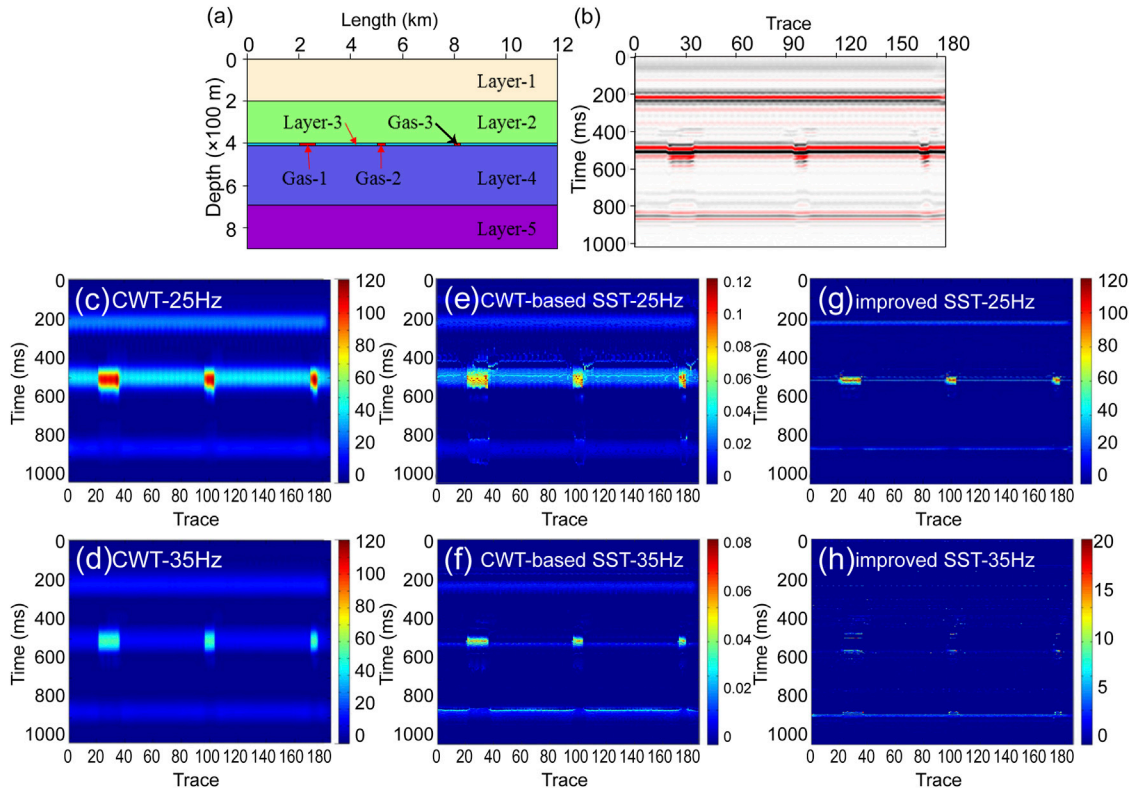

FIGURE 4
Application of the 2-D horizontal model and analysis of the instantaneous frequency used the isofrequency section. **(A)** Forward model with horizontal layers. The third layer contains three gas layers with large transverse width variations. Model data are created by using the Tesseral 2-D; **(B)** pre-stack time migration profile of the 2-D forward model. **(C)** 25 Hz-isofrequency section of the continuous wavelet transform (CWT); **(D)** 35 Hz-isofrequency section of the CWT; **(E)** 25 Hz-isofrequency section of the CWT-based SST; **(F)** 35 Hz-isofrequency section of the CWT-based SST; **(G)** 25 Hz-isofrequency section of the improved synchrosqueezing transform (SST) in this study; **(H)** 35 Hz-isofrequency section of the improved SST (these are all plotted with MATLAB, with the "jet" colormap; red indicates higher amplitude).

TABLE 1 Geological parameters of the 2-D forward model.

Layer	Velocity (m/s)	Density (g/cm^3)	Thickness (m)	Width (m)
Layer-1	1,300	1.20	200	
Layer-2	1,500	1.25	200	
Layer-3	1,600	1.30	10	
Layer-4	1700	1.35	290	
Layer-5	1800	1.40	800	
Gas-1	1,400	1.20	10	600
Gas-2	1,400	1.20	10	300
Gas-3	1,400	1.20	10	200

(Daubechies et al., 2011), and improved SST methods. The model designed in Figure 4A consisted of five horizontal layers; the third layer was a thin reservoir with a thickness of 10 m, in which, three gas layers with large transverse width variations were developed. The widths of the layers from left to right were 600, 300, and 200 m, respectively. The specific design parameters are shown in Table 1. The geological model was forward modeled with a 30 Hz zero-phase Ricker wavelet. Figure 4B is the pre-stack time migration profile by forward modeling. It can be seen from the migration profile that although a depression existed in the in-

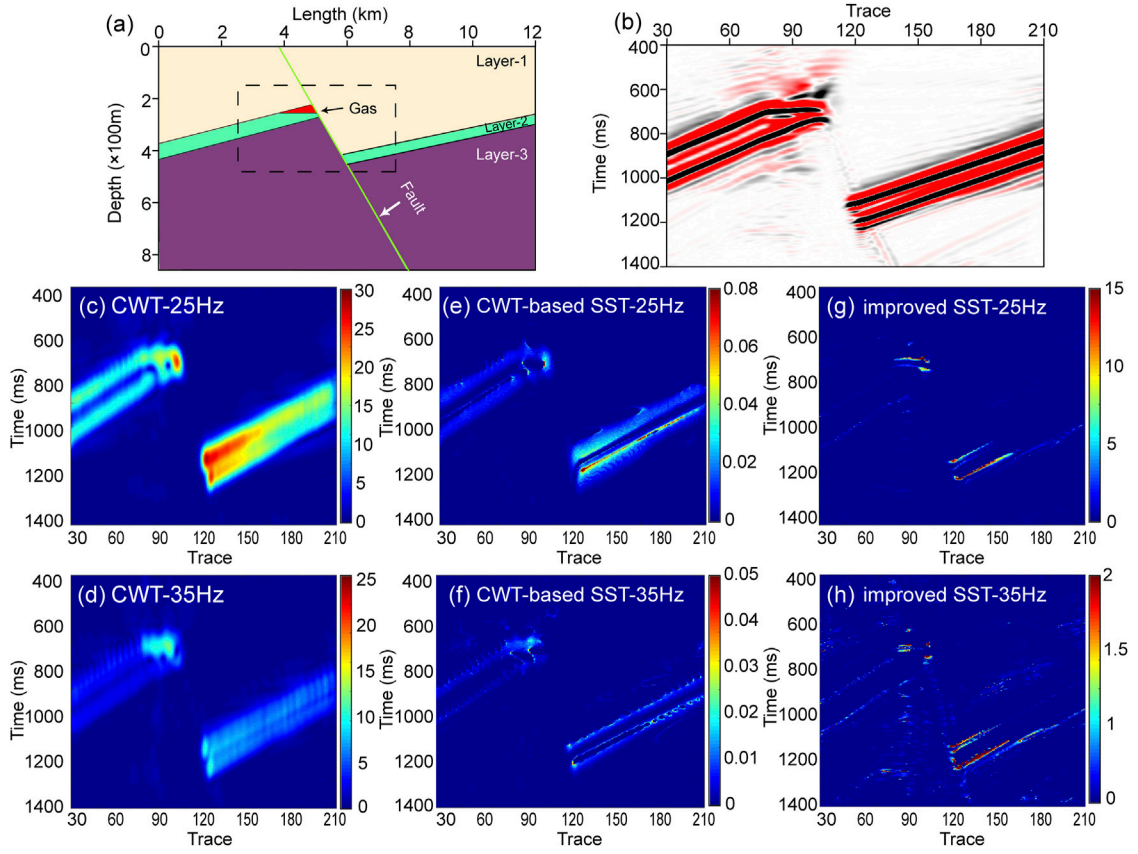

FIGURE 5
Application of the 2-D non-horizontal model and analysis of the instantaneous frequency used the isofrequency section. **(A)**Forward model, which is created by using the Tesseral 2-D; the black dotted box shows the location of the profile in Panel **(B)**; **(B)** pre-stack time migration profile of the 2-D forward model in Panel **(A)**. **(C)** 25 Hz-isofrequency section of the continuous wavelet transform (CWT); **(D)** 35 Hz-isofrequency section of the CWT; **(E)** 25 Hz-isofrequency section of the CWT-based SST; **(F)** 35 Hz-isofrequency section of the CWT-based SST; **(G)** 25 Hz-isofrequency section of the improved synchrosqueezing transform (SST) in this study; **(H)** 35 Hz-isofrequency section of the improved SST (these are all plotted with MATLAB, with the "jet" colormap; red indicates higher amplitude).

TABLE 2 Geological parameters of the fault model.

Layer	Velocity (m/s)	Density (g/cm^3)
Layer-1	1,300	1.20
Layer-2	1,600	1.30
Layer-3	1,800	1.40
Gas	1,400	1.20

phase axis at the gas-bearing location, the presence of fluid cannot be confirmed.

Figures 4C—H represent the single-frequency profile near the target location extracted by applying CWT, CWT—based SST, and improved SST to Figure 4B. They represent the 25 and 35 Hz single-frequency profiles of CWT, CWT—based SST, and improved SST, respectively. The comparison of the three methods shows that the improved SST has the best time–frequency resolution. The three methods can reflect the phenomenon of high-frequency attenuation of gas reservoirs, but the improved SST was more sensitive to frequency changes due to its higher resolution. In particular, the energy group of the gas layer in Figure 4H can hardly be seen in the 35 Hz single-frequency profile, which is sufficient to demonstrate the feasibility of the improved SST method in gas-bearing detection. In addition, it was found that the energy difference between the gas reservoir and surrounding rock in the time spectrum (Figure 4G) was larger than that of the CWT (Figure 4A) and CWT-based SST (Figure 4A), which is helpful for qualitative identification of reservoir boundaries.

3.3 2D unhorizontal layered model

In order to further study the applicability of the improved SST in irregular gas reservoir exploration, we developed a 2D

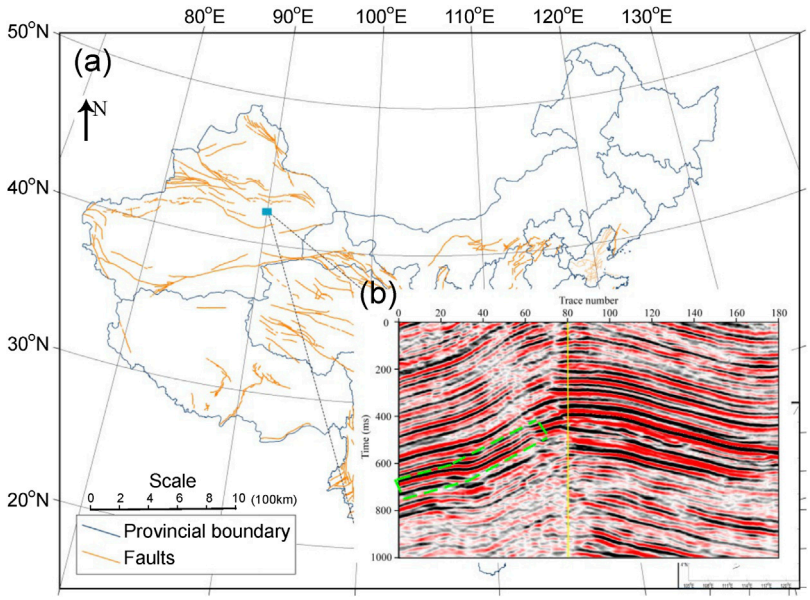

FIGURE 6
Location of the real seismic data. **(A)** Location of the exploration area where data were collected (blue square). This is created by using the Generic Mapping Tools (GMT) 4, accessed on 1 May 2022; **(B)** original pre-stack time migration profile of a through-well line from 3-D seismic data; the yellow vertical line represents extracted single-channel seismic data for subsequent analysis; the green box indicates a reservoir by drilling data.

fault model as an example and compared the results to those of the CWT, CWT-based SST, and improved SST methods. This model shown in Figure 5A perceived a gas reservoir at a depth of 300 m. Table 2 displays the specific parameters for each layer. This 2D unhorizontal layer geological model was also forward modeled with a 30 Hz zero-phase Ricker wavelet. Figure 5B displays the pre-stack time migration profile after processing from forward modeling. It is evident that compared with the horizontal layer model, it is more difficult to identify the gas-bearing boundary in the migration profile of the inclined horizon.

Figures 5C–H represent the single-frequency profile near the target location extracted by applying CWT (Figures 5C,D), CWT-based SST (Figures 5E,F), and improved SST (Figures 5G,H) methods to Figure 5B. They represent the 25 and 35 Hz single-frequency profiles of CWT, CWT—based SST, and improved SST, respectively. Figure 5 shows that the improved SST can identify the boundary of the reservoir more accurately than the other two methods (Figure 5G). CWT displayed the lowest resolution of the three models. The energy mass of the gas reservoir was not concentrated, and the upper and lower boundaries of the sand body on the right side of fault overlapped. The resolution of the time–frequency distribution of the CWT-based SST was higher than that of CWT, and the sand boundary on both sides of the fault could be identified more accurately. However, it was still difficult to identify the gas reservoir, especially in the 25 single-frequency profiles (Figure 5E).

4 Applications to seismic signals

We used real seismic data from the Tuha basin in Xinjiang as an example to deeply discuss the advantages of the improved SST in gas-bearing reservoir prediction. Due to the influence of many factors, such as attenuation and Earth absorption, in the propagation process of a seismic wave, it showed a high degree of non-stationarity. In the low-frequency profile, shadows appeared beneath the gas reservoir, and the low-frequency shadows gradually disappeared as the frequency increased (Castagna et al., 2003; Chen et al., 2009; Shi et al., 2014). Therefore, we can use these characteristics to detect gas reservoirs. Figure 6 shows a through-well line from 3-D seismic data. The green box indicates a reservoir that has been confirmed to be gas-bearing using drilling data. However, the sand body in the study area changed rapidly in the transverse direction, and a low-frequency, high-amplitude area was present under the gas-bearing layer, namely, a “low-frequency shadow” phenomenon (Ebrom, 2004; Liu 2004; Liu X. et al., 2018). It was difficult to determine the boundary of the sand body with conventional interpretation methods.

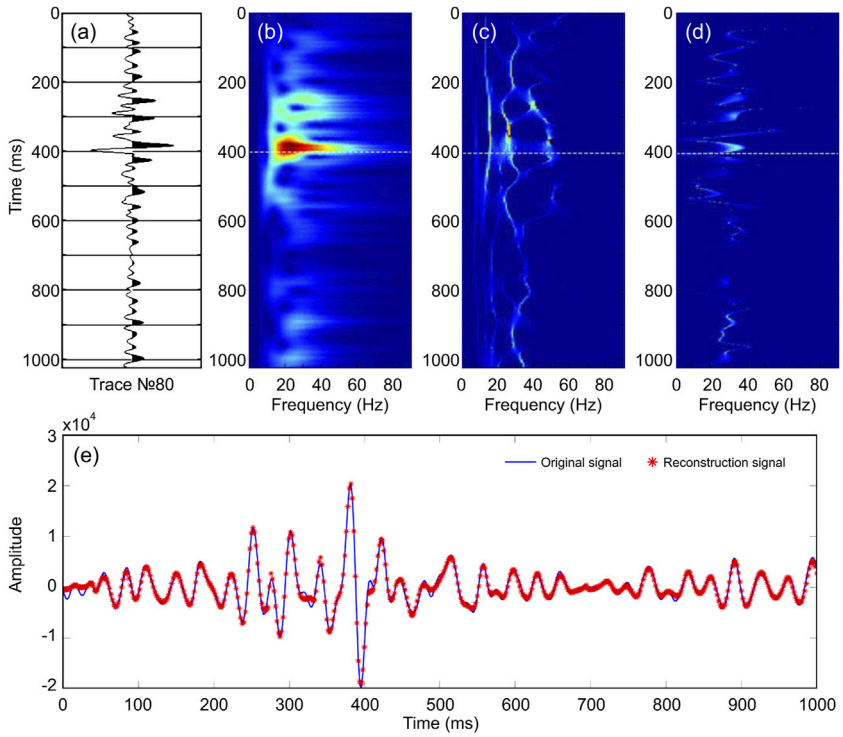

FIGURE 7
Comparison of single-channel seismic data. **(A)** Single-channel seismic data for trace No. 80; **(B)** time–frequency spectra of synthetic seismic trace using the continuous wavelet transform (CWT); **(C)** time–frequency spectra of synthetic seismic trace using the CWT-based synchrosqueezing transform (SST); **(D)** time–frequency spectra of synthetic seismic trace using the improved SST; **(E)** Comparison between the original seismic signal and reconstructed seismic signal by the improved SST. The blue solid line represents the original signal s(t); the red asterisk represents the reconstruction signal [these are all plotted with MATLAB; **(B–D)** are displayed with the 'jet' colormap; red indicates higher amplitude].

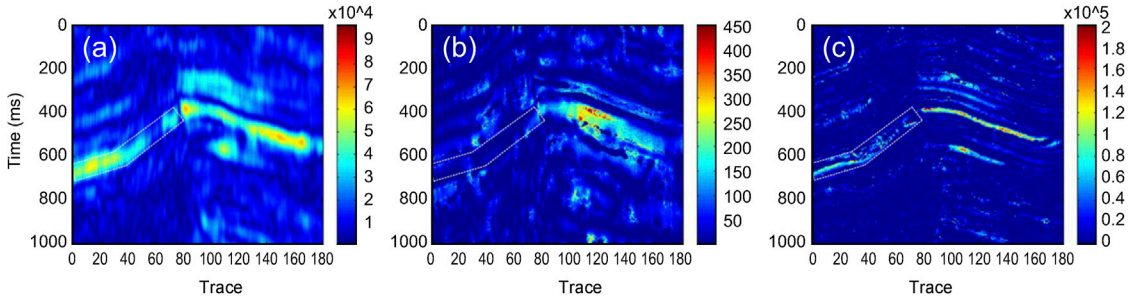

FIGURE 8
30 Hz-isofrequency profile processed with different approaches. **(A)** Continuous wavelet transform (CWT); **(B)** CWT-based synchrosqueezing transform (SST); and **(C)** improved SST. The white dotted box marks the location of the gas-bearing reservoir (these are all plotted with MATLAB, with the "jet" colormap; red indicates higher amplitude).

4.1 Single trace

Figure 7A shows the interception of single-channel seismic data of trace No. 80 in Figure 6 and the gas-bearing reservoir near 400 ms. The time spectra of CWT, SST, and improved SST are shown in Figures 7B–D, respectively. It can be seen that compared with CWT, SST had a greater improvement in the adhesion of the energy group, but the vertical time–frequency distribution showed a certain continuity. The improved SST had a higher time–frequency resolution, which could not only

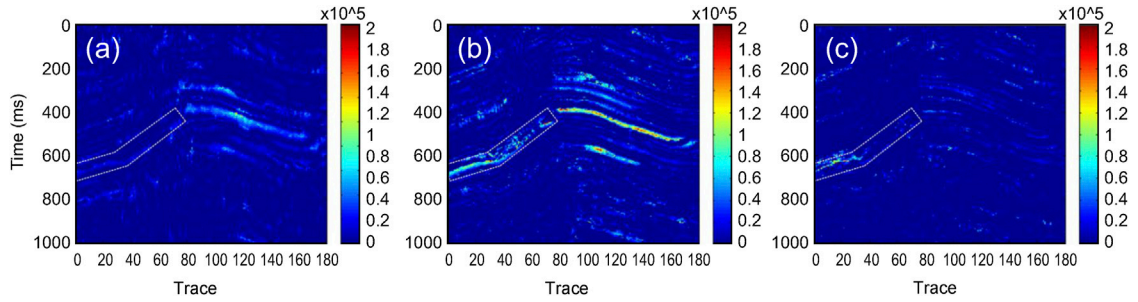

FIGURE 9
Isofrequency profile of data processed by the improved synchrosqueezing transform (SST). **(A)** 20 Hz-isofrequency profile; **(B)** 30 Hz-isofrequency profile; and **(C)** 40 Hz-isofrequency profile. The white dotted box marks the location of the gas-bearing reservoir (these are all plotted with MATLAB, with the "jet" colormap; red indicates higher amplitude).

improve the problem of energy group diffusion but could also clearly distinguish the gas reservoir from other horizons in the longitudinal direction. The time–frequency characteristics of the wavelet could be accurately determined, especially in the vicinity of the 200–400 ms gas-bearing reservoir. As shown in Figures 7B–D, the dominant frequency for the trace was approximately 30 Hz. Figure 7E shows the comparison between the reconstructed and original seismic data, verifying that the improved synchrosqueezing transform has good reversibility.

4.2 Vertical cross section

Next, we applied the three methods to all traces and computed the time–frequency representation of 30 Hz-signal frequency components to qualitatively identify reservoir boundaries in Figure 8.

It can be seen from Figure 8 that, in general, for the gas reservoirs indicated by the white box, the SST and improved SST had the worst and best time–frequency resolution, respectively. This is because the continuous frequency of the actual data varied greatly, and the original SST could not effectively solve the energy divergence caused by the rapid frequency change, while the improved SST had good adaptability to it. The 20, 30, and 40 Hz single-frequency–time-frequency spectra of the improved synchrosqueezing transform were further extracted and compared (Figure 9). It can be seen that, from 20 to 30 Hz, the time–frequency energy of the reservoir, indicated by the white box, increased with the increasing low-frequency portion. From 30 to 40 Hz, the reservoir time–frequency energy decreased with the increase in high-frequency components. In particular, the boundary range of the isolated gas-bearing reservoir, indicated by the white box, could clearly be determined from the 20–40 Hz variation characteristics.

5 Discussion

In essence, the SST rearranges the energy of each point in the time–frequency spectrum to a position closer to the real time–frequency coordinate of the signal. Specifically, it rearranges the complex spectrum of the WT along the frequency axis. The model test results show that the SST can improve the focusing ability of the original WT and ensure the reversibility of the WT, which has better prospects for application than the time spectrum rearrangement method.

In order to solve the problem that the spectrum energy is not concentrated at a fast frequency change rate in the SST, in this study, we introduced a phase factor before WT using the idea of GFT to improve the SST and enhance its applicability to the frequency change while improving the energy focus. The key to this method was to find $x_0(t)$ and map the frequency $\omega(t)$ of the original signal to ω_0 by transformation (ω_0 is here a constant frequency with a rate of change of zero). For a signal $s(t)$ with a specific expression, if ω_0 is given, $x_0(t)$ can be calculated by the specific expression of $s(t)$. However, obtaining $x_0(t)$ is the key problem for the unstable seismic signal $s(t)$. Olhede and Walden (2005) only used an estimated linear function to obtain $x_0(t)$ in the improved discrete wavelet packet transform, which was estimated on the time–frequency diagram of the original signal after the discrete wavelet transform. In this study, we used the instantaneous attribute of seismic signal $\omega(t)$ to obtain $x_0(t)$ indirectly so as to achieve the purpose of improving the SST. The application results of the model and actual seismic data prove the feasibility of the improved method. On the basis of retaining the inverse transformation, the improved method has high energy focusing ability and applicability to frequency changes.

When the seismic wave propagates in the gas zone, the high-frequency signal attenuates, and the frequency moves toward lower frequencies. At the same time, the low-frequency strong amplitude area will appear below the gas zone, which is often

called the "low-frequency shadow" phenomenon (Sheriff, 2002). Taner et al. (1979) identified the low-frequency features under oil and gas reservoirs through complex seismic trace analysis. Castagna et al. (2003) adopted the matching pursuit method to decompose signals in the time–frequency domain and used the anomaly of different instantaneous frequency spectrum energies to directly indicate the existence of oil and gas, that is, the direct hydrocarbon indicator (DHI) technology. Ebrom (2004) studied the correlation between low-frequency shadows and oil and gas storage, and summarized the possible mechanism of low-frequency shadows generated by pre-stack and post-stack seismic data.

Taking Figures 7B–D as an example, the low-frequency shadow phenomenon of the oil and gas reservoir in the target formation was analyzed. As shown in the figure, the location of the reservoir showed a strong energy cluster in both the high frequency and low-frequency bands (dotted line), whereas the low-frequency band below the reservoirs showed a strong energy cluster, which gradually disappeared at the higher band. Due to the insufficient resolution of CWT, the energy group of the reservoir overlapped the low-frequency shadow below (Figure 7B). The CWT-based SST displayed a strong energy distribution in both low- and high-frequency bands (Figure 7C). Compared with the other two methods, the improved synchrosqueezing transform provides high time–frequency resolution to identify the reservoir location more accurately.

Regarding the field data application shown in Figures 8, 9, there was stronger energy distribution in the right part (trace No. 80-160) of the 20-, 30- and 40-isofrequency sections than in the reservoir. Although we have no direct data to confirm whether it is a reservoir or not, based on the geological characteristics of the area and the time–frequency analysis results of this study, we speculate that this part may not be gas-bearing. From the perspective of the geological structure, the gas-bearing layer in the study area is thin, and transverse continuity is poor, while the strong energy mass on the right side is obviously inconsistent with those features. In addition, from the analysis of time–frequency distribution characteristics, as shown in Figure 9, the gas-bearing layer has the weakest energy in the low-frequency band (20 Hz) and strong energy in the high-frequency band (30–40 Hz), while the right strong energy group has strong energy in the 20–30 Hz band and weak energy in the 40 Hz band, which is inconsistent with the time–frequency distribution characteristics of the gas-bearing layer. Combined with the similar phenomenon in the forward model displayed in Figure 5, we speculate that the cause of this phenomenon may be the physical characteristics of the fault itself.

The improved synchrosqueezing transform was applied to the gas reservoir forward model and actual profile; the results showed that the synchrosqueezing transform had higher time-frequency resolution, was more sensitive to the high-frequency attenuation phenomenon, and could describe the gas reservoir distribution range more accurately than the conventional CWT method. It is, therefore, likely to be beneficial for gas detection and the boundary identification of reservoirs in production gas fields.

Data availability statement

The original contributions presented in the study are included in the article/supplementary material; further inquiries can be directed to the corresponding author.

Author contributions

Writing—original draft preparation, CY. Collection of database and the geological interpretation, LC. Methodology, SW. All authors have read and agreed to the published version of the manuscript.

Funding

This research was funded by the National Key Research and Development Program of China (No. 2018YFE0109700) and the Joint Funds of the National Natural Science Foundation of China (No.U2039205).

Acknowledgments

We thank the editors and reviewers for their careful reviews and constructive comments.

Conflict of interest

Author SW was employed by China Electronics Technology Group Corporation.

The remaining authors declare that the research was conducted in the absence of any commercial or financial relationships that could be construed as a potential conflict of interest.

Publisher's note

References

Abry, P., Goncalves, P., and Flandrin, P. (1993). Wavelet-based spectral analysis of 1/f processes. I.E. *E.E. Int. Conf. Acoust.* 3 (3), 237–240. doi:10.1007/978-1-4612-2544-7_2

Auger, F., and Flandrin, P. (1995). Improving the readability of time-frequency and time-scale representations by the reassignment method. *IEEE Trans. Signal Process.* 43 (5), 10681053–1089587X. doi:10.1109/78.382394

Castagna, J. P., Sun, S. J., and Siegfried, R. W. (2003). Instantaneous spectral analysis: Detection of low-frequency shadows associated with hydrocarbons. *Lead. Edge* 22 (2), 120–127. doi:10.1190/1.1559038

Chen, W. C., and Gao, J. H. (2007). Characteristic analysis of seismic attenuation using MBMSW wavelets. *Chin. J. Geophys.* 50 (3), 722–728. doi:10.1002/cjg2.1086

Chen, X. H., He, Z. H., Huang, D. j., and Wen, X. T. (2009). Low frequency shadow detection of gas reservoirs in time-frequency domain. *Chin. J. Geophys.* 52 (1), 215–221. (in Chinese).

Daubechies, I., Lu, J. F., and Wu, H. T. (2011). Synchrosqueezed wavelet transforms: An empirical Mode decomposition-like tool. *Appl. Comput. Harmon. Anal.* 30 (2), 243–261. doi:10.1016/j.acha.2010.08.002

Daubechies, I., and Maes, S. (1996). "A nonlinear squeezing of the continuous wavelet transform based on auditory nerve models," in *Wavelets in medicine and biology*. Editors A. Aldroubi and M. Unser (Boca Raton, FL: CRC Press), 527–546.

Daubechies, I. (2004). *Ten lectures on wavelets*. Philadelphia: Society for Industrial and Applied Mathematics.

Daubechies, I., Wang, Y., and Wu, H. T. (2016). ConceFT: Concentration of frequency and time via a multitapered synchrosqueezed transform. *Phil. Trans. R. Soc. A* 374, 20150193. doi:10.1098/rsta.2015.0193

Detka, C. S., and El-Jaroudi, A. (1996). The generalized evolutionary spectrum. *IEEE Trans. Signal Process.* 44 (11), 2877–2881. doi:10.1109/78.542447

Ebrom, D. (2004). The low frequency gas shadow on seismic sections. *Lead. Edge* 23 (8), 772. doi:10.1190/1.1786898

Gao, J. H., Wan, T., Chen, W. C., and Jian, M. (2006). Three parameter wavelet and its applications to seismic data processing. *Chin. J. Geophys.* 49 (6), 1802–1812. *(in Chinese)*. doi:10.1016/j.apgeochem.2006.08.012

Han, J., and Van der Baan, M. (2013). Empirical Mode decomposition for seismic time-frequency analysis. *Geophysics* 78 (2), 9–19. doi:10.1190/GEO2012-0199.1

Han, L. (2013). *Research on the methods of high-resolution full spectrum decomposition*. Changchun: Jinlin University. [dissertation]. [Changchun, China (in Chinese)].

Herrera, R. H., Han, J. J., and van der Baan, M. (2014). Applications of the synchrosqueezing transform in seismic time-frequency analysis. *Geophysics* 79 (3), 55–64. doi:10.1190/geo2013-0204.1

Herrera, R. H., Tary, J. B., van der Baan, M., and Eaton, D. W. (2015). Body wave separation in the time-frequency domain. *IEEE Geosci. Remote Sens. Lett.* 12 (2), 364–368. doi:10.1109/lgrs.2014.2342033

Huang, Z., Zhang, J., Zhao, T., and Sun, Y. (2016). Synchrosqueezing S-transform and its application in seismic spectral decomposition. *IEEE Trans. Geosci. Remote Sens.* 54 (2), 817–825. doi:10.1109/TGRS.2015.2466660

Kahoo, A. R., and Siahkoohi, H. R. (2009). "Random noise suppression from seismic data using time-frequency peak filtering," in *Proceedings of the EAGE conference and exhibition* (Amsterdam,Netherlands.

Kodera, K., De Villedary, C., and Gendrin, R. (1976). A new method for the numerical analysis of nonstationary signals. *Phys. Earth Planet. Interiors* 12 (2–3), 142–150. doi:10.1016/0031-9201(76)90044-3

Li, C., and Liang, M. (2012). A generalized synchrosqueezing transform for enhancing signal time-frequency representation. *Signal Process.* 92 (9), 2264–2274. doi:10.1016/j.sigpro.2012.02.019

Li, H. B., Zhao, W. Z., Gao, H., Yao, F. C., and Shao, L. Y. (2004). Characteristics of seismic attenuation of gas reservoirs in wave domain. *Chin. J. Geophys.* 47 (5), 892–899. doi:10.3321/j.issn:0001-5733.2004.05.022

Liu, N., Gao, J., Jiang, X., Zhang, Z., and Wang, P. (2018a). Seismic instantaneous frequency extraction based on the SST-MAW. *J. Geophys. Eng.* 15 (3), 995–1007. doi:10.1088/1742-2140/aa8cb6

Liu, W., Cao, S., Wang, Z., Jiang, K., Zhang, Q., and Chen, Y. (2018b). A novel approach for seismic time-frequency analysis based on high-order syschrosqueezing transform. *IEEE Geosci. Remote. Sens. Lett.* 99, 1–5. doi:10.1109/LGRS.2018.2829340

Liu, X., Liu, H., Xing, L., Yin, Y., and Wang, J. (2018c). Seismic low-frequency shadow beneath gas hydrate in the shenhu area based on the stereoscopic observation system. *J. Earth Sci.* 29 (3), 669–678. doi:10.1007/s12583-017-0807-8

Liu, Y. (2004). Seismic "low frequency shadows" for gas sand reflection. *Seg. Tech. Program Expand. Abstr.* 23, 1563–1566. doi:10.1190/1.1851138

Morlet, J., Arens, G., Fourgeau, E., and Giard, D. (1982b). Wave propagation and sampling theory-Part II: Sampling theory and complex waves. *Geophysics* 47 (2), 222–236. doi:10.1190/1.1441329

Morlet, J., Arens, G., Fourgeau, E., and Glard, D. (1982a). Wave propagation and sampling theory-Part I: Complex signal and scattering in multilayered media. *Geophysics* 47 (2), 203–221. doi:10.1190/1.1441328

Oberlin, T., Meignen, S., and Perrier, V. (20142014). "The Fourier-based synchrosqueezing transform," in *Proceedings on IEEE international conference on acoustics, speech and signal processing (ICASSP)* (Florence: Italy), 315–319. doi:10.1109/ICASSP.2014.6853609

Odegard, J. E., Baraniuk, R. G., and Oehler, K. L. (1997). "Instantaneous frequency estimation using the reassignment method," in *Proceedings of the SEG meeting 1941–1944* (Dallas, USA.

Olhede, S., and Walden, A. T. (2005). A generalized demodulation approach to time-frequency projections for multicomponent signals. *Proc. R. Soc. A* 461, 2159–2179. doi:10.1098/rspa.2005.1455

Pedersen, H. A., Mars, J. I., and Amblard, P. O. (2003). Improving surface-wave group velocity measurements by energy reassignment. *Geophysics* 68 (2), 677–684. doi:10.1190/1.1567238

Potter, R. K., Kopp, G. A., and Green, H. C. (1966). *Visible speech*. New York: Dover Publications, Inc.

Potter, R. K., and Steinberg, J. C. (1950). Toward the specification of speech. *J. Acoust. Soc. Am.* 22 (6), 807–820. doi:10.1121/1.1906694

Shang, S. (2014). *High-resolution seismic spectral decomposition and its application [dissertation]*. Changchun: Jinlin University. [Changchun, China (in Chinese)].

Sheriff, R. (2002). *Encyclopedic dictionary of applied Geophysics*. Fourth Edition. Houston: The Society of Exploration Geophysicists.

Shi, Z. Z., Pang, S., Tang, X. R., and He, Z. H. (2014). Carbonate reservoir characterization based on low-frequency shadow method by matching pursuit algorithm. *Lithol. Reserv.* 26 (3), 114–118. (in Chinese). doi:10.3969/j.issn.1673-8926.2014.03.019

Siahsar, M., Gholtashi, S., Kahoo, A., Marvi, H., and Ahmadifard, A. (2016). Sparse time-frequency representation for seismic noise reduction using low-rank and sparse decomposition. *Geophysics* 81 (2), 117–124. doi:10.1190/geo2015-0341.1

Sinha, S., Routh, P. S., Anno, P. D., and Castagna, J. P. (2005). Spectral decomposition of seismic data with continuous-wavelet transform. *Geophysics* 70 (6), P19–P25. doi:10.1190/1.2127113

Taner, M. T., Koehler, F., and Sheriff, R. E. (1979). Complex seismic trace analysis. *Geophysics* 44 (6), 1041–1063. doi:10.1190/1.1440994

Thakur, G., Brevdo, E., Fučkar, N., and Wu, H. (2013). The Synchrosqueezing algorithm for time-varying spectral analysis: Robustness properties and new paleoclimate applications. *Signal Process.* 93 (5), 1079–1094. doi:10.1016/j.sigpro.2012.11.029

Wang, Q., and Gao, J. (2017). Application of synchrosqueezed wave packet transform in high resolution seismic time-frequency analysis. *J. Seismic Explor.* 26, 587–599.

Wang, Q., Gao, J., Liu, N., and Jiang, X. (2018). High-resolution seismic time-frequency analysis using the synchrosqueezing generalized s-transform. *IEEE Geosci. Remote Sens. Lett.* 15 (3), 374–378. doi:10.1109/LGRS.2017.2789190

Wu, G., and Zhou, Y. (2018). Seismic data analysis using synchrosqueezing short time Fourier transform. *J. Geophys. Eng.* 15 (4), 1663–1672. doi:10.1088/1742-2140/aabf1d

Wu, X. Y., and Liu, T. Y. (2009). Spectral decomposition of seismic data with reassigned smoothed pseudo wigner-ville distribution. *J. Appl. Geophy.* 68 (3), 386–393. doi:10.1016/j.jappgeo.2009.03.004

Xue, Y., Cao, J., Wang, X., Li, Y., and Du, J. (2019). Recent developments in local wave decomposition methods for understanding seismic data: Application to seismic interpretation. *Surv. Geophys.* 40 (5), 1185–1210. doi:10.1007/s10712-019-09568-2

Yu, G., Yu, M., and Xu, C. (2017). Synchroextracting transform. *IEEE Trans. Ind. Electron.* 64, 8042–8054. doi:10.1109/TIE.2017.2696503

frontiers | Frontiers in Earth Science

TYPE Original Research
PUBLISHED 12 August 2022
DOI 10.3389/feart.2022.919130

OPEN ACCESS

EDITED BY
Amin Beiranvand Pour,
INOS University Malaysia Terengganu, Malaysia

REVIEWED BY
Mohamed Abdel-Fattah,
University of Sharjah, United Arab Emirates
Yasir Bashir,
Universiti Sains Malaysia (USM), Malaysia

*CORRESPONDENCE
Syed Adnan Ahmed,
sadnan84@hotmail.com

SPECIALTY SECTION
This article was submitted to Solid Earth Geophysics, a section of the journal Frontiers in Earth Science.

RECEIVED 13 April 2022
ACCEPTED 29 June 2022
PUBLISHED 12 August 2022

CITATION
Ahmed SA, MonaLisa, Hussain M and Khan ZU (2022), Supervised machine learning for predicting shear sonic log (DTS) and volumes of petrophysical and elastic attributes, Kadanwari Gas Field, Pakistan.
Front. Earth Sci. 10:919130.
doi: 10.3389/feart.2022.919130

Supervised machine learning for predicting shear sonic log (DTS) and volumes of petrophysical and elastic attributes, Kadanwari Gas Field, Pakistan

Syed Adnan Ahmed[1,2]*, MonaLisa[1], Muyyassar Hussain[1,2] and Zahid Ullah Khan[1,2]

[1]Department of Earth Sciences, Quaid-I-Azam University, Islamabad, Pakistan, [2]LMK Resources (Private) Limited, Islamabad, Pakistan

Shear sonic log (DTS) availability is vital for litho-fluid discrimination within reservoirs, which is critical for field development and production. For certain reasons, most of the wells in the Lower Indus Basin (LIB) lack DTS logs, which are modeled using conventional techniques based on empirical relations and rock physics modeling. However, in their extensive computation, these approaches need assumptions and multiple prerequisites, which can compromise the true reservoir characteristics. Machine learning (ML) has recently emerged as a robust and optimized technique for predicting precise DTS with fewer input data sets. To predict the best DTS log that adheres to the geology, a comparison was made between three supervised machine learning (SML) algorithms: random forest (RF), decision tree regression (DTR), and support vector regression (SVR). Based on qualitative statistical measures, the RF stands out as the best algorithm, with maximum determination of correlation (R^2) values of 0.68, 0.86, 0.56, and 0.71 and lower mean absolute percentage error (MAPE) values of 4.5, 2.01, 4.79, and 4.65 between the modeled and measured DTS logs in Kadanwari-01, -03, -10, and -11 wells, respectively. For detailed reservoir characterization, the RF algorithm is further employed to generate elastic attributes such as P-impedance (Zp), S-impedance (Zs), lambda-rho ($\lambda\rho$), mu-rho ($\mu\rho$), as well as petrophysical attributes such as effective porosity (PHIE) and clay volumetric (Vcl) utilizing seismic and well data. The resultant attributes helped to establish a petro-elastic relationship delineated at the reservoir level. Possible gas zones were determined by zones with high PHIE (8%–10%) and low values of other attributes like Vcl (30%–40%), Zp (10,400–10,800 gm/cc*m/s), and Zs (6,300–6,600 gm/cc*m/s). The potential bodies are also validated by low $\lambda\rho$ (27–30 GPa*g/cc) cross ponding to higher $\mu\rho$ (38–44 GPa*g/cc).

KEYWORDS

DTS log prediction, supervised learning, random forest, rock physics modeling, petrophysics, reservoir characterization

Introduction

With the advancement of computer science algorithms, machine learning (ML) has emerged as the most recent tool in geosciences due to its capacity to uncover relationships in provided data to predict the desired output (Gupta et al., 2021). ML has been applied in many fields of earth science, such as geochemistry (Dornan et al., 2020), petrophysics (Song et al.,

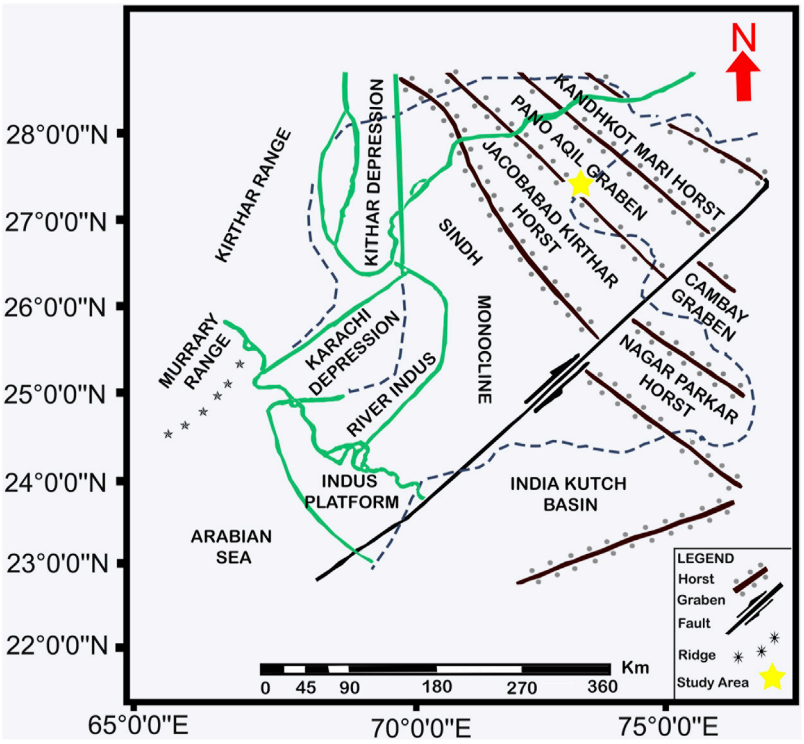

FIGURE 1
Location of the study area with major tectonic features in the surrounding, (modified after Saif-Ur-Rehman et al. 2016).

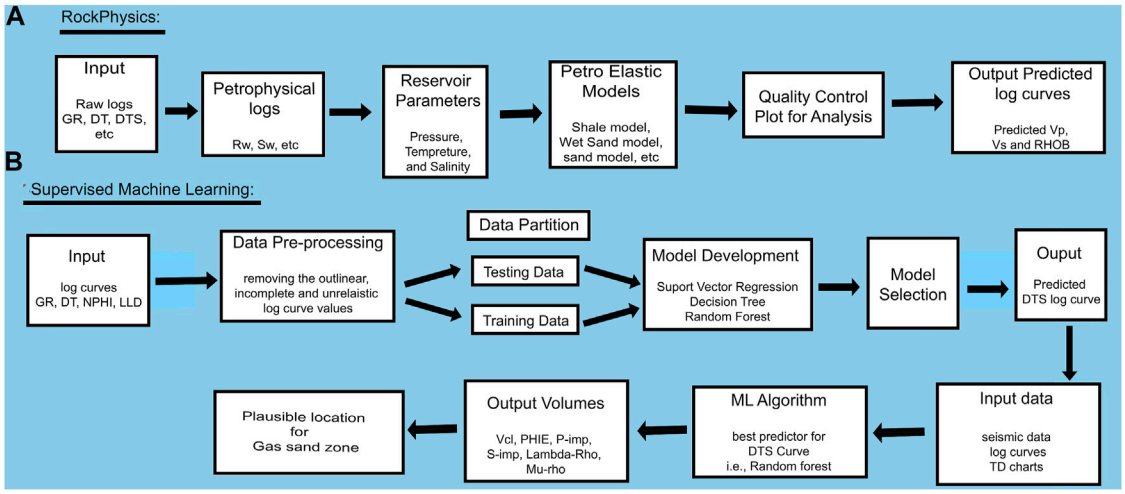

FIGURE 2
(A) Steps for conventional rock physics modeling workflow, and **(B)** SML procedure for prediction of DTS along with other elastic, and petrophysical attributes.

TABLE 1 Identified litho-facies based on the petrophysical cutoff values.

Litho-facies	Cutoff values
Shale	Clay volume >0.30
Wet sands	Clay volume ≤0.30, Sw ≥ 0.45
Gas sands	Clay volume ≤0.30, Sw < 0.45

2020), geology (Bai and Tan, 2020), and geophysics (Chen et al., 2020; Feng et al., 2020; Grana et al., 2020) to delineate subsurface hydrocarbon potentials. According to Mohammed et al. (2016), SML is a subcategory of ML that employs artificial intelligence to train an algorithm on labeled input data to recognize patterns and trends without the need for explicit programming (Hall, 2016). To predict the DTS curve, three of the most successful and widely adopted SML algorithms, RF, DTR, and SVR, have been applied in this study.

The petro-elastic relationship was established for detailed reservoir characterization by modeling the important elastic (Zp, Zs, $\lambda\rho$, and $\mu\rho$ relationships) and petrophysical (PHIE and Vcl) properties using SML algorithms, which was useful in highlighting potential sand facies at the reservoir level.

The interpretation of elastic properties, that is, sonic (DTP), DTS, and density (RHOB), is highly important as they are closely related to seismically quantified reservoir properties (Munyithya et al., 2019).

When combined with Vp, that is, the Vp/Vs ratio (Hamada, 2004), DTS is useful for identifying litho-fluid types and differentiating wet sands from gas sands. The $\lambda\rho$ and $\mu\rho$ relationship is employed for better fluid and lithology delineation, which also highlights the gas sand zone and is strongly dependent on precise DTS (Young and Tatham, 2007). In many situations, DTS is not calibrated or has poor quality due to poor logging, failure of logging instruments, and high cost (Liu et al., 2021). Previously, rock physics modeling was used to compensate for these deficiencies by generating a set of

TABLE 2 Petrophysical and elastic properties of the reservoir utilized in PEMs.

Reservoir parameter	Avg. porosity	Avg. shale			Avg. water (Sw)				Pressure (PSI)	Temp. (°C)	Salinity (g/l)	Gas gravity
Values	15%	25%			42%				2,500	130	0.15	0.689
Elastic parameters	Bulk modulus (GPA)				Shear modulus (GPA)					RHOB (g/cm^3)		
	Quartz	Clay	Sw	Gas	Quartz	Clay	Sw	Gas	Quartz	Clay	Sw	Gas
Values	37	15	2.38	0.02	44	5	0	0	2.65	2.6	1.0	0.1

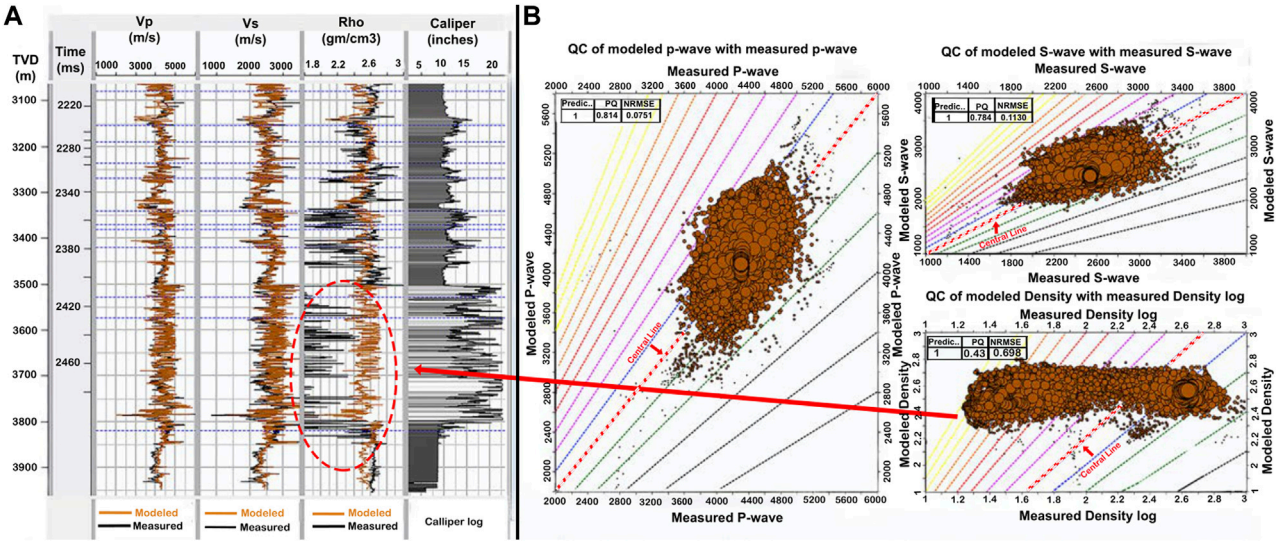

FIGURE 3
(A) Modeled Vp and Vs logs follow the measured log trend, whereas density log shows mismatch due to poor borehole condition highlighted through polygon, also illustrated by caliper log, and **(B)** QC cross plot displaying log points aligned at the central line for Vp and Vs; however, RHOB shows deviation due to error in wellbore measurement.

TABLE 3 Statistical description of the test data (Kadanwari-03).

Test data	Mean	Minimum	Maximum	Standard dev
GR (API)	98.15	23.87	152	25.56
DT (usec/ft)	72.92	56.06	91.71	5.62
NPHI (fraction)	16.75	1.44	36.44	5.27
LLD	11.1	1.76	71.62	7.38

consistent elastic logs. In conventional seismic inversion procedures, these modeled logs are utilized to properly delineate the litho-facies of the reservoir, which are further employed for petrophysical property (PHIE and Vcl) predictions (Khan et al., 2021).

Depending upon the situation and availability of information about reservoirs, three types of rock physics models are assumed: theoretical, empirical, and heuristic (Avseth et al., 2010).

TABLE 4 Statistical description of the training data (average out of three wells, i.e., Kadanwari-01, -10, and -11).

Training data	Mean	Minimum	Maximum	Standard dev
GR (API)	118	50.51	185.59	22.53
DT (usec/ft)	72.22	58.41	96.44	6.16
NPHI (fraction)	16.92	1.62	33.25	5.29
LLD	14.89	1.62	57.95	8.54

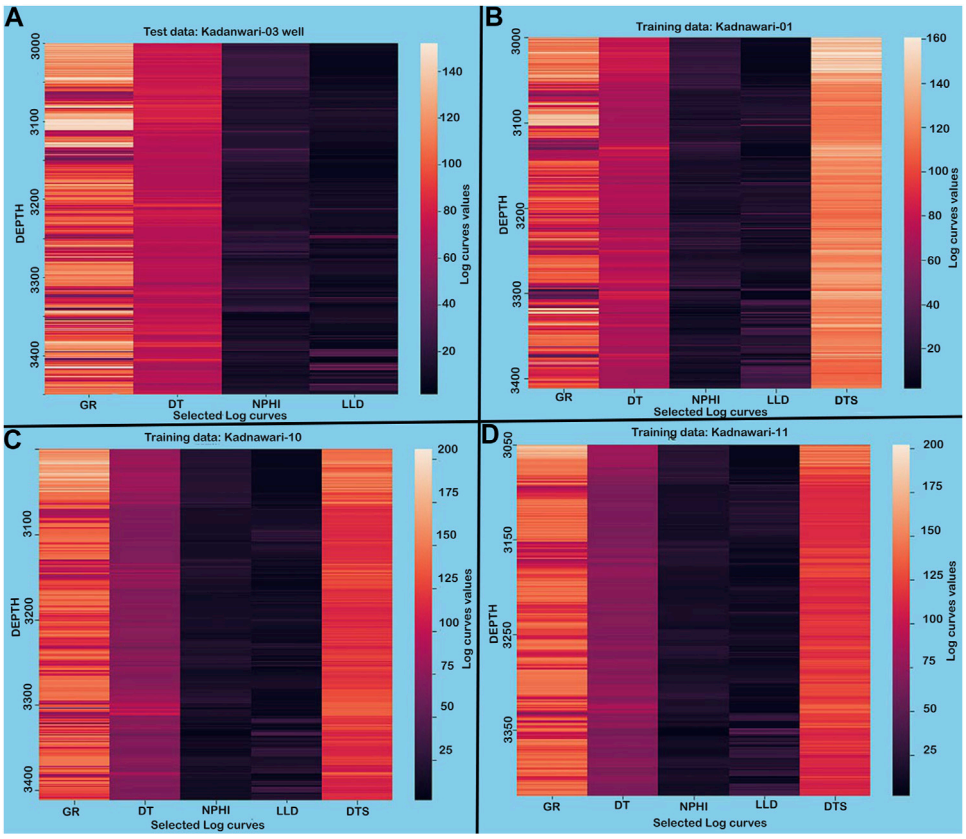

FIGURE 4
Heat map depicting values for selected logs against subsurface depth demonstrates that the data set is smooth and does not carry unrealistic values.

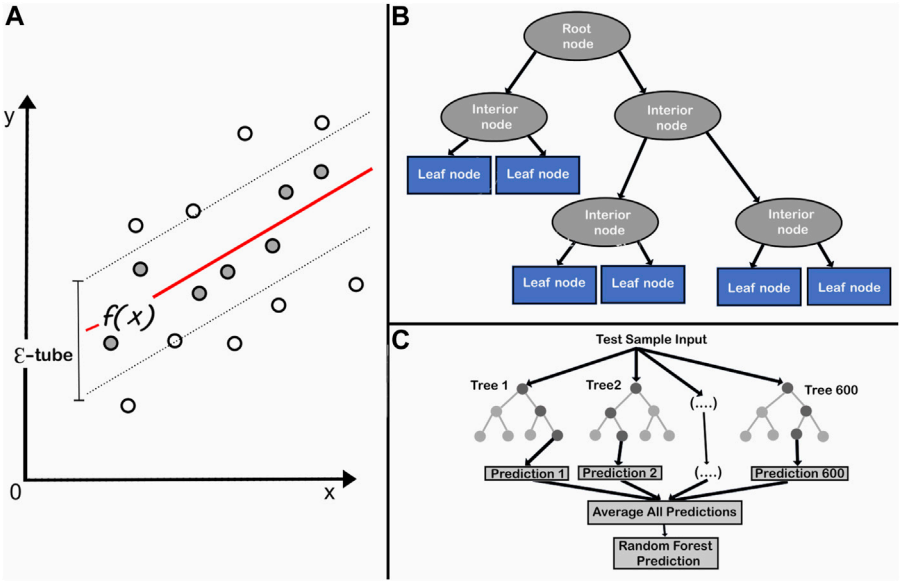

FIGURE 5
Supervised machine learning algorithms: **(A)** support vector regression (modified after Naganathan and Babulal, 2019), **(B)** decision tree regression (modified after Charbuty and Abdulazeez, 2021), and **(C)** random forest (modified after Rudd, 2020).

However, each method incorporates some assumptions, like theoretical models assuming that pores have a regular shape (Jakobsen et al., 2003), in contrast to heuristic models, which incorporate irregular pores with few real scenarios but skip detailed rock complexities. Castagna et al. (1985) and Han (1987) used empirical models to replicate the real cases, but they also acted as a subset of real cases.

Azeem et al. (2019), Shakir et al. (2021), and Khan et al. (2021) have used conventional rock physics modeling approaches to optimize and predict the missing logs without implementing the advanced ML technique in LIB. In this study, the successful execution of a novel ML approach for this basin helped in predicting accurate DTS along with elastic and petrophysical attributes to delineate reservoir potentials. This approach can be applied worldwide in basins having similar geological conditions and short comes.

Geological settings

This study was conducted in the Kadanwari Gas Field, which lies within the Panno-Aqil graben surrounded by Jacobabad–Khairpur and Mari–Kandhkot High, Lower Indus Basin, Pakistan (Figure 1) (Saif-Ur-Rehman et al., 2016). The structural configuration in this area was influenced by three tectonic events: Late Cretaceous uplift and erosion, Late Paleocene wrench faulting, and Late Tertiary to recent uplift (Kadri 1995; Kazmi and Jan 1997). This area has been separated into horst and graben structures due to the wrench faulting. The Lower Goru Formation (LGF), which is primarily composed of interbedded sand and shale deposits, produces the majority of the production for the area (Ehsan et al., 2018).

The cretaceous LGF was deposited in a shallow marine deltaic environment, during sea-level low stand as detached medium-to-coarse–grained sediments on the top of the distal (shale and siltstone) sediments of the previous high stand system tract (Berger et al., 2009). These sands exhibit characteristics similar to those of Indian shields in the neighborhood (Ahmad et al., 2007). The Cretaceous Sembar Formation serves as a confirmed source rock, with interbedded LGF and Upper Goru Formation shales serving as seal rock (Abbasi et al., 2016). Numerous large and enormous fields, including Miano, Sawan, and Mari, have been discovered in this roughly north–south reservoir fairway (Dar et al., 2021).

Materials and methods

This study incorporated wireline logs and well tops from four wells (Kadanwari-01, Kadanwari-03, Kadanwari-10, and Kadanwari-11) in the 3-D seismic volume of the study area. Except for a few problems, the data quality was fair for all mandatory log curves. For example, the RHOB curve was compromised in Kadanwari-01 well by poor borehole condition, that is, washout, while DTS was only recorded in

Kadanwari-03 well. The Castagna relationship, which is an empirical link between compressional and shear velocities, was initially used to estimate the DTS log in wells with missing DTS (Castagna et al., 1985).

Well log constraints such as low RHOB and missing DTS curve have been addressed using the traditional rock physics method, which needs comprehensive petrophysical analysis, *in situ* reservoir parameters, and petro-elastic models as an input data set (Figure 2A). ML, on the other hand, has only used raw logs as input data from available wells, that is, GR, DT, DTS, LLD, and NPHI, which are divided into test and training data sets. The test data consist of log curves from the well where the DTS must be predicted, whereas the training data consist of log curves from wells that are involved in the DTS prediction process. Multiple SML methods, such as RF, DTR, and SVR, were used to train the data set (seismic and well), with the best algorithm (based on R2 and MAPE values) being used to derive elastic and petrophysical attributes (Figure 2B).

TABLE 5 Values of R^2 between predicted and measured DTS curves.

Well name	Random forest	DTR	SVR
Kadanwari-01	0.68	0.57	0.11
Kadanwari-03	0.86	0.86	0.52
Kadanwari-10	0.56	0.56	0.25
Kadanwari-11	0.71	0.69	0.49

TABLE 6 Values of MAPE between predicted and measured DTS curves.

Well name	Random forest	DTR	SVR
Kadanwari-01	4.57	4.96	8.33
Kadanwari-03	2.01	2.16	4.76
Kadanwari-10	4.79	5.04	7.62
Kadanwari-11	4.65	4.8	6.53

Rock physics modeling

The litho-facies were identified based on petrophysical cutoff values (Table 1), and then, a comprehensive rock physics model was developed by utilizing petro-elastic models (PEMs). The PEMs for shale, wet, and gas sands are generated in HampsonRussels software, incorporating reservoir *in situ* properties along with elastic constants of identified litho-facies (Table 2) (Miraj et al., 2021).

The rock physics modeled elastic logs rectified the abnormal values, especially in poor RHOB, which is affected by bad borehole conditions (Figure 3A), and also predicted a reliable DTS curve (Figure 3A). The quantitative QC plots of modeled and measured DTP and DTS curves revealed consistent behavior along the central line (zero-error), while the RHOB deviated as the measured RHOB contained erroneous values (Figure 3B).

Supervised machine learning

ML has emerged as a new way to approach technical problems, that is, unrecorded logs of wellbore or deficiencies in measured logs, by analyzing and generating reliable logs (Liu et al., 2021). SML is the basic technique of ML, and its algorithms create a model to link the data (or feature) vector to a matching label or target vector using training data when both the input and the related label are known and provided to the algorithm (Litjens, 2017). Log curve prediction or correction is the part of the regression model used to forecast the continuous numerical variables (Liu et al., 2021).

Before training with the selected model, unrealistic or incomplete data points were eradicated from selected log curves. Outliers were defined as data points with a value that was away from the mean of the data by three times the standard deviation. After removing the outliers, the statistical properties of log curves used as test and training data sets are illustrated in Tables 3, 4.

The log curves used to predict the DTS curve are displayed in the form of heat maps that provide the log values against subsurface depth through various color shades (Figure 4), demonstrating that the data are clear and smooth without any unrealistic values.

The DTS curve was only accessible in the Kadanwari-03 well; so, it had to be predicted in other wells by establishing a relationship with measured logs. The empirically derived DTS curve is used as training data by following the major procedures, which involve writing Python code, employing the most commonly used SML algorithms such as RF, DTR, and SVR with "scikit-learn" (Pedregosa et al., 2011), and to develop a Python framework (Figure 2). The best algorithm for the prediction among the applied algorithms is labeled based on R^2 and MAPE values.

The SVR method is used for regression analysis (Chen et al., 2020), and it estimates real values using the kernel function (Steinwart, 2008) and predicts rock properties (Kang and Wang, 2010). An Ɛ-tube is introduced around the function that best approximates the continuous-value function f(x) in SVR and tries to balance model complexity and prediction error (Figure 5A) by assessing multiple kernel functions, values for kernel option, epsilon, and regularization. The DTR algorithm tackles regression problems using a tree structure, with the root node representing the sample data, interior nodes and branches displaying data attributes and decision rules, and leaf nodes expressing the outcome (Figure 5B). DTR has several advantages, including minimal data cleansing, non-linear performance, and a small number of hyperparameters to tune. The RF approach handled the over-fitting problem with decision trees.

RF as a combination of multiple individual decision trees (Figure 5C) acted as an ensemble where multiple learners were trained to solve the complex relationships by voting among a collection ("forest") of randomized decision trees (Breiman, 2001). The RF algorithm offered an advantage over opaque approaches, such as neural networks, which required a large number of hyperparameters to be tuned. RF has had a wide range of applications in solid earth geoscience (Bergen et al., 2019).

The missing DTS log was generated in the remaining wells using the aforementioned ML algorithms. To verify the adopted approach for DTS prediction, the predicted DTS logs (Kadanwari-01, -10, and -11) were combined to predict the DTS in the Kadanwari-03 well while keeping the measured DTS curve blind in Kadanwari-03 well. Figure 8 depicts the accuracy of the prediction, that is, the modeled log for Kadanwari-03 is in good agreement with the measured DTS, while in other wells, the predicted DTS and empirically derived DTS also delineate similarities in trends.

The RF algorithm, the best algorithm to predict the DTS curve based on R^2 and MAPE, has been further employed to establish the relationship between the seismic amplitude of PSTM volume and well logs for estimating elastic and petrophysical properties. For the plausible gas sand location, the elastic properties (Zp, Zs, and λ-μ relation) and petrophysical properties (PHIE and Vcl) were mapped within the reservoir, that is, E-sands.

Results and discussion

The missing DTS log curve in Kadanwari-01, -03, -10, and -11 wells was predicted using traditional methods such as rock physics and by employing the algorithms of the most recent technique of SML such as RF, DTR, and SVR. These wells contain mandatory logs along with important information such as formation tops, time–depth relationships, and lithological information. For the identification of plausible sands, all wells are utilized for petrophysical interpretation and formation evaluation. To establish a petro-elastic relationship, rock physics bridges the gap between elastic and petrophysical properties.

Many researchers have successfully used rock physics techniques in the past to predict the DTS log in various fields such as the Middle Indus Basin (Azeem et al., 2015), Barnett Shale

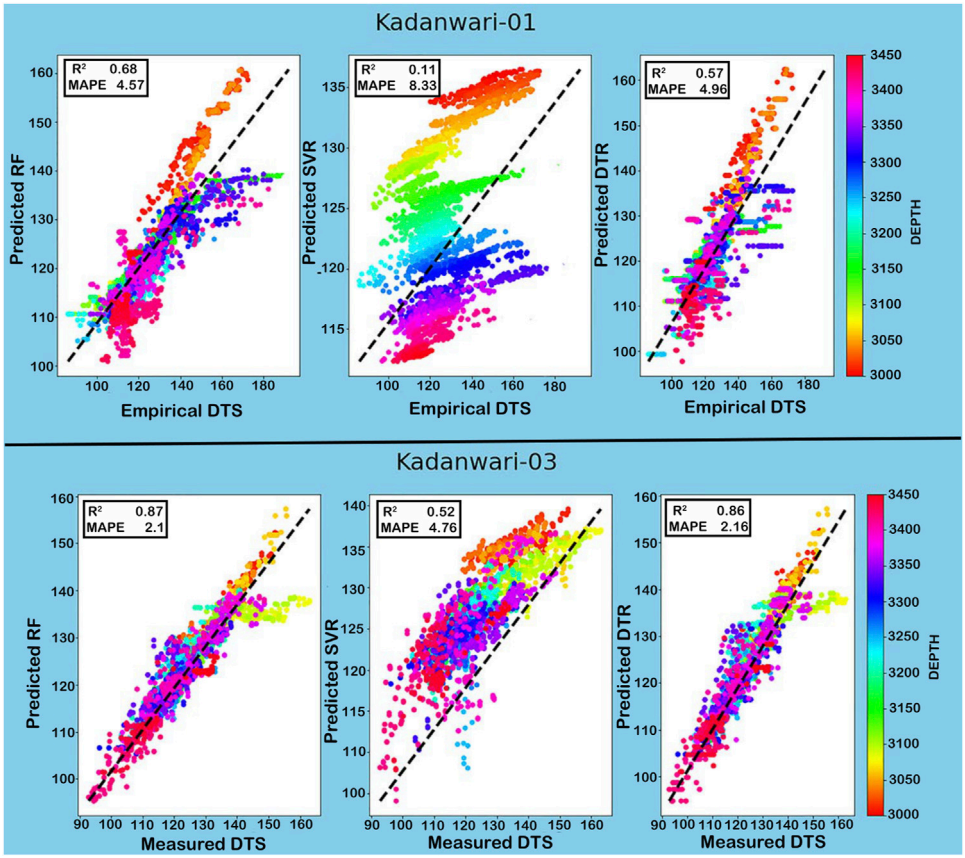

FIGURE 6
Cross plot between empirically derived and predicted DTS curve in the Kadanwari-01 well and between measured and predicted DTS curve in Kadanwari-03 depicting RF as the best algorithm.

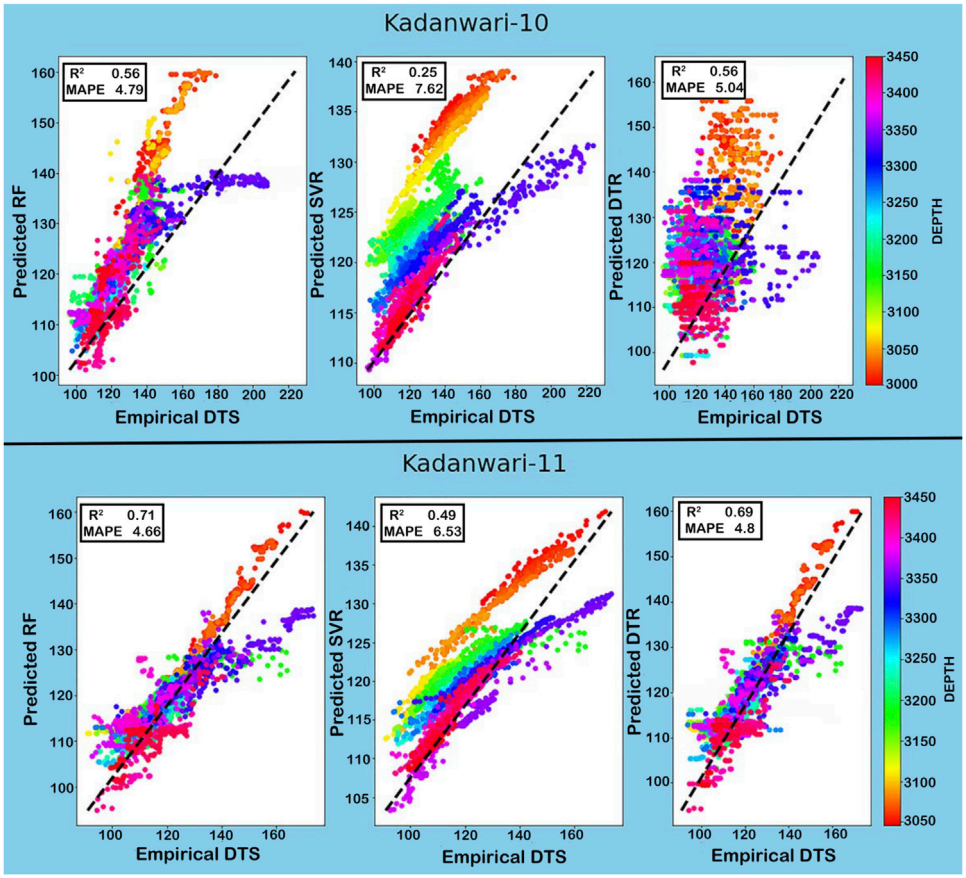

FIGURE 7
Cross plot between predicted and empirically derived DTS curves in Kadanwari-10 and -11 wells depicting RF as the best algorithm for DTS curve prediction.

Formation (Guo and Li, 2015), North Poland (Wawrzyniak-Guz, 2019), LIB (Durrani et al., 2020), Zamzama Gas Field (Khan et al., 2021), and Mehar Block (Shakir et al., 2021) and further utilized these techniques in improving reservoir characterization based on seismic inversion techniques. Rock physics modeling has provided a decent estimation of the DTS curve, which was evaluated statistically through a QC plot, that is, prediction quality, which assesses the quality of the match between predicted and measured logs ranging from 0 to 1, was equal to 0.78 (Figure 3B). Another QC factor is the normalized root mean square error (NRMSE), which deals with the degree of difference, such as 0 for identical curves and 2 for the greatest difference, which was equal to 0.11 (Figure 3B). The abnormal values of RHOB (minimum of 1 gm/cc) at a depth of 3,500–3,820 m are rectified by the modeled logs that bring the ranges to the standard of the clastic reservoir (2.3–2.6 g/cc) (Figure 3B). Despite the reliable results of rock physics modeling, it is highly subject to the number of interdependent procedures, and if some error arises, it floats up to the final output. For example, the miscalculations made in petrophysical properties are added into petro-elastic models built for the facies and hence deteriorate the rock physics–modeled properties. Different procedures are incorporated into rock physics that need experts to find the exact reservoir properties, and it also increases the process cost.

On other hand, ML appeared to be a successful tool capable of constructing a relationship between log curves based on their effective features for DTS prediction to evaluate the reservoir properties. Many researchers have recently used ML for predicting the DTS curve, that is, Bukar et al. (2019), Anemangely et al. (2019), Miah (2021), Gamal et al. (2022), Gupta et al. (2019), and Liu et al. (2021). Due to complex reservoir attributes and limited data set, ML is a critical and optimized tool in the most productive LIB for predicting the DTS curve. This technique was developed for the first time to get maximum information from the produced well locations with missing DTS logs.

The accuracy of the predicted DTS curve is evaluated through R^2 and MAPE (Saad et al., 2018). For Kadanwari-03 well, the only well having DTS run in its wellbore, RF proved to be the best algorithm for prediction with high values for R^2 and low values for MAPE between predicted and measured DTS (Tables 5, 6). In the remaining wells, that is, Kadanwari-01, -10, and -11, the missing DTS is calculated by empirical

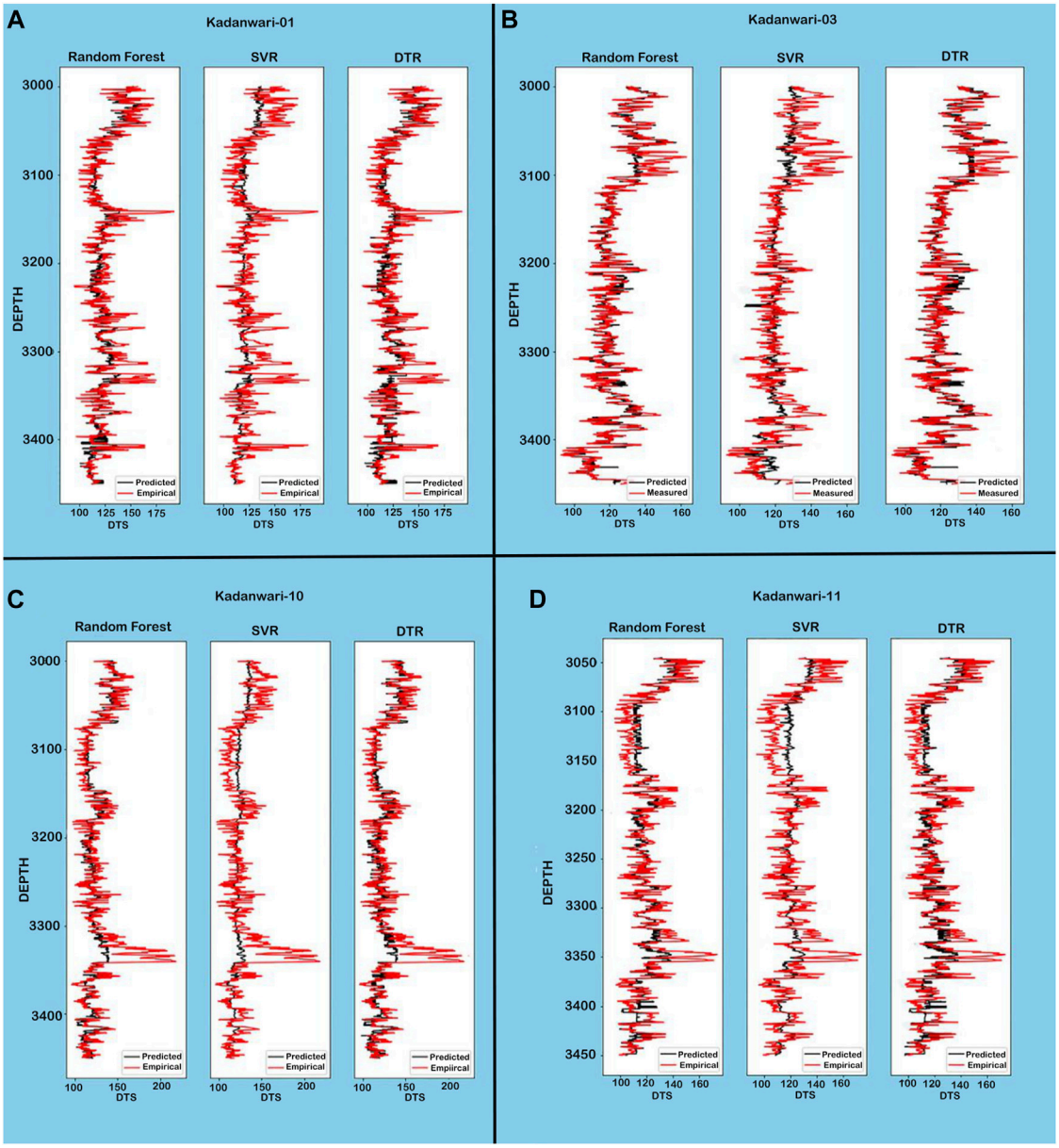

FIGURE 8
Comparison of trends between measured and predicted DTS curves depicts that RF is the most efficient technique.

relation and correlated with the predicted DTS log for comparison (Tables 5, 6). The SVR algorithm's accuracy was reduced overall, even though it provided the same R^2 value in Kadanwari-03 and -10, but its values decreased in Kadanwari-01 and -11, that is, 0.57 and 0.69, and MAPE values were overall higher, that is, 4.96, 2.16, 5.04, and 4.8 for all wells. The DTR algorithm proved to be the least accurate in DTS prediction, with the lowest values of R^2, that is, 0.11, 0.52, 0.25, and 0.49, and highest values of MAPE, that is, 8.33, 4.76, 7.62, and 6.53 in Kadanwari-01, -03, -10, and -11, respectively. Few researchers have successfully utilized the RF approach for DTS prediction, that is, Gamal et al. (2022) employed RF for building sonic prediction models in complex lithology rocks including sandstone, limestone shale, and carbonate formations. The RF model accuracy was checked in comparison with the DTR approach through the correlation coefficient (R), that is, 0.986 for RF and 0.93 for DTR, and an average absolute percentage error (AAPE) of 1.12% for RF and 1.95% for DTR between actual values and predicted model. Gupta et al. (2019) have compared several machine learning

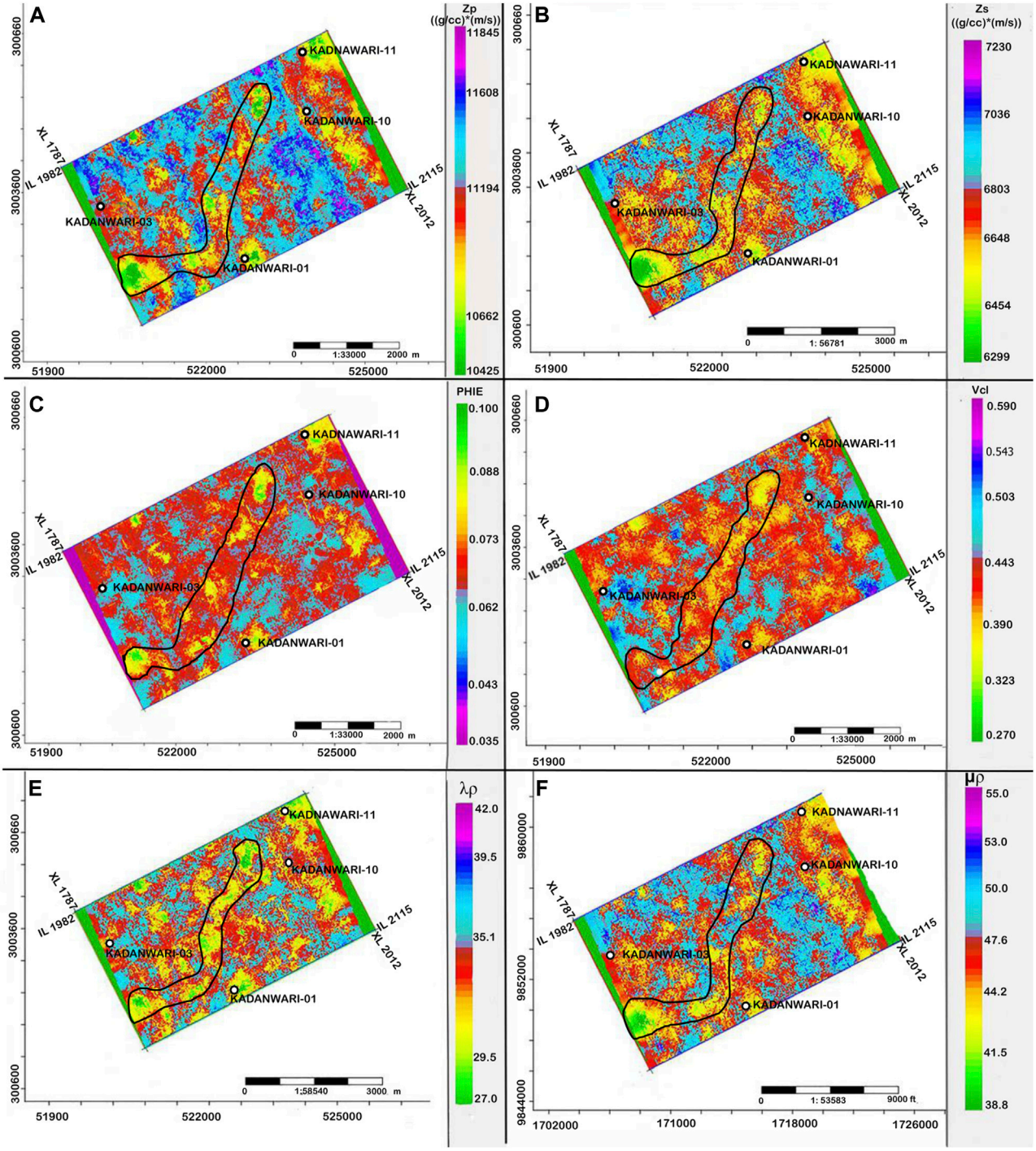

FIGURE 9
Average value maps extracted within E-sands exhibiting **(A)** low Zp, **(B)** low Zs, **(C)** high PHIE, and **(D)** low Vcl response around the producing Kadanwari-01, while polygon indicates plausible channelized gas sands, **(E)** $\lambda\rho$, and **(F)** $\mu\rho$ supporting the presence of gas sands at the same location.

regression techniques, such as multilinear regression (MLR), least absolute shrinkage and selection operator regression, support vector regression, random forest (RF), gradient boosting (GB), and alternating conditional expectations, to predict the synthetic sonic (Vp and Vs) and mechanical properties. Their results showed RF and GB as the best predictors with low uncertainties in the prediction, with R^2 and adjusted R^2 around 0.95 and RMS error around 0.18.

The correlation between the measured and predicted DTS curves is displayed through cross plots, that is, *x*-axis (measured/empirical DTS), *y*-axis = predicted DTS, and Z = depth values (3,000–3,450 m). The cross plots show the correlation of the applied ML technique at each well by observing the curve values along the zero-error line. This correlation also clearly shows that the RF technique performed efficiently and shows maximum alignment with centerline (Figures 6, 7).

The predicted DTS curve using various techniques, such as RF, SVM, and DTR, overlapped with the measured DTS for Kadanwari-03 and empirically derived DTS in other wells to evaluate the trends and curve ranges (Figure 8). In comparison to the DTR and SVR algorithms, the RF algorithm was more accurate in dealing with the heterogeneous reservoir sands of LGF (Dar et al., 2021), as it predicted DTS curves that were more consistent with measured curves across all wells (Figure 8).

The RF algorithm further utilizes the predicted DTS log, along with other significant elastic logs such as DTP and RHOB, to build a relationship with the 3-D seismic volume of the study area. This relationship was trained to predict elastic (Zp, Zs, $\lambda\rho$, and $\mu\rho$) and petrophysical (PHIE and Vcl) attribute volumes. The maps generated by taking the average values within reservoir E-sands exhibited low values of Zp (10,400–10,800 gm/cc*m/s), Zs (6,300–6,600 gm/cc*m/s), and Vcl (30%–40%) with high PHIE (8–10%) around the producing well, Kadanwari-01 (Figure 9). Such a response from elastic and petrophysical properties indicates a potential area with good sand quality (Khan et al., 2021), that is, around the producing Kadanwari-01 well and channelized potential sands bound by the polygon (Figure 9). Low values for $\lambda\rho$ (27–30 GPa*g/cc) cross ponding to higher $\mu\rho$ (38–44 GPa*g/cc) also support the presence of gas sands around the Kadanwari-01 well and within the polygon (Figure 9). Low values of $\lambda\rho$ indicate the compressibility of gas, while the rigidity of quartz is delineated by a high $\mu\rho$ value (Young and Tatham, 2007).

Conclusion

Rock physics, a conventional but extensively used method, and ML, a new technology that employs artificial intelligence, are combined in this study to predict the missing DTS curve. However, the input data set and prerequisites for both approaches differ significantly. Rock physics, for example, demands petrophysical logs, reservoir *in situ* parameters, and petro-elastic models of the litho-facies identified in the area, all of which add time and cost to the operation. ML, on the other hand, is more accurate, faster, and less prone to errors, as well as able to work with a smaller data set. Three different SML algorithms, that is, RF, DTR, and SVR, are applied in the study, among which RF is proved to be more accurate in dealing with heterogeneous sand and it is further utilized for estimating elastic (Zp, Zs, $\lambda\rho$, and $\mu\rho$) and petrophysical (PHIE and Vcl) volumes. In the stratigraphic slice extracted at the E-sand level, the reservoir in the area, gas sands zones were discovered with low Zp, Zs, and Vcl in contrast to higher PHIE which is also supported by the λ–μ relation with higher $\mu\lambda$ corresponding to lower $\lambda\rho$ values. Therefore, the ML technique will be effective in areas with missing log curve data, particularly in the LIB, which has older wells that lack DTS due to high drilling costs or insufficient drilling equipment at the time of drilling.

Data availability statement

The data used for this research work is highly confidential and it is property of the DGPC that provide this to university students for research work only. The permission will be required from DGPC to use it for the research purpose.

Author contributions

SA: conceptualization, methodology, and software. ML: supervision and writing—reviewing and editing. MH: visualization, investigation, and validation. ZK: data curation, formal analysis, and investigation.

Acknowledgments

The data were provided by the Directorate General for Petroleum Concession (DGPC), Pakistan, while software was provided by LMK Resources (Private) Limited, Islamabad, Pakistan and Compagnie Générale de Géophysique (CGG).

Conflict of interest

SA, MH, and ZK were employed by the company LMK Resources (Private) Limited.

The remaining author declares that the research was conducted in the absence of any commercial or financial relationships that could be construed as a potential conflict of interest.

Publisher's note

References

Ahmad, N., Spadini, G., Palekar, A., and Subhani, M. A. (2007). Porosity prediction using 3D seismic inversion Kadanwari gas field, Pakistan. *Pak. J. Hydrocarb. Res.* 17, 95–102.

Ahmed Abbasi, S., Asim, S., Solangi, S., and Khan, F. (2016). Study of fault configuration related mysteries through multi seismic attribute analysis technique in Zamzama gas field area, southern Indus Basin, Pakistan. *Geodesy Geodyn.* 7, 132–142. doi:10.1016/j.geog.2016.04.002

Anemangely, M., Ramezanzadeh, A., Amiri, H., and Hoseinpour, S. A. (2019). Machine learning technique for the prediction of shear wave velocity using petrophysical logs. *J. Petroleum Sci. Eng.* 174, 306–327. doi:10.1016/j.petrol.2018.11.032

Avseth, P., Mukerji, T., and Mavko, G. (2010). *Quantitative seismic interpretation: Applying rock physics tools to reduce interpretation risk*. Cambridge, UK: Cambridge University Press, doi:10.1017/CBO9780511600074

Azeem, T., Chun, W. Y., MonaLisa, P., Khalid, L. X., Qing, M. I., Ehsan, M. J., et al. (2017). An integrated petrophysical and rock physics analysis to improve reservoir characterization of Cretaceous sand intervals in Middle Indus Basin, Pakistan. *J. Geophys. Eng.* 14 (2), 212–225. doi:10.1088/1742-2140/14/2/212

Bai, Y., and Tan, M. (2021). Dynamic committee machine with fuzzy-c-means clustering for total organic carbon content prediction from wireline logs. *Comput. Geosciences* 146, 104626. doi:10.1016/j.cageo.2020.104626

Bergen, K. J., Johnson, P. A., de Hoop, M. V., and Beroza, G. C. (2019). Machine learning for data-driven discovery in solid Earth geoscience. *Science* 363 (6433), eaau0323. doi:10.1126/science.aau0323

Berger, A., Gier, S., and Krois, P. (2009). Porosity-preserving chlorite cements in shallow-marine volcaniclastic sandstones: Evidence from Cretaceous sandstones of the Sawan gas field, Pakistan. *Bulletin* 93 (5), 595–615. doi:10.1306/01300908096

Breiman, L. (2001). Random forests. *Mach. Learn.* 45 (1), 5–32. doi:10.1023/A:1010933404324

Bukar, I., Adamu, M. B., and Hassan, U. (2019). "A machine learning approach to shear sonic log prediction," in Proceedings of the SPE Nigeria Annual International Conference and Exhibition, Lagos, Nigeria, August 2019. doi:10.2118/198764-ms

Castagna, J. P., Batzle, M. L., and Eastwood, R. L. (1985). Relationships between compressional-wave and shear-wave velocities in clastic silicate rocks. *geophysics* 50 (4), 571–581. doi:10.1190/1.1441933

Charbuty, B., and Abdulazeez, A. (2021). Classification based on decision tree algorithm for machine learning. *J. appl. sci. technol. trends* 2 (01), 20–28.

Chen, G., Chen, L., and Li, Q. (2020). Comparison and application of neural networks in LWD lithology identification. *IOP Conf. Ser. Earth Environ. Sci.IOP Publ.* 526 (1), 012146. doi:10.1088/1755-1315/526/1/012146

Chen, W., Yang, L., Zha, B., Zhang, M., and Chen, Y. (2020). Deep learning reservoir porosity prediction based on multilayer long short-term memory network. *Geophysics* 85 (4), WA213–WA225. doi:10.1190/geo2019-0261.1

Dar, Q. U. Z., Renhai, P., Ghazi, S., Ahmed, S., Ali, R. I., and Mehmood, M., (2021). Depositional facies and reservoir characteristics of the early cretaceous lower Goru Formation, lower Indus basin Pakistan: Integration of petrographic and gamma-ray log analysis. *Petroleum*. doi:10.1016/j.petlm.2021.09.003

Dornan, T., O'Sullivan, G., O'Riain, N., Stueeken, E., and Goodhue, R. (2020). The application of machine learning methods to aggregate geochemistry predicts quarry source location: An example from Ireland. *Comput. Geosciences* 140, 104495. doi:10.1016/j.cageo.2020.104495

Durrani, M. Z. A., Talib, M., and Sarosh, B. (2020). Rock physics-driven quantitative seismic reservoir characterization of a tight gas reservoir: A case study from the lower Indus basin in Pakistan. *First Break* 38 (11), 43–53. doi:10.3997/1365-2397.fb2020079

Ehsan, M., Gu, H., Akhtar, M. M., Abbasi, S. S., and Ehsan, U. (2018). A geological study of reservoir formations and exploratory well depths statistical analysis in Sindh Province, Southern Lower Indus Basin, Pakistan. *Kuwait J. Sci.* 45 (2), 84–93.

Feng, R., Mejer Hansen, T. M., Grana, D., and Balling, N. (2020). An unsupervised deep-learning method for porosity estimation based on poststack seismic data. *Geophysics* 85 (6), M97–M105. doi:10.1190/geo2020-0121.1

Gamal, H., Alsaihati, A., and Elkatatny, S. (2022). Predicting the rock sonic logs while drilling by random forest and decision tree-based algorithms. *J. Energy Resour. Technol.* 144, 043203. doi:10.1115/1.4051670

Grana, D., Azevedo, L., and Liu, M. (2020). A comparison of deep machine learning and Monte Carlo methods for facies classification from seismic data. *Geophysics* 85 (4), WA41–WA52. doi:10.1190/geo2019-0405.1

Guo, Z., and Li, X. Y. (2015). Rock physics model-based prediction of shear wave velocity in the Barnett Shale formation. *J. Geophys. Eng.* 12 (3), 527–534. doi:10.1088/1742-2132/12/3/527

Gupta, I., Devegowda, D., Jayaram, V., Rai, C., and Sondergeld, C. (2019). Machine learning regressors and their metrics to predict synthetic sonic and mechanical properties. *Interpretation* 7 (3), SF41–SF55. doi:10.1190/INT-2018-0255.1

Gupta, R., Srivastava, D., Sahu, M., Tiwari, S., Ambasta, R. K., and Kumar, P., (2021). Artificial intelligence to deep learning: Machine intelligence approach for drug discovery. *Mol. Divers.* 25 (3), 1315–1360. doi:10.1007/s11030-021-10217-3

Hall, B. (2016). Facies classification using machine learning. *Lead. Edge* 35 (10), 906–909. doi:10.1190/tle35100906.1

Hamada, G. M. (2004). Reservoir fluids identification using Vp/Vs ratio? *Oil Gas Sci. Technol. - Rev. IFP* 59 (6), 649–654. doi:10.2516/ogst:2004046

Han, D. H. (1987). *Effects of porosity and clay content on acoustic properties of sandstones and unconsolidated sediments* (CA, USA: Stanford University). Doctoral dissertation.

Jakobsen, M., Hudson, J. A., and Johansen, T. A. (2003). T-matrix approach to shale acoustics. *Geophys. J. Int.* 154 (2), 533–558. doi:10.1046/j.1365-246X.2003.01977.x

Kadri, I. B. (1995). *Petroleum geology of Pakistan*. Karachi, Pakistan: Graphic Publishers, 93–108.

Kang, Y., and Wang, J. (20102010). A support-vector-machine-based method for predicting large-deformation in rock mass. *Seventh Int. Conf. Fuzzy Syst. Knowl. Discov.* 3, 1176–1180. doi:10.1109/FSKD.2010.5569148

Kazmi, A. H., and Jan, M. Q. (1997). *Geology and tectonics of Pakistan*. Oregon, USA: Graphic publishers.

Khan, Z. U., Lisa, M., Hussain, M., and Ahmed, S. A. (2021). Gas-bearing sands appraisal through inverted elastic attributes assisted with PNN approximation of petrophysical properties. *Kuwait J. Sci.* doi:10.48129/kjs.15915

Litjens, G., Kooi, T., Bejnordi, B. E., Setio, A. A. A., Ciompi, F., Ghafoorian, M., et al. (2017). A survey on deep learning in medical image analysis. *Med. image Anal.* 42, 60–88. doi:10.1016/j.media.2017.07.005

Liu, S., Zhao, Y., and Wang, Z. (2021). Artificial intelligence method for shear wave travel time prediction considering reservoir geological continuity. *Math. Problems Eng.* 2021, 5520428–18. doi:10.1155/2021/5520428

Miah, M. I. (2021). Improved prediction of shear wave velocity for clastic sedimentary rocks using hybrid model with core data. *J. Rock Mech. Geotechnical Eng.* 13 (6), 1466–1477. doi:10.1016/j.jrmge.2021.06.014

Miraj, M. A. F., Javaid, H., Ali, N., Javaid, P. W. S., Rathore, R. F., Ahsan, N., et al. (2021). An integrated approach to evaluate the hydrocarbon potential of jurassic samana suk formation in Middle Indus basin, Pakistan. *Kuwait J. Sci.* 48 (4), 1–11. doi:10.48129/kjs.v48i4.9193

Mohammed, M., Khan, M. B., and Bashier, E. B. M. (2016). *Machine learning: Algorithms and applications*. Boca Raton, Florida: CRC Press. doi:10.1201/9781315371658

Munyithya, J. M., Ehirim, C. N., and Dagogo, T. (2019). Rock physics models and seismic inversion in reservoir characterization, "MUN" onshore Niger delta field. *Ijg* 10 (11), 981–994. doi:10.4236/ijg.2019.1011056

Naganathan, G. S., and Babulal, C. K. (2019). Optimization of support vector machine parameters for voltage stability margin assessment in the deregulated power system. *Soft Computing* 23 (20), 10495–10495. doi:10.1007/s00500-018-3615-x

Pedregosa, F., Varoquaux, G., Gramfort, A., Michel, V., Thirion, B., Grisel, O., et al. (2011). Scikit-learn: Machine learning in Python. *J. Mach. Learn. Res.* 12, 2825–2830.

Saif-Ur-Rehman, K. J., Mehmood, M. F., Shafiq, Z., and Jadoon, I. A. (2016). Structural styles and petroleum potential of Miano block, central Indus Basin, Pakistan. *Ijg* 7 (10), 1145–1155. doi:10.4236/ijg.2016.710086

Rudd, J. M. (2020). "An Empirical Study of Downstream Analysis Effects of Model Pre-Processing Choices. *Open journal of statistics* 10 (5), 735–809. doi:10.4236/ojs.2020.105046

Saad, B., Negara, A., and Syed Ali, S. (2018). "Digital rock physics combined with machine learning for rock mechanical properties characterization," in Proceedings

of the Abu Dhabi International Petroleum Exhibition & Conference, Abu Dhabi, UAE, November 2018. doi:10.2118/193269-MS

Shakir, U., Ali, A., Amjad, M. R., and Hussain, M. (2021). Improved gas sand facies classification and enhanced reservoir description based on calibrated rock physics modelling: A case study. *Open Geosci.* 13 (1), 1476–1493. doi:10.1515/geo-2020-0311

Song, S., Hou, J., Dou, L., Song, Z., and Sun, S. (2020). Geologist-level wireline log shape identification with recurrent neural networks. *Comput. Geosciences* 134, 104313. doi:10.1016/j.cageo.2019.104313

Steinwart, I., and Christmann, A. (2008). *Support vector machines*. Berlin, Germany: Springer Science & Business Media.

Wawrzyniak-Guz, K. (2019). Rock physics modelling for determination of effective elastic properties of the lower Paleozoic shale formation, North Poland. *Acta Geophys.* 67 (6), 1967–1989. doi:10.1007/s11600-019-00355-6

Young, K. T., and Tatham, R. H. (2007). "Lambda-mu-rho inversion as a fluid and lithology discriminator in the columbus basin, offshore trinidad," in *Seg. Tech. Program Expand. Abstr. 2007*, 214–218.

frontiers | Frontiers in Earth Science

TYPE Original Research
PUBLISHED 29 August 2022
DOI 10.3389/feart.2022.979039

OPEN ACCESS

EDITED BY
Amin Beiranvand Pour,
INOS University Malaysia Terengganu, Malaysia

REVIEWED BY
Bo Liu,
Northeast Petroleum University, China
Peng Li,
SINOPEC Petroleum Exploration and Production Research Institute, China

*CORRESPONDENCE
Jinxian He,
jxhe@cumt.edu.cn

SPECIALTY SECTION
This article was submitted to Economic Geology, a section of the journal Frontiers in Earth Science

RECEIVED 27 June 2022
ACCEPTED 04 August 2022
PUBLISHED 29 August 2022

CITATION
Shi S, He J, Zhang X, Wu H, Yu Z, Wang J, Yang T and Wang W (2022), Fractal analysis of pore structures in transitional shale gas reservoirs in the Linxing area, Ordos Basin.
Front. Earth Sci. 10:979039.
doi: 10.3389/feart.2022.979039

Fractal analysis of pore structures in transitional shale gas reservoirs in the Linxing area, Ordos Basin

Shuai Shi[1,2], Jinxian He[1,2]*, Xiaoli Zhang[1,2], Hongchen Wu[3], Ziqi Yu[4], Jian Wang[1,2], Tiantian Yang[1,2] and Wei Wang[1,2]

[1]Key Laboratory of Coalbed Methane Resource and Reservoir Formation Process, Ministry of Education, China University of Mining and Technology, Xuzhou, China, [2]School of Resources and Geoscience, China University of Mining and Technology, Xuzhou, China, [3]Institute of Geochemistry, Chinese Academy of Sciences, Guiyang, China, [4]School of Public Policy and Management, China University of Mining and Technology, Xuzhou, China

Studying complex pore structures and fractal characteristics of gas shale provides significant guidance for clarifying the mechanism of shale gas accumulation and realizing its efficient development. In this paper, 12 samples of Taiyuan Formation shale are used as the research object, and the fractal theory is combined with mercury intrusion porosimetry and N_2 adsorption technology to innovatively solve the problem of splicing point selection, which can reveal the full-scale pore size distribution of shale. The results demonstrate that the most common types of pores in the chosen samples are pores between or within clay minerals, micropores and mesopores inside organic matter, and microfractures, based on scanning electron microscopy imagery analyses. The pores of shale samples have fractal geometries. The fractal dimension D_{M1} values in the mercury intrusion porosimetry experiments range from 2.3060 to 2.6528. Two fractal dimensions, D_{N1} and D_{N2}, may be obtained using the Frenkel-Halsey-Hill fractal method. D_{N1} values vary from 2.4780 to 2.6387, whereas D_{N2} values range from 2.5239 to 2.7388. Most macropores in shale samples have a size range of about 0.2 mm, with a wide pore size distribution, and the largest peak of the micro-mesopore volume is generally about 50 nm. The fractal dimension correlates positively with the corresponding pore volume, although the correlation between volume and composition is weak. The relatively strong correlation between fractals and the basic compositions of shale proves the fractal theory's relevance in defining pore inhomogeneity. This study would contribute to the development of a fractal perspective-based method for pore splicing while also expanding our understanding of pore morphology and structure in transitional shale.

KEYWORDS

linxing area, pore structure, fractal analysis, full-scale PSD, shale gas

1 Introduction

The world's energy supply is undergoing a third significant transition, and many nations have aggressive energy development strategies in place to promote the quick advancement of this transition (Zou et al., 2020). To achieve carbon peak and neutrality goals, the focus of the energy in China will remain on stable supply, clean and low-carbon energy, and economic convenience in the long run while addressing the difficulty of upgrading for high-quality development (Dai et al., 2021). Natural gas is an indispensable, relatively clean, and efficient high-quality energy source for use in the process of energy structure transformation, and its demand will continue to expand in the future. Shale gas, a representative of unconventional gas, has emerged as one of the most essential natural gas resources in the last decades. Influenced by the rapid development of the shale gas industry in many countries (Jarvie et al., 2007), research and exploration of shale gas in China are also increasing.

Shale gas reservoirs are an integrated source and storage reservoir system, which means that large amounts of natural gas in them have a complex storage state (Curtis, 2002). Gas enrichment is strongly influenced by the shale features, including the content and type of organic matter (OM), mineral composition, and pore structure parameters such as specific surface area (SSA), pore volume (PV), and pore size distribution (PSD). The complex characteristics of pore structure type and evolution, which are usually dominated by nanometer- or micron-scale pores, have an important impact on the storage and seepage capacity of shale. The SSA, mainly attributed to micropores and mesopores, determines the storage potential of adsorbed gas, the PV of macropores influences the storage ability of free gas, and the diffusion and seepage capacity of shale gas is mainly controlled by the PSD (Li et al., 2019). Therefore, a detailed and in-depth study of the pore feature of shale reservoirs has important meaning for clarifying the mechanism of shale gas accumulation and developing shale gas resources.

Scholars have put forward a host of experimental methods to research the development characteristics of reservoir pores, including three types of methods: microscopic imaging methods, radiographic methods, and fluid injection methods. Specifically, they include scanning electron microscopy (SEM) (Jiao et al., 2014), atomic force microscopy (Chen et al., 2021a), helium ion microscopy (Wang et al., 2020), confocal laser scanning microscopy (Liu et al., 2020), computed tomography (Liu et al., 2021a), nuclear magnetic resonance (NMR) (Li et al., 2016), small-angle scattering (Sun et al., 2020), mercury intrusion porosimetry (MIP) (Li et al., 2021a), and low-temperature N_2 adsorption (N_2 adsorption) (Hu et al., 2019). Because of the complex pore structure of gas shale, various methods have limitations, and it is difficult to analyze the pore structure with a single method (Jiang et al., 2017). Therefore, scholars usually combine techniques to study shale pores (Chen et al., 2021b; Wang et al., 2021; Zhang et al., 2018). Due to their efficiency and extensive testing range, MIP and N_2 adsorption are combination procedures that are frequently employed for quantitative pore characterization. However, the selection of splice points also has a significant impact on the collection of the full-scale PSD.

At present, there are three main methods of pore splicing, as follows: 1) From experience, three splicing points—25, 50, and 100 nm—are widely applied (Zhang et al., 2017; Xu et al., 2021); 2) According to the PSD image, the intersection of two curves or the midpoint of their parallel segments is usually selected for the splicing location (Xu et al., 2018); 3) The splicing point can be determined from an NMR T_2 curve (Xiao et al., 2020; Zheng et al., 2019a). The problems with these methods are also obvious: For method 1, the splicing points are frequently chosen based on the splicing findings of similar lithologies or study areas, making the points chosen highly subjective. For method 2, it is very difficult to determine the splicing point since intersections or parallel segments often cannot be found, or there may be multiple intersections or parallel segments. For method 3, NMR experiments are relatively expensive, and there is no unified understanding of the T_2 curve correction method, which essentially introduces another pore size characterization method.

The fractal method is typically used to examine patterns and characteristics that are self-similar but lack a distinctive length (Liu et al., 2019a). The microscopic pore structure of rock reservoirs has good statistical self-similarity and exhibits good fractal characteristics within a certain pore size range (Clarkson et al., 2013), which can be quantitatively described by the fractal dimension. N_2 adsorption and MIP provide fast, efficient, and economical acquisition of fractal dimensions. A large body of scholarly work has found that fractal dimension can quantitatively characterize the non-homogeneity of reservoir pore structure, which is suitable for reservoir description and evaluation (Jiang et al., 2016; Liu et al., 2019b; Wang & Zai, 2021).

In this study, we conducted SEM morphology observation, MIP, and N_2 adsorption analysis on the Taiyuan Formation shale collected from the Linxing area to obtain the morphological characteristics of the pores and quantitative parameters of the pore structure. The fractal dimensions of different pore ranges were calculated, which can be used to characterize the pore structure and inhomogeneity of the shale. An attempt is made to select suitable splicing points from the fractal perspective, and then to obtain full-scale PSD curves and PVs at each stage. Based on this, the relationship between fractal dimension, PV, and basic compositions of transitional shale, is discussed.

2 Geologic background

The Ordos Basin (Figure 1A) is located in the North China Craton (Li et al., 2021b). According to the basement material composition and structural characteristics, it can be divided into

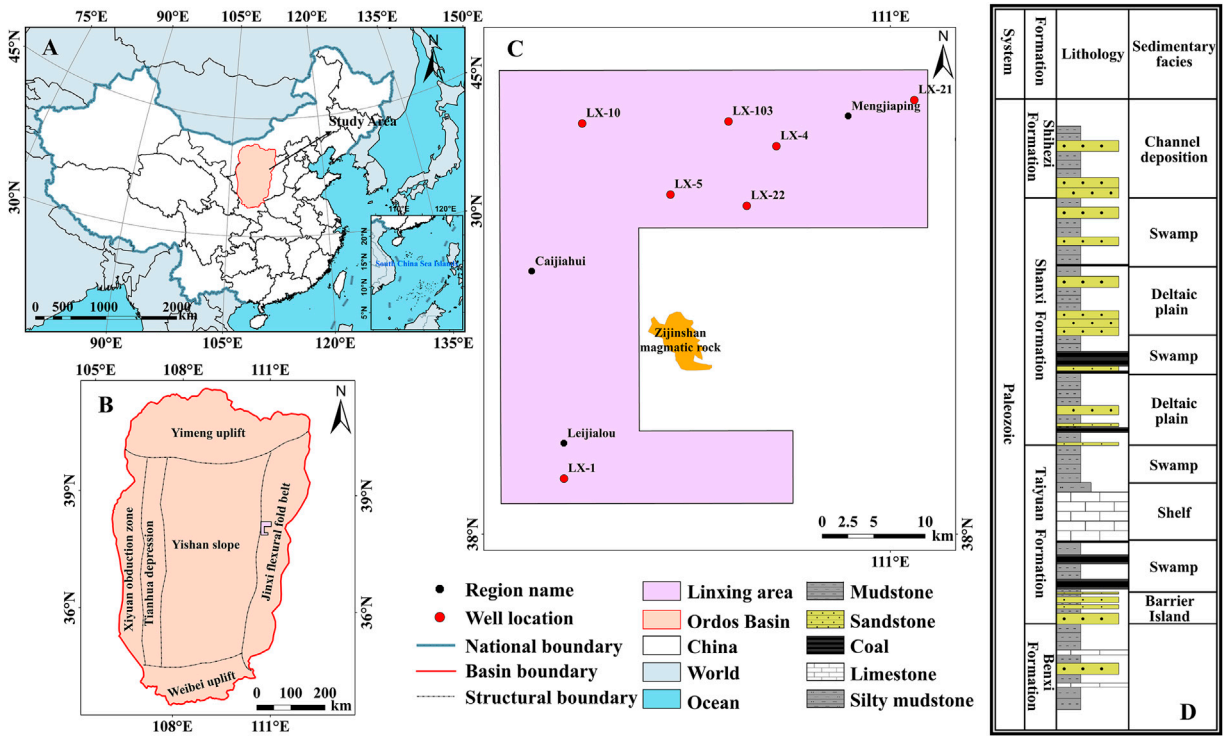

FIGURE 1
Geological settings of the Ordos Basin: **(A)** showing the location of the Ordos Basin; **(B,C)** showing the location of Linxing area and sampling well; **(D)** stratigraphic histogram of Shihezi Formation-Benxi Formation in Linxing area, modified after Li et al. (2016).

six subsidiary parts (Figure 1B) (Li et al., 2019). The Linxing area is located on the eastern edge of the Ordos Basin, and its structure is relatively simple (Figures 1B,C). Controlled by the Zijinshan magmatic rock intrusion and regional tectonic movement, the stratigraphic trend is NE–SW, with a dip of 5°–10° to the west (Xu et al., 2015; Shu et al., 2021). The paleogeographic evolution of the strata in the Ordos Basin underwent a transition from sea to land during the Late Paleozoic. In the Taiyuan stage, the study area's sedimentary environment is the main barrier coastal sedimentary system (Figure 1D) (Shen et al., 2017). The Taiyuan Formation of the Upper Carboniferous is a major coal-bearing stratum in North China (Ju et al., 2017), mainly comprising grayish-black shale, silty mudstone, argillaceous siltstone, sandstone, micrite limestone, bioclastic limestone, and coal seams.

3 Samples and experiments

A total of 12 shale samples were collected from depths of 1659–2067 m in the Taiyuan Formation, and then the samples were crushed and divided into several parts to complete different experimental tests. Organic geochemical and mineralogical composition tests were used to clarify the developmental status of the samples. SEM was used to observe the pore morphology of each sample to obtain a visual understanding of the pore morphology, and MIP and N_2 adsorption were used for quantitative and comprehensive analysis of the pore structure of the samples. The pore classification system of the International Union of Pure and Applied Chemistry (IUPAC) (Thommes et al., 2015) is widely applicable and comparable, so this scheme is used for the classification of pores in this paper.

3.1 Organic geochemical and mineral composition tests

Each sample was subjected to tests on its total organic carbon (TOC) concentration, OM type, vitrinite reflectance (R_o), and whole-rock X-ray diffraction (XRD) to determine its fundamental geochemical characteristics and mineral compositions. The TOC content was determined by a carbon/sulfur analyzer (multi EA4000, Analtik Jena, Germany). Microfraction microscopy was used to distinguish among the OM types, and the R_o was then measured using a matching photometer. The mineral compositions of the shale sample can be obtained by the XRD experiment (D8 ADVANCE, Bruker, Germany).

TABLE 1 Sample properties for the Taiyuan shale in the Linxing area.

Sample	Well	Depth (m)	TOC (%)	OM Type	R_o (%)	Whole rock (%)				
						Quartz	feldspar	Carbonate	Pyrite	Clay
1	LX-1	2037.7	1.66	II_2	1.31	55.99	0	18.46	6.12	19.43
2	LX-1	2067.5	2.14	II_2	1.29	47.33	0	2.56	4.96	45.15
3	LX-4	1736.4	22.58	III	1.21	26.55	10.11	0	0	63.34
4	LX-5	1722.6	2.20	II_2	1.13	50.05	5.19	1.62	5.58	37.56
5	LX-10	1659.6	4.58	II_2	1.00	40.93	0	1.30	6.69	51.08
6	LX-21	1952.1	1.87	II_2	1.29	37.98	0	0	3.04	58.98
7	LX-21	1991.6	2.06	II_1	1.26	42.47	5.27	1.54	2.43	48.29
8	LX-21	1993.7	1.59	II_1	1.30	45.50	0	3.73	0	50.77
9	LX-22	1947.6	2.12	II_1	1.34	20.15	8.08	4.48	2.87	64.42
10	LX-103	1714.5	4.50	II_1	1.23	49.45	0	0	0	50.55
11	LX-103	1716.3	1.74	II_1	1.20	34.62	0	0	0	65.38
12	LX-103	1717.9	6.06	II_2	1.24	21.92	0	0	0	78.08

3.2 Scanning electron microscopy characterization

Using a scanning electron microscope (Quanta 250, FEI company, United States), we acquired SEM images of the microscopic pores. The SEM imaging on the fresh broken surfaces of the samples was conducted at 25°C and 35% relative humidity. The qualitative structural information of the microscopic pores was obtained from the acquired SEM images, see Section 4.2 for more detailed results.

3.3 Mercury intrusion porosimetry

The mercury intrusion analyses were done using a mercury porosimeter (Poremaster 60GT, Quantachrome Instruments, United States) at pressures up to 40,000 pounds per square inch absolute (psia; approximately 275.8 MPa). Crushed shale samples with diameters between 1 and 3 mm were prepared according to standard operating guidelines, and all samples were dried at a constant temperature of 100°C for 5 h before being tested for MIP.

3.4 Low-temperature N_2 adsorption

The low-temperature N_2 adsorption experiments were performed on an automatic SSA and pore analyzer (Tristar II 3020, Micromeritics Instruments, United States). After the sample was pulverized to 0.25–0.425 mm diameter particles (Chen et al., 2018), weighed 1–2 g, and placed in a desiccator where it was dried at 100°C for 8 h. Using liquid nitrogen, we measured a range of relative pressures (P/P_0) from 0.002 to 0.995 for N_2 adsorption under a temperature of −195.85°C. After the N_2 adsorption tests were completed, the density function theory (DFT) model was used for PV and PSD acquisition. With the support of mercury intrusion data, it can be confirmed that the samples contain a large number of macropores, so after considering the applicability of each model, the DFT model is most suitable for obtaining the PSD.

4 Results

4.1 Organic geochemical characteristics and mineral composition

The basic geochemical characteristics and mineral composition of each sample were tested experimentally, and Table 1 lists the test results. The TOC content of shale samples of Taiyuan formation in the Linxing area ranges from 1.59% to 22.58%, with a mean value of 2.77%. The OM types are mainly typed II kerogen, and the vitrinite reflectance ranges from 1.00% to 1.34%, with a mean value of 1.23%, which is in the middle maturity stage. According to the North American shale evaluation standard, the Taiyuan shale in the Linxing area is a fine gas-producing source rock (Burnaman & Shelton, 2009). Based on the XRD test results, the main mineral components in the shale samples are clay minerals, quartz, carbonate minerals, pyrite, and feldspar, in order of abundance.

4.2 Qualitative analysis of pore morphology

The qualitative analysis of shale pore morphology is helpful to determine the pore structure. Micronmeter-scale pores and

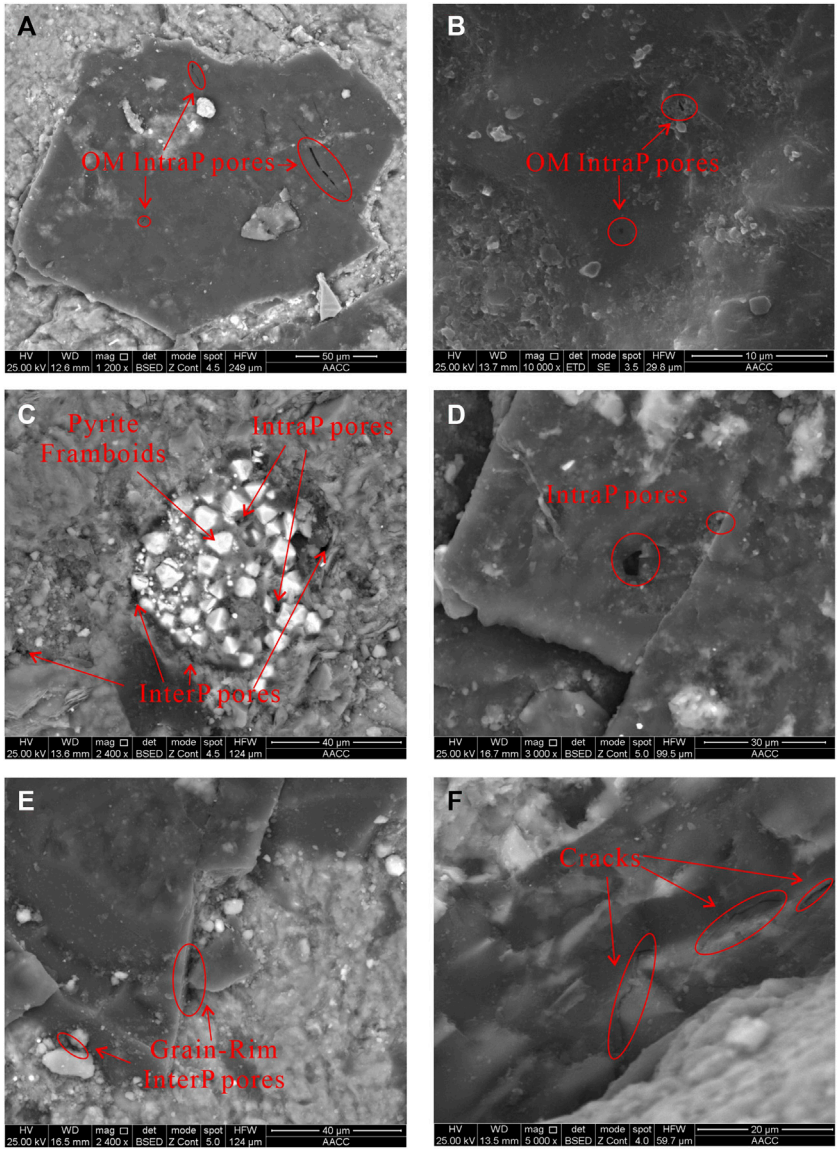

FIGURE 2
Scanning electron microscopy (SEM) imageries of Taiyuan Formation shale: **(A)** sample 3, LX-4, 1736.4 m; **(B)** sample 9, LX-22, 1947.6 m; **(C)** sample 7, LX-21, 1991.6 m; **(D,E)** sample4, LX-5, 1722.6 m; **(F)** sample 11, LX-103, 1716.3 m.

nanometer-scale pores are abundant in the SEM imageries. According to the SEM imagery characterizations, there are three main types of pores in the Taiyuan shale: intraparticle (intraP) pores that are located inside mineral grains, interparticle (interP) pores that are located between mineral grains, and microfractures. The intraP pores located within kerogen, are also known as OM pores.

The OM pores in the Taiyuan Formation shale have different shapes and sizes, and exist in isolation or are connected. Pore diameters range from a few nanometers to several hundreds of nanometers, and pores of several microns can also be seen (Figures 2A,B). Typically, the interP pores are observed around or between particles in minerals. These interP pores are tens to hundreds of nanometers in diameter and usually have elongated shapes or polygonal cross-sections (Figures 2C,E). Clay minerals, pyrite framboids, and OM contain the most intraP pores (Figures 2C,D). Microfractures in the Taiyuan Formation shale can develop in and between particles of minerals or OM, mainly as organic hydrocarbon-generating fractures, mineral interlayer fractures, or mineral tension fractures caused by temperature and pressure changes during diagenesis. The morphologies of microcracks extend linearly or curvilinearly,

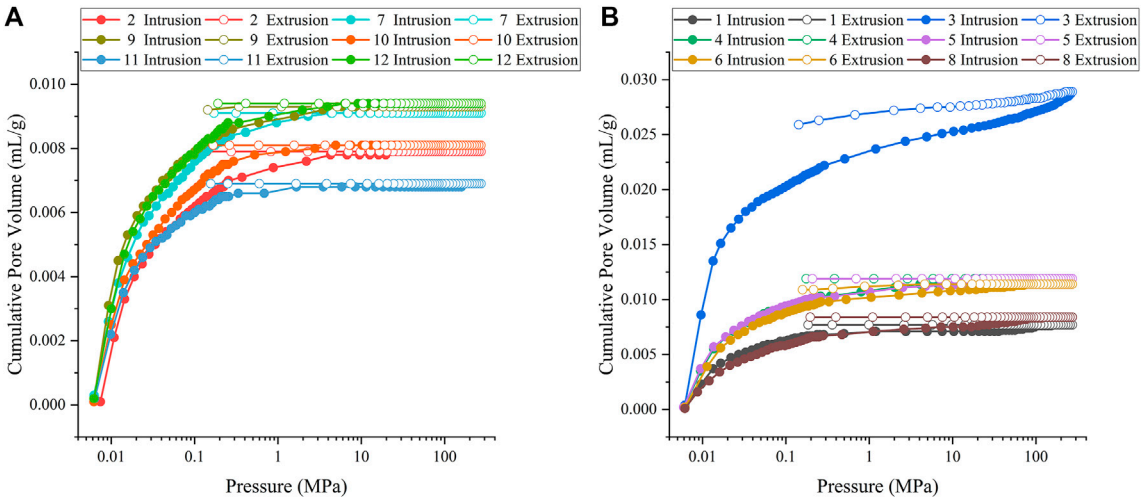

FIGURE 3
Mercury intrusion/extrusion curves of the Taiyuan Formation shales.

and the lengths are usually several microns to tens of micrometers (Figure 2F). The existence of microcracks provides good channels for the communication of different types of reservoir spaces and the seepage of gas.

4.3 Quantitative analyses of pore structure

4.3.1 Pore characterization using mercury intrusion porosimetry measurements

For the MIP method, the form of the in-extrusion mercury curve shows various pore space expansion and connectivity. According to the intrusion mercury curves of the Taiyuan Formation shales in the study area, although the cumulative mercury intrusion differs between various shale samples, the intrusion curve often has the same shape. All of them have a low-pressure section ($p < 0.011$ MPa, corresponding to a pore size of 150 μm), with the steepest slope, suggesting the presence of numerous macropores that are micron-sized in diameter. The mercury intrusion rate is modest after this point and the intrusion curve gradually flattens out.

The mercury intrusion curve of the samples could be divided into two categories when the pressure was greater than 10 MPa, with one category's mercury intrusion remaining nearly constant after 10 MPa (Figure 3A), and the other category's mercury intrusion gradually increasing with pressure until it reached its maximum mercury intrusion (Figure 3B). The majority of the Taiyuan Formation shale samples are well closed based on the degree of closure of the intrusion and extrusion curves. Some samples even have practically overlapping intrusion/extrusion curves, indicating that the bulk of the samples' pores is open or cracked.

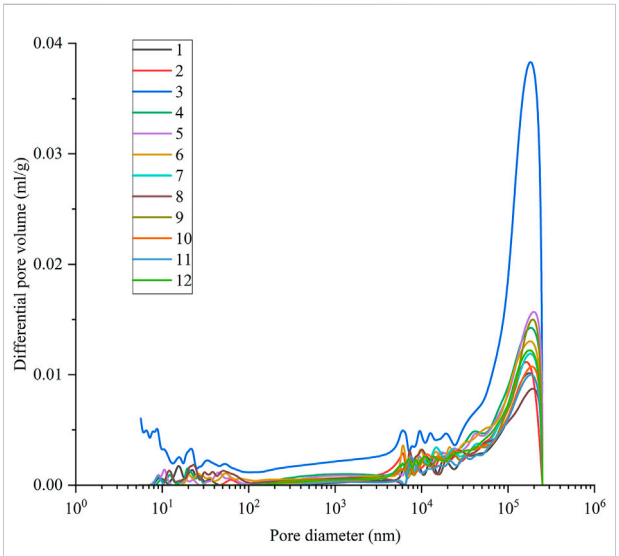

FIGURE 4
Pore size distributions (PSDs) of shales estimated from mercury intrusion porosimetry (MIP) analyses.

The pores of the Taiyuan Formation shale are widely distributed, ranging from mesopores to micron-scale fractures (Figure 4). Among them, samples 1, 3, 4, 5, 6, and 8, have a bimodal distribution. The two main peaks consist of meso–macropores and cracks, respectively. The right peak area (8000–200,000 nm) is larger than the left peak area (5–100 nm). Samples 2, 7, 9, 10, 11, and 12, have only a single peak, indicating that the reservoir space is mainly composed of fractures. The PV of sample 3 is significantly

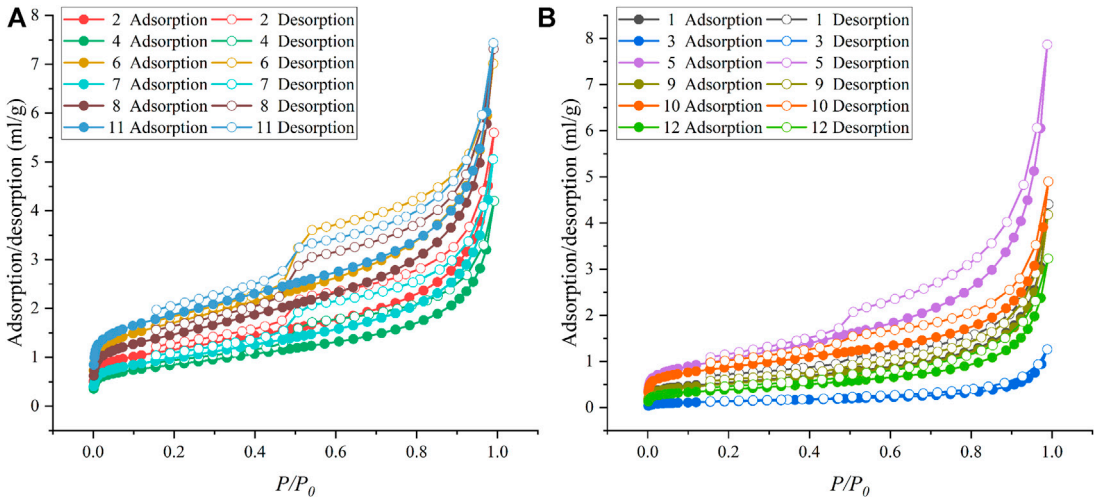

FIGURE 5
Isotherms of samples **(A)** samples with clear inflection points; **(B)** samples without inflection points.

higher than that of the other samples at each stage, which may be caused by the higher TOC content (Table 1).

4.3.2 Pore structure from N_2 adsorption isotherms

The IUPAC report in 2015 divided the gas adsorption isotherms into eight categories, adding two subclasses to represent the characteristics of different pores in porous materials (Thommes et al., 2015). The morphological characteristics of adsorption-desorption curves of the twelve shale samples are similar in general. They all show an inverse S shape with a hysteresis loop. In the early stage of adsorption ($P/P_0 < 0.1$), the nitrogen adsorption capacity increases slowly, the curve is slightly convex upward, and there is an inflection point. In the middle section of the adsorption curve ($P/P_0 = 0.1–0.7$), the nitrogen adsorption capacity increases gently, and the adsorption curve is almost a straight line. In the late stage of adsorption ($P/P_0 > 0.7$), the nitrogen adsorption capacity increases rapidly with the increase of the P/P_0 and the adsorption curve is steep, but when the adsorption curve was close to the nitrogen saturation vapor pressure the shale samples did not reach the maximum adsorption capacity. The above adsorption-desorption curve characteristics show that the adsorption isotherm of the Taiyuan Formation shale samples is similar to the type IV isotherm, but it is still not saturated at the adsorption end-point, which is a characteristic of the type II isotherm. This evidence indicates that the shale samples include a substantial number of macropores that exceed the detection limit of N_2 adsorption. Based on the IUPAC classifications of hysteresis loops, the Taiyuan shale samples belong to H3 (Thommes et al., 2015). The desorption curves for samples 2, 4, 6, 7, 8, and 11 show prominent inflection points near the P/P_0 of 0.5 and large hysteresis loops (Figure 5A), indicating that ink bottle-shaped pores exist. By contrast, Figure 5B illustrates that the desorption curves for 1, 3, 5, 9, 10, and 12 have no inflection points. And the hysteresis lines of these samples are relatively small, indicating the presence of conical pores. This is consistent with what is seen in the SEM images, such as the cone-shaped OM pores (Figure 2A) observed in sample 3.

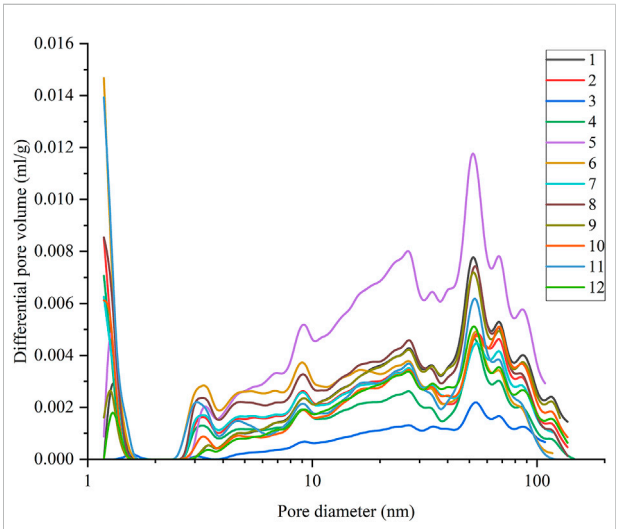

FIGURE 6
PSDs of shales estimated from N_2 adsorption analyses.

From the PSD diagram (Figure 6), it can be seen that the pore spaces in the shale are mainly concentrated in mesopores and macropores. The maximum peak value of the differential PV is usually around 50 nm, which is near the boundary between mesopores and macropores. The PSD characteristics also show

TABLE 2 Fractal dimension of mercury intrusion porosimetry (MIP) in shale samples.

Sample ID	p < 14.7 MPa			p > 14.7 MPa		
	k_1	D_{M1}	R^2	k_2	D_{M2}	R^2
1	−1.6940	2.3060	0.9445	−0.8548	3.1452	0.1196
2	−1.4320	2.5680	0.9721			
3	−1.3472	2.6528	0.9666	−0.6305	3.3695	0.8535
4	−1.4516	2.5484	0.9529	−0.5413	3.4587	0.1189
5	−1.4414	2.5586	0.9797	−0.8947	3.1053	0.2459
6	−1.4345	2.5655	0.9448	−1.0490	2.9510	0.3718
7	−1.4561	2.5439	0.9778			
8	−1.4457	2.5543	0.9644	−1.0431	2.9569	0.4538
9	−1.4896	2.5104	0.9781			
10	−1.5023	2.4977	0.9803			
11	−1.5013	2.4987	0.9666			
12	−1.4870	2.5130	0.9713			

that mesopores and macropores provide the most pore space and are the main components of the Taiyuan Formation shale pores. Some samples can also show higher peaks in the range of micropores, indicating that the Taiyuan shale also contains a certain number of micropores. Due to the limitation of N_2 adsorption experiments, some micropore (<1 nm) volumes may be neglected.

5 Discussion

5.1 Pore fractal analysis of the shale samples

5.1.1 Pore fractal analysis using mercury intrusion porosimetry measurements

The fractal theory had been successfully applied by many scholars to the analysis of shale reservoirs. The MIP experiment was mainly solved based on the Washburn formula and Menger sponge model (Cai et al., 2011), the calculation formula can be derived as follows:

$$\ln(dV_P/dP)/\ln P = D_M - 4 \quad (1)$$

where: D_M is the shale pore fractal dimension using MIP, dimensionless; P is the experimental pressure, MPa; and V_P is the mercury injection volume at P, mL/g.

According to the Eq. 1, the mercury intrusion data was obtained, and then the linear fitting was performed according to the relationship between ln (dV_P/dP) and ln$P$ of the shale sample to obtain the slope (Figure 6), thereby obtaining the fractal dimension D_M of different shale samples, listed in Table 2.

There were two cases for the fitting results of ln(dV_P/dP) and ln$P$, corresponding to the two PSD characteristics. There are two stages in the relationship between ln(dV_P/dP) and ln$P$ in Figure 7A, corresponding to samples with bimodal PSD, indicating that the pore fractal dimension of the Taiyuan shale in the Linxing area has a boundary point, and its pressure limit is approximately 14.7 MPa; the corresponding pore size range is approximately 100 nm. Figure 7B only exists in the first stage, corresponding to the sample with only a single peak. The macropore–fracture fractal dimension was recorded as D_{M1}, and the mesopore–macropore fractal dimension was recorded as D_{M2}. D_{M1} ranged from 2.3060 to 2.6528, with a mean value of 2.5264; D_{M2} ranged from 2.9510 to 3.4587, with a mean value of 3.1644. According to fractal theory, the D value was only meaningful when it was between 2 and 3. This means that D_{M2} was unreliable, and it could be noted that its correlation index, R^2, was also low. Research by other scholars had shown that matrix compression may result from excessive mercury intrusion pressure (Zhang, et al., 2019a; Zhang et al.,. 2019b). In other words, the loss of reliability for D_{M2} was a sign that the pore structure is damaged.

5.1.2 Pore fractal analysis from N_2 adsorption isotherms

Many methods had been used to calculate the fractal dimension of porous materials using nitrogen adsorption data. The more commonly used methods included the Frenkel–Halsey–Hill (FHH) model, the Brunauer–Emmett–Teller (BET) model, and the Niemark–Kiselev (NK) model. Among them, the FHH method was the most widely used, and the fractal characteristics obtained are also effective (Liu et al., 2019b). Therefore, this model was chosen to calculate the fractal dimension of nitrogen adsorption in this study. The calculation method of the FHH model is as follows:

$$\ln V = (D_N - 3)\ln[\ln(P_0/P)] + C \quad (2)$$

where: D_N is the shale pore fractal dimension using N_2 adsorption, dimensionless; P is the equilibrium pressure of the gas, MPa; P_0 is the gas saturation pressure, MPa; V is the volume of adsorbed gas molecules at P, and C is a constant.

It can be seen from Eq. 2 that the fractal dimension D_N can be obtained by making a relationship diagram between lnV and ln [ln(P_0/P)] and obtaining the slope between them through the least-squares regression. Based on the original N_2 adsorption isotherm data for the shale samples, a scatter diagram (Figure 8) can be drawn. It can be seen from the figure that the relationship between ln[ln(P_0/P)] and lnV has two stages with a good linear fitting relationship, and the demarcation point is at P/P_0 = 0.5. The discrepancies between the scatter diagram at P/P_0 of 0–0.5 and 0.5–1 indicate diverse adsorption behaviors. Intermolecular forces dominated the adsorption behavior in

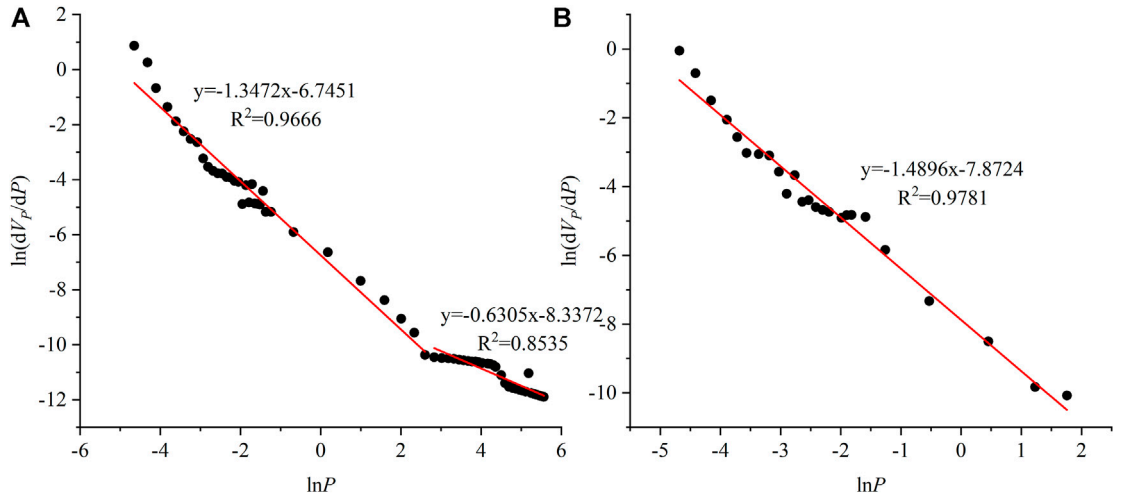

FIGURE 7
Fractal calculation results from ln (dV_P/dP) vs. ln$P$ reconstructed from MIP for two representative shale samples **(A)** sample 3; **(B)** sample 9.

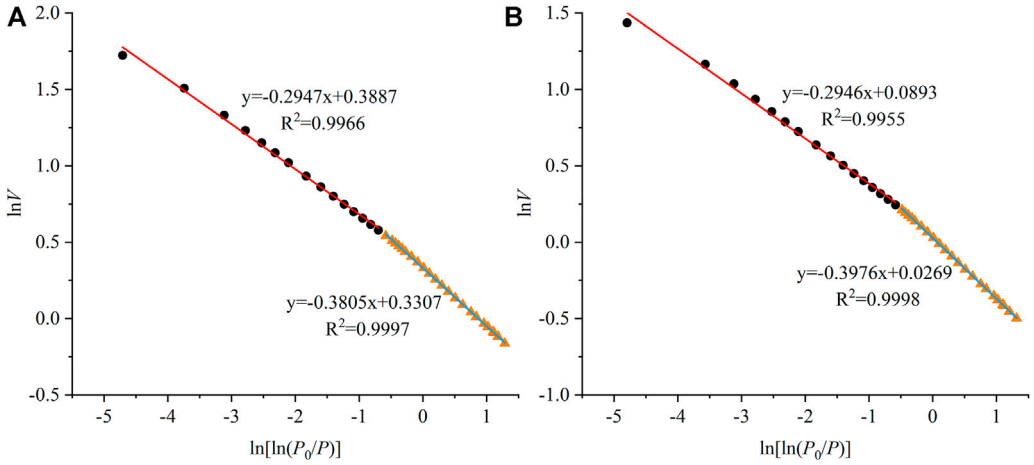

FIGURE 8
Scatter diagrams of ln$V$ vs. ln[ln(P_0/P)] for two typical shale samples, both with a demarcation point at P/P_0 = 0.5 **(A)** sample 2; **(B)** sample 4.

the early stage ($P/P_0 < 0.5$) of N_2 adsorption, while the behavior was controlled by capillary coalescence in the later stage ($P/P_0 >$ 0.5) of N_2 adsorption (Wang et al., 2016). So D_{N1} was computed in the early stage. At lower P/P_0, as N_2 molecules were adsorbed and arranged on the surface of the pores, monolayer adsorption occurs, in which surface adsorption dominates. Therefore, D_{N1} responded to the surface roughness of the pore structure and could be referred to as the surface fractal dimension. In contrast, D_{N2} has computed in the $P/P_0 > 0.5$ regions. At higher relative pressures, pore-filling adsorption and multilayer adsorption dominated, and N_2 molecules manifested capillary condensation features. Consequently, D_{N2} was used as the fractal dimension of the pore structure.

Two characteristic FHH model scatter plots of ln$V$ vs. ln[ln(P_0/P)] from N_2 adsorption data for samples 2 and 3 are plotted in Figure 8. The slopes obtained from the fits are presented in Table 3, and it can be found that all R^2 values are greater than 0.99, indicating a good correlation between the linear fits. It can be seen from Table 3 that D_{N1} ranges from 2.4780 to 2.6387 with a mean value of 2.5757, and D_{N2} ranges from 2.5239 to 2.7388 with a mean value of 2.6487. D_{N1} was smaller than D_{N2} for each sample. Studies conducted on shale reservoirs in different basins had shown the same results,

TABLE 3 Fractal dimension of N_2 adsorption isotherms in shale samples.

Sample ID	$P/P_0 < 0.5$			$P/P_0 > 0.5$		
	k_3	D_{N1}	R^2	k_4	D_{N2}	R^2
1	−0.4249	2.5751	0.9993	−0.4179	2.5821	0.9965
2	−0.3805	2.6195	0.9997	−0.2947	2.7053	0.9966
3	−0.5220	2.4780	0.9934	−0.4761	2.5239	0.9978
4	−0.3976	2.6024	0.9998	−0.2946	2.7054	0.9955
5	−0.4849	2.5151	0.9997	−0.4069	2.5931	0.9960
6	−0.3928	2.6072	0.9998	−0.2649	2.7351	0.9932
7	−0.4277	2.5723	0.9998	−0.3140	2.6860	0.9974
8	−0.4173	2.5827	0.9998	−0.2984	2.7016	0.9965
9	−0.4366	2.5634	0.9998	−0.4237	2.5763	0.9969
10	−0.3936	2.6064	0.9995	−0.3340	2.6660	0.9985
11	−0.3613	2.6387	0.9990	−0.2612	2.7388	0.9985
12	−0.4524	2.5476	0.9999	−0.4296	2.5704	0.9944

suggesting that lower D_{N1} values than D_{N2} values might be a more general phenomenon (Hazra et al., 2019; Jiang et al., 2016; Liu et al., 2021b). According to the research of relevant scholars, D_{N1} was positively correlated with the amount of methane gas adsorption, so the relatively high D_{N1} values of the Taiyuan Formation shale indicated that it had a higher gas adsorption potential (Yang et al., 2014). The higher D_{N2} values compared with D_{N1} values might result from the enhanced accessibility of N_2 to porous structures at higher relative pressures. (Hazra et al., 2019).

5.2 The full-scale pore size distribution of transitional shales

MIP and N_2 adsorption had specific pore size test ranges. Shale samples had a wide range of pore sizes, and neither of these two techniques alone could reliably characterize all the pores in a shale, making it inappropriate to analyze full-scale PSDs by only a single experiment. Therefore, in this section, it will be discussed how to effectively couple the PSD values obtained from MIP and N_2 adsorption experiments to characterize the full-scale PSD of shales.

The core of rebuilding the full-scale PSD is to give full play to the advantages of the two test methods, that is, to capitalize on the most reliable parts of the two data sets. When a piece of data is no longer reliable, it should not be present in the final result of the full-scale PSD images. The fractal theory had been wildly used to characterize the distribution of pores in various rocks. Therefore, we can use fractal dimension to solve the problem of splicing point selection. When the rock fractal dimension value loses its physical meaning or there is no fractal dimension value, the corresponding method can no longer effectively characterize the pore structure of the rock and that data should be discarded. Through the previous calculation, we found that for the Taiyuan shale, the D_M values lose physical meaning in the part of pore size less than 100 nm; while the D_N values are always meaningful, thus the reasonable splicing point should be at 100 nm.

Compared our approach to the standard method 2 to further validate its dependability. By comparing the PSD plots (Figure 9) of the N_2 adsorption and MIP across the whole test range of the N_2 adsorption test. Except for sample 3, the MIP generally underestimated the PV below 100 nm. The PSD curves of samples 1, 2, 4, 5, 6, and 8 retain some morphological similarity (peak heights change but peak positions remain similar), and there are crossings or exhibit the same monotonicity near 100 nm, however, this pore splicing approach fails for samples 7, 9, 10, 11, and 12. This demonstrates that the fractal theory is viable and more extensively relevant in the problem of splicing point selection. This shows that the fractal theory is valid and more widely applicable in the problem of the selection of splicing points. It should be observed that the two curves of sample 3 have multiple intersections in the 50–100 nm pore size section, and the measured stage pore volume increases as the intrusion pressure increases. This is similar to the usual overestimation of mesopore and micropore volumes in coal rocks reported by certain authors due to matrix compression effects (Li et al., 2021a). Combined with the significantly higher TOC of sample 3 (22.58%), it suggests that organic matter pores and mineral pores are different when they are disrupted. OM particles may be disrupted due to larger intrusion pressure, thus making the internally contained closed pores disrupted and communicated. Mineral pores, on the other hand, tend to collapse as a whole, i.e., they are supported by the clay mineral skeleton and still maintain a certain pore morphology (Kuila & Prasad, 2013).

Figure 10 exhibits the volume differential full-scale PSD of 12 shale samples gained from the above fractal method. The figure shows that the distributions of the studied samples range from 1.5 nm to 200 μm, and nanoscale pores act as an important storage space for the Taiyuan shale. The porosity values gained from the full-scale PSD curve are significantly larger than those obtained from the MIP or N_2 adsorption techniques alone, which indicates that pores at micron and larger scales are not negligible for shale gas reservoirs. The full-scale PSD curves exhibit a multimodal character, and several peaks can be found, corresponding to pore diameters of approximately 1.5 nm, 25 nm, 50 nm, 10 μm, and 0.2 mm, from left to right.

The foregoing research shows that the pore structure of shale is complicated, diversified, and has a wide range of PSD. The pore volume distribution features of full pore size vary substantially among different Taiyuan Formation shale samples. However, in general, it is still characterized by macropores providing the majority of PV, followed by mesopores, and micropores providing a small amount of PV (Figure 11). The mean volumes of micropores, mesopores, and macropores are 0.00045 ml/g, 0.0031 ml/g, and 0.011 ml/g, respectively. The mean percentages are 3.4%, 21.7%, and 74.9%, respectively.

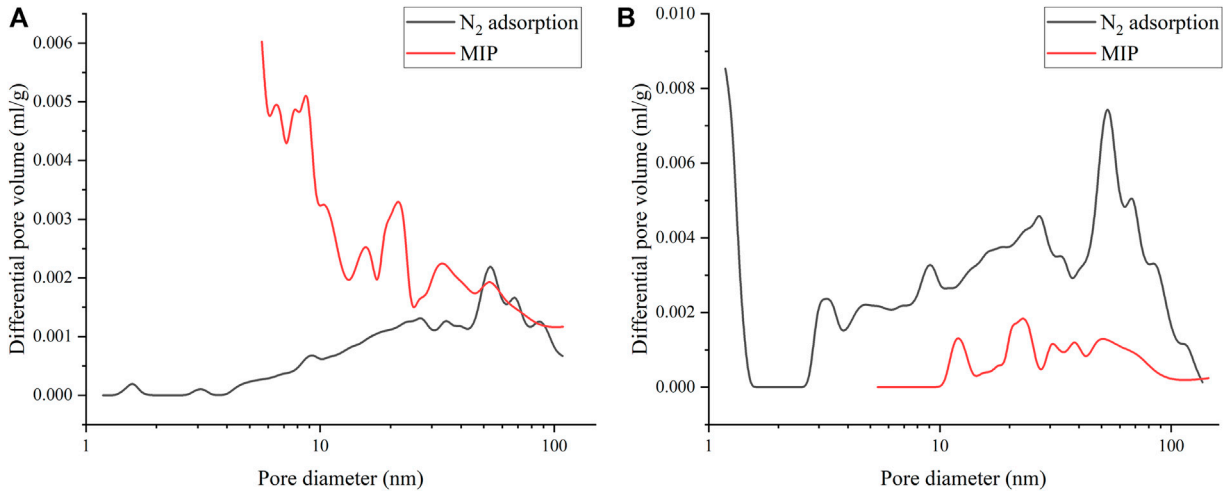

FIGURE 9
Comparison of pore size distribution obtained from MIP and N_2 adsorption data **(A)** sample 3; **(B)** sample 8.

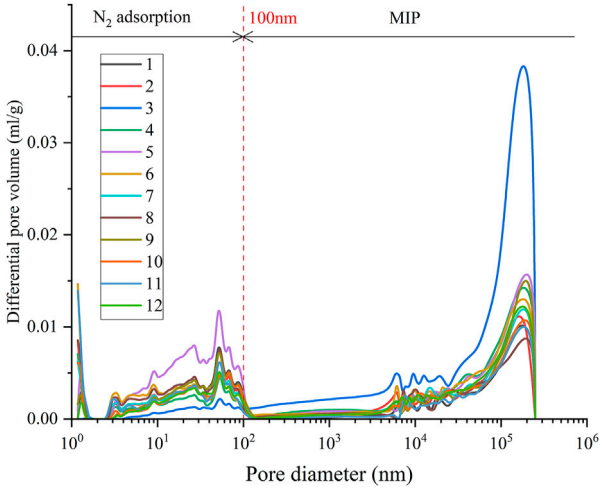

FIGURE 10
Full-scale PSDs of 12 samples gained by combining N_2 adsorption and MIP measurements.

5.3 The correlation between fractal dimensions and the pore volume and compositions of shales

To determine the effect of the fractal characteristics of Taiyuan shale on pore anisotropy, it is essential to survey the correlation between fractal dimensions, PV, and the basic compositions of transitional shale, including TOC content, quartz content, and clay content. A total of three effective fractal dimensions were obtained in this study, D_{M1}, D_{N1}, and D_{N2}, which correspond to most of the macropores, micropores, and mesopores, respectively.

Figure 12 illustrates the positive relationship between fractal dimensions and related pore volume. Micropores show a clearer correlation between D_{N1} and pore volume than mesopores and macropores do (Figure 12B). In shale reservoirs, heterogeneity and irregular pore structure are mostly caused by micropores, as demonstrated by Yang et al. (2014), and the fractal dimension in such shales indicates the degree of micropore development.

The growth of shale reservoir pores, particularly organic pores, is significantly influenced by TOC, which is a prerequisite for shale gas enrichment. The relationship between PV and TOC at each scale reveals that macropore volume has a positive correlation with TOC, indicating that high TOC content positively affects macropores development; for mesopores, there is no obvious relationship between TOC and mesopore volume; and for micropores, there is a weak negative relationship between the two (Figure 13A). It should be noted that sample 3 has a substantially greater TOC than the other samples, which may obfuscate the association between the other samples, hence it has been omitted from the graph in Figure 13A and Figure 14A.

The correlation analysis between the quartz content and the PV of each scale shows that the macropore volume is negatively correlated with the quartz content as a whole, but there is no obvious correlation between the mesopore and micropore volumes and the quartz content (Figure 13B). According to the negative relationship between macropore volume and quartz concentration, secondary quartz formed during diagenesis may be the primary source of quartz crystals. Because different types of clay minerals have vastly different morphological structures and physicochemical properties that

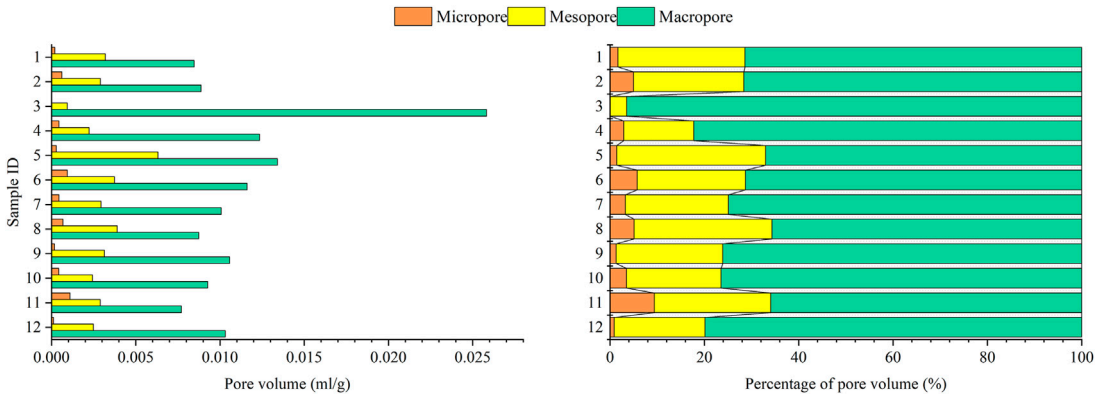

FIGURE 11
Pore volume and percentage of pore volume distributions based on IUPAC pore classification.

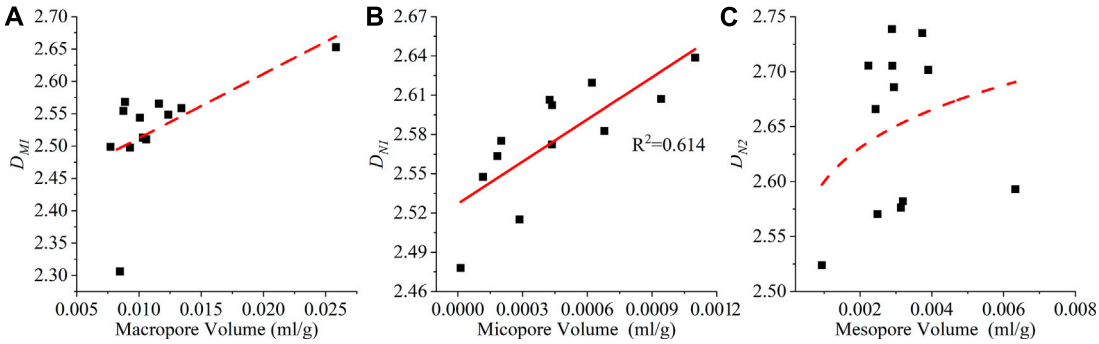

FIGURE 12
Relationship between fractal dimensions and corresponding pore volume: **(A)** D_{M1}; **(B)** D_{N1}; **(C)** D_{N2}.

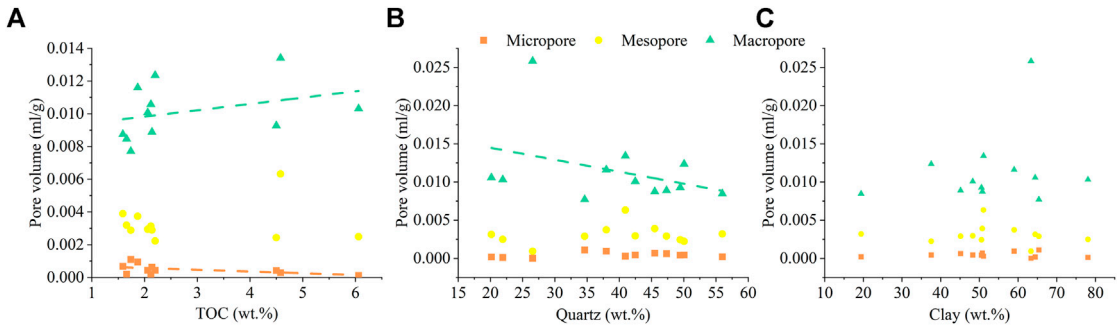

FIGURE 13
Relationship between PV and compositions of transitional shale: **(A)** TOC; **(B)** Quartz; **(C)** Clay.

have different effects on pore growth in shale reservoirs, there is no clear relationship between clay and pore volume at any scale (Figure 13C).

TOC shows no significant relationship with D_{M1}, and is negatively correlated with both D_{N1} and D_{N2} (Figure 14A). This phenomenon contradicts the shale recorded in the Qingshankou

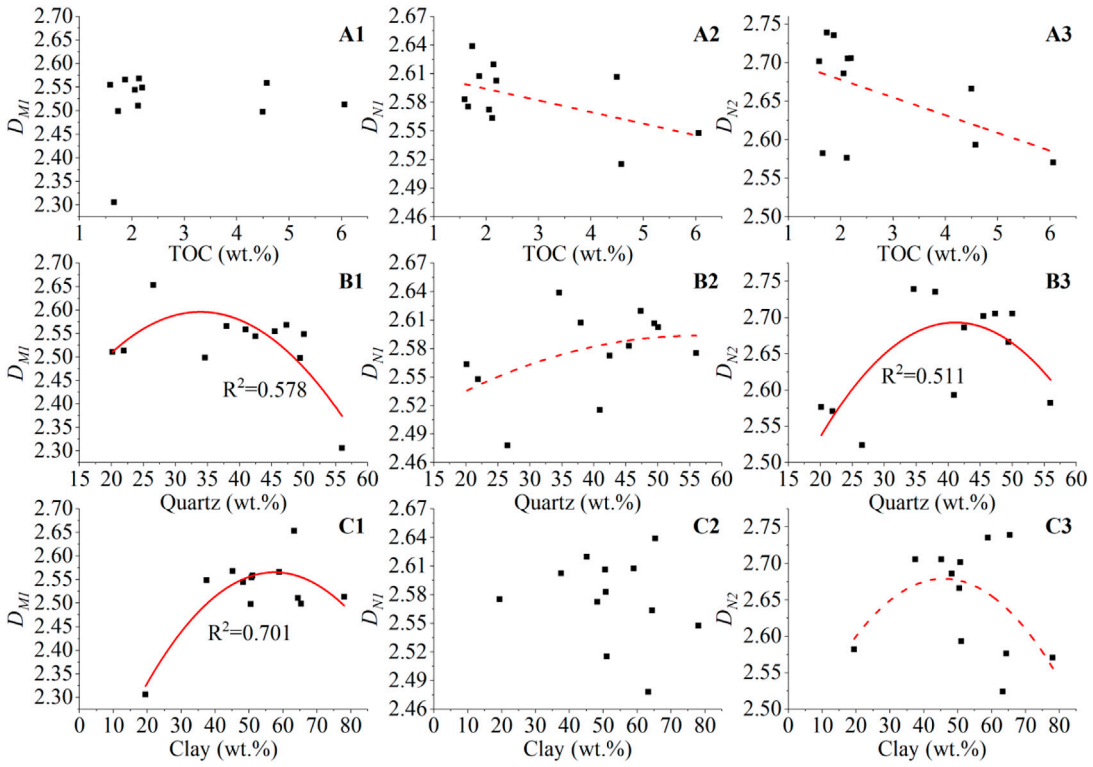

FIGURE 14
Relationship of fractal dimensions versus shale compositions. **(A)** total organic carbon (TOC) vs. fractal dimensions: (1) D_{M1}, (2) D_{N1}, (3) D_{N2}; **(B)** quartz contents vs. fractal dimensions: (1) D_{M1}, (2) D_{N1}, (3) D_{N2}; **(C)** clay contents vs. fractal dimensions: (1) D_{M1}, (2) D_{N1}, (3) D_{N2}.

Formation lacustrine shale (Wang et al., 2015), where the relationship indicates a decrease followed by an increase, with a minimum value of *D* at about 3% TOC content. Our findings varied from previously published maritime shale gas data (Yang et al., 2014; Xi et al., 2018), in which *D* was positively linked with TOC concentration. It is discovered that the discrepancy might be due to differences in sedimentary facies by further analyzed related studies. The transitional facies are the Taiyuan Formation shale's sedimentary facies, whereas other researchers have concentrated on lacustrine and marine shales.

The relationship between quartz minerals and various fractal dimensions is not the same, there is a parabolic correlation between D_{M1} and D_{N2}, and a positive correlation with D_{N1} (Figure 14B). Some scholars believed that the quartz content is independent of the fractal dimension (Xi et al., 2018), which contradicted the current findings, and the varied behavior of quartz at different phases merits further exploration. Clay minerals show a parabolic relationship with D_{M1} and D_{N2}, and no significant correlation with D_{N1} (Figure 14C). The correlation analysis between clay mineral content and fractal dimensions at different scales shows that the maximum non-homogeneity occurs around 50% of clay mineral content. The correlation with the fractal dimension of the pore surface is not strong, indicating that clay is not the main cause of hole surface roughness

It is discovered that the connections between fractal dimension and shale composition are typically nonlinear. This was consistent with previous researchers' findings that shale reservoirs were sensitive to multiple geological variables that interact with one another and had a complicated pore network (Ross & Bustin, 2009). In the previous analysis, the Taiyuan Formation and marine and lacustrine shale samples showed different correlations in fractal and component correlations, and even some components were close in content. This phenomenon can be attributed to differences in depositional environments, as we know that different depositional environments bring about differences in OM types, sources of quartz, types of clay minerals, and more. The difference between Taiyuan Formation shale and marine and lacustrine shale also indicates that the study of the sedimentary process deserves attention.

6 Conclusion

The scanning electron microscopy, mercury intrusion porosimetry, and N_2 adsorption experiments were employed in this work to examine the pore morphology and structure of 12 transitional shale samples. The mercury intrusion porosimetry and N_2 adsorption were applicable complementary techniques to investigate the diverse characteristics of shale. The optimal splicing point was successfully chosen based on the physical meaning of fractal dimension combined with mercury intrusion porosimetry and N_2 adsorption technology, and a full-scale pore size distribution image was obtained. Furthermore, the relationships between the basic components of shale and the fractal dimension have been studied. The following five conclusions have been obtained.

(1) The scanning electron microscopy imageries provided qualitative information on the Taiyuan shale pore size and morphology. The pore structure and network in the shale were very complicated. Micropores and mesopores within organic matter, interP pores between mineral grains, and microfractures were the most common types of pores in the Taiyuan shale.
(2) The pore structure and size range of the Taiyuan shale was quantitatively characterized by the mercury intrusion porosimetry and N_2 adsorption experiments. According to the mercury intrusion porosimetry analyses, unimodal and multimodal pore size distributions can be found, with most pores ranging in size by approximately 0.2 mm. For micropores and mesopores, multimodal pore size distributions were found based on the results of N_2 adsorption characterization. Typically, the maximum peak value of the differential pore volume was usually around 50 nm.
(3) The pores of the Taiyuan shale samples had fractal geometries. The fractal dimension D_{M1} was determined via the mercury intrusion porosimetry experiments, and its value ranged from 2.3060 to 2.6528. The Taiyuan shale had significantly different adsorption behaviors and fractal characteristics at relative pressures <0.5 and >0.5. Two fractal dimensions, D_{N1} and D_{N2}, can be determined using the Frenkel–Halsey–Hill model, with D_{N1} ranging between 2.4780 and 2.6387, and D_{N2} ranging between 2.5239 and 2.7388.
(4) The Taiyuan shale samples had a wide pore size distribution and macropores were the main source of the pore volume. The mean percentages of micropores, mesopores, and macropores are 3.4%, 21.7%, and 74.9%, respectively.
(5) There were various correlations between fractal dimension, pore volume, and basic composition of shale. The correlation between fractal dimension and corresponding pore volume was positive, the correlation between pore volume and component was weak, but the correlation between fractal and component was mostly non-linear. The good correlation between fractals reflected the validity of the fractal theory in the characterization of pore inhomogeneity.

Data availability statement

The original contributions presented in the study are included in the article/Supplementary material, further inquiries can be directed to the corresponding author.

Author contributions

Conceptualization: SS, JH; Methodology: SS, XZ; Formal analysis and investigation: HW, ZY, and JW; Writing–original draft preparation: SS; Writing–review and editing: SS, JH; Funding acquisition: JH, XZ; Resources: HW, TY, and WW; Supervision: JH.

Funding

The National Key R&D Program of China (2021YFC2902003); The National Natural Science Foundation of China (41702170).

Conflict of interest

The authors declare that the research was conducted in the absence of any commercial or financial relationships that could be construed as a potential conflict of interest.

Publisher's note

References

Burnaman, M. D., and Shelton, J. (2009). Shale gas play screening and evaluation criteria. *China Pet. Explor.* 14 (03), 51–64.

Cai, Y. D., Liu, D. M., Yao, Y. B., Li, J. Q., and Liu, J. L. (2011). Fractal characteristics of coal pores based on classic geometry and thermodynamics models. *Acta Geol. Sin. - Engl. Ed.* 85 (5), 1150–1162. doi:10.1111/j.1755-6724.2011.00547.x

Chen, S. B., Gong, Z., Li, X. Y., Wang, H. J., Wang, Y., and Zhang, Y. K. (2021a). Pore structure and heterogeneity of shale gas reservoirs and its effect on gas storage capacity in the Qiongzhusi Formation. *Geosci. Front.* 12 (6), 101244. doi:10.1016/j.gsf.2021.101244)

Chen, Y., Jiang, C., Leung, J. Y., Wojtanowicz, A. K., and Zhang, D. (2021b). Multiscale characterization of shale pore-fracture system: Geological controls on gas transport and pore size classification in shale reservoirs. *J. Petroleum Sci. Eng.* 202, 108442. Article 108442. doi:10.1016/j.petrol.2021.108442

Chen, Y. L., Qin, Y., Wei, C. T., Huang, L. L., Shi, Q. M., Wu, C. F., et al. (2018). Porosity changes in progressively pulverized anthracite subsamples: Implications for the study of closed pore distribution in coals. *Fuel* 225, 612–622. doi:10.1016/j.fuel.2018.03.164

Clarkson, C. R., Solano, N., Bustin, R. M., Bustin, A. M. M., Chalmers, G. R. L., He, L., et al. (2013). Pore structure characterization of North American shale gas reservoirs using USANS/SANS, gas adsorption, and mercury intrusion. *Fuel* 103, 606–616. doi:10.1016/j.fuel.2012.06.119

Curtis, J. B. (2002). Fractured shale-gas systems. *Aapg Bull.* 86 (11), 1921–1938. doi:10.1306/61EEDDBE-173E-11D7-8645000102C1865DAvailable at: https://www.scopus.com/inward/ record.uri?eid=2-s2.0-0036860861&partnerID=40&md5=92ff1a872d03ebc16123055d2458e727

Dai, H. L., Su, Y. A., Kuang, L. C., Liu, J. Z., Gu, D. Z., and Zou, C. N. (2021). Contemplation on China's energy-development strategies and initiatives in the context of its carbon neutrality goal. *Engineering* 7 (12), 1684–1687. doi:10.1016/j.eng.2021.10.010

Hazra, B., Chandra, D., Singh, A. K., Varma, A. K., Mani, D., Singh, P. K., et al. (2019). Comparative pore structural attributes and fractal dimensions of Lower Permian organic-matter-bearing sediments of two Indian basins: Inferences from nitrogen gas adsorption. *Energy Sources Part A Recovery Util. Environ. Eff.* 41 (24), 2975–2988. doi:10.1080/15567036.2019.1582737

Hu, H., Hao, F., Guo, X., Yi, J., Shu, Z., Bao, H., et al. (2019). Effect of lithofacies on the pore system of over-mature Longmaxi shale in the Jiaoshiba area, Sichuan Basin, China. *Mar. Petroleum Geol.* 109, 886–898. doi:10.1016/j.marpetgeo.2019.06.050

Jarvie, D. M., Hill, R. J., Ruble, T. E., and Pollastro, R. M. (2007). Unconventional shale-gas systems: The Mississippian Barnett Shale of north-central Texas as one model for thermogenic shale-gas assessment. *Am. Assoc. Pet. Geol. Bull.* 91 (4), 475–499. doi:10.1306/12190606068

Jiang, F., Chen, D., Chen, J., Li, Q., Liu, Y., Shao, X., et al. (2016). Fractal analysis of shale pore structure of continental gas shale reservoir in the Ordos Basin, NW China. *Energy fuels.* 30 (6), 4676–4689. doi:10.1021/acs.energyfuels.6b00574

Jiang, S., Xiao, D., Tang, X., Xing, F., Xiang, C., Pahnke, P., et al. (2017). Nano to micron-sized pore types and pore size distribution revealed by innovative test methods-case studies from fluvial, lacustrine and marine tight and shale oil and gas plays in China and US. *J. Nanosci. Nanotechnol.* 17 (9), 6296–6306. doi:10.1166/jnn.2017.14433

Jiao, K., Yao, S. P., Liu, C., Gao, Y. Q., Wu, H., Li, M. C., et al. (2014). The characterization and quantitative analysis of nanopores in unconventional gas reservoirs utilizing FESEM-FIB and image processing: An example from the lower Silurian Longmaxi Shale, upper Yangtze region, China. *Int. J. Coal Geol.* 128, 1–11. doi:10.1016/j.coal.2014.03.004

Ju, W., Shen, J., Qin, Y., Meng, S., Wu, C., Shen, Y., et al. (2017). *In-situ* stress state in the Linxing region, eastern Ordos Basin, China: Implications for unconventional gas exploration and production. *Mar. Petroleum Geol.* 86, 66–78. doi:10.1016/j.marpetgeo.2017.05.026

Kuila, U., and Prasad, M. (2013). Specific surface area and pore-size distribution in clays and shales. *Geophys. Prospect.* 61 (2), 341–362. doi:10.1111/1365-2478.12028

Li, G., Qin, Y., Wu, M., Zhang, B., Wu, X., Tong, G., et al. (2019). The pore structure of the transitional shale in the Taiyuan formation, Linxing area, Ordos Basin. *J. Petroleum Sci. Eng.* 181, 106183. doi:10.1016/j.petrol.2019.106183

Li, Y. B., Song, D. Y., Liu, S. M., Ji, X. F., and Hao, H. J. (2021b). Evaluation of pore properties in coal through compressibility correction based on mercury intrusion porosimetry: A practical approach. *Fuel* 291, 120130. doi:10.1016/j.fuel.2021.120130

Li, Y., Song, D., Liu, S., Ji, X., and Hao, H. (2021a). Evaluation of pore properties in coal through compressibility correction based on mercury intrusion porosimetry: A practical approach. *Fuel* 291, 120130. doi:10.1016/j.fuel.2021.120130

Li, Y., Tang, D., Wu, P., Niu, X., Wang, K., Qiao, P., et al. (2016). Continuous unconventional natural gas accumulations of Carboniferous-Permian coal-bearing strata in the Linxing area, northeastern Ordos basin, China. *J. Nat. Gas Sci. Eng.* 36, 314–327. doi:10.1016/j.jngse.2016.10.037

Liu, B., Gao, Y., Liu, K., Liu, J., Ostadhassan, M., Wu, T., et al. (2021a). Pore structure and adsorption hysteresis of the middle Jurassic Xishanyao shale formation in the Southern Junggar Basin, northwest China. *Energy Explor. Exploitation* 39 (3), 761–778. doi:10.1177/0144598720985136

Liu, B., Jin, L., and Hu, C. (2019a). Fractal characterization of silty beds/laminae and its implications for the prediction of shale oil reservoirs in Qingshankou formation of Northern Songliao Basin, Northeast China. *Fractals* 27 (1), 1940009. doi:10.1142/s0218348x19400097)

Liu, B., Yan, M., Sun, X., Bai, Y., Bai, L., and Fu, X. (2020). Microscopic and fractal characterization of organic matter within lacustrine shale reservoirs in the first member of cretaceous Qingshankou Formation, songliao basin, Northeast China. *J. Earth Sci.* 31 (6), 1241–1250. doi:10.1007/s12583-020-1345-3

Liu, W., Wang, G., Han, D. Y., Xu, H., and Chu, X. Y. (2021b). Accurate characterization of coal pore and fissure structure based on CT 3D reconstruction and NMR. *J. Nat. Gas Sci. Eng.* 96, 104242. Article 104242. doi:10.1016/j.jngse.2021.104242

Liu, Y., Zhu, Y., Wang, Y., and Chen, S. (2019b). Fractal characteristics of nanoscale pores in shale and its implications on methane adsorption capacity. *Fractals* 27 (1), 1940014. doi:10.1142/s0218348x19400140)

Ross, D. J. K., and Bustin, R. M. (2009). The importance of shale composition and pore structure upon gas storage potential of shale gas reservoirs. *Mar. Petroleum Geol.* 26 (6), 916–927. doi:10.1016/j.marpetgeo.2008.06.004

Shen, Y., Qin, Y., Wang, G. G. X., Guo, Y., Shen, J., Gu, J., et al. (2017). Sedimentary control on the formation of a multi-superimposed gas system in the development of key layers in the sequence framework. *Mar. Petroleum Geol.* 88, 268–281. doi:10.1016/j.marpetgeo.2017.08.024

Shu, Y., Sang, S.-X., Lin, Y.-X., Zhou, X.-Z., Wang, H., and Wang, Z.-L. (2021). The influence of magmatic-hydrothermal activities on porosity and permeability of sandstone reservoirs in the Linxing area, Ordos Basin, Northern China. *J. Asian Earth Sci.* 213, 104741. Article 104741. doi:10.1016/j.jseaes.2021.104741

Sun, M. D., Zhao, J., Pan, Z. J., Hu, Q. H., Yu, B. S., Tan, Y. L., et al. (2020). Pore characterization of shales: A review of small angle scattering technique. *J. Nat. Gas Sci. Eng.* 78, 103294. Article 103294. doi:10.1016/j.jngse.2020.103294

Thommes, M., Kaneko, K., Neimark, A. V., Olivier, J. P., Rodriguez-Reinoso, F., Rouquerol, J., et al. (2015). Physisorption of gases, with special reference to the evaluation of surface area and pore size distribution (IUPAC Technical Report). *Pure Appl. Chem.* 87 (9-10), 1051–1069. doi:10.1515/pac-2014-1117

Wang, F., and Zai, Y. (2021). Fractal and multifractal characteristics of shale nanopores. *Results Phys.* 25, 104277. doi:10.1016/j.rinp.2021.104277

Wang, M., Xue, H., Tian, S., Wilkins, R. W. T., and Wang, Z. (2015). Fractal characteristics of upper cretaceous lacustrine shale from the songliao basin, NE China. *Mar. Petroleum Geol.* 67, 144–153. doi:10.1016/j.marpetgeo.2015.05.011

Wang, P., Zhang, C., Li, X., Zhang, K., Yuan, Y., Zang, X., et al. (2020). Organic matter pores structure and evolution in shales based on the he ion microscopy (him): A case study from the triassic yanchang, lower silurian longmaxi and lower cambrian niutitang shales in China. *J. Nat. Gas Sci. Eng.* 84, 103682. doi:10.1016/j.jngse.2020.103682

Wang, Y., Liu, L., and Cheng, H. (2021). Gas adsorption characterization of pore structure of organic-rich shale: Insights into contribution of organic matter to shale pore network. *Nat. Resour. Res.* 30 (3), 2377–2395. doi:10.1007/s11053-021-09817-5

Wang, Y., Zhu, Y., Liu, S., and Zhang, R. (2016). Pore characterization and its impact on methane adsorption capacity for organic-rich marine shales. *Fuel* 181, 227–237. doi:10.1016/j.fuel.2016.04.082

Xi, Z., Tang, S., Wang, J., Yi, J., Guo, Y., and Wang, K. (2018). Pore structure and fractal characteristics of niutitang shale from China. *Minerals* 8 (4), 163. Article 163. doi:10.3390/min8040163

Xiao, Q., Yang, Z., Wang, Z., Qi, Z., Wang, X., and Xiong, S. (2020). A full-scale characterization method and application for pore-throat radius distribution in tight oil reservoirs. *J. Petroleum Sci. Eng.* 187, 106857. doi:10.1016/j.petrol.2019.106857

Xu, H., Tang, D., Zhao, J., and Li, S. (2015). A precise measurement method for shale porosity with low-field nuclear magnetic resonance: A case study of the carboniferous-permian strata in the linxing area, eastern Ordos Basin, China. *Fuel* 143, 47–54. doi:10.1016/j.fuel.2014.11.034

Xu, L., Yang, K., Wei, H., Liu, L., Li, X., Chen, L., et al. (2021). Full-scale pore structure characteristics and the main controlling factors of mesoproterozoic xiamaling shale in zhangjiakou, hebei, China. *Nanomaterials* 11 (2), 527. doi:10.3390/nano11020527

Xu, Y., Wang, Y., Yuan, H., Zhang, D., Agostini, F., and Skoczylas, F. (2018). Pore structure characterization of tight sandstone from Sbaa Basin, Algeria: Investigations using multiple fluid invasion methods. *J. Nat. Gas Sci. Eng.*, 59, 414–426. doi:10.1016/j.jngse.2018.09.021

Yang, F., Ning, Z., and Liu, H. (2014). Fractal characteristics of shales from a shale gas reservoir in the Sichuan Basin, China. *Fuel* 115, 378–384. doi:10.1016/j.fuel.2013.07.040

Zhang, L., Lu, S., Xiao, D., and Gu, M. (2017). Characterization of full pore size distribution and its significance to macroscopic physical parameters in tight glutenites. *J. Nat. Gas Sci. Eng.* 38, 434–449. doi:10.1016/j.jngse.2016.12.026

Zhang, S., Tang, S., Zhang, J., and Pan, Z. (2018). Pore structure characteristics of China sapropelic coal and their development influence factors. *J. Nat. Gas Sci. Eng.* 53, 370–384. doi:10.1016/j.jngse.2018.03.022

Zheng, S., Yao, Y., Liu, D., Cai, Y., and Liu, Y. (2019a). Nuclear magnetic resonance surface relaxivity of coals. *Int. J. Coal Geol.* 205, 1–13. doi:10.1016/j.coal.2019.02.010

Zheng, S., Yao, Y., Zhang, S., Liu, Y., and Yang, J. (2019b). Insights into multifractal characterization of coals by mercury intrusion porosimetry. *Energies* 12 (24), 4743. doi:10.3390/en12244743)

Zou, C., Pan, S., and Hao, Q. (2020). On the connotation, challenge and significance of China's "energy independence" strategy. *Petroleum Explor. Dev.* 47 (2), 449–462. doi:10.1016/S1876-3804(20)60062-3

frontiers | Frontiers in Earth Science

TYPE Original Research
PUBLISHED 29 August 2022
DOI 10.3389/feart.2022.978647

OPEN ACCESS

EDITED BY
Luan Thanh Pham,
VNU University of Science, Vietnam

REVIEWED BY
Bikash Sinha,
Schlumberger Doll Research,
United States
Nicolás Barbosa,
Université de Lausanne, Switzerland

*CORRESPONDENCE
Jack Dvorkin,
jackdvorkin007@gmail.com

SPECIALTY SECTION
This article was submitted to Earth and Planetary Materials,
a section of the journal
Frontiers in Earth Science

RECEIVED 26 June 2022
ACCEPTED 27 July 2022
PUBLISHED 29 August 2022

CITATION
Muqtadir A, Al-Dughaimi S, Alzaki T and Dvorkin J (2022), Vertical velocity at hydrostatic and anisotropic stresses. *Front. Earth Sci.* 10:978647.
doi: 10.3389/feart.2022.978647

Vertical velocity at hydrostatic and anisotropic stresses

Arqam Muqtadir, Saud Al-Dughaimi, Taqi Alzaki and Jack Dvorkin*

College of Petroleum Engineering and Geosciences, King Fahd University of Petroleum and Minerals, Dhahran, Saudi Arabia

Sonic and dipole wireline tools measure V_p and V_s along the vertical direction. The state of stress in the subsurface is predominantly anisotropic, while most laboratory experiments measuring the dynamic elastic properties are conducted under hydrostatic stress. The question we ask is whether such laboratory experiments provide the velocities that are close to those measured in the vertical wellbore where the stresses are anisotropic. To address this question, we conducted ultrasonic pulse transmission experiments on several room-dry rock samples. The comparison was made between the P- and S-wave velocities obtained at pure hydrostatic loading conditions and those at a smaller hydrostatic stress with added axial stress, so that the total stress along the axis of a cylindrical plug was the same as under pure hydrostatic loading. These differences were significant in the extreme case of only 1 MPa hydrostatic confining stress with the axial stress increasing up to 40 MPa. However, as the hydrostatic (confining) stress increased, the differences between the velocities along the axis of the sample became smaller and smaller. For example, at 1 MPa confining and 30 MPa axial stress, the relative difference in V_p was about 10%, while that in V_s was about 20%. However, at 10 MPa confining stress, these differences became about 3% and 6%, respectively, and further decreased as the confining stress increased. This means that even at strong *in-situ* contrasts between the vertical and horizontal stresses, the results of laboratory hydrostatic experiments can be used for *in-situ* velocity estimates. These results also appear to be consistent with a theoretical model that predicts the directional velocities at any triaxial stress conditions from those measured versus hydrostatic stress.

KEYWORDS

velocity, anisotropy, stress, elastic moduli, hydrostatic

Introduction

The elastic-wave velocities in porous rocks are practically always sensitive to stress, especially so for the samples extracted from the deep subsurface. Many laboratory tests indicate that both the P- and S-wave velocities increase with increasing stress. The commonly accepted reason for such behavior is the closure of compliant cracks present in the pore space, as well as the stiffening of compliant grain contacts (e.g., Hudson, 1980; Johnson, 1985). These subtle features may occupy only a small portion of the entire rock

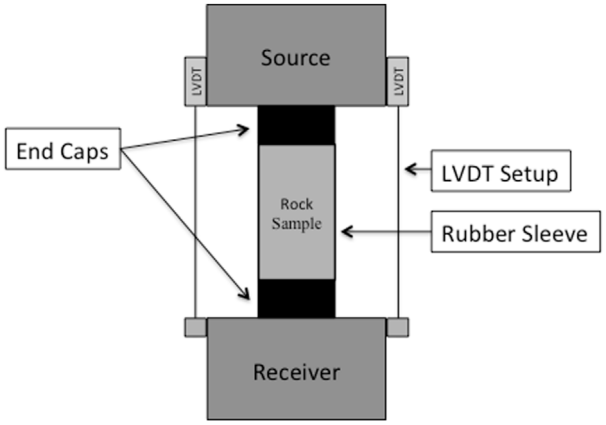

FIGURE 1
Schematic depiction of the experimental setup.

volume, yet their contribution to the compliance of rock material is enormous. The smaller the aspect ratio of the crack the more compliant it is (e.g., Hudson, 1980). Hence, once these cracks close, the stiffnesses of the sample and the respective velocities strongly increase.

Literature on stress-induced anisotropy is massive. Arguably, the first quantitative and rigorous report on stress-related velocity anisotropy is by Nur and Simmons (1969). The authors show that a granite sample subject to uniaxial stress makes the P-wave velocity highest along the direction of the applied stress and makes this velocity substantially slower along the direction normal to the stress. Moreover, this work, for the first time reported the so-called S-wave splitting, meaning that these polarized waves travel with different speeds in any direction. S-wave splitting, also called seismic birefringence, is the phenomenon that occurs when a polarized shear wave enters an anisotropic medium, whereby the incident S-wave splits into two polarized shear waves.

This work was followed by Nur's (1971) theoretical investigation on the effect of the directional distribution of cracks on velocity anisotropy. These theoretical results matched the experimental data obtained on two granite samples.

These two pioneering publication have been since followed by an avalanche of experimental and theoretical publications. It is simply impossible to refer to all of them here. Instead, we will quote only selected ones.

Crampin (1985) shows that shear-wave splitting in seismographs may be interpreted, under a set of assumptions, in terms of crack orientation, thus also implying the anisotropy of permeability in reservoirs. Zamora and Poirier (1990) experimentally investigate the P-wave velocity anisotropy, as well as S-wave splitting in Fountainebleau sandstone in two orthogonal directions. They also show that the crack orientation inferred from these experiments and using the Crampin (1985) theory qualitatively match the orientations observed in the respective Scanning Electron Microscope (SEM) images. An experimental study by Dillen et al. (1999) explores stress-induced velocity anisotropy due to triaxial state of stress in a low-porosity sandstone. Once again, these authors confirm the already known fact that anisotropic stresses result in anisotropic speeds of wave propagation. Another elaborate study on stress-induced velocity anisotropy using a spherical sample is by Nadri et al. (2011). Later, Bhuiyan and Holt (2016) presented experimental results on velocity anisotropy in dry and saturated sand as the axial stress varied between 1 and 15 MPa.

Recent publications by Gong et al. (2018) and Ramos et al. (2019) explore, experimentally and theoretically, the effects of clay mineralogy and lamination, respectively, on elastic anisotropy in shale samples. Let us also bring the reader's attention to a recent important publication by Barbosa et al. (2019), where the authors estimate fracture compliance from attenuation and velocity analysis using full-waveform wireline data.

Because the elastic anisotropy is sometimes related to crack orientation that, in turn, may affect the transport property anisotropy, many attempts have been made to infer the latter from the former. One of the most recent examples is by Falcon-Suarez et al. (2020) whose experiments indicate that in a weakly consolidated sandstone, the stress orientation affects the elastic and electrical properties in a congruent way. Recent work by Cilli and Chapman (2021) presents a fundamental theoretical analysis linking the elastic and electrical properties of rocks with the crack aspect ratio being a critical variable.

Earlier rigorous experimental and theoretical studies linking the elastic to permeability anisotropy are by Rasolofosaon and Zinszner (2002), as well as by Gueguen and Schubnel (2003). Teng (1998) explores relations between the seismic anisotropy of fractured formations and fluid flow. This study also provides an extensive overview of the theories of fracture-induced elastic anisotropy.

Needless to say that stress-induced anisotropy (and anisotropy in general) has provided a comfortable target for numerous, often unnecessary elaborate, theories. Once again, we have no way of quoting all these theories here. Ciz and Shapiro (2009) discuss the applicability of theoretically derived stress-induced anisotropy in transversely isotropic media to experimental data from shale samples. A series of publications by Gurevich et al. (2011); Collet and Gurevich (2013); and Collet et al. (2014) puts forward an elaborate analytical apparatus for modeling elastic anisotropy resulting from triaxial state of stress. Bandyopadhyay (2009) presented an exhaustive theoretical study on stress-induced anisotropy invoking third-order elasticity, as well as discussing contact-based effective-medium models for stress-induced anisotropy in granular materials.

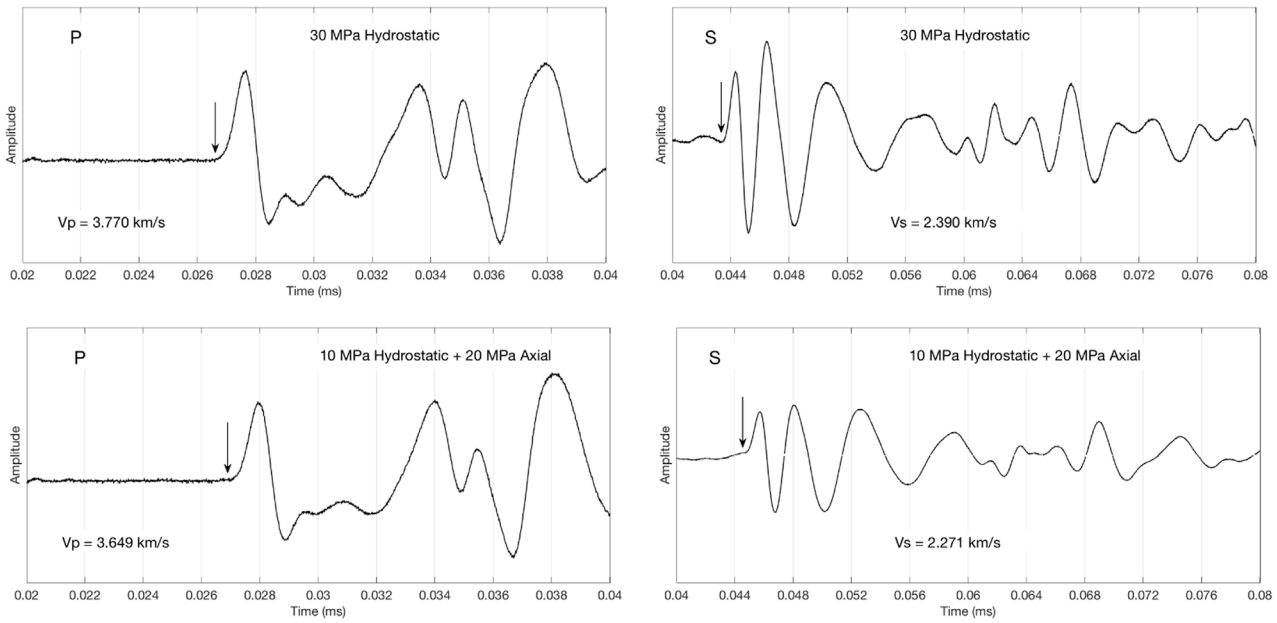

FIGURE 2
P-wave (left) and S-wave (right) waveforms in Berea sandstone at 30 MPa pure hydrostatic stress (top) and 10 MPa hydrostatic stress plus 20 MPa axial stress (bottom), equivalent to 30 MPa total axial stress. The arrows show the first arrival picks.

It is important to mention a substantial body of theoretical work by Mark Chapman and collaborators discussing elastic and attenuation anisotropy, as well as the effects of the pore fluid saturation and viscosity and frequency on velocity anisotropy (e.g., Chapman et al., 2003; Chapman, 2009; and Amalokwu et al., 2015).

Additional references on the subject follow. Smith (1963) reviews various theories existed at the time and compares them to experimental data concentrating mostly on the effect of shear wave birefringence in metals. A rigorous report discussing the theoretical and experimental aspects of stress-induced seismic anisotropy is by Rasolofosaon (1998). Yin (1992) presents pioneering experimental results on stress-induced attenuation and elastic anisotropy under three-dimensional polyaxial loading. Majmudar and Behringer (2005) present an experimental study on stress-induced anisotropy in granular materials. They address the fundamental phenomenon of the heterogeneity of the contact stress chains in such dry particulates under different boundary conditions. Hu et al. (2010) report the emergence of stress-induced anisotropy in sands due to cyclic loading and only using numerical two-dimensional discrete element method simulations. Johnson and Rasolofosaon (1996) discuss, in detail, stress-induced anisotropy in rocks on the basis of non-linear elasticity, as well as compare their theoretical results with the existing experimental data. Kuhn et al. (2015) employ three-dimensional discrete element method simulations, together with the Lattice-Boltzmann method for simulating fluid flow to numerically explore the elastic and permeability anisotropy in granular packs as a result of biaxial plane-strain compression with constant mean stress. An early experimental work on two-dimensional granular assemblies made of plastic is by Oda et al. (1985).

We believe that the most relevant and, coincidentally, elegant theoretical development came from Mavko et al. (1995), by far preceding (and perhaps triggering) the avalanche of the later theories. These authors derived a simple analytical transform to predict stress-induced elastic anisotropy in stress-sensitive materials just from the isotropic V_p and V_s measured versus hydrostatic pressure. This is the theory we will use here to support and explain our new experimental data.

The question that triggered the new experimental work presented here is whether the elastic-wave velocities measured in the laboratory under hydrostatic stress conditions are approximately the same as the vertical velocities in the crust where the stresses are anisotropic but the vertical stress is the same as the hydrostatic stress in the laboratory. Perhaps the answer is buried in the multitude of earlier experimental and theoretical results. Yet, to the best of our knowledge, nobody before has explicitly asked this question and provided a clear answer.

To this end and to clearly answer the question posed, we have conducted experiments on 6 samples, including sandstones, glass beads, and carbonates. These experiments were done 1) at pure hydrostatic stress and 2) at a uniaxial state of stress. In the latter experiments, the confining hydrostatic stress was kept constant,

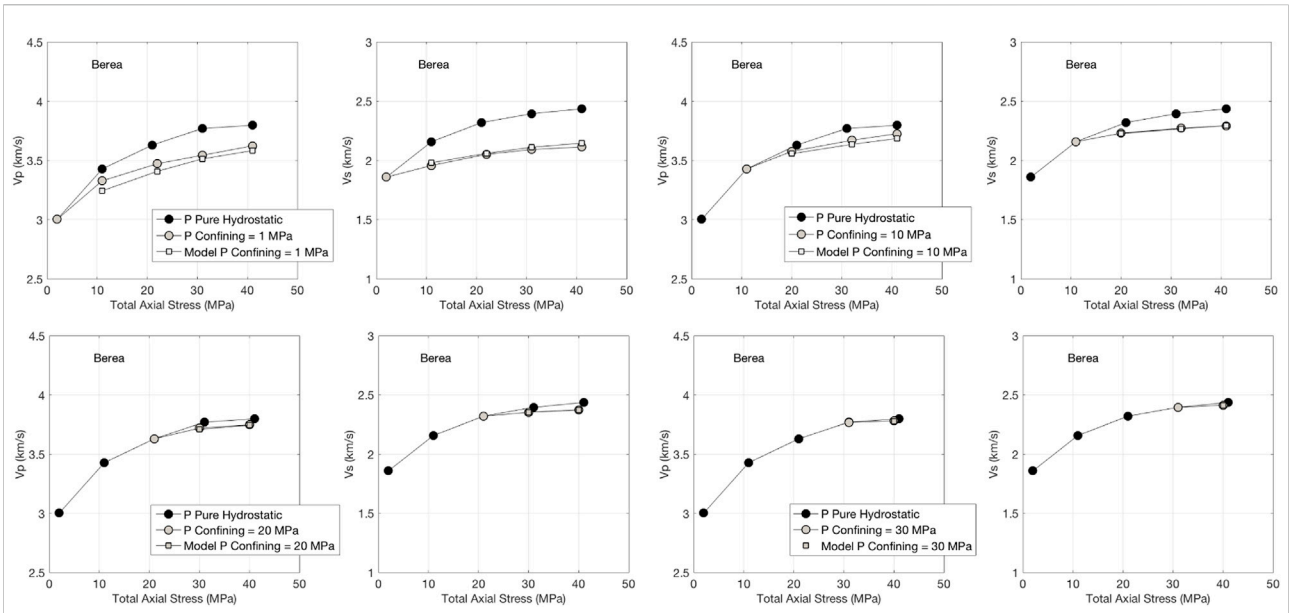

FIGURE 3
P-wave and S-wave velocities in Berea sandstone for pure hydrostatic loading as denoted by black symbols; and fixed hydrostatic stress 1 and 10 MPa (top) and 20 and 30 MPa (bottom) with the increasing axial stress as denoted by open symbols. The latter results are compared to those from the Mavko et al. (1995) model (denoted by open-square symbols).

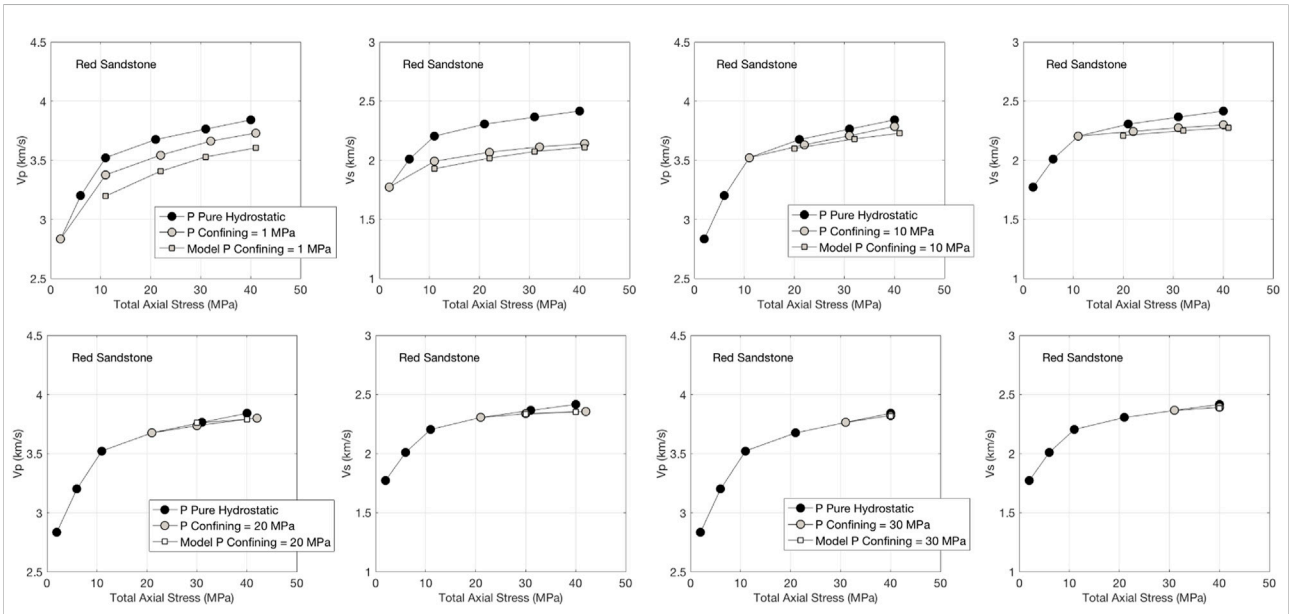

FIGURE 4
Same as Figure 3, but for Red sandstone.

while the axial stress was gradually increased. The vertical velocities were compared to those measured at pure hydrostatic stress matching the total axial stress.

This comparison indicates that the answer to the posed question is "yes, approximately." These results are confirmed by the Mavko et al. (1995) theory.

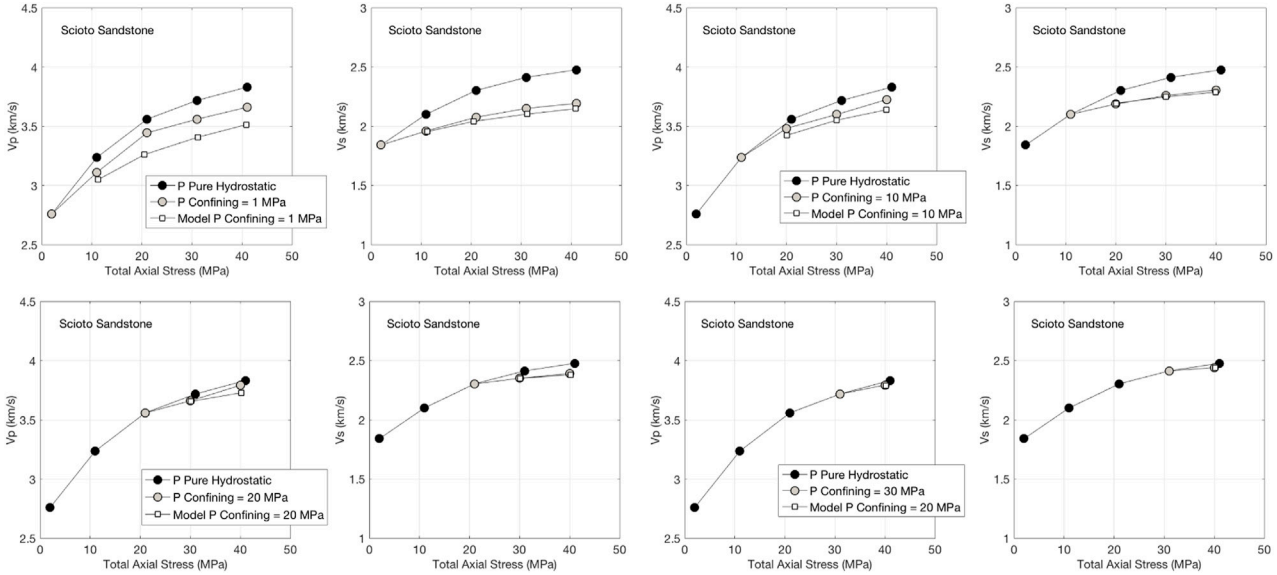

FIGURE 5
Same as Figure 3, but for Scioto sandstone.

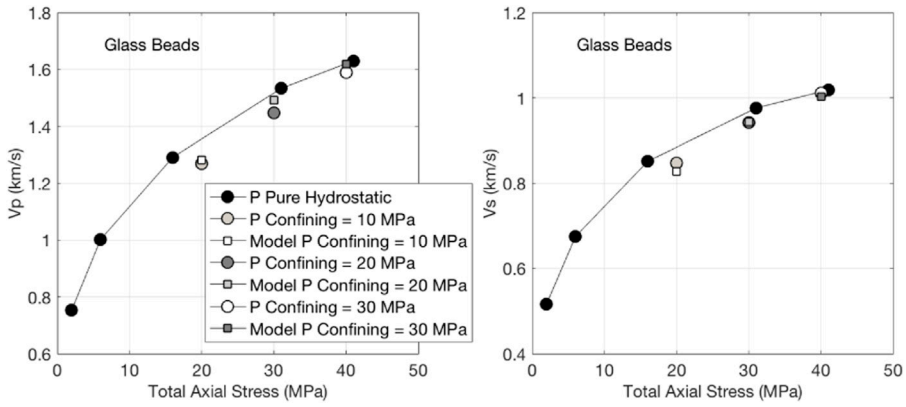

FIGURE 6
Same as Figure 3, but for glass beads.

Theory

The Mavko et al. (1995) theory allows for inferring the velocities along the axial direction at anisotropic uniaxial loading from those measured at pure hydrostatic stress. The essence of this theory is that the part of the pore space represented by compliant cracks is characterized by compressional and shear compliances that are derived from V_p and V_s measured at hydrostatic loading.

Two important assumptions allow us to transform the compliances under hydrostatic stress to those under uniaxial stress: 1) The compliant cracks that are solely responsible for the stress dependence of the elastic-wave velocities are planar and, hence, their normal and shear deformations can be decoupled from each other. So is the in-plane and out-of-plane deformation. Mathematically this means that the crack compliance tensor is sparse. 2) For a thin crack under any stress field, it is predominantly the normal stress component, as resolved on the crack's face, that is responsible for the crack's closure and, hence, for the stress-dependence of the elastic properties of the rock containing these cracks.

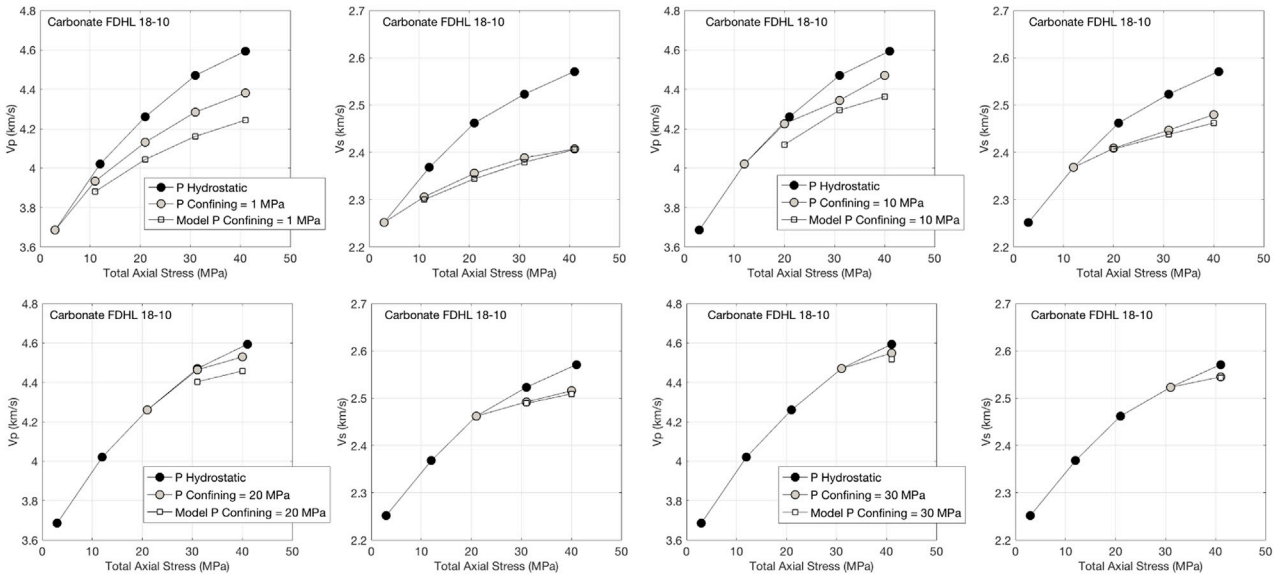

FIGURE 7
Same as Figure 3, but for carbonate CA 18-10.

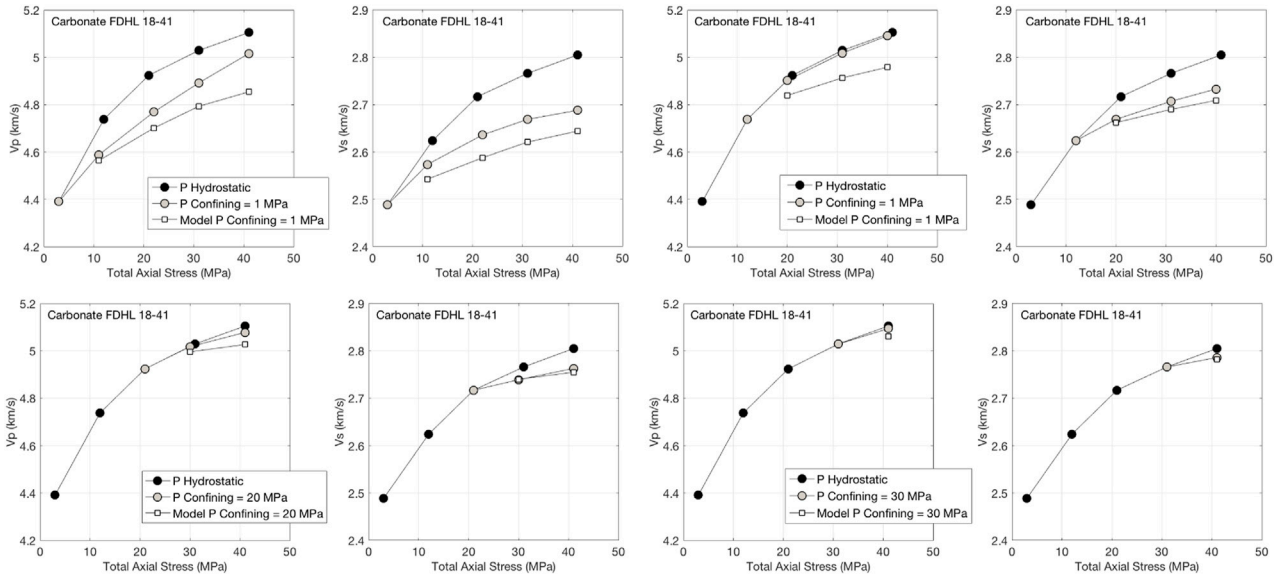

FIGURE 8
Same as Figure 3, but for carbonate CA 18-41.

These assumptions allow one to use the elastic-wave velocities measured versus hydrostatic stress to be mapped to those at any applied anisotropic state of stress. Hence, the only required inputs are V_p and V_s obtained during hydrostatic loading.

This theory is formulated in terms of the compliance tensor S_{ijkl} that is defined as:

$$\delta\varepsilon_{ij} = S_{ijkl}(\sigma)\delta\sigma_{kl}, \quad (1)$$

TABLE 1 Samples used in the experiments, their porosities, mineralogies, and dimensions (length by diameter in inches).

Sample	Sample type	Porosity	Quartz	Clay	Calcite	Glass	Dimensions
Berea	Sandstone	0.1920	0.95	0.05	0.00	0.00	2.5 x 1.5
Red Sandstone	Sandstone	0.2103	0.90	0.10	0.00	0.00	2.0 x 1.5
Scioto	Sandstone	0.1330	0.80	0.20	0.00	0.00	3.0 x 1.5
Glass Beads	Granular	0.3400	0.00	0.00	0.00	1.00	2.0 x 1.0
CA 18-10	Carbonate	0.0931	0.00	0.00	1.00	0.00	2.0 x 1.0
CA 18-41	Carbonate	0.1089	0.00	0.00	1.00	0.00	2.0 x 1.0

where $\delta\varepsilon_{ij}$ are small increments of the stress tensor elements due to the small increments $\delta\sigma_{kl}$ of the stress tensor σ.

The change in the elastic compliance at any state of stress σ is:

$$\Delta S_{ijkl}(\sigma) = S_{ijkl}(\sigma) - S^0_{ijkl} = \sum_q \phi^{(q)}(\sigma) W^{(q)}_{ijkl}(\sigma), \quad (2)$$

where S^0_{ijkl} are the compliances at the ultimate (very large) stress at which all the compliant parts of the pores are closed, $\phi^{(q)}$ is the porosity of the q-th crack, and $W^{(q)}_{ijkl}$ is the q-th crack's compliance. This equation is general under the assumptions of (a) elastic behavior and (b) homogeneity of the mineral matrix.

Next, all cracks having approximately the same orientation are combined into $n < q$ sets of cracks. The unit vector $\hat{m}$ for each such set is defined as:

$$\hat{m} = (\sin\theta\cos\gamma, \sin\theta\sin\gamma, \cos\theta)^T, \quad (3)$$

where θ and γ are the Euler angles describing the orientation of the normal to each of the n-th crack set and T means transposition.

The final equation for the compliance increments versus stress σ is:

$$\Delta S_{ijkl}(\sigma) = \int_{\theta=0}^{\pi/2}\int_{\gamma=0}^{\pi} W^H_{rstu}(\hat{m}^T\sigma\hat{m})\beta^n_{ir}\beta^n_{js}\beta^n_{kl}\beta^n_{lu}\sin\theta d\theta d\gamma, \quad (4)$$

where W^H_{rstu} are the compliances determined from the *hydrostatic* experiments and β^n_{ij} are the direction cosines between each crack set coordinates axes and the global coordinate axes. All theoretical equations were coded in Matlab with the code supplied to us by the authors of the Mavko et al. (1995) theory.

Mavko et al. (1995) illustrate the applicability of their theory by using the Barre granite and Massillon sandstone examples. Here we apply this theory to the new experimental data reported in the previous sections. These theoretical computations are based on the pure hydrostatic velocity data shown as black circles in Figures 3–8. The resulting velocities computed at uniaxial stress are shown in the same figures as light squares and compared to the respective velocities measured at the same uniaxial stress (light circles). The theory is reasonably close to the data even in the presence of strong stress anisotropy with the confining stress 1 MPa. As this stress increases, the match between the theory and experiment further improves and becomes practically perfect at high stress.

Not only does this theoretical exercise somewhat validate our experimental data. It also presents a "yes" answer to the question posed that motivated this work.

Samples and experiments

A total of six samples were selected for this study, three sandstones, two carbonates, and loose glass beads. The three sandstone samples were low-clay-content medium porosity rocks. The glass beads used were well-sorted and had high sphericity. The two carbonates, essentially pure calcite, had porosity about 10%. The porosities and mineralogies of these samples are listed in Table 1, together with the dimensions of the samples.

The velocity measurements were conducted in AutoLab1500 machine manufactured by New England Research. It is a triaxial frame used for ultrasonic, triaxial, as well as permeability and resistivity tests. The ultrasonic module contains a set of piezoelectric sensors located in the coreholders with the frequency 750 kHz. The source sends three input impulses: one P- and two S-waves (the latter two with the normal to each other polarization) through the sample. The arrivals are captured at the receiver at the base of the coreholder.

Each sample was placed in a rubber sleeve (holder) subject to hydrostatic pressure exerted by the surrounding mineral oil. Additional vertical axial stress was applied by a piston through the end caps in the holder. All samples were room-dry. The length of the sample was recorded by a pair of linear variable differential transformers (LVDT). The schematic depiction of the experimental setup is shown in Figure 1.

The P- and S-wave velocities were computed by dividing the sample length by the signal arrival time (first break). The sample length used was variable as recorded by LVDT. The latter was picked at the first arrival as shown in Figure 2 (an example for Berea sandstone).

The P-wave arrival was picked at the first break while the S-wave arrivals were picked at the first trough (as shown in

Figure 2). These picks were first determined at high stress where the arrivals appeared very clear. Then the waveform features thus established were tracked to the lower-stress arrivals. The errors in velocity determination did not exceed 1%.

Each sample was subject to five separate experiments: 1) pure hydrostatic loading from zero to 40 MPa with a 10 MPa increment and 2) four constant confining stress stations of 1, 10, 20, and 30 MPa with the axial stress gradually increasing at each station with a 10 MPa increment. Maximum stress never exceeded 40 MPa. In all cases, the samples were subjected to several loading/unloading cycles to arrive at repeatable velocity-stress behaviors. During the final two cycles (loading and unloading) the velocity versus stress curves were practically the same. No hysteretic behaviors were observed.

In the case of glass beads, we were only able to obtain reliable results with the 10 MPa difference between the hydrostatic and axial stress. Past that stress difference, the sample simply collapsed.

In all cases, the S-wave splitting was minimal, hence indicating very small (practically negligible) anisotropy in the relevant direction.

Results: Sandstones

The experimental results for Berea sandstone are shown in Figure 3. Here, we compare V_p and V_s measured at pure hydrostatic stress with those measured at the equivalent total axial stress. The differences appear to be significant at the 1 MPa fixed hydrostatic stress station, but become small at 10 MPa station even where the contrast between the total axial and fixed hydrostatic stress is as high as 30 MPa.

These velocity differences become hardly noticeable at the 20 and 30 MPa fixed hydrostatic stress stations hence proving that even in the presence of large stress anisotropy, the vertical velocities at pure hydrostatic stress are approximately the same as at the equivalent total axial stress.

The same results, but for the "Red Sandstone" sample are shown in Figure 4. The conclusion here is the same as in the case of Berea sandstone. This conclusion also holds for Scioto sandstone sample (Figure 5).

Results: Glass beads

Because the glass beads sample was very friable, we could only register coherent ultrasonic signals at uniaxial loading where the difference between the axial and confining hydrostatic stress did not exceed 10 MPa. Past this threshold, the sample uncontrollably deformed. Specifically, we can only compare the velocities measured at 1) the total axial stress 20 MPa with 10 MPa confining pressure to those measured at pure hydrostatic stress 20 MPa; 2) at the total axial stress 30 MPa with 20 MPa confining pressure to those measured at pure hydrostatic stress 30 MPa; and 3) at the total axial stress 40 MPa with 30 MPa confining pressure to those measured at pure hydrostatic stress 40 MPa.

The results shown in Figure 6 indicate that the relative difference in V_p in the first case is about 3%, while that in V_s is about 6%. In the second case, these differences are even smaller, while they are practically zero in the third case.

Results: Carbonates

The measurement results for the carbonate CA 18-10 are shown in Figure 7. The relative velocity difference at 40 MPa total axial stress and 1 MPa confining hydrostatic stress is about 5% in V_p and 7% in V_s. However, as the confining hydrostatic stress increases, these differences are reduced and become very small at 30 MPa confining hydrostatic stress.

Similarly, the differences between the velocities measured at pure hydrostatic stress and those measured at the equivalent total axial stress, the latter at anisotropic loading, appear quite small for carbonate CA 18-41 (Figure 8). These results confirm the conclusion derived from the experiments conducted on sandstones and glass beads that the vertical velocities even at significant stress anisotropy are close to those at the equivalent hydrostatic stress.

Discussion

We show, by example, that the vertical P- and S-wave velocities measured at uniaxial stress are close to those measured at the same hydrostatic stress even in the presence of very strong stress anisotropy. Predictably, this match improves as the stress anisotropy is reduced. These velocities are practically the same even where the axial stress exceeds the confining hydrostatic pressure by 10 MPa and at 40 MPa total axial stress, which amounts to 25% stress anisotropy.

The Mavko et al. (1995) theory confirms this conclusion, albeit only for materials approximately elastically isotropic under isotropic stress. The match between the theory and experiment is practically perfect at high stress and deteriorates at very small stress. One reason is the idealization present in the theoretical assumptions. For example, some cracks may open at very high anisotropic stress, while the theory assumes uniform crack closure. Also, the theory assumes the initially elastically isotropic material, while some of the samples used may be structurally anisotropic. Finally, due to these theoretical assumptions, the theory underestimates the data at high anisotropic stress differences. Mavko et al. (1995) show a similar behaviors in some of their examples.

Of course, as in any robust scientific argumentation, a counterexample is needed to show where this conclusion is

invalid, thus hedging the realm of its applicability. To address this issue, additional experiments are in order, perhaps dealing with naturally strongly anisotropic rocks, such as laminated shale.

Another issue not covered by the present study is that of spatial scale. Namely, how these results obtained on inch-sized samples can be translated into the reservoir and/or basin scales. Clearly, controlled experiments at such scales are hardly tenable. Perhaps analytical techniques can be used to address this question in the future.

Conclusion

We have provided clear proof that the elastic-wave velocities measured in a vertical borehole under generally anisotropic state of stress are very close to those measured in the laboratory at purely hydrostatic stress equal to the vertical stress in the crust. This proof is by example. The examples include medium-porosity sandstones, an unconsolidated glass bead pack, and low-to-medium porosity carbonates. An existing analytical theory confirms this result. A practical aspect of this conclusion is that the velocities measured on the samples extracted from the borehole and at variable hydrostatic stress can be used to predict and interpret the time-lapse seismic data as the pore pressure changes during production. Another practical implication is for seismic processing, as well as impedance inversion. Specifically, the elastic properties measured in a vertical borehole or obtained in hydrostatic laboratory experiments can be used in the aforementioned procedures. Finally, our results can be relevant in digital rock physics experiments where a hydrostatic laboratory experiment can serve as a calibration for digitally-derived elastic property computations.

Data availability statement

The raw data supporting the conclusions of this article will be made available by the authors, without undue reservation.

Author contributions

All authors listed have made a substantial, direct, and intellectual contribution to the work and approved it for publication.

Funding

This work was provided by the Center for Integrative Petroleum Research of College of Petroleum Engineering and Geosciences at King Fahd University of Petroleum and Minerals, the Kingdom of Saudi Arabia.

Acknowledgments

We thank Gary Mavko for providing the code to compute the velocities at uniaxial stress from those measured at hydrostatic stress. Thanks go to our imaging team, Rizwanullah Hussaini, Nadeem Ahmed, and Hani Al-Mukainah for supplying CT-scan images of the samples under examination. We thank Marjory Matic for editing the text.

Conflict of interest

The authors declare that the research was conducted in the absence of any commercial or financial relationships that could be construed as a potential conflict of interest.

Publisher's note

All claims expressed in this article are solely those of the authors and do not necessarily represent those of their affiliated organizations, or those of the publisher, the editors and the reviewers. Any product that may be evaluated in this article, or claim that may be made by its manufacturer, is not guaranteed or endorsed by the publisher.

References

Amalokwu, K., Chapman, M., Best, A. I., Minshull, T. A., and Li, X.-Y. (2015). Water saturation effects on P-wave anisotropy in synthetic sandstone with aligned fractures. *Geophys. J. Int.* 202, 1088–1095. doi:10.1093/gji/ggv192

Bandyopadhyay, K. (2009). *Seismic anisotropy: Geological causes and its implications to reservoir geophysics*. Stanford, CA: Stanford University. Ph.D. thesis.

Barbosa, N. D., Caspari, E., Rubino, J. G., Greenwood, A., Baron, L., and Holliger, K. (2019). Estimation of fracture compliance from attenuation and velocity analysis of full-waveform sonic log data. *J. Geophys. Res. Solid Earth* 124, 2738–2761. doi:10.1029/2018jb016507

Bhuiyan, M. H., and Holt, R. M. (2016). Anisotropic parameters of dry and saturated sand under stress. *Geophysics* 81, C229–C241. doi:10.1190/geo2015-0354.1

Chapman, M., Maultzsch, S., Liu, E., and Li, X.-Y. (2003). The effect of fluid saturation in an anisotropic multi-scale equant porosity model. *J. Appl. Geophys.* 54, 191–202. doi:10.1016/j.jappgeo.2003.01.003

Chapman, M. (2009). Modeling the effect of multiple sets of mesoscale fractures in porous rock on frequency-dependent anisotropy. *Geophysics* 74, D97–D103. doi:10.1190/1.3204779

Cilli, P. A., and Chapman, M. (2021). Linking elastic and electrical properties of rocks using cross-property DEM. *Geophys. J. Int.* 225, 1812–1823. doi:10.1093/gji/ggab046

Ciz, R., and Shapiro, S. A. (2009). Stress-dependent anisotropy in transversely isotropic rocks: Comparison between theory and laboratory experiment on shale. *Geophysics* 74, D7–D12. doi:10.1190/1.3008546

Collet, O., and Gurevich, B. (2013). Fluid dependence of anisotropy parameters in weakly anisotropic porous media. *Geophysics* 78, WC137–WC145. doi:10.1190/geo2012-0499.1

Collet, O., Gurevich, B., Madadi, M., and Pervukhina, M. (2014). Modeling elastic anisotropy resulting from the application of triaxial stress. *Geophysics* 79, C135–C145.

Crampin, S. (1985). Evaluation of anisotropy by shear-wave splitting. *Geophysics* 50, 142–152. doi:10.1190/1.1441824

Dillen, M. W. P., Cruts, H. M. A., Groenenboom, J., Fokkema, J. T., and Duijndam, A. J. W. (1999). Ultrasonic velocity and shear-wave splitting behavior of a Colton sandstone under a changing triaxial stress. *Geophysics* 64, 1603–1607. doi:10.1190/1.1444664

Falcon-Suarez, I. H., North, L., Callow, B., Bayrakci, G., Bull, J., and Best, A. (2020). Experimental assessment of the stress-sensitivity of combined elastic and electrical anisotropy in shallow reservoir sandstones. *Geophysics* 85, MR271–MR283. doi:10.1190/GEO2019-0612.1

Gong, F., Di, B., Wei, J., Ding, P., Pan, X., and Zu, S. (2018). Ultrasonic velocity and mechanical anisotropy of synthetic shale with different types of clay minerals. *Geophysics* 83, MR57–MR66. doi:10.1190/GEO2016-0590

Gueguen, Y., and Schubnel, A. (2003). Elastic wave velocities and permeability of cracked rocks. *Tectonophysics* 370, 163–176. doi:10.1016/S0040-1951(03)00184-7

Gurevich, B., Pervukhina, M., and Makarynska, D. (2011). An analytic model for the stress-induced anisotropy of dry rocks. *Geophysics* 76, WA125–WA133. doi:10.1190/1.3567950

Hu, M., O'Sullivan, C., Jardine, R. R., and Jiang, M. (2010). Stress-induced anisotropy in sand under cyclic loading. *Granul. Matter* 12, 469–476. doi:10.1007/s10035-010-0206-7

Hudson, J. A. (1980). Overall properties of a cracked solid. *Math. Proc. Camb. Phil. Soc.* 88, 371–384. doi:10.1017/S0305004100057674

Johnson, P. A., and Rasolofosaon, P. N. J. (1996). Nonlinear elasticity and stress-induced anisotropy in rock. *J. Geophys. Res.* 101, 3113–3124. doi:10.1029/95jb02880

Johnson, K. L. (1985). *Contact mechanics*. Cambridge, England: Cambridge University Press, 452. doi:10.1017/CBO9781139171731

Kuhn, M. R., Sun, W, C., and Wang, Q. (2015). Stress-induced anisotropy in granular materials: Fabric, stiffness, and permeability. *Acta Geotech.* 10, 399–419. doi:10.1007/s11440-015-0397-5

Majmudar, T. S., and Behringer, R. P. (2005). Contact force measurements and stress-induced anisotropy in granular materials. *Nature* 435, 1079–1082. doi:10.1038/nature03805

Mavko, G., Mukerji, T., and Godfrey, N. (1995). Predicting stress-induced velocity anisotropy in rocks. *Geophysics* 60, 1081–1087. doi:10.1190/1.1443836

Nadri, D., Bona, A., Brajanovski, M., and Lokajicek, T. (2011). Estimation of stress-dependent anisotropy from P-wave measurements on a spherical sample. *Geophysics* 76, WA91–WA100. doi:10.1190/1.3552703

Nur, A., and Simmons, G. (1969). Stress-induced velocity anisotropy in rock: An experimental study. *J. Geophys. Res.* 74, 6667–6674. doi:10.1029/jb074i027p06667

Nur, A. (1971). Effects of stress on velocity anisotropy in rocks with cracks. *J. Geophys. Res.* 76, 2022–2034. doi:10.1029/jb076i008p02022

Oda, M., Nemat-Nasser, S., and Konishi, J. (1985). Stress-induced anisotropy in granular masses. *Soils Found.* 25, 85–97. doi:10.3208/sandf1972.25.3_85

Ramos, M. J., Espinosa, D. N., Laubach, S. E., and Torres-Verdin, C. (2019). Quantifying static and dynamic stiffness anisotropy and nonlinearity in finely laminated shales: Experimental measurement and modeling. *Geophysics* 84, MR25–MR36. doi:10.1190/GEO2018-0032.1

Rasolofosaon, P. N. J., and Zinszner, B. E. (2002). Comparison between permeability anisotropy and elasticity anisotropy of reservoir rocks. *Geophysics* 67, 230–240. doi:10.1190/1.1451647

Rasolofosaon, P. N. J. (1998). Stress-induced seismic anisotropy revisited. *Rev. Inst. Fr. Pet.* 53, 679–692. http://hal-ifp.archives-ouvertes.fr/hal-02079038. doi:10.2516/ogst:1998061

Smith, R. T. (1963). Stress-induced anisotropy in solids—the acousto-elastic effect. *Ultrasonics* 1, 135–147. doi:10.1016/0041-624X(63)90003-9

Teng, L. (1998). *Seismic and rock-physics characterization of fractured reservoirs*. Stanford, CA: Stanford University. Ph.D. thesis.

Yin, H. (1992). *Acoustic velocity and attenuation in rocks: Isotropy, intrinsic anisotropy, and stress-induced anisotropy*. Stanford, CA: Stanford University. Ph.D. thesis.

Zamora, M., and Poirier, J. P. (1990). Experimental study of acoustic anisotropy and birefringence in dry and saturated Fontainebleau sandstone. *Geophysics* 55, 1455–1465. doi:10.1190/1.1442793

frontiers | Frontiers in Earth Science

TYPE Original Research
PUBLISHED 23 September 2022
DOI 10.3389/feart.2022.1018105

OPEN ACCESS

EDITED BY
Ahmed M. Eldosouky,
Suez University, Egypt

REVIEWED BY
Sadegh Karimpouli,
University of Zanjan, Iran
Yang Yang,
Guilin University of Technology, China
Faisal Ur Rahman Awan,
Edith Cowan University, Australia

*CORRESPONDENCE
Wanzhong Shi,
shiwz@cug.edu.cn
Shucheng Tan,
shchtan@ynu.edu.cn

†These authors have contributed equally to this work and share first authorship

SPECIALTY SECTION
This article was submitted to Solid Earth Geophysics, a section of the journal Frontiers in Earth Science

RECEIVED 15 August 2022
ACCEPTED 06 September 2022
PUBLISHED 23 September 2022

CITATION
Anees A, Zhang H, Ashraf U, Wang R, Thanh HV, Radwan AE, Ullah J, Abbasi GR, Iqbal I, Ali N, Zhang X, Tan S and Shi W (2022), Sand-ratio distribution in an unconventional tight sandstone reservoir of Hangjinqi area, Ordos Basin: Acoustic impedance inversion-based reservoir quality prediction. *Front. Earth Sci.* 10:1018105. doi: 10.3389/feart.2022.1018105

Sand-ratio distribution in an unconventional tight sandstone reservoir of Hangjinqi area, Ordos Basin: Acoustic impedance inversion-based reservoir quality prediction

Aqsa Anees[1†], Hucai Zhang[1], Umar Ashraf[1†], Ren Wang[2,3], Hung Vo Thanh[4], Ahmed E. Radwan[5], Jar Ullah[6], Ghazanfer Raza Abbasi[7], Ibrar Iqbal[8], Nafees Ali[9,10], Xiaonan Zhang[1], Shucheng Tan[11]* and Wanzhong Shi[2,3]*

[1]Institute for Ecological Research and Pollution Control of Plateau Lakes, School of Ecology and Environmental Science, Yunnan University, Kunming, China, [2]School of Earth Resources, China University of Geosciences, Wuhan, China, [3]Key Laboratory of Tectonics and Petroleum Resources, Ministry of Education, China University of Geosciences, Wuhan, China, [4]School of Earth and Environmental Sciences, Seoul National University, Seoul, South Korea, [5]Faculty of Geography and Geology, Institute of Geological Sciences, Jagiellonian University, Kraków, Poland, [6]Institute of Geophysics and Geomatics, China University of Geosciences, Wuhan, China, [7]Physical Science and Engineering Division, King Abdullah University of Science and Technology (KAUST), Thuwal, Saudi Arabia, [8]School of Earth Sciences, Zhejiang University, Hangzhou, China, [9]State Key Laboratory of Geomechanics and Geotechnical Engineering, Institute of Rock and Soil Mechanics, Chinese Academy of Sciences, Wuhan, China, [10]University of Chinese Academy of Sciences, Beijing, China, [11]School of Resource Environment and Earth Science, Yunnan University, Kunming, China

Future gas field development and prospect assessment depend on accurate reservoir parameter characterization. The understanding of the tight sand distribution of the Shanxi and Taiyuan Formations within the Hangjinqi area is ambiguous due to the presence of coal and mudstone lithofacies, high heterogeneity, and poor resolution of the seismic data. Thus, it is difficult to determine the reservoir's thickness. To cope with this challenge, we have employed the advanced method of constrained sparse spike inversion (CSSI) utilizing 3D seismic and nine wells for the distinction of tight sandstone facies from the coal and mudstone facies. Results of petrophysical analysis of studied well J54 show that the coal and mudstone facies are dominant towards the T9c horizon, whereas tight sandstone facies are present towards the T9d horizon. The obtained findings show that the CSSI accurately identified the spatial distribution of sand-ratio in the zone of interest (ZOI) that lies between the T9c and T9d horizons. The acoustic impedance (AI) of coal shows the lowest AI values, whereas the tight sandstone shows the highest AI values. The tight sandstone facies shows moderate values of AI in the range of 8.5×10^6 kg/m^{2}s to 1.20×10^7 kg/m^{2}s. The impedance map of T9c suggested the presence of coal and mud facies, whereas the T9d impedance map suggest the presence of maximum tight sandstone facies. The sand-ratio map of T9d showed maximum reservoir thickness that ranges from 0.65-0-95, whereas the sand-ratio value

mostly ranges from 0 to 0.5 on the T9c map. The maximum sand-ratio values on T9d show that the lower Shanxi Formation has good reservoir characteristics. Whereas, due to the presence of coal and mudstone in the Taiyuan Formation, the T9c map shows low values of sand-ratio. The maximum sand-ratio regions within the targeted T9c-T9d layers should be exploited for future gas explorations.

KEYWORDS

acoustic impedance inversion, sand-ratio, shanxi and taiyuan formations, tight sandstone, reservoir characterization, Hangjinqi area

1 Introduction

Tight sandstone gas is the world's top unconventional natural gas source and has emerged as a crucial characteristic for natural gas production. Also, unconventional tight gas contributes the most to China's yearly production of natural gas, accounting for 24.6% of total output (Dai et al., 2012). Tight sandstone is generally defined as a reservoir with porosity of around 12% and less than 1mD (Dai et al., 2012). Henceforth, reservoir characterization and reservoir quality prediction are thus being studied by a large number of geologists, geophysicists, petrophysicist and petroleum engineers (Ehsan et al., 2018; Abdulaziz et al., 2019; Ashraf et al., 2019; Ehsan et al., 2019; Qiang et al., 2020; Radwan, 2020; Vo Thanh et al., 2020; Ashraf et al., 2021; Kassem et al., 2021; Radwan, 2021; Radwan et al., 2021; Dar et al., 2022; Jiang et al., 2022; Ullah et al., 2022; Vo Thanh and Lee, 2022). The Ordos Basin has China's biggest yearly gas production (Duan et al., 2008; Yang et al., 2015). The Hangjinqi area lies in the Ordos Basin. Pure gas exploration began here a decade ago (Anees et al., 2022b). Hangjinqi has several wells, however, the distribution of sand-ratio in many zones is unclear. Reliable reservoir property calculations such as reservoir sand distribution in relation to the acoustic impedance (AI) are crucial for production policy and decision-making (Pendrel, 2006).

Seismic inversion calculates rock parameters for reservoir characterization (Saussus and Sams, 2012) and identifies reservoir parameters such as the distribution of tight sand in relation to the mud that can be exploited for future drilling and field development (Avadhani et al., 2006). Post-stacked seismic data is converted to p-impedance layer data for AI inversion (Latimer et al., 2000). The constrained sparse spike inversion (CSSI) is an advanced approach used by geoscientists in oil and gas (Wang and Guo, 2008). In previous studies, many authors have utilized CSSI as an advanced and effective tool to measure the elastic properties of gas hydrate-bearing sediments (Riedel et al., 2010), and to estimate the coal-strata thickness (Zhu, 2011). In a recent study, authors utilized the CSSI to evaluate the sand-ratio of a heterogeneous reservoir for reservoir-quality estimation (Ashraf et al., 2020). Traditional inversion methods are difficult to use because of their dependence on the starting model. As a result, CSSI is included in our analysis since it is independent of the model and relies only on the characteristics of the original data. CSSI offers a benefit over current approaches since it can be used to analyze whole bandwidth reflectivity (Simm et al., 2014).

The recent studies within the Shanxi and Tiayun Formations were focused on the pore-structure features (Wang and Guo, 2019), fractal characteristics (Gaoyuan et al., 2021), shale gas potential within the southern region of the Ordos Basin (Li et al., 2021; Wang et al., 2021), and sedimentary facies modeling (Li et al., 2021; Zhang et al., 2022). However, a comprehensive study addressing the tight sandstone facies within the Shanxi and Taiyuan Formations is still missing. Much attention is needed to address the accurate tight sandstone reservoir distribution. Therefore, in this study, we have focused on the identification of the horizontal and vertical distribution of lithofacies by means of the AI model *via* regional 3D seismic and well-log data. Also, we aim to highlight the low-impedance sandstone reservoir zones that can be exploited for future gas explorations.

2 Geology of the study area

The clastic rocks from the upper Paleozoic are the most important exploration prospects for natural gas in the Hangjinqi area. The black mudstone and coal of the tidal flat-delta-lake facies make up the majority of the gas source rocks and are found in the Shanxi and Taiyuan Formations (Wu et al., 2017). The cap rocks are comprised of the upper Shihezi Formation and Shiqianfeng Formation, while the reservoirs are composed of shore sand bodies, deltaic braided channels, interdistributary channels, and channel-bar sand bodies (all of which are found in the Shanxi and Lower Shihezi Formations). The tight sandstones of the Lower Shihezi Formation, which include sandy fluvial conglomerate and coarse-to-fine-grained sandstones, are acting as the primary reservoir within the Hangjinqi area (Zhang et al., 2009; Anees et al., 2019). Recent studies show that the member-1 of the Lower Shihezi Formation has good reservoir quality and has the potential to develop gas reserves on a regional and commercial scale (Anees et al., 2022a). In addition, the northern region of the member-2 and member-3 of the Lower Shihezi Formation also suggested good favorable zones for gas exploration (Anees et al., 2022b).

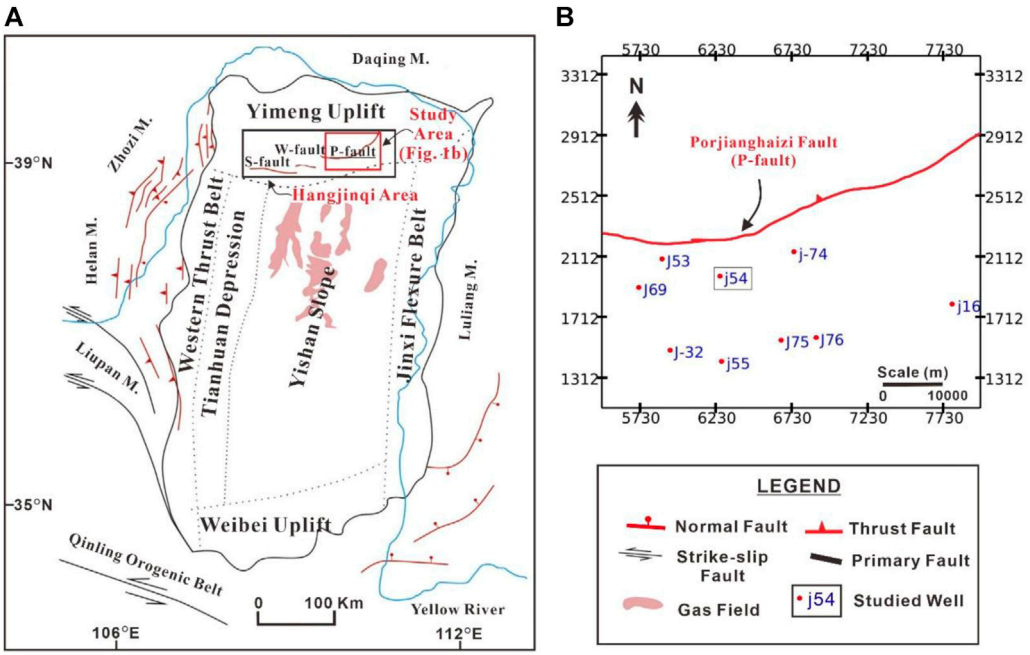

FIGURE 1
(A) The Ordos Basin's primary tectonic units. The red colored text and box show the Hangjinqi study area. **(B)** 3D seismic grid along with wells utilized to execute the research. The P-fault is the main fault within the Hangjinqi area.

The Hangjinqi lies at the Yishan ramp and Yimeng uplift (Figure 1A). The paleo-high in the northern Ordos Basin makes Hangjinqi ideal for hydrocarbon migration (Xue et al., 2009). From west to east, three primary faults are dispersed throughout the research area, with Porjianghaizi Fault (P-fault) separating the Hangjinqi area into north and south (Xu et al., 2018; Liu et al., 2020) (Figure 1B). According to the present geomorphology, the central region of the Ordos Basin is relatively stable and does not contain many structures. On the other hand, the margins of the basin have been subjected to multiple tectonic activities, which has resulted in structural complexity (Ju et al., 2017). Since the end of the Carboniferous era, the whole area had subsided, marking the beginning of a period in which sedimentation was shifting from the ocean (marine) to the land (continental) settings (Ju et al., 2017). At the beginning of the Triassic period, the basin began to experience an intracontinental phase, and as a result, there were collisions that occurred between the North China Block and the South China Block, as well as the collision between the Qiangtang Block and the Eurasian Plate. Tectonic forces shifted from exerting compressional to exerting extensional stress throughout the Cenozoic epoch (Ju et al., 2017). During the Cenozoic, the Ordos Basin and North China Block parted, creating six tectonic areas on the Archean-Proterozoic basement. These includes Weibei uplift, Yimeng uplift, Western thrust belt, Jinxi flexural belt, Yishan slope, and Tianhuan depression (Yang et al., 2005).

In the current study, we focus on the geological characteristics of the Lower Permian Shanxi (P_1s) and Carboniferous Taiyuan (C_3t) Formations (Figure 2). The Shanxi Formation further comprises of Shanxi-1 and Shanxi-2 members. The Taiyuan Formation was mostly formed in a marine sedimentary environment, while the Shanxi Formation was primarily deposited in a terrestrial sedimentary environment (Xu et al., 2015).

3 Data and methods

A vast grid of 3D post-stacked seismic data that incorporates around 1,000 km^2 including nine wells (J16, J32, J53, J54, J55, J69, J74, J75, and J76) is utilized in our study to identify the tight sand thickness of the reservoir within the Hangjinqi area. In order to achieve the aim of the research, several geophysical logs, such as sonic (DT) (us/m), density (RHOB) (g/cm^3), deep resistivity (LLD) (ohm.m), shallow resistivity (LLS) (ohm.m), caliper (CAL) (in), compensated neutron log(CNL) (dec), and gamma-ray (GR) (API), were included (Ehsan and Gu, 2020). The study was accomplished with the help of the Jason software package. In the first step of the interpretation, the stratigraphic and structural interpretations were done using seismic sections and well logs. Initially, we employed the petrophysical analysis to interpret the lithofacies and reservoir zone. Afterward, to create a synthetic seismogram, the seismic to well-tie

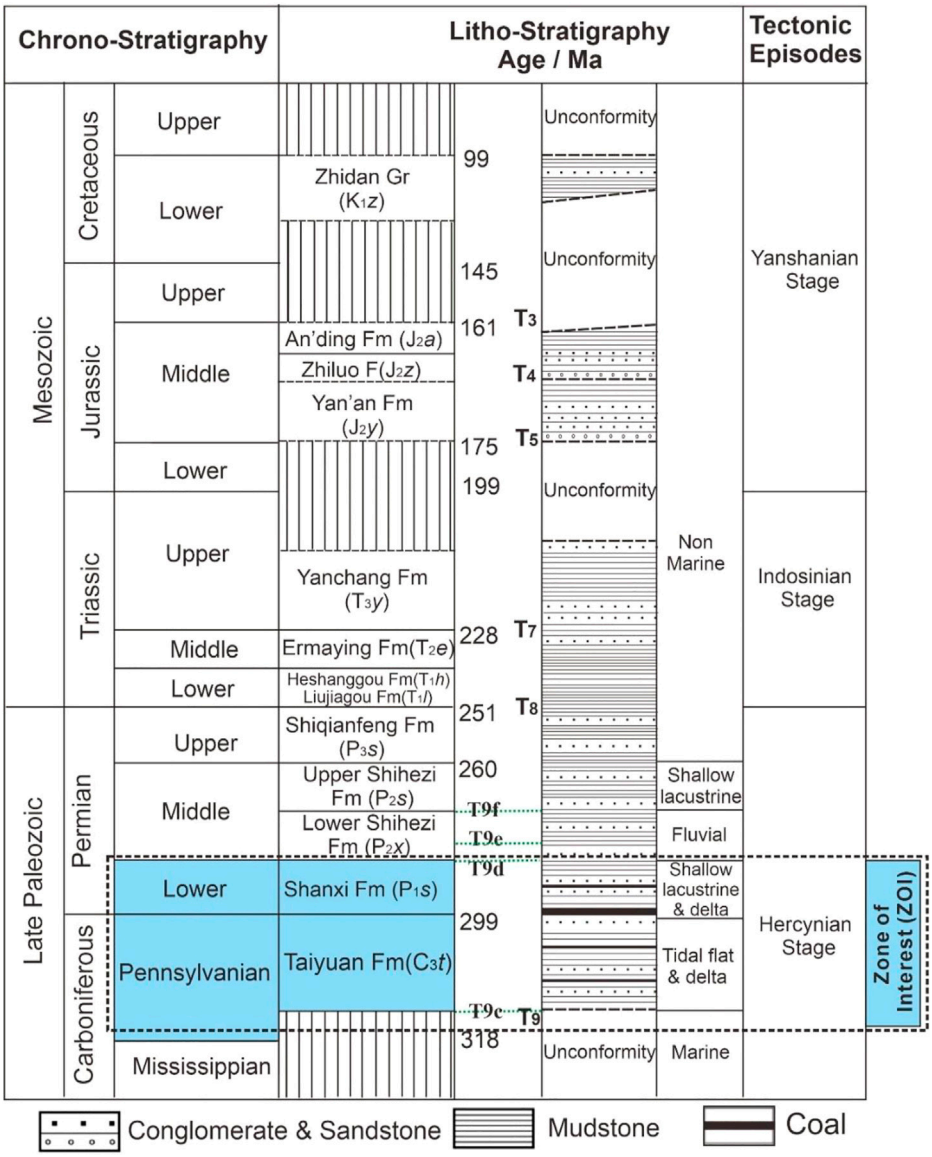

FIGURE 2
Simplified stratigraphic diagram of the study area. The highlighted blue colored text shows the studied region.

approach was used (Ashraf et al., 2016). The T9c and T9d layers were identified as two distinct horizons within the Shaanxi and Taiyuan Formations which encompass the whole zone of interest (ZOI). The interpolation of the geological models was run along the T9c and T9d horizons. The two targeted horizons were utilized to help understand the extent of the reservoir facies and tight sand thickness distribution. In the second step, the thickness of ZOI was calculated using well-logging data on geophysical logs of the studied well J54. In the next step, to get the average wavelet, a wavelet was created for each well. It was integrated with a band-limited model to improve the inverted broadband model's resolution by extracting average wavelet, seismic, log, and horizon data. A series of quality control (QC) tests followed to ensure the inversion results were accurate. The geostatistical analysis was used to examine the impedance maps and thickness maps in order to determine the distribution of lithofacies.

4 Results

4.1 Petrophysical analysis

In order to examine the generalized pattern of the vertical distribution of tight sand and coal facies, well J54 was selected as

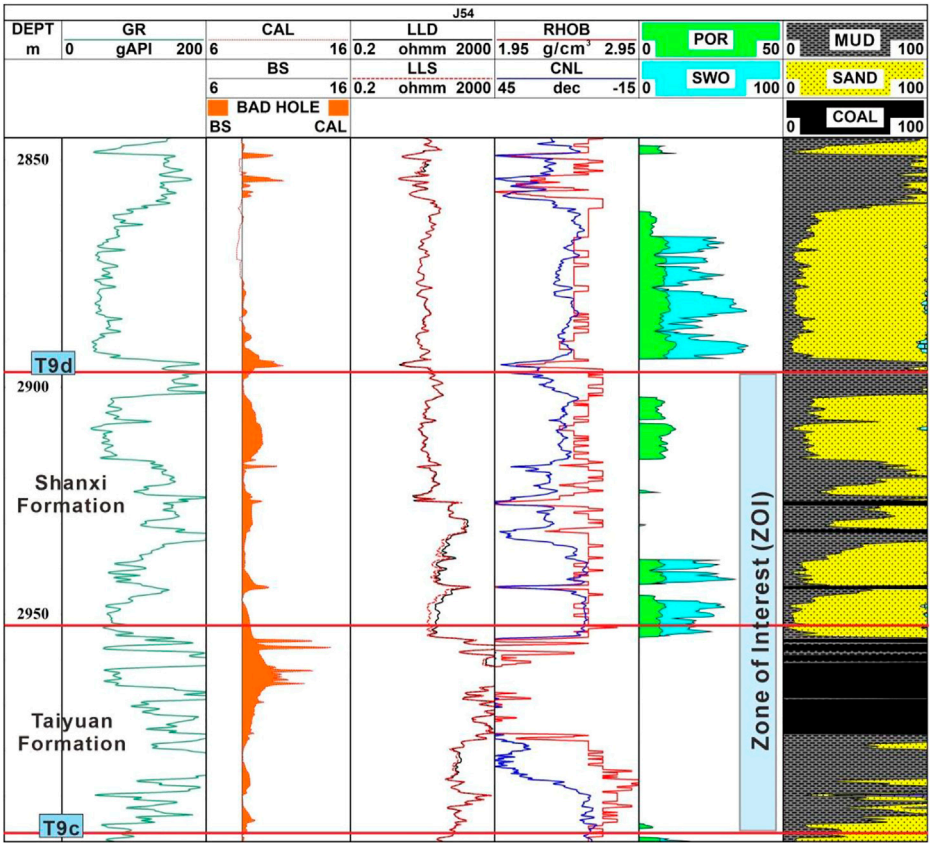

FIGURE 3
Well J54 interpretation shows the interpreted tight sandstone, mudstone and coal facies within the ZOI. The ZOI lies between the Shanxi and Taiyuan Formations.

a case study to use as an example. The layer T9c lies at the bottom of the Taiyuan Formation, whereas T9d is situated at the top of the Shanxi (including the Shanxi-1 and Shanxi-2) Formation which is marked by red lines in Figure 3 to show the ZOI. The results of petrophysical analysis within the ZOI show the vertical distribution of coal, tight sandstone and mud lithofacies. There are three thin coal layers between 2,905–2,950 m, and a thick zone of coal lies between 2,957–2,978 m. The coal facies shows high resistivity values, low RHOB, high CNL, and low GR. The minor variations in logs values are associated with the different type of coal rank, type, gas content, and adsorption content (Mangi et al., 2020; Mangi et al., 2022; Wood and Cai, 2022). On the other hand, as compared to coal facies, the tight sandstone facies shows comparatively high GR, low resistivity values, high RHOB and low CNL. The particularly moderate values of porosity give the indication of tight sandstone in the study area. There are four porous zones that lie above the thick zone of coal facies. The tight sandstone facies are mainly present near the T9d layer. Whereas, towards the bottom of the ZOI, the region near the T9c layer shows the presence of mainly mudstone facies. The coal facies are acting as a source rock within the study, whereas the porous tight sandstone facies above the thick coal zone near 2950 m suggesting good porous zones that can act as a reservoir within the Hangjinqi area.

4.2 Acoustic impedance inversion

4.2.1 Horizon interpretation

In order to make the interpretation mapping of the horizons as smooth as possible, the smoothing technique that is offered in the Jason software was used for the loaded horizons. This was done in order to limit the number of troughs and peaks in the data. The interpolation of the geological model runs along the horizons while this procedure creates a smoothed version of the interpolated well-log AI over the whole survey. The interpreted T9c and T9d horizons on the seismic section are shown in Figure 4A, while their interpolated structural maps are shown in Figure 4B and Figure 4C, respectively.

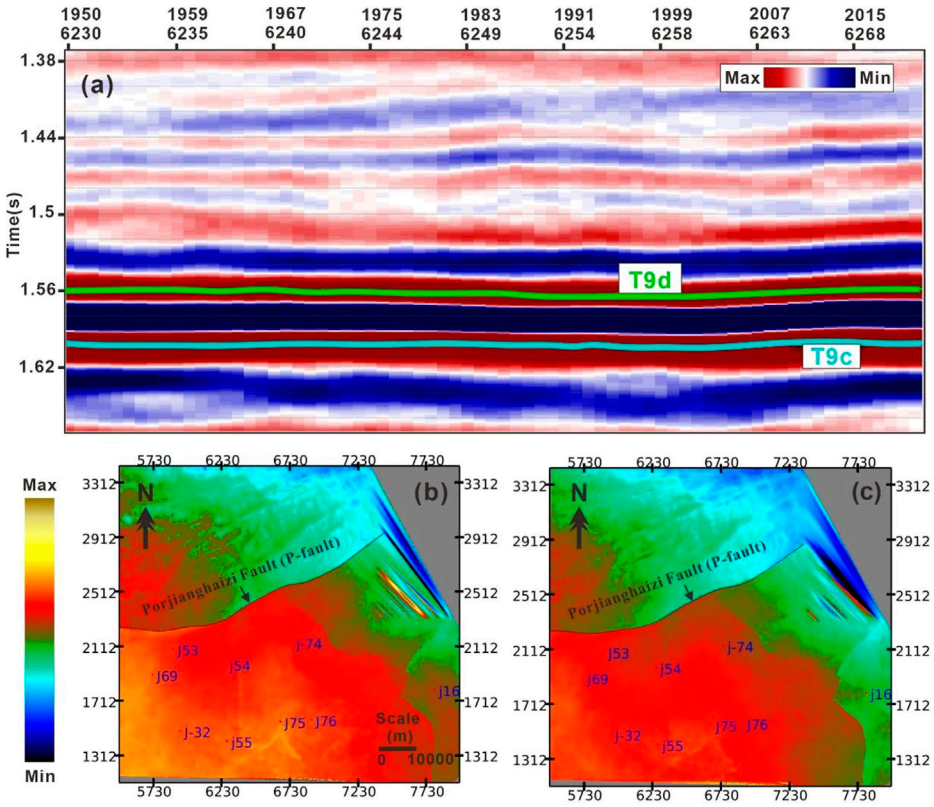

FIGURE 4
(A) Interpreted horizons T9c and T9d on the seismic section. Interpolations of horizons **(B)** T9c, and **(C)** T9d.

4.2.2 Generating missing logs

At the beginning of the investigation, the p-impedance log was not accessible for all of the study wells. As part of the process of completing the inversion, an AI log is required which was created by employing the Backus' averaging of the DT log on the ZOI for the successful completion of the time-to-depth conversion. Since AI comprises RHOB and DT, therefore corrected DT log of some wells was utilized to generate the missing RHOB. The Jason suite has an in-built algorithm that can generate the missing RHOB log by applying Gardner's equation (Eq. 1) to the data (Gardner et al., 1974).

$$\text{Density} = (0.23)\,\text{X}\,(\text{p} - \text{wave velocity})\,0.25 \qquad (1)$$

4.2.3 Wavelet estimation and synthetic seismogram

In order to accomplish a reliable seismic inversion, an accurate wavelet estimate is required first and foremost. The amplitude spectrum and phase spectrum of a wavelet are the two main components. Also, it is more challenging to define the phase spectrum in comparison to the amplitude spectrum. Since the phase spectrum is the primary cause of producing errors in the inversion, it is of the utmost importance to take into consideration the correct phase spectrum, which ultimately leads to the correct inversion and the right results. The generation of synthetic seismograms for each well, which is the critical initial stage in the process of wavelet estimate, was completed so that the seismic and well data could be linked (Anees et al., 2017; Abbas et al., 2019). Because high-quality good ties are required in order to obtain the low-frequency AI trend, the step of creating a synthetic seismogram is followed by an iterative method for the tie process to improve the quality of the tie.

The amplitude spectrum is derived from the seismic data by performing an autocorrelation analysis on them. We have employed the autocorrelation technique to remove the phase from the seismic data by employing the temporal taper to the autocorrelation function in order to smooth out the spectrum (Table 1).

The seismic data was zero phase, therefore a zero phase wavelet was developed for the research region. This was done to ensure that there was a strong connection between the data from the well logs and the seismic data. The wavelet extraction was performed during the process of stretching and squeezing, and

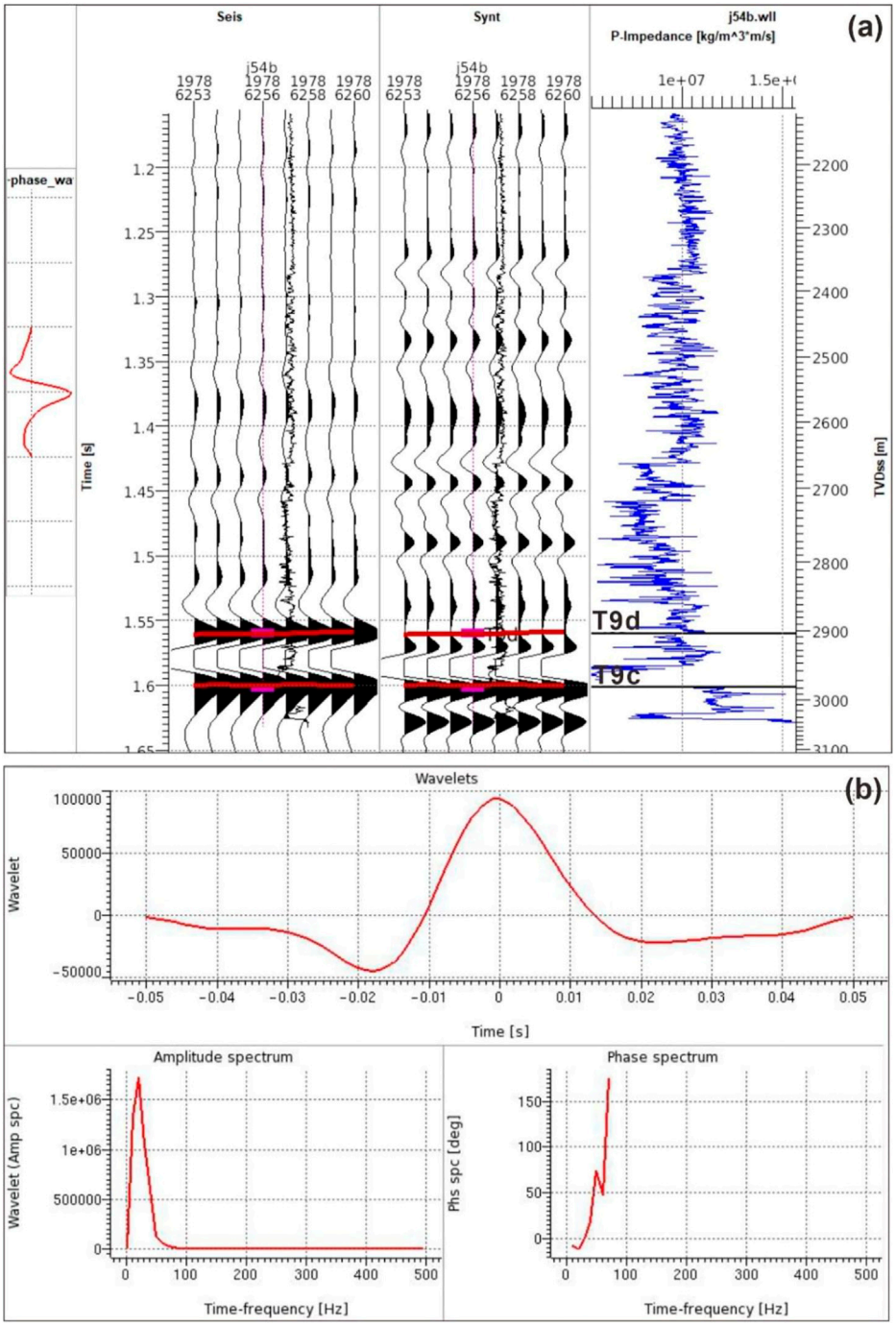

FIGURE 5
(A) Well editing window of well J54. The seismic data from chosen traces surrounding the well is shown on the left-hand panel. The synthetic from the acoustic impedance and the well logs are shown in the second and third panels, respectively. The integrated sonic was used to transform this data from depth to time from a vertical well. **(B)** The amplitude and phase spectrum of the average wavelet retrieved from the study wells.

the resulting extracted wavelet was updated throughout the process of tying. This iterative procedure verifies the accurate extraction of the wavelet and creates a reliable connection between the data from the well log and the seismic data (Figure 5A). The sensitivity of the inversion procedure was evaluated with the aid of the various wavelets that were retrieved. Within the context of the seismic survey, the well placements and overall quality served as the primary

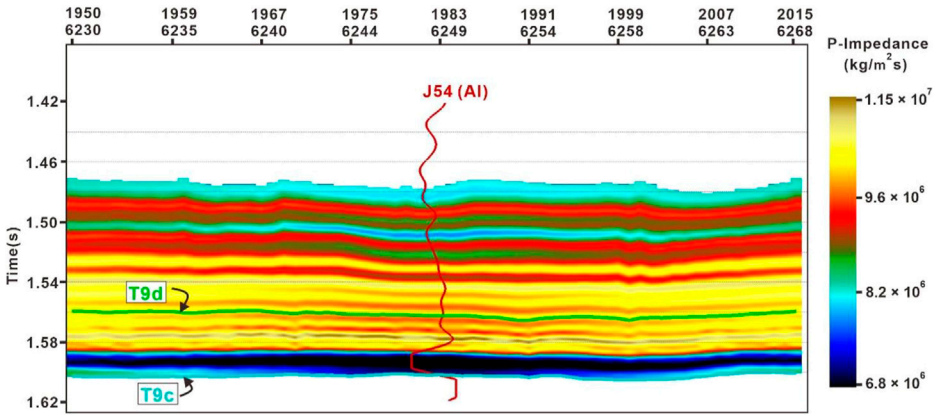

FIGURE 6
Low-frequency model created for study area.

considerations for the extraction of the average wavelet. The wavelet was derived from the targeted horizons of T9c to T9d, which entirely enclosed the reservoir (Figure 5B). All those wells were used to obtain the average wavelet for the available consistent wavelets which were having the DT and RHOB logs reaching the targeted depths of T9c and T9d.

4.2.4 Low-frequency model

To construct a low-frequency model, the phrases relative and absolute AI are often used to describe AI. The computation of relative AI does not take into account the development of a low-frequency model, despite the fact that it is a feature of the relative layer. The absolute AI, on the other hand, is a feature of the absolute layer that is employed for both qualitative and quantitative interpretations, as well as for the construction of low-frequency models. It is possible, however, to achieve absolute AI by using an inversion method that includes a low-frequency component (0–15 Hz) (Cooke and Cant, 2010). Sparse-spike inversion uses a distinct inversion technique for the low-frequency model, rather than using the inversion algorithm itself (Cooke and Schneider, 1983).

The presence of low-frequency disturbances in the seismic data spoils the low-frequency information, which in turn causes the low-frequency information to be disturbed in the recorded seismic data. The incorporation of the low-frequency model resulted in the generation of a zero-hertz component, which converted the relative AI values to the absolute AI values. As a result, the detection and resolution of the tight sandstone, mudstone, and coal facies were improved.

Ferguson and Margrave, 1996 provided the low-frequency AI model and algorithm that was employed in our study (Ferguson and Margrave, 1996). This model and technique are based on an approach known as iterative forward modeling (Veeken and Da Silva, 2004). This approach improved the low-frequency information by using integrated well-log data (mainly DT and RHOB logs), an estimate of seismic wavelet, 3D seismic data (band limited), and seismic horizons taken from the seismic reflectivity data. To create a low-frequency model, all wells that had logs extending to at least T9c horizon were utilized for seismic data. Figure 6 shows the generated low-frequency model for the Hangjinqi 3D seismic survey. The overlay AI log of well J54 show deflection towards the left side presenting low impedance values that are associated with the coal facies. In addition, the deflection of AI curve towards the right side shows high AI values gives the indication of mudstone and tight sandstone facies.

Since AI inversion was band-limited, a low-frequency model was needed to create a broadband model. This low-frequency model was retrieved from well-log data and incorporated into a seismic-derived band-limited AI model. Because the distribution of the wells within the research region is not uniform, the inverse distance weighted and kriging interpolation approaches were not delivering the most accurate information. The triangulation approach was selected as the preferable method of interpolation since it was determined to be the most appropriate for the regional available data for the research. Due to the fact that it generates an interpolation of data that is continuous and smooth, this approach really produced the best interpolation results over the whole of the survey. In order to lead the interpolation between the well-logs, two different horizons (T9c and T9d) were incorporated. The low-frequency model that was produced provided a better understanding of the lateral and vertical variance of the facies that are present in the Taiyuan and Shanxi Formations.

4.2.5 Constrained sparse spike inversion

After completing the computation of the wavelets and the interpolation of the AI logs, the inversion process was completed

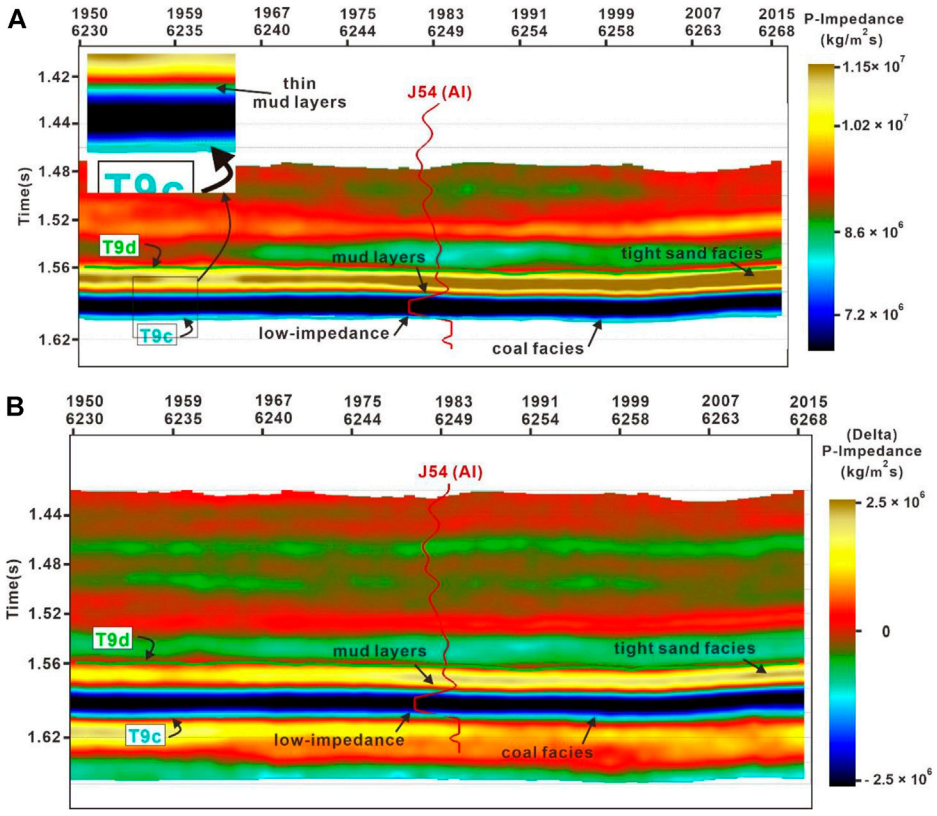

FIGURE 7
(A) Inverted broadband acoustic impedance model. Zoomed image shows the presence of thin mudstone layers **(B)**. Inverted bandlimited acoustic impedance model. Well J54 is overlaying on the inverted models showing the vertical distribution of the p-impedance log.

by establishing additional parameters. They consist of the selection of lambda, trend mismatch, the maximum and lowest values of AI that the inversion is capable of achieving, as well as the p and q parameters for reflectivity and the seismic misfit term. The following is a description of the stages that were carried out in the process of inversion:

a) The preliminary step was composed of editing the trends. In most cases, the value of the p-impedance increases with the increase in the depth of the well logs. Therefore, the trends of all the wells using a targeted area (T9c-T9d) were edited.
b) Trace merging was carried out in order to combine two data sets: one that had information about the low-frequency band, and the other that contained information about the seismic bandwidth or above. The band-pass filter was applied. The frequency of the cut-off was determined to be between 0-50 (lowest to highest frequency) Hz.
c) Different QC procedures for the CSSI were carried out with the lambda factor serving as the testing variable.

After making adjustments to all of the QC parameters, CSSI was accomplished to get the results of the inverted bandlimited AI. In order to fill the missing element regarding the low-frequency, a low-frequency model was included in the model. To get the most accurate interpretation of the inversion, all of its many components were utilized. Since the full bandwidth contains the maximum bandwidth and the least amount of wavelet effects, the results of the full bandwidth inversion provided the most reliable information for interpretation. To carry out the quantitative analysis, these results were tied directly to the p-impedance logs of the wells. Once regions and ZOI on the full bandwidth result were recognized, the bandlimited and low-frequency components were further analyzed to define the underlying coalbeds from the channel tight sandstone and mudstone facies.

The results of the CSSI model are shown in Figure 7. After being integrated with the low-frequency model, the CSSI approach proves to be an efficient tool for the delineation of vertical and lateral changes in impedances of the various lithofacies. The broadband model that was generated displayed the maximum resolution possible and exhibited a vibrant variation in the AI. This variation made it possible to differentiate between the vertical and lateral extent of the coal and the tight sandstone reservoir facies that are present in the Hangjinqi region. The low-velocity

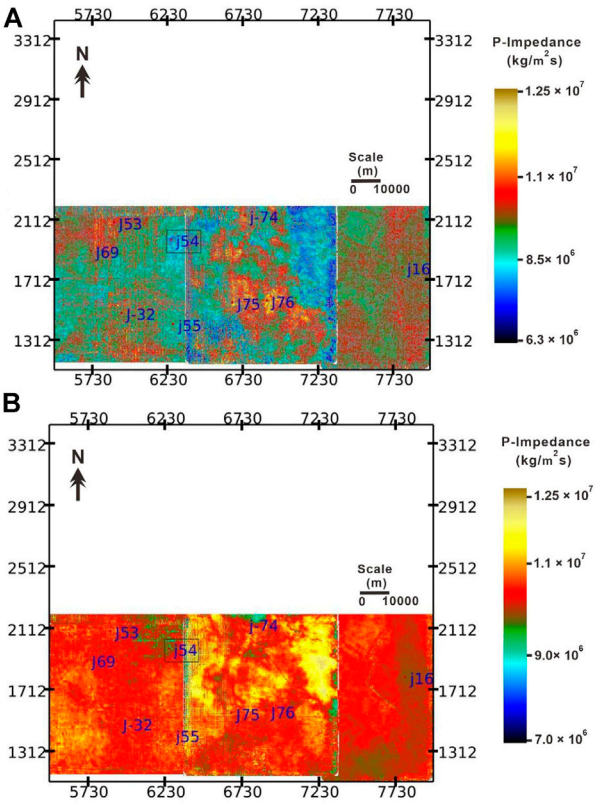

FIGURE 8
Impedance maps of **(A)** T9c horizon and **(B)** T9d horizon. The highlighted well J54 is utilized in the study to assess the vertical distribution of lithofacies.

influence of coal obscures the amplitude response of tight sandstone. Seismic resolution is insufficient to distinguish between coal and tight sandstone. As a result of the seismic section's low-velocity coalbed layer producing such a high amplitude reflection, it creates a thick reflector. When it comes to interpretation, the thick reflector might be deceiving. An inversion of limited sparse spike inversion data evidently showed the coal deposit to be distinct from mudstone and tight sandstone. The coal bed (dark blue) is present between the T9d to T9c horizons in Taiyuan and Shanxi Formations. Furthermore, the AI broadband model shows that various lithologies are present in between T9c-T9d horizons which were not easily resolvable on the seismic section. The tight sandstone (yellow-brown color) is evidently differentiated from the coal layer (dark blue) and mudstone (cyan-green color). The impedance value of coal is quite low as compared to tight sandstone and mudstone facies. Whereas, the impedance of mudstone facies is moderate to high, and tight sandstone shows moderate-to-highest impedance. The impedance of coal facies lies around 6.5 × 10^6 kg/m^2s, 8.5 × 10^6 kg/m^2s for mudstone facies, and about 1 × 10^7 kg/m^2s for tight sand facies near J54 well location.

Geoscientists often find worth in impedance sections that are placed between wells and overlay them with logs. As a result of the fact that impedance sections often demonstrate reservoir connection which can be correlated with porosity and impedance sections that are able to provide valuable information to geological models. For this reason, overlay log was utilized in order to validate the dependability of the inverted model. Because the seismic has a lower vertical resolution than the well logs, many beds that can be observed in the wells were not evident in the seismic. In order to make a more accurate comparison between the well logs and the inversion result, a high-cut filter was applied to the p-impedance (AI) log and then filtered back to the frequency of the inversion result. Following the completion of the filtering process, the Al log was then superimposed over the inverted AI sections.

At the J54 well site, a p-impedance log curve was superimposed on an inverted AI absolute (broadband) model (Figure 7A) and bandlimited model (Figure 7B). This indicates that the coal facies exhibit the lowest impedance values that range from 4.5 × 10^6 kg/m^2s to 6.5 × 10^6 kg/m^2s. Whereas, tight sandstone facies exhibits the highest impedance values that range from 8.5 × 10^6 kg/m^2s to 1.20 × 10^7 kg/m^2s at J54 well location. However, the mudstone facies shows a moderate value of impedance that ranges around 6.0 × 10^6 kg/m^2s to 1.15 × 10^7 kg/m^2s. For a conventional case, low AI is one of the key features of good gas reservoirs. In a previous study of conventional sand-shale reservoir, authors showed that the high-quality gas reservoirs fall somewhere in the region of 7.5 × 10^6 kg/m^2s to 9.9 × 10^6 kg/m^2s, whereas the higher values show the features of shales (Ibrahim, 2007). But, in our case, the tight sandstone shows unconventional behavior due to presence of coal. Since, the AI values of tight sandstone in the ZOI is highest as compared to mudstone and coal facies, therefore it suggests the presence of unconventional tight sandstone facies. In many recent studies, authors have showed that the tight sandstone within the Ordos Basin shows unconventional pattern where coal shows lowest impedance and tight sandstone shows highest impedance values as compared to mudstone facies (Liu et al., 2022; Pan et al., 2022).

Furthermore, the test confirmed that the inverted AI model is reliable and can be used for further reservoir characterization of sand-ratio identification.

5 Discussion

5.1 Distribution of the acoustic impedance on the targeted intervals

The AI maps of layers T9c to T9d (Taiyuan and Shanxi Formations) were generated to interpret the coal seams and the fluvial channel sandstone facies distribution of the targeted area. The AI map of T9c horizon shows the distribution of tight sandstone,

TABLE 1 Selected parameters for optimum wavelet estimation within the study area.

Sample interval	Phase rotation	Ricker wavelet frequency (Hz)	Correlation factor	Correlation range	Scale factor	No. Of traces	Trace gate (horizons)
0.004	180°	22	0.703916	0.02	72401.9	10	T9d—T9c

TABLE 2 Statistics for T9c-T9d sand-ratio and p-Impedance of nine studied wells.

Well name	Sand-ratio	P-impedance
J54	0.336	5,784,960
J75	0.3319	6,509,350
J76	0.538	7,605,100
J69	0.45	6,975,790
J32	0.414	7,101,000
J16	0.65	8,056,030
J55	0.472	6,888,270
J74	0.69	8,569,050
J53	0.59	7,771,210

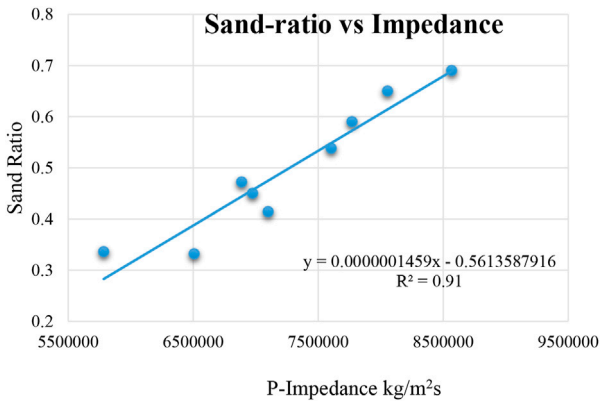

FIGURE 9
Cross-plot between the AI and sand-ratio with a good correlation coefficient value. The relationship shows a linear relationship with a positive slope. The nine points shows the AI and sand-ratio values of nine studied wells that lie within the targeted T9c-T9d horizons.

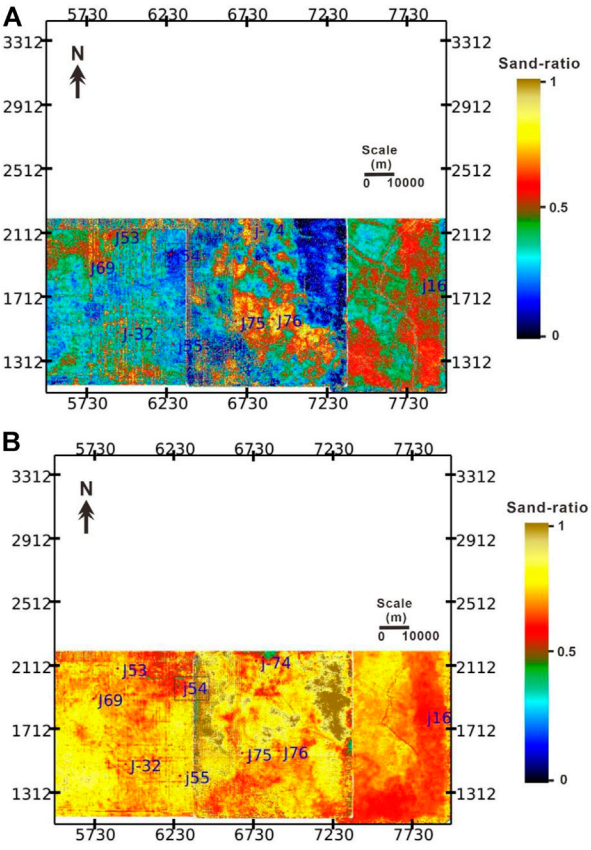

FIGURE 10
Sand-ratio maps of **(A)** T9c horizon & **(B)** T9d horizon. The highlighted well J54 is utilized in the study to assess the vertical distribution of lithofacies.

mudstone and coal seam in the Taiyuan and Lower Shanxi Formations (Figure 8A). The AI map of T9d horizon shows the distribution of only tight sandstone and mudstone. Since this horizon lies at the top of the Shanxi Formation and the bottom of the Lower Shihezi-1 Formation, the majority of the area within the T9d map shows the distribution of the mainly reservoir tight sandstone (Figure 8B). The sand bodies are developed and overlapped with each other. It can also be seen from the T9d map that the effect of coal from the underlying Shanxi and Taiyuan Formations is negligible on this horizon map.

5.2 Reservoir sand-ratio distribution

We exported the lithofacies and depth columns of well-logging data of the ZOI. It was determined how thick each lithology was by noting the top and bottom depths of each lithology and then calculating the thickness of each lithology. After that, the thicknesses of the tight sandstone intervals were put together to

get the overall thickness of the tight sand. In addition to this, the whole thickness of the targeted formation intervals was computed. The sand-ratio was determined by utilizing the ratio of sandstone-thickness and formation-thickness (Ashraf et al., 2020).

After the calculation of formation thickness and cumulative tight sandstone thickness within the ZOI, following steps were undertaken to measure the sand-ratio.

1. Initially, horizon attribute extraction was conducted between the T9c and T9d impedance map. By utilizing the horizon-to-horizon attribute map between T9c-T9d, we noted the impedance values at each well location.
2. By employing the formula of sand-ratio = sandstone thickness/formation thickness, we have the calculated the sand-ratio of each well.
3. A table was constructed using the above mentioned points for further analysis (Table 2). After plotting the results with p-impedances along the *x*-axis and sand-ratio along the *y*-axis, a linear connection (trend-line) and an equation was obtained (Figure 9). Since the tight sandstone showed highest impedance as compare to mudstone and coal facies, therefore a positive slope was obtained due to the unconventional characteristics of tight sandstone in the Hangjinqi area. The trendline with a positive slope also suggest that the sand-ratio is increasing with increasing p-impedance value. Cross plot of AI and sand-ratio with a correlation coefficient showed an excellent $R^2 = 0.91$ value.
4. The acquired equation was entered into the FunctionMod Jason program, where it was utilized to generate the framework (statistics) by using the inverted AI model. The final result, which was also produced, was then presented on the map for the results (Figure 10).

$$y = 0.0000001459x - 0.5613587916 \quad (2)$$

The sand-ratio map of T9c and T9d (Taiyuan and Shanxi Formations) was generated to measure the facies distribution of the targeted area. The sand-ratio thickness map supports the results of the impedance maps. The results show that T9d is the reservoir horizon that has the maximum distribution of tight sandstone as compared to T9c. The sand-ratio distribution is less than 25% in the majority of the area on T9c map due to the presence of excessive mudstone and coal facies (Figure 10A), whereas it is more than 80% in majority of the area on the T9d map due to mainly tight sandstone facies (Figure 10B). The T9d map gives the indication of thick braided channels and braided bars where the tight sand facies were deposited, and mudstone facies were deposited in the inter-distributary channels. On the other hand, the T9c map displays multi-characteristics of sedimentary facies distribution where coal facies were deposited in the swamp region. The tight sand and mud facies were deposited in the deltaic and inter-distributary channels. Corollary, our research indicates that the T9d horizon that lies at the interface of Shanxi and Shihezi-1 Formations has the best potential for exploring gas reservoirs due to the presence of maximum sand-ratio distribution.

Conclusion

We have utilized regional 3D seismic and nine well logs by employing the advanced CSSI to evaluate the spatial distribution of lithofacies within the T9c and T9d horizons that covers the Shanxi and Taiyuan Formations of the Hangjinqi area.

The conclusions of the study are as follows;

1. The formation evaluation of well J54 shows the vertical distribution of lithofacies. The coal facies are composed of thin and thick layers towards the bottom of the zone of interest. Mudstone facies are distributed mainly in Taiyuan Formation, whereas the tight sandstone facies are present in the middle and top regions. The thick zone of coal is present at 2,957–2,978 m, whereas the four tight sandstone porous zones lie between 2,905–2,950 m.
2. The CSSI provided the reliable horizontal and spatial distribution of various lithofacies through broadband and bandlimited inverted models. Results of CSSI also supported the results of well logging which showed that the coal facies were accumulated at the bottom and displayed low-impedance values that range between 4.5×10^6–6.5×10^6 kg/m^{2}s, mudstone facies had moderate AI values of about 6.0×10^6–1.5×10^7 kg/m^{2}s, and reservoir tight sandstone facies lie between 8.5×10^6 kg/m^{2}s to 1.20×10^7 kg/m^{2}s at J54 well location.
3. The sand-ratio and AI relationship yielded a strong association of $R^2 = 0.91$. The sand-ratio of T9c lies between 0 and 0.5 and 0.65-0.95 for the T9d horizon map. The T9d horizon suggested the presence of thick fluvial braided channels and braided bars where tight sandstone is accumulated. The mudstone facies are present in the inter-distributary channels in the Hangjinqi. The coal facies are mostly present in the T9c map that suggest the swamp settings. Overall, the T9d has good quality reservoir characteristics and should be targeted for future gas explorations.

Data availability statement

The data analyzed in this study is subject to the following licenses/restrictions: The data is confidential. Requests to access these datasets should be directed to umarash2010@hotmail.com.

Author contributions

AA, WS, and UA conceived this study. WS supervised this project. RW undertook the responsibility of arranging the data

for this project. AA and UA wrote the manuscript. AR, HT, GA, JU, II, and NA helped in validation and software. XZ discussed the data. ST and HZ reviewed the manuscript and provided the necessary funding. All authors have read and agreed to the published version of the manuscript.

Funding

This research was supported by the National Natural Science Foundation of China (Grant Nos 4162134 and 41820104008), the National Key R and D program of China (2017YFE0106300), the 13th Five year Plan of the Ministry of Science and Technology of China (2016ZX05034-002003), the Fundamental Research Funds for the Central Universities, China University of Geosciences (Wuhan) (CUGCJ1712), and the Open Fund of the Key Laboratory of Tectonics and Petroleum Resources (China University of Geosciences in Wuhan) (TPR-2018-18), and Yunnan Provincial Government Leading Scientist Program, No. 2015HA024.

Acknowledgments

AA is grateful to my former supervisor Prof. Shi Wanzhong for providing the necessary data, guidance, support, software, and technical help to accomplish this research. I am also thankful for my labmates at the China University of Geosciences. I also acknowledge the China University of Geosciences, Wuhan, and Yunnan University for funding this project.

Conflict of interest

The authors declare that the research was conducted in the absence of any commercial or financial relationships that could be construed as a potential conflict of interest.

The reviewer YY declared a shared affiliation with the author II to the handling editor at the time of review.

The reviewer FR declared a shared affiliation with the author GR to the handling editor at the time of review.

Publisher's note

All claims expressed in this article are solely those of the authors and do not necessarily represent those of their affiliated organizations, or those of the publisher, the editors and the reviewers. Any product that may be evaluated in this article, or claim that may be made by its manufacturer, is not guaranteed or endorsed by the publisher.

References

Abbas, A., Zhu, H., Anees, A., Ashraf, U., and Akhtar, N. (2019). Integrated seismic interpretation, 2D modeling along with petrophysical and seismic attribute analysis to decipher the hydrocarbon potential of Missakeswal area. *Pak. J. Geol. Geophys* 7, 1–12. doi:10.4172/2381-8719.1000455

Abdulaziz, A. M., Mahdi, H. A., and Sayyouh, M. H. (2019). Prediction of reservoir quality using well logs and seismic attributes analysis with an artificial neural network: A case study from farrud reservoir, Al-ghani field, Libya. *J. Appl. Geophys.* 161, 239–254. doi:10.1016/j.jappgeo.2018.09.013

Anees, A., Shi, W., Ashraf, U., and Xu, Q. (2019). Channel identification using 3D seismic attributes and well logging in lower Shihezi Formation of Hangjinqi area, northern Ordos Basin, China. *J. Appl. Geophys.* 163, 139–150. doi:10.1016/j.jappgeo.2019.02.015

Anees, A., Zhang, H., Ashraf, U., Wang, R., Liu, K., Abbas, A., et al. (2022a). Sedimentary facies controls for reservoir quality prediction of lower shihezi member-1 of the Hangjinqi area, Ordos Basin. *Minerals* 12, 126. doi:10.3390/min12020126

Anees, A., Zhang, H., Ashraf, U., Wang, R., Liu, K., Mangi, H., et al. (2022b). Identification of favorable zones of gas accumulation via fault distribution and sedimentary facies: Insights from Hangjinqi area, northern Ordos Basin. *Front. Earth Sci. (Lausanne).* 9, 822670. doi:10.3389/feart.2021.822670

Anees, A., Zhong, S. W., Ashraf, U., and Abbas, A. (2017). Development of a computer program for zoeppritz energy partition equations and their various approximations to affirm presence of hydrocarbon in missakeswal area. *Geosciences* 7, 55–67. doi:10.5923/j.geo.20170702.02

Ashraf, U., Zhang, H., Anees, A., Ali, M., Zhang, X., Shakeel Abbasi, S., et al. (2020). Controls on reservoir heterogeneity of a shallow-marine reservoir in Sawan Gas Field, SE Pakistan: Implications for reservoir quality prediction using acoustic impedance inversion. *Water* 12, 2972. doi:10.3390/w12112972

Ashraf, U., Zhang, H., Anees, A., Mangi, H. N., Ali, M., Zhang, X., et al. (2021). A core logging, machine learning and geostatistical modeling interactive approach for subsurface imaging of lenticular geobodies in a clastic depositional system, SE Pakistan. *Nat. Resour. Res.* 30, 2807–2830. doi:10.1007/s11053-021-09849-x

Ashraf, U., Zhu, P., Anees, A., Abbas, A., and Talib, A. (2016). Analysis of Balkassar area using velocity modeling and interpolation to affirm seismic interpretation, Upper Indus Basin. *Geosciences* 6, 78–91. doi:10.5923/j.geo.20160603.02

Ashraf, U., Zhu, P., Yasin, Q., Anees, A., Imraz, M., Mangi, H. N., et al. (2019). Classification of reservoir facies using well log and 3D seismic attributes for prospect evaluation and field development: A case study of sawan gas field, Pakistan. *J. Petroleum Sci. Eng.* 175, 338–351. doi:10.1016/j.petrol.2018.12.060

Avadhani, V., Anandan, M., Thattacherry, B., Murthy, K., Gariya, B., and Dwivedi, A. (2006). Acoustic impedance as a lithological and hydrocarbon indicator—A case study from cauvery basin. *Lead. Edge* 25, 854–858. doi:10.1190/1.2221363

Cooke, D. A., and Schneider, W. A. (1983). Generalized linear inversion of reflection seismic data. *Geophysics* 48, 665–676. doi:10.1190/1.1441497

Cooke, D., and Cant, J. (2010). Model-based seismic inversion: Comparing deterministic and probabilistic approaches. *CSEG Rec.* 35, 29–39.

Dai, J., Ni, Y., and Wu, X. (2012). Tight gas in China and its significance in exploration and exploitation. *Petroleum Explor. Dev.* 39, 277–284. doi:10.1016/s1876-3804(12)60043-3

Dar, Q. U., Pu, R., Baiyegunhi, C., Shabeer, G., Ali, R. I., Ashraf, U., et al. (2022). The impact of diagenesis on the reservoir quality of the early Cretaceous Lower Goru sandstones in the Lower Indus Basin, Pakistan. *J. Pet. Explor. Prod. Technol.* 12, 1437–1452. doi:10.1007/s13202-021-01415-8

Duan, Y., Wang, C., Zheng, C., Wu, B., and Zheng, G. (2008). Geochemical study of crude oils from the Xifeng oilfield of the Ordos basin, China. *J. Asian Earth Sci.* 31, 341–356. doi:10.1016/j.jseaes.2007.05.003

Ehsan, M., Gu, H., Ahmad, Z., Akhtar, M. M., and Abbasi, S. S. (2019). A modified approach for volumetric evaluation of shaly sand formations from conventional well logs: A case study from the talhar shale, Pakistan. *Arab. J. Sci. Eng.* 44, 417–428. doi:10.1007/s13369-018-3476-8

Ehsan, M., Gu, H., Akhtar, M. M., Abbasi, S. S., and Ullah, Z. (2018). Identification of hydrocarbon potential of Talhar shale: Member of lower Goru Formation using well logs derived parameters, southern lower Indus basin, Pakistan. *J. Earth Sci.* 29, 587–593. doi:10.1007/s12583-016-0910-2

Ehsan, M., and Gu, H. (2020). An integrated approach for the identification of lithofacies and clay mineralogy through Neuro-Fuzzy, cross plot, and statistical analyses, from well log data. *J. Earth Syst. Sci.* 129, 101–113. doi:10.1007/s12040-020-1365-5

Ferguson, R. J., and Margrave, G. F. (1996). A simple algorithm for band-limited impedance inversion. *CREWES Res. Rep.* 8, 1–10.

Gaoyuan, Y., Junjian, Z., Guanwen, L., and Fangkai, Q. (2021). Fractal characteristics of shale pores from Taiyuan Formation to Shanxi Formation in qinshui basin. *Xinjiang Pet. Geol.* 42, 548. doi:10.7657/XJPG20210505

Gardner, G., Gardner, L., and Gregory, A. (1974). Formation velocity and density—the diagnostic basics for stratigraphic traps. *Geophysics* 39, 770–780. doi:10.1190/1.1440465

Ibrahim, M. (2007). "Seismic inversion data, a tool for reservoir characterization/modeling, sawan gas field—a case study," in Proceedings of the Annual Technical Conference, Islamabad, Pakistan, 27-28 March 2007.

Jiang, R., Zhao, L., Xu, A., Ashraf, U., Yin, J., Song, H., et al. (2022). Sweet spots prediction through fracture Genesis using multi-scale geological and geophysical data in the karst reservoirs of Cambrian Longwangmiao Carbonate Formation, Moxi-Gaoshiti area in Sichuan Basin, South China. *J. Pet. Explor. Prod. Technol.* 12, 1313–1328. doi:10.1007/s13202-021-01390-0

Ju, W., Shen, J., Qin, Y., Meng, S., Wu, C., Shen, Y., et al. (2017). *In-situ* stress state in the linxing region, eastern Ordos Basin, China: Implications for unconventional gas exploration and production. *Mar. Petroleum Geol.* 86, 66–78. doi:10.1016/j.marpetgeo.2017.05.026

Kassem, A. A., Hussein, W. S., Radwan, A. E., Anani, N., Abioui, M., Jain, S., et al. (2021). Petrographic and diagenetic study of siliciclastic Jurassic sediments from the Northeastern Margin of Africa: Implication for reservoir quality. *J. Petroleum Sci. Eng.* 200, 108340. doi:10.1016/j.petrol.2020.108340

Latimer, R. B., Davidson, R., and Van Riel, P. (2000). An interpreter's guide to understanding and working with seismic-derived acoustic impedance data. *Lead. edge* 19, 242–256. doi:10.1190/1.1438580

Li, P., Zhang, J., Tang, X., Huo, Z., Li, Z., Luo, K., et al. (2021). Assessment of shale gas potential of the lower Permian transitional Shanxi-Taiyuan shales in the southern North China Basin. *Aust. J. Earth Sci.* 68, 262–284. doi:10.1080/08120099.2020.1762737

Liu, B., Chang, S., Zhang, S., Chen, Q., Zhang, J., Li, Y., et al. (2022). Coalbed methane gas content and its geological controls: Research based on seismic-geological integrated method. *J. Nat. Gas Sci. Eng.* 101, 104510. doi:10.1016/j.jngse.2022.104510

Liu, K., Wang, R., Shi, W., Zhang, W., Qi, R., Qin, S., et al. (2020). Tectonic controls on Permian tight gas accumulation: Constrains from fluid inclusion and paleo-structure reconstruction in the Hangjinqi area, northern Ordos Basin, China. *J. Nat. Gas Sci. Eng.* 83, 103616. doi:10.1016/j.jngse.2020.103616

Mangi, H. N., Chi, R., Detian, Y., Sindhu, L., He, D., Ashraf, U., et al. (2022). The ungrind and grinded effects on the pore geometry and adsorption mechanism of the coal particles. *J. Nat. Gas Sci. Eng.* 100, 104463. doi:10.1016/j.jngse.2022.104463

Mangi, H. N., Detian, Y., Hameed, N., Ashraf, U., and Rajper, R. H. (2020). Pore structure characteristics and fractal dimension analysis of low rank coal in the Lower Indus Basin, SE Pakistan. *J. Nat. Gas Sci. Eng.* 77, 103231. doi:10.1016/j.jngse.2020.103231

Pan, H., Yin, X., Li, K., and Pei, S. (2022). An improved matching pursuit method for coal seam identification driven by seismic inversion. *Chin. J. Geophys.* 65, 2276–2293. doi:10.6038/cjg2022P0211

Pendrel, J. (2006). Seismic inversion-a critical tool in reservoir characterization. *Scand. oil-gas Mag.* 34.

Qiang, Z., Yasin, Q., Golsanami, N., and Du, Q. (2020). Prediction of reservoir quality from log-core and seismic inversion analysis with an artificial neural network: A case study from the sawan gas field, Pakistan. *Energies* 13, 486. doi:10.3390/en13020486

Radwan, A. E. (2020). *Hydrocarbon type estimation using the synthetic logs: A case study in baba member*. Gulf of Suez, Egypt: AAPG/datapages search and discovery. *Article* 20475.

Radwan, A. E. (2021). Modeling the depositional environment of the sandstone reservoir in the middle miocene sidri member, badri field, gulf of Suez basin, Egypt: Integration of gamma-ray log patterns and petrographic characteristics of lithology. *Nat. Resour. Res.* 30, 431–449. doi:10.1007/s11053-020-09757-6

Radwan, A. E., Trippetta, F., Kassem, A. A., and Kania, M. (2021). Multi-scale characterization of unconventional tight carbonate reservoir: Insights from October oil filed, Gulf of Suez rift basin, Egypt. *J. Petroleum Sci. Eng.* 197, 107968. doi:10.1016/j.petrol.2020.107968

Riedel, M., Lee, W., and Bellefleur, G. (2010). 7. Inversion of Seismic Data for Elastic Parameters: A Tool for Gas-Hydrate Characterization. *Geophys. Dev. Ser.*, 109–120. doi:10.1190/1.9781560802197.ch7

Saussus, D., and Sams, M. (2012). Facies as the key to using seismic inversion for modelling reservoir properties. *First Break* 30, 45–52. doi:10.3997/1365-2397.2012009

Simm, R., Bacon, M., and Bacon, M. (2014). *Seismic amplitude: An interpreter's handbook*. United Kingdom: Cambridge University Press.

Ullah, J., Luo, M., Ashraf, U., Pan, H., Anees, A., Li, D., et al. (2022). Evaluation of the geothermal parameters to decipher the thermal structure of the upper crust of the Longmenshan fault zone derived from borehole data. *Geothermics* 98, 102268. doi:10.1016/j.geothermics.2021.102268

Veeken, P., and Da Silva, M. (2004). Seismic inversion methods and some of their constraints. *First break* 22. doi:10.3997/1365-2397.2004011

Vo Thanh, H., and Lee, K.-K. (2022). 3D geo-cellular modeling for oligocene reservoirs: A marginal field in offshore vietnam. *J. Pet. Explor. Prod. Technol.* 12, 1–19. doi:10.1007/s13202-021-01300-4

Vo Thanh, H., Sugai, Y., and Sasaki, K. (2020). Impact of a new geological modelling method on the enhancement of the CO2 storage assessment of E sequence of Nam Vang field, offshore Vietnam. *Energy Sources, Part A Recovery, Util. Environ. Eff.* 42, 1499–1512. doi:10.1080/15567036.2019.1604865

Wang, H., Zhang, L., Zhao, Q., Qiu, Z., Liu, D., Zhang, Q., et al. (2021). Reservoir characteristics of the lower permian marine-continental transitional shales: Example from the Shanxi Formation and Taiyuan Formation in the Ordos Basin. *Geofluids*, 1–17. doi:10.1155/2021/9373948

Wang, J., and Guo, S. (2019). The whole-aperture pore-structure characteristics of marine-continental transitional shale facies of the Taiyuan and Shanxi Formations in the Qinshui Basin, North China. *Interpretation* 7, T547–T563. doi:10.1190/int-2018-0157.1

Wang, Q., and Guo, K. (2008). Constrained sparse spike inversion applied in the reservoir prediction. *Well Logging Technol.* 32, 35–37. doi:10.16489/j.issn.1004-1338.2008.01.02

Wood, D. A., and Cai, J. (2022). "Coal-bed methane reservoir characterization using well-log data," in *Sustainable geoscience for natural gas subsurface systems* (Oxford, United Kingdom: Elsevier), 243–274.

Wu, X., Ni, C., Liu, Q., Liu, G., Zhu, J., and Chen, Y. (2017). Genetic types and source of the upper paleozoic tight gas in the Hangjinqi area, northern Ordos Basin, China. *Geofluids* 2017, 1–14. doi:10.1155/2017/4596273

Xu, H., Tang, D., Tang, S., Zhang, W., Meng, Y., Gao, L., et al. (2015). Geologic and hydrological controls on coal reservoir water production in marine coal-bearing strata: A case study of the carboniferous Taiyuan Formation in the liulin area, eastern Ordos Basin, China. *Mar. Petroleum Geol.* 59, 517–526. doi:10.1016/j.marpetgeo.2014.10.005

Xu, Q., Shi, W., Xie, X., Busbey, A. B., Xu, L., Wu, R., et al. (2018). Inversion and propagation of the late paleozoic Porjianghaizi Fault (north Ordos Basin, China): Controls on sedimentation and gas accumulations. *Mar. Petroleum Geol.* 91, 706–722. doi:10.1016/j.marpetgeo.2018.02.003

Xue, H., Wang, Y., Mao, X., Xu, P., Nie, H., Yin, Y., et al. (2009). The timing of gas pooling in the upper paleozoic in the northern Ordos Basin: A case study of the Hangjinqi Block. *Nat. Gas. Ind.* 29, 9–12. doi:10.3787/j.issn.1000-0976.2009.12.003

Yang, M., Li, L., Zhou, J., Jia, H., Sun, X., Qu, X., et al. (2015). Mesozoic structural evolution of the Hangjinqi area in the northern Ordos Basin, north China. *Mar. Petroleum Geol.* 66, 695–710. doi:10.1016/j.marpetgeo.2015.07.014

Yang, Y., Li, W., and Ma, L. (2005). Tectonic and stratigraphic controls of hydrocarbon systems in the Ordos Basin: A multicycle cratonic basin in central China. *Am. Assoc. Pet. Geol. Bull.* 89, 255–269. doi:10.1306/10070404027

Zhang, L., Bai, G., Luo, X., Ma, X., Chen, M., Wu, M., et al. (2009). Diagenetic history of tight sandstones and gas entrapment in the Yulin Gas Field in the central area of the Ordos Basin, China. *Mar. Petroleum Geol.* 26, 974–989. doi:10.1016/j.marpetgeo.2008.05.003

Zhang, X., Fu, J., Hou, F., Zheng, X., Zhang, Y., Wang, R., et al. (2022). Sand-mudstone modeling of fluvial fan sedimentary facies: A case study of Shanxi Formation reservoir in Ordos Basin. *J. Pet. Explor. Prod. Technol.*, 1–14. doi:10.1007/s13202-022-01496-z

Zhu, H. (2011). Application of multiple wells-constrained sparse pulse inversion technology in coalfield 3D seismic prospecting. *Procedia Earth Planet. Sci.* 3, 401–407. doi:10.1016/j.proeps.2011.09.112

frontiers | Frontiers in Earth Science

TYPE Original Research
PUBLISHED 28 September 2022
DOI 10.3389/feart.2022.972125

OPEN ACCESS

EDITED BY
Amin Beiranvand Pour,
INOS University Malaysia Terengganu, Malaysia

REVIEWED BY
Bo Liu,
Northeast Petroleum University, China
Ebong D. Ebong,
University of Calabar, Nigeria

*CORRESPONDENCE
Mingchuan Wang,
wangmc.syky@sinopec.com

SPECIALTY SECTION
This article was submitted to Economic Geology, a section of the journal Frontiers in Earth Science

RECEIVED 17 June 2022
ACCEPTED 05 September 2022
PUBLISHED 28 September 2022

CITATION
Wang M, Yang F, Zhang Y, Zhang D, Feng J, Luo J and Zeng Y (2022), Probabilistic geothermal resource assessment in Maichen Sag, south China.
Front. Earth Sci. 10:972125.
doi: 10.3389/feart.2022.972125

Probabilistic geothermal resource assessment in Maichen Sag, south China

Mingchuan Wang*, Fan Yang, Ying Zhang, Dianwei Zhang, Jianyun Feng, Jun Luo and Yan Zeng

SINOPEC Petroleum Exploration and Production Research Institute, Beijing, China

It is crucial for financial providers, investment groups, resource developers, and exploration companies to rate new geothermal projects in terms of resources and reserves. In general, the existing volumetric method is constrained by limited information when projects are at the early stage of development. The main objective of this study is to estimate the probabilistic potential thermal energy of the M research area in the Maichen Sag, a geothermal prospect in South China, through stochastic methodologies. The probabilistic assessment methodology provides a way to embody the uncertainty and risk in geothermal projects and to quantify the power potential in a probable range. In this study, proxy numerical models were built by combining the Experimental Design (ED) and Response Surface Methodology (RSM) with the Monte Carlo Simulation technique. An improved workflow for combined ED-RSM that uses two-level Full Factorial and Box–Behnken designs was proposed. For comparative analysis, the typical volumetric technique was also implemented in this study. The ED-RSM results show that the M area has P10, P50, and P90 reserves of 5.7×10^{14} J, 5.3×10^{14} J, and 5×10^{14} J, respectively, and these numbers from the typical volumetric method are 1.5×10^{15} J, 9×10^{14} J, and 5.1×10^{14} J, respectively. In this study, the operability, applicability, and accessibility of ED-RSM in the assessment of geothermal potential and its ability to provide a reliable output are demonstrated.

KEYWORDS

south China, maichen sag, probabilistic geothermal energy assessment, experimental design, response surface methodology, temperature field, geothermal geological model

1 Introduction

Global energy demand has soared tremendously because of rapid industrial advancement and human activities, at the same time, it has been found that the available geothermal resources are adequate to meet this energy demand. At present, 80 countries have geothermal resources that are being harnessed for direct use applications; however, currently, only 24 countries are using geothermal resources for generating electricity (Bertani, 2012; Bertani, 2016; Lund and Boyd, 2016). Resource evaluation, which is the first step toward improvement of the commercial development of

geothermal resources, is the practice of characterizing a geothermal system and estimating its potential power or thermal energy capacity (Ciriaco et al., 2018; Ciriaco A. E. et al., 2020). The estimated capacity of the resource is usually calculated by using volumetric heat storage method or numerical models. Of these two methods, numerical modeling has been widely used in various industries and can provide more reliable estimates (Ciriaco A. E. et al., 2020). It can be used to simulate the fluid flow and heat transfer of actual complex geothermal systems, and its performance is better than that of the heat storage method (Quinao and Zarrouk, 2018). However, numerical modeling of geothermal systems still cannot provide error-free results and cannot make subjective predictions on its modeling parameters. Therefore, quantification of the mismatches and errors in numerical modeling predictions is not only necessary, but also challenging because these models produce deterministic results (Santner et al., 2003; Ciriaco et al., 2018). The quantification of uncertainty in numerical model predictions requires a series of simulation experiments. These steps include the construction of multiple versions of the calibrated reservoir model through reverse modeling. However, under normal circumstances, simulation experiments require intense labor and time (Doherty et al., 2017). The method involving combination of Experimental design (ED) and Response surface methodology (RSM), together denoted as ED-RSM method has been employed to build polynomial models rather than numerical models and several authors have verified the techniques (Pasikki et al., 2016; Quinao and Zarrouk, 2018). The ED-RSM method allows for the consideration of uncertainty in numerical model predictions in a more practical manner (Ciriaco A. E. et al., 2020).

In experimental research, ED and RSM are two separate statistical techniques that are used to describe the relationship between input variables and specific output variables (Ciriaco A. E. et al., 2020). The output variable is the parameter of interest, which is the goal or product of the experiment. On the other hand, the input variables are variables that affect output. ED uses the least number of simulations to understand the impact of input variables on output variables, while RSM optimizes output variables by conducting sequential experiments (Ciriaco et al., 2018). Notably, ED was first introduced in the 1920s mainly to provide a method for systematic planning and research (Box, 1979; Box et al., 1978; Myers and Montgomery, 2002). Nowadays, the ED-RSM framework has been applied in many fields such as metallurgy, transportation, medicine, industrial machinery, and oil and gas. However, in the geothermal industry, only a few published studies on this technology are available. For example, Acuna et al., 2002 and Hoang et al. (2005) described the relationship between factors that affected power capacity, by considering one factor at a time and created a simple equation as a function of important reservoir parameters, including rock permeability, boundary conditions of aquifers, productivity (Ciriaco A. E. et al., 2020), upwelling velocity, and deep reservoir temperature. Pasikki et al., 2016 evaluated green fields by developing a polynomial model for calculating the average decline rate of MWe using ED. Quinao and Zarrouk (2018) succeeded in estimating oil reserves by adopting a stochastic method to construct a surrogate model used in the oil industry for estimating oil reserves and revealed that Plackett–Burman and Full Factorial designs were sufficient to evaluate Ngatamariki Reservoir of New Zealand. Recently, the use of Full Factorial design and Box–Behnken design was investigated to screen and construct a second-order polynomial model and the ED-RSM method was applied to the Rotorua geothermal model (Ciriaco et al., 2018). The screening phase not only reduced the number of required simulation runs by removing insignificant variables, but also provided insights into the next experimental setup (Ciriaco et al., 2018). The results also confirmed that the second-order polynomial model is the most suitable for simulating experimental data. The results of the two studies mentioned above show that Full Factorial, Plackett–Burman, and Box–Behnken designs work well for creating geothermal reservoir models. The polynomial surrogate model from the ED-RSM method also provides a way to evaluate probabilistic resources by applying the Monte Carlo method, thus each parameter in the polynomial model can be described by using a probability distribution (Ciriaco A. E. et al., 2020).

The main objective of this study was to optimize the ED-RSM workflow to quantify uncertainty screening parameters before constructing a proxy model. The experiment involved a case study of a potential hydrothermal field in the Beibuwan Basin in China. The reservoir models of this field were established according to the natural conditions. Six reservoir parameters were selected to build the experimental design reservoir model. These parameters were horizontal (kx and ky) and vertical (kz) permeability, porosity, volumetric specific heat, and volume of a single rock type. For each reservoir model, two-level Full Factorial design and Box–Behnken design were implemented. The Box–Behnken design requires three levels; therefore, the final regression model was combined with the Monte Carlo method to generate the heat storage probability distribution, and the result was compared with the result obtained from the traditional volumetric heat storage method (Ciriaco A. E. et al., 2020). These six parameters were selected based on expert knowledge and experimental requirement. These specific rock parameters (kx, ky, kz, porosity, volumetric specific heat) and different lithology rock volumes exhibit a significant impact on amount of stored geothermal energy (q). Although other model parameters could also be included in the survey (such as upstream location parameters and

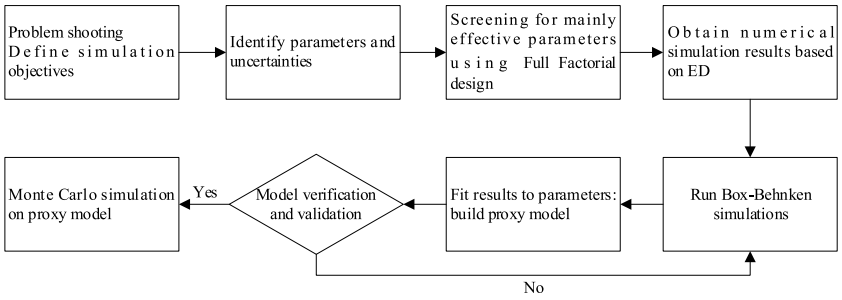

FIGURE 1
The ED-RSM workflow used in this study for probabilistic resource assessment by using numerical models.

reservoir model boundaries), based on experience, it was concluded herein that these six selected parameters were the most suitable for this study. It is strongly believed that this new type of numerical simulation-Monte Carlo method for probabilistic resource assessment is a useful and convenient method. Therefore, it is very important to use the ED-RSM framework to establish a powerful working framework to construct polynomial models for numerical modeling.

2 Methodology

A predictive model is a statistical model constructed from a collection of data for a system of interest, which is then used to predict the future behavior of the system (Ciriaco A. E. et al., 2020). In this study, a prediction model was created to predict the geothermal capacity of potential geothermal fields by using detailed geological models and numerical temperature fields. Three important components were identified to improve the geothermal ED-RSM workflow to predict geothermal capacity: 1) experimental design, 2) model parameters and parameter values, and 3) modeling acceptance criteria. In this experimental design process, two ED methods were fully utilized, and the key influencing parameters were identified by the two-level Full Factorial method, and then several types of parameters exhibiting the greatest impact on the results were selected as the basis of numerical simulation for geothermal energy. Based on obtaining the simulation calculation results, the second-order Fractional Factor experimental design method, i.e., Box–Behnken method was used to establish the proxy model. After the proxy model was established, it was judged whether it was reasonable through a set model acceptance standard. In case, it was unreasonable, the simulation sets for proxy model were optimized again until they reached the standard, and the probability distribution of geothermal energy was calculated by using the proxy model and via the Monte Carlo method. Use of this approach not only solves the problem of too many experimental parameters and cumbersome calculations, but also retains the characteristics of each parameter to the greatest extent. Moreover, the process of numerical calculation using a computer system can be omitted (Figure 1).

2.1 Experimental design

In the ED-RSM workflow, the parameters in the reservoir model are changed simultaneously according to the experimental design (Amudo et al., 2009). In this study, two experimental designs, namely, Full Factor and Fractional Factor were considered to simultaneously evaluate the response of a given output parameter to changes in input variables. The main advantage of Full Factorial design is that it allows for the evaluation of all possible parameter combinations and the collection of every possible data point, thus providing a simple method for selecting the best conditions. When using the Fractional Factorial design, part of the factorial design can simultaneously change and evaluate various factors (Walpole et al., 2012). The two most commonly used Fractional factorial designs are the Plackett–Burman design and the Box–Behnken design. The Plackett–Burman design is the most widely used in geothermal applications (Hoang et al., 2005; Quinao and Zarrouk, 2014, 2018). However, in this study, it was decided to perform a two-level Full Factorial design instead of a Plackett–Burman design to obtain more detailed factor information. Box–Behnken design is a high-order design that can be used to estimate interaction and quadratic effects. It is an independent quadratic design, with each factor requiring three levels, and it can be achieved with fewer model runs. Previous studies have shown that the fitting of modeling results requires a second-order polynomial model (Simpson et al., 1998), and this model has been successfully applied in the model of the Rotorua geothermal field (Ciriaco et al., 2018).

TABLE 1 Input parameters applied in the experimental design model.

Parameter/Variable	Unit	Low (−1)	Mid (0)	High (+1)
Permeability (x and y)	10^{-3} μm^2	0.5	1	1.5
Permeability (z)	μm^2	0.05	0.1	0.15
Porosity	%	10	15	20
Volumetric specific heat	10^6 J (k·m^3)$^{-1}$	2	2.5	3
Sandstone volume	10^8 m^3	400	900	1,500
Mudstone volume	10^8 m^3	3,000	2,500	1900

2.2 Simulation parameters and parameter values

The next step after selecting the most appropriate experimental design is the determination of the parameters or factors, their values, and their levels. The level of the factor refers to the setting of the parameter value. Each parameter is assigned a minimum (low) setting and a maximum (high) setting, and in a factorial design, these settings are assigned codes of −1 and +1, respectively. This range of values illustrates the possible uncertainty of parameters. Table 1 summarizes all the parameters and their values used in this study. The low range and high range are initially based on expert knowledge, and the range of consideration is very wide. The number of factors and their levels affects the number of simulation runs required to execute a particular design. Box–Behnken design requires a three-level factorial design (Friedmann et al., 2003; Hoang et al., 2005; Ciriaco et al., 2018; Fukuda et al., 2018). To evaluate the performance of the Full Factorial design, two-level setting was carried out.

2.3 Acceptance criteria

A residual graph was used to verify the effectiveness of the regression model (Quinao and Zarrouk, 2014). The polynomial model was evaluated based on the goodness of fit. The two measures of goodness of fit are R-squared (R^2) and adjusted R^2. For a given set of predictors, a higher R^2 value usually indicates that the polynomial model is better able to explain the change in response surface. However, even if the added predictor variable is not significant, R^2 increases naturally with the number of predictor variables. The adjusted R^2 performs better than R^2 because it adds independent variables that do not contribute to the explanatory power of the model. Monte Carlo simulation was performed on the final regression model. A simple triangular distribution based on the most probable minimum and maximum value was assigned to each important variable. A simple triangular distribution is usually sufficient to describe the uncertainty level of key reservoir parameters (Parini and Riedel, 2000). Thus, 8,000 random samples were created to generate the probability distribution of thermal energy q.

2.4 Thermal energy calculation

The thermal energy q stored in a reservoir can be calculated by dividing the reservoir into n different regions of volume Vi and temperature T_i, where i = 1, 2, ..., n, using the equation (Muffler and Cataldi, 1978):

$$q = \sum_{i=1}^{n} \rho_i c_i V_i \left(T_i - T_f\right) \quad (1)$$

where:

$\rho_i c_i$ is the volumetric specific heat capacity of the saturated rock, J (°Cm^3)$^{-1}$.
V_i is the volume of the i^{th} region of n numbers of lithology.
T_i is the initial temperature of the i^{th} lithology, °C, and T_f is the cut-off or final abandoned reservoir temperature, °C.

This study considers the influence of porosity on the above-mentioned equation. Therefore, the thermal energy in the rock (q_r) and in the fluid (q_f) was calculated separately by introducing porosity φ.

According to the geological model of a geothermal reservoir and the results of three-dimensional (3D) temperature field finite element model, the energy calculation of the finite element grid can be carried out by the above-mentioned method, and the energy of partition, layering, and rock-splitting type can be obtained. Further, the relationship among different geological parameters can be established by the ED method introduced herein, and an estimate of the geothermal reservoir's energy can be obtained quickly, and other favorable targets can be evaluated more quickly and easily.

3 Case studies

In order to improve the existing methods of constructing polynomial models, the ED-RSM workflow was applied to the geothermal potential field in the Beibuwan Basin in South China. The geothermal systems are in the South China Volcanic Zone, and their hot geothermal fluids are used for residential and commercial energy purposes.

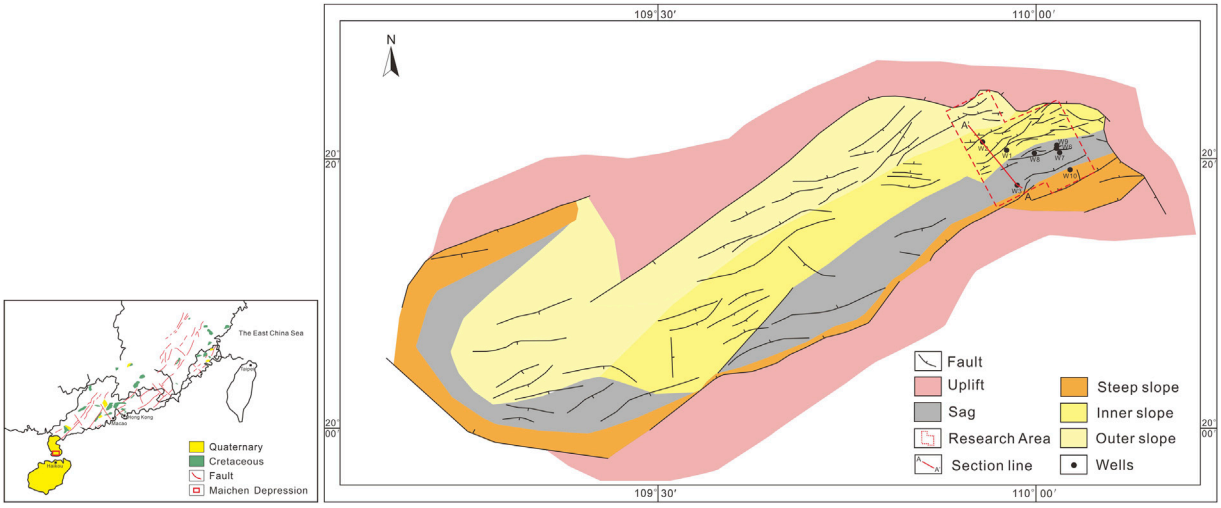

FIGURE 2
Location of the research area.

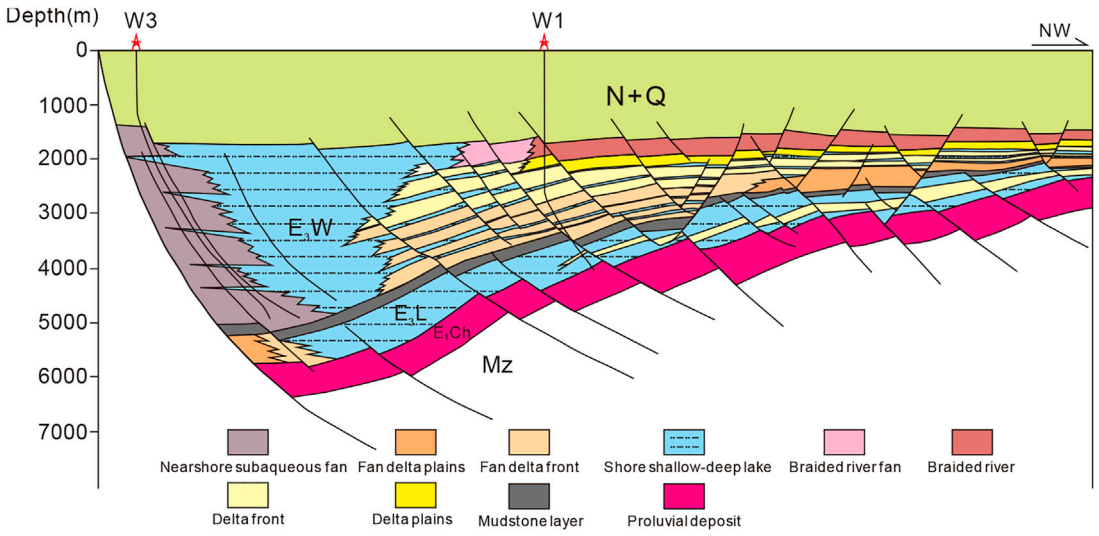

FIGURE 3
Section view and stratigraphy of the research area.

3.1 Research area background

The research area, which is in the easternmost part of the Maichen depression of the Beibuwan Basin, is an oil and gas exploration block. The area, which spans 6,256 km^2, is located in the Leizhou Peninsula, Guangdong Province, China. The structural location belongs to the eastern part of the Beibuwan Basin on the continental shelf of the South China Sea (Figure 2).

In the Cenozoic, the Beibuwan Basin underwent extensional faulting to form the basin; there is a double-layer structure of a vertical superimposed Paleogene faulted (or rifted) basin and a Neogene depression basin. In the Paleogene, extensional structures with twisted structures mainly developed, while in the Neogene-Quaternary period, extensional structures mainly developed. Huge, thick Paleogene sands and mudstone strata (Changliu Formation, Liushagang Formation, and Weizhou

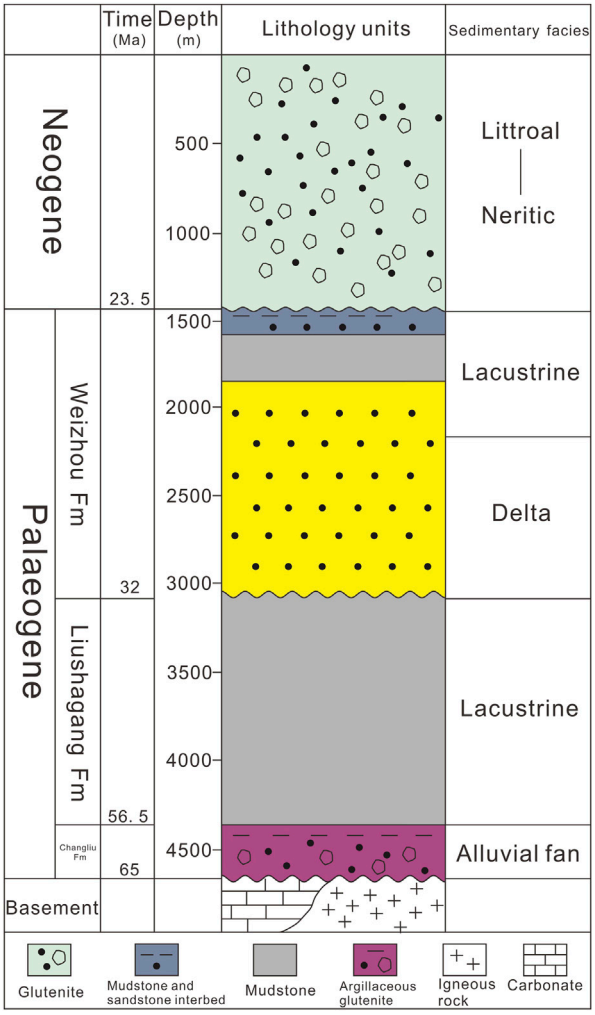

FIGURE 4
Sedimentary column of the research area.

Formation) have been deposited in the various depressions in the Beibuwan Basin (Figure 3). Among them, the Liushagang Formation is a set of shallow and middle-deep lacustrine mudstone deposits. The reservoirs are mainly sandstones of the Liushagang and Weizhou Formations, and the regional caprock is a large set of dark mudstone and shale of the Liushagang Formation (Figure 4). The Maichen depression can be divided into five structural units: the southern steep slope zone, the deep depression zone, the inner gentle slope zone, the outer gentle slope zone, and the western depression. Faults (mainly normal faults) are developed in the area. The depression-controlling faults mainly have NE strike. The boundary faults at both ends of the depression (X fault and M2 fault) have NW strikes. The secondary faults have mostly NE strikes in the deep part and NE strikes in the shallow part. In general, in the Paleogene, the Beibuwan Basin experienced the initial fault-sag period of the Paleocene, the strong fault-sag period of the Eocene, and the stable subsidence period of the Oligocene. The tectonic activity indicates a weak–strong–weak change. More importantly, the Maichen depression experienced a strong tectonic inversion in the late period of the first stage, and the strata suffered strong denudation.

According to the previous studies, the land heat flow value of the South China Sea coast varies between 60 and 80 mW m^{-2} (Zhao et al., 2019), and the heat flow value increases in the direction of the ocean basin. The surface heat flow value of each basin is different. The scale of the Beibuwan Basin is relatively small. The panoramic view of the basin is near the east to the Hainan and Leizhou areas, which are separated by the Hainan uplift and Qiongdongnan depression. The average surface heat flow value of the Beibuwan Basin is 61.2 mW m^{-2} (Chen et al., 2014). The geothermal energy in the area mainly comes from mantle-source heat and crustal reflective elements. According to a previous study, the temperature of the Moho in the Beibuwan Basin varies in the range of 700–800°C, the heat flow composition of the Beibuwan Basin is stable, and the heat flow of the crust surface varies between 38% and 42%. This previous study used the Mckenzie model and the Hutchison heat balance formula to comprehensively study the heat flow history of the Beibuwan Basin since the Cenozoic, based on measured ground temperature data. The corresponding time of the Himalayan movement leading to the thermal event is the period of intense volcanic activity since the Neogene. Previous studies have shown that the Beibuwan Basin has a relatively high current geothermal gradient, with an average value of 3.72°C/100 m, and there is a relatively low geothermal gradient in the Maichen Sag. In this study, the ground temperature was obtained and calculated from well temperature logging data in the study area. Then, a profile diagram of the relationship between underground temperature and depth was drawn (Figure 5); the temperature values were obtained from both well temperature logging data and actual measured underground temperature data. The measured data are generally higher than the well temperature data, and the measured data more truly reflect the underground temperature; however, the well temperature logging data exhibit better continuity and can better reflect the change of temperature with depth. In the temperature logging curve of Well W1, there are abnormal temperature areas that are distributed in the middle of the Liushagang Formation, and the characteristics of the measured well temperature data are not obvious. The temperature logging curve of Well W6 exhibits an increasing inflection point at the depth of 2,800 m, which may be related to the presence of the top layer containing the oil and gas reservoir. Herein, the current ground temperature gradient was calculated by plotting the measured ground temperature and depth profile. According to statistics, the annual average temperature of the surface in the Maichen depression is 22–26°C, and the average temperature is 24°C. The average temperature gradient is 3.19°C/100 m, which is calculated based on the reference surface.

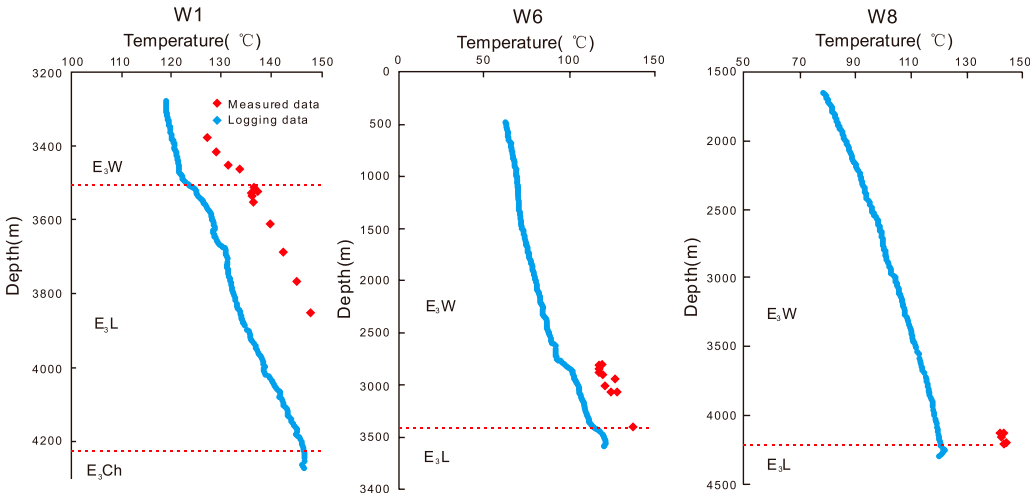

FIGURE 5
Temperature gradient from the measured and logging data.

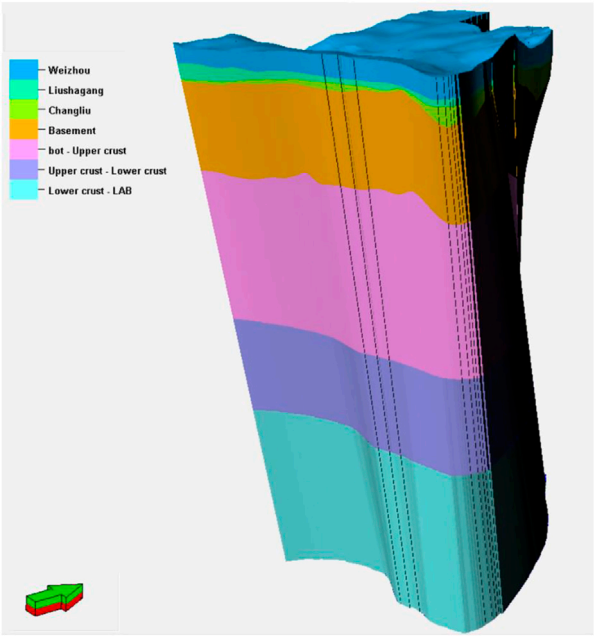

FIGURE 6
Geological model of the research area.

3.2 Geological model

The 3D information of the configuration of the underground structure was compiled, visualized, and interpolated (Ebong et al., 2019). The model is 18 km wide from east to west and 20 km wide from north to south (Figure 6). The model has seven formation layers, two sedimentary facies, and two lithological characteristics, thus the vertical grid spacing of the 3D model incorporates the number of layers and their respective thickness changes. The bottom of the model extends down to the Lithosphere–Asthenosphere Boundary (LAB) at a depth of nearly 30 km. In the horizontal direction, the 3D structure of each geological layer is defined with 170,392 grid nodes, corresponding to a grid spacing of 50 m.

The lithological model of the research area was also created by combining geostatistical and geological information (Figure 7) (Ebong et al., 2020; Ebong et al., 2021). In the 3D geological model, there are two sets of sandstone reservoirs in the target layers Weizhou and Liushagang; in the southern part of the research area, sandstone is mainly distributed locally in the ascending plate of the fault, and the deep depression of the settlement center at the descending plate contains some turbidite sandstone. In the gentle slope to the north, there are mainly deposits of river sand bodies, with obvious belt distribution characteristics, and the other locations mainly contain delta front mud and shallow lacustrine mudstone. The sand body is unevenly distributed and has great variability in lithology, porosity, and permeability. Therefore, the thermal storage correlation coefficients related to lithology and horizontal rock spatial structure also exhibit great variability. In this study, the thermal conductivity (TC), thermal diffusivity (TD), and specific heat capacity of a single well were calculated by using logging calculation methods and acoustic wave, neutron, density, natural gamma, and resistivity curves (Fuchs et al., 2015). Therefore, geostatistical method was used herein to build the geological model based on information of rocks from various single wells.

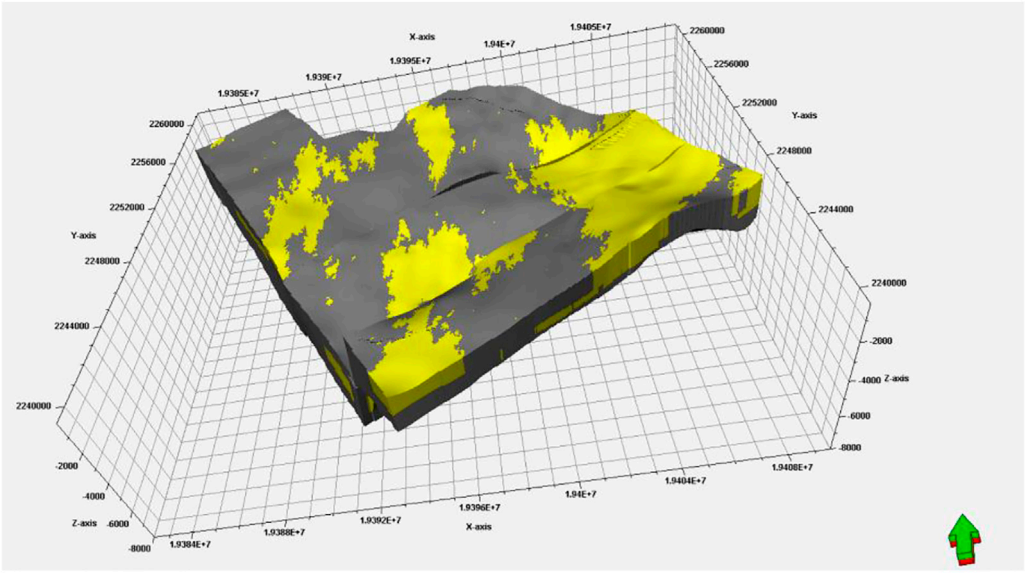

FIGURE 7
Lithological model of Weizhou and Liushagang layers of the research area (the yellow area is sand and the dark gray area is mudstone).

The thermal correlation coefficient can be used to form a 3D thermal correlation coefficient attribute model, which is of great significance for temperature calculation. The model reveals that the TC of sandstone is higher, with an average value of 3.01 W $(m{\cdot}K)^{-1}$, and the average TC of the mudstone is 2.1 W $(m{\cdot}K)^{-1}$, with a large spatial variation. The general rule is that the TC of sandstone is greater; however, it is affected by different lithofacies of sandstone, thus the TC of the sandstone also varies in space. The general rule is that the TC of river sand bodies is better than that of turbidite sand bodies, and the TC of lacustrine mudstone is larger than that of delta mudstone (Chen, 1988; Qiu et al., 2004; Guo et al., 2020).

3.3 Thermal modeling approaches

To predict the temperature distribution at depth, the steady-state conduction heat field was calculated at the scale of the entire lithosphere.

For purely conductive temperature calculations, it was assumed that heat is mainly transmitted through conduction throughout the Earth's lithosphere. The formula of the related equation is as follows (Sippel et al., 2013):

$$(\rho c)^{(b)}\frac{\partial T}{\partial t} = -\nabla\times\left(\lambda^{(b)}\nabla T\right) + S \tag{2}$$

Under the assumption of thermal equilibrium, the first term on the left side of Eq. 2 can be ignored (i.e., $\frac{\partial T}{\partial t} = 0$). Therefore, Eq. 2 takes the simplified form of:

$$\nabla\times\left(\lambda^{(b)}\nabla T\right) = S \tag{3}$$

Eq. 3 indicates that the calculated temperature is only sensitive to the radiogenic heat generation (S), the bulk thermal conductivity ($\lambda^{(b)}$), and the boundary conditions.

To calculate the 3D heat conduction field, each unit of the 3D geological model is provided with radiant heat generation values and bulk (solid and fluid) thermal conductivity. The lateral boundary conditions of the model are considered to be closed, and a constant temperature of 24°C at the topographic surface of the Earth is defined as the upper boundary condition. The lower boundary condition for the purely conductive thermal modeling corresponds to a temperature of 1,300°C at the LAB.

3.4 Results and discussion

3.4.1 Temperature simulation result

Figure 8A,B shows the temperature field distribution result calculated by using numerical simulation under the Mid value of the six main influencing factors (permeability (x and y), permeability (z), porosity, volumetric specific heat, sandstone volume, mudstone volume) selected according to ED. The temperature distribution results indicate that the Weizhou and Liushagang target layers have similar overall temperature distributions. The highest temperatures are concentrated in the subsidence center of the descending disk of the fault and the temperatures increase unevenly to the north. However, the overall temperature of the ascending disk is

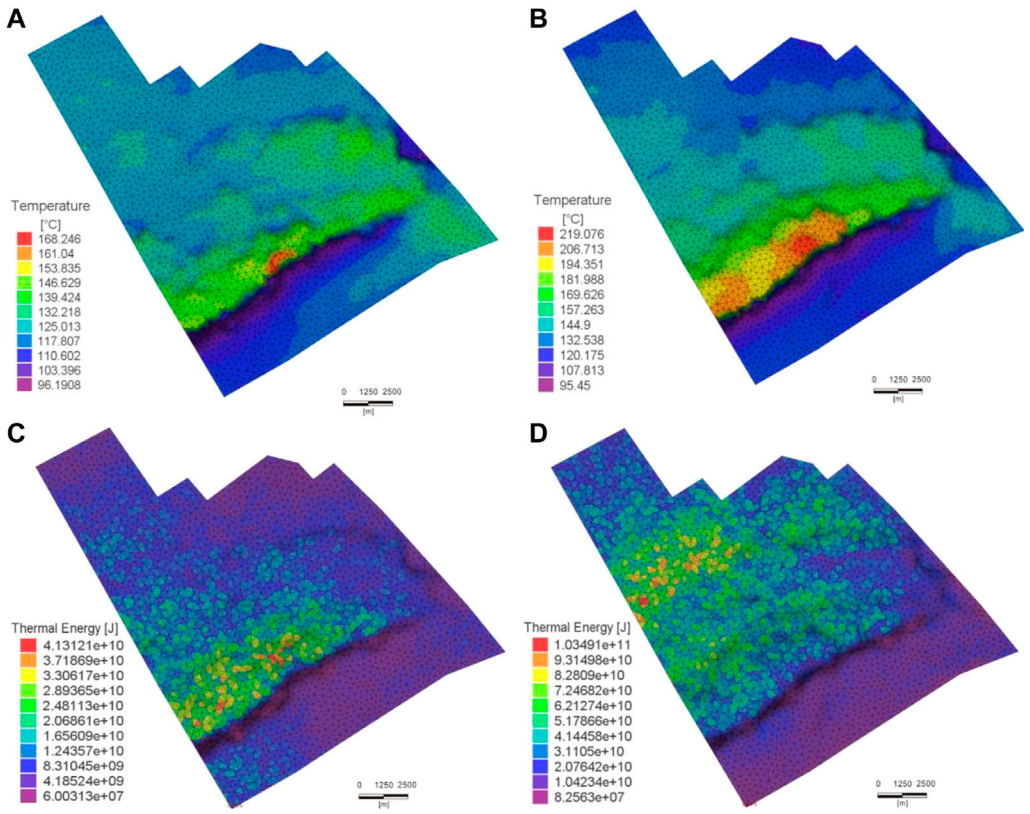

FIGURE 8
(A) The temperature distribution of the bottom of Weizhou Formation, **(B)** The temperature distribution of the bottom of Liushagang Formation, **(C)** The thermal energy of the bottom of Weizhou Formation and **(D)** The thermal energy of the bottom of Liushagang Formation.

relatively low. Specifically, for the Weizhou group, the highest temperature reaches 168°C and the lowest temperature is 96°C; nonetheless, the highest temperatures exhibit a very small distribution range, and it is difficult to use the areas with these high temperatures as an effective thermal reservoir. The geothermal energy in the area where the temperature is above 130°C can be used as a geothermal resource for power generation, but overall, there are fewer geothermal resources. However, the overall temperature of the Liushagang group is higher, reaching a maximum of 219°C, which is distributed in the fault descending disk and the range of high temperature is small. The temperature of the nearby area is above 130°C, and the range of the temperature is wide. If Liushagang group is used as a geothermal reservoir for power generation, significant amount of energy can be obtained. Therefore, the Liushagang group can be considered as the main layer for geothermal reservoir power generation development, and the shallower Weizhou formation can be used to provide energy for refrigeration, heating, and other purposes. Furthermore, 3D multi-layer well pattern development should be implemented to obtain the maximum recovery rate.

3.4.2 Thermal energy

Thermal energy is a vital factor in the evaluation process. Various evaluation methods are available for exploration of geothermal resources. So far, the main calculation methods can be divided into two categories, namely, volumetric method and numerical simulation method. For geothermal projects that have not yet been developed or are in the early stages of development, the volumetric method is the recommended method. In contrast, numerical simulation is more suitable for predicting sustainable production capacity after exploration drilling. Obviously, this study is related to long-term geothermal resource estimation for untapped geothermal projects, thus the volumetric method is used in thermal energy calculations. The thermal energy q generated in the rock can be calculated by dividing the model into n different elements of volume V_i [m³] and the temperature of the elements T_i.

Similar to the above-mentioned temperature field calculation, the Mid values of several main parameters were considered and the thermal energy was calculated according to the volumetric method (Figure 8C,D). Compared with the

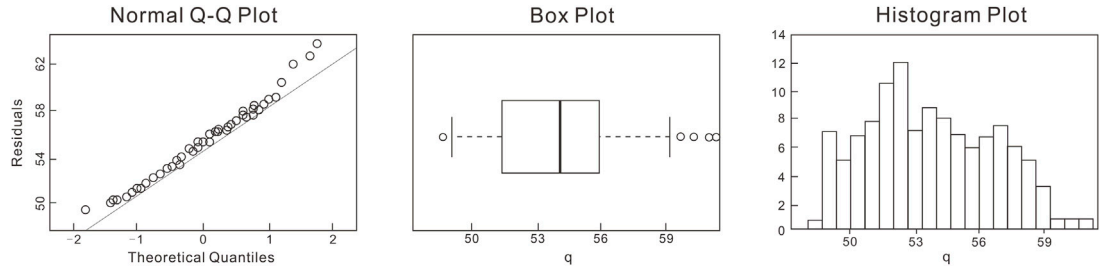

FIGURE 9
Diagnostic plots for all 64 successful two-level Full Factorial design simulation runs.

TABLE 2 The *p*-value of parameters applied in a first-order regression model with interactions.

	kx	ky	kz	Porosity	Volume heat	Lithology volume	R^2	Adjusted R^2
	$<1 \times 10^{-18}$	$<1 \times 10^{-18}$	$<1 \times 10^{-18}$	$<2.1 \times 10^{-10}$	0.0504	$<1 \times 10^{-18}$		
kx	—	$<1 \times 10^{-18}$	$<3.1 \times 10^{-18}$	0.0312	0.0705	$<1 \times 10^{-18}$		
ky	$<1 \times 10^{-18}$	—	0.2812	0.0329	0.9751	$<1 \times 10^{-18}$		
kz	$<3.1 \times 10^{-18}$	0.2812	—	$<4.1 \times 10^{-10}$	0.6512	$<1 \times 10^{-18}$		
porosity	0.0312	0.0329	$<4.1 \times 10^{-10}$	—	0.4555	0.2311		
volume specific heat	0.0201	0.8173	0.6512	0.4555	—	0.2411		
lithology volume	$<1 \times 10^{-18}$	$<1 \times 10^{-18}$	$<1 \times 10^{-18}$	0.2311	0.2411	—		
							0.9875	0.9867

traditional simplified calculation method, by using the calculated finite element model, all elements were assigned with heterogeneous volumetric specific heat capacity and temperature, which is more convincing than the results obtained by assuming that the volumetric specific heat capacity and temperature of each layer are homogeneous. The calculated result shows that the total thermal energy of the sand geothermal reservoirs is 5.6×10^{14} J. According to the conversion standard that 1 ton of standard coal can generate energy of 2.9×10^{10} J, the amount of geothermal resources is equivalent to 1.9×10^{4} tons of standard coal. Taking the depth of the reservoir into consideration, herein it was initially believed that the reservoir has a certain economic value.

The above-mentioned results are only the numerical simulation calculation results when each parameter takes the Mid value. When the ED-RSM method was employed, it was required to design experiments according to the numerical values of different experimental designs and corresponding simulation result was calculated. Then, the parameters and results were analyzed by the response surface method, which is direct correspondence analysis and forms surrogated numerical models.

3.4.3 Two-level full factorial

Out of 64 runs, a total of five possible outliers were identified and extracted from Regression analysis, which is indicated in normal Q–Q plot and Box plot, and a skewed histogram plot of q was generated from all successful runs (Figure 9). A review of the outlier input parameters shows that the horizontal and vertical permeability values for all failed runs were set at 10^{-16} m^2, which is the lowest meaningful value. Moreover, in all failed cases, the lithology volume was set to a low value, while the volumetric specific heat was set to a Mid value (Table 1). These early indications suggest that permeability, lithology volume, and volumetric specific heat could have a significant impact on the resource potential of the M field (Table 2). Plots without outliers are shown in Figure 10 (a). Regression analysis was performed after removing the outliers from the result to construct: 1) The first-order main effect, and 2) the first-order with interaction. A higher R^2 and adjusted R^2 values were obtained from the latter, as presented in Table 2. Figure 10 (a) shows the curvature that indicates the need to build a second-order polynomial model (Simpson, 1998). According to the results of R^2 and adjusted R^2, and compared with the subsequent second-order *Box–Behnken* calculation results, a second-order simulation better fits the data based on the residual plots (Figure 11).

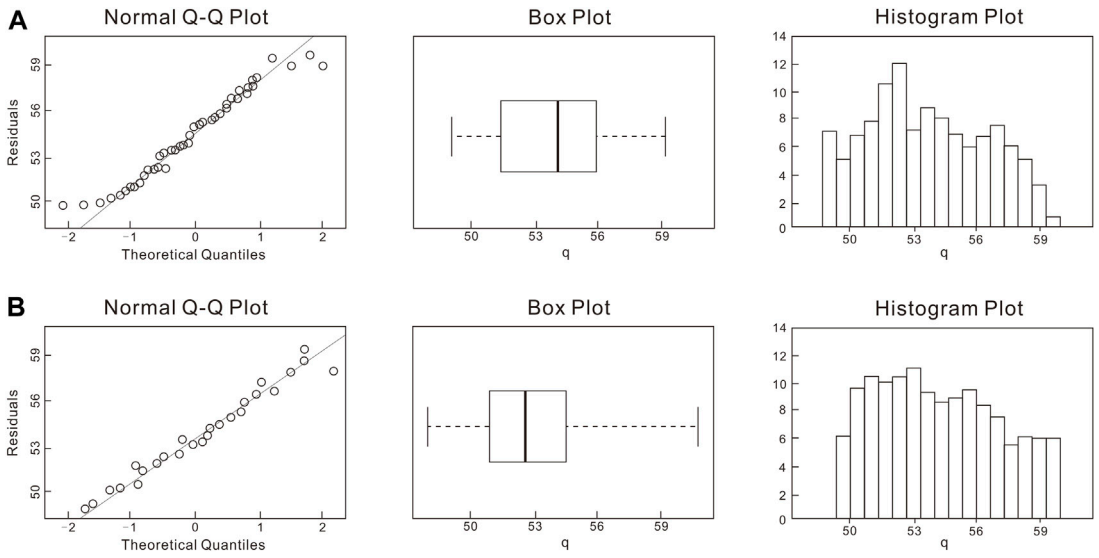

FIGURE 10
Diagnostic plots for the **(A)** two-level Full Factorial simulation without outliers and **(B)** Box–Behnken simulation runs.

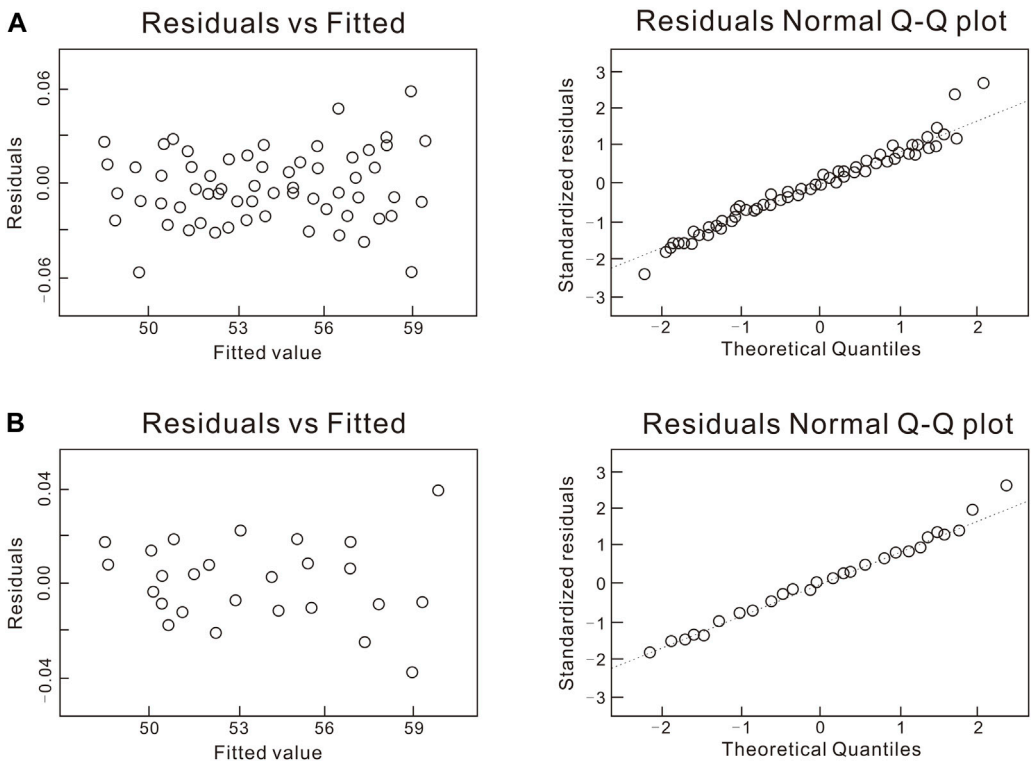

FIGURE 11
Residual plots of the **(A)** first-order regression model with interactions and **(B)** Box–Behnken second-order regression model with interactions among significant parameters plus kz.

TABLE 3 The *p*-value of parameters applied in building a Box–Behnken design second-order model with interactions.

	kz	Porosity	Volumetric heat	Lithology volume	R^2	Adjusted R^2
	$<2.1 \times 10^{-13}$	$<1.4 \times 10^{-10}$	$<2.4 \times 10^{-5}$	$<1.6 \times 10^{-12}$		
kz	—	—	—	—		
porosity	—	—	0.0105	0.1322		
volumetric specific heat	—	0.0305	—	0.0411		
lithology volume	—	0.1322	0.0411	—		
					0.9944	0.9921

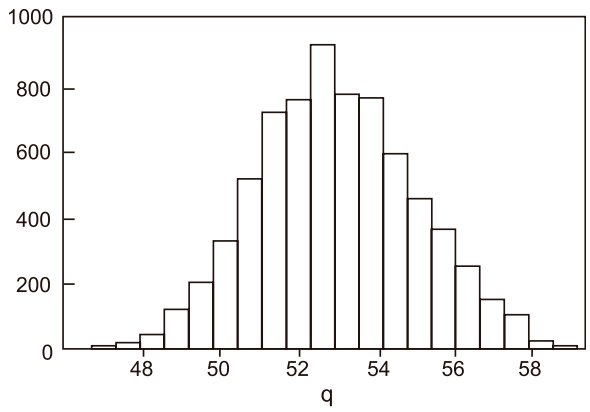

FIGURE 12
Geothermal probabilistic resource assessment.

3.4.4 Box–Behnken

Based on the result of the two-level Full Factorial, further, three significant parameters and kz were adopted for the subsequent second-order model with interaction regression analysis (Figure 11). The multi-factor relationship of Box–Behnken design second-order model with interaction is presented in Table 3, and the R^2 and adjusted R^2 shows a better fit than that of the two-level Full Factorial design. The experiment exhibited a total of 29 runs and three of the results were outliers [Figure 10 (b)]. Table 2 summarizes that the lithology volume was a significant predictor and the R^2 and the adjusted R^2 were 0.9875 and 0.9867, respectively. The results (Table 3) from the second-order polynomial models provided a higher R^2 and adjusted R^2 values and indicated that a second-order model better fitted the data based on the residual plots [Figure 11B]. A *p*-value of less than 0.05 indicates that the parameter is a significant predictor of the response variable, so the first and second order of kx, ky, kz, porosity, volumetric specific heat, lithology volume, and their interactions turned out to be significant predictors of q. The residuals are not distributed normally as shown in Figure 11 (b), so a polynomial equation can also be included in the design and a probabilistic distribution of q was formed by using the Monte Carlo method. A simple triangular distribution was assigned to each parameter. The result of the ED-RSM method improved by two-level Factorial and Box–Behnken designs is presented in Figure 12. Clearly, the M geothermal field consists of a thermal energy resource of 5×10^{14} J (90th percentile), 5.3×10^{14} J (50th percentile), and 5.7×10^{14} J (10th percentile). The potential energy is also calculated by the volumetric stored heat method (Muffler P and Caraldi R, 1978), and the resultsare 5.1×10^{14} J (90th percentile), 9×10^{14} J (50th percentile), and 1.5×10^{15} J (10th percentile). By comparing the results obtained by the two methods, the ED-RSM results have a significantly narrower distribution than that of the volumetric method, which can be attributed to the constrained reservoir model.

4 Conclusion

The current evaluation process of a favorable target requires long-term geological research and model establishment and calculation. In many cases, project evaluation is faced with many uncertain parameters and incomplete geological understanding. The commonly used Monte-Carlo method for uncertainty evaluation often offers a wide range result, which makes it difficult to obtain appropriate decisions. In this study, two-level Full Factorial and Box–Behnken designs were combined to simplify the three-level experimental design and strengthen the two-level experimental design, then integrated with RSM, a proxy model was built to carry out evaluation. The results are reliable and have a narrow interval, and can provide better guidance than that of the simple Monte–Carlo method.

The proxy polynomial model of the ED-RSM workflow was derived from the calibrated numerical temperature field and the geological model, a 3D geological model of M geothermal field was established, and the 3D uneven temperature field is built horizontally and vertically in the model. The geological model can accurately predict the petrophysical and thermal properties of sandstone reservoirs. The 3D temperature field model is extremely important for characterizing geothermal reservoirs because temperature is the primary resource of geothermal reservoirs; the higher the temperature, the better the evaluation result. The establishment of the comprehensive model provides a scientific basis for ED-RSM.

Three-level Full Factorial design is not applicable for multi-factor implementation in geothermal projects, because the numerical simulation is very time-consuming. Therefore, we are looking to combine two-level Full Factorial design and three-level Fractional Factorial design methods. Through first-order regression analysis, effective parameters are optimized and the number of insignificant parameters are reduced, then the maximum information can be obtained by the simulation of three-level Fractional Factorial design with least work. Finally, the improved ED-RSM method with two-stage design, which combined two-level Full Factorial design and Box–Behnken design, is proposed. The proposed method more quickly and accurately provides a narrower interval of probabilistic geothermal resource than that provided by the volumetric method, thus it provides more valuable information. In addition, the permeability does not much affect the thermal energy, partially because only a conductive thermal model was used to calculate the temperature.

Data availability statement

The original contributions presented in the study are included in the article/supplementary material, further inquiries can be directed to the corresponding author.

Author contributions

WM contributed the conception of the paper, the establishment of geothermal model, the calculation of geothermal resources and the review of the paper; YF designed the experiment and wrote the draft of the paper; ZY, ZD and FJ provided the research results and understanding of geothermal geology in Maichen Depression; LJ and ZY were responsible for the clear drawing of maps.

Funding

This study was financially supported by National Key Research and Development Projects (No. 2019YFC0604903, No. 2021YFA0716004) and Joint Fund of the National Natural Science Foundation of China (Grant No. U20B6001).

Conflict of interest

The authors declare that the research was conducted in the absence of any commercial or financial relationships that could be construed as a potential conflict of interest.

Publisher's note

All claims expressed in this article are solely those of the authors and do not necessarily represent those of their affiliated organizations, or those of the publisher, the editors and the reviewers. Any product that may be evaluated in this article, or claim that may be made by its manufacturer, is not guaranteed or endorsed by the publisher.

References

Acuna, J. A., Parini, M. A., and Urmeneta, N. A. (2002). *Using A large reservoir model in the probabilistic assessment of field management studies. 27th workshop on geothermal reservoir engineering*. Stanford, CA: Stanford University.

Amudo, C., Graf, T., and Dandekar, R. R. (2009). *The pains and gains of experimental design and response surface applications in reservoir simulation studies*. The Woodlands, Texas: SPE Reservoir Simulation Symposium.

Bertani, R. (2012). Geothermal power generation in the world 2005–2010 update report. *Geothermics* 41, 1–29. doi:10.1016/j.geothermics.2011.10.001

Bertani, R. (2016). Geothermal power generation in the world 2010–2014 update report. *Geothermics* 60, 31–43. doi:10.1016/j.geothermics.2015.11.003

Box, G. E. P., Hunter, W. G., and Hunter, J. S. (1978). *Statistics for experimenters, an introduction to design, data analysis, and model building*. New York, NY: John Wiley & Sons.

Box, G. E. P. (1979). "Robustness in the strategy of scientific model building," in *Robustness in statistics*, 201–236.

Chen, M. X. (1988). *North China geothermal energy*. Beijing: China Science Press.

Chen, S. B., Gan, H. J., and Xia, C. Y. (2014). History simulation of thermal evolution and hydrocarbon generation of source rocks in Bailian Sub-Sag, Fushan Sag, Beibuwan Basin. *Xinjiang Pet. Geol.* 35 (6), 672–677. (In Chinese with English abstract).

Ciriaco, A. E., Zarrouk, S. J., Zakeri, G., and Mannington, W. I. (2020b). Refined experimental design and response surface methodology workflow using proxy numerical models for probabilistic geothermal resource assessment. *Geothermics* 88, 101911–101934. doi:10.1016/j.geothermics.2020.101911

Ciriaco, A. E., Zarrouk, S. J., and Zakeri, G. (2020a). Geothermal resource and reserve assessment methodology: Overview, analysis and future directions. *Renew. Sustain. Energy Rev.* 119, 109515. doi:10.1016/j.rser.2019.109515

Ciriaco, A. E., Zarrouk, S. J., and Zakeri, G. (2018). *Probabilistic resource assessment using experimental design and second order proxy model: Rotorua geothermal system, New Zealand. 40th New Zealand geothermal workshop*.

Doherty, J., Yeh, A., and Colina, R. (2017). *Experiments with inverse modelling and uncertainty quantification with a geothermal model. 39th New Zealand Geothermal Workshop*.

Ebong, E. D., Akpan, A. E., Ekwok, S. E., Esu, E. O., and Ebong, L. A. (2021). 3-D reservoir characterization and hydrocarbon volumetric estimation of parts of Niger delta basin-Nigeria. *J. Afr. Earth Sci.* 180, 104207. doi:10.1016/j.jafrearsci.2021.104207

Ebong, E. D., Akpan, A. E., and Ekwok, S. E. (2020). Stochastic modelling of spatial variability of petrophysical properties in parts of the Niger delta basin, southern Nigeria. *J. Pet. Explor. Prod. Technol.* 10, 569–585. doi:10.1007/s13202-019-00787-2

Ebong, E. D., Akpan, A. E., and Urang, J. G. (2019). 3D structural modelling and fluid identification in parts of Niger delta basin, southern Nigeria. *J. Afr. Earth Sci.* 158, 103565. doi:10.1016/j.jafrearsci.2019.103565

Friedmann, F., Chawathe, A., and Larue, D. K. (2003). Assessing uncertainty in channelized reservoirs using experimental designs. *SPE Reserv. Eval. Eng.* 6 (4), 264–274. doi:10.2118/85117-pa

Fuchs, S., Balling, N., and Forster, A. (2015). Calculation of thermal conductivity, thermal diffusivity and specific heat capacity of sedimentary rocks using petrophysical well logs. *Geophys. J. Int.* 203 (3), 1977–2000. doi:10.1093/gji/ggv403

Fukuda, I. M., Pinto, C. F. F., Moreira, C. D. S., Saviano, A. M., and Lourenco, F. R. (2018). Design of experiments (DoE) applied to pharmaceutical and analytical quality by design (QbD). *Braz. J. Pharm. Sci.* 54, 1–16. doi:10.1590/s2175-97902018000001006

Guo, P. Y., Bu, M. H., Li, Q. B., and He, M. C. (2020). Research progress of accurate measurement and characterization model of effective thermal conductivity of rock. *Chin. J. Rock Mech. Eng.* 39 (10), 1983–2013.

Hoang, V., Alamsyah, O., and Roberts, J. (2005). *Darajat geothermal field expansion performance - a probabilistic forecast*. Antalya, Turkey: World Geothermal Congress.

Lund, J. W., and Boyd, T. L. (2016). *Direct utilization of geothermal energy 2015 worldwide review*. Geothermics 60, 66–93. doi:10.1016/j.geothermics.2015.11.004

Muffler, P., and Cataldi, R. (1978). Methods for regional assessment of geothermal resources. *Geothermics* 7 (2-4), 53–89. doi:10.1016/0375-6505(78)90002-0

Myers, R. H., and Montgomery, D. C. (2002). Response surface methodology. New York: Wiley.

Parini, M., and Riedel, K. (2000). "Combining probabilistic volumetric and numerical simulation approaches to improve estimates of geothermal resource capacity," in *Proceedings: World geothermal congress* (Japan: Kyushu-Tohoku).

Pasikki, R. G., Cita, F., and Hernawan, A., (2016). "Application of experimental design." in *Geothermal greenfield size assessment. Indonesia international geothermal convention and exhibition*.

Qiu, L. S., Hu, S. B., and He, L. J. (2004). *Theory and application of geothermal regime research in sedimentary basin*. Beijing: China Petroleum Industry Press.

Quinao, J. J. D., and Zarrouk, S. J. (2018). Geothermal resource assessment using experimental design and response surface methods: The Ngatamariki geothermal field, New Zealand. *Renew. Energy* 116, 324–334. doi:10.1016/j.renene.2017.09.084

Quinao, J. J., and Zarrouk, S. J. (2014). "Applications of experimental design and response surface method in probabilistic geothermal resource assessment – preliminary results," in *Proceedings: Thirty-Ninth workshop on geothermal reservoir engineering* (Stanford).

Santner, T. J., Williams, B. J., and Notz, W. (2003). *The design and analysis of computer experiments*. 2nd ed. New York: Springer-Verlag.

Simpson, T. W., Mauery, T. M., and Korte, J. J. (1998). "Comparison of response surface and kriging models in the multidisciplinary design optimization," in *7th AIAA/USAF/NASA/ISSMO symposium on multidisciplinary analysis and optimization*.

Sippel, J., Fuchs, S., Cacace, M., Braatz, A., Kastner, O., Huenges, E., et al. (2013). Deep 3D thermal modelling for the city of Berlin (Germany). *Environ. Earth Sci.* 70 (8), 3545–3566. doi:10.1007/s12665-013-2679-2

Walpole, R. E., Myers, R. H., and Myers, S. L. (2012). "Probability and statistics for engineers and scientists," in *Pearson*. 9th ed. (Zealand: Prentice-Hall).

Zhao, Y. D., Bai, K. L., and Zhao, Y. J. (2019). Characteristics of a geothermal anomaly in the fushan sag, Beibuwan Basin, China, and its effects on oil and gas reservoirs. *Arab. J. Geosci.* 12, 698. doi:10.1007/s12517-019-4889-8

frontiers | Frontiers in Earth Science

TYPE Original Research
PUBLISHED 11 October 2022
DOI 10.3389/feart.2022.970614

OPEN ACCESS

EDITED BY
Mourad Bezzeghoud,
Universidade de Évora, Portugal

REVIEWED BY
Yves Shandini,
University of Douala, Cameroon
Zhaohai Meng,
Tianjin Navigation Instrument Research Institute, China

*CORRESPONDENCE
Franck Eitel Ghomsi,
franckeitel@gmail.com
Ahmed M. Eldosouky,
dr_a.eldosoky@yahoo.com
Alain Rodrigue Nzeuga,
alainzeuga@yahoo.fr
Luan Thanh Pham,
luanpt@hus.edu.vn

SPECIALTY SECTION
This article was submitted to Solid Earth Geophysics,
a section of the journal
Frontiers in Earth Science

RECEIVED 16 June 2022
ACCEPTED 23 September 2022
PUBLISHED 11 October 2022

CITATION
Nzeuga AR, Ghomsi FE, Pham LT, Eldosouky AM, Aretouyap Z, Kana JD, Yasmine ZT, Fokem ABK, Nouayou R, Abdelrahman K, Fnais MS and András P (2022), Contribution of advanced edge-detection methods of potential field data in the tectono-structural study of the southwestern part of Cameroon. *Front. Earth Sci.* 10:970614. doi: 10.3389/feart.2022.970614

Contribution of advanced edge-detection methods of potential field data in the tectono-structural study of the southwestern part of Cameroon

Alain Rodrigue Nzeuga[1]*, Franck Eitel Ghomsi[2,3]*, Luan Thanh Pham[4]*, Ahmed M. Eldosouky[5]*, Zakari Aretouyap[6], Janvier Domra Kana[7], Zambou Tsopgni Yasmine[3], Alpha Baster Kenfack Fokem[8], Robert Nouayou[3], Kamal Abdelrahman[9], Mohammed S. Fnais[9] and Peter András[10]

[1]Department of Petroleum, Gas and Exploration, School of Geology and Mining Engineering, University of Ngaoundéré, Meiganga, Cameroon, [2]Geodesy Laboratory, National Institute of Cartography, Yaoundé, Cameroon, [3]Department of Physics, University of Yaoundé 1, Yaoundé, Cameroon, [4]Department of Geophysics, Faculty of Physics, University of Science, Vietnam National University, Hanoi, Vietnam, [5]Geology Department, Faculty of Science, Suez University, Suez, Egypt, [6]Department of Architecture and Engineering Art, Institute of Fine Arts, University of Dschang, Foumban, Cameroon, [7]Department of Mines, Petroleum and Water Resource Exploration, Faculty of Mines and Petroleum Industries, University of Maroua, Maroua, Cameroon, [8]Department of Mining Geology, School of Geology and Mining Engineering, University of Ngaoundéré, Meiganga, Cameroon, [9]Department of Geology and Geophysics, College of Science, King Saud University, Riyadh, Saudi Arabia, [10]Faculty of Natural Sciences, Matej Bel University in Banska Bystrica, Banska Bystrica, Slovakia

The southwest part of Cameroon is composed of a range of geological structures and sedimentary basins, whose geological history dates from the Cretaceous, and their establishment would have originated from the opening of the South Atlantic. Among these structures, the most important is the Cameroon Volcanic Line, generally denoted CVL, followed by the southern part of the Central African Shear Zone (CASZ) called the Foumban Shear Zone (FSZ), the Ntem Complex, the Benue Trough, the northern margin of the Congo Craton, and many others. The major structures identified in this part are formed as a result of geodynamic activity between the Oligocene and the recent period, to which we can add the volcanism that exists along with the continental limit. The XGM201e_2159 model is used to highlight the geological structures of Southwestern Cameroon. First, we separated the regional and residual anomalies from Bouguer gravity data. Then, we used a combination of filters to enhance the signature of the residual anomalies in Southwest Cameroon. These filters identified various geological structures in the area. Finally, we applied the enhanced horizontal gradient amplitude (EHGA) and multi-scale horizontal derivative of the vertical derivative (MSHDVD) methods to reveal the geological contacts, allowing us to establish the corresponding structural map of the region. In addition, the results obtained in this study are the first to precisely define the circumferential demarcation of the continental and oceanic expansions of Mount Cameroon, while clearly illustrating the Bao, Bomana, Tiko, and Ekona faults that extend to the Bakassi Peninsula and the Douala

outlet. Furthermore, they highlight the strike–slip faults in the summit vicinity. The structural map shows that most of the geological boundaries identified in the area are trending in the NE–SW, NNE–SSW, ENE–WSW, N–S, and NW–SE directions.

KEYWORDS

gravity, potential field data, edge detection, structural mapping, southwestern Cameroon

1 Introduction

Located in the south-west of Cameroon, the study area spanned between longitudes 8°00′ E and 11°25′ E and latitudes 3°00′ N and 7°25′ N (Figure 1). It encompasses various geological structures and sedimentary basins whose origins remain subjects of reflection within the scientific community. Among these structures, the most important would be the succession of mountain ranges that form the Cameroon Volcanic Line (CVL). The CVL owes its origin to a large subvolcanic and volcanic sequence to which it belongs, which in turn would originate from its presence within several hot spots (Ngounouno et al., 2000; Ngounouno et al., 2003). This great lineament, which extends till the West African coast, is composed of both an oceanic and a continental part. It separates the sedimentary Rio Del Rey Basin from that of Douala–Kribi Campo. The mountain range that forms it is generally alkaline and formed between the Tertiary and the recent period (Fitton, 1987). This mountain range is subject to volcanism, which extends from the Atlantic islands of Pagulu to the interior of the African continent (Lee et al., 1994). The islands of Bioko and Sao Tomé et Principe constitute the marine component, while the Manengouba, Bamboutos, Oku, and Mandara mountains constitute the continental portion (Figure 1). This continental part has an average crustal density of 400 kg/m^3, with an average Moho depth of about 32.5 km (Ghomsi et al., 2020; Ghomsi et al., 2022b). In addition to the CVL, we can see other structures in this area, including the Ntem Complex and the Mamfe Sedimentary Basin, which is a part of the Central Cameroonian Shear Zone.

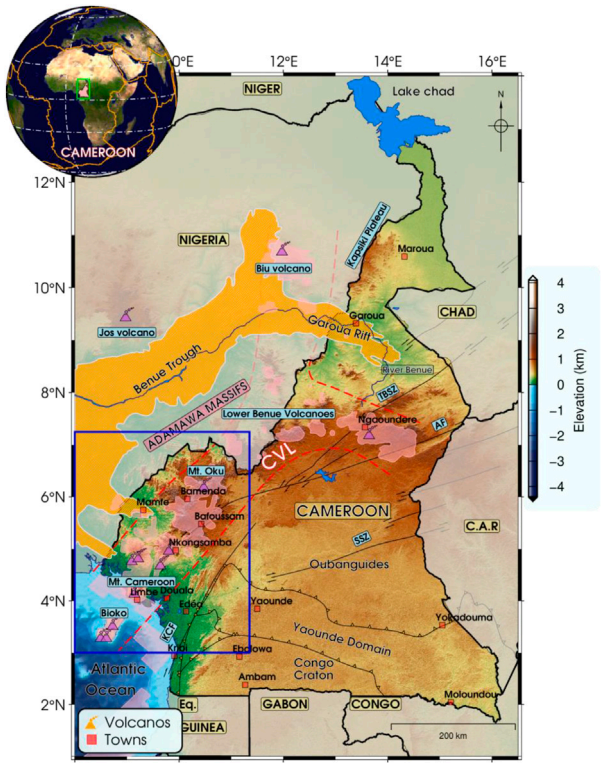

FIGURE 1
Map location of the study area with the representation of the Cameroon Volcanic Line.

According to Ubangoh et al. (2005), the positive anomalies seen along the CVL point are due to the presence of multiple active volcanic craters and cones as well as a strong geothermal gradient. Also, an analysis of the samples collected along the CVL highlights the existence of a predominant magnetization spectrum within it. The main lineaments of the region are highlighted in the past research by Nzeuga et al. (2019) and Ghomsi et al. (2022a) based on the interpretation of aeromagnetic data. Noutchogwé et al. (2011) and Ndikum et al., 2014; Ndikum et al., 2017 highlighted the geological contacts of this part of Cameroon from the interpretation of gravity data using the MSHDVD method. Koumetio et al. (2012) applied multi-scale elevation of the maxima of the horizontal derivative on the vertical gradient of the Bouguer anomaly, followed by 3D modeling to highlight geological structures in the region, visible on the signal as negative gravity anomalies. The basement of this region is intruded by bodies of variable shapes and sizes located at a depth varying between 1 and 10 km and a density range from 2.57 to 2.87 g/cm^3. These intrusions observed in the crust of this region could be potential reservoirs of rare minerals (Fosso-Téguia et al., 2020), and the crust thickness is between 35 and 39 km (Tokam et al., 2010; Ghomsi et al., 2020; Ghomsi et al., 2022b).

Considering the results of previous work in the study area (Ghomsi et al., 2020; Ghomsi et al., 2021; Tchoukeu et al., 2021; Ghomsi et al., 2022b), the use of the recent XGM 2019e2159 Gravity Field Model presented by Zingerle et al. (2020) and the regional/residual separation of the Bouguer anomaly map by using the method of Zeng et al. (2007) could

increase the signature gravity anomalies. Additionally, determining gravity source parameters is crucial for finding new mineral deposits and helps maximize exploratory drilling operations (Pham et al., 2019; Pham et al., 2020a; Duong et al., 2021; Long et al., 2021).

Gravity and magnetic data can provide vital information on the subsurface structures (Dung and Minh, 2017; Hang et al., 2019; Eldosouky et al., 2021a; Eldosouky et al., 2021b; Oksum 2021). The determination of geological boundaries from the interpretation of gravity data has been the subject of several studies, and many different techniques have been introduced (Melouah et al., 2021; Eldosouky et al., 2022a; Pham et al., 2022a; Eldosouky et al., 2022b; Pham et al., 2022b; Eldosouky et al., 2022c; Ghomsi et al., 2022c; Eldosouky et al., 2022d; Ghomsi et al., 2022d), such as, for example, the peak detection methods (Blakely and Simpson, 1986; Hang et al., 2017; Pham et al., 2018; Pham et al., 2021), vertical derivatives, the filters of horizontal gradient (Cordell, 1979; Cordell and Grauch, 1985), the analytical signal (Nabighian, 1972; Nabighian, 1984; Roest et al., 1992), tilt angle (Miller and Singh, 1994), the horizontal gradient amplitude of tilt angle (Verduzco et al., 2004), enhanced horizontal gradient amplitude (Pham et al., 2020a), improved logistic function (Pham et al., 2020b), and balanced horizontal gradient amplitude filters (Prasad et al., 2022a; Prasad et al., 2022b).

From the Bouguer anomaly data, we shall extract anomalies of importance in this study. Then, in order to emphasize the various contacts, we will use the first-order derivation, the horizontal gradient (HG), the analytical signal (AS), the tilt angle (TDR), the horizontal gradient of the tilt angle (HG_TDR), and the enhanced horizontal gradient amplitude (EHGA) filters. Finally, we will compare the geological contacts obtained on the TDR, HG_TDR, and EHGA maps with those obtained by using the MSHDVD method to reveal a new tectono-structural map of the region.

2 Geological setting

The geology of the southwestern part of Cameroon illustrated in Figure 2 is very large and complex. The CVL consists of a succession of mountains ranging in age from the Tertiary to the recent period (Fitton and Dunlop, 1985). Among the elements that constitute it, we can cite the Adamaoua–Yade Plateau and the Western Cameroon Highlands, generally called the Cameroon Highlands. The highlands of Cameroon form the androgenic plutonic complexes of the CVL and encompass a succession of volcanoes oriented at 30°E with peaks ranging from 900 to 1,800 m for the smallest to 3,010 m for Mount Oku and 4,020–4,100 m for Mount Cameroon, located near the coastal plain (Deruelle et al., 2007; Beckline et al., 2018; Wembenyui et al., 2020). The CVL consists of eight monogenetic volcanic fields with an estimated total area of 17,000 km^2, with individual fields ranging in size from 700–4,000 km^2 (Schmidt et al., 2022). Because the CVL is located in a unique tectonic environment at the transition from the oceanic to continental crust, it serves as a natural laboratory for the study of the geochemical evolution of alkaline magmas with varying degrees of crustal contamination and mixing. Mount Cameroon is the only active mountain in the mountain range that constitutes the CVL, and its last seven eruptions date from 1909, 1922, 1954, 1959, 1982, 1999, and 2000 (Geze, 1943; Fitton et al., 1983; Suh et al., 2003). The basanitic and alkaline basaltic nature of its flows, adding small quantities of pyroclastic materials and volcanic cinder cones, make it a composite volcano (Suh et al., 2003; Yokoyama et al., 2007; Suh et al., 2008). The CVL has a crystalline basement embedded in the mobile orogenic Ubangid belt, bounded by the Pan-African range and located between the Saharan Metacraton, the Congo Craton, and the West African cratons (Meyers et al., 1998; Ghomsi et al., 2020; Ghomsi et al., 2021; Ghomsi et al., 2022b). Ghomsi et al. (2022a) applied the intensity of the enhanced horizontal gradient amplitude (EHGA) on the aeromagnetic data to highlight the major geological structures of the CVL and their effects on the topography and the cross-correlation analysis to highlight the principal directions of magnetization of certain anomalies. The Central African Shear Zone (CASZ), a component of the Pan-African Range, is a major fault belt still active. Its nature is identical to that of its counterpart, known as the Pernambuco lineament, located in Northeast Brazil, which would be an extension of the CVL in South America (Torsvik et al., 2009; Aslanian and Moulin, 2010; Moulin et al., 2010).

The Ntem Complex, part of which is in our study area, represents the northern part of the Congo Craton. It is formed mainly of Archean rocks, intrusive rocks, leptynites, and gneisses (Tchameni et al., 2001). The intrusions encountered in the Ntem Complex are mainly granites, tonalites, and syenites. The Nyong unit is the part of the Ntem Complex which appears in our study area. This unit consists mainly of gneisses and greenstones in the form of a belt and represents the NW section of the Ntem Complex (Maurizot et al., 1986; Minyem and Nedelec, 1990; Tchameni, 1997). Basic and ultrabasic rocks and ferriferous and barren quartzites are the constituent elements of greenstone belts. The blastomylonitic shear zones observed irregularly on the Nyong and Ntem units owe their origin to faulting deformation. Neoproterozoic intrusions of nepheline syenite in a sinistral shear zone in the Nyong unit also owe their origin to the last magmatic episode in this one (Maurizot et al., 1986; Nsifa, 2005).

Another part of our study area is the Benue Trough. It is a large sedimentary basin oriented in the NE–SW direction, distributed over a length of about 1,000 km, which extends from the Niger Delta in Southern Nigeria to the vicinity of Lake Chad. Its origin dates from the Cretaceous with the opening of the South Atlantic (Guiraud and Maurin, 1992; Nouayou, 2005). The Benue Trough includes many faults of various kinds in its upstream part, and the main ones are oriented along the N115°E structural direction (Regnoult, 1986). It is represented in Cameroon in the North by the Garoua Rift, also called Yola Trough, and in the south-east region by the Mamfe Sedimentary Basin. The volcanic massifs of Cameroon are at the origin of the

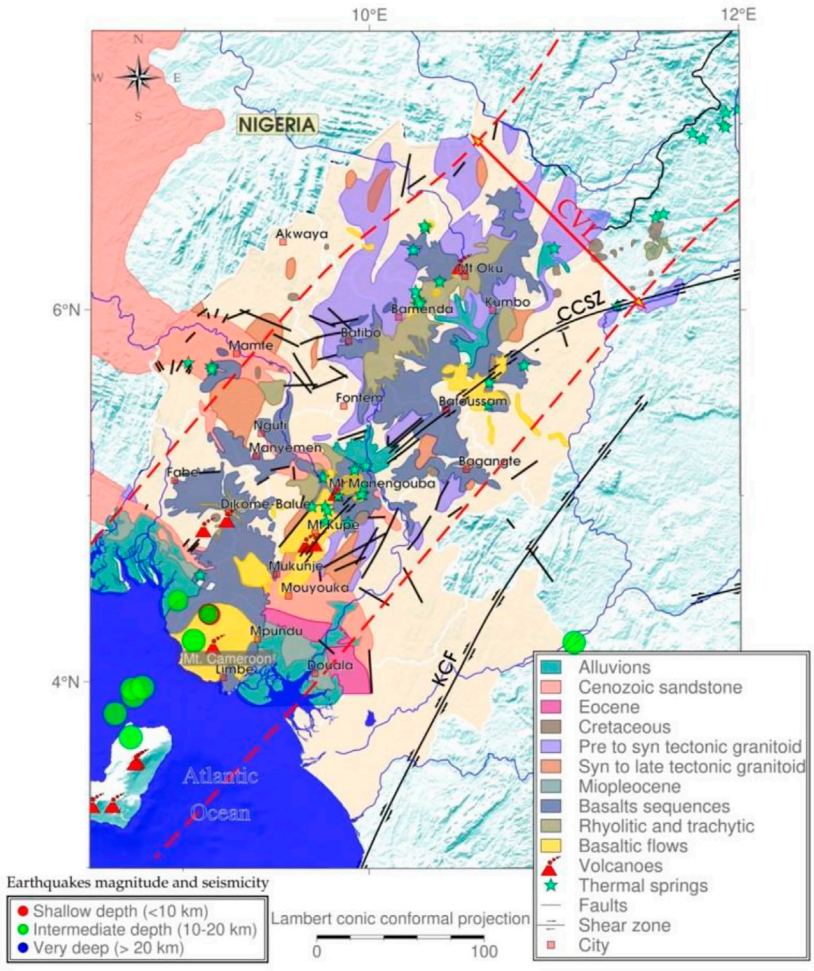

FIGURE 2
Geology map of Southern Cameroon (after Ghomsi et al., 2022a).

interruption of the extension of the Cameroonian coastal basins of Douala/Kribi–Campo toward the Benue Trough, and these basins (Mamfé, Rio Del Rey, and Douala/Kribi-Campo) would have the same geological history as this one (Nzeuga et al., 2019).

3 Data

The satellite-derived gravity data for the entire Southwest Cameroon are derived from the XGM 2019e_2159 (eXperimental Gravity field Model 2019) (Zingerle et al., 2020), which is represented through spheroidal harmonics, corresponding to a spatial resolution of 2' (~4 km), and has lesser artifacts. It is developed from altimetry, satellite-only model GOCO06s (Kvas et al., 2021), topography (Amante and Eakins, 2009), and ground data. It is a static global combined gravity field model with degree and order of 5,399. It has the long wave from GRACE+GOCE v5 and the short wave from land gravity averaged at 1/15° and marine and altimetric gravity (DTU15) provided by the National Geospatial-Intelligence Agency (NGA). The topographic heights are calculated from the spherical harmonic model of the topography (ETOPO1) used up to the same maximum degree as the gravity field model.

4 Methodology

To determine the lineaments and propose a geological model of the subsoil, highlighting the intrusions of igneous bodies in the southwestern part of Cameroon, many filtering operations are needed and should be applied to the gravity anomaly data. First, we have performed the regional–residual separation from the Bouguer anomalies using the method of Zeng et al. (2007). Then, the filters such as the horizontal gradient, analytical signal, tilt

angle, and enhanced horizontal gradient amplitude have been applied to the residual anomaly data to enhance the geological edges. Finally, we have applied the improved maximum detection method (Pham et al., 2020c) to the multi-scale horizontal derivative of the vertical derivative to detect the geological contacts.

4.1 Regional/residual separation

The observed gravity anomaly is the sum of gravity effects of density differences at various depths (Oksum et al., 2019; Pham et al., 2022c; Ghomsi et al., 2022d). Here, we used the method of Zeng et al. (2007) for separating the regional anomaly resulting from deep sources from the observed gravity. Then, the residual anomaly generated by the shallow sources was calculated by removing the regional anomaly from the observed anomaly. This method calculates a series of cross-correlations between the upward continuations at two successive heights (Zeng et al., 2007). The height associated with the maximum deflection of these cross-correlation values yields the optimum height for regional/residual separation (Zeng et al., 2007).

4.2 Use of derivative filters

We consider ΔT as the value of the total gravimetric field caused by a random distribution of the density sources in the soil. When the gravity fields of several sources interfere, the application of the derived filters is important to dissociate them and to determine the location of the contacts at the origin of each source (Fedi and Florio, 2001). It also has the advantage of operating calculations at different heights *via* the upward extension stable operator (Jacobsen, 1987).

The first-order horizontal and vertical derivatives can be written as follows:

$$\frac{\partial \Delta T}{\partial x} = \frac{\Delta T_{i+1,j} - \Delta T_{i-1,j}}{2\Delta x} \tag{1}$$

$$\frac{\partial \Delta T}{\partial y} = \frac{\Delta T_{i,j+1} - \Delta T_{i,j-1}}{2\Delta y} \tag{2}$$

$$\frac{\partial \Delta T}{\partial z} = F^{-1}\{|k| F(\Delta T)\} \tag{3}$$

where Δx is the sampling distance along the longitudes; Δy is the sampling distance along the latitudes; i and j represent the data collection points of ΔT in x and y, respectively; F and F^{-1} represent the Fourier transform and inverse Fourier transform, respectively; and $|k|$ is the radial wave number.

We can combine these elements to calculate the horizontal gradient (HG) (Cordell, 1979; Cordell and Grauch, 1985) and the analytical signal (AS) (Nabighian, 1972; Nabighian, 1984; Roest et al., 1992) as follows:

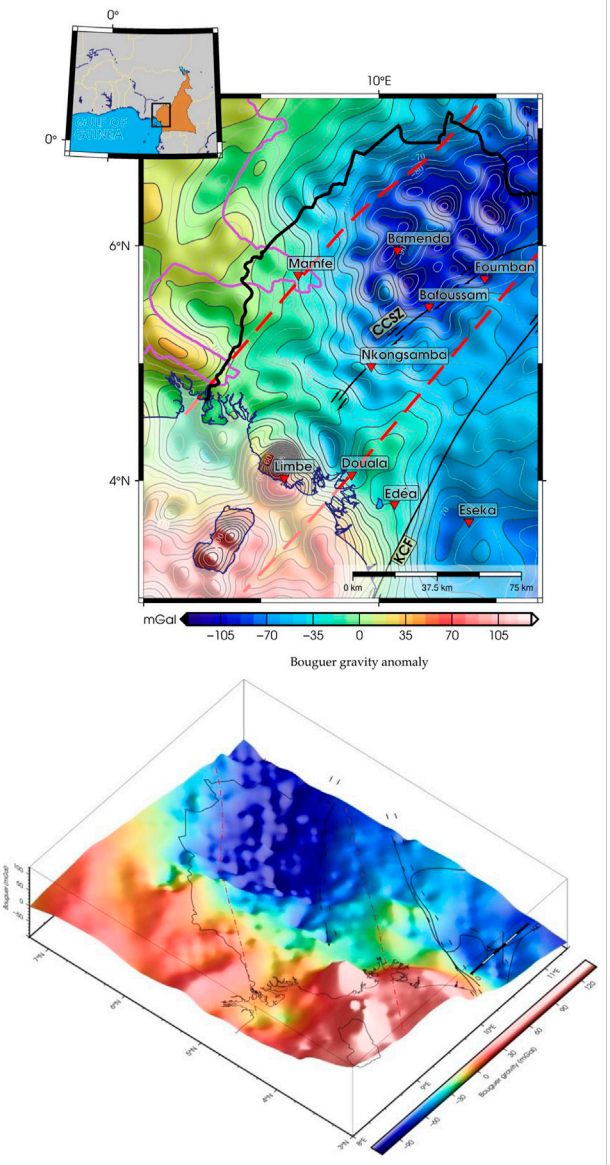

FIGURE 3
Bouguer anomaly map of the study area with its perspective representation, estimated on a 0.1° × 0.1° geographical grid (black lines represent national boundaries).

$$HG = \sqrt{\left(\frac{\partial \Delta T}{\partial x}\right)^2 + \left(\frac{\partial \Delta T}{\partial y}\right)^2} \tag{4}$$

$$AS = \sqrt{\left(\frac{\partial \Delta T}{\partial x}\right)^2 + \left(\frac{\partial \Delta T}{\partial y}\right)^2 + \left(\frac{\partial \Delta T}{\partial z}\right)^2} \tag{5}$$

The maximum value of the HG and AS is used to detect the source edges (Grauch and Cordell, 1987; Phillips, 2000).

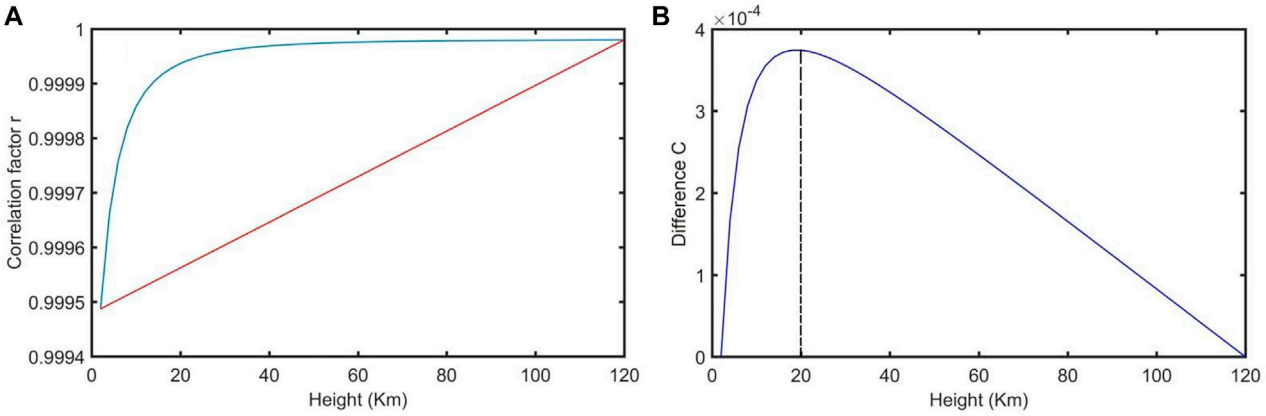

FIGURE 4
(A) Cross-correlations between the upward continuations at two successive heights. **(B)** Deflection C *versus* the height.

4.3 Tilt angle

The tilt angle (TDR) is also known as a phase filter. The tilt angle and its total horizontal gradient are recommended for the mapping of geological structures buried in the ground at medium depths and for the determination of ore deposits (Miller and Singh, 1994). This filter is applied on potential data, and it is defined as the ratio of the vertical derivative in the z-direction to the amplitude of the horizontal gradient as follows:

$$TDR = tan^{-1}\left[\frac{\frac{\partial \Delta T}{\partial z}}{\sqrt{\left(\frac{\partial \Delta T}{\partial x}\right)^2 + \left(\frac{\partial \Delta T}{\partial y}\right)^2}}\right] \tag{6}$$

The horizontal gradient of the tilt angle (HG_TDR) was developed by Verduzco et al. (2004) to optimize the geological information given by the tilt angle. It is given by

$$HG\_TDR = \sqrt{\left(\frac{\partial TDR}{\partial x}\right)^2 + \left(\frac{\partial TDR}{\partial y}\right)^2} \tag{7}$$

4.4 Enhanced horizontal gradient amplitude

Pham et al. (2020a) proposed to use the enhanced horizontal gradient amplitude (EHGA) filter to highlight both the shallow and deep geological contacts responsible for the gravity anomalies observed at the surface. It can be given as follows:

$$EHGA = \mathcal{R}\left(asin\left(p\left(\frac{HG_z}{\sqrt{HG_x^2 + HG_y^2 + HG_z^2}} - 1\right) + 1\right)\right) \tag{8}$$

where $\mathcal{R}$ is the real part of the function and p is a positive number. The EHGA ranges from—$\pi/2$ to + $\pi/2$ when the peaks are directly located over the edges, and we obtained optimal results when using $p \geq 2$ (Pham et al., 2020a).

4.5 Multi-scale horizontal derivative of the vertical derivative

As explained previously, the upward continuation on the data field is indicated to enhance the geological information in the ground at greater depths. For determination of geological contacts, the greater the extension height, the more information is enhanced on the deep contacts. Suppose the contact is located vertically from the source, then the maxima of the horizontal gradient of the extended map will make it possible to determine it, and the direction of shift of the maxima in question defines the dip direction of said contact (Fedi and Florio, 2001).

The following is a summary of the steps used for the MSHDVD method:

- Computing the first-order vertical gradient of the gravity data extended upward at different experimental altitudes, called multi-scale vertical derivative (MSVD).
- Determining the maxima of the horizontal gradient of the maps resulting from the MSVD method.

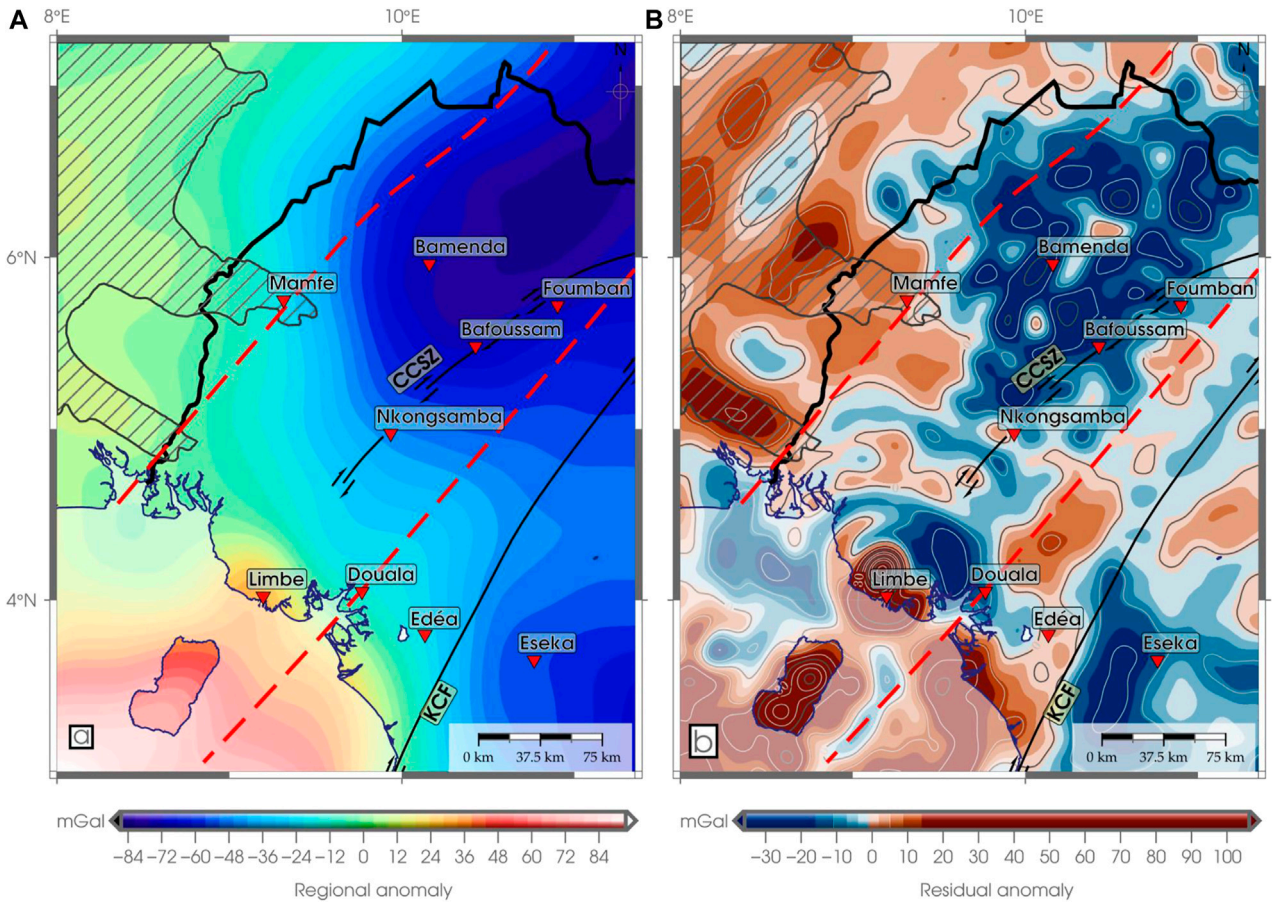

FIGURE 5
(A) Bouguer regional map; and **(B)** Bouguer residual map (black lines represent national boundaries).

- Superposing the results determined for different continuation heights.

5 Results

5.1 Bouguer anomaly map

In this section, we outlined the Bouguer anomalies resulting from the combination of the XGM 2019e_2159 and the ETOPO1 models to plot the Bouguer anomaly map. A 5 min × 5 min gridded spatial distribution of the Bouguer gravity anomaly was obtained. The total gravity intensity (TGI) clearly showed the differences in the locations of high and low gravimetric intensities (Figure 3). Due to the effects of region on the distribution of gravity anomalies observed on this map, the interpretation may contain errors, and we must first eliminate these effects to interpret it. This will be the subject of the next section.

5.2 Regional/residual separation

The Bouguer anomalies map (Figure 3) showed positive long-wavelength anomalies reaching ~174 mGal at the coast and negative anomalies in the eastern part of the study area, reaching peaks of −130 mGal. These positive anomalies would be the extension of the oceanic crust, which has a high density put in place during the opening of the South Atlantic (Torsvik et al., 2009; Lawrence et al., 2017). The negative anomalies observed to the northeast would be the deposits of ancient Precambrian rocks that would form the region's bedrock. Furthermore, the 3D Bouguer anomalies map showed a high correlation between the regional distribution of anomalies and the topography, thus indicating the presence of isostatic compensation. In addition, we observed a great correlation between the Bouguer anomalies map and the geological map of the study area.

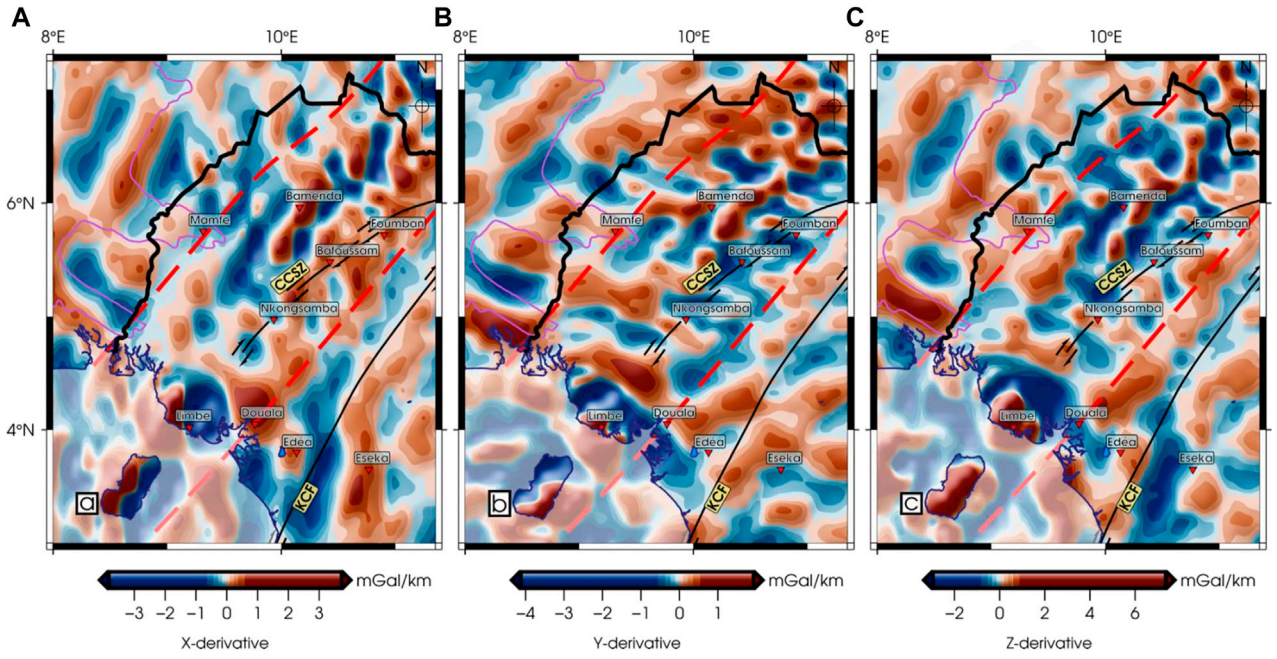

FIGURE 6
First-order derivative of the Bouguer residual anomaly map: **(A)** in the *X*-direction; **(B)** in *Y*-direction; and **(C)** in *Z*-direction (black lines represent national boundaries).

Figure 4A shows the cross-correlations between continuations to two successive heights *versus* the height. Figure 4B shows the deflection C *versus* the height for the Bouguer anomaly of the southwestern part of Cameroon. The curve of the deflection shows a maximum at a height of 20 km (Figure 4B). Thus, this height is regarded as the optimal height (Figure 4B). The upward continuation of the Bouguer anomaly data at a height of 20 km yields the regional anomaly (Figure 5A). The regional anomaly map obtained by extension shows a large positive anomaly at the coast and a large negative anomaly in the northwest region, separated by a medium-density structure. These anomalies would be caused by the effects of surface structures present in the study area. The residual anomaly caused by localized gravity effects was calculated by removing the regional anomaly data in Figure 5A from the observed anomaly. The calculated residual field anomaly map is shown in Figure 5B. The residual anomaly map provides precision on the distribution of gravity anomalies in the region. The positive anomalies observed along the coast and at the east of the region would be the representation of the CVL. The negative anomalies represent ancient Precambrian deposits, and mid-density anomalies represent sedimentary deposits.

5.3 Derivatives

To highlight the gravimetric signatures of the study area, the first-order derivative filters were applied, as explained in Section 4. Figure 6 shows the X, Y, and Z derivatives of gravimetric data. The X-derivative map shows that the positive anomalies observed are oriented NE–SW and the existence of sedimentary deposits along the coast and in the bordering part between the north-west and the south-west of Cameroon. This information is practically contradictory to that observed on the Y-derivative map. On the other hand, the Z-derivative map is similar to the residual anomaly map with positive anomalies oriented NE–SW, well dissociated compared to those observed in this one. Furthermore, Z-derivative presented anomalies of higher amplitudes, ranging between −4 and 8 mGal/km, than those observed on the X- and Y-derivatives and corroborated the existing information on the geological map.

5.4 Gradient filters

The HG and AS were applied to the Bouguer residual map to characterize the isolated sources since, in most cases, the filtered

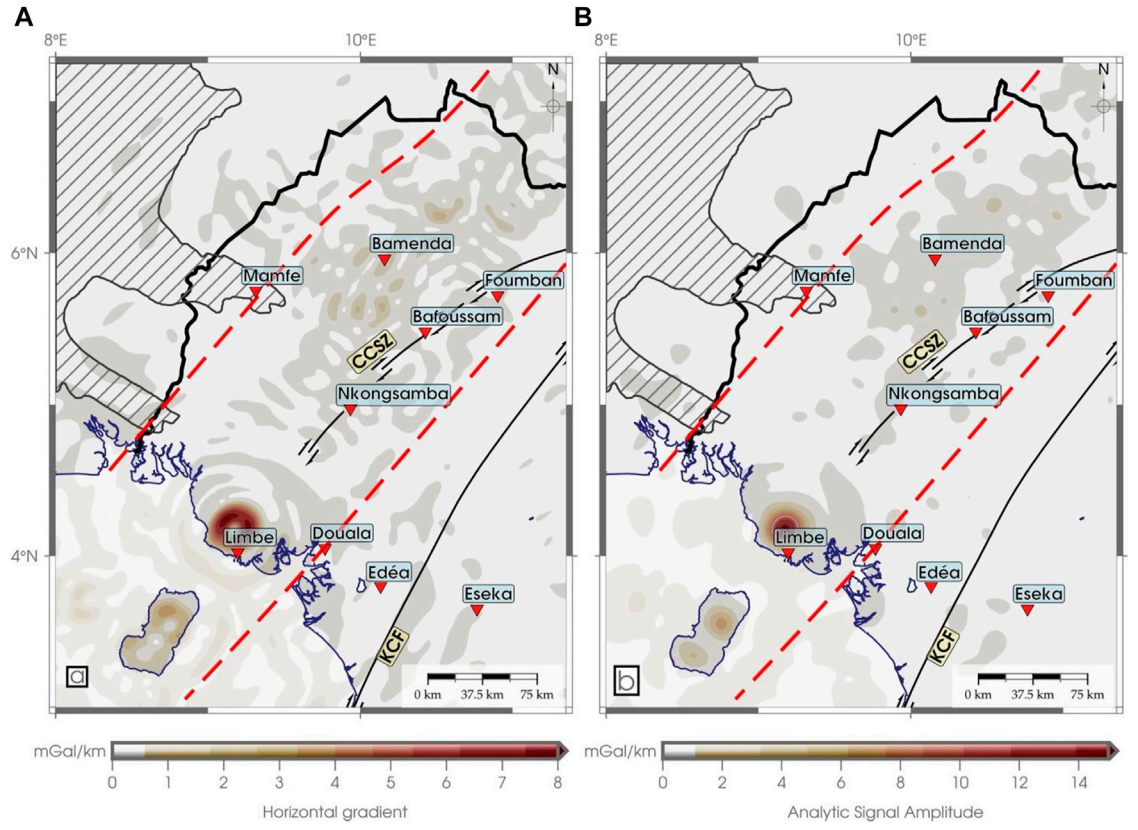

FIGURE 7
(A) Horizontal gradient and **(B)** analytical signal amplitude of the Bouguer residual map (black lines represent national boundaries).

anomaly is generally positive, and its maxima are located over the source edges. The gradient maps represented in Figure 7 show that the anomalies grouped in the Bouguer regional map are isolated, and the gradient filters aim to center the gravity anomalies below their geological sources. We can observe that the HG is more effective than the AS in mapping the source edges from gravity data. Here, Figure 7A also shows more edges than Figure 7B.

5.5 Filters based on the ratio of gradients

The TDR and HG_TDR maps of the residual data are shown in Figures 8A, B, respectively. On the TDR map, the observed positive anomalies well-corroborate the information of the geological map distinguished by the Eocene, Miopleocene, and Paleo-Neogene age sand covers that cover the Douala and Rio Del Rey sedimentary basins. Pham (2020) showed that the TDR filter is useful for enhancing information on discordant signals. However, it is not an ideal filter for edge detection because it does not provide sharpened responses at the source edges. The HG_TDR map represents the same anomalies observed on the TDR map but in the form of geological contacts existing below them. The EHGA map (Figure 8C) isolates edges better than TDR and HG_{TDR} since it can extract the edges of both shallow and deep structures.

5.6 Determination of geological contacts using the multi-scale horizontal derivative of the vertical derivative method

The detailed methodology used to apply this method has been elaborated in Section 4. In order to reveal the geological contacts between the depths of 1–5 km, first, the first-order Z-vertical derivative was calculated on the residual map and extended successively to depths of 1, 2, 3, 4, and 5 km. Second, we calculated the horizontal gradient amplitudes of these vertical derivatives and used the improved maximum detection method (Pham et al., 2020c) to determine the source edges (Figure 9). It is noticed that there is a great similarity between the maps in Figure 9 and those in Figure 8.

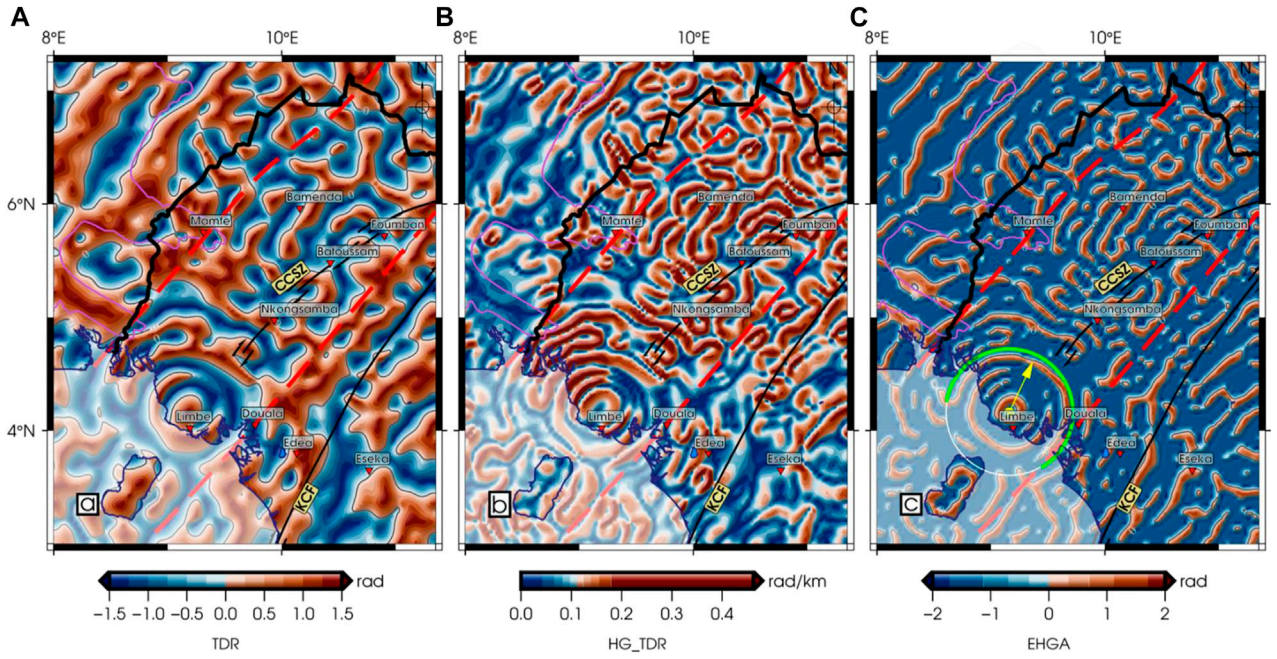

FIGURE 8
(A) Tilt derivative (TDR); **(B)** the horizontal gradient of the tilt derivative (HG_TDR); and **(C)** the enhanced horizontal gradient amplitude (EHGA) of the Bouguer residual map (black lines represent national boundaries). In green: the Fako and Tiko faults meet in a ring formation constituting the continental junction, spreading out to the Bakassi Peninsula and the Douala outlet. The yellow arrow denotes the average of the green arc.

The rose diagram of EHGA and MSHDVD lineaments represented in Figure 10 shows the distribution and orientations of the main faults identified in Southwestern Cameroon. As can be seen, most of the geological boundaries identified in the area are trending in the NE–SW, NNE–SSW, ENE–WSW, N–S, and NW–SE directions. Based on the information from the geological map, these maps will be analyzed to propose a tectono-structural map of the southwest part of Cameroon as shown in Figure 11. This map (Figure 11) highlights the main structures highlighted by the results of previous studies and corroborates the information provided by the geological map.

6 Discussion

The Bouguer anomaly map (Figure 3) highlights a large positive anomaly at the coast and a large negative anomaly at the northeast region of the study area. This positive anomaly would have originated from the extension of the oceanic crust at the level of the coast set up during the opening of the Atlantic Ocean in the Cretaceous and corroborates the results of Guiraud and Maurin (1992), Torsvik et al. (2009), and Lawrence et al. (2017). The negative anomaly observed indicates the presence of isostatic compensation as presented by Balogun (2019) and would be an accumulation of syn-tectonic granite. Moreover, we can observe an accumulation of low-intensity positive gravity anomalies covering the upper cretaceous sandstone of the Mamfe Basin. Thus, these observations are consistent with the existing geological and tectonic information in the study area.

The regional map (Figure 5A) highlights all the regional effects that interfere with the gravity signal. It is similar to the Bouguer anomaly map but is smoother than this one. Its resemblance rate to the Bouguer anomaly map justifies the chosen separation method and validates the height of 20 km for upward continuation. The residual map (Figure 5B) represents the anomaly map after removing the regional anomaly from the Bouguer anomaly. It presents the distribution of the different anomalies of the region more precisely. The positive anomalies observed are all oriented along the mean structural direction of N75° E, which is the major structural direction of the CVL (Tokam et al., 2010; Nzeuga et al., 2017), and this anomaly would be due to a melting point in the form of a "Y" below the crust (Fitton, 1980). The negative gravimetric anomalies observed in the northeast and southeast of the region would represent old syn-tectonic granitic rocks to which are added felsic gneisses and meta-sediments which constitute the crystalline basement (Toteu et al., 2004; Nzenti et al., 2006; Reusch et al., 2010; Anderson et al., 2014). According to Jacobsen (1987) and Kebede et al. (2020), when the gravity field is upward continued to a height z, it maps the sources located at and below the depth z/2. Since the Bouguer anomalies continuing upward to 20 km represent the regional field and were

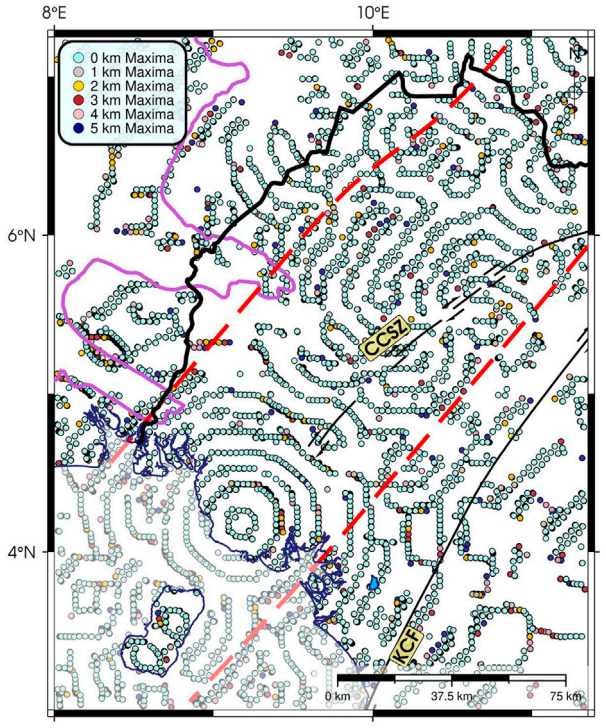

FIGURE 9
Source edges of the study area obtained by using the MSHDVD method.

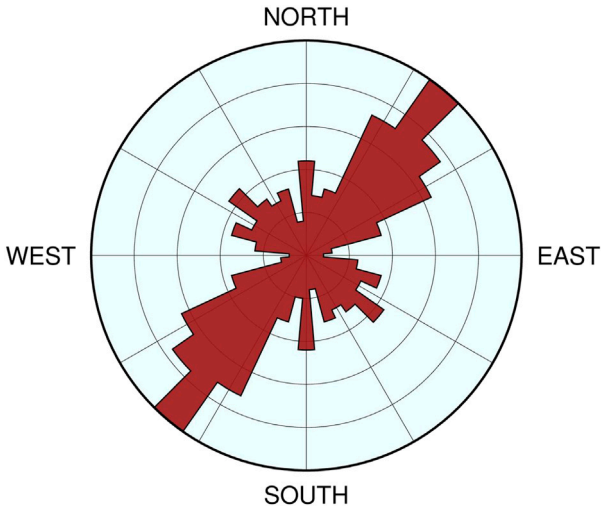

FIGURE 10
Rose diagram that shows the fault orientations within Southern Cameroon.

subtracted from the Bouguer anomaly map to obtain the corresponding residual, our results are related to the sources located at and above 10 km.

The first-order derivative maps (Figure 6) enhance the geological information contained in the residual map. The Z-derivative shows some positive anomalies that were not visible on the residual map east of the region. The HG and AS maps (Figure 7) isolated the different sources that were arranged as a block and placed the gravity anomalies directly above their sources. Since the THG and AS use the derivative amplitude to outline the edges, they cannot balance anomalies from shallow and deep structures. In other words, these methods cannot determine geological boundaries located at different depths at the same time. Both methods are dominated by large-amplitude responses from the shallow structures. In addition, for thin or deep sources, the peaks of the AS are shifted inward from the edges, making the structural bodies seem smaller than they are, as reported by Pham et al. (2020a), Pham et al. (2020b).

The TDR map (Figure 8A) highlights the different gravimetric domains, while the HG_{TDR} map (Figure 8B) highlights the different contacts that delimit these different domains. It should be noted that the contacts obtained from the TDR and HGTDR are connected, complicating the geological interpretation (Eldosouky et al., 2022e). The EHGA filter is effective in highlighting a wide range of density structures in southwestern Cameroon. Since the EHGA is based on the ratio of derivatives of the horizontal gradient, it can balance anomalies from different structures. Thus, the use of this method brings clearer images for all the edges of both the shallow and deep sources. In other words, the EHGA can outline the geological boundaries located at different depths at the same time. In addition, the EHGA map can avoid bringing false information in the edge maps, as reported by Pham et al. (2020a) and Ghomsi et al. (2020). Thus, we believe that the edges in the EHGA map are suitable for highlighting geological contacts as faults.

The source edges determined by the MSHDVD method represented in Figure 9 highlight most of the contacts shown on the EHGA map. The presence of a wide range of structures in the MSHDVD map is also verified by the results of the EHGA. So, we can observe in Figure 9 that these contacts bound the anomalies. Thus, contacts that form closed contours delineate intrusions, while those that are linear determine the presence of structures like faults. The combined analysis of the maps in Figures 8, 9 highlights the geological structures in this region. We also compared the density structures determined in Figures 8, 9 to the geological structures in Figure 2 (Figure 11). The present study is the first of its kind to accurately determine the circular margin of the continental and oceanic extensions of Mount Cameroon, while perfectly illustrating the Bao, Bomana, Tiko, and Ekona faults, as well as highlighting the strike–slip faults at the top as simulated by Mathieu et al. (2011) and Kervyn et al. (2014). We can see that our results not only highlighted some structures that already existed according to the observations of the geological map but also highlighted new faults.

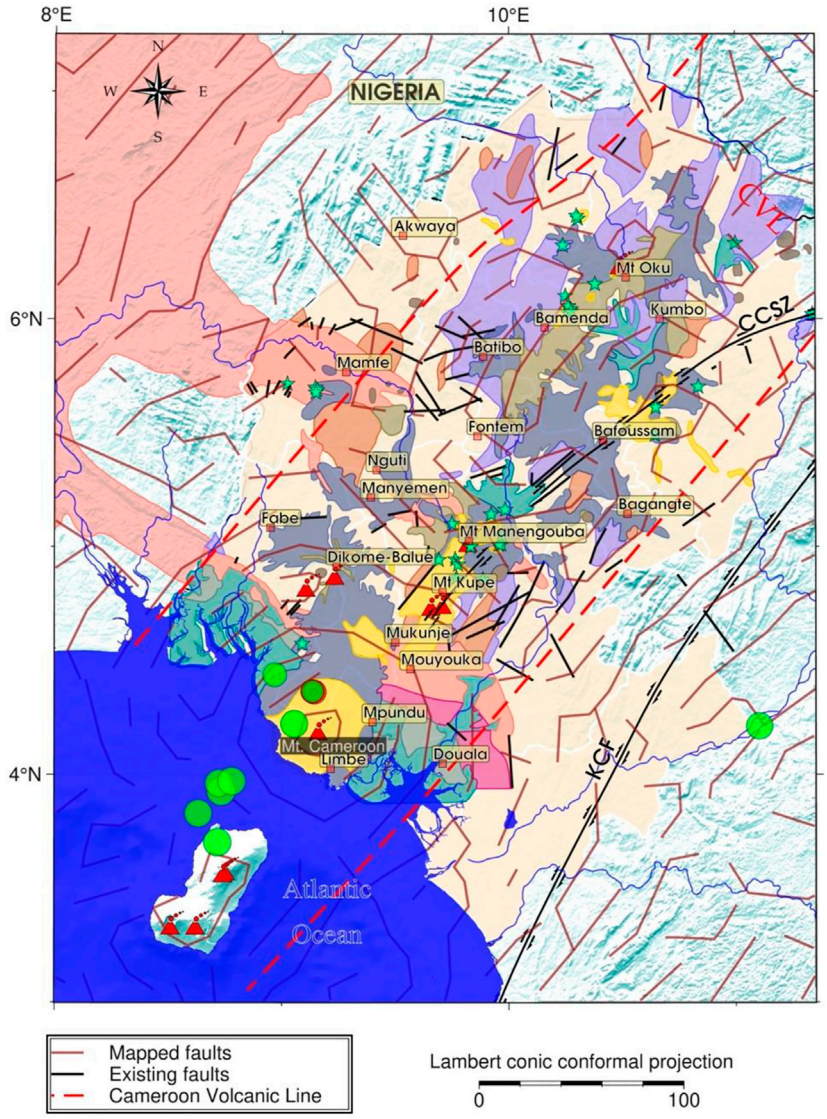

FIGURE 11
Representation of new faults compared to the existing ones. Legend and abbreviations as shown in Figure 2.

7 Conclusion

In this study, we separated the regional/residual anomalies from the Bouguer anomaly data to obtain the best map of residual anomalies for the southwestern part of Cameroon. Then, we applied filters such as the HG, AS, TDR, HG_{TDR} gradient, and EHGA to the residual anomaly data to highlight the geological source edges. Finally, we used the MSHDVD method to highlight the same contacts. The main results of this work show with precision the region's major lineaments, which in turn made it possible to highlight the CVL, intrusions of rocks of low densities known as syn to late tectonic granitoid, and faults of various directions. These results are comparable to those of the existing one and corroborate the information that the basement of the studied region would be made up of Precambrian volcanic rocks with a large concentration of basalt and gneiss. The observed geological structures show that the tectonic activity in this region is still ongoing. The current study is the first of its type to precisely define the circular boundary of Mount Cameroon's continental and oceanic expansions, while also perfectly displaying the Bao, Bomana, Tiko, and Ekona faults

and highlighting the strike–slip faults near the peak. However, it would be important to delineate the depths of the structures that form the CVL by quantitative analysis by inversion and/or by 2D or 3D modeling. Also, the use of remote sensing data will make it possible to highlight a structural map of the said region precisely.

Data availability statement

The raw data supporting the conclusion of this article will be made available by the authors, without undue reservation.

Author contributions

ARN contributed to writing, scientific development and early computations of this study. FEKG contributed to writing, result interpretation, scientific development, review, data curation and figure preparation. LTP contributed to writing, result interpretation, scientific development, review and performed the computations. AME contributed to writing, result interpretation, review and scientific development. ZA, JDK, ABKF, and RN contributed to writing and scientific development. KA, MSF, and PA reviewed, provided critical feedback and helped shape the research.

Funding

This research was supported by Researchers Supporting Project number (RSP-2021/249), King Saud University, Riyadh, Saudi Arabia.

Conflict of interest

The authors declare that the research was conducted in the absence of any commercial or financial relationships that could be construed as a potential conflict of interest.

Publisher's note

All claims expressed in this article are solely those of the authors and do not necessarily represent those of their affiliated organizations, or those of the publisher, the editors, and the reviewers. Any product that may be evaluated in this article, or claim that may be made by its manufacturer, is not guaranteed or endorsed by the publisher.

References

Amante, C., and Eakins, B. W. (2009). ETOPO1 1 arc-minute global relief model: procedures, data sources and analysis. *NOAA, Tech. Memo. NESDIS, NGDC* 24, 19. doi:10.1594/PANGAEA.769615

Anderson, K. F., Wall, F., Rollinson, G. K., and Moon, C. J. (2014). Quantitative mineralogical and chemical assessment of the Nkout iron ore deposit, Southern Cameroon. *Ore Geol. Rev.* 62, 25–39. doi:10.1016/j.oregeorev.2014.02.015

Aslanian, D., and Moulin, M. (2010). Comment on 'A new scheme for the opening of the south Atlantic Ocean and the dissection of an aptian salt basin' by trond H. Torsvik, sonia rousse, cinthia labails and mark A. Smethurst. *Geophys. J. Int.* 183, 20–28. doi:10.1111/j.1365-246x.2010.04727.x

Balogun, O. B. (2019). Preliminary interpretation of isostatic residual gravity anomalies within the central portion of the Equatorial Atlantic African region. *SN Appl. Sci.* 1 (5), 495. doi:10.1007/s42452-019-0440-5

Beckline, M., Yujun, S., Etongo, D., Saeed, S., and Mannan, A. (2018). Assessing the drivers of land use change in the Rumpi hills forest protected area, Cameroon. *J. Sustain. For.* 37, 592–618. doi:10.1080/10549811.2018.1449121

Blakely, R. J., and Simpson, R. W. (1986). Approximating edges of source bodies from magnetic or gravity anomalies. *Geophysics* 51, 1494–1498. doi:10.1190/1.1442197

Cordell, L., and Grauch, V. J. S. (1985). "16. mapping basement magnetization zones from aeromagnetic data in the san juan basin, New Mexico," in *The utility of regional gravity and magnetic anomaly maps* (Texas: Society of Exploration Geophysicists), 181–197. doi:10.1190/1.0931830346.ch16

Cordell, L. (1979). "Gravimetric expression of graben faulting in santa fe country and the espanola basin: New Mexico geological society guidebook," in 30th Field Conference, New Mexico, Jan 1 1979, 59–64.

Deruelle, B., Ngounouno, I., and Demaiffe, D. (2007). The Cameroon hot line (CHL): a unique example of active alkaline intraplate structure in both oceanic and continental lithospheres. *Comptes Rendus Geosci.* 339, 589–600. doi:10.1016/j.crte.2007.07.007

Dung, T. T., and Minh, N, Q. (2017). Eruptive-volcanic-basalt structures in the Truong Sa-Spratly Islands and adjacent areas from interpreting gravity and magnetic data. *Vietnam J. Earth Sci.* 39 (1), 1–13. doi:10.15625/0866-7187/39/1/9167

Duong, T. N., Phong, L. H., Pham, D. N., Chen, C. H., and Dinh, V. T. (2021). Relationship between seismicity and active faults in Thanh Hoa province detected by local seismic network. *Vietnam J. Earth Sci.* 43 (2), 199–219. doi:10.15625/0866-7187/15931

Eldosouky, A. M., Pham, L. T., El-Qassas, R. A. Y., Hamimi, Z., and Oksum, E. (2021a). "Lithospheric structure of the arabian–nubian shield using satellite potential field data," in *The geology of the arabian-nubian shield. Regional geology reviews*. Editors Z. Hamimi, A. R. Fowler, J. P. Liégeois, A. Collins, M. G. Abdelsalam, and M. Abd EI-Wahed (Cham: Springer). doi:10.1007/978-3-030-72995-0_6

Eldosouky, A. M., El-Qassas, R. A. Y., Pour, A. B., Mohamed, H., and Sekandari, M. (2021b). Integration of ASTER satellite imagery and 3D inversion of aeromagnetic data for deep mineral exploration. *Adv. Space Res.* 68 (9), 3641–3662. doi:10.1016/j.asr.2021.07.016

Eldosouky, A. M., El-Qassas, R. A. Y., Pham, L. T., Abdelrahman, K., Alhumimidi, M. S., El Bahrawy, A., et al. (2022a). Mapping main structures and related mineralization of the arabian shield (Saudi Arabia) using sharp edge detector of transformed gravity data. *Minerals* 12, 71. doi:10.3390/min12010071

Eldosouky, A. M., Ekwok, S. E., Akpan, A. E., Achadu, O. I. M., Pham, L. T., Abdelrahman, K., et al. (2022b). Delineation of structural lineaments of Southeast Nigeria using high resolution aeromagnetic data. *Open Geosci.* 14 (1), 331–340. doi:10.1515/geo-2022-0360

Eldosouky, A. M., Pham, L. T., Abdelrahman, K., Fnais, M. S., and Gomez-Ortiz, D. (2022c). Mapping structural features of the Wadi Umm Dulfah area using aeromagnetic data. *J. King Saud Univ. - Sci.* 34 (2), 101803–103647. doi:10.1016/j.jksus.2021.101803

Eldosouky, A. M., Pham, L. T., and Henaish, A. (2022d). High precision structural mapping using edge filters of potential field and remote sensing data: A case study from wadi umm ghalqa area, south eastern desert, Egypt. *Egypt. J. Remote Sens. Space Sci.* 25 (2), 501–513. doi:10.1016/j.ejrs.2022.03.001

Eldosouky, A. M., Pham, L. T., Duong, V. H., Ghomsi, F. E. K., and Henaish, A. (2022e). Structural interpretation of potential field data using the enhancement techniques: a case study. *Geocarto Int.*, 1–26. doi:10.1080/10106049.2022.2120548

Fedi, M., and Florio, G. (2001). Detection of potential fields source boundaries by enhanced horizontal derivative method. *Geophys. Prospect.* 49, 40–58. doi:10.1046/j.1365-2478.2001.00235.x

Fitton, J. G., and Dunlop, H. M. (1985). The Cameroon line, West Africa, and its bearing on the origin of oceanic and continental alkali basalt. *Earth Planet. Sci. Lett.* 72, 23–38. doi:10.1016/0012-821X(85)90114-1

Fitton, J. G., Kilburn, C. R. J., Thirlwall, M. F., and Hughes, D. J. (1983). 1982 eruption of mount Cameroon, west Africa. *Nature* 306, 327–332. doi:10.1038/306327a0

Fitton, J. (1980). The Benue trough and Cameroon line — a migrating rift system in west Africa. *Earth Planet. Sci. Lett.* 51 (1), 132–138. doi:10.1016/0012-821x(80)90261-7

Fitton, J. G. (1987). "The Cameroon line, west Africa: A comparison between oceanic and continental alkaline volcanism," in *Alkaline igneous rocks, 30*. Editors J. G. Fitton and B. G. J. Upton (London: Geological Society London Special Publications), 273–291. doi:10.1144/GSL.SP.1987

Fosso-Téguia, E. M. E., Nana, V. G., Alain, L. T. S., Olivier, N. B. E., Albert, E. Y., Alain, Z. A., et al. (2020). Exploration of potential ore deposits along the Cameroon volcanic line from gravity and magnetic studies. *Open J. Geol.* 10, 1009–1026. doi:10.4236/ojg.2020.1010047

Geze, B. (1943). Géographie physique et géologie du Cameroun Occidental, 17. *Mem. Mus. Natl. Hist. Nat. Paris, Nouv. Ser.*, 1–272.

Ghomsi, F. E. K., Sévérin, N., Mandal, A., Nyam, F. E. A., Tenzer, R., Kamga, A. P. T., et al. (2020). Cameroon's crustal configuration from global gravity and topographic models and seismic data. *J. Afr. Earth Sci.* 161, 103657. doi:10.1016/j.jafrearsci.2019.103657

Ghomsi, F. E. K., Ribeiro-Filho, N., Baldez, R., Tenzer, R., Martins, C. M., Chisenga, C., et al. (2021). Identification of Cameroon's geological structures through a gravity separation and using seismic crustal models. *J. Afr. Earth Sci.* 173, 104027. doi:10.1016/j.jafrearsci.2020.104027

Ghomsi, F. E. K., Domra, K. J., Aretouyap, Z., Ribeiro-Filho, N., Pham, L. T., Baldez, R., et al. (2022a). Main structural lineaments of the southern Cameroon volcanic line derived from aeromagnetic data. *J. Afr. Earth Sci.* 186, 104418. doi:10.1016/j.jafrearsci.2021.104418

Ghomsi, F. E. K., Tenzer, R., Njinju, E., and Steffen, R. (2022b). The crustal configuration of the West and Central African Rift System from gravity and seismic data analysis. *Geophys. J. Int.* 230 (2), 995–1012. doi:10.1093/gji/ggac089

Ghomsi, F. E. K., Pham, L. T., Tenzer, R., Esteban, F. D., Van Vu, T., and Kamguia, J. (2022c). Mapping of fracture zones and structural lineaments of the Gulf of Guinea passive margins using marine gravity data from CryoSat-2 and Jason-1 satellites. *Geocarto Int.*, 1–24. doi:10.1080/10106049.2022.2040602

Ghomsi, F. E. K., Pham, L. T., Steffen, R., Ribeiro-Filho, N., and Tenzer, R. (2022d). Delineating structural features of North Cameroon using the EIGEN6C4 high-resolution global gravitational model. *Geol. J*, 1–15. doi:10.1002/gj.4544

Grauch, V. J. S., and Cordell, L. (1987). Limitations of determining density or magnetic boundaries from the horizontal gradient of gravity or pseudogravity data. *Geophysics* 52, 118–121. doi:10.1190/1.1442236

Guiraud, R., and Maurin, C. J. (1992). Early cretaceous rifts of western and central africa: an overview. *Tectonophysics* 213, 153–168. doi:10.1016/0040-1951(92)90256-6

Hang, N. T. T., Thanh, D. D., and Minh, L. H. (2017). Application of directional derivative method to determine boundary of magnetic sources by total magnetic anomalies. *Vietnam J. Earth Sci.* 39 (4), 360–375. doi:10.15625/0866-7187/39/4/10731

Hang, N. T. T., Oksum, E., Minh, L. H., and Thanh, D. D. (2019). An improved space domain algorithm for determining the 3-D structure of the magnetic basement. *Vietnam J. Earth Sci*. 41 (1), 69–80. doi:10.15625/0866-7187/41/1/13550

Jacobsen, B. H. (1987). A case for upward continuation as a standard separation filter for potential-field maps. *Geophysics* 52, 1138–1148. doi:10.1190/1.1442378

Kebede, H., Alemu, A., and Fisseha, S. (2020). Upward continuation and polynomial trend analysis as a gravity data decomposition, case study at Ziway-Shala basin, central Main Ethiopian rift. *Heliyon* 6 (1), e03292. doi:10.1016/j.heliyon.2020.e03292

Kervyn, M., Van Wyk De Vries, B., Walter, T. R., Njome, M. S., Suh, C. E., and Ernst, G. G. J. (2014). Directional flank spreading at Mount Cameroon volcano: Evidence from analogue modeling. *J. Geophys. Res. Solid Earth* 119 (10), 7542–7563. doi:10.1002/2014JB011330

Koumetio, F., Njomo, D., Tabod, C. T., Noutchogwe, T. C., and Manguelle-Dicoum, E. (2012). Structural interpretation of gravity anomalies from the kribi–edea zone, south Cameroon: a case study. *J. Geophys. Eng.* 9 (6), 664–673. doi:10.1088/1742-2132/9/6/664

Kvas, A., Brockmann, J. M., Krauss, S., Schubert, T., Gruber, T., Meyer, U., et al. (2021). GOCO06s–a satellite-only global gravity field model. *Earth Syst. Sci. Data* 13 (1), 99–118. doi:10.5194/essd-13-99-2021

Lawrence, S. R., Beach, A., Jackson, O., and Jackson, A. (2017). Deformation of oceanic crust in the eastern gulf of Guinea: role in the evolution of the Cameroon volcanic line and influence on the petroleum endowment of the douala-rio muni basin. *Geol. Soc. Lond. Spec. Publ.* 438 (1), 7–26. doi:10.1144/SP438.7

Lee, D. C., Halliday, A., Fitton, J. G., and Poli, G. (1994). Isotopic variations with distance and time in the volcanic islands of the Cameroon line: evidence for a mantle plume origin. *Earth Planet. Sci. Lett.* 123 (1–4), 119–138. doi:10.1016/0012-821x(94)90262-3

Long, H. V., Thanh, N. T., Tuan, V. T., Tung, N. T., Anh, N. L., Din, D. B., et al. (2021). Holocene sedimentation offshore Southeast Vietnam based on geophysical interpretation and sediment composition analysis. *Vietnam J. Earth Sci.* 43 (3), 336–379. doi:10.15625/2615-9783/16268

Mathieu, L., Kervyn, M., and Ernst, G. G. (2011). Field evidence for flank instability, basal spreading and volcano-tectonic interactions at Mt Cameroon, West Africa. *Bull. Volcanol.* 73 (7), 851–867. doi:10.1007/s00445-011-0458-z

Maurizot, P., Abessolo, A., Feybesse, J. L., Johan, V., and Lecomte, P. (1986). *Etude et prospection minière du sudouest Cameroun. Synthèse des travaux de 1978 à 1985*. Rapport: BRGM, 274.

Melouah, O., Eldosouky, A. M., and Ebong, W. D. (2021). Crustal architecture, heat transfer modes and geothermal energy potentials of the Algerian Triassic provinces. *Geothermics* 96, 102211. ISSN 0375-6505. doi:10.1016/j.geothermics.2021.102211

Meyers, J. B., Rosendahl, B. R., Harrison, C. G., and Ding, Z. D. (1998). Deep-imaging seismic and gravity results from the offshore Cameroon volcanic line, and speculation of african hotlines. *Tectonophysics* 284, 31–63. doi:10.1016/s0040-1951(97)00173-x

Miller, H. G., and Singh, V. (1994). Potential field tilt—a new concept for location of potential field sources. *J. Appl. Geophy.* 32, 213–217. doi:10.1016/0926-9851(94)90022-1

Minyem, D., and Nedelec, A. (1990). "Origin and evolution of the eseka gneisses (Cameroon). Archean TTG reworked in the panafrican mobile belt," in Proceeding of the 15th Colloquium of African Geology Nancy, 21–24.

Moulin, M., Aslanian, D., and Unternehr, P. (2010). A new starting point for the south and equatorial atlantic ocean. *Earth. Sci. Rev.* 98, 1–37. doi:10.1016/j.earscirev.2009.08.001

Nabighian, M. N. (1972). The analytic signal of two-dimensional magnetic bodies with polygonal cross-section: its properties and use for automated anomaly interpretation. *Geophysics* 37, 507–517. doi:10.1190/1.1440276

Nabighian, M. N. (1984). Toward a three-dimensional automatic interpretation of potential field data via generalized hilbert transforms: fundamental relations. *Geophysics* 49, 780–786. doi:10.1190/1.1441706

Ndikum, E. N., Tabod, C. T., and Tokam, A. P. K. (2014). Frequency time analysis (FTAN) and moment tensor inversion solutions from short period surface waves in Cameroon (central africa). *Open J. Geol.* 4, 33–43. doi:10.4236/ojg.2014.42004

Ndikum, E. N., Tabod, C. T., Koumetio, F., Tatchum, N. C., and Victor, K. J. (2017). Evidence of some major structures underlying the Douala sedimentary sub-basin: West african coastal basin. *J. Geoscience Environ. Prot.* 5, 161–172. doi:10.4236/gep.2017.57013

Ngounouno, I., D´eruelle, B., and Demaiffe, D. (2000). Petrology of the bimodal cenozoic volcanism of the kapsiki plateau (northernmost Cameroon, central Africa). *J. Volcanol. Geotherm. Res.* 102, 21–44. doi:10.1016/s0377-0273(00)00180-3

Ngounouno, I., D´eruelle, B., Demaiffe, D., and Montigny, R. (2003). Petrology of the cenozoic volcanism in the upper benue valley, northern Cameroon (central Africa). *Contrib. Mineral. Pet.* 145, 87–106. doi:10.1007/s00410-002-0438-6

Nouayou, R. (2005). "Contribution à l'étude géophysique du bassin sédimentaire de Mamfé par prospections Audio et Hélio Magnétotelluriques," Thèse de Doctorat d'Etat ès Sciences. (Cameroon: Université de Yaoundé I), 212.

Noutchogwe, T. C., Tabod, C. T., Koumetio, F., and Manguelle-Dicoum, E. (2011). A gravity model study for differentiating vertical and dipping geological contacts with application to a bouguer gravity anomaly over the foumban shear zone, Cameroon. *Geophysica* 47, 43–55.

Nsifa, E. N. (2005). "Magmatisme et évolution géodynamique de l'Archéen au Protérozoïque de la bordure nord-ouest du craton du Congo (complexe du Ntem) au Sud-Ouest Cameroun," Thèse Doctorat d'Etat. (Yaounde: Université de Yaoundé I), 248.

Nzenti, J. P., Kapajika, B., Wörner, G., and Lubala, T. R. (2006). Synkinematic emplacement of granitoids in a Pan-African shear zone in Central Cameroon. *J. Afr. Earth Sci.* 45 (1), 74–86. doi:10.1016/j.jafrearsci.2006.01.005

Nzeuga, A. R., Nouayou, R., Enyegue-à-Nyam, F., and Fairhead, J. D. (2017). The use of aeromagnetic data interpretation to characterize the features in the mamfe sedimentary basin Cameroon and a part of the east of Nigeria. *Int. J. Sci. Res.* 6, 2319–7064. doi:10.21275/ART20177759

Nzeuga, A. R., Nyam, F. E., Nouayou, R., and Fairhead, J. D. (2019). Impact of the south atlantic opening on the origin and the tectonic of the mamfe, Douala and Rio Del Rey sedimentary basins, geodynamics implication. *Open J. Earthq. Res.* 8, 299–312. doi:10.4236/ojer.2019.84017

Oksum, E., Dolmaz, M. N., and Pham, L. T. (2019). Inverting gravity anomalies over the Burdur sedimentary basin, SW Turkey. *Acta Geod. geophys.* 54 (4), 445–460. doi:10.1007/s40328-019-00273-5

Oksum, E. (2021). Grav3CH_inv: a GUI-based MATLAB code for estimating the 3-D basement depth structure of sedimentary basins with vertical and horizontal density variation. *Comput. Geosci.* 155, 104856. doi:10.1016/j.cageo.2021.104856

Pail, R., Fecher, T., Barnes, D., Factor, J. F., Holmes, S. A., Gruber, T., et al. (2018). Short note: the experimental geopotential model XGM2016. *J. Geod.* 92 (4), 443–451. doi:10.1007/s00190-017-1070-6

Pham, L. T., Le, M. H., Oksum, E., and Do, T. D. (2018). Determination of maximum tilt angle from analytic signal amplitude of magnetic data by the curvature-based method. *Vietnam J. Earth Sci.* 40 (4), 354–366. doi:10.15625/0866-7187/40/4/13106

Pham, L. T., Do, T. D., Oksum, E., and Le, S. T. (2019). Estimation of Curie point depths in the Southern Vietnam continental shelf using magnetic data. *Vietnam J Earth Sci* 41 (3), 216–228. doi:10.15625/0866-7187/41/3/13830

Pham, L. T., Eldosouky, A. M., Oksum, E., and Saada, S. A. (2020a). A new high resolution filter for source edge detection of potential field data. *Geocarto Int.* 37, 3051–3068. doi:10.1080/10106049.2020.1849414

Pham, L. T., Vu, T. V., Le-Thi, S., and Trinh, P. T. (2020b). Enhancement of potential field source boundaries using an improved logistic filter. *Pure Appl. Geophys.* 177, 5237–5249. doi:10.1007/s00024-020-02542-9

Pham, L. T., Oksum, E., Vu, M. D., Vo, Q. T., Le-Viet, K. D., and Eldosouky, A. M. (2020c). An improved approach for detecting ridge locations to interpret the potential field data for more accurate structural mapping: A case study from vredefort dome area (South Africa). *J. Afr. Earth Sci.* 175, 104099. doi:10.1016/j.jafrearsci.2020.104099

Pham, L. T., Kafadar, O., Oksum, E., and Hoang-Minh, T. (2021). A comparative study on the peak detection methods used to interpret potential field data: A case study from vietnam. *Geocarto Int.* 37, 3679–3696. doi:10.1080/10106049.2021.2007297

Pham, L. T., Oksum, E., Kafadar, O., Trinh, P. T., Nguyen, D. V., Vo, Q. T., et al. (2022a). Determination of subsurface lineaments in the Hoang Sa islands using enhanced methods of gravity total horizontal gradient. *Vietnam J. Earth Sci.* 44 (3), 395–409. doi:10.15625/2615-9783/17013

Pham, L. T., Oliveira, S. P., Eldosouky, A. M., Abdelrahman, K., Fnais, M. S., Xayavong, V., et al. (2022b). Determination of structural lineaments of northeastern Laos using the LTHG and EHGA methods. *J. King Saud Univ. – Sci.* 34, 101825. doi:10.1016/j.jksus.2022.101825

Pham, L. T., Oksum, E., Eldosouky, A. M., Gomez-Ortiz, D., Abdelrahman, K., Altinoglu, F. F., et al. (2022c). Determining the Moho interface using a modified algorithm based on the combination of the spatial and frequency domain techniques: a case study from the arabian shield. *Geocarto Int.*, 1–16. doi:10.1080/10106049.2022.2037733

Pham, L. T. (2020). A comparative study on different filters for enhancing potential field source boundaries: synthetic examples and a case study from the song hong trough (vietnam). *Arab. J. Geosci.* 13, 723. doi:10.1007/s12517-020-05737-5

Phillips, J. D. (2000). *Locating magnetic contacts: A comparison of the horizontal gradient, analytic signal, and local wavenumber methods: Presented at the SEG technical program expanded abstracts 2000*. Texas: Society of Exploration Geophysicists. doi:10.1190/1.1816078

Prasad, K. N. D., Pham, L. T., and Singh, A. P. (2022a). Structural mapping of potential field sources using BHG filter. *Geocarto Int.*, 1–28. doi:10.1080/10106049.2022.2048903

Prasad, K. N. D., Pham, L. T., and Singh, A. P. (2022b2022). A novel filter "ImpTAHG" for edge detection and a case study from cambay rift basin, India. *Pure Appl. Geophys.* 179, 2351–2364. doi:10.1007/s00024-022-03059-z

Regnoult, T. M. (1986). *Synthèse géologique du Cameroun. Ministère des Mines et de l'Energie*. Yaoundé. Direction des Mines et de la Géologie, 119.

Reusch, A. M., Nyblade, A. A., Wiens, D. A., Shore, P. J., Ateba, B., Tabod, C., et al. (2010). Upper mantle structure beneath Cameroon from body wave tomography and the origin of the Cameroon Volcanic Line. *Geochem. Geophys. Geosyst.* 11, Q10W07. doi:10.1029/2010gc003200

Roest, W. R., Verhoef, J., and Pilkington, M. (1992). Magnetic interpretation using the 3-D analytic signal. *Geophysics* 57, 116–125. doi:10.1190/1.1443174

Schmidt, C., Laag, C., Whitehead, M., Profe, J., Aka, F. T., Hasegawa, T., et al. (2022). The complexities of assessing volcanic hazards along the Cameroon Volcanic Line using spatial distribution of monogenetic volcanoes. *J. Volcanol. Geotherm. Res.* 427, 107558. doi:10.1016/j.jvolgeores.2022.107558

Suh, C. E., Sparks, R. S. J., Fitton, J. G., Ayonghe, S. N., Annen, C., Nana, R., et al. (2003). The 1999 and 2000 eruptions of mount Cameroon: Eruption behaviour and petrochemistry of lava. *Bull. Volcanol.* 65, 267–281. doi:10.1007/s00445-002-0257-7

Suh, C. E., Luhr, J. F., and Njome, M. S. (2008). Olivine-hosted glass inclusions from scoriae erupted in 1954-2000 at mount Cameroon volcano, west Africa. *J. Volcanol. Geotherm. Res.* 169, 1–33. doi:10.1016/j.jvolgeores.2007.07.004

Tchameni, R., Mezger, K., Nsifa, N. E., and Pouclet, A. (2001). Crustal origin of early proterozoic syenites in the Congo craton (Ntem complex), south Cameroon. *Lithos* 57, 23–42. doi:10.1016/S0024-4937(00)00072-4

Tchameni, R. (1997). "Géochimie et Géochronologie des formations de l'Archéen et du Paléoprotérozoïque du SudCameroun (groupe du Ntem, craton du Congo),". Thèse Doctorat Université d'Orléans, Orléans, 356.

Tchoukeu, C. D. N., Sobh, M., Basseka, C. A., Mouzong, M., Djomani, Y. P., and Etame, J. (2021). The mechanical behaviour of the lithosphere beneath the Chad Basin and the Bangui Magnetic Anomaly. Insights from Moho depth and effective elastic thickness estimates. *J. Afr. Earth Sci.* 182, 104299. doi:10.1016/j.jafrearsci.2021.104299

Tokam, K. A. P., Tabod, C. T., Nyblade, A. A., Julia, J., Wiens, D. A., and Pasyanos, M. (2010). Structure of the crust beneath Cameroon, West Africa, from the joint inversion of Rayleigh wave group velocities and receiver functions. *Geophys. J. Int.* 183, 1061–1076. doi:10.1111/j.1365-246x.2010.04776.x

Torsvik, T. H., Rousse, S., Labails, C., and Smethurst, M. A. (2009). A new scheme for the opening of the south atlantic ocean and the dissection of an aptian salt basin. *Geophys. J. Int.* 177, 1315–1333. doi:10.1111/j.1365-246x.2009.04137.x

Toteu, S. F., Penaye, J., and Poudjom-Djomani, Y. (2004). Geodynamic evolution of the panAfrican belt in central Africa with special reference to Cameroon. *Can. J. Earth Sci.* 41 (1), 73–85. doi:10.1139/e03-079

Ubangoh, R. U., Pacca, I. G., Nyobe, J. L., Hell, J., and Ateba, B. (2005). Petromagnetic characteristics of Cameroon Line volcanic rocks. *J. Volcanol. Geotherm. Res.* 142 (3–4), 225–241. doi:10.1016/j.jvolgeores.2004.11.006

Verduzco, B., Fairhead, J. D., Green, C. M., and MacKenzie, C. (2004). New insights into magnetic derivatives for structural mapping. *Lead. Edge* 23, 116–119. doi:10.1190/1.1651454

Wembenyui, E. W., Collerson, K. D., and Xin-Zhao, J. (2020). Evolution of Mount Cameroon volcanism: geochemistry, mineral chemistry and radiogenic isotopes (pb, sr, nd). *Geosci. Front.* 11, 2157–2168. doi:10.1016/j.gsf.2020.03.015

Yokoyama, T., Aka, F. T., Kusakabe, M., and Nakamura, E. (2007). Plume-Lithosphere interaction beneath Mt. Cameroon volcano, west Africa: Constraints from 238U-230Th-226Ra and Sr-Nd-Pb isotope systematics. *Geochimica Cosmochimica Acta* 71, 1835–1854. doi:10.1016/j.gca.2007.01.010

Zeng, H., Xu, D., and Tan, H. (2007). A model study for estimating optimum upward-continuation height for gravity separation with application to a Bouguer gravity anomaly over a mineral deposit, Jilin province, northeast China. *Geophysics* 72 (4), I45–I50. doi:10.1190/1.2719497

Zingerle, P., Pail, R., Gruber, T., and Oikonomidou, X. (2020). The combined global gravity field model XGM2019e. *J. Geod.* 94 (7), 66–12. doi:10.1007/s00190-020-01398-0

frontiers | Frontiers in Earth Science

TYPE Original Research
PUBLISHED 24 October 2022
DOI 10.3389/feart.2022.1025110

OPEN ACCESS

EDITED BY
Luan Thanh Pham,
VNU University of Science, Vietnam

REVIEWED BY
Huong Phan,
Hanoi University of Mining and Geology, Vietnam
Michela Giustiniani,
Istituto Nazionale di Oceanografia e di Geofisica Sperimentale, Italy
Tran Danh Hung,
Hanoi University of Mining and Geology, Vietnam

*CORRESPONDENCE
Seung-Goo Kang,
ksg9322@kopri.re.kr

SPECIALTY SECTION
This article was submitted to Earth and Planetary Materials, a section of the journal Frontiers in Earth Science

RECEIVED 22 August 2022
ACCEPTED 14 October 2022
PUBLISHED 24 October 2022

CITATION
Choi Y, Kang S-G, Jin YK, Hong JK, Shin S-R, Kim S and Choi Y (2022), Estimation of the gas hydrate saturation from multichannel seismic data on the western continental margin of the Chukchi Rise in the Arctic Ocean. *Front. Earth Sci.* 10:1025110. doi: 10.3389/feart.2022.1025110

Estimation of the gas hydrate saturation from multichannel seismic data on the western continental margin of the Chukchi Rise in the Arctic Ocean

Yeonjin Choi[1,2], Seung-Goo Kang[1]*, Young Keun Jin[1], Jong Kuk Hong[1], Sung-Ryul Shin[2], Sookwan Kim[3] and Youngil Choi[1]

[1]Division of Earth Sciences, Korea Polar Research Institute, Incheon, South Korea, [2]Department of Ocean Energy and Resource Engineering, Korea Maritime and Ocean University, Busan, South Korea, [3]Marine Active Fault Research Unit, Korea Institute of Ocean Science and Technology, Busan, South Korea

A multichannel seismic survey was conducted to investigate the geophysical characteristics of gas hydrates along the western continental margin of the Chukchi Rise around an ARAON mound cluster, which was first recovered in 2016. In the seismic data, gas hydrate-related bottom simulating reflection was widely distributed along the western continental margin of the Chukchi Rise. High-precision seismic P-wave velocity was obtained to investigate the geophysical characteristics of the gas hydrate structures in the BSR areas. Iterative migration velocity analysis was used to construct a detailed P-wave velocity model from the acquired seismic data. The gas hydrate and free gas layers have abnormally high- and low-seismic P-wave velocities; the precise velocity model allows us to understand the detailed spatial distribution of gas hydrate and free gas structures. The effective medium theory model enables estimations of the gas hydrate saturation from constructed seismic P-wave velocity model. We propose the P-wave velocity and gas hydrate saturation models from acquired multichannel seismic data in the western continental margin of the Chukchi Rise for the first time.

KEYWORDS

gas hydrates along the western continental margin of the chukchi rise in the arctic ocean, bottom simulating reflections (BSRs), seismic P-wave velocity model, iterative migration velocity analysis, estimation of gas hydrate saturation by the effective medium theory (EMT) model, characteristic of free gas-bearing sediment

1 Introduction

Gas hydrates are ice-like crystalline solids composed of natural gas and water molecules under low-temperature and high-pressure conditions, which are known as the gas hydrate stability zone (GHSZ) (Kvenvolden, 1988; Sloan and Koh, 2008). Since gas hydrates were first discovered in the 1970's, they have attracted attention as a potential energy source, a geological hazard, and a scientific issue related to climate change It has been reported that gas hydrates are distributed in the marine settings on the continental shelf and continental slope areas, which satisfy the gas hydrate stability conditions. In the Arctic regions, it is known that permafrost is closely related to the formation and distribution of gas hydrates. During the Pleistocene, cold temperature conditions were maintained beneath the Arctic permafrost region, and many gas hydrates were formed in this period (Collett et al., 2011). Nowadays, the relic gas hydrates remain under the Arctic permafrost regions (Kvenvolden, 1988; Kvenvolden et al., 1993; Kvenvolden, 1994; Collett et al., 2011; Ruppel, 2014; Chadburn et al., 2017; Kang et al., 2021b).

Geophysical techniques have been used to confirm the occurrence of gas hydrates, including well-logging analysis, seismic surveys, electromagnetic surveys, multibeam echo sounders, sub-bottom profilers, and side scan sonar (Sloan and Koh, 2008; Osadetz and Chen, 2010; Riedel et al., 2010; Tóth et al., 2014; Lu et al., 2017; Ruppel and Kessler, 2017; Singhroha et al., 2019; Kang et al., 2021a; Choi et al., 2021; Monteleone et al., 2022). Among these techniques, seismic surveys are widely used to confirm the occurrence of gas hydrates because the presence of gas hydrates brings about bottom simulating reflections (BSRs) in seismic data (Shipley and Houston, 1979; Yoo et al., 2013; Lu et al., 2017). BSRs are located in the seismic section at the base of the GHSZ, where the physical interface between gas hydrate-bearing sediments and free gas-saturated sediments has different seismic velocities and densities. A BSR has a reverse polarity reflector with high amplitude and shows a parallel trend to the seafloor topography (Yoo et al., 2013; Lu et al., 2017). However, a BSR may not appear in seismic data if there is an absence of free gas beneath the gas hydrate-bearing sediments or the seismic velocity of the sediment layer is higher than that of the gas hydrate-bearing sediments. The negative reflection coefficient of BSRs in seismic data is occurred due to a contrast between the upper high-velocity anomalies of gas hydrates and the lower low-velocity anomalies of the free gas layer. The seismic velocity is increased where gas hydrates exist in the pore space of the sediments because the seismic velocity of the pure gas hydrate is generally higher than that of the water-filled sediments. Conversely, the seismic velocity of the free gas-saturated sediments is decreased. Thus, the seismic velocity anomalies can be considered evidence of the presence of gas hydrates and free gas. The size of the anomalies in the velocity models is proportional to the volume of gas hydrates and free gas contained within the pore space. As a result, the velocity anomaly provides quantitative information regarding the gas hydrate and free gas saturation in the pore space of the sediments (Ecker et al., 2000; Riedel et al., 2010).

In the Arctic region, subsea permafrost-related gas hydrates are distributed at shallow water depths because the Arctic permafrost possesses temperature and pressure conditions in which gas hydrates can form in a relatively shallow continental shelf (Collett et al., 2011). Alaska/US and the Beaufort Sea continental shelf/Canada are regions where permafrost-related gas hydrates have been discovered (Dallimore et al., 2002; Carcione and Gei, 2004; Osadetz and Chen, 2010; Majorowicz et al., 2012; Riedel et al., 2017). The East Siberian Arctic Shelf is reportedly an area where a methane eruption was actively caused by permafrost and gas hydrate dissociation (Shakhova et al., 2010; Shakhova et al., 2017; Shakhova et al., 2019). Many studies have been conducted in this area, with a focus on the interaction between permafrost and gas hydrate dissociation, changes in the seabed environment, and the relationship to climate change (Shakhova et al., 2010; Shakhova et al., 2015; Shakhova et al., 2017). Additionally, various gas hydrate-bearing venting structures on the seafloor, such as gas flares, Pingo, and mud volcanoes, were observed in the Vestnesa Ridge in northwest Svalbard (Hustoft et al., 2009). In this area, gas hydrate-related studies are being conducted using state-of-the-art geophysical exploration technology (Hustoft et al., 2009; Singhroha et al., 2019). The seismic velocity and saturation models of the Vestnesa Ridge were proposed based on seismic data analysis. The distribution of gas hydrates, which were controlled by the topography and faults, was presented for the Vestnesa Ridge (Singhroha et al., 2019). However, the Chukchi Sea and East Siberian Sea regions remain unknown; no published gas hydrate-related research or information is available.

The Korea Polar Research Institute (KOPRI) has conducted geological and geophysical explorations in the East Siberian and Chukchi Seas continental margin regions to study changes in the Arctic seafloor environment and seafloor resources with the icebreaker research vessel ARAON in 2016 and 2018 (Jin and Party, 2017, 2018; Kim et al., 2020a; Kim et al., 2020b). In the first research cruise in 2016, mound morphologies were discovered in the western continental margin of the Chukchi Rise, and gas hydrate samples were obtained through gravity coring (Jin and Party, 2017). In the second cruise in 2018, intensive gas hydrate explorations, including sparker single channel seismic surveys, were conducted in the surrounding area of the mound structures (Jin and Party, 2018). As a result, a total of eight mound morphologies (ARAON mound) were discovered in the survey area, and the gas hydrate samples were obtained from two different mound morphologies. Additionally, the seismic data on 15 lateral lines were obtained, and heat flow and CTD (conductivity, temperature, and depth) profiles were acquired from five stations over the Chukchi Rise continental shelf area down to the continental margin. The single channel sparker seismic data showed that high-amplitude reflections with reversed polarity were widely distributed from the clustered mounds toward the continental margin and under the seafloor (Kang et al., 2021a). The depth of

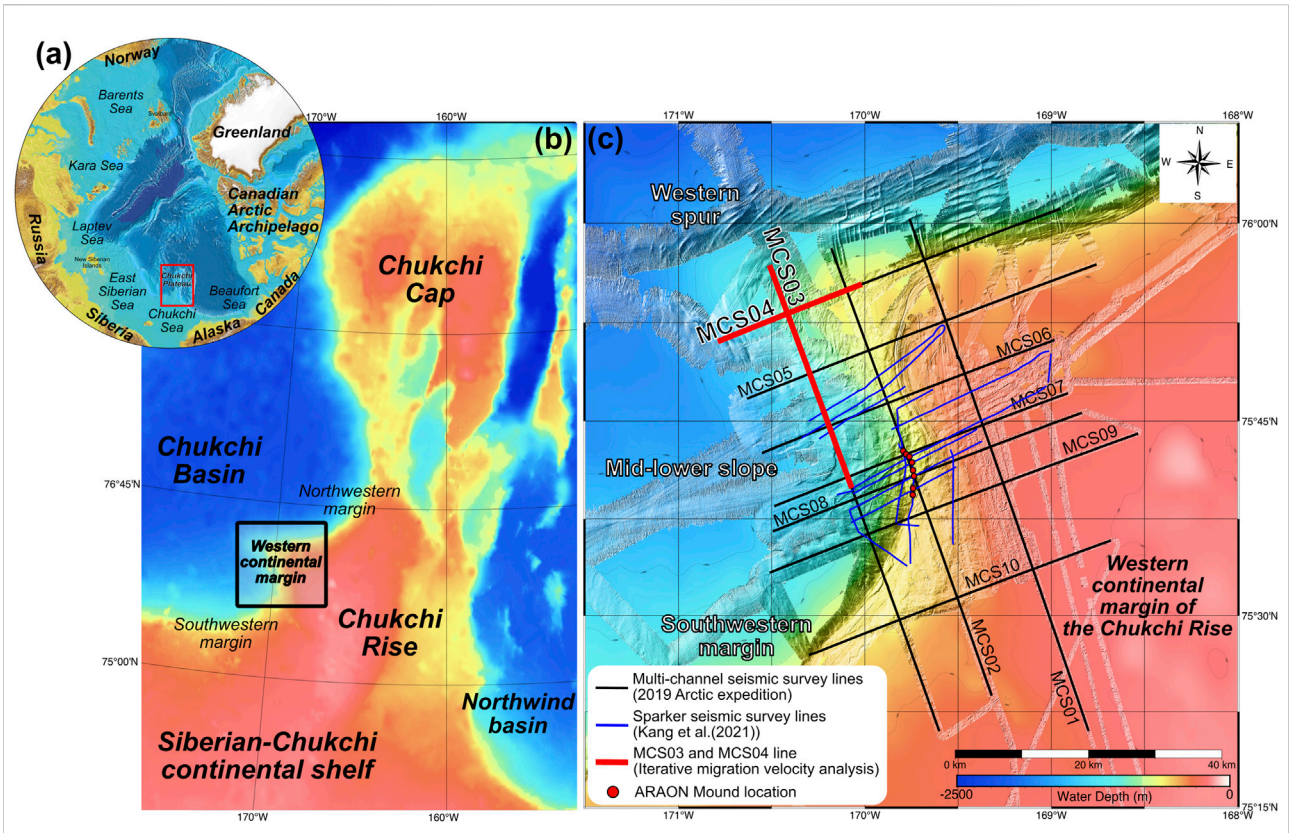

FIGURE 1
Map of the study area. **(A)** Bathymetric map of the Arctic Ocean. **(B)** is the map of the Chukchi Plateau, and the study area is located on the western continental margin of the Chukchi Rise (black box). **(C)** Map of the seismic track lines in the 2018 and 2019 Arctic expeditions.

the lower boundary of the GHSZ was calculated using the geothermal gradient and seafloor water temperature measurements obtained during the exploration and then compared with the depth at which strong reflective structures with reversed polarity have appeared in seismic images (Dickens and Quinby-Hunt, 1994; Miles, 1995; Andreassen et al., 2006). Gas hydrate-related BSRs were considered if the depth of the strong reflective structure with reversed polarity in the cross-section was the same as the calculated depth of the lower boundary of the GHSZ (Dickens and Quinby-Hunt, 1994; Miles, 1995; Andreassen et al., 2006). This case is the first in which geophysical evidence and distribution information have been presented regarding the occurrence of gas hydrates along the western continental margin of the Chukchi Rise (Kang et al., 2021a).

A multichannel seismic survey (MCS) was conducted during the third expedition in 2019 to investigate the geophysical characteristics of gas hydrates along the western continental margin of the Chukchi Rise around the ARAON mound cluster. In the MCS data, gas hydrate-related BSRs were widely distributed along the western continental margin of the Chukchi Rise. The acquired MCS data were applied to the iterative migration velocity analysis (IMVA) method to construct seismic P-wave velocity models to investigate the geophysical characteristics of the gas hydrate structures. By applying the IMVA method, we present the geophysical model of the gas hydrate and free gas in the western continental margin of the Chukchi Rise. The seismic velocity model recovered the high-velocity and low-velocity structures near a BSR. These velocity anomalies provide strong evidence that gas hydrates and free gas exist within the pore space of the sediments. Additionally, we employed the effective medium theory (EMT) in the seismic velocity model to derive the gas hydrate and free gas saturation model. In this model, the spatial distribution and characteristics of the gas hydrates and free gas are well represented. As a result of this study, we presented several geophysical evidence of the presence of gas hydrate in the western continental margin of the Chukchi rise.

2 Geological setting

Chukchi Rise is the southern part of the Chukchi Plateau, and the northern part of the Chukchi Rise is the Chukchi Cap of the Chukchi Plateau. On the southern side, the Chukchi Rise is directly connected to the Siberian-Chukchi continental shelf, and it is connected to the Chukchi Basin to the west, as shown in Figure 1A. The average depth of the Chukchi Rise is 0.2 km, and

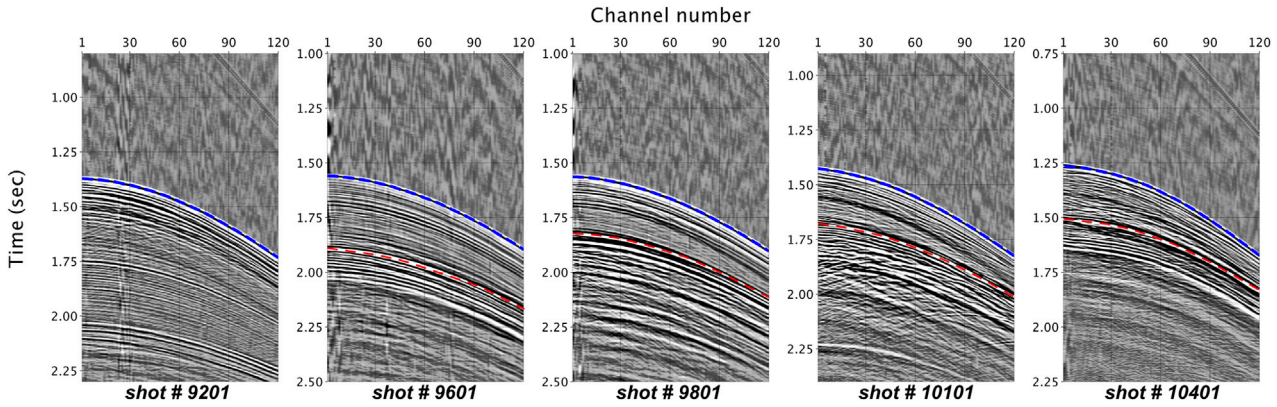

FIGURE 2
Raw shot-gathers on MCS03 lines. The blue dashed line is marked on the seafloor reflections, and the red dashed line is marked on the polarity-reversed reflections.

it has a relatively flat top (Kim et al., 2021). The study area is the western continental margin of the Chukchi Rise (black box in Figure 1B), where the water depth ranges from 0.5 km (shelf break) to 2.5 km (Chukchi Basin). In the center of the study area, a triangular-shaped highland, named the western spur, protrudes 20 km toward the Chukchi Basin (Kim et al., 2021). Hegewald and Jokat (2013) interpreted the seismic section obtained from the Chukchi Rise to the Chukchi Basin and classified three stratigraphic horizons (Base Tertiary, Top Oligocene, and Top Miocene). The average thickness of the sedimentary layer of the Chukchi Rise is 0.6 km, and it was confirmed that many normal faults have developed from the acoustic basement to the seafloor. Additionally, the average velocity of the upper sedimentary layer of the acoustic basement was suggested to be 2.3 km/s based on sonar buoy data (Hegewald and Jokat, 2013). The other study was suggested that the P-wave velocity of the upper sedimentary layer of the Chukchi Plateaus was 1.7 km/s and the P-wave velocity of the lower sedimentary layer was 3.8–4.0 km/s using the wide-angle multichannel seismic reflection survey (Kashubin et al., 2018).

3 Data

The MCS data acquired in 2019 were used to identify the geophysical characteristics of the gas hydrates in the western continental margin of the Chukchi Rise (Jin and Party, 2019). The seismic source comprised two GI-gun with a total volume of 710 cubic inches, and the receiver comprised a 120-channel solid-type streamer. The shot and group spacings were 25.0 m and 12.5 m, respectively. The recording time was 7.0 s, and the sampling interval was 0.001 s. Figure 1C shows the map of survey tracks for the MCS data. Our survey area is the western continental margin of the Chukchi Rise, as shown in the black box in Figure 1B. Ten survey lines (marked with the solid black lines in Figure 1C) were acquired around the ARAON mound cluster area (marked with the red circles in Figure 1C), where the gas hydrate samples were recovered by gravity coring in 2016 and 2018 (Jin and Party, 2017, 2018). The total length of the seismic survey tracks was 617.49 km.

Figure 2 shows the seismic shot gathers extracted from the MCS03 line containing the BSR. The seafloor reflections appeared at 1.3–1.6 s (blue dashed line), and polarity-reversed reflections (red dashed line), which are assumed to be a BSR, can be found below the seafloor reflection in the presented seismic shot-gathers.

In this study, we select two seismic tracks (MCS03 and MCS04, marked with the solid-red lines in Figure 1C) to construct the precise seismic P-wave velocity model by IMVA and estimate the gas hydrate and saturation model.

4 Materials and methods

4.1 Data processing and iterative migration velocity analysis

Seismic data processing, including the iterative migration velocity analysis (IMVA), was performed on the raw seismic data obtained from the above-mentioned geophysical survey. First, the raw seismic data was needed to check the survey geometry and add missing information or corrections (Yilmaz, 2001). Additionally, the seismic data applied several data processing algorithms in the prestack step, such as the Butterworth low-frequency filtering, static correction, spherical divergence correction, and deconvolution techniques, to improve the data quality, certainty, and signal-to-noise (S/N) ratio. After the prestack data processing step, the seismic data (preprocessed

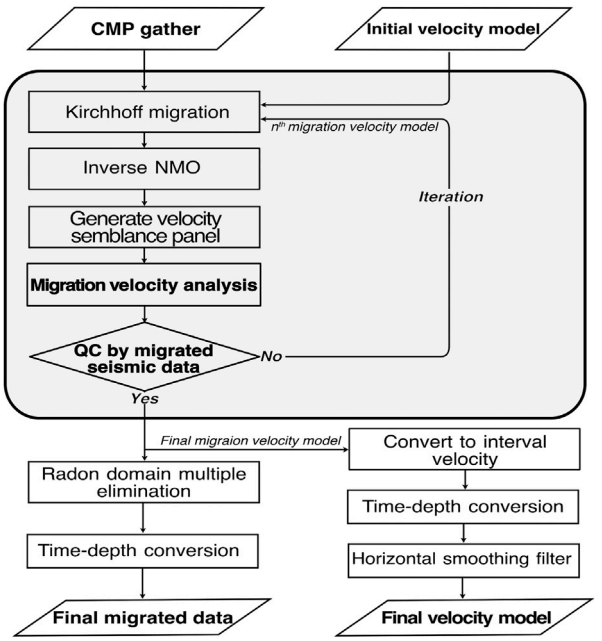

FIGURE 3
Detailed workflow of the iterative migration velocity analysis to construct the seismic velocity model.

and CMP sorted) were applied to the first velocity analysis to generate the initial seismic velocity model for the next IMVA step and multiple attenuations.

We used the IMVA method to construct an accurate P-wave velocity model to confirm the spatial distribution of the gas hydrate and estimate the gas hydrate saturation. The IMVA method was operated by the Iterative Velocity Analysis module in the Omega2 seismic data processing platform by Schlumberger. Figure 3 illustrates the detailed IMVA workflow. The first step of the IMVA is a Kirchhoff migration for preprocessed seismic data (CMP sorted) based on an initial seismic P-wave velocity model. The migrated seismic data were applied to the inverse NMO procedure to generate a semblance panel for the migration velocity analysis. The velocity model was constructed by migration velocity analysis for the first iteration. Then it was used for the initial velocity of the Kirchhoff migration in the second iteration of the IMVA.

The final migration velocity model constructed from sufficient iterative steps was evaluated by a quality control procedure based on analysis of the NMO correlated gathers and migrated seismic data. The iteration number of the IMVA is five for each seismic track. The P-wave velocity model from IMVA, constructed in the last iteration step, was used to build the final migrate seismic image. The final velocity model was converted from RMS to interval velocity using Dix's equation. Then, time-to-depth conversion was applied to confirm the spatial distribution of gas hydrates at each depth in the survey area. In Figure 4, we present the seismic semblance panels for IMVA with NMOed seismic data. Figure 4A shows the seismic semblance panel and NMOed seismic data for the survey area without BSR, which is the typical subsea sediment environment. Figure 4B illustrates the seismic panel and NMOed seismic data for the survey area with a BSR, where free gas and gas hydrates exist. In the seismic semblance panels, the solid black line represents the RMS velocity profile, and the solid white line represents the estimated interval velocity profile. Generally, the seismic velocity of gas hydrates is higher than that of water-filled sediment. Therefore, the seismic velocity profile on the seismic panel shows a trend of a rapid increase in the hydrate layer compared to the typical sediment layer. A free gas layer exists below the gas hydrate layer, and the seismic velocity in the free gas layer shows a rapidly decreasing trend because the seismic velocity of free gas is very slow. The estimated interval (P-wave) velocity for the seafloor is 1.45 km/s; the gas hydrate layer velocity is 1.8 km/s, and that of free gas is 0.8 km/s.

The accuracy and resolution of the velocity model derived from a semblance-based velocity analysis are affected by several factors, including the streamer length, stacking fold, signal-to-noise ratio, and the main frequencies (Yilmaz, 2001). Assuming that the velocity analysis error in this study is approximately ±15 m/s of the RMS velocity based on the width of the velocity semblance spectrum. This RMS velocity error causes an error of 0.15 km/s in the interval velocity, which implies an inaccuracy of up to 10%, assuming a sediment velocity of around 1.5 km/s (Hajnal and Sereda, 1981; Tóth et al., 2014). Considering that an acceptable RMS velocity error is 2%–10% in general (Yilmaz, 2001), this study's velocity errors are considered reliable.

4.2 Estimation of the gas hydrate saturation

In a rock physics model, there is a quantitative relationship theory between the elastic properties (P-wave velocity, S-wave velocity, density) and physical properties (porosity, clay volume, lithology, fluid material within the pore, and fluid saturation) of the rock. This method is mostly used in oil and gas reservoir characterization for petrophysical analysis. Nevertheless, many rock physics models, such as the weighted equation, three-phase biot equation, EMT, and SCA-DEM model, have been used to quantify gas hydrate resources (Lee et al., 1996; Jakobsen et al., 2000; Lee, 2002; Chand et al., 2004). In this paper, we applied the EMT model to estimate the gas hydrates saturation from a seismic velocity model. The EMT model is a theoretical or numerical theory used to analyze the properties of an effective medium composed of several constituent materials. The EMT model was proposed by Dvorkin et al. (1999); it is assumed to be the unconsolidated marine sediments with high porosity (0.36–0.4). In addition, Ecker et al. (2000) estimated the gas

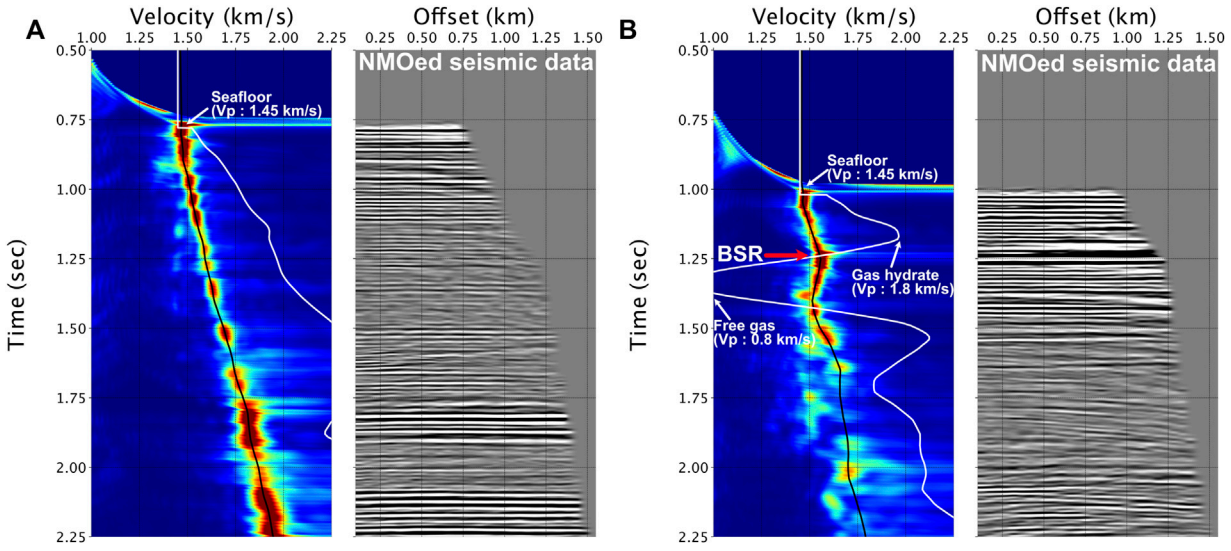

FIGURE 4
Velocity semblance panel (left) and NMO-corrected seismic data (right) for the iterative migration velocity analysis. **(A)** is the area without a BSR, and **(B)** is the area with a BSR.

hydrate saturation by applying the EMT model to the gas hydrate-rich sedimentary layer for the first time. Also, several additional cases have been reported that used the EMT model to verify the gas hydrate saturation in various regions (Ghosh et al., 2010; Chhun et al., 2018; Pan et al., 2019). In this method, the elastic modulus of the gas hydrate-bearing sediments is related to mineralogy, effective pressure, porosity, and characteristics of the fluid material within the pore space.

4.2.1 Effective medium theory model of water-filled sediments without gas hydrates

In water-filled sediments, the bulk and shear moduli of the dry frame of sediments are expressed by the Hashin-Shtrikman-Hertz–Mindlin theory as follows:

1) $\varnothing < \varnothing_c$

$$K_{dry} = \left[\frac{\phi/\phi_c}{K_{HM} + \frac{4}{3}G_{HM}} + \frac{1 - \phi/\phi_c}{K + \frac{4}{3}G_{HM}} \right]^{-1} - \frac{4}{3}G_{HM} \quad (1)$$

$$K_{dry} = \left[\frac{\phi/\phi_c}{K_{HM} + \frac{4}{3}G_{HM}} + \frac{1 - \phi/\phi_c}{K + \frac{4}{3}G_{HM}} \right]^{-1} - \frac{4}{3}G_{HM} \quad (2)$$

2) $\varnothing > \varnothing_c$

$$K_{dry} = \left[\frac{(1-\phi)/(\phi_c)}{K_{HM} + \frac{4}{3}G_{HM}} + \frac{(\phi - \phi_c)/(1-\phi_c)}{K + \frac{4}{3}G_{HM}} \right]^{-1} - \frac{4}{3}G_{HM} \quad (3)$$

$$G_{dry} = \left[\frac{(1-\phi)/(1-\phi_c)}{G_{HM} + Z} + \frac{(\phi - \phi_c)/(1-\phi_c)}{G + Z} \right]^{-1} - Z \quad (4)$$

$$Z = \frac{G_{HM}}{6}\left[\frac{9K_{HM} + 8G_{HM}}{K_{HM} + 2G_{HM}} \right] \quad (5)$$

where $\varnothing$ is the porosity and $\varnothing_c$ is the critical porosity. The critical porosity has a range of 0.36–0.4, according to Nur et al. (1998), and we used a value of 0.4. K_{HM} and G_{HM} are calculated from Hertz–Mindlin theory as follows:

$$K_{HM} = \left[\frac{G^2 n^2 (1 - \varnothing_c)^2}{18\pi^2 (1 - \upsilon)^2} P \right]^{1/3} \quad (6)$$

$$G_{HM} = \frac{5 - 4\upsilon}{10 - 5\upsilon}\left[\frac{3G^2 n^2 (1 - \varnothing_c)^2}{2\pi^2 (1 - \upsilon)^2} P \right]^{1/3} \quad (7)$$

where υ is Poisson's ratio, and n is the average number of contacts per grain (generally 8.5). P is the effective pressure, followed by

$$P = (\rho_b - \rho_f) g D \quad (8)$$

where g is gravity accretion and D is depth below the seafloor. Finally, the bulk and shear moduli of water-filled sediment is expressed by the Gassmann equation as follows:

$$K_{sat} = K_s \frac{\phi K_{dry} - (1 + \phi) K_f K_{dry} / K_s + K_f}{(1 - \phi) K_f + \phi K - K_f K_{dry} / K_s} \quad (9)$$

$$G_{sat} = G_{dry} \quad (10)$$

where K_s and G_s are the bulk and shear moduli of the solid phase, respectively. The solid phase represents the minerals that comprise the sediments. The bulk and shear moduli of the solid phase can be calculated as follows:

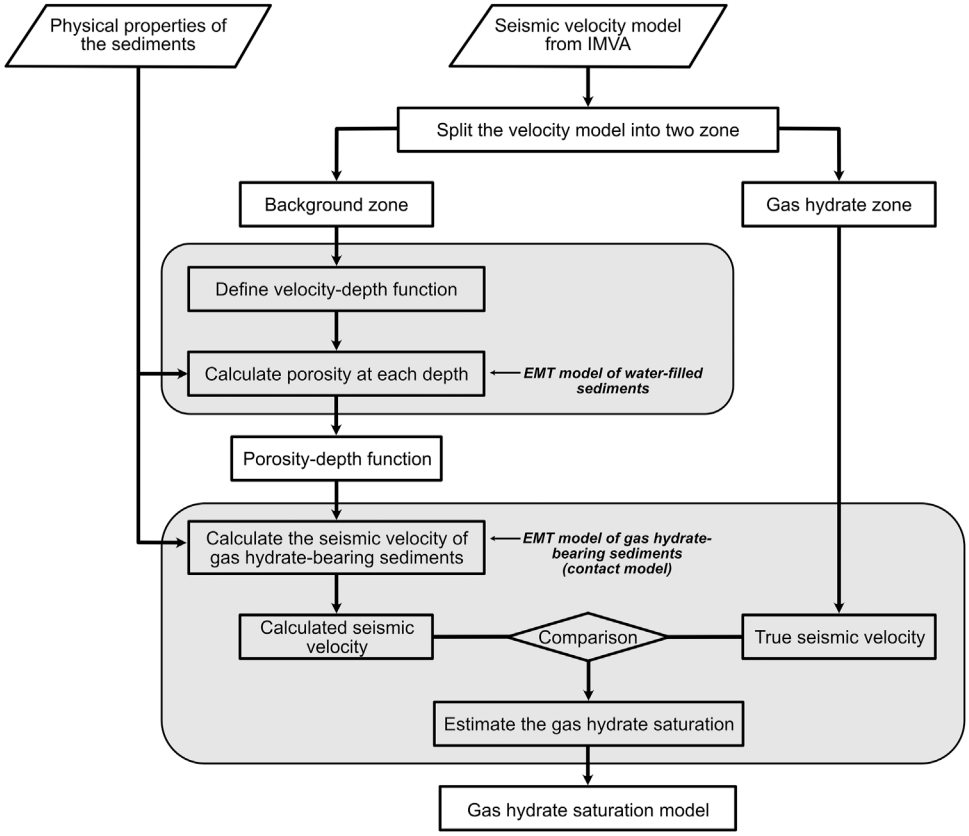

FIGURE 5
Detailed workflow to estimate the gas hydrate saturation model using the EMT model.

TABLE 1 Elastic modulus and density of sediment.

Material	Bulk modulus (K, GPa)	Shear modulus (G, GPa)	Density (ρ, g/cm^3)
Sediment (67.6% Quartz + 16.8% Plagioclases + 3.2% K-feldspars + 12.4% Aggregates)	44.76	37.10	2.650
Gas hydrates	5.60	2.40	0.767
Water	2.58	—	1.036
Methane	0.125	—	0.250

$$K_s = \frac{1}{2}\left[\sum_{i=1}^{m} f_i K_i + \left(\sum_{i=1}^{m} \frac{f_i}{K_i}\right)^{-1}\right] \quad (11)$$

$$G_s = \frac{1}{2}\left[\sum_{i=1}^{m} f_i G_i + \left(\sum_{i=1}^{m} \frac{f_i}{G_i}\right)^{-1}\right] \quad (12)$$

$$\rho_s = \sum_{i=1}^{m} f_i \rho_i \quad (13)$$

where F_i is the volume ratio of each mineral consisting of the solid phase and K_i and G_i are the bulk and shear moduli of each mineral, respectively. Substring i means the index of each mineral, and m is the total number of minerals. K_f is the bulk modulus of the fluid phase, which means the pore-filled material. In water-filled sediments, K_f is the same as K_w (bulk modulus of water).

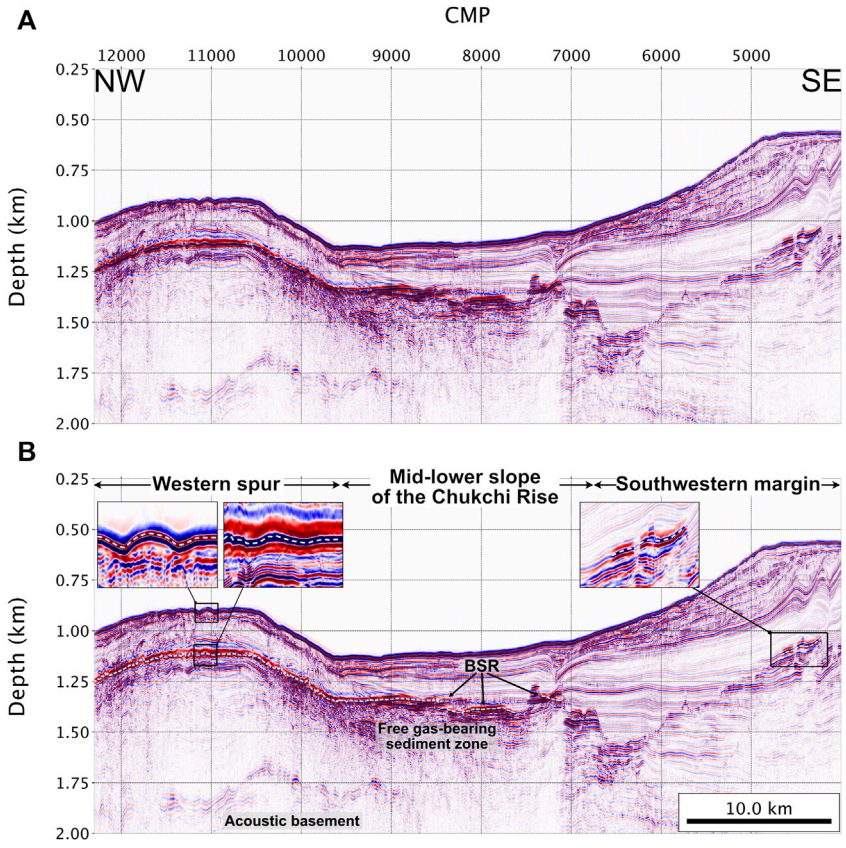

FIGURE 6
(A) Uninterpreted and **(B)** interpreted migrated seismic images obtained from the MCS03 line.

4.2.2 Contact model

Ecker et al. (2000) introduced two different types of EMT models based on the sediment abundance type of gas hydrates. The contact model represents the gas hydrates that are in contact with or surrounding the mineral grains; thus, the gas hydrates are part of the solid phase. Therefore, the reduced porosity is obtained as follows:

$$\phi_r = \phi S_w = \varnothing (1 - S_h) \tag{14}$$

where ϕ_r is the reduced porosity from gas hydrates and S_h is the gas hydrate saturation. The bulk and shear moduli of the solid phase of the contact model is modified as follows:

$$K_s = \frac{1}{2}\left[f_h K_h + (1 - f_h) K_s + \left(\frac{f_h}{K_h} + \frac{1 - f_h}{K_s} \right)^{-1} \right] \tag{15}$$

$$G_s = \frac{1}{2}\left[f_h G_h + (1 - f_h) G_s + \left(\frac{f_h}{G_h} + \frac{1 - f_h}{G_s} \right)^{-1} \right] \tag{16}$$

where K_s and G_s on the right side are the elastic modulus of the mineral material computed by Eqs 11, 12, and K_h and G_h are the bulk and shear moduli of gas hydrates, respectively. F_h is the volume ratio of gas hydrates within the solid phase.

4.2.3 Noncontact model

The other model introduced by Ecker et al. (2000) is the noncontact model, in which gas hydrates are floating in the pore-filling material. Therefore, gas hydrates are not in contact with the mineral grains, so they do not affect the solid phase. Hence, the bulk and shear moduli of the solid phase are not changed, and only the bulk modulus of the fluid phase is modified as follows:

$$K_f = \left[\frac{1 - S_h}{K_w} + \frac{S_h}{K_h} \right]^{-1} \tag{17}$$

The modified bulk modulus of the fluid phase is replaced by K_f in Eq. 9.

Finally, the P-wave (V_p) and S-wave (V_s) velocities of the saturated sediments are expressed as follows:

$$V_p = \sqrt{\frac{K_{sat} + 4/3 G_{sat}}{\rho_b}} \tag{18}$$

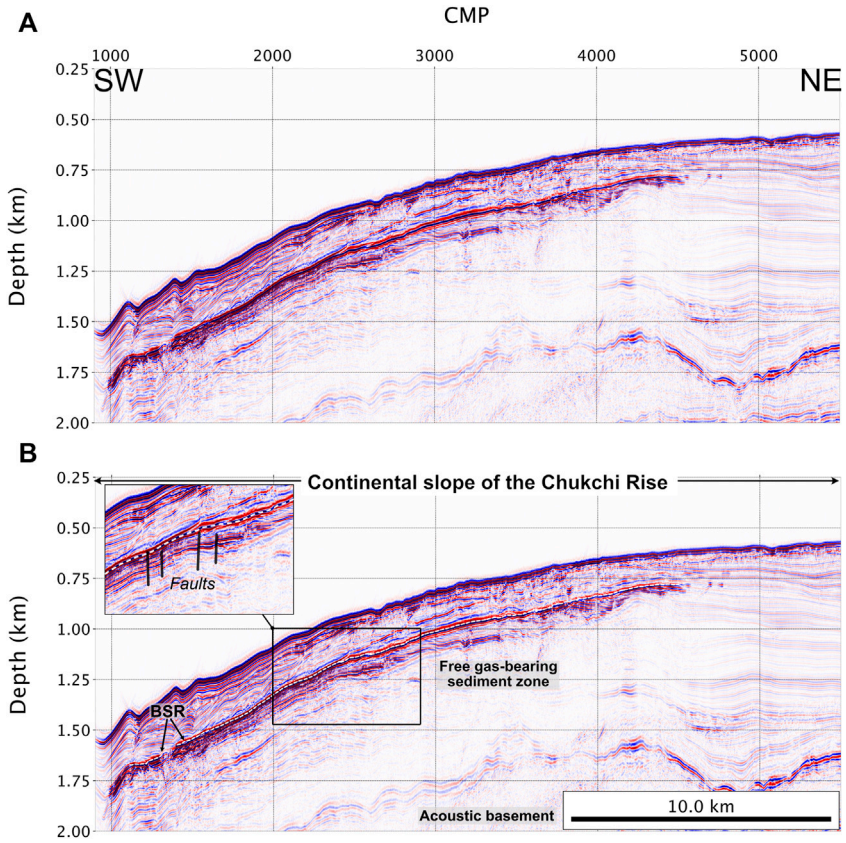

FIGURE 7
(A) Uninterpreted and **(B)** interpreted migrated seismic images obtained from the MCS04 line.

$$V_s = \sqrt{\frac{G_{sat}}{\rho_b}} \tag{19}$$

Figure 5 illustrates the workflow used to estimate the gas hydrate saturation. This workflow is based on the methods described in Ghosh et al. (2010). The seismic velocity model from IMVA and the physical properties of sediment were used as input parameters in this workflow. The physical properties of sediments include the volume ratio, the elastic modulus of the minerals within the sediment, and the elastic modulus of the water, gas hydrates, and free gas. Table 1 shows the values of the elastic modulus in this study. Due to the absence of physical property information for the sediments in this area, the bulk and shear moduli of the sediments were computed using constituent mineral information from the southern margin of the Siberian-Chukchi shelf, as investigated by Kolesnik et al. (2019).

The seismic velocity model from IMVA was split into two zones: the background zone and the gas hydrate zone. The background zone means the water-filled sediment, in which pore space is filled with water without gas hydrate and free gas. The gas hydrate zone is the area where gas hydrates are present. In this study, the background zone for estimating the gas hydrate saturation in the EMT model was determined to be along the MCS03 line between CMP#6501 and CMP#7000 (Figure 6), and the gas hydrate zone was selected as the area where a BSR exists (Figures 6, 7)This workflow was started to define the velocity-depth function using linear regression from the velocity profile extracted from the background zone. Then, the porosity–depth function was calculated from the velocity-depth function using the EMT model of the water-filled sediments Eqs. 1–13. In this step, several assumptions were included. First, the background zone is fully saturated water within the pore space. Second, the mineralogical properties were similar throughout the study area. The porosity–depth function derived from the background zone is also used for the gas hydrate zone in this assumption.

In the second step, shown in the red box in Figure 5, we calculated the seismic velocity of the gas hydrate-bearing sediments using the EMT model of gas hydrate-bearing sediments, which is the contact model (Eqs 14–16). The

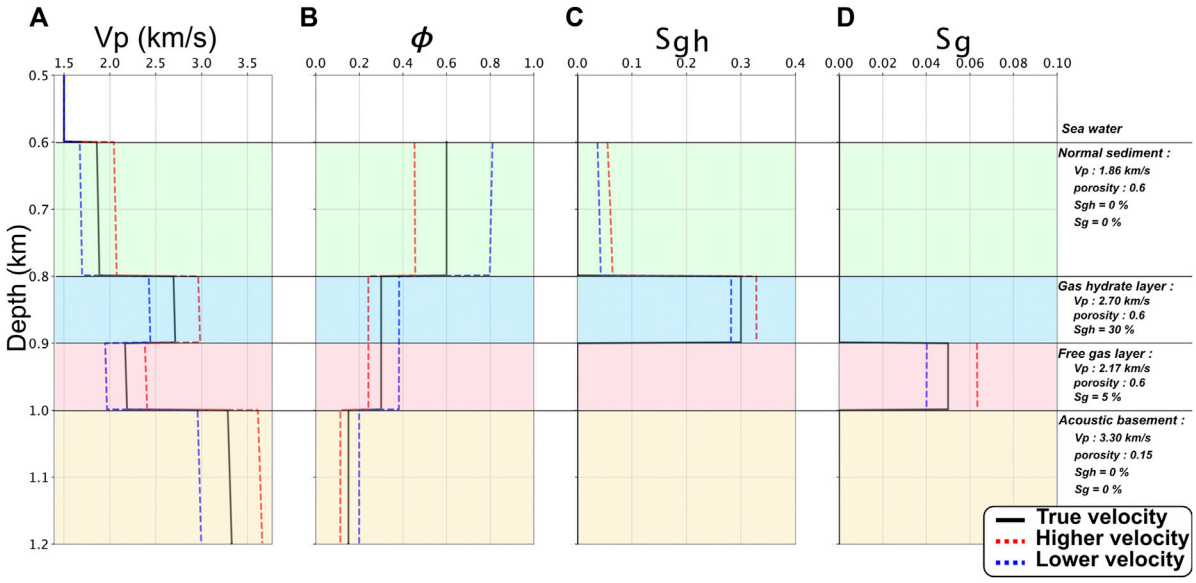

FIGURE 8
The results of the quantified error analysis **(A)** 4-layer velocity profiles **(B)** calculated porosity-depth profiles **(C)** estimated gas hydrate saturation profiles, and **(D)** estimated free gas saturation profiles. The black solid line is the true velocity. The dashed line is the 10% higher (red) and 10% lower (blue) velocity than the true velocity.

precalculated porosity–depth function and the physical properties of sediments were used as input parameters. Then, the gas hydrate saturation model can be constructed by comparing the calculated seismic velocity with the true velocity extracted from the gas hydrate zone. The free gas saturation can be estimated using the same method; however, the noncontact model (Eq. 17) is applied instead of the contact model.

4.3 Quantified error analysis related to the estimation of gas hydrate saturation by the effective medium theory model

This study used the EMT model to estimate the gas hydrate and free gas saturation from seismic velocity. This method only used seismic P-wave velocity and assumed that the other factors were the same in all areas. Therefore, we will obtain inaccurate results when we use the incorrect velocity to estimate the gas hydrate saturation. Therefore, the incorrect velocity caused inaccuracy in the estimated gas hydrate saturation.

The quantitative error analysis was conducted using the numerical test using a simple 4-layer velocity model comprised of a sediments layer near the seafloor, gas hydrate, free gas, and an acoustic basement, as shown in Figure 8. Figure 8A shows the 4-layer velocity profiles for the numerical test. The solid black line represents the true velocity profile, whereas the dashed line represents the incorrect velocity profile when+/-10% velocity errors occur. The Red dashed line shows a 10% higher velocity profile than the true velocity, while the blue dashed line shows a 10% lower velocity profile than the true velocity. Figure 8B demonstrates the porosity profile derived when+/-10% velocity errors occur. As a result, the error in porosity was 20% caused by the+/-10% inaccurate velocity. Figures 8C,D represent the estimated gas hydrate and free gas saturation profile when+/-10% velocity errors occur. The inaccuracy of the results was 9% for gas hydrate saturation and 20%–26% for free gas saturation, respectively. We note that when an erroneous velocity is used, the EMT model's estimated gas hydrate and free gas saturations are inaccurate, and the result of free gas saturation is more sensitive to inaccurate velocity than the result of the gas hydrate saturation.

In our IMVA methods, we determined that the velocity model contained a maximum of 10% of the inaccuracy of the interval velocity (see Section 4.1). Therefore, according to the quantified error analysis, saturation models can expect an inaccuracy of 9% for gas hydrate saturation and 20%–26% for free gas saturation, respectively.

5 Results

5.1 Final migrated seismic images

To identify the geophysical characteristics of the gas hydrate along the western continental margin of the Chukchi Rise, we

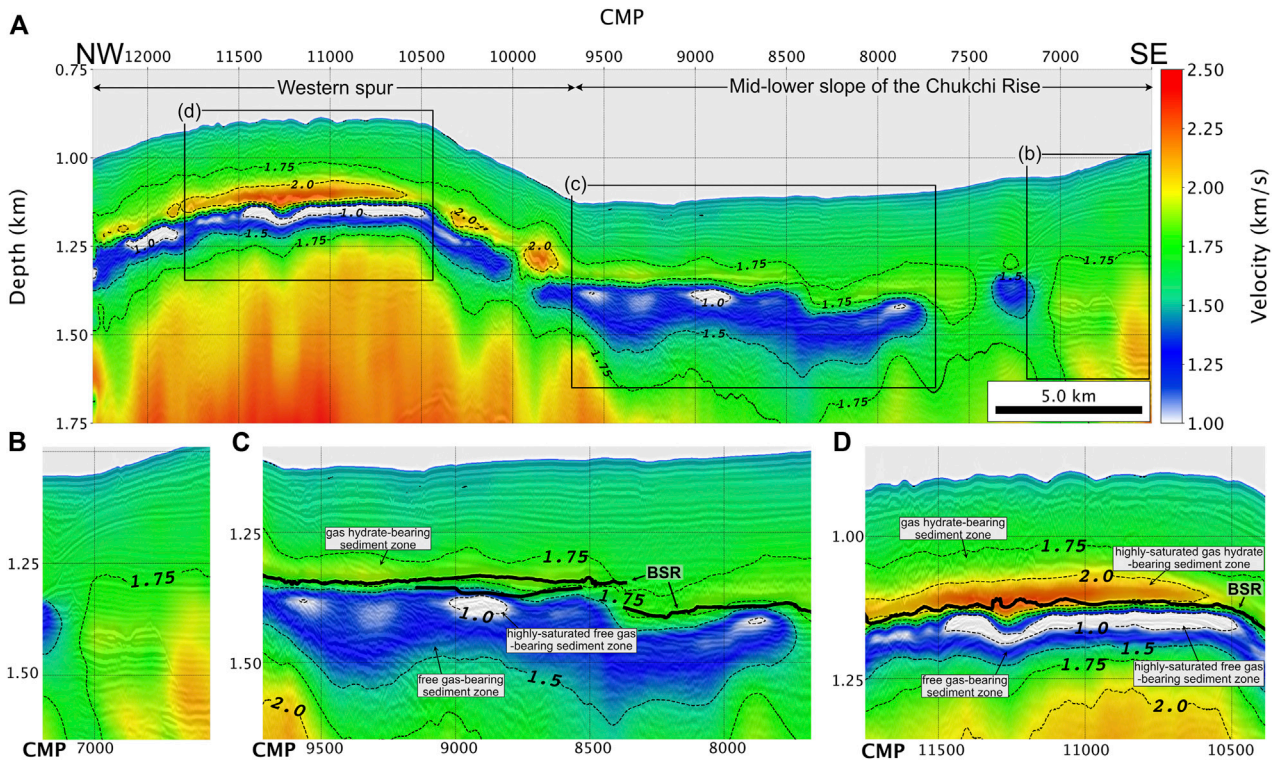

FIGURE 9
(A) Constructed P-wave velocity model overlaid with migrated seismic images using the IMVA of the MCS03 line. The analysis range is marked on the solid red line in Figure 1C. **(B)**–**(D)** is the enlarged velocity model: **(B)** absence area of the gas hydrate, **(C)** mid-lower slope of the western continental margin, and **(D)** crest of the western spur area.

applied seismic data processing, including static and spherical divergence correction, noise attenuation, deconvolution, IMVA, and migration. As a result, an interpretable P-wave velocity model and final seismic section (migrated), which confirm the geological structures below the seafloor, were successfully constructed from the acquired multichannel seismic data. The migrated seismic images for seismic tracks MCS03 and MCS04, as shown in Figures 6, 7, present the information on the sediment and subsea geological structures and BSR, which is parallel to the seafloor with a reversed polarity, strong amplitude, and cross-cutting of the strata.

Figure 6 shows the migrated seismic image for the MCS03 line, which was obtained from the southwestern margin to the western spur through the mid-lower slope of the western continental margin of the Chukchi Rise. Figure 6A is the final migrated seismic image of the MCS03 line, and Figure 6B is the same as the final migrated seismic image of the MCS03 line, including the descriptions and interpretations related to gas hydrates and free gas. The migrated seismic image describes the typical continuous BSR between CMP#7150 and CMP#12300 (Shedd et al., 2012). The length of the continuous BSR is 32.18 km horizontally, and the depth is 1.3 km at the mid-lower slope of the western continental margin of the Chukchi Rise and 1.1 km at the western spur. The high-amplitude dipping reflection is shown beneath the BSR (Figure 6B). Similar to several previous studies, our results also imply that free gas exists in the pore space of the sediments (White, 1979; Lin et al., 2009; Yoo et al., 2013). At the southwestern margin, a continuous BSR was not present, but it showed a partial high-amplitude reflection on the migrated seismic images, which can be considered to be a gas-charged layer (Figure 6B).

Figure 7 shows the migrated seismic image for the MCS04 line, which was acquired along the continental slope of the western spur. Figure 7A is the final migrated seismic image of the MCS04 line, and Figure 7B is the same as the final migrated seismic image of the MCS04 line, including the descriptions and interpretations related to gas hydrates and free gas. The CMP#2800 on the MCS04 line intersects the CMP#11050 on the MCS03, and the two migrated seismic images represent a similar BSR characterization. Similar to the results of Shedd et al. (2012), the MCS04 migration images revealed a well-developed, continuous BSR along the slope of the western spur. The length of the continuous BSR is 21.25 km, and it extends from the shallow

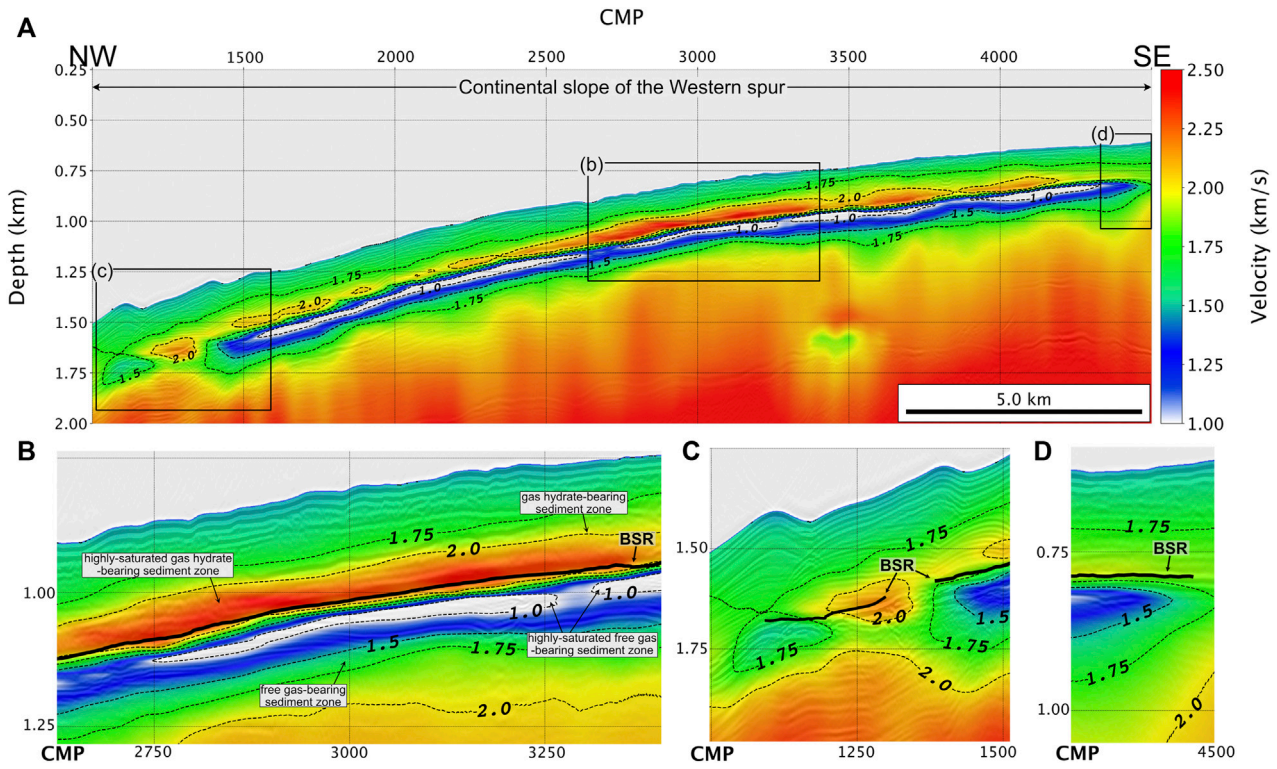

FIGURE 10
(A) Constructed P-wave velocity model overlaid with migrated seismic images using the IMVA of the MCS04 line. The analysis range is marked on the solid red line in Figure 1C. **(B)**–**(D)** Enlarged velocity model: **(B)** continental slope of the western spur, **(C)** deepest area showing the BSR of the western spur, and **(D)** shallower area showing the BSR of the western spur.

part of the western spur to the deeper part. The shallowest water depth that appeared in the BSR is 0.6 km, and the BSR depth is 0.78 km (Figure 7B). The deepest water depth that appeared in the BSR is 1.25 km. Several faults developed from CMP#2000 to CMP#3000, which are expected to play a key role in the methane migration pathway.

The gas hydrate-related BSR at the western continental margin of the Chukchi Rise was confirmed by migrated seismic images. Our results imply that gas hydrates are widely distributed throughout the study area because gas hydrate-related BSR considers the geophysical evidence of the presence of the gas hydrate.

5.2 P-wave velocity models constructed by the iterative migration velocity analysis method

We used the IMVA method to construct an interpretable P-wave velocity model from the seismic data. A constructed P-wave velocity model was used to understand the spatial distribution of the gas hydrate and free gas layers near the BSR in each survey area. The P-wave velocity models of the MCS03 and MCS04 lines are presented with the velocity contours in Figures 9, 10, respectively. The P-wave velocity models constructed by the IMVA method contain high-velocity anomalies (1.9–2.5 km/s) above the BSR and low-velocity anomalies (1.0–1.5 km/s) below the BSR.

Figure 9 presents the images overlaid on the seismic velocity model with the migrated seismic images for the MCS03 lines. Figure 9A is the seismic velocity model for the entire MCS03 line. The velocity model between CMP#6500 and CMP#7200 is considered a background velocity zone, where the BSR did not appear. This background velocity zone shows the linear trend of increasing velocity with respect to depth without any velocity anomalies (Figure 9B). Between the CMP#7700 and CMP#9950 areas in the velocity model (Figure 9C), which contains the continuous BSR in the migrated seismic images, high- and low-velocity zones were constructed near the BSR. The area between CMP#10450 and CMP#11775 in the velocity model also contains the continuous BSR with the high- and low-velocity zones, as shown in Figure 9D.

The low-velocity anomaly suggests the presence of free gas. In the P-wave velocity model between CMP#7700 and

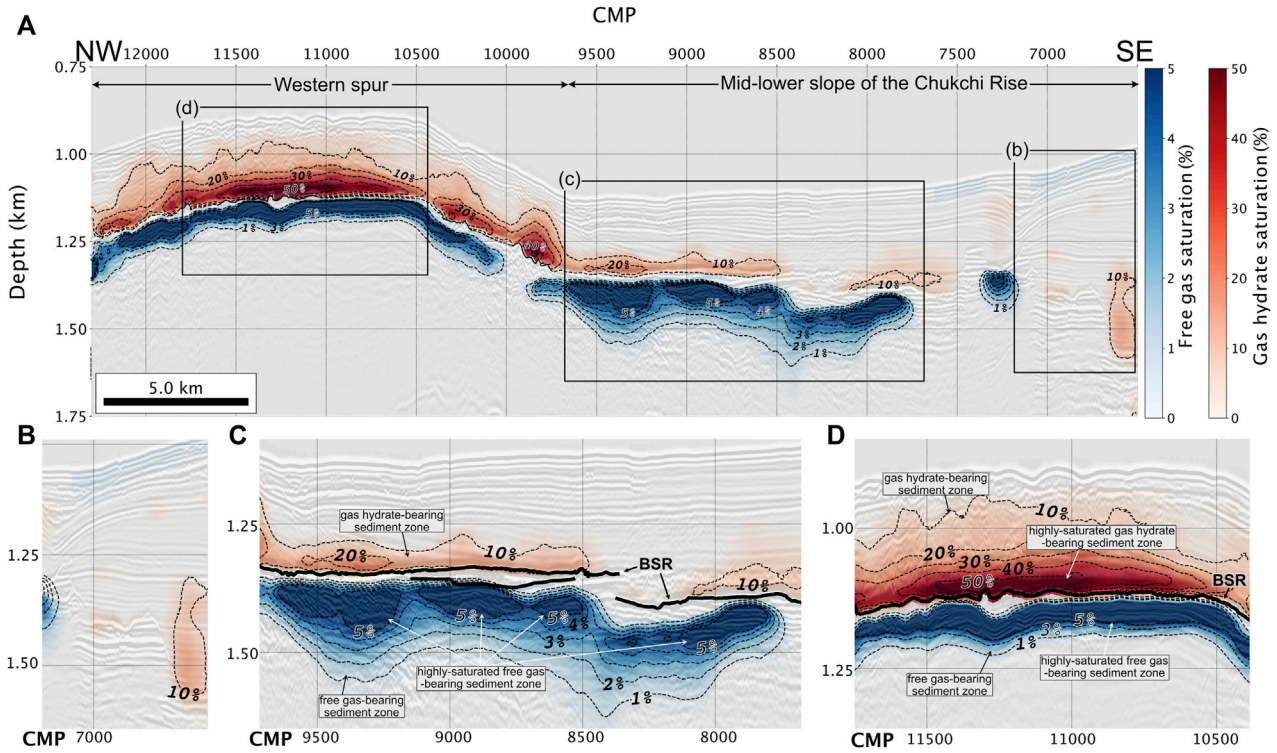

FIGURE 11
(A) Estimated gas hydrate and free gas saturation model overlaid with migrated seismic images using the IMVA of the MCS03 line. The analysis range is marked on the solid red line in Figure 1C. **(B)**–**(D)** is the enlarged velocity model: **(B)** absence area of the gas hydrate, **(C)** mid-lower slope of the western continental margin, and **(D)** crest of the western spur area.

CMP#9950, a thick low-velocity zone was identified in the mid-lower slope, as shown in Figure 9C. The low-velocity zone has a width of 12.5 km, a maximum thickness of 0.25 km, and a velocity range of 1.0–1.5 km/s. In the P-wave velocity model between CMP#8800 and CMP#9000, the lowest velocity below 1.0 km/s was observed, shown in Figure 9D. We note that the highly saturated free gas-bearing sediments exist along the crest of the western spur.

The high-velocity anomalies with a velocity range of 1.7–1.8 km/s, indicating a gas hydrate-bearing sediment zone, appeared above the BSR in the western spur (Figure 9D). The velocity anomalies in the western spur area are more noticeable than those in the mid-lower slope. The highest velocity (>2.0 km/s) and lowest velocity (<1.0 km/s) in this model are distributed on the ridge of the western spur. Notably, the western spur contains more gas hydrates and free gas than the mid-lower slope. On the other hand, the thickness of the low-velocity zone in the western spur is 0.05 km, confirming that the mid-lower slope has a thicker low-velocity zone than the western spur.

Figure 10 presents the images overlaid on the P-wave velocity model with the migrated seismic images for the MCS04 lines. Figure 10A shows the entire P-wave velocity model, which covers the slope side of the western spur, with 0.7–1.5 km of water depth. High-velocity anomalies (velocity ranges are 1.75–2.25 km/s) were discovered above the BSR. The highest velocity structures (P-wave velocity over 2.25 km/s) are distributed between CMP#2650 and CMP#3400, as shown in Figure 10B. Low-velocity anomalies (P-wave velocity ranges 0.5–1.75 km/s) were discovered from CMP#1450 to CMP#4450 beneath the BSR. The thickness of this low-velocity structure averages 0.125 km.

In our P-wave velocity model obtained by the IMVA method, the high-and low-velocity anomalies caused by gas hydrate and free gas are well represented. Because the velocity anomalies suggest the presence of gas hydrate and free gas within the pore space of the sediments, these results provide additional evidence that gas hydrate exists in the study area.

5.3 Gas hydrate saturation estimated by the Effective medium theory model

We used the EMT model to construct gas hydrate saturation models from the seismic P-wave velocity model of the MCS03 and MCS04 lines. The gas hydrate saturation model is used to understand the geophysical characteristics and indirectly

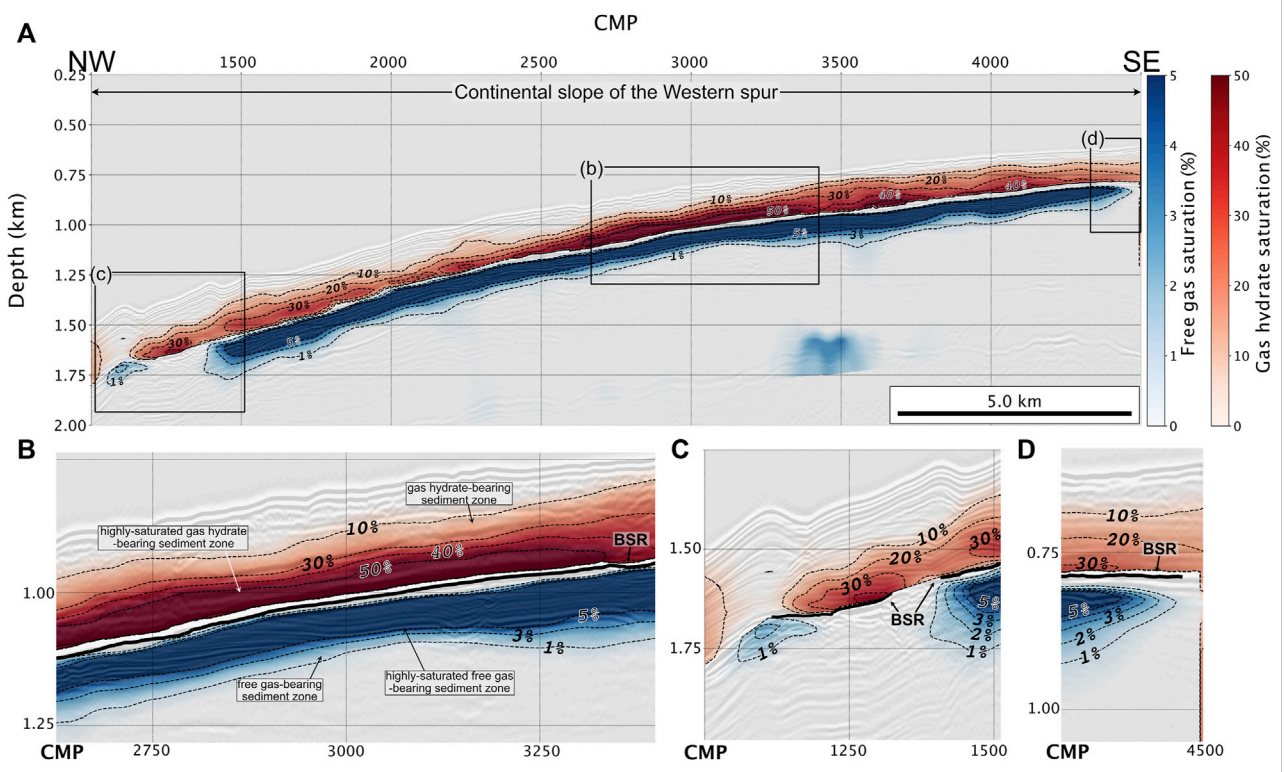

FIGURE 12
(A) Estimated gas hydrate, and free gas saturation model overlaid with migrated seismic images using the IMVA of the MCS04 line. The analysis range is marked on the solid red line in Figure 1C. **(B)**–**(D)** Enlarged velocity model: **(B)** continental slope of the western spur, **(C)** deepest area showing the BSR of the western spur, and **(D)** shallower area showing the BSR of the western spur.

estimate the total amount of subsurface gas hydrates in the study area. The gas hydrate saturation model is presented with the saturation contours in Figures 11, 12.

Figure 11A represents the gas hydrate and free gas saturation models of the MCS03 line. The saturation model shows that 10–50% of the gas hydrate is saturated above the BSR, and 1–5% of the free gas is saturated below the BSR throughout the western continental margin of the Chukchi Rise. In the mid-lower slope of the Chukchi Rise, an average of 7.8% ± 0.7% and a maximum of 25.6% ± 2.3% of gas hydrates and an average of 2.7% ± 0.5% of free gas are saturated (Figure 11C). The thickness of the gas hydrate layer is approximately 0.085 km, and the free gas layer is approximately 0.176 km thick. In the western spur, an average of 16.9% ± 1.5%, a maximum of 56.7% ± 5.1% of gas hydrates, and an average of 6.2% ± 1.2% of free gas are saturated (Figure 11D). The thicknesses of gas hydrates and free gas are 0.181 km and 0.091 km, respectively. The mid-lower slope of the Chukchi Rise has a lower gas hydrate saturation than the western spur, but it has a thicker free gas zone.

Figure 12A illustrates the gas hydrate and free saturation models derived from the MCS04 line. This model shows a similar trend to the western spur area of the MCS03 line. Above the BSR, the gas hydrate layer is 0.155 km thick, and 10%–50% (an average of 23.1% ± 2.1%) of the gas hydrate saturation is estimated. Between CMP#2650 and CMP#3400, the gas hydrate is highly saturated at 67.5% ± 6.1% (Figure 12B). However, a low gas hydrate saturation of 10%–20% is estimated in the deeper part (CMP#4300-CMP#4500) and shallower part (CMP#1000-CMP#1250) (Figures 12C,D). The free gas saturation is determined to be 7.1% ± 1.4% on average (Figure 12A).

The distribution and structures of the gas hydrate in the western continental margin of the Chukchi Rise are well represented in the saturation model obtained from the P-wave velocity model using the EMT model. In our saturation model, the mid-lower slope contains low-saturated gas hydrate and free gas, whereas the western spur contains high-saturated gas hydrate and free gas. It is inferred that the western spur and mid-lower slope have two different environments for the formation of gas hydrates.

6 Discussion

The BSR provides evidence of the presence of gas hydrates and related free gas in the seismic images. Figure 13A is the distribution map of the BSR that was confirmed by the seismic

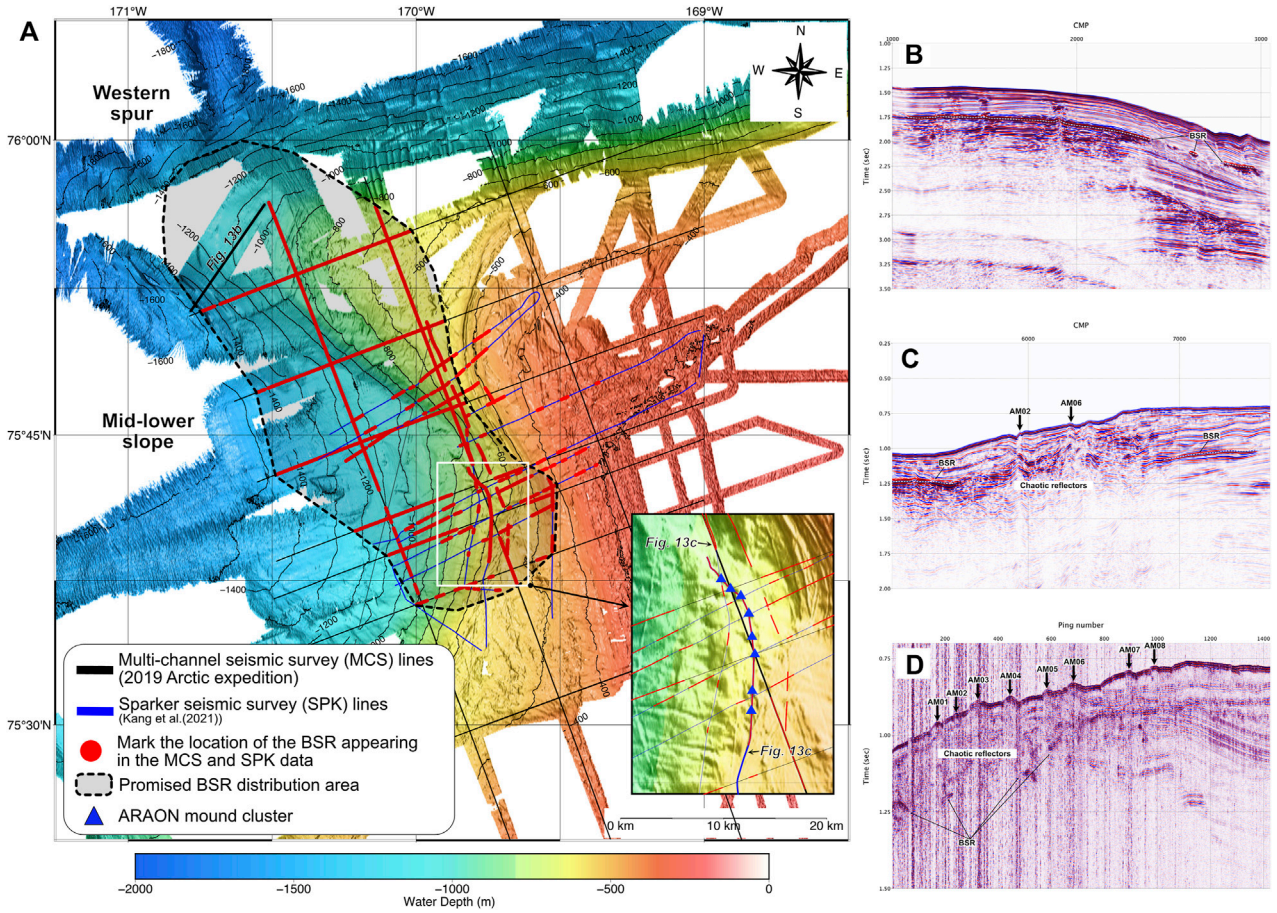

FIGURE 13
(A) Distribution map of the BSR in the western continental margin of the Chukchi Rise. **(B)**–**(D)** are the MCS and sparker seismic images: **(B)** migrated seismic images of the MCS03T transit line, **(C)** migrated seismic images of the MCS02 line, and **(D)** seismic images of the ES_SP004 line modified from Kang et al. (2021a).

images from the multichannel seismic and sparker seismic tracks acquired in 2018 and 2019 in the western spur of the Chukchi Rise (Jin and Party, 2018; Kang et al., 2021a). According to the distribution map, the BSR was widely distributed around the ARAON mound cluster, as marked by blue triangular symbols in Figure 13A. The shallowest BSR is located in the area where the water depth of 0.5–0.6 km corresponds to the shelf break. Most of the BSR is observed at a water depth of 0.8–1.4 km, which is marked with a black dashed line. The black dashed line in Figure 13A depicts the distribution area of the BSR on the northern slope of the western spur. Due to a lack of seismic data, the distribution of the BSR cannot be clearly confirmed in these areas. The deepest limit of the BSR appeared in the mid-lower slope of the Chukchi Rise at a water depth of 1.3–1.5 km, extending to the southern slope and the western spur ridge. Therefore, it is presumed that the BSR is distributed in up to 1.4 km of water depth, even on the northern slope of the western spur. Additionally, the migrated seismic images of the MCS03T transit line between MCS03 and MCS04 were taken from parts of the northern slope of the western spur (Figures 13A,B), confirming the BSR to some extent.

The BSR is not clearly confirmed in the ARAON mound cluster area because chaotic reflections appeared beneath the mound morphologies in the seismic images, as shown in Figures 13C,D. Figure 13C shows part of the migrated seismic images obtained from the MCS02 line, and Figure 13D illustrates the sparker seismic images of the ES_SP004 line. In these seismic images, acoustic blanking and irregular strong amplitude reflectors appear beneath the mound morphologies, and the BSR is observed on both sides of the ARAON mound area (Figures 13C,D). According to the analysis of the heat flow measurement from the ARAON mound, the fluid is supplied to the mound structure (Kim et al., 2020b). Considering the result of Kim et al. (2020b), it is probable that the upward-moving fluid disturbed the strata of the sedimentary layer and disrupted the continuity of the BSR.

In our results, the low-velocity range of 0.8–1.5 km/s was estimated on the slope side of the western spur. The previous studies suggest that the low-velocity of the free gas-bearing sediment is related to an overpressure environment (Tinivella, 2002; Dash et al., 2004; Chhun et al., 2018). Tinivella (2002) and Dash et al. (2004) demonstrated that the seismic velocity of free gas-bearing sediments was decreased under overpressure conditions. Chhun et al. (2018) evaluated an abnormally high gas saturation of 20% in the Kumano basin. They interpreted that the high gas saturation was caused by the overpressure condition based on the permeability-porosity relationship through the laboratory test from the core samples. Because the study area does not have borehole samples, we cannot prove that the subsurface environment is in an overpressure condition. However, considering the overpressure condition makes it possible to describe the abnormally low velocity and high free gas saturation on the western spur.

Several analyses of the gas hydrate samples obtained from the ARAON mounds indicated that a gas hydrate of an s1 structure composed of more than 99% methane migrated from deep sediment to the surface layer (Kim et al., 2020a; Kim et al., 2020b; Choi et al., 2021). Therefore, it is reasonable to assume that the gas hydrate along the western spur and mid-lower slope of the western continental margin of the Chukchi Rise is also composed of pure methane originating from the deep structures. The western spur showed a higher saturation when we compared our saturation model in the western spur to the mid-lower slope. This finding implies that the western spur has favorable conditions for gas hydrate formation. Several previous studies have shown that gas hydrate and free gas are highly saturated along crests in ridge-type topography (Baba and Yamada, 2004; Singhroha et al., 2019). The reason for the high saturation was the abundance of methane supplied during gas hydrate formation because methane prefers to migrate to the crests in ridge-shaped topography (Singhroha et al., 2019). Additionally, the several faults shown in the migrated seismic images obtained from the western spur are connected to the BSR by deep structures. These faults may have acted as the main pathway for the upward migration process of methane (Kim et al., 2020a).

7 Summary and conclusion

The spatial distribution and geophysical characteristics of the gas hydrate in the western continental margin of the Chukchi Rise were proposed by the P-wave velocity and gas hydrate saturation models from the seismic data. An accurate seismic velocity model was derived using IMVA to confirm the spatial distribution of gas hydrates. The EMT model was used to estimate the gas hydrate saturation. In the saturation model, highly saturated gas hydrates are distributed along the ridge of the western spur region. In the western spur, the maximum gas hydrate saturation is 56.7% ± 5.1%, with an average of 16.9% ± 1.5% of gas hydrates being distributed in the area. The free gas below the BSR has an average of 6.2% ± 1.2% saturation in the western spur. Approximately 7.8% ± 0.7% of gas hydrates and 2.7% ± 0.5% of free gas exists in the mid-lower slope. The gas hydrates and free gas are highly saturated on the western spur ridge because the gas migrated to the top of the ridge-shaped topography. Our result will provide the basic information to estimate the methane flux from sediments to the ocean, verify the gas hydrate formation environments, and analyze the behavior of Arctic gas hydrate related to climate change.

Data availability statement

The datasets presented in this study can be found in online repositories. The names of the repository/repositories and accession number(s) can be found below: https://kpdc.kopri.re.kr/search/c854a4e8-5012-471c-9976-9fa77e31ce6c.

Author contributions

YC processed, analyed and interpretated the data, and writing the manuscript. S-GK designed and coordinate the study, and led the writting of the manuscript. YJ desinged and directed the survey as the chief scientist, and reviewed the manuscript. JH and S-RS reviewd the manuscript. SK reviewed the manuscript, specifically geological setting. YC participated the survey and reviewd the manusciprt. All authors contributed to the writing of the manuscript.

Funding

This work is supported by the research project entitled “Survey of Geology and Seabed Environmental Change in the Arctic Seas,” which was funded by the Korean Ministry of Ocean and Fisheries (KIMST Grant 20210632).

Conflict of interest

The authors declare that the research was conducted in the absence of any commercial or financial relationships that could be construed as a potential conflict of interest.

Publisher’s note

References

Andreassen, K., Mienert, J., Bryn, P., and Singh, S. C. (2006). A double gas-hydrate related bottom simulating reflector at the Norwegian continental margin. *Ann. N. Y. Acad. Sci.* 912, 126–135. doi:10.1111/j.1749-6632.2000.tb06766.x

Baba, K., and Yamada, Y. (2004). BSRs and associated reflections as an indicator of gas hydrate and free gas accumulation: An example of accretionary prism and forearc basin system along the nankai trough, off central Japan. *Resour. Geol.* 54, 11–24. doi:10.1111/j.1751-3928.2004.tb00183.x

Carcione, J. M., and Gei, D. (2004). Gas-hydrate concentration estimated from P- and S-wave velocities at the Mallik 2L-38 research well, Mackenzie Delta, Canada. *J. Appl. Geophys.* 56, 73–78. doi:10.1016/j.jappgeo.2004.04.001

Chadburn, S. E., Burke, E. J., Cox, P. M., Friedlingstein, P., Hugelius, G., and Westermann, S. (2017). An observation-based constraint on permafrost loss as a function of global warming. *Nat. Clim. Chang.* 7, 340–344. doi:10.1038/nclimate3262

Chand, S., Minshull, T. A., Gei, D., and Carcione, J. M. (2004). Elastic velocity models for gas-hydrate-bearing sediments—a comparison. *Geophys. J. Int.* 159, 573–590. doi:10.1111/j.1365-246x.2004.02387.x

Chhun, C., Kioka, A., Jia, J., and Tsuji, T. (2018). Characterization of hydrate and gas reservoirs in plate convergent margin by applying rock physics to high-resolution seismic velocity model. *Mar. Petroleum Geol.* 14, 719–732. doi:10.1016/j.marpetgeo.2017.12.002

Choi, W., Lee, J., Kim, Y. G., Kim, H., Rhee, T. S., Jin, Y. K., et al. (2021). The impact of the abnormal salinity enrichment in pore water on the thermodynamic stability of marine natural gas hydrates in the Arctic region. *Sci. Total Environ.* 799, 149357. doi:10.1016/j.scitotenv.2021.149357

Collett, T. S., Lee, M. W., Agena, W. F., Miller, J. J., Lewis, K. A., Zyrianova, M. V., et al. (2011). Permafrost-associated natural gas hydrate occurrences on the Alaska North Slope. *Mar. Petroleum Geol.* 28, 279–294. doi:10.1016/j.marpetgeo.2009.12.001

Dallimore, S. R., Uchida, T., and Collett, T. S. (2002). *Scientific results from JAPEX/JNOC/GSC mallik 2L-38 gas hydrate research well, mackenzie delta, northwest territories, Canada*. Ottawa, ON (Canada): Geological Survey of Canada, Natural Resources Canada.

Dash, R. K., Sain, K., and Thakur, N. K. (2004). Overpressure detection from seismic amplitude versus offset response: An application to gas-hydrates. *Curr. Sci.* 86, 985–990.

Dickens, G. R., and Quinby-Hunt, M. S. (1994). Methane hydrate stability in seawater. *Geophys. Res. Lett.* 21, 2115–2118. doi:10.1029/94gl01858

Dvorkin, J., Prasad, M., Sakai, A., and Lavoie, D. (1999). Elasticity of marine sediments: Rock physics modeling. *Geophys. Res. Lett.* 26, 1781–1784. doi:10.1029/1999gl900332

Ecker, C., Dvorkin, J., and Nur, A. M. (2000). Estimating the amount of gas hydrate and free gas from marine seismic data. *Geophysics* 65, 565–573. doi:10.1190/1.1444752

Ghosh, R., Sain, K., and Ojha, M. (2010). Estimating the amount of gas-hydrate using effective medium theory: a case study in the blake ridge. *Mar. Geophys. Res. (Dordr).* 31, 29–37. doi:10.1007/s11001-010-9084-y

Hajnal, Z., and Sereda, I. T. (1981). Maximum uncertainty of interval velocity estimates. *Geophysics* 46, 1543–1547.

Hegewald, A., and Jokat, W. (2013). Tectonic and sedimentary structures in the northern Chukchi region, Arctic Ocean. *J. Geophys. Res. Solid Earth* 118, 3285–3296. doi:10.1002/jgrb.50282

Hustoft, S., Bünz, S., Mienert, J., and Chand, S. (2009). Gas hydrate reservoir and active methane-venting province in sediments on <20 Ma young oceanic crust in the Fram Strait, offshore NW-Svalbard. *Earth Planet. Sci. Lett.* 284, 12–24. doi:10.1016/j.epsl.2009.03.038

Jakobsen, M., Hudson, J. A., Minshull, T. A., and Singh, S. C. (2000). Elastic properties of hydrate-bearing sediments using effective medium theory. *J. Geophys. Res. Solid Earth* 105, 561–577. doi:10.1029/1999jb900190

Jin, Y. K., and Party, O. S. S. (2017). *ARA07C cruise report : 2016 Korea-Russia-Germany East Siberian Sea research program*. Incheon: Korea Polar Research Institute.

Jin, Y. K., and Party, O. S. S. (2018). *ARA09C cruise report : 2018 Korea-Russia-Japan East Siberian Sea/Chukchi Sea research program*. Incheon: Korea Polar Research Institute.

Jin, Y. K., and Party, O. S. S. (2019). *ARA10C cruise report : 2019 Korea-Russia East Siberian/Chukchi Sea research program*. Incheon: Korea Polar Research Institute.

Kang, S.-G., Jang, U., Kim, S., Choi, Y., Kim, Y.-G., Hong, J. K., et al. (2021a). Exploration of the gas hydrates on the southwestern continental slope of the Chukchi Plateau in the Arctic Ocean. *ksmer.* 58, 418–432. doi:10.32390/ksmer.2021.58.5.418

Kang, S.-G., Jin, Y. K., Jang, U., Duchesne, M. J., Shin, C., Kim, S., et al. (2021b). Imaging the P-wave velocity structure of arctic subsea permafrost using laplace-domain full-waveform inversion. *J. Geophys. Res.* 124. doi:10.1029/2020jf005941

Kashubin, S. N., Petrov, O. V., Artemieva, I. M., Morozov, A. F., Vyatkina, D. V., Golysheva, Y. S., et al. (2018). Crustal structure of the mendeleev rise and the Chukchi Plateau (Arctic Ocean) along the Russian wide-angle and multichannel seismic reflection experiment "arctic-2012". *J. Geodyn.* 119, 107–122. doi:10.1016/j.jog.2018.03.006

Kim, J. H., Hachikubo, A., Kida, M., Minami, H., Lee, D.-H., Jin, Y. K., et al. (2020a). Upwarding gas source and postgenetic processes in the shallow sediments from the ARAON Mounds, Chukchi Sea. *J. Nat. Gas Sci. Eng.* 76, 103223. doi:10.1016/j.jngse.2020.103223

Kim, Y.-G., Kim, S., Lee, D.-H., Lee, Y. M., Kim, H. J., Kang, S.-G., et al. (2020b). Occurrence of active gas hydrate mounds in the southwestern slope of the Chukchi Plateau, Arctic Ocean. *Episodes* 43, 811–823. doi:10.18814/epiiugs/2020/020053

Kim, S., Polyak, L., Joe, Y. J., Niessen, F., Kim, H. J., Choi, Y., et al. (2021). Seismostratigraphic and geomorphic evidence for the glacial history of the northwestern Chukchi margin, Arctic Ocean. *J. Geophys. Res. Earth Surf.* 126, 29. doi:10.1029/2020jf006030

Kolesnik, O. N., Kolesnik, A. N., Vologina, E. G., and Maryash, A. A. (2019). Mineralogical characteristics of the sand fraction in quaternary sediments from the southern margin of the Chukchi Plateau, Arctic Ocean. *Oceanology* 59, 556–576. doi:10.1134/s000143701904009x

Kvenvolden, K. A., Ginsburg, G. D., and Soloviev, V. A. (1993). Worldwide distribution of subaquatic gas hydrates. *Geo-Marine Lett.* 13, 32–40. doi:10.1007/bf01204390

Kvenvolden, K. A. (1988). Methane hydrate — a major reservoir of carbon in the shallow geosphere? *Chem. Geol.* 71, 41–51. doi:10.1016/0009-2541(88)90104-0

Kvenvolden, K. A. (1994). Natural gas hydrate occurrence and issues. *Ann. N. Y. Acad. Sci.* 715, 232–246. doi:10.1111/j.1749-6632.1994.tb38838.x

Lee, M. W., Hutchinson, D. R., Collett, T. S., and Dillon, W. P. (1996). Seismic velocities for hydrate-bearing sediments using weighted equation. *J. Geophys. Res.* 101, 20347–20358. doi:10.1029/96jb01886

Lee, M. W. (2002). Biot–Gassmann theory for velocities of gas hydrate-bearing sediments. *Geophysics* 67, 1711–1719. doi:10.1190/1.1527072

Lin, C.-C., Lin, A. T.-S., Liu, C.-S., Chen, G.-Y., Liao, W.-Z., and Schnurle, P. (2009). Geological controls on BSR occurrences in the incipient arc-continent collision zone off southwest Taiwan. *Mar. Petroleum Geol.* 14, 1118–1131. doi:10.1016/j.marpetgeo.2008.11.002

Lu, Y., Luan, X., Lyu, F., Wang, B., Yang, Z., Yang, T., et al. (2017). Seismic evidence and formation mechanism of gas hydrates in the Zhongjiannan Basin, Western margin of the South China Sea. *Mar. Petroleum Geol.* 84, 274–288. doi:10.1016/j.marpetgeo.2017.04.005

Majorowicz, J., Safanda, J., and Osadetz, K. (2012). Inferred gas hydrate and permafrost stability history models linked to climate change in the Beaufort-Mackenzie Basin, Arctic Canada. *Clim. Past.* 8, 667–682. doi:10.5194/cp-8-667-2012

Miles, P. R. (1995). Potential distribution of methane hydrate beneath the European continental margins. *Geophys. Res. Lett.* 22, 3179–3182. doi:10.1029/95gl03013

Monteleone, V., Marín-Moreno, H., Bayrakci, G., Best, A., Shaon, F., Hossain, M. M., et al. (2022). Seismic characterization and modelling of the gas hydrate system in the northern Bay of Bengal, offshore Bangladesh. *Mar. Petroleum Geol.* 141, 105690. doi:10.1016/j.marpetgeo.2022.105690

Nur, A., Mavko, G., Dvorkin, J., and Galmudi, D. (1998). Critical porosity: A key to relating physical properties to porosity in rocks. *Lead. Edge* 17, 357–362. doi:10.1190/1.1437977

Osadetz, K. G., and Chen, Z. (2010). A re-evaluation of Beaufort Sea-mackenzie delta basin gas hydrate resource potential: Petroleum system approaches to non-conventional gas resource appraisal and geologically-sourced methane flux. *Bull. Can. PETROLEUM Geol.* 58, 56–71. doi:10.2113/gscpgbull.58.1.56

Pan, H., Li, H., Grana, D., Zhang, Y., Liu, T., and Geng, C. (2019). Quantitative characterization of gas hydrate bearing sediment using elastic-electrical rock physics models. *Mar. Petroleum Geol.* 105, 273–283. doi:10.1016/j.marpetgeo.2019.04.034

Riedel, M., Willoughby, E. C., and Chopra, S. (2010). *Geophysical characterization of gas hydrates*. Tulsa: Society of Exploration Geophysicists.

Riedel, M., Brent, T. A., Taylor, G., Taylor, A. E., Hong, J. K., Jin, Y. K., et al. (2017). Evidence for gas hydrate occurrences in the Canadian Arctic Beaufort Sea

within permafrost-associated shelf and deep-water marine environments. *Mar. Petroleum Geol.* 81, 66–78. doi:10.1016/j.marpetgeo.2016.12.027

Ruppel, C. D., and Kessler, J. D. (2017). The interaction of climate change and methane hydrates. *Rev. Geophys.* 55, 126–168. doi:10.1002/2016rg000534

Ruppel, C. (2014). Permafrost-Associated gas hydrate: Is it really approximately 1 % of the global system? *J. Chem. Eng. Data* 60, 429–436. doi:10.1021/je500770m

Shakhova, N., Semiletov, I., Salyuk, A., Yusupov, V., Kosmach, D., and Gustafsson, O. (2010). Extensive methane venting to the atmosphere from sediments of the East siberian arctic shelf. *Science* 327, 1246–1250. doi:10.1126/science.1182221

Shakhova, N., Semiletov, I., Sergienko, V., Lobkovsky, L., Yusupov, V., Salyuk, A., et al. (2015). the East siberian arctic shelf: Towards further assessment of permafrost-related methane fluxes and role of sea ice. *Phil. Trans. R. Soc. A* 373, 20140451. doi:10.1098/rsta.2014.0451

Shakhova, N., Semiletov, I., Gustafsson, O., Sergienko, V., Lobkovsky, L., Dudarev, O., et al. (2017). Current rates and mechanisms of subsea permafrost degradation in the East Siberian Arctic Shelf. *Nat. Commun.* 8, 15872. doi:10.1038/ncomms15872

Shakhova, N., Semiletov, I., and Chuvilin, E. (2019). Understanding the permafrost–hydrate system and associated methane releases in the East siberian arctic shelf. *Geosciences* 9, 251. doi:10.3390/geosciences9060251

Shedd, W., Boswell, R., Frye, M., Godfriaux, P., and Kramer, K. (2012). Occurrence and nature of "bottom simulating reflectors" in the northern Gulf of Mexico. *Mar. Petroleum Geol.* 34, 31–40. doi:10.1016/j.marpetgeo.2011.08.005

Shipley, T. H., and Houston, M. H. (1979). Seismic evidence for widespread possible gas hydrate horizons on continental slopes and rises. *Am. Assoc. Pet. Geol. Bull.* 63. doi:10.1306/2f91890a-16ce-11d7-8645000102c1865d

Singhroha, S., Chand, S., and Bünz, S. (2019). Constraints on gas hydrate distribution and morphology in Vestnesa Ridge, western svalbard margin, using multicomponent ocean-bottom seismic data. *J. Geophys. Res. Solid Earth* 124, 4343–4364. doi:10.1029/2018jb016574

Sloan, E. D., and Koh, C. A. (2008). *Clathrate hydrates of natural gases*. Boca Raton, FL: CRC Press.

Tinivella, U. (2002). The seismic responce to overpressure versus gas hydrate and free gas concentration. *J. Seismic Explor.* 11, 283–305.

Tóth, Z., Spiess, V., Mogollón, J. M., and Jensen, J. B. (2014). Estimating the free gas content in Baltic Sea sediments using compressional wave velocity from marine seismic data. *J. Geophys. Res. Solid Earth* 119, 8577–8593. doi:10.1002/2014jb010989

White, R. S. (1979). Gas hydrate layers trapping free gas in the Gulf of Oman. *Earth Planet. Sci. Lett.* 42, 114–120. doi:10.1016/0012-821x(79)90196-1

Yilmaz, Ö. (2001). *Seismic data analysis*. Tulsa: Society of Exploration Geophysicists.

Yoo, D. G., Kang, N. K., Yi, B. Y., Kim, G. Y., Ryu, B. J., Lee, K., et al. (2013). Occurrence and seismic characteristics of gas hydrate in the ulleung basin, East sea. *Mar. Pet. Geol.* 47, 236–247. doi:10.1016/j.marpetgeo.2013.07.001

frontiers | Frontiers in Earth Science

TYPE Original Research
PUBLISHED 05 January 2023
DOI 10.3389/feart.2022.1041596

OPEN ACCESS

EDITED BY
Biswajeet Pradhan,
University of Technology Sydney, Australia

REVIEWED BY
Wansheng Pei,
Northwest Institute of Eco-Environment and Resources (CAS), China
Youjun Ning,
Southwest Petroleum University, China

*CORRESPONDENCE
Zhe Wang,
wangzhe@lsu.edu.cn

SPECIALTY SECTION
This article was submitted to Solid Earth Geophysics, a section of the journal Frontiers in Earth Science

RECEIVED 11 September 2022
ACCEPTED 27 September 2022
PUBLISHED 05 January 2023

CITATION
Chen G, Wu D, Wang Z, Liu S, Zhou P and Hu J (2023), Shear behaviors of recycled aggregate sand in constant volume simple shear tests interrelated with particle shape.
Front. Earth Sci. 10:1041596.
doi: 10.3389/feart.2022.1041596

Shear behaviors of recycled aggregate sand in constant volume simple shear tests interrelated with particle shape

Guanyu Chen[1], Dazhi Wu[1], Zhe Wang[2,3]*, Shu Liu[4], Pan Zhou[2] and Juntao Hu[1]

[1]School of Civil Engineering and Architecture, Zhejiang Sci-Tech University, Hangzhou, China, [2]Department of Civil Engineering, Faculty of Engineering, Lishui University, Lishui, China, [3]College of Information Engineering, Zhejiang University of Technology, Hangzhou, China, [4]Ningbo Nottingham New Materials Institute, The University of Nottingham Ningbo, Ningbo, China

Compared with quartz sand, recycled aggregate sand is characterized by the high liquefaction and shear resistance because of its irregular particle shape. However, the interrelationship between its particle shape and shear behaviors is seldom investigated. This paper investigates the role of the particle shape on the shear behaviors of recycled aggregate sand by conducting a series of monotonic and cyclic simple shear tests under undrained constant volume conditions. The particles' morphology parameters are assessed in terms of sphericity, roundness and regularity with microscopic observation and image processing. According to the experimental results, the recycled aggregate sand with irregular shapes mobilizes greater gradients of the flow liquefaction lines under monotonic shear conditions. The irregularity of the particle shape also leads to greater peak shear stress and dynamic shear modulus, indicating stronger shear and liquefaction resistances under the cyclic shearing. Furthermore, the interrelationships between the peak shear stress, dynamic shear modulus and particle shape of the samples are revealed and established by well fitted functions, which could serve as references for the selection of recycled aggregate sand and corresponding designs of the foundation.

KEYWORDS

recycled aggregate sand, particle shape, shear behavior, liquefaction resistance, simple shear test

1 Introduction

Owing to the surge of international infrastructure construction in the last decades, the consumption of natural sand resources has been significantly increasing. It is inevitable that environmentally friendly, resource-rich, and sustainable recycled aggregate sand (RA) will replace natural sand because of its abundant mining resources, including rocks, mine tailings and industrial waste (Yang et al., 2019; Li et al., 2021; Alqarni et al., 2022).

Recently, RA has received considerable attention as an emerging construction material used in foundation backfilling. Compared with natural quartz sand (QS), RA

has two noticeable characteristics. One characteristic is the chemical composition. The QS is mainly composed by silica, while the compositions of RA are various, including carbonate, ferric oxide and aluminium oxides. Another significant characteristic is the particle shape, which has been reported to have a significant impact on the mechanical behaviors of granular materials (Rui et al., 2021; Li et al., 2022; Wang et al., 2022). Compared with QS, the particle shapes of RA are more irregular and could vary in a wide range due to different production process and chemical composition. In past a few years, a number of researchers have studied the influence of particle shape on the responses of sand by experimental and numerical methods (Jensen et al., 2001; Mirghasemi et al., 2002; Chuhan et al., 2003; Tang-Tat, 2009; Ueda et al., 2013). Shinohara et al. (2000) pointed out that the irregular shapes show more intense interlocking between particles and have a noticeable impact on the internal friction angle. Yang and Wei (2012) carried out a series of undrained triaxial tests on both angular crushed silica and rounded glass beads and found that the increase of roundness could result in a decrease of the critical state angle. Maeda et al. (2010) emphasized that the shear strength, stiffness and compressibility are highly correlated to the particle shape. These studies manifest that there is an obvious interrelationship between the particle shape and mechanical behaviors of sand, especially under cyclic loading conditions (Rousé et al., 2008; Tsomokos and Georgiannou, 2010; Suh et al., 2017). Consequently, quantifying the shape of sand particles and selecting the material with suitable particles could effectively enhance its mechanical shear performance in foundation backfilling. However, although there are a number of studies about the particle

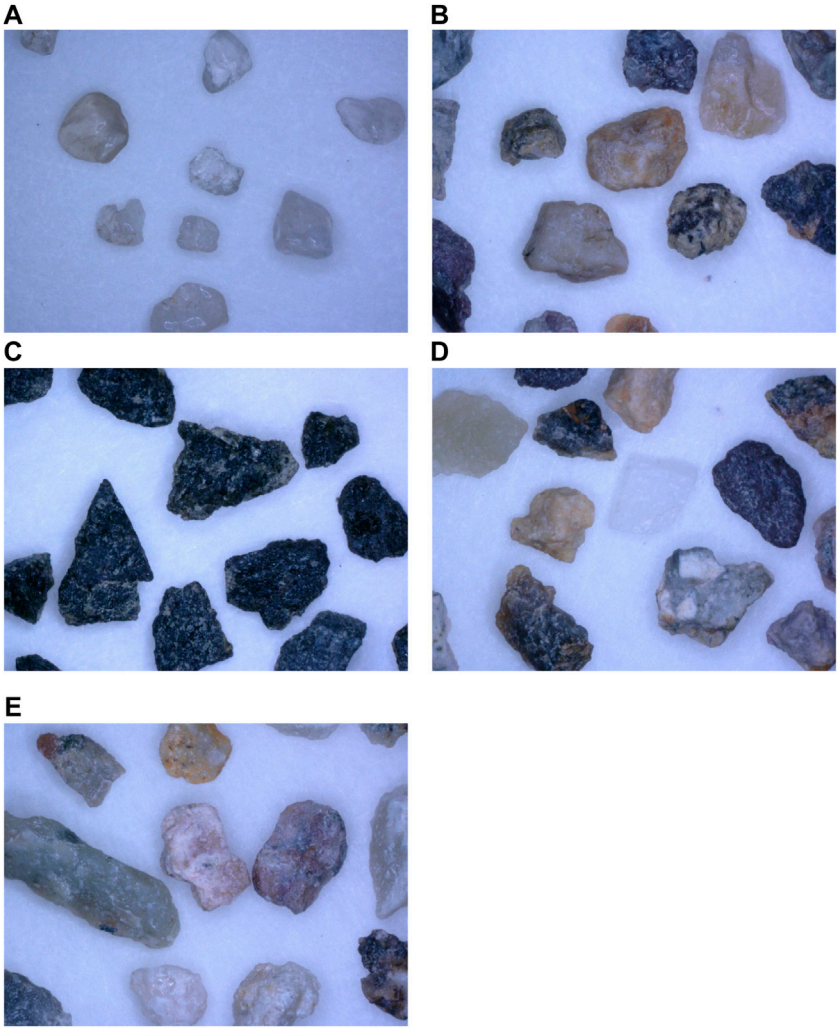

FIGURE 1
Particle images of: **(A)** QS; **(B)** RASR; **(C)** RAB; **(D)** RAS; **(E)** RAR.

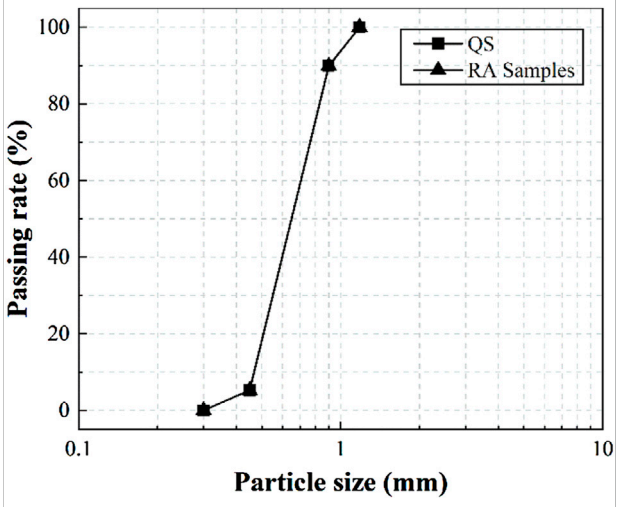

FIGURE 2
The grading of QS and RA samples.

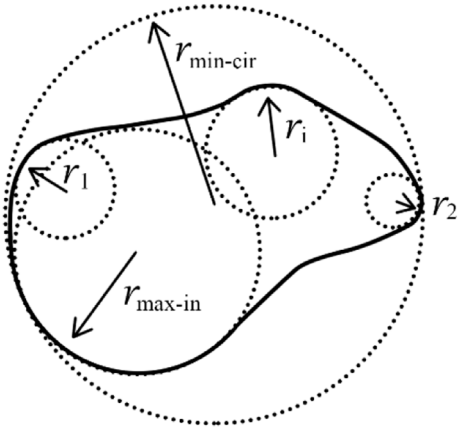

FIGURE 3
Illustration of particle shape parameters.

shape of granular materials, the particle shape of RA and its impact on the shear behaviors have rarely been quantitatively and systematically investigated.

Meanwhile, with the rising complexity of seismic and traffic loadings, the risks of foundation deformation and sand liquefaction, which could lead to various damage, such as road collapse and pipeline leakage, kept increasing, bringing immeasurable harm to the traffic and pedestrian. A few researchers have conducted a series of experiments to evaluate the mechanical characteristics of RA under cyclic loadings and found that compared with natural sand, RA has higher liquefaction resistance and better dynamic performance. According to Wang et al. (2018), under the cyclic loading, the majority of RA materials show less permanent strain than that of natural sand. Arulrajah et al. (2013) and Li et al. (2019) conducted a series of cyclic triaxial tests to evaluate the liquefaction properties of RA and concluded that its liquefaction and shear resistance is higher than that of quartz sand. Otsubo et al. (2016) suggested that using RA for backfilling could effectively improve the shear strength and liquefaction resistance of the foundation. Huang et al. (2021) analyzed the influence of the particle grading on the cyclic shear characteristics of RA and found that the shear strength of well graded RA is higher than that of poorly graded RA. However, these experiments mainly investigated the mechanical properties of RA from macro aspects. Factors in micro scale, such as the particle shape, were paid too little attention.

Therefore, this paper aims to investigate the impact of the particle shape on shear behaviors of RA under undrained shear loading conditions by a series of monotonic and cyclic simple shear tests. The particle shapes of four kinds of RA which are crushed from different rocks were quantitatively determined and compared with natural quartz sand (QS). Based on the derived shape parameters, the connections between the particle shape and variations of the slope of liquefaction line, maximum shear stress and dynamic shear modulus were investigated and described. It should be noted that except for the particle shape, the shear behaviors could be also influenced by other factors including the grading, particle size and uniformity coefficient, which are not within the scope of this study. Therefore, these parameters are kept identical for the sample as control factors. The

TABLE 1 Properties of QS and RA samples.

Materials	Parent rocks	Maximum void ratio, e_{max}	Minimum void ratio, e_{min}
QS	Quartzite	0.79	0.52
RASR	Rhyolitic crystal tuff	1.023	0.606
RAB	Basalt	0.992	0.589
RAS	Sandstone	1.016	0.585
RAR	River pebbles	1.09	0.636

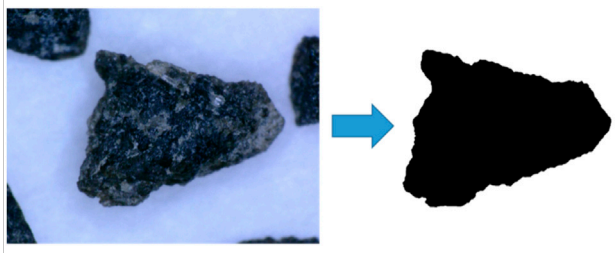

FIGURE 4
Binarized photos and image processing method for the particles.

TABLE 2 Computed shape parameters of samples.

Samples	Roundness (R)	Sphericity (S)	Regularity (ρ)
QS	0.821	0.735	0.778
RASR	0.721	0.531	0.626
RAB	0.646	0.416	0.531
RAS	0.601	0.389	0.495
RAR	0.472	0.380	0.426

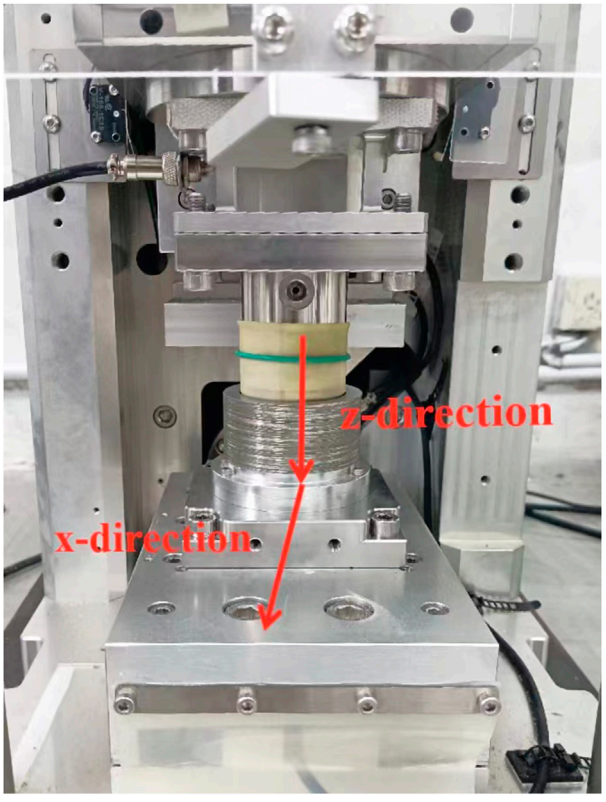

FIGURE 5
Samples prepared for monotonic and cyclic simple shear testing.

TABLE 3 Design of the monotonic and cyclic simple shear tests.

Test No.	Test type	Samples	Shear strain amplitude
1	Monotonic shear	QS	—
2		RASR	—
3		RAB	—
4		RAS	—
5		RAR	—
6–9	Cyclic shear	QS	0.1, 0.2, 0.3, 0.4
10–13		RASR	0.1, 0.2, 0.3, 0.4
14–17		RAB	0.1, 0.2, 0.3, 0.4
18–21		RAS	0.1, 0.2, 0.3, 0.4
22–25		RAR	0.1, 0.2, 0.3, 0.4

research findings could provide theoretical supports and reference values for the selection of RA in geotechnical engineering and facilitate the application of RA in the design and construction of foundations under cyclic loading conditions, for example, the earthquake loading condition.

2 Materials and methods

2.1 Experimental materials

Four types of RA with irregular particle shapes produced in Zhejiang Province, China, were used in this study. Each type of sand was crushed from different kinds of rocks, denoted as RASR, RAB, RAS, RAR corresponding to parent rocks of sandstone with rhyolitic crystal tuff, basalt, sandstone and river pebble respectively. The material used in the control group was quartz sand—Leighton Buzzard sand (fraction B), a type of natural sand from England, whose particles are relatively round and smooth, denoted as QS. The digital microscope photographs of the particles for each type of sand are presented in Figure 1. The compositions of RA and QS were evaluated by the XRD chemical analyze. It was found that the silicon dioxide content of QS is approximately 94.6%, while the others' ranges from 57.4 to 74.3%.

To evaluate the shear behavior of different samples and examine the impact of the particle shape on their dynamic behaviors, the particle gradations were kept consistent for the samples of both QS and RA, as shown in Figure 2, giving the identical mean particle diameter d_{50} of 0.62 mm and the coefficient of uniformity C_u of 1.51. The maximum and minimum void ratio were assessed and utilized to control the relative density of the samples in the tests and are presented in Table 1, following the ASTM standard D4253 (2016a) and D4254 (2016b).

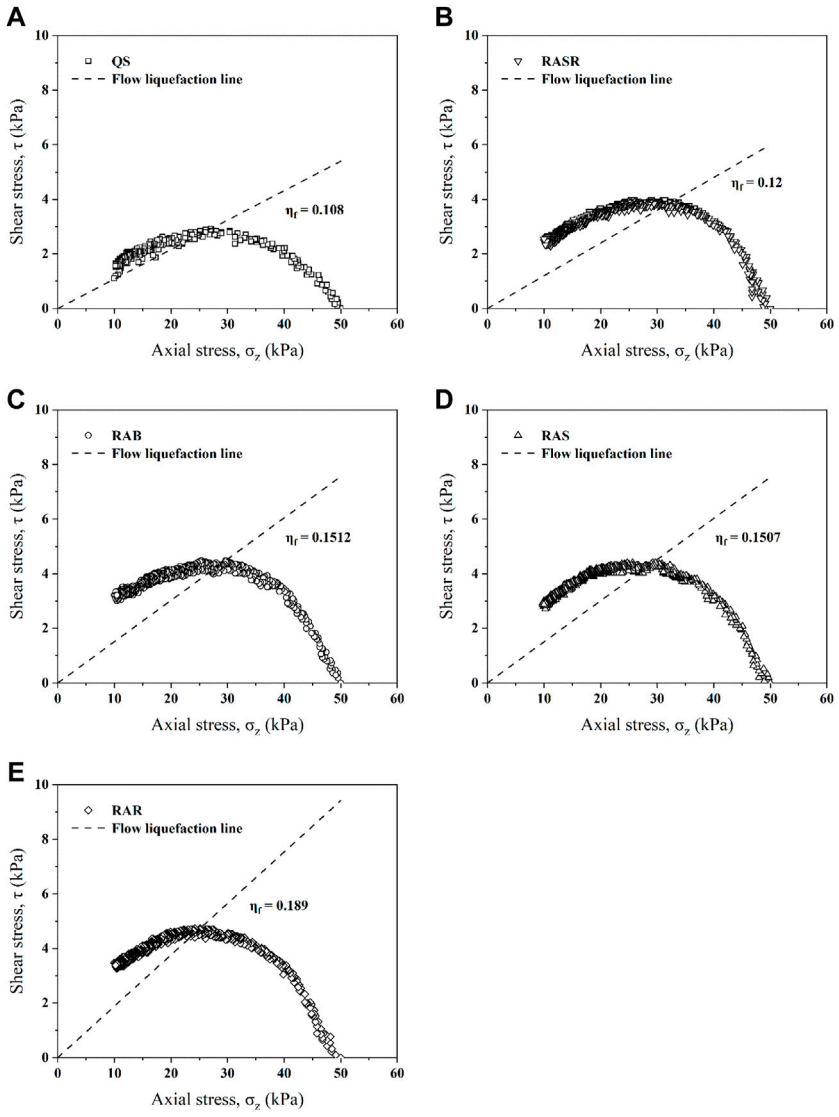

FIGURE 6
Flow liquefaction lines in the space of shear stress *t versus* axial stress σ_z in the monotonic simple shear tests for: **(A)** QS; **(B)** RASR; **(C)** RAB; **(D)** RAS; **(E)** RAR.

2.2 Particle shape evaluation

In the existing studies, a variety of parameters were proposed by researchers to quantify the particle shape (Jennings et al., 1988; Shigehisa et al., 1998; Fonseca et al., 2012; Lee et al., 2017). In this paper, the well established parameters—sphericity (S), roundness (R), and regularity (ρ) were adopted to quantitatively represent the particle shape (Wadell, 1932; Cho et al., 2007). The sphericity (S) could well describe the overall shape of the particle including the length and width while the roundness (R) could illustrate the regional shape of the principal circular surfaces. To comprehensively quantify the particle shape, the regularity (ρ) is adopted and calculated from the sphericity and roundness. The parameters can be defined as follows:

$$S = \frac{r_{max-in}}{r_{min-cir}}, \tag{1}$$

$$R = \frac{\sum_{i=1}^{n} r_i / r_{max-in}}{n_c}, \tag{2}$$

$$\rho = \frac{S + R}{2}, \tag{3}$$

where r_i and n_c are the radius and the number of corner circles, while $r_{max\text{-}in}$ is the maximum radius of the inscribe circle of the particle and $r_{min\text{-}cir}$ is the minimum radius of the circumcircle.

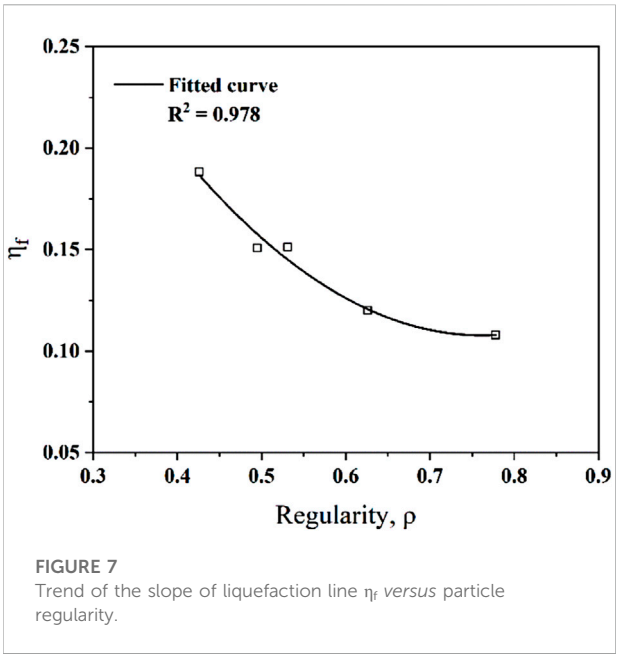

FIGURE 7
Trend of the slope of liquefaction line η_f *versus* particle regularity.

The definitions of r_i, $r_{max\text{-}in}$ and $r_{min\text{-}cir}$ are illustrated in Figure 3. More details can be found in Cho et al. (2006).

In this study, a large number of grains were picked randomly for each type of sand to quantify the shape features. The particle morphologies were obtained by the microscope. Captured pictures were firstly binarized and then the shape parameters were calculated by the MATLAB software for individual particles. The processing procedure for the pictures are shown in Figure 4. The particle regularity (ρ), which is a representative factor of sphericity and roundness, was used to quantify the overall shape for each type of samples. The computed average values o0066 for QS, RASR, RAB, RAS, RAR were 0.778, 0.626, 0.531, 0.495, 0.426 respectively (Table 2).

2.3 Experimental apparatus and methods

The simple shear tests were carried our using an electromechanical dynamic cyclic simple shear system (EMDCSS), which is capable of performing dynamic cyclic experiments with shear strain amplitudes from 0.005 to 10%, as shown in Figure 5. This device allows the stress or strain to be imposed in both the vertical direction (z-direction) and horizontal direction (x-direction). Each sample was tested in cylindrical shape with the diameter of 50 mm and the height of 30 mm. The pre-weighted and oven-dried samples were confined by an impermeable membrane and covered with low-friction stacked rings made of polytetrafluoroethylene (PTFE), which ensures a constant cross-sectional area for the sample. The rigidity of the stacked rings ensures a K0 consolidation of the sample before the shearing.

The initial relative density of samples was controlled according to the weight and void ratio and set to be 46% before the shearing. After samples were prepared in the shear box, an axial stress σ_z of 50 kPa was imposed for K_0 consolidation, lasting for 30 min.

The samples' height remained unchanged when the shearing started, so the volume of the samples could be kept unchanged. It has been proved that the shear behavior of sand samples in constant volume is equivalent to that of those in truly undrained conditions and it is demonstrated that the loss of axial stress is equivalent to the increase of pore pressure (Dyvik et al., 1987). The method is widely adopted because the saturation of samples as well as the pore pressure sensors are not required (Mao and Fahey, 2003; Porcino et al., 2008).

Two different types of simple shear tests were carried out in this study. One is the monotonic simple shear test and the other one is the cyclic simple shear test. The test conditions are presented in Table 3. Both the monotonic and cyclic shear tests are strain-controlled. For the monotonic simple shear tests, the shear rate was set to be 0.05 mm/min. For the cyclic simple shear tests, the strain-controlled symmetric sine loading curve was applied. The loadings were imposed for 20 cycles for each sample with the frequency of 0.1 Hz to fully record the stress-strain relationship during the shearing. Four cyclic shear strain amplitudes (0.1, 0.2, 0.3, and 0.4%) were exerted to the samples in this study to investigate their cyclic shear responses.

3 Results and discussion

3.1 Results of the monotonic simple shear tests

The results of the monotonic simple shear tests are shown in Figure 6. It can be seen that during the constant volume monotonic shearing, the axial stress reduces gradually, indicating the accumulation of the pore pressure. Meanwhile, the shear stress increases with the decreasing axial stress until it reaches the peak value and then reduces gradually. The peak stress ratio is determined by the ratio of the peak shear stress and the corresponding axial stress (τ_{max}/σ_z), which is identical to the slope of the flow liquefaction line and could reflect the stability of sandy soils (Hill, 1958). The flow liquefaction line is presented to demonstrate the initiation of failure as the instability is prone to be triggered beyond the line (Yang et al., 2022). Comparing the experimental results in Figures 6A–E, it is evident that the slope of flow liquefaction line of QS is obviously lower than RA, demonstrating its lower liquefaction resistance.

Combining the slope of liquefaction line and particle shape parameter of the samples, the influence of particle shape on the value of η_f is demonstrated in Figure 7. In general, the slope of the flow liquefaction lines tends to decrease with the increasing particle regularity in a nonlinear pattern, reflecting the instability and greater liquefaction potential of rounder particles under monotonic shear tests.

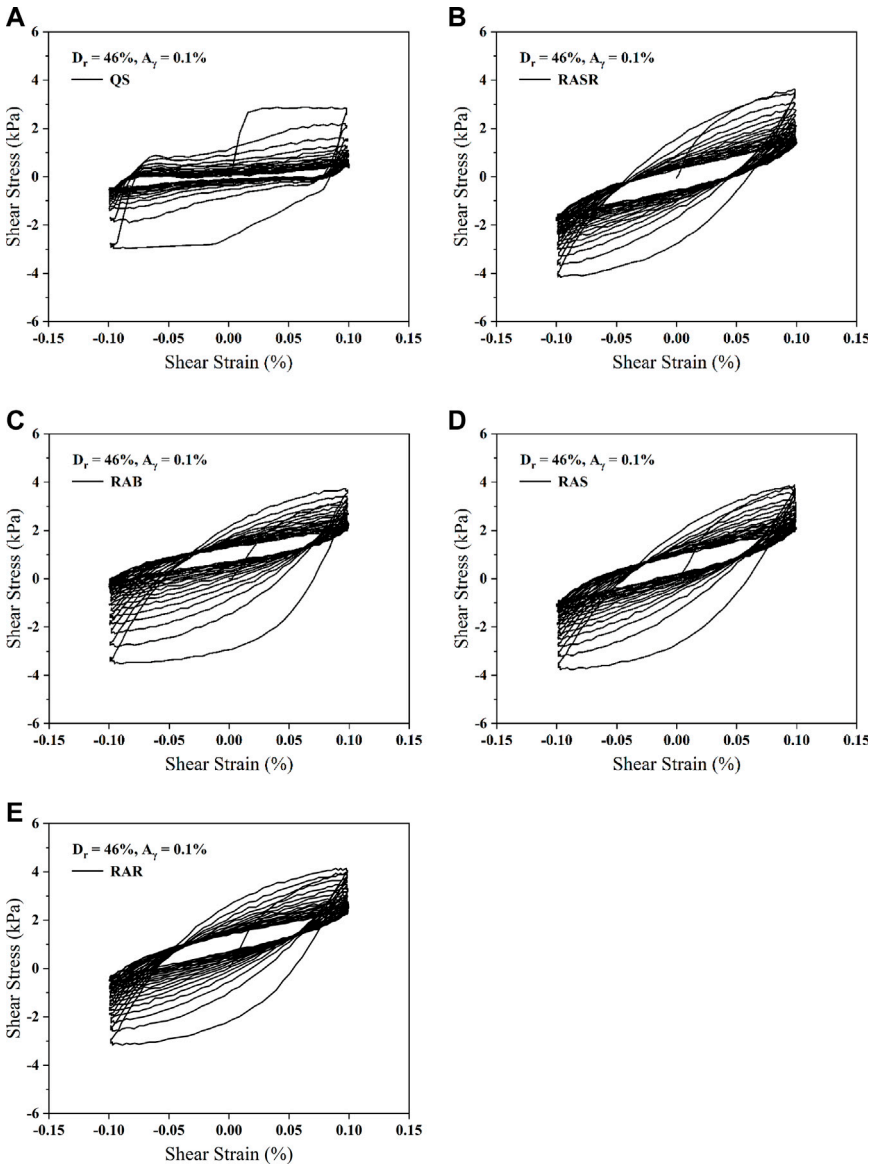

FIGURE 8
Hypothesis shear strain-stress loops of samples: **(A)** QS; **(B)** RASR; **(C)** RAB; **(D)** RAS; **(E)** RAR.

3.2 Results of the cyclic simple shear tests

The typical stress-strain hysteresis loops obtained from the cyclic simple shear tests with the shear strain amplitude of 0.1% are shown in Figure 8. The shear stress of RA samples comes to a peak value in the first few cycles then decreases gradually, while the shear stress of QS decreases much quicker due to its rounder particles. During the cyclic shearing, the maximum shear stress for QS, RASR, RAB, RAS, and RAR were 2.835, 3.639, 3.724, 3.893, and 4.147kPa, corresponding to the particle regularity of 0.778, 0.626, 0.531, 0.495, and 0.426. The peak shear stress is found to increase as the regularity of the particles decreases because the particle shape with greater irregularity strengthens the inter-particle locking of the samples (Yang and Elgamal, 2002; Ueng et al., 2017).

3.2.1 Influence of the particle shape on the maximum cyclic shear stress

From the hypothesis shear stress-strain loops, it is found that the maximum cyclic shear stress is correlated with the particle shape. Figures 9A–D show the peak value of shear stress against the particle regularity under the cyclic shearing with different shear strain amplitudes under initial normal stress of 50 kPa and relative density of 46%. A linear relationship between the peak

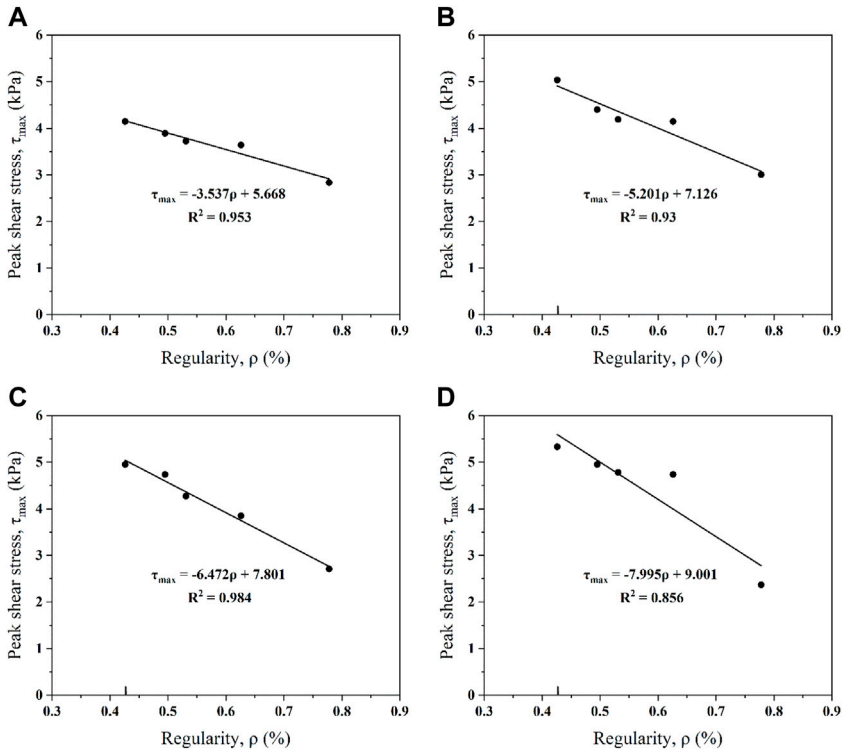

FIGURE 9
Influence of particle regularity on the maximum cyclic shear stress under different shear strain amplitudes: **(A)** A_γ = 0.1%; **(B)** A_γ = 0.2%; **(C)** A_γ = 0.3%; **(D)** A_γ = 0.4%.

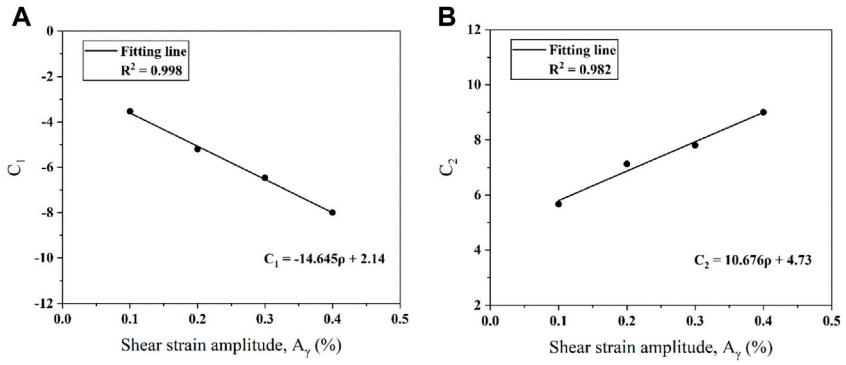

FIGURE 10
Influence of shear strain amplitude on the fitting parameters: **(A)** C_1; **(B)** C_2.

cyclic shear stress and the particle regularity could be obtained with a given shear amplitude, which could be expressed as:

$$\tau_{max} = C_1 \cdot \rho + C_2, \quad (4)$$

where C_1 and C_2 are fitting parameters for the function, depending on the initial normal stress and shear strain amplitude. In these figures, the values of C_1 and C_2 for the fitting lines both vary with the shear amplitudes. The values of C_1 are -3.537, -5.201, -6.472, and -7.995; the values of C_2 are 5.668, 7.126, 7.801, and 9.001; corresponding to the shear strain amplitude of 0.1, 0.2, 0.3, and 0.4%.

To further analyze the relationship, the correlation between shear strain amplitudes and these two parameters is presented in Figures 10A,B. The results demonstrate that as the shear strain increases, the value of C_1 presents a decreasing trend, while the value of C_2 shows an increasing trend in

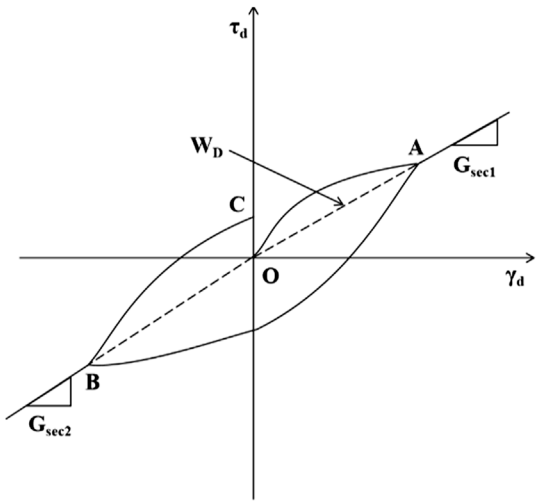

FIGURE 11
Definition of the dynamic shear modulus based on the hysteretic shear stress-strain loop.

contrast. The impact of shear strain amplitude on the values of C_1 and C_2 could be expressed as:

For value C_1

$$C_1 = -14.645A_\gamma + 2.14. \quad (5)$$

For value C_2

$$C_2 = 10.676A_\gamma + 4.73, \quad (6)$$

where A_γ is the shear strain amplitude. Combined Eqs 4–6, the maximum cyclic shear stress can be defined as:

$$\tau_{max} = F_1(A_\gamma) \cdot \rho + F_2(A_\gamma), \quad (7)$$

where the F_1 (A_γ) and F_2 (A_γ) are functions of the shear strain amplitude.

3.2.2 Influence of the particle shape on the dynamic shear modulus

The dynamic shear modulus is investigated in the study as it could reflect the dynamic characteristics of granular materials

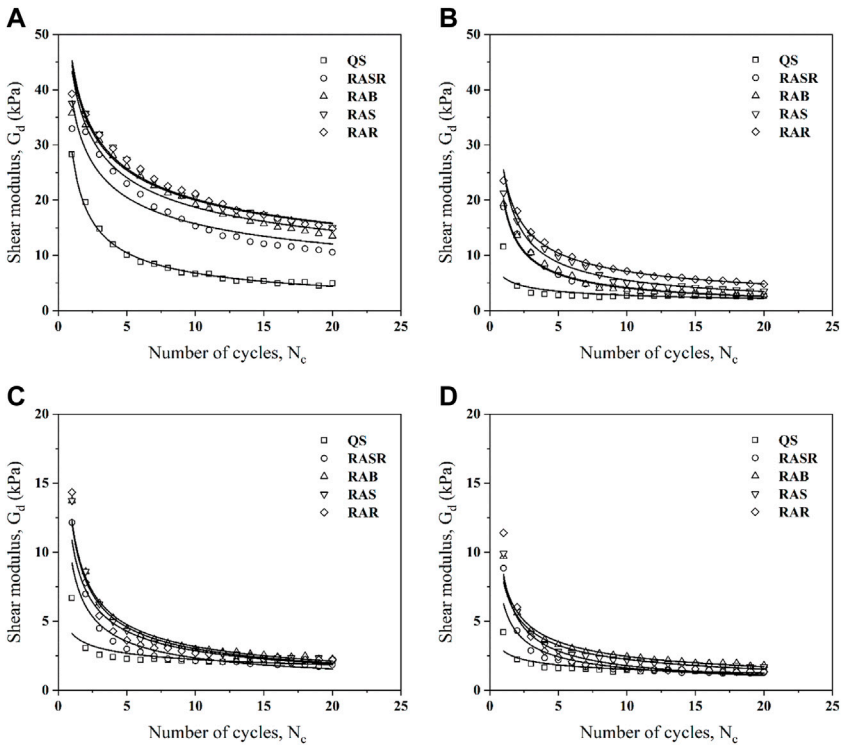

FIGURE 12
Influence of the particle regularity on the dynamic shear modulus under different shear strain amplitudes: **(A)** A_γ = 0.1%; **(B)** A_γ = 0.2%; **(C)** A_γ = 0.3%; **(D)** A_γ = 0.4%.

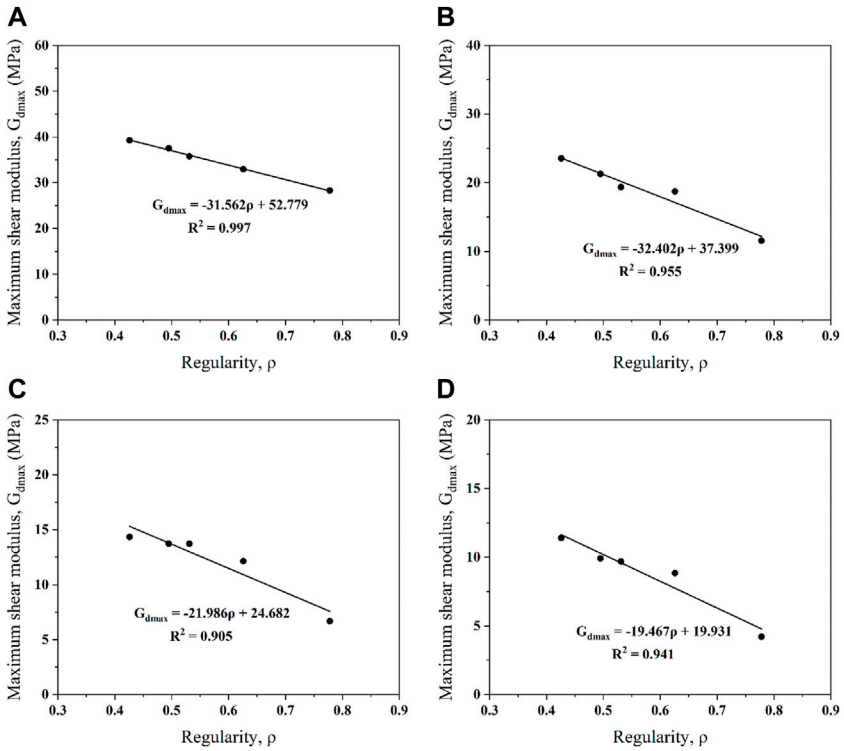

FIGURE 13
Relationship between the maximum dynamic shear modulus and particle regularity for samples under different shear strain amplitudes: **(A)** A_γ = 0.1%; **(B)** A_γ = 0.2%; **(C)** A_γ = 0.3%; **(D)** A_γ = 0.4%.

under cyclic loadings, such as the earthquake loading (Nye and Fox, 2007; Vieira et al., 2013; Wang et al., 2016). Based on the hypothesis loops, the dynamic shear modulus (G_d) is defined as (Kumar et al., 2017):

$$G_d = \frac{G_{sec\,1} + G_{sec\,2}}{2}, \tag{8}$$

where the slope between the vertex of the positive half-axis and the origin of the hysteresis curve, known as G_{sec1}, is used to calculate the dynamic shear modulus of the loading portion while G_{sec2} is used to calculate the reverse-loading part, which is determined by the slope between the vertex of the negative half-axis and the origin of the hysteresis curve. The parameter definition of dynamic shear modulus G_d in hypothesis curves is shown in Figure 11.

Figure 12 shows the variation of dynamic shear modulus against the cyclic number. Different from the shear stress, the peak value of the dynamic shear modulus is reached in the first cycle. During the constant volume cyclic shearing, the dynamic shear modulus generally decreases with the imposed cyclic number as the sample contracts. The maximum dynamic shear modulus for a given tested material reduces with the increasing shear strain amplitude. Furthermore, as the shear strain amplitude increases, the reduction rate of the dynamic shear modulus increases as well. It is obvious that the value of the dynamic shear modulus of QS is less than that of RA in the same cycle and reduces faster as well. The relationship between the dynamic shear modulus and the number of cycles could be described as:

$$G_d = A \cdot (N_c)^{-B}, \tag{9}$$

where A and B are parameters associated with sample properties. Generally, the given power function fits well with the reduction of dynamic shear modulus under the cyclic shearing except for the first cycle in the results of Figures 12B–D when the dramatic reduction of the dynamic shear modulus occurs, which can be difficult to predict. For a specific shear strain amplitude, it can be observed that the fitted curves of the RAR, RAS, RAB, RASR and QS are located from the top to the bottom, corresponding to the particle regularity of 0.426, 0.495, 0.531, 0.626 and 0.778. The results present a decreasing trend of the liquefaction resistance among the samples, which consists with the results obtained in Figure 7.

Figure 13 shows variations of the maximum dynamic shear modulus with the particle regularity under different shear strain amplitudes. For a given shear amplitude, the maximum dynamic shear modulus decreases with the increasing particle regularity

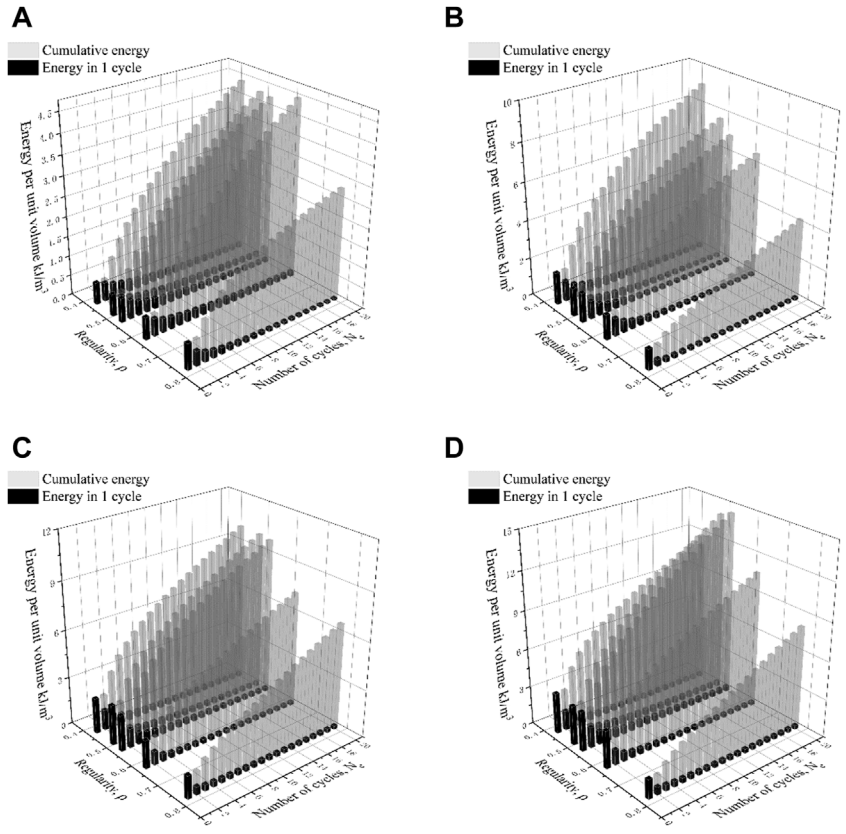

FIGURE 14
Cumulative energy consumed and energy consumed per cycle for samples under different shear strain amplitudes: **(A)** A_γ = 0.1%; **(B)** A_γ = 0.2%; **(C)** A_γ = 0.3%; **(D)** A_γ = 0.4%.

and a linear regression is found between them. As the shear amplitude increases, the maximum dynamic shear modulus generally shows a decreasing trend. It can be observed from the fitting lines that the R^2 are larger than 0.9 for all the samples, which reflects the reliability of the fitting formulas. The relationship between the maximum dynamic shear modulus and the particle regularity could be established as:

$$G_{d\,\max} = -S_m \cdot \rho + C_m, \tag{10}$$

where S_m and C_m can be determined by the shear amplitude.

3.2.3 Energy dissipation

It is reported that the movement and relocation of sand particles would consume large energy under the cyclic loading, which is also highly related to the stability of sand (Baziar and Jafarian, 2007; Sonmezer, 2019). Therefore, the energy dissipation under the cyclic shearing is investigated as well. In this paper, the energy dissipated in one cycle is calculated by the area of the corresponding hypothesis stress-strain loop as follows (Figueroa et al., 1994):

$$\delta W = \sum_1^i \frac{\tau_{i+1} + \tau_i}{2} \cdot (\gamma_{i+1} - \gamma_i), \tag{11}$$

where τ_i and γ_i are the shear stress and shear strain recorded in one cycle. To analyze the difference of cyclic shearing resistance of sand with different particle regularity, the energy dissipation per cycle and the cumulative energy are calculated and presented in Figures 14A–D. The figures illustrate that the cumulative energy grows rapidly at the beginning of the cyclic shearing and then the increasing rate drops gradually. In the last a few cycles, the energy consumed in one cycle tend to reach a constant value, resulting in the total energy to accumulate linearly and indicating the approaching of the liquefaction. Furthermore, as the shear strain amplitude increased, the energy dissipation in one cycle drops more quickly and less cycles are required for the total energy to achieve the linear increasing rate. In general, the particles with larger regularity dissipate less energy under the same loading cycles, indicating the greater instability of the corresponding material under the cyclic shearing.

4 Conclusion

In order to explore the influence of the particle shape on the shear and liquefaction behaviors of recycled aggregate sand, a series of monotonic and cyclic simple shear tests were performed on QS and four types of RA. The shape of the particles was quantitatively evaluated in terms of sphericity, roundness and regularity. Then the regularity is selected as the representative factor to reflect the particle shape of the samples. The shear behaviors under constant volume shearing for samples with different shape characteristics were analyzed and the key findings are summarized as follows:

1) The particle regularity of QS is higher than that of RA, reflecting that the particles of RA are more irregular and angular.
2) In the monotonic simple shear tests, the shear strength and the slope of the flow liquefaction line of RA are greater than that of QS and the slope of the liquefaction line tends to decrease with the increasing particle regularity, indicating the better liquefaction resistance of RA compared with QS.
3) In the cyclic simple shear tests, the shear stress of QS decreases more quickly compared with RA because of its rounder and more regular particle shape. A linear correlation between the peak shear stress and particle shape parameters of the samples was derived under undrained cyclic shearing with different shear amplitudes.
4) During the cyclic shearing, an exponential relation was established to describe the variation of the dynamic shear modulus and imposed number of cycles of different samples. The reduction of the dynamic shear modulus is accelerated with greater shear amplitudes. A linear relationship between the particle regularity and the maximum dynamic shear modulus was proposed as well.
5) The samples with irregular particles dissipate larger energy and more cycles are required for the total energy to achieve the linear increasing rate under the same cyclic loading condition, indicating their need of greater energy to trigger instability.

The shear characteristics found in this paper and the proposed relationships between the particle shape parameters and the flow liquefaction line, peak shear stress and dynamic shear modulus could be used to predict the responses of RA under both monotonic and cyclic shear loading conditions, thus serving as the reference for its selection and application in the foundation engineering.

Data availability statement

The original contributions presented in the study are included in the article/supplementary material, further inquiries can be directed to the corresponding authors.

Author contributions

All authors listed have made a substantial, direct, and intellectual contribution to the work and approved it for publication.

Funding

The research was funded by Zhejiang Provincial Natural Science Foundation of China (grant number LQ19E090003) and National Natural Science Foundation of China (grant number 51678533).

Conflict of interest

The authors declare that the research was conducted in the absence of any commercial or financial relationships that could be construed as a potential conflict of interest.

Publisher's note

All claims expressed in this article are solely those of the authors and do not necessarily represent those of their affiliated organizations, or those of the publisher, the editors and the reviewers. Any product that may be evaluated in this article, or claim that may be made by its manufacturer, is not guaranteed or endorsed by the publisher.

References

Alqarni, A. S., Abbas, H., Al shwikh, K. M., and Al salloum, Y. A. (2022). Influence of treatment methods of recycled concrete aggregate on behavior of high strength concrete. *Buildings* 12 (4), 494. doi:10.3390/buildings12040494

Arulrajah, A., Piratheepan, J., Disfani, M. M., and Bo, M. W. (2013). Geotechnical and geoenvironmental properties of recycled construction and demolition materials in pavement subbase applications. *J. Mat. Civ. Eng.* 25 (8), 1077–1088. doi:10.1061/(ASCE)MT.1943-5533.0000652

ASTM D4253 (2016a). *Standard test methods for maximum index density and unit weight of soils using vibratory table*. ASTM International, West Conshohocken, PA.

ASTM D4253 (2016b). *Standard test method for minimum index density and unit weight of soils and calculation of relative density*. ASTM International, West Conshohocken, PA.

Baziar, M. H., and Jafarian, Y. (2007). Assessment of liquefaction triggering using strain energy concept and ANN model: Capacity Energy. *Soil Dyn. Earthq. Eng.* 27 (12), 1056–1072. doi:10.1016/j.soildyn.2007.03.007

Cho, G. C., Dodds, J., and Santamarina, J. C. (2007). Closure to "Particle shape effects on packing density, stiffness, and strength: Natural and crushed sands by Gye-Chun Cho, Jake Dodds, and J. Carlos Santamarina. *J. Geotech. Geoenviron. Eng.* 133133 (11), 147411. doi:10.1061/(asce)1090-0241(2007)133:11(1474)

Cho, G. C., Dodds, J., and Santamarina, J. C. (2006). Particle shape effects on packing density, stiffness, and strength: Natural and crushed sands. *J. Geotech. Geoenviron. Eng.* 133 (5), 591–602. doi:10.1061/(asce)1090-0241(2006)132:5(591)

Chuhan, F. A., Høeg, K., Kjeldstad, A., and Bjørlykke, K. (2003). Experimental compression of loose sands: Relevance to porosity reduction during burial in sedimentary basins. *Can. Geotech. J.* 40, 995–1011. doi:10.1139/t03-050

Dyvik, R., Berre, T., Lacasse, S., and Raadim, B. (1987). Comparison of truly undrained and constant volume direct simple shear tests. *Geotechnique* 37 (1), 3–10. doi:10.1680/geot.1987.37.1.3

Figueroa, J. L., Saada, A. S., Liang, L., and Dahisaria, N. M. (1994). Evaluation of soil liquefaction by energy principles. *J. Geotech. Engrg.* 120 (9), 1554–1569. doi:10.1061/(asce)0733-9410(1994)120:9(1554)

Fonseca, J., O'Sullivan, C., Coop, M. R., and Lee, P. D. (2012). Non-invasive characterization of particle morphology of natural sands. *Soils Found.* 52 (4), 712–722. doi:10.1016/j.sandf.2012.07.011

Hill, R. (1958). A general theory of uniqueness and stability in elastic-plastic solids. *J. Mech. Phys. Solids* 6 (3), 236–249. doi:10.1016/0022-5096(58)90029-2

Huang, Y., Wang, J., Ying, M., Ni, J., and Li, M. (2021). Effect of particle-size gradation on cyclic shear properties of recycled concrete aggregate. *Constr. Build. Mater.* 301 (3), 124143. doi:10.1016/j.conbuildmat.2021.124143

Jennings, B., and Parslow, R. (1988). Particle size measurement: The equivalent spherical diameter. *Proc. Royal Soc. A Math.* 419 (1856), 137–149. doi:10.1098/rspa.1988.0100

Jensen, R. P., Plesha, M. E., Edil, T. B., Bosscher, P. J., and Kahla, N. B. (2001). DEM simulation of particle damage in granular media — structure interfaces. *Int. J. Geomech.* 1 (1), 21–39. doi:10.1061/(asce)1532-3641(2001)1:1(21)

Kumar, S. S., Krishna, A. M., and Dey, A. (2017). Evaluation of dynamic properties of sandy soil at high cyclic strains. *Soil Dyn. Earthq. Eng.* 99, 157–167. doi:10.1016/j.soildyn.2017.05.016

Lee, C., Suh, H. S., Yoon, B., and Yun, T. S. (2017). Particle shape effect on thermal conductivity and shear wave velocity in sands. *Acta Geotech.* 12 (3), 615–625. doi:10.1007/s11440-017-0524-6

Li, B., Wang, Y., Jin, Q., and Chen, H. (2019). Liquefaction characteristics of recycled concrete aggregates. *Soil Dyn. Earthq. Eng.* 120, 85–96. doi:10.1016/j.soildyn.2019.01.038

Li, C., Liu, T., Fu, H., Zhang, X., Yang, Y., and Zhao, S. (2021). Test and evaluation of the flexural properties of reinforced concrete beams with 100% recycled coarse aggregate and manufactured sand. *Buildings* 11 (9), 420. doi:10.3390/buildings11090420

Li, W., Wang, D., Chen, B., Hua, K., Su, W., Xiong, C., et al. (2022). Research on three-dimensional morphological characteristics evaluation method and processing quality of coarse aggregate. *Buildings* 12 (3), 293. doi:10.3390/buildings12030293

Maeda, K., Sakai, H., Kondo, A., Yamaguchi, T., Fukuma, M., and Nukudani, E. (2010). Stress-chain based micromechanics of sand with grain shape effect. *Granul. Matter* 12 (5), 499–505. doi:10.1007/s10035-010-0208-5

Mao, X., and Fahey, M. (2003). Behaviour of calcareous soils in undrained cyclic simple shear. *Geotechnique* 53 (8), 715–727. doi:10.1680/geot.2003.53.8.715

Mirghasemi, A. A., Rothenburg, L., and Matyas, E. L. (2002). Influence of particle shape on engineering properties of assemblies of two-dimensional polygon-shaped particles. *Geotechnique* 52 (3), 209–217. doi:10.1680/geot.2002.52.3.209

Nye, C. J., and Fox, P. J. (2007). Dynamic shear behavior of a needle-punched geosynthetic clay liner. *J. Geotech. Geoenviron. Eng.* 133 (8), 973–983. doi:10.1061/(asce)1090-0241(2007)133:8(973)

Otsubo, M., Towhata, I., Hayashida, T., Liu, B., and Goto, S. (2016). Shaking table tests on liquefaction mitigation of embedded lifelines by backfilling with recycled materials. *Soils Found.* 56 (3), 365–378. doi:10.1016/j.sandf.2016.04.004

Porcino, D., Caridi, G., and Ghionna, V. N. (2008). Undrained monotonic and cyclic simple shear behaviour of carbonate sand. *Geotechnique* 58 (8), 635–644. doi:10.1680/geot.2007.00036

Rousé, P. C., Fannin, R. J., and Shuttle, D. A. (2008). Influence of roundness on the void ratio and strength of uniform sand. *Geotechnique* 58 (3), 227–231. doi:10.1680/geot.2008.58.3.227

Rui, S., Guo, Z., Si, T., Zhou, W., and Zha, X. (2021). Particle shape influence on the deformation resistance of carbonate sands under drained condition. *Soil Dyn. Earthq. Eng.* 144, 106688. doi:10.1016/j.soildyn.2021.106688

Shigehisa, E., Yoshikazu, K., Hitoshi, O., Ikeda, C., and Iwata, H. (1998). Shape estimation of anisometric particles using size measurement techniques. *Part. Part. Syst. Charact.* 15 (3), 145–149. doi:10.1002/(SICI)1521-4117(199817)15:3<145::AID-PPSC145>3.0.CO;2-B

Shinohara, K., Oida, M., and Golman, B. (2000). Effect of particle shape on angle of internal friction by triaxial compression test. *Powder Technol.* 107 (1-2), 131–136. doi:10.1016/S0032-5910(99)00179-5

Sonmezer, Y. B. (2019). Energy-based evaluation of liquefaction potential of uniform sands. *Geomechanics Eng.* 17 (2), 145–156. doi:10.12989/gae.2019.17.2.145

Suh, H. S., Kim, K. Y., Lee, J., and Yun, T. S. (2017). Quantification of bulk form and angularity of particle with correlation of shear strength and packing density in sands. *Eng. Geol.* 220, 256–265. doi:10.1016/j.enggeo.2017.02.015

Tang-Tat, N. (2009). Particle shape effect on macro- and micro-behaviors of monodisperse ellipsoids. *Int. J. Numer. Anal. Methods Geomech.* 33 (4), 511–527. doi:10.1002/nag.732

Tsomokos, A., and Georgiannou, V. N. (2010). Effect of grain shape and angularity on the undrained response of fine sands. *Can. Geotech. J.* 47 (5), 539–551. doi:10.1139/T09-121

Ueda, T., Matsushima, T., and Yamada, Y. (2013). DEM simulation on the one-dimensional compression behavior of various shaped crushable granular materials. *Granul. Matter* 15 (5), 675–684. doi:10.1007/s10035-013-0415-y

Ueng, T. S., Wang, Z. F., Chu, M. C., and Ge, L. (2017). Laboratory tests for permeability of sand during liquefaction. *Soil Dyn. Earthq. Eng.* 100, 249–256. doi:10.1016/j.soildyn.2017.05.037

Vieira, C. S., Lopes, M. L., and Caldeira, L. M. (2013). Sand-geotextile interface characterisation through monotonic and cyclic direct shear tests. *Geosynth. Int.* 20 (1), 26–38. doi:10.1680/gein.12.00037

Wadell, H. (1932). Volume, shape, and roundness of rock particles. *J. Geol.* 40 (5), 443–451. doi:10.1086/623964

Wang, J., Fang, Z., Cai, Y., Chai, J., Wang, P., and Geng, X. (2018). Preloading using fill surcharge and prefabricated vertical drains for an airport. *Geotext. Geomembranes* 46 (5), 575–585. doi:10.1016/j.geotexmem.2018.04.013

Wang, J., Liu, F. Y., Wang, P., and Cai, Y. Q. (2016). Particle size effects on coarse soil-geogrid interface response in cyclic and post-cyclic direct shear tests. *Geotext. Geomembranes* 44 (6), 854–861. doi:10.1016/j.geotexmem.2016.06.011

Wang, T., Ma, L., Wang, M., Li, Z., Zhang, X., and Geng, H. (2022). Effects of particle shape on dynamic mechanical behaviours of coral sand under one-dimensional compression. *Eng. Geol.* 304, 106624. doi:10.1016/j.enggeo.2022.106624

Yang, J., Liang, L. B., and Chen, Y. (2022). Instability and liquefaction flow slide of granular soils: The role of initial shear stress. *Acta Geotech.* 17 (1), 65–79. doi:10.1007/s11440-021-01200-1

Yang, J., and Wei, L. M. (2012). Collapse of loose sand with the addition of fines: The role of particle shape. *Geotechnique* 62 (12), 1111–1125. doi:10.1680/geot.11.P.062

Yang, R., Yu, R., Shui, Z., Guo, C., Wu, S., Gao, X., et al. (2019). The physical and chemical impact of manufactured sand as a partial replacement material in Ultra-High Performance Concrete (UHPC). *Cem. Concr. Compos.* 99, 203–213. doi:10.1016/j.cemconcomp.2019.03.020

Yang, Z., and Elgamal, A. (2002). Influence of permeability on liquefaction-induced shear deformation. *J. Eng. Mech.* 128 (7), 720–729. doi:10.1061/(asce)0733-9399(2002)128:7(720)

Frontiers in Earth Science

Investigates the processes operating within the major spheres of our planet

Advances our understanding across the earth sciences, providing a theoretical background for better use of our planet's resources and equipping us to face major environmental challenges.

Discover the latest Research Topics

See more →

Frontiers

Avenue du Tribunal-Fédéral 34
1005 Lausanne, Switzerland
frontiersin.org

Contact us

+41 (0)21 510 17 00
frontiersin.org/about/contact